SOME THEORETICAL PROBLEMS RELATED TO FLOWS INDUCED IN LIQUID METALS BY LINEAR MOTORS

BY

IAIN C. RAE

A Thesis submitted to the University of Keele for the degree of Doctor of Philosophy.

November, 1977.

ABSTRACT

We obtain results which describe the electromagnetic (EM) field and some aspects of the fluid flow induced in a liquid metal by a linear induction motor. The need for a theoretical description of the motor and its influence arises from recent developments in the production of flat glass. The EM equations are simplified by initially assuming the liquid metal (which we refer to as 'the conductor') moves as a solid. In this way we include some magnetohydrodynamic effects in the partially coupled hydrodynamic and EM differential equations.

In chapter one we describe the float glass process, provide a physical description of a linear motor, discuss the appropriate EM and hydrodynamic equations and give a survey of the relevant literature. In chapter two we describe an experiment in which liquid mercury is induced to move under the action of a linear motor. In chapter three we derive expressions for a simplified model of a linear motor and obtain velocity profiles for a given Hartmann number. This work is extended in chapter four to include the effect of a superimposed shear flow. In chapters five and six we describe the EM boundary layer region of the conductor. Two-dimensional numerical results are obtained in chapters seven and nine for the EM field induced in the conductor. In chapter eight we examine the flow induced by a rectangular body force, of constant magnitude at a fixed depth, decaying exponentially into the conductor. Chapter eleven extends the magnetic dipole analysis of chapter ten and gives three-dimensional numerical results for the EM field induced in the conductor by a linear motor. Some aspects of the results of chapters two (the experiment) ten and eleven are discussed in chapter twelve using magnetic field line theory.

PREFACE

Pilkington Brothers Limited have been concerned with the use of linear motors to control tin flows in the bath used in the manufacture of float glass. The travelling magnetic field produced by a linear motor interacts with the induced currents in the molten tin which causes the metal to move. A need has arisen for a theoretical description of the electromagnetic field produced by a linear motor and its effect on the molten tin.

The work for this thesis was undertaken with financial assistance from the Science Research Council under the Co-operative Awards in Science and Engineering (CASE) scheme. I thank the collaborating body, Pilkington Brothers Limited, for the opportunity to work on this industrial problem and for providing experimental facilities in St. Helens. I must also thank Mr S Wolfenden for his help in the aquisition and construction of equipment for the experiment described in chapter two. I give sincere thanks to my supervisors Professor P C Kendall and Dr P Smith of the University of Keele, and Mr A D Cunningham of Latham Research Laboratories for their help, encouragement and thoughts. Finally I thank Miss Janette Hudon for her invaluable help in the typing of this thesis.

CONTENTS

1. INTRODUCTION

1.1 The Pilkington Float Glass Process.

For more than 250 years the principal method of plate glass production was that of the cast type. Essentially, an amount of glass is melted in a cast, rolled flat, then ground and polished. The process developed by Pilkington in the period 1920 to 1950 extended the ideas of this traditional method. In the final form of this process a continuous ribbon of glass was rolled from the melting tank and passed through an annealing kiln. The ribbon was then ground on both surfaces at the same time with enormous grinding wheels fed with progressively finer sand. The twin grinder was driven by 1.5 MW and this power was expended in grinding the ribbon. However, this power output and the 20 per cent glass wastage never made the process a good economic proposition (PILKINGTON, 1969,1977)

In 1957, after five years of development, the float glass process came into production. In this process a continuous ribbon of glass moves out of a melting furnace and floats along the surface of an enclosed bath of molten tin (figure 1.1).

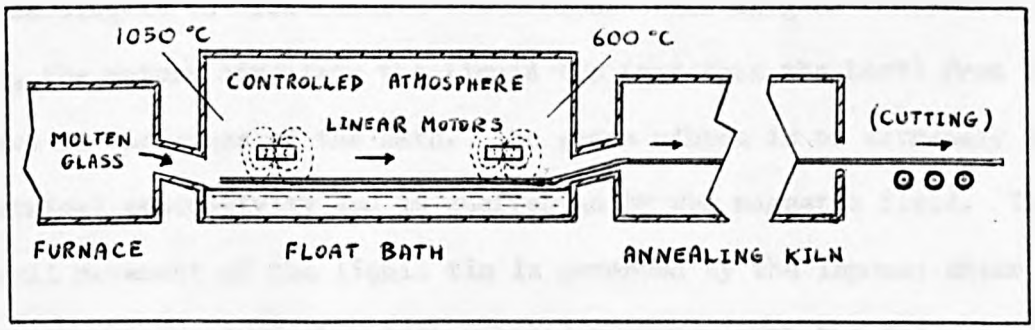

Fig. 1.1 The Float Glass Process

The ribbon is held in a chemically controlled atmosphere long enough for the irregularities to melt out and for the surfaces to become flat and parallel . The ribbon is lifted from the tin at the entrance to the kiln and is eventually cut into plates at the exit. To enable the lifting to

take place the glass ribbon must be brought to a plastic state before the kiln entrance, and so a temperature gradient is enforced along the bath. Because the surface of the molten tin is level, the glass becomes flat and a ribbon is produced with uniform thickness, also the surfaces do not require grinding or polishing. The thickness of the ribbon (from 1.5 mm to 50 mm, but typically 6 mm) is altered by, amongst other things, increasing its withdrawal speed. During the initial production of float glass it was found that the large heat loss through the refractory side walls of the bath caused an increase in the viscosity of the molten glass there, which in turn produced irregularities in the ribbon. In order to eliminate this effect it was found necessary to eliminate the temperature gradient transverse to the bath, and a method of circulating the (hot) liquid tin from the centre to the (cooler)edges of the bath was required. The constraint of minimum effect on the surface and flatness of the ribbon had to be observed. In 1961 some linear induction motors were built at Pilkington's in St. Helens, and later introduced into the float bath suspended above the glass ribbon. The linear motors produce axial travelling magnetic fields which interact with the electrically conducting tin causing it to flow beneath the ribbon. When aligned transverse to the bath, the motors circulate the liquid tin (and thus the heat) from the centre to the edges of the bath. The glass ribbon is of extremely low electrical conductivity and is unaffected by the magnetic field. The overall movement of the liquid tin is governed by the imposed shear flow (from the movement of the glass ribbon) together with the induced velocity profiles from the linear motor's electromagnetic field. Linear motors are also used to move the molten tin past heat sources.

At present the float process supplies 40 per cent of the Western world's flat glass demand. Recent innovations include a bronze solar control glass and the pulsed electrofloat. The solar glass is made using an electrochemical system which drives metallic ions into the advancing

glass ribbon, at a controlled depth and intensity. The pulsed electro-float allows a range of patterns and colours to be put inside the glass, leaving the surfaces free from the uneven textures of traditional patterned glass.

In all of these processes a linear motor can be used to advantage and a study of the electromagnetic field and velocity profiles induced in the liquid tin is both relevant and necessary. Because of the hostile environment inside the bath, no measurements of any kind are possible using today's technology. Neither has there been a study of the magnetic field produced by a plant linear induction motor.

The aim of this thesis is to describe the electromagnetic field produced by a linear induction motor and to describe the velocity profiles it induces in molten tin. Because of the industrial nature of the thesis and for ease of future research, a literature survey is also included.

1.2 Electromagnetic Induction and Magnetohydrodynamics.

Magnetohydrodynamics (MHD) is the study of the motion of an electrically conducting fluid in the presence of a magnetic field. The subject is also sometimes called 'magnetofluid dynamics' or 'hydromagnetics'. The motion of a conducting material across magnetic field lines induces an electric field in the system which causes electric currents to flow in the conductor. This is an extension of the results discovered independently by Henry and Faraday in 1831 for a closed circuit in a magnetic field. Faraday named this phenomenon electromagnetic (EM) induction. Lenz gave the direction of the induced currents. The direction is such that the magnetic field produced by the currents opposes the charge in the magnetic field which created them. In addition, the flow of an electric current across a magnetic field produces a body force, the Lorentz force, which modifies the motion of the conductor. It is this inter-dependance between hydrodynamics and electromagnetism which renders many MHD

problems both theoretically and practically difficult.

1.3 The Analysis of a Linear Induction Motor.

A flat linear induction motor (FLIM) is an 'unwound' version of its rotary counterpart (LAITHWAITE, 1975), and the methods of analysis for the rotational motor may be carried over to the FLIM - with suitable changes to account for the finite length of the motor.

Electrical engineers are mainly concerned with the electrical characteristics of induction motors, and have long used the equivalent circuit concept and circuit theory (eg.KESAVAMURTHY and BEDFORD 1958) and solutions to Laplace's equation (e.g. PIGGOT, 1962) in their analysis. Recently CULLIN and BARTON 1958 constructed a theory of the induction motor based on transmission line theory. We are mainly interested in the spatial variation of the EM field and here Maxwell's equations yield the best results - especially when combined with the travelling wave theory (BARLOW, 1965) of induction motors. Further approaches to the study of induction motors may be found in the comprehensive review of NASAR (1964).

1.4 Equations

1.4.1 Notation. The right hand Cartesian coordinate system is used throughout; the vectors $\underline{e}_1$, $\underline{e}_2$, $\underline{e}_3$ denote unit vectors along the x, y and z axis respectively. Subscripts 1, 2 and 3 denote the components of a vector quantity, e.g. $\underline{B} = [B_1, B_2, B_3] = B_1 \underline{e}_1 + B_2 \underline{e}_2 + B_3 \underline{e}_3$ Alphabetical superscripts and subscripts will often be used to denote parameters of significance or for clarification purposes, e.g. $\underline{J}^e$, K_s. The superscript ^ denotes quantities in Fourier transformation space. Script letters $\mathcal{L}, \mathcal{U}, \mathcal{T}, \mathcal{B}$ denote scales of length, speed, time and magnetic field respectively. Unless otherwise stated, rationalised MKS units are used throughout. Finally we define the gradient and Laplacian operators to be $\nabla = \underline{e}_1 \frac{\partial}{\partial x} + \underline{e}_2 \frac{\partial}{\partial y} + \underline{e}_3 \frac{\partial}{\partial z}$ $\nabla^2 = \frac{\partial^2}{\partial x^2} + \frac{\partial^2}{\partial y^2} + \frac{\partial^2}{\partial z^2}$

1.4.2 Electrodynamic Equations. If we neglect displacement currents and Hall currents, then Maxwell's equations are

$$\nabla . \underline{B} = 0 \tag{1}$$

$$\nabla . \underline{E} = q/\epsilon \tag{2}$$

$$\nabla \wedge \underline{E} = -\frac{\partial \underline{B}}{\partial t} \tag{3}$$

$$\nabla \wedge \underline{B} = \mu \underline{J} \tag{4}$$

where $\underline{B}$ is the magnetic induction in webers m^{-2} (=volt sec m^{-2}); $\underline{E}$ is the electric field in volts m^{-1}; $\underline{J}$ is the electric current density in amps m^{-2} (coulomb $m^{-2} s^{-2}$); q is the charge density; ϵ the dielectric constant and μ is the magnetic permeability in henry m^{-1} (=newton amp^{-2}). The magnetic induction is related to the magnetic field $\underline{H}$ (sometimes called the magnetising force, its units are amp-turns m^{-1}), by

$$\underline{B} = \mu \underline{H} \tag{5}$$

We shall assume, unless otherwise stated, that $\mu = \mu_0$, the permeability of free space, where $\mu_0 = 4\pi \times 10^{-7}$ henry m^{-1}. SHERCLIFF (1965) gives a detailed derivation of (1) to (5) and fully discusses the implication behind the assumptions made above, in the MHD context. From (4) we have the additional result for charge continuity

$$\nabla . \underline{J} = 0 \tag{6}$$

If $\underline{E}'$ is the total electric field and σ is the electric conductivity in mho m^{-1}, (mho=ohm^{-1}, ohm=volt amp^{-1}), then Ohm's law gives

$$\underline{J} = \sigma \underline{E}' \tag{7}$$

If the conductor is moving with a velocity $\underline{v}$ in a magnetic induction $\underline{B}$, the total electric field $\underline{E}'$ experienced by a moving fluid element is $\underline{E} + (\underline{v} \wedge \underline{B})$, where $\underline{E}$ is the electric field in fixed axes. Thus Ohm's law (7) becomes

$$\underline{J} = \sigma (\underline{E} + \underline{v} \wedge \underline{B}) \tag{8}$$

If we take the divergence of (8), using (6) and (2) we obtain

$$q/\epsilon = -\nabla . (\underline{v} \wedge \underline{B}) \tag{9}$$

In general the right of (9) is non-zero in a fluid conductor and we conclude

that there is a volume charge density inside a moving fluid; deviations from this induced charge are dissipated extremely rapidly by displacement currents (SCHWARTZ et al. 1964). From the MHD viewpoint, setting $\nabla.\underline{\mathcal{E}}=0$ over-describes the electric field and the solutions will be inconsistent. Taking the curl of (4) , using (8) and (3) we obtain the result

$$\eta \nabla_\wedge (\nabla_\wedge \underline{\mathcal{B}}) = \nabla_\wedge (\underline{v}_\wedge \underline{\mathcal{B}}) - \frac{\partial \underline{\mathcal{B}}}{\partial t} \tag{10}$$

or, using (1) and the operator relation, curl curl = grad div $-\ \nabla^2$,

$$\eta \nabla^2 \underline{\mathcal{B}} + \nabla_\wedge (\underline{v}_\wedge \underline{\mathcal{B}}) = \frac{\partial \underline{\mathcal{B}}}{\partial t} \tag{11}$$

where $\eta = (\mu\sigma)^{-1}$ is the magnetic diffusivity, or magnetic viscoscity, in $m^2 s^{-1}$. The relative importance of the terms on the left of (11) can be determined using dimensional analysis. We have

$$\frac{|\nabla_\wedge (\underline{v}_\wedge \underline{\mathcal{B}})|}{|\eta \nabla^2 \mathcal{B}|} \sim \frac{u\mathcal{B}/\mathcal{L}}{\eta \mathcal{B}/\mathcal{L}^2} = \frac{u\mathcal{L}}{\eta} = \mathcal{R}_m \tag{12}$$

The parameter $\mathcal{R}_m$ is called the magnetic Reynolds number. If $\mathcal{R}_m$ is small compared with unity (11) may be reduced to the diffusion equation

$$\eta \nabla^2 \underline{\mathcal{B}} = \frac{\partial \underline{\mathcal{B}}}{\partial t} \tag{13}$$

Equation (13) shows that the magnetic field leaks or diffuses through the (now stationary) electrical conductor. We conclude that for small $\mathcal{R}_m$ the magnetic field is not greatly affected by the motion of the conductor. The time scale T for the penetration of the magnetic field into the conductor of depth $\mathcal{L}$ is of order $\mathcal{L}^2/\eta$. If we denote the time scale for the magnetic field variation by $\mathcal{T}$ then using (13) we can identify a depth of penetration, δ , of the magnetic field into the conductor given by $\delta \sim (\eta \mathcal{T})^{1/2}$. When $\mathcal{T} \ll T$ the magnetic field is concentrated close to the surface of the conductor and the regions at distances greater than δ below the conductor have little effect on the induced EM field. The parameter δ is referred to as the 'skin depth'. If the magnetic Reynolds number is large compared with unity the first term on the left of (11) may be neglected and we have

$$\nabla_\wedge (\underline{v}_\wedge \underline{\mathcal{B}}) = \frac{\partial \underline{\mathcal{B}}}{\partial t} \tag{14}$$

This equation is identical to that satisfied by the vorticity $\underline{\omega}$ in an ideal fluid, namely

$$\nabla \wedge (\underline{v} \wedge \underline{\omega}) = \frac{\partial \underline{\omega}}{\partial t} \tag{15}$$

Equations (14) and (15) describe the convection of the magnetic field and vorticity through the fluid. The interpretation of (15) is that vortex lines move with the fluid, so we interpret (14) to mean that the magnetic field lines are 'frozen into' and move with the conductor. This result was first stated by ALFVÉN (1942). In the laboratory R_m is seldom large and the frozen-in effect is barely noticeable. If R_m is neither large nor small both terms on the left of (11) must be considered. In this case both diffusion and convection of the magnetic field lines occur. The field lines are 'dragged' through the conductor as they diffuse into it.

The force $\underline{\mathcal{F}}$ exerted by an EM field on a conductor is given by

$$\underline{\mathcal{F}} = q(\underline{\mathcal{E}} + \underline{v} \wedge \underline{\mathcal{B}}) = q\,\underline{\mathcal{E}} + \underline{\mathcal{J}} \wedge \underline{\mathcal{B}} \tag{16}$$

However from (3) we see that $|\underline{\mathcal{E}}| \sim \mathcal{L}|\underline{\mathcal{B}}|\mathcal{T}^{-1}$, and (2) gives $|q| \sim \epsilon |\underline{\mathcal{E}}| \mathcal{L}^{-1}$ whilst (4) gives $|\underline{\mathcal{J}}| \sim |\underline{\mathcal{B}}|/\mu\mathcal{L}$, so that the ratio of the first and second terms on the right of (16) is

$$\frac{|q\underline{\mathcal{E}}|}{|\underline{\mathcal{J}} \wedge \underline{\mathcal{B}}|} \sim \epsilon\mu \cdot \frac{|\underline{\mathcal{E}}|^2}{|\underline{\mathcal{B}}|^2} \sim \left(\frac{\mathcal{L}}{c\,\mathcal{T}}\right)^2 \ll 1$$

where $\epsilon\mu = c^{-2}$ and c is the velocity of light. Thus in a moving liquid the volume charge does not appreciably contribute to the body force and we may take the force as

$$\underline{\mathcal{F}} = \underline{\mathcal{J}} \wedge \underline{\mathcal{B}} \tag{17}$$

The force $\underline{\mathcal{F}}$ is a true body force, like gravity, and is usually called the Lorentz body force. It is possible to show COWLING (1957) that the Lorentz force may be interpreted as a tension $\mathcal{B}^2/\mu$ along the magnetic field lines together with a hydrostatic pressure $\mathcal{B}^2/2\mu$.

1.4.3 Hydrodynamic Equations. The equation of momentum is

$$\rho \frac{d\underline{v}}{dt} = -\nabla P + \underline{\mathcal{F}} + \tfrac{1}{3}\nu \nabla(\nabla.\underline{v}) + \nu \nabla^2 \underline{v} \tag{18}$$

where ρ is the density of the fluid in kg m ; P the (scalar) internal

fluid pressure; $\underline{\mathcal{F}}$ the body force and ν the viscosity of the fluid in Pascal(=kg m^{-1} s^{-1}). For a conducting fluid moving in a magnetic and gravitational field we have, using (16)

$$\underline{\mathcal{F}} = \mathcal{J} \wedge \underline{\mathcal{B}} + \rho g \tag{19}$$

where g is the gravitational acceleration. The mobile operator $\frac{d}{dt}$ is defined by

$$\frac{d}{dt} = \frac{\partial}{\partial t} + \underline{v}.\nabla \tag{20}$$

The last two terms of (18) are the viscous forces. To the above we now add the equation of continuity

$$\frac{\partial \rho}{\partial t} + \nabla.(\rho \underline{v}) = 0 \tag{21}$$

which is a mathematical representation of the conservation of mass. In this thesis we shall assume that all liquids are incompressible so that ρ is a constant, and the thermodynamic equations required for compressible flow are not necessary. Thus (21) reduces to

$$\nabla.\underline{v} = 0 \tag{22}$$

It is apparent that ρg in (19) may be included in the pressure term of (18) so we choose to ignore the gravitational force throughout this thesis. From (18) to (22) we obtain the Navier-Stokes hydromagnetic equation

$$\rho\left\{\frac{\partial \underline{v}}{\partial t} + (\underline{v}.\nabla)\underline{v}\right\} = -\nabla P + \mathcal{J} \wedge \underline{\mathcal{B}} + \nu \nabla^2 \underline{v} \tag{23}$$

We can investigate the relative importance of the terms in (23) using dimensional analysis. The ratio of the inertia term to the viscous term is

$$\frac{|\rho(\underline{v}.\nabla)\underline{v}|}{|\nu \nabla^2 \underline{v}|} \sim \frac{\rho U^2/L}{\nu U/L^2} = \frac{\rho U L}{\nu} = R_e \tag{24}$$

where R_e is the Reynolds number for the flow. When R_e is large the inertia term dominates the viscous term and (23) remains non-linear in $\underline{v}$. When R_e is small (the 'slow flow' approximation) we can neglect the inertia term and (23) becomes linear in $\underline{v}$. If the Reynolds number is

large, the effect of viscosity is only important in regions close to the boundaries (the boundary layers) or in regions of large velocity gradients.

Using (8) we see that the ratio of the Lorentz term to the viscous term is

$$\frac{|\underline{J}\wedge\underline{B}|}{|\nu\nabla^2\underline{v}|} \sim \frac{\sigma B^2 U}{\nu U/L^2} = B^2L^2\left(\frac{\sigma}{\nu}\right) = H_m^2 \qquad (25)$$

where $H_m = BL\left(\frac{\sigma}{\nu}\right)^{1/2}$ is the Hartmann number. This dimensionless parameter was first used by Hartmann in 1937. It gives a direct estimate of the relative importance of the Lorentz and viscous forces. When H_m is large the viscous term can only compete with the magnetic term in regions of large velocity gradients. These regions occur close to the boundaries, and we can associate a boundary layer of width $\delta = \frac{1}{B}\left(\frac{\nu}{\sigma}\right)^{1/2}$ (the Hartmann boundary layer) with these regions.

The ratio of the Lorentz term to the inertia term in (23) is

$$\frac{|\underline{J}\wedge\underline{B}|}{|\rho(\underline{v}.\nabla)\underline{v}|} \sim \frac{\sigma B^2 U}{\rho U^2 L} = \frac{B^2L}{U}\left(\frac{\sigma}{\rho}\right) = \frac{H_m^2}{R_e} \qquad (26)$$

The ratio H_m^2/R_e is sometimes denoted by R_H, the magnetic pressure number. In large Reynolds number flow we require $H_m > R_e^{1/2}$ for the Lorentz force to compete with the inertia term. If the Hartmann number is not large enough the magnetic field lines are partially excluded from the moving liquid and concentrate in the boundary layers.

1.4.4 Time Variation. Throughout we shall be considering EM sources which oscillate with an angular frequency ω. In our analysis all solutions of Maxwell's equations will also oscillate with this angular frequency. We shall write, ($i^2=-1$),

$$\underline{J}(\underline{r},t) = \underline{J}(\underline{r})e^{i\omega t} \quad \underline{B}(\underline{r},t) = \underline{B}(\underline{r})e^{i\omega t} \quad \underline{E}(\underline{r},t) = \underline{E}(\underline{r})e^{i\omega t} \qquad (27)$$

where only the real parts of $\underline{J}$, $\underline{B}$ and $\underline{E}$ have physical meaning. Using (16) we see that the Lorentz body force is

$$\underline{F} = \mathcal{R}(\underline{J})\wedge\mathcal{R}(\underline{B}) \qquad (28)$$

where $\mathcal{R}$ denotes 'real part of'. It can be seen that $\underline{\mathcal{F}}$ may be written as the sum of two parts, one dependent on time (having an angular frequency 2ω), $\underline{\mathcal{F}}^t$, and the other, $\underline{F}$, independent of time. Thus

$$\underline{\mathcal{F}} = \underline{\mathcal{F}}^t + \underline{F} \tag{29}$$

If we average $\underline{\mathcal{F}}$ over a period of oscillation $\left(\frac{2\pi}{\omega}\right)$ it is easily shown that the time averaged Lorentz force $\underline{\mathcal{F}}$ is equal to $\underline{F}$ and we have

$$\underline{F} = \tfrac{1}{2}\,\mathcal{R}\left\{ \underline{J}(\underline{r}) \wedge \underline{B}^*(\underline{r}) \right\} \tag{30}$$

where $*$ denotes the complex conjugate. In component form (30) becomes

$$\underline{F} = \tfrac{1}{2}\,\mathcal{R}\left[J_2 B_3^* - J_3 B_2^* \,,\; J_3 B_1^* - J_1 B_3^* \,,\; J_1 B_2^* - J_2 B_1^* \right] \tag{31}$$

1.4.5 The Fourier Transformation. In much of this thesis we are concerned with the three dimensional behaviour of the EM field and velocity profiles. One extremely important tool in analyses of this type is the double exponential Fourier transformation. Sufficiency conditions for the transform to exist may be found in TITCHMARSH (1937) or CHAMPENEY (1973), but for our purposes the sufficient condition is that the function to be transformed has a finite number of discontinuities.

We shall define the n-dimensional Fourier transformation, although we only use the cases n=1 and n=2. Writing $\underline{r} = [x_1, x_2, x_3, \ldots\ldots, x_n]$, $\underline{r}' = [x_1', x_2', \ldots\ldots, x_n']$, $\underline{s} = [p_1, p_2, p_3, \ldots, p_n]$, $\underline{s}' = [p_1', p_2', \ldots p_n']$ we define the Fourier transformation of the (n+1)-dimensional function $M(\underline{r}, z)$ with respect to $\underline{r}$ as $\hat{M}(\underline{s}, z)$ where

$$\hat{M}(\underline{s}, z) = \mathcal{F}_n^+\left\{M(\underline{r}, z)\right\} = \int_{-\infty}^{\infty}\!\!\ldots\ldots\int_{-\infty}^{\infty} M(\underline{r}, z)\, e^{i\,\underline{r}\cdot\underline{s}}\, d\underline{r} \tag{32}$$

The corresponding inverse transformation is defined to be

$$M(\underline{r}, z) = \mathcal{F}_n^-\left\{\hat{M}(\underline{s}, z)\right\} = \frac{1}{(2\pi)^n}\int_{-\infty}^{\infty}\!\!\ldots\ldots\int_{-\infty}^{\infty} \hat{M}(\underline{s}, z)\, e^{-i\,\underline{r}\cdot\underline{s}}\, d\underline{s} \tag{33}$$

We also have the following convolution results for the functions $M(\underline{r}, z)$ and $N(\underline{r}, z)$:

$$\mathcal{F}_n^+\left\{ M(\underline{r}, z)\, N(\underline{r}, z)\right\} = \int_{-\infty}^{\infty}\!\!\ldots\int_{-\infty}^{\infty} \hat{M}(\underline{s}', z)\, \hat{N}(\underline{s}-\underline{s}', z)\, d\underline{s}' \tag{34}$$

$$\mathcal{F}_n^-\left\{ \hat{M}(\underline{s}, z)\, \hat{N}(\underline{s}, z)\right\} = \int_{-\infty}^{\infty}\!\!\ldots\int_{-\infty}^{\infty} M(\underline{r}', z)\, N(\underline{r}-\underline{r}', z)\, d\underline{r}' \tag{35}$$

We shall also require Parseval's formula (see Champeney):

$$\int_{-\infty}^{\infty}\cdots\int_{-\infty}^{\infty} M(\underline{r},z)\,N^{*}(\underline{r},z)\,d\underline{r} = \int_{-\infty}^{\infty}\cdots\int_{-\infty}^{\infty} \hat{M}(\underline{s},z)\,\hat{N}(\underline{s},z)\,d\underline{s} \qquad (36)$$

1.4.6 Electromagnetic boundary conditions.

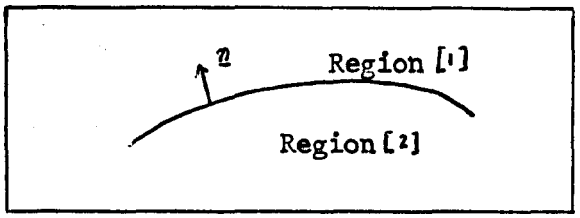

Fig. 1.2 Defining Boundary Conditions.

A boundary between two media is shown in figure 1.2. For the field vectors $\underline{\mathcal{E}}$, $\underline{\mathcal{H}}$ and $\underline{\mathcal{B}}$ we have

(a) The tangential component of $\underline{\mathcal{E}}$ is continuous across the boundary thus

$$\underline{n} \wedge (\underline{\mathcal{E}}_1 - \underline{\mathcal{E}}_2) = \underline{0} \qquad (37)$$

(b) The tangential component of $\underline{\mathcal{H}}$ is discontinuous across the boundary by an amount $\underline{\mathcal{K}}$ which measures the surface current density. We note that the current density is to be interpreted as $\underline{\mathcal{K}} = \lim_{\delta \to 0}(\delta \underline{\mathcal{J}})$ where δ is the depth of penetration of $\underline{\mathcal{J}}$ into [1] and [2]. Using (5) we have

$$\underline{n} \wedge \left(\frac{\underline{\mathcal{B}}_1}{\mu_1} - \frac{\underline{\mathcal{B}}_2}{\mu_2}\right) = \underline{\mathcal{K}} \qquad (38)$$

where μ_1 and μ_2 are the magnetic permeabilities of [1] and [2] respectively. When the regions are of finite conductivity $\underline{\mathcal{K}} = \underline{0}$. When the conductivity of [2] becomes infinite the EM field is excluded from [2] and a surface current $\underline{\mathcal{K}}$ exists.

(c) The normal component of magnetic induction is continuous across the boundary, thus

$$\underline{n} \cdot (\underline{\mathcal{B}}_1 - \underline{\mathcal{B}}_2) = 0 \qquad (39)$$

The boundary conditions above still apply when the two media are in relative motion (see ROBERTS, 1967). To the above conditions we add the requirement that the EM field decays at infinity.

1.4.7 Hydrodynamic Boundary Conditions. We use figure 1.2 but the region [2] is now occupied by an incompressible viscous fluid moving with velocity $\underline{V}(t) = [u, v, w]$.

(a) For a plane boundary moving with velocity $\underline{V}_0(t)$ we have

$$\underline{V} = \underline{V}_0 \qquad (40)$$

at the boundary.

(b) If the surface shear stress $\underline{\tau}$ is specified along a plane boundary with unit normal $\underline{e}_3$, we have

$$\tau = \left[\nu \frac{du}{dz} , \nu \frac{dv}{dz} , 0 \right] \quad \text{and} \quad W = \underline{V}_0 \cdot \underline{e}_3 \qquad (41)$$

If [1] is a vacuum, the surface shear stress is zero.

1.5 The Float Parameters

1.5.1 A Linear Induction Motor.

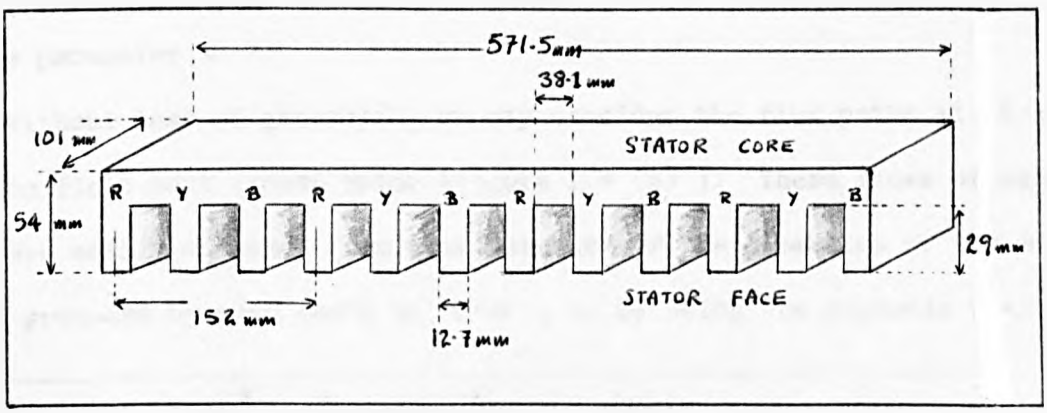

Fig. 1.3 The Float Bath Linear Motor

One of the float bath's linear motors is shown in figure 1.3. The stator core is constructed of soft iron, laminated to minimise eddy current losses. Thus the core's electrical conductivity may be taken as zero. Twelve teeth are attached to the stator core, each tooth wound with four turns of insulated water cooled copper tubing except the end teeth which have two turns. The teeth are connected in series according to the colour coding: R (red), Y (yellow) and B (blue) - see figure 1.3. A three phase electric current is applied to the colour group and the supply is said to

be 'balanced' if a phase difference in time of $\frac{2\pi}{3}$ radians is maintained between the colours. The whole arrangement is enclosed in a refractory jacket able to withstand the high temperatures inside the bath (British Patent: 1,107,099).

A section of the float bath linear motor is shown in figure 1.4(a). We assume the group Y and group B windings are respectively phase advanced and phase retarded by the amount $\frac{2\pi}{3}$ radians over the group R windings. From the phase vectors in the circle diagrams we can deduce the shown variation in magnetic flux with position along the motor axis. The upper graph is assumed to correspond with the time $t=0$. It is apparent that the magnetic flux moves along the motor axis in the direction of increasing phase difference in the windings with a speed given by $\omega/(2\pi/\lambda)$,where $\lambda\ (=2\tau)$ is the wavelength of the excitation and 2τ is the distance between adjacent teeth in the same phase. Can we attach a significance to the parameter τ ?

Without loss of generality we may consider the flux paths at $t=0$ for the float bath linear motor (figure 1.4 (b)). These lines of magnetic flux are easily obtained from consideration of the direction of the magnetic field produced by each tooth at $t=0$, or by using the magnetic field line

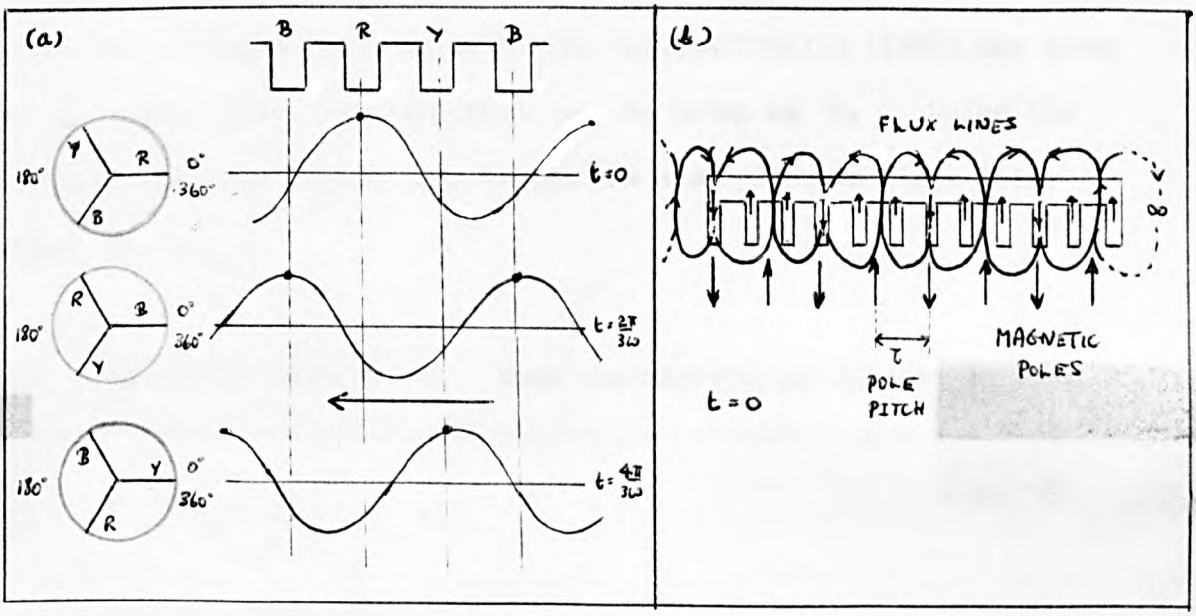

Fig. 1.4 Flux Variation

analysis of chapter 12. It is apparent that the flux paths for this motor are equivalent to an array of eight magnetic poles (an extra pole arises from the closure of flux at infinity). The distance τ is seen to be the magnetic pole pitch.

We shall now define the technical terms used throughout this thesis when discussing linear motors; the stator (or primary) constitutes the stator core and stator face (tooth/slot region); the electrical conductor (plate or liquid metal) upon which the FLIM acts is called the rotor (or secondary); the tooth pitch (c) is the distance between the centres of adjacent teeth; the pole pitch (τ) is half the distance between the centres of adjacent teeth in the same phase and the wavelength of the stator excitation is twice the pole pitch ($\lambda = 2\tau$). The equivalent airgap (g_e) is the distance between the stator face and the secondary (g) corrected for the serrated topology of the tooth/slot region. It is equal to $K_c g$, where K_c, the CARTER (1926) airgap fringing coefficient, is given by

$$K_c = \frac{c(5g_m + \omega_s)}{c(5g_m + \omega_s) - \omega_s^2} \qquad (42)$$

In (42) the parameter ω_s is the width of the slot opening and g_m is the length of the magnetic flux path. For machines with an open magnetic circuit ie: a single inductor as in the FLIM, LAITHWAITE (1966) has shown that g_m, to a first approximation, may be taken as τ/π. Using the dimensions shown in figure 1.3, (which are also given in table 1.1), we find $K_c = 1.22$.

1.5.2 The Stator Excitation. When the magnetising current is balanced the fundamental term of the magnetomotive force (MMF) for a three phase induction motor may be represented by a forward moving travelling wave. For an infinitely long and infinitely wide ('idealised') FLIM we have (WATT, 1955)

$$MMF = F_m \sin(\omega t - \alpha y - \pi) \qquad (43)$$

where the peak MMF is given by

$$F_m = \frac{3\sqrt{2}\, N I K_\omega}{P\pi} \tag{44}$$

In (43) and (44) α is the wavenumber ($\alpha = \pi/\tau$); N is the total turns per phase; I the winding current; $K_\omega = \sin\left(\frac{c_p}{\tau}\cdot\frac{\pi}{2}\right)$ is the pitch factor (c_p is the coil pitch) and P is the number of poles . The coordinate y is chosen along the FLIM axis. If V_s is the synchronous speed of the travelling wave then $V_s = \omega/\alpha$. If the magnetising current is unbalanced a backward moving travelling wave is created which introduces extra power losses. We shall assume the currents are balanced.

In theoretical analyses there are two main methods of representing the winding configuration. The first method replaces the winding currents and tooth slots by a distributed surface current on the stator face, (for example FUKUSHIMA et al. 1963, OOI and WHITE 1970). This method we call the case S . It is valid when the induction motor is series wound (LAITHWAITE, 1965). The stator surface current density $\underline{K}$ is found by differentating the MMF (43) with respect to y . Changing to complex notation we have

$$\underline{K} = K_s e^{i(\omega t - \alpha y)} \underline{e}_1 \tag{45}$$

where

$$K_s = \frac{3\sqrt{2}\, N I K_\omega \alpha}{P\pi} \tag{46}$$

The magnetic permeability of iron is not constant, but depends upon the magnitude of the magnetic field. However, because it is of the order 10^{-4} henry m^{-1} we may assume $\mu_{iron} \sim \infty$. From the boundary conditions at the stator face (38) we see that case S excitation is equivalent to specifying the tangential component of magnetic induction at the stator face. Thus we have the following boundary condition at the stator face:

Case S :

$$B_2 = \mu_0 K_s e^{i(\omega t - \alpha y)} \tag{47}$$

Where K_s is given by (46). Using the parameters of table 1.1 we find $K_s = 7850$ Amp m^{-1} for $K_\omega = 0.5$

In the second method we specify the normal component of magnetic induction B_m at the stator face, (for example; WANG, 1971), which is valid when analysing parallel-wound motors. This method of analysis we call case P , and the condition at the stator face is

Case P: $$B_3 = B_m e^{i(\omega t - \alpha y)} \tag{48}$$

We can obtain B_m in terms of the MMF using Ampéres circuital rule (SAY, 1963)

$$MMF = \frac{1}{\mu_0} \oint_C \underline{B} \cdot d\underline{r} \tag{49}$$

where the contour C is any closed flux path. It is easy to show that under no load conditions (in the abscence of a rotor)

$$B_m = \mu_0 K_s \tag{50}$$

1.5.3 Finite Excitation Effects. The results of 5.2 are in reality applicable only to the central regions of a FLIM where the excitation does not 'see' the stator edges. However, a real FLIM if of finite length and the discontinuities in the excitation at the ends of the stator introduce pulsating components of the EM field which are superimposed on the travelling field. This is called the 'longitudinal end effect', (OKHREMENKO , 1960). The pulsating components induce shunt currents which add to the power losses but they can be removed in several ways.

(a) Compensating poles. This is an external method proposed by ELLIOT et al. (1966). Extra poles are added to the ends of the FLIM and wound with a single phase a.c. supply (figure 1.5) so as to cancel the pulsating components of the EM field in the travelling wave region. This eliminates end loss but adds substantially to the

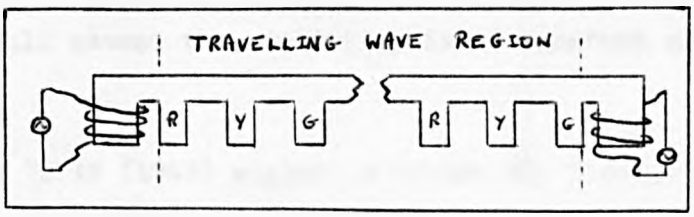

Fig. 1.5 FLIM with Compensating Poles

length of the FLIM. The MMF in this case is given by

$$MMF = F_m \left\{ \cos(\omega t - \alpha y) - \cos \omega t + g_1 \sin \omega t \right\} \qquad (51)$$

where g_1 is a parameter which includes the length of the compensating poles.

(b) Grading the Winding. There are a number of ways of reducing the MMF to zero at the ends of the stator (BLAKE, 1956). One of these is to wind the end-poles of a FLIM with half the standard number of turns. In this way the magnetic field is reduced to zero at the stator ends and no pulsating components appear. The MMF here is of the form

$$MMF = \tfrac{1}{2} F_m \left\{ \cos(\omega t - \alpha y) - \cos \omega t \right\} \qquad (52)$$

Grading the winding was the method used in the design of the float bath linear motors.

(c) Sudan's method. This internal method, first proposed by SUDAN (1963) removes the pulsating components by adding additional windings within the travelling wave region. Sudan proposed to eliminate the zero order end effects by using three instead of only one travelling wave excited winding. The MMF in this case is of the form

$$MMF = \sum_n F_{m_n} \cos(\omega t - \alpha_n y) \qquad (53)$$

It is not difficult to consider boundary conditions (51), (52) and (53) at the stator face but we choose to assume the excitation is a pure travelling wave.

A real FLIM is also of finite width. The change in structure of the EM field at the edges of a FLIM because of the discontinuity of the winding current there, is called the 'transverse edge effect' (VILNITIS, 1966). Throughout, we shall assume the excitation is of constant magnitude across the stator width.

LIELPETER and TUTIN (1959) suggest a factor K_ℓ 0.8-0.9 should be introduced in K_s to include the longitudinal end effect.

1.5.4 Float Parameters. The physical parameters involved in the float process relevant to our work are given in table 1.1 .

Table 1.1 - Bath Parameters (mixed units)

FLIM PARAMETERS

Width ($2a$)	4 in. 101 mm	Current (I)	150 A
Length ($2b$)	22.5 in. 571.5mm	Voltage	10 V
Height	$2\frac{1}{8}$ in. 54 mm	Frequency (f)	50 Hz
Airgap (g)	0.5-3 in. 12-76mm	Angular Freq. (ω)	100π Rad
Slot Width (ω_s)	1.5 in. 38.10mm	Wavelength (λ)	6 in. 152 mm
Pole Pitch (τ)	3 in. 76 mm	Wave Speed (V_s)	7.6 m/s 25 ft/s
Tooth Pitch (c)	2 in. 51 mm	Current Density (K_s)	7850 A/m
Coil Pitch (c_p)	1 in. 25.4mm	Turns/Phase (N)	15

TIN PARAMETERS (SMITHELLS, 1955)

TEMP ^oC	DENSITY ρ Kg/litre	VISCOSCITY ν Pascal (Poise.10^{-1})	ELECTRICAL CONDUCTIVITY σ mho/m	HARTMANN NUMBER $\mu_0 K_s L \left(\frac{\sigma}{\nu}\right)^{1/2}$	MAGNETIC REYNOLDS NUMBER $V_s L \mu_0 \sigma$
400	6.85	0.00137	1.946×10^6	23.6	1.19
500	6.78	0.00118	1.852×10^6	24.8	1.13
600	6.71	0.00105	1.761×10^6	25.7	1.07
800	6.57	0.00087	1.595×10^6	26.3	0.98
Tin Depth (L) 2.5 in. 63.5 mm					

GLASS PARAMETERS

Ribbon Speed (u_o)	152-254 mm 6-10 in/s
Thickness	2-10 mm.
Density	2.5 Kg/litre
Viscoscity	$10^3 - 10^{10}$ Pa
Electrical conductivity	1.7 mho/m

1.6 The Applications of a Linear Motor

The use of a FLIM in conjunction with solid rotors has been adequately described by GOLDHAMMER et al. (1968) and LAITHWAITE (1975). Its use in the liquid metal industry ranges from the pumping of liquid metal coolants in the nuclear reactor (MULLER, 1966) to MHD power generation (WOMACK, 1969) and the control of molten metal flow in the foundry industry (ARMSTRONG, 1964). Other applications are given in PANHOLZER(1963) and ROBINSON et al. (1972).

The use of a FLIM in the production of stainless steel is similar to that in the production of float glass and so it is relevant to this thesis. AEG-Elotherm's ELDOMET system (HOEY et al. 1974) involves the movement of molten iron along an inclined channel from the furnace to a casting ladle, by a FLIM placed underneath the channel (von STARCK 1971; EADY et al 1972). BLOCK (1973) gives some experimental results for the ELDOMET system and other EM runners and pumps. The ASEA company of Sweden developed (in 1939) a FLIM to stir the molten iron inside an arc furnace, thereby increasing the rate of metallurgical processes (REZIN, 1965; ELIASON & KALLING, 1968). This two-phase FLIM is placed underneath the furnace and is capable of developing a force of 500 N/m^2 which drives the shallow layer of molten iron at a surface speed of 1 m/s when V_s = 4 m/s (SUNDBERG , 1969). The FLIM operates on a very low frequency supply (0.5-2 Hz) to allow diffusion of the magnetic field through the thick furnace base. Further references on induction stirring may be obtained from the files of the STUDSVIK company (Sweden), and COCHET et al. (1972).

1.7 A Survey of Linear Induction Motor/Pump Analyses

1.7.1 Definitions. A FLIM may be used in conjunction with a solid rotor or with a liquid metal rotor. The latter configuration is that of a flat linear induction pump (FLIP). It is possible to have a single (SLIM, SLIP) or double (DLIM, DLIP) inductor arrangement (figure 1.6).

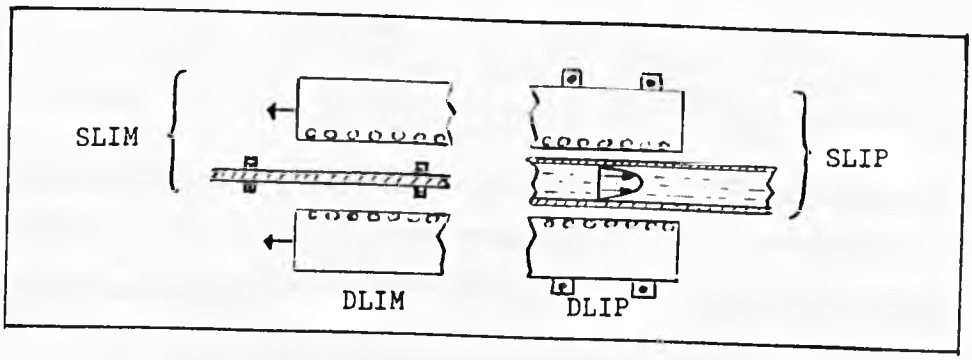

Fig. 1.6 FLIM and FLIP Longitudinal sections.

Usually a FLIM is used to drive a vehicle (for example, a train) along a fixed rotor (the'reaction rail' in this context). A FLIP, however, is fixed and it is the liquid metal which is induced to move. In all FLIM analyses the solutions are found assuming the FLIM moves with a constant speed V; the excitation wavespeed relative to the fixed rotor is then sV_s, where the slip s is given by

$$s = (V_s - V) / V_s \qquad (54)$$

Thus the induced EM field is a function of s. At start-up the slip is unity and the induced propulsion forces are at a maximum. When the slip is zero, the wavespeed equals the FLIM speed and the induced propulsion forces are zero. The analysis of a FLIP is a true MHD problem and the velocity of the liquid metal must be determined from the coupled Maxwell and Navier-Stokes equations. However if we assume the liquid moves as a solid with a constant velocity V the equations uncouple and we can obtain first approximation solutions. Thus the analyses for a FLIM and a FLIP may be considered identical.

Some possible models for the longitudinal and transverse sections of a SLIM/SLIP are shown in figures 1.7 and 1.8 respectively.

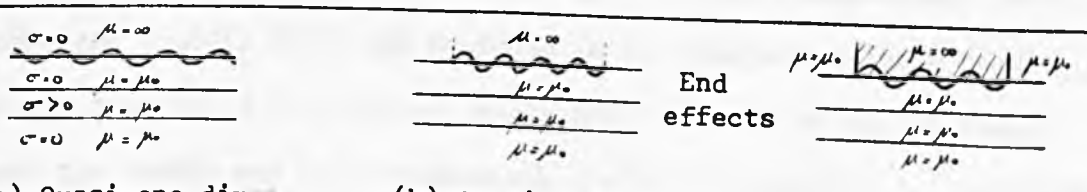

(a) Quasi-one dim. (Idealised excitation)

(b) Quasi-two dim. (Finite excitation)

(c) Two dimensional (Finite stator)

Fig. 1.7 Longitudinal Models

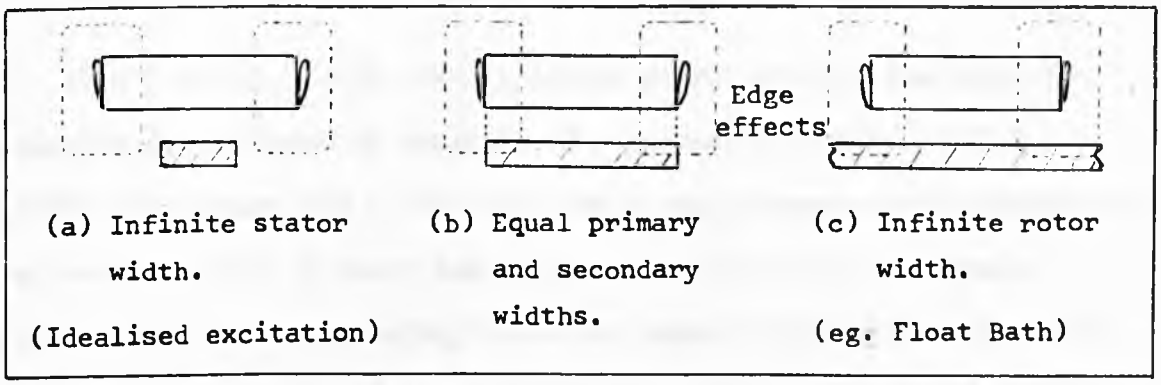

(a) Infinite stator width. (Idealised excitation)

(b) Equal primary and secondary widths.

(c) Infinite rotor width. (eg. Float Bath)

Fig. 1.8 Transverse Configurations

1.7.2 Survey.

(a) One dimensional analyses. Here it is assumed the decay of the EM field away from the stator excitation is negligible (no skin effect) enabling the rotor to be replaced by a thin conducting sheet. Using flux linkage arguments WILLIAMS et al. (1956) and KARO (1963) assess the properties of short stator machines, of which the FLIM is but one example, and discuss the longitudinal end effect. LAITHWAITE (1957, et.al.1960) gives some applications for the short stator machine. Building on previous work LAITHWAITE (1965) introduces a design parameter G, the 'goodness factor', which gives an indication of the usefulness of a machine, where

$$G = \frac{\sigma \mu_0 V_s}{\alpha^2 g} \tag{55}$$

It can be seen that G is equivalent to the magnetic Reynolds number (12) A machine is 'good' or 'bad' according as $G \gg 1$ or $G < 1$. Using G and the equivalent circuit concept NIX and LAITHWAITE (1966) perform a detailed study of SLIMs for low speed applications. BOLDEA and NASAR (1975) consider a finite stator with half wound end poles for case S excitation. A transverse edge effect factor (BOLTON, 1969) and a skin effect factor (KLIMAN and ELLIOT, 1974) are included in the analysis. Their results indicate that the $1/e$ folding length for the decay of the EM field beyond the stator end is approximately $(\alpha G^{1/2})^{-1}$, when $S \sim 1$, which is similar to the folding length derived by Bolton for the transverse edge effect.

ELLIOT et al. (1966) develop design parameters for the induction generator and included an analysis of compensating poles. CERINI and ELLIOT (1968) show that i) the end loss in an uncompensated generator is the ohmic loss due to shunt end currents, and ii) the fluid ohmic losses due to the compensating fields are small compared with the shunt end loss. We note that the end effect results of Laithwaite's work are unfortunately of little use. He assumes zero induced current before the stator entrance end and merely indicates that the induced currents are non-zero beyond the stator exit end.

SCHEIBER (1973) uses the Fitzgerald vector superpotential (the time derivative of the electric Hertz vector) to produce streamlines indicating the end and edge effects for a rectangular travelling wave excitation placed above a finite sheet. KIRILLOV and LAVRENT'EV (1972) also produce some results for a finite sheet but these are difficult to interpret. Further references on the transverse edge effect may be found in the review of VILNITIS (1966).

(b) Quasi-one dimensional analyses. All of the studies below use Maxwell's equations to analyse FLIM models of type (a) in figure 1.7

(i) Induction machines. WEST and HESMONDALGH (1961) investigate (case S) the problem of flux penetration in conducting media and determine the properties of induction machines with large air gaps. Their results indicate that 63 per cent of the flux from an iron stator lies within a distance τ/π from the stator face. The case S analysis of STOLL and HAMMOND (1965) can be applied to the SLIM. They show that the rotor may be regarded as infinitely thick if its thickness is greater than the skin depth of the EM field or if its thickness is greater than τ/π . If neither of these instances hold the authors conclude that the rotor can be treated as a thin sheet with the neglect of eddy currents.

(ii) High speed ground transportation. The following papers deal with the propulsion and levitation aspects of linear motors with

application to rail transport. OOI and WHITE (1970) with a sheet rotor case S analysis and WANG (1971) with a thick rotor case P analysis, consider the DLIM. LIPKIS et al (1971) uses both case P and case S analyses for the problem of a SLIM with a half space rotor.

(iii) MHD power generation, (DLIP configuration). JACKSON and PIERSON (1966) analyse (case S) the material limitations in a MHD generator channel whilst WANG and DUDZINSKY(1967a) obtain (case P) a generator's electrical characteristics. A comprehensive review of induction generator experiments and theoretical analyses is given in DUDZINSKY and WANG (1968).

(iv) Liquid metal pumps, (also see (f) and (g)). VEZE and KRUMIN (1965) consider (case S) the force solutions for a DLIP with phased bilateral inductors. VEZE and MIKEL'SON (1970) show their solutions suggest a contactless method of exciting vibrations in a solidifying ingot of liquid metal to control its structure.

(c) Quasi-two dimensional analysis. The following papers analyse the longitudinal end effect with an infinite stator length (figure 1.7.(4))

(i) MHD induction generator. The papers of JESTER and FANUCCI (1969) and PIERSON (1971) use SUDAN's (1963) superimposed winding analysis as a means of increasing the generator efficiency. Sudan used the Fourier transformation technique to analyse a finite DLIP and obtained series solutions. The zero modes of these solutions are the major contributory factors in the end loss terms but by having three different but suitably chosen windings on the stator face Sudan found they could be eliminated. ENGELN and PESCHICA (1966) develop electrical characteristics for a finite excitation (case S) generator using the two sided Laplace transformation. MOSZYNSKI (1966) and SUTTON and SHERMAN (1965) use the conformal transformation to map the end regions into a rectangle within which the analysis

is performed. Moszynski also discusses the use of insulating vanes to reduce shunt end currents.

(ii) FLIM studies. NASAR (1969) gives a theoretical (case S) and experimental account of the variations of the magnetic field inside a DLIM using the Fourier transformation technique. He also gives a survey of end effect studies. This work is extended to a SLIM in NASAR and del CID's (1973a) paper.

Further references to end effect studies may be found in the review of VALDAMIS (1966). The papers of KOZYRENKO (1971a, 1971b) suggest a method of solving discontinuous boundary value problems for elliptic systems of first order equations. The author assumes the velocity profile in a MHD channel may be written as $\underline{V} = G(\alpha,\gamma)\,\nabla\alpha \wedge \nabla\gamma$, $\alpha = \alpha(\xi)$, $\gamma = \gamma(\xi)$ and $\nabla\alpha \wedge \nabla\gamma = \nabla\beta$, $\beta = \beta(\xi)$. Maxwell's equations are then reduced to first order elliptic form in a canonical (α , β , γ) domain. For a given $G(\alpha, \gamma)$ the author obtains integral solutions for the end and edge effects.

(d) Two dimensional studies. NASAR and del CID (1973a, 1973b) analyse a finite length SLIM for high speed ground transportation using the model of figure 1.7(b) and finite difference techniques. The theoretical results of paper (a) agree favourably with the computational solutions.

(e) Three dimensional studies. As far as we are aware, the only three dimensional analytic study of a FLIM configuration is that of OBERRETL (1973) for the DLIM. He takes the longitudinal and transverse edge effects, the end-winding field and the MMF harmonics into consideration. The rotor is of finite thickness and finite width. The magnetic permeability of the iron stators is taken as infinite enabling the magnetic field to be directly related to the MMF at the stator surfaces.

(f) DLIP design studies.

(i) No edge effects. WATT (1955, 1957) and ELLIOT et al (1965) consider one dimensional analyses and derive expressions for such quantities as the power developed, pressure head and efficiency.

BLAKE (1956) gives a general analysis of all types of EM pump - both induction and conduction. LIELPETER and TUTIN (1959) discuss the optimum dimensions for a DLIP and give expressions for edge effect and hydraulic loss factors. Apart from the compensating pole analysis of Elliot et al., all of the papers above treat an idealised DLIP where there are no end effects. ELLIOT (1969) discusses the effect of the number of slots, on the electrical efficiency of an MHD generator, comparing the calculated efficiencies with that of the ideal generator, $(1-S)^{-1}$.

(ii) With edge effects. Here the channel width is assumed to be that of the stator faces, allowing a Fourier representation in the transverse variations of the EM field. The papers of OKHREMENKO (1959, 1965a, 1965b) and VESKE (1965), besides considering the overall aspects of pumping, derive such quantities as the pressure attenuation factor and the demagnetisation coefficient. The longitudinal end effect is not included in the above analyses

(g) DLIP flow profiles. Apart from the work of HARRIS (1967) there seems to be no published work in the West on the velocity profiles induced in travelling wave MHD pumps and generators. Harris' solutions indicate the velocity profiles under a bilateral travelling wave excitation (case S) may be taken as those of ordinary d.c. Hartmann flow, provided we introduce a slip factor into the Hartmann number.

A large amount of work on this problem has been undertaken in the U.S.S.R. TROPP (1968, 1969) uses the matched asymptotic expansion technique to obtain (case P) solutions for the velocity field in a DLIP in inverse powers of the Hartmann number. PETROVICH and ULMANIS (1969) solve numerically, using a pursuit method, the non-linear system of MHD equations for the DLIP configuration. The papers of TKACHENKO (1970, 1972, 1973) are very important in that they produce second approximation analytic MHD solutions for the induced flow in a DLIP. Maxwell's equations are solved initially for a constant velocity stream and the Lorentz force produced

is substituted in the Navier-Stokes equations, which can be solved (under certain circumstances) to obtain the second approximation velocity profiles. The solutions contain the parameters S (slip) and Hm (Hartmann number) and averaging the profiles across the channel gives, after some manipulation, S = S(Hm). Thus MHD back reaction is included in the analysis. KIM (1970) shows how to calculate the induced magnetic field in a DLIM by constructing minimising sequences, using experimental velocity profile data, which are to be substituted in a functional form of Maxwell's equations.

All of the above papers consider velocity profiles induced by time averaged Lorentz forces in an idealised DLIP. MERKULOV et al. (1973) treat the periodic flow of an inviscid fluid in the channel and give a pictorial representation of the flow development from t=0. Finally TROPP (1972) treats the development of the flow when a viscous fluid moves into a finite length DLIP, by the singular pertubation method, but the analysis is extremely complicated. It should be noted that TROPP does not actually give the flow development in the entrance region of the DLIP, but merely shows how it may be found.

Harris' observation on the similarity of DLIP flow to Hartmann flow is not reiterated by the Russian authors.

(h) Miscellaneous. An experimental study of a DLIM has been performed by VASIL'EV et al (1965), who conclude that an assumption of plane parallel EM field in the gap can produce reasonable results. A complete discussion of the physical, electrical and hydraulic aspects of the DLIP are given in the books of LIYELPETER (1966) and VOLDEK (1970) whilst the physical and electrical aspects of the DLIM are given in LAITHWAITE (1966) and YAMAMURA (1972). Yamamura's book is a 'state of the art survey' of Japanese publications. There have been many symposia on MHD (for example, SALZBURG, 1966 and RIGA, 1972) and further references may be found in their proceedings.

1.8 Coplanar Flow with Constant Applied Magnetic Fields

Throughout we deal with steady state phenomena and simplified MHD flow. No consideration is given here (and to our knowledge, elsewhere) on the stability of the flow, the flow development and decay with time or the entrance and exit flow profiles in a finite excitation induction pump. However, there has been a great deal of work on the above topics in constant applied magnetic field (Hartmann-type) flow, and for completness we include a brief survey of these approaches. We shall confine the review to the author, method of analysis and assumptions made.

(a) Stability. STUART (1954; parallel field), WOOLER (1961; non-parallel field), LOCK (1955; transverse field - Hartmann flow), CHEN and EATON (1972; parabolic inlet profile, asymptotic form agrees with LOCK), C. WANG (1974; free surface).

(b) Flow development. ERASLAN (1967; parabolic profile at t=0, Laplace/Fourier transform analysis), SLOAN (1971, 1973) extends a particular case of Eraslan's work, SNEYD (1972; vorticity study at switch on and switch-off)

(c) Inlet profiles (finite fields). SHERCLIFF (1956; heuristic analysis, inviscid flow), SUTTON and CARLSON (1961; perturbation study, conformal mapping of entrance region),HWANG and FAN (1963; finite difference, uniform inlet profile), YUFEREV (1967; boundary layer analysis, Blasius inlet profile). A new method of hydrodynamic inlet profile analysis between parallel planes was formulated by SPARROW et al. (19) based on a linearisation of the inertia terms using a stretched axial coordinate. The following authors have applied this analysis to MHD inlet problems: SNYDER (1965; constant inlet profile),CHEN and CHEN (1972; parabolic inlet profile). HWANG et al. (1966) use a finite difference approach for a uniform inlet profile.

References to analyses of MHD channel flow are given in the reviews of RYABININ and KHOZHAINOV (1969), HUNT and SHERCLIFF (1971) and LIELAUSIS (1975). An interesting paper by TODD (1966) gives precise conditions which distinguish between the Hartmann flow MHD generator, EM pump,EM brake and MHD accelerator.

2. A MAGNETOHYDRODYNAMIC EXPERIMENT

2.1 The Experiment

A model, designed* to analyse the effect of linear induction motors upon liquid tin, was used to obtain flow profiles for mercury (liquid at room temperature), under the Lorentz force produced by a linear induction motor placed $\frac{1}{4}$" above the mercury's free surface (plate 2.1).

The model (figure 2.1) consisted of an oval channel (7" wide) with perspex base and sidewalls (electrically non-conducting) allowing a depth of $1\frac{1}{2}$" of mercury. (Total weight : 155 Kg, 3 cwt.) The flow profiles were measured at stations (a) - (k), (1) - (7), using a pitot tube/bulb manometer/microammeter system, which measured the total head (Bernoulli) pressure. Results were subsequently corrected for internal fluid pressure using a pitot-static arrangement.

The three laminated iron teeth of the motor (figure 2.2) were each wound with a coil consisting of seven turns of insulated, water cooled copper tubing, overlapping the width of the iron core at each end. A three phase mains frequency supply used in conjunction with a Berco rotary regavolt (type number 121 AG 3E; 0-440V output at 25 A) and a Transformer (type number P.1352; 6.25KVA), gave a power of 2.25KW from a current of 250A at an E.M.F. of 10V. The travelling magnetic field produced had a wavelength twice the length of the motor, and effectively (because of the relative dimensions of channel and motor width) had no component across the width of the channel.

2.2 Results

A film of oxide and dust repeatedly formed on the mercury surface reducing the surface speed to zero. In order to perform the experiment we had to frequently clean the mercury, which interrupted the recording of measurements. Other difficulties included the variation in room temperature, and the leakage of air through the sealed joints in the recording apparatus.

* Designed by M.Abrams, Models Laboratory, Pilkington Bros., St Helens.

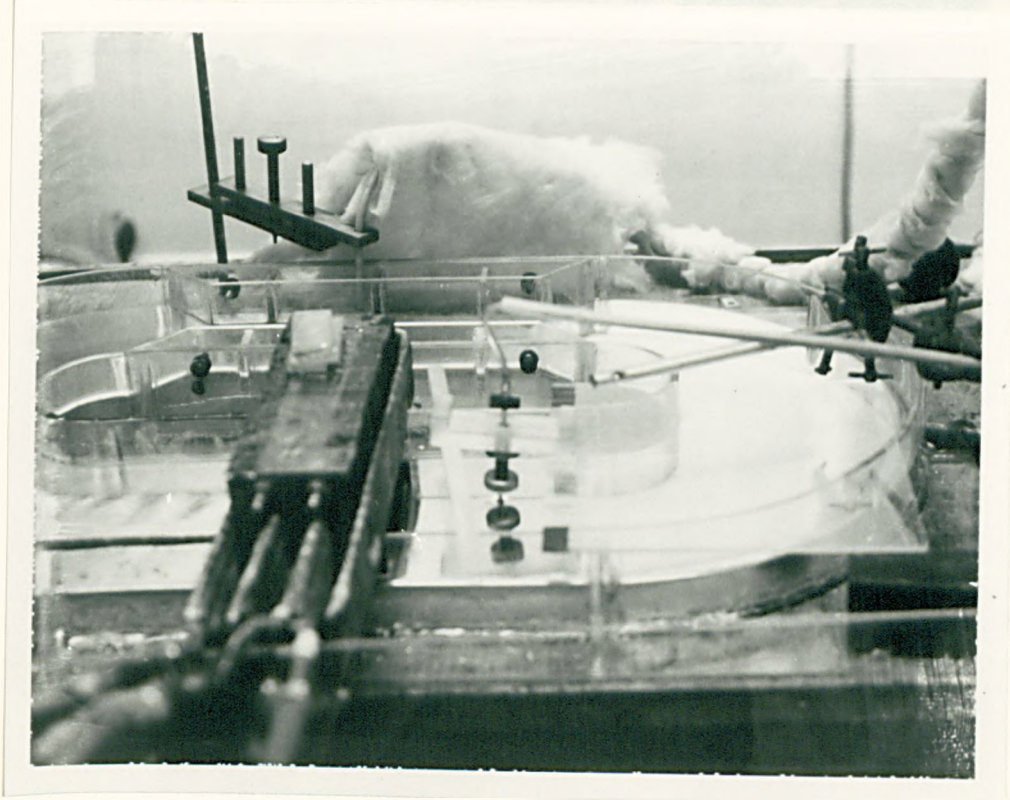

Plate 2.1 The Model

Plate 2.2 The Near Channel (Downstream)

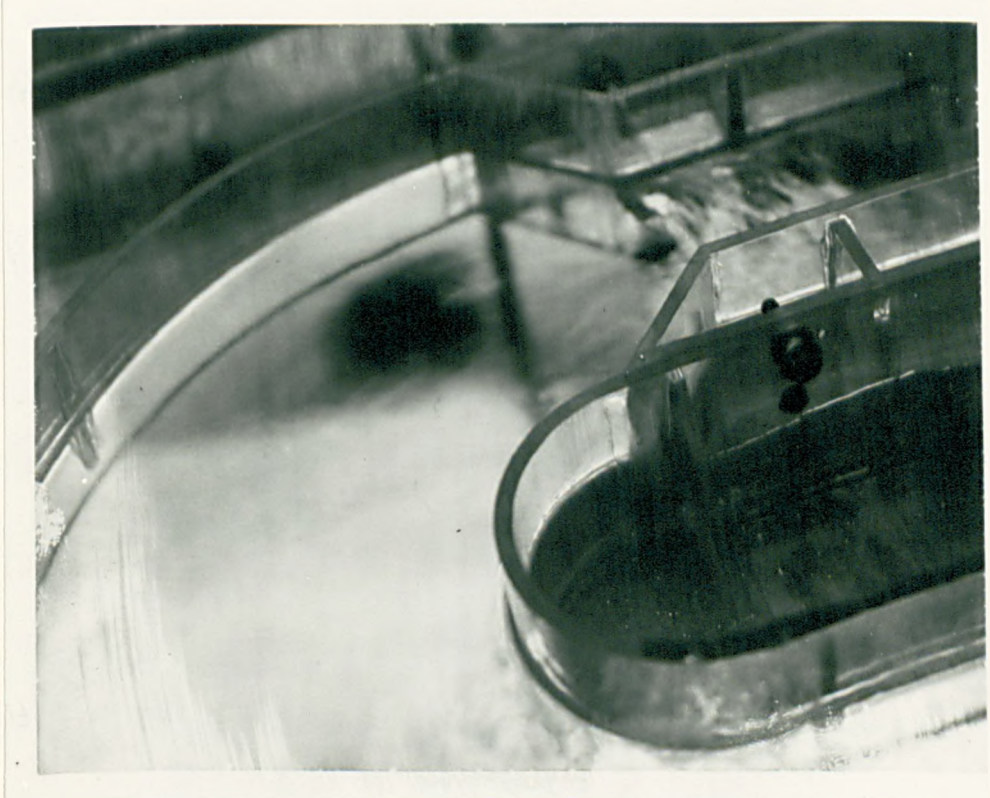

Plate 2.3 The Far Channel

The mercury was quite turbulent throughout the near channel flow (less turbulent in the far channel), and this was indicated by the variable readings of the microammeter, which measured the total head pressure in inches of water. Thus to obtain velocity profiles, the readings were effectively 'time-averaged'; the error involved in the profiles, relative to the mean (time-averaged) velocity, is +30% at 2"/sec and ± 7% at 10"/sec.

The effect of the motor on the fluid when the power was turned on was immediate: a streaming of fluid downstream of the motor appeared to produce a slowly moving wave which returned around the channel until the motion settled to a mean steady state with approximately zero pressure gradient. All readings were taken in this mean steady state of motion.

Depth profiles across the near channel are shown in figures 2.3. and 2.3a. The progression of the fluid beneath the motor is clearly shown by a comparison of profiles at stations (c) and (d). Turbulent flow effects (eddies, vortices) produced unreliable results (dashed lines indicate possible profiles), and the effect of the channel walls can be clearly seen by the small velocities recorded at stations 1 and 7. All profiles show a hydrodynamic boundary layer of thickness $\delta < \frac{1}{12}$ mercury depth. (Taking a typical velocity and length as 10"/ sec and 15" respectively, the theoretical boundary layer thickness $\left(\delta = \frac{\nu \ell}{U}\right)$ is $o(\frac{1}{16})$ mercury depth). The flow into the motor is more or less uniform with depth along the outside (more 'laminar') region of the upstream channel.

Figure 2.4 illustrates the near-surface velocity profiles and the visual effects of the surface motion, with dashed lines indicating the probable profiles. The downstream flow was definitely not purely normal to the motor face: the mercury was streamed in the direction shown by the arrows, producing a vortex which moved as indicated. There was some backflow near the inside edge of the channel, below the input side of the motor - probably caused by the non-symmetric flow into the motor, local eddy flows, and the unbalanced windings (see table 2.3). The unbalanced

windings produce backward travelling EM waves which oppose the motion. (see §1.5 and plates 2.2, 2.3)

Approximate flow rates were calculated from the root mean square velocity at each station (Table 2.1), including station (k), (figure 2.5) in the far channel. Although results for the latter are more accurate than those elsewhere (due to less turbulence because of the aligning of the flow from the angle pieces), the flow rate calculated is not necessarily an exact indication of the efficiency of the motor. The true flow rate produced by the motor in the steady state is likely to lie near the downstream flow rate, with local circulation accounting for a large part of the difference.

When copper strips were placed along the side walls beneath the motor and short circuited, thereby allowing return flow of electric currents (conductivity of copper >> mercury) and thus an increased Lorentz force, the flow rate increased (in the far channel) by 16%. Time did not permit the measurement of near channel profiles for this case.

Table 2.1 Flow Parameters

Station	RMS Velocity "/s cm/s	Volumetric Flow Rate litre/sec	Mass Flow Rate Kg/sec
(a)	4.04 10.26	0.69	9.5
(b)	3.69 9.37	0.63 Av. 0.65	8.6 Av. 8.9
(c)	3.70 9.40	0.64	8.7
(d)	4.80 12.19	0.83	11.3
(e)	5.04 12.8	0.87	11.8
(f)	5.25 13.34	0.90 Av. 0.88	12.2 Av. 12.0
(g)	5.10 12.95	0.88	12.0
(h)	5.3 13.46	0.91	12.4
(j)	5.21 13.23	0.90	12.2
A (k)	5.2 13.21	0.45	6.10
B (k)	5.96 15.14	0.51	7.00 +16%

The magnitudes of the magnetic induction components $\mathcal{B}_1$ and $\mathcal{B}_3$ were estimated using a search coil / oscilloscope system. The standing waves obtained on the oscilloscope screen were photographed (with Polaroid film) and the height of each wave was measured from the subsequent photographic image (with an error of approximately 5%). Unfortunately we did not have access to instruments with which the absolute magnitudes of the components could be measured so the results in figures 2.6 and 2.7 have been made dimensionless, taking $\mathcal{B}_3$ at the surface ($z=0$) of the mercury, below the centre of the end tooth, as the scale magnetic field. The reduction in magnitude (figure 2.6) of $\mathcal{B}_3$ with distance is large (90% fall in 2.5 inches) whilst the fall in $\mathcal{B}_1$ is more gradual (about 60% fall in 2.5 inches). We also found that the normal magnetic induction was the dominant component

Table 2.2 Physical Parameters

Channel width	7in (178mm)	Coil span (c_p)	0.81in (20.6mm)
Mercury depth (L)	1.5in (38mm)	Turns per phase	7
Motor length / Channel length	1 / 5	Number of poles	2
Stator length	2.75in (70mm)	Electrical conductivity mho/m	
Tooth width	0.5in (12.7mm)	σ_m Mercury (20°C)	1.05×10^6
Tooth gap	0.635in (15.9mm)	σ_c Copper	5.8×10^7
Tooth height	3in (76mm)	Density Hg(20°C)	=13.55gms/cc
Maximum velocity (V)	10in (25.4cm)/sec	Viscosity Hg(20°C)	=0.00155poise
Winding current (I)	250 A	Reynolds number $R_e = \rho\frac{VL}{\nu}$	=85000
Power supplied	2.25 KW	Magnetic Reynolds Numbers	
Supply frequency	50 Hz	$R_{mp} = \mu_o\sigma_m V L$	=0.073
Angular frequency (ω)	100π rad.	$R_m = \mu_o\sigma_m V_s L$	=0.23
Pole pitch (τ)	1.8 in (46mm)	Skin depth $\delta = (\mu_o\sigma_m\omega)^{-1/2}$	=3.46cms
Wave number (α)	$1.75\,in^{-1}(6.83.10^{-2}mm^{-1})$	Exponential decay factor	= 1.12.z
Wave speed ($V_s = \omega/\alpha$)	4.6 m/sec		

close to the FLIP; in fact we have $|\mathcal{B}_2| \sim 3.5\,|\mathcal{B}_1|$ at the stator edge. The measured variation of $\mathcal{B}_3$ with depth (figure 2.7) is indicative of an exponential decay and we estimate the decay factor to be approximately $1.8z$ where z is the dimensionless ordinate pointing away from the mercury, (the scale length for the system is taken to be the depth of mercury). However, this factor is quite different from the theoretical factor

Table 2.3 Electrical Data

OVER MERCURY

PHASE	RED	BLUE	YELLOW	NEUTRAL	
Voltage (v)	2.9	4.4	3.9	To neutral	
Power (KW)	.13	.82	.64		Total 1.59 KW
Current (A)	290	240	165	120	
KVA	.841	1.056	.644		
Power factor (KW/KVA)	.1546	.7765	.9945		

OVER AIR

PHASE	RED	BLUE	YELLOW	NEUTRAL	
Voltage (v)	2.9	4.4	3.9		
Power (KW)	0.1	.82	.65		Total 1.592 KW
Current (A)	290	235	170	155	

COOLING WATER

	TEMPERATURE ^{o}C			VOLUME OF FLOW (Q cm^3)	TIME OF FLOW (t secs)	POWER SUPPLIED
	IN	OUT	$\Delta\theta$			
Over Mercury	15.6	48.9	33.3	4×10^3	350	1600 W
Over Air	14.5	47.6	33.1	4×10^3	338	1600 W

(value 1.1) obtained using the physical data in table 2.2. The difference is largely due to the curvature of the magnetic field lines at the edges of the SLIM which decrease the skin depth of the induced EM field (see §6.3) Some electrical data (collected by S. WOLFENDEN) is given in table 2.3.

It is clear from the power data that the windings are very unbalanced and it is likely that a strong backward-travelling wave was produced by the SLIP (see § 1.5). This wave would produce a force opposing the flow which perhaps explains the occurrence of backflow underneath face 1 in figure 2.4. The heat absorbed by the cooling water was measured using a standard thermometer and the figures obtained give a reasonable indication of the power ($=4.2 \times \Delta\theta \times Q/T$ Watts) supplied to heat the water. Using (3.34), which is an expression for the total resistance of the copper windings we find the power loss from the windings (I^2 x resistance) to be of a similar value. Comparing the active power ($\sim$1.59 KW) with the heat loss we conclude that most of the power supplied is dissipated in the form of heat and that the SLIP operates on a very low efficiency. This latter conclusion is verified by consideration of the mercury flow. Following a streamline from face 1 to face 2 of the SLIP we can obtain an expression for the average pressure drop (ΔP) across the stator, viz: $\Delta P = \rho (V_2^2 - V_1^2)/2g$, where V_2 and V_1 are the average velocities at face 2 and face 1 respectively and g is the gravitational acceleration, (9.8 m/sec). The power required to maintain the average flow rate Q across the stator is $Q\Delta P$ where $Q \sim (0.88 - 0.65)$ litre /sec, (from table 2.1) Using the data of tables 2.1 and 2.2 we find this power is approximately 0.001 W; the electrical efficiency of the SLIP is thus extremely small. Applying Newton's second law (force = mass x acceleration) to the data in table 2.1 we estimate the force developed by the SLIP is 270 N/m^3 .

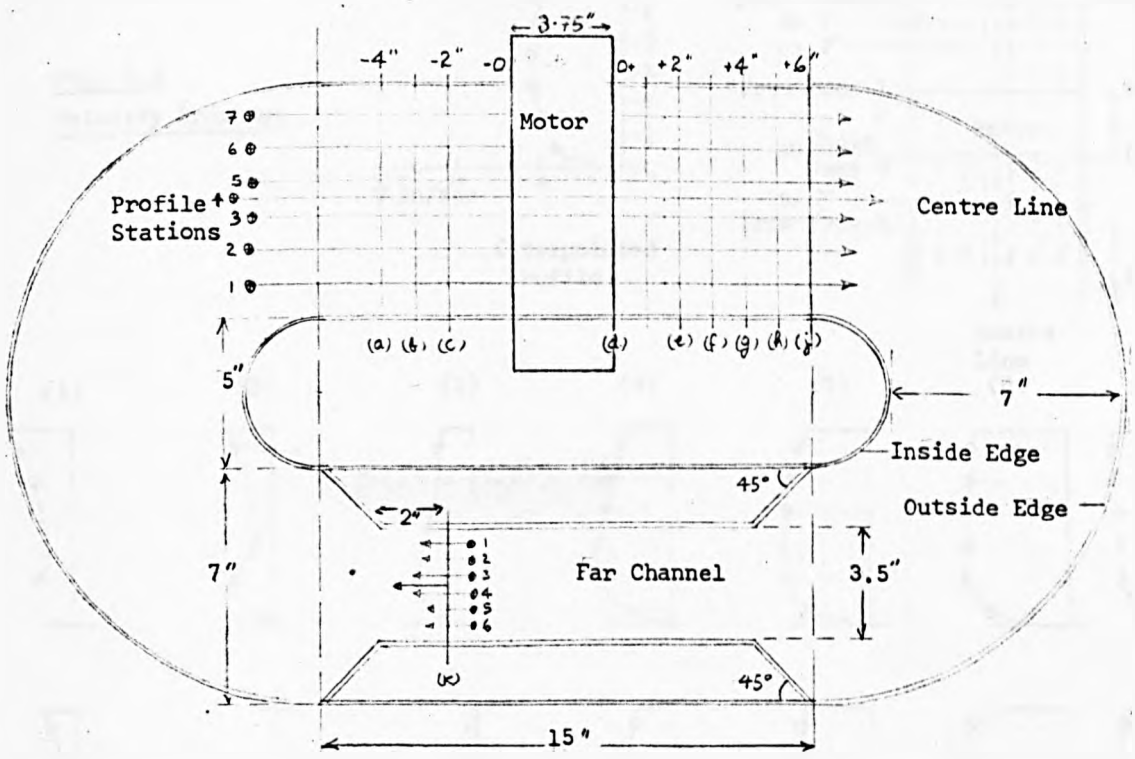

Fig. 2.1 The Model

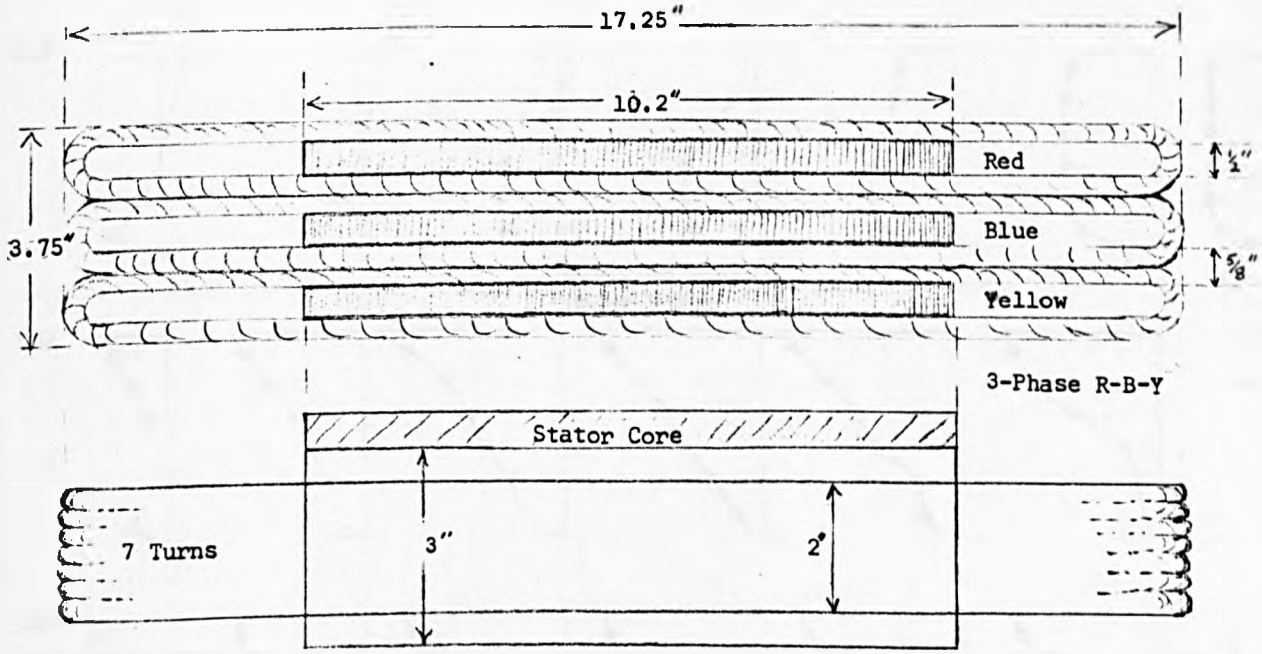

Fig. 2.2 The Motor

Fig. 2.3
Velocity Profiles

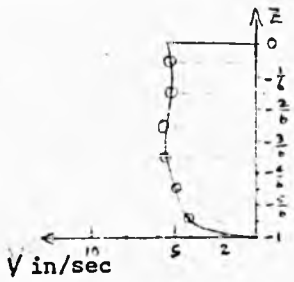

---- Extrapolated Profile

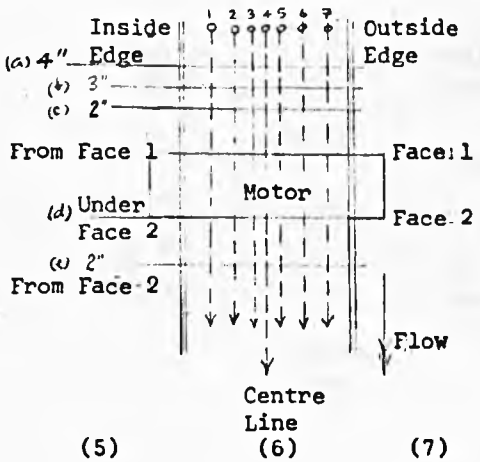

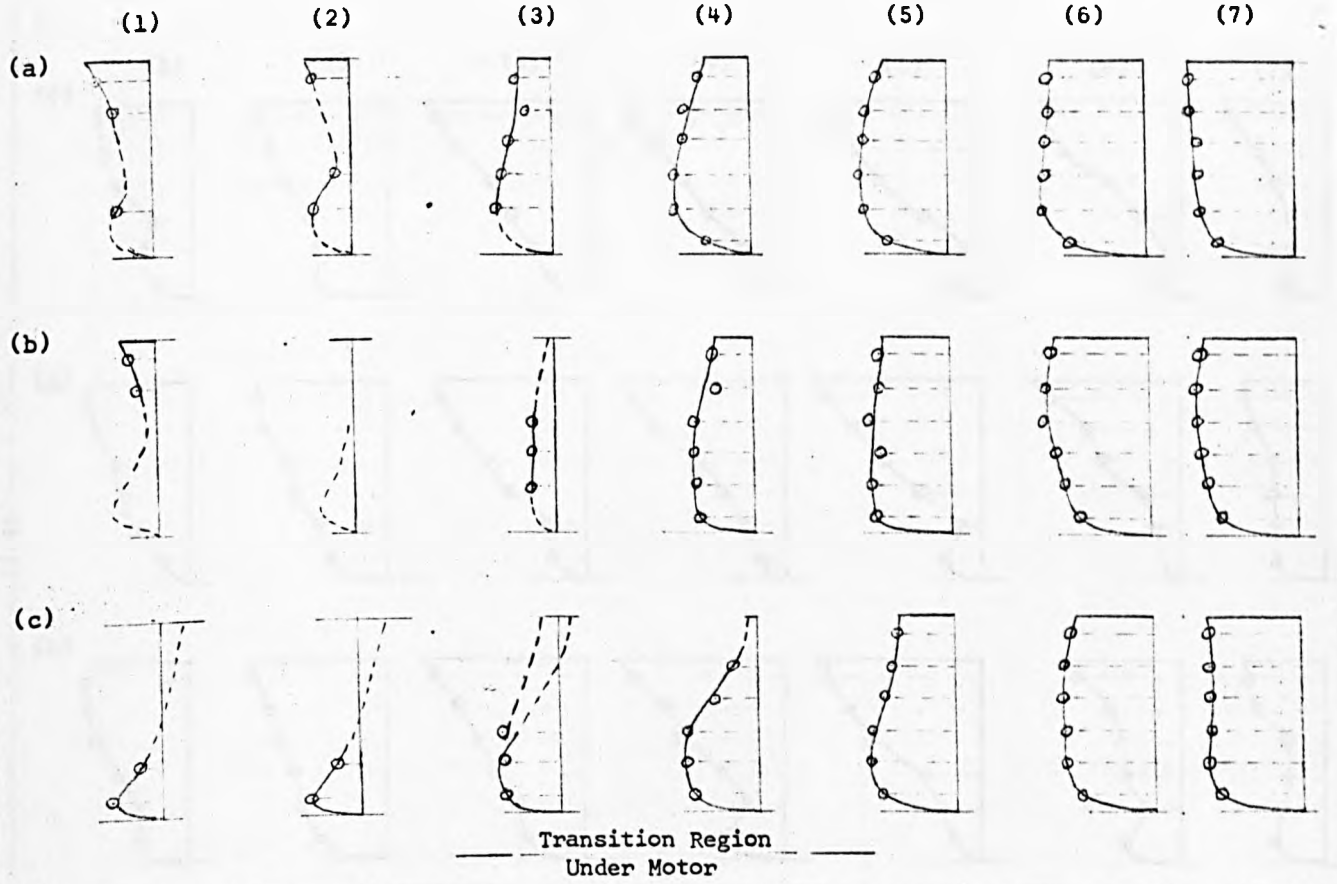

Fig. 2.3(a)
Velocity Profiles

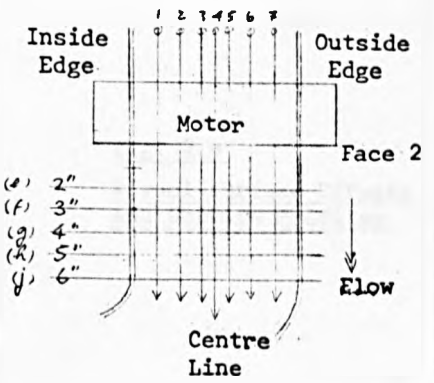

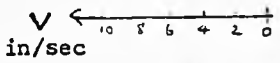

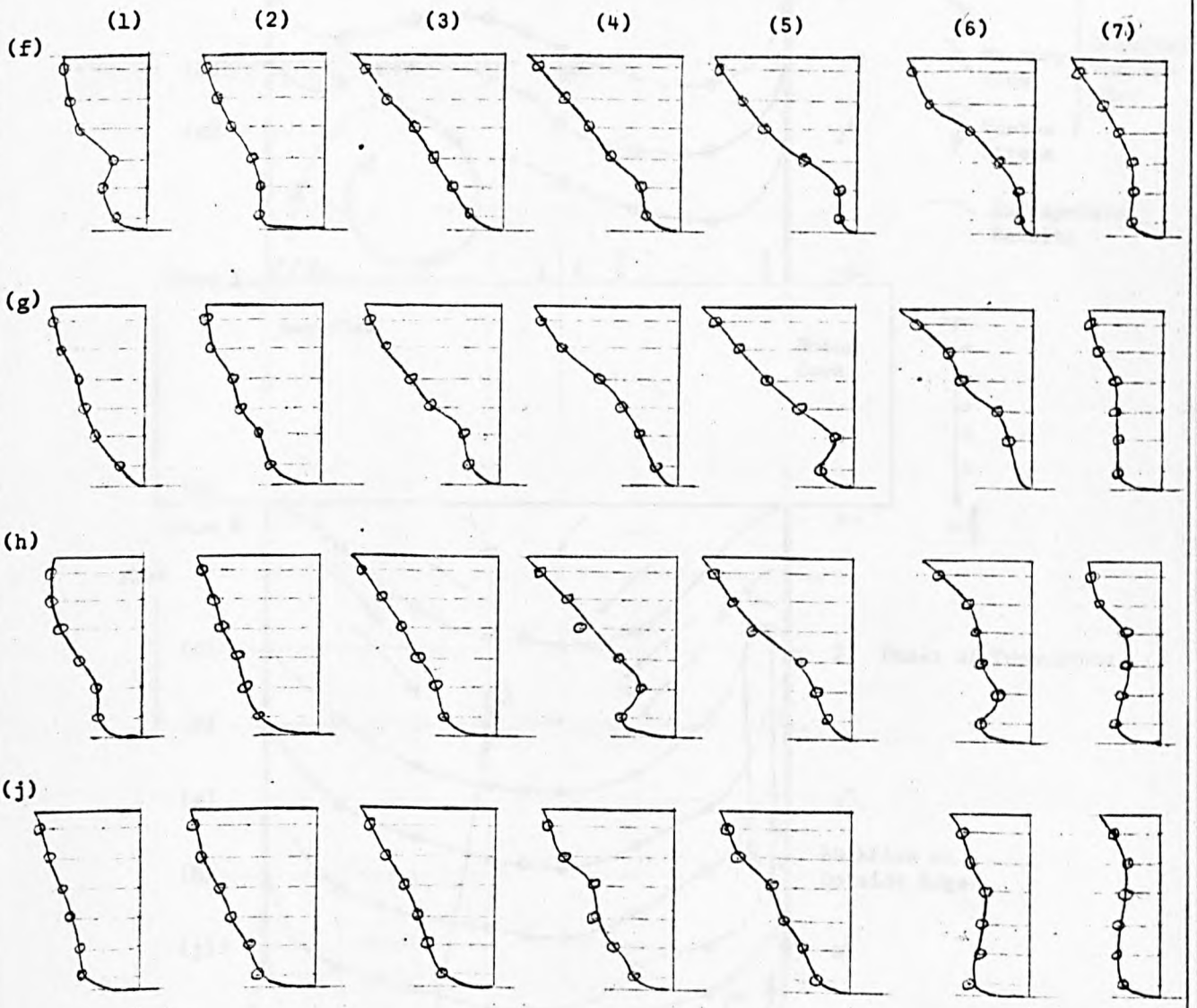

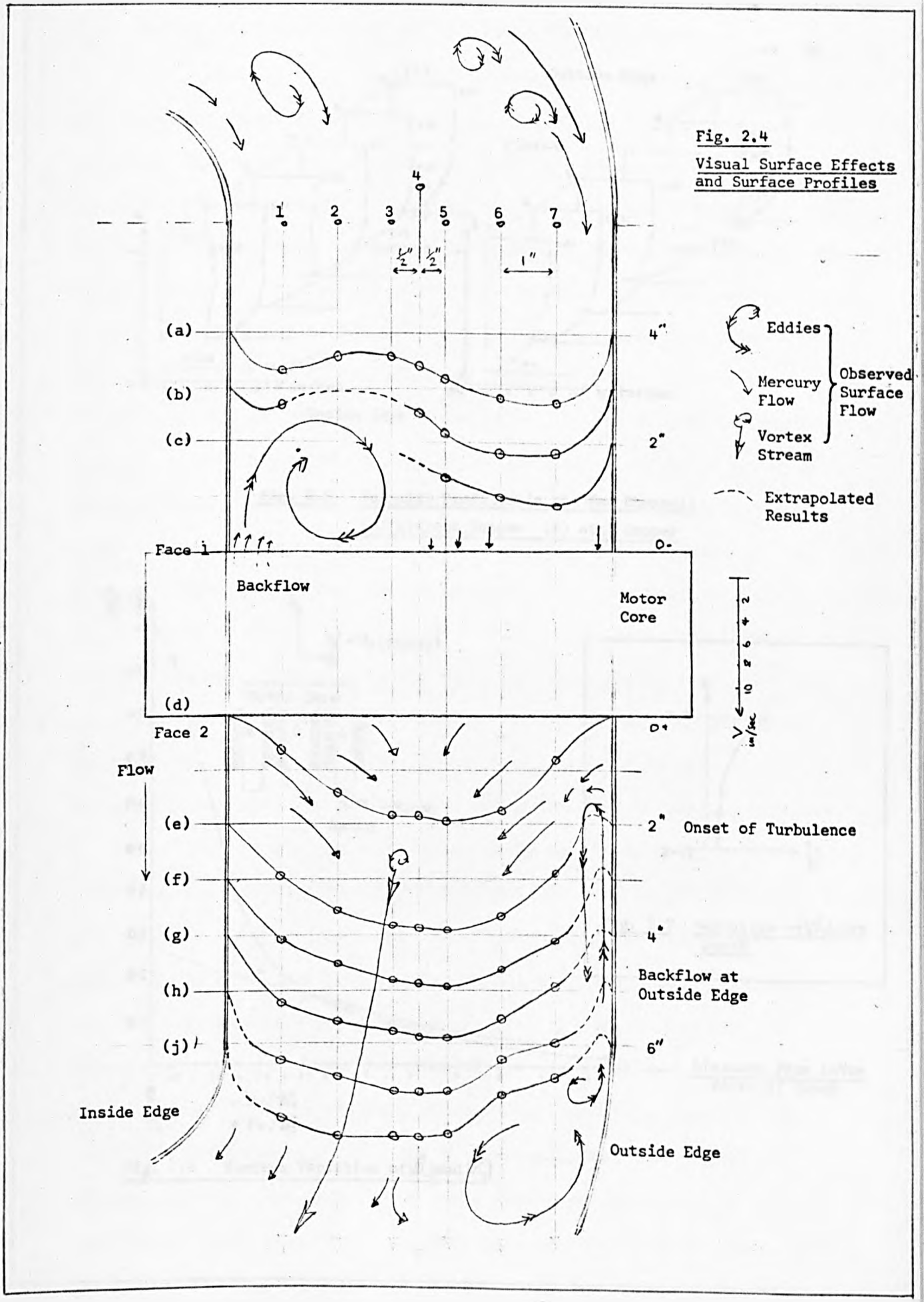
Fig. 2.4
Visual Surface Effects and Surface Profiles
4
1
2
3
5
6
7
½"
½"
1"
(a)
(b)
(c)
4"
2"
0"
Eddies
Mercury Flow
Vortex Stream
Observed Surface Flow
Extrapolated Results
Face 1
Backflow
Motor Core
(d)
Face 2
V in/sec
Flow
(e)
(f)
(g)
(h)
(j)
2"
Onset of Turbulence
4"
Backflow at Outside Edge
6"
Inside Edge
Outside Edge

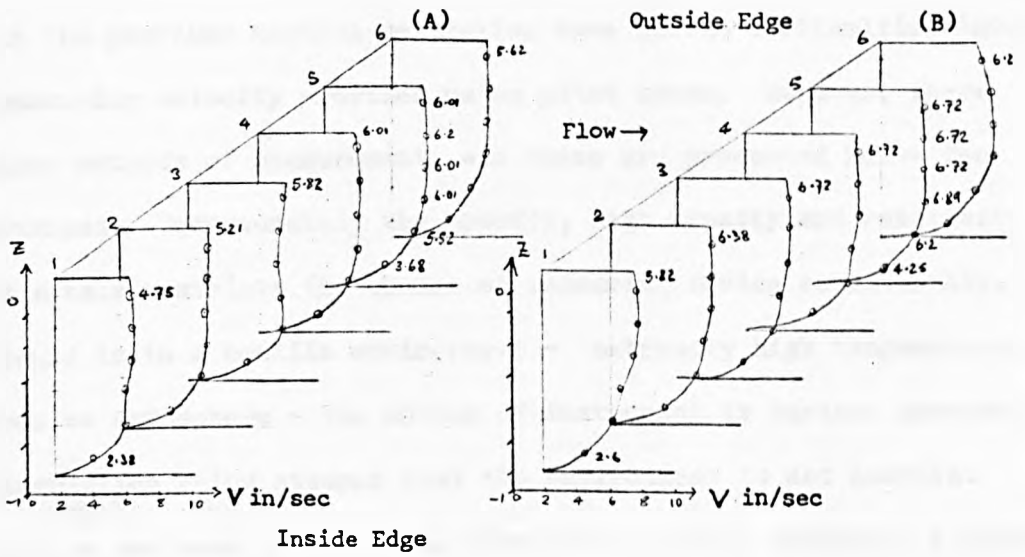

Fig. 2.5 Velocity Profiles in the Far Channel:
(A) without Copper (B) with Copper

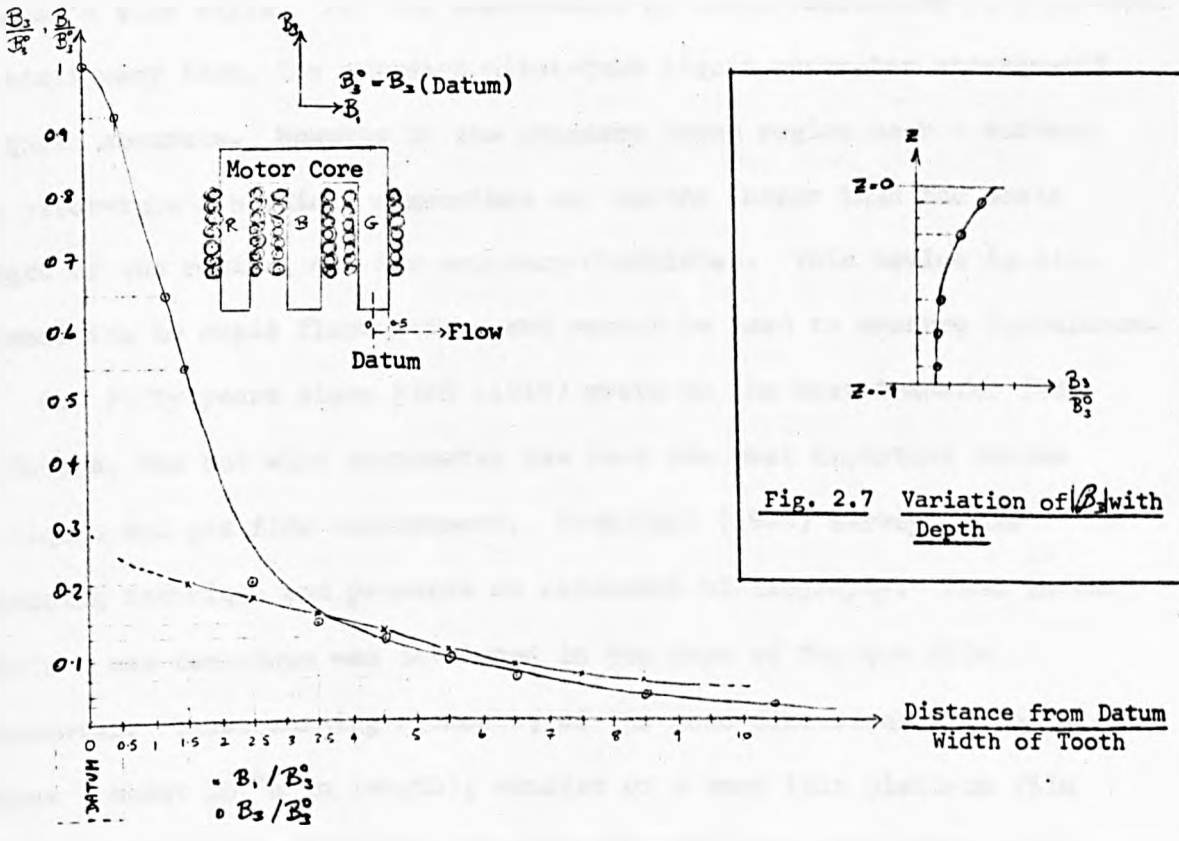

Fig. 2.6 Surface Variation of $|B_1|$ and $|B_2|$

Fig. 2.7 Variation of $|B_3|$ with Depth

2.3 The measurement of liquid metal velocity profiles

In the previous section we mention some of the difficulties involved when measuring velocity profiles using pitot tubes. However, there are other methods of measurement, and these are presented below for completeness. Unfortunately the opacity, high density and reactivity of liquid metals restricts the choice of measuring device considerably. If the liquid is in a hostile environment - extremely high temperatures or a corrosive atmosphere - the choice of instrument is further narrowed. The description below assumes that the environment is not hostile.

For an estimate of the local flow rate a device called an electromagnetic flowmeter (SHERCLIFF, 1962) may be used. A constant magnetic field is applied across the channel or pipe and fluctuations in the induced currents are recorded through conducting plates placed on the channel's side walls. For the measurement of large velocities ($V > 0.05$m/s) in stationary flow, the standard pitot-tube liquid manometer arrangement is quite accurate. However in the boundary layer region near a surface the pitot-tube's physical dimensions may become larger than the scale length of the region, and its accuracy diminishes. This device is also insensitive to rapid fluctuations and cannot be used to measure turbulence.

For fifty years since KING (1914) wrote on the heat transfer from cylinders, the hot wire anemometer has been the most important device in liquid and gas flow measurement. KOVASZNAY (1965) surveys this measuring technique and presents an extensive bibliography. Then in the 1950's a new technique was developed in the form of the hot film anemometer. These sensing elements, of the same dimensions as the hot-wire probes (about 10^{-4}m in length), consist of a very thin platinum film fused to a glass surface (LING and HUBBARD, 1956 and LING 1960), but are more accurate than hot wire sensors when used for liquid or high temperature supersonic flow. The principle of both types of sensor is the same - the transfer of heat from the probe surface to the moving liquid.

The hot-wire and hot-film devices work in two modes of operation. If the heating current of the wire is kept constant and the variations in sensor temperature are recorded as voltage drops across the sensor, then this is called the constant current operation. The second mode of operation, the constant temperature mode, is when the sensor temperature is kept constant, and fluctuations in the heating current are recorded. For a comparison of the two types of sensors and their modes of operation, see WASSERMAN and GRANT (1973) and the DISA Probe Manual. Unfortunately liquid metals tend to react with probe surfaces - both chemically and electrically. For early work with mercury see SABJEN (1965) and MALCOLM (1968), who deal with hot-wire and hot-film probes respectively. The high conductivity of the mercury can also lead to local MHD effects: interactions between the current carrying sensors and the immediate environment produce induced currents which can modify the liquid motion around the probes (MALCOLM , 1970).

After the completion of the experiment described in this chapter an opportunity was provided for further work of a more accurate nature. We had planned to set up a model of the plant conditions. A FLIM was to be placed above a bath of liquid mercury and the three dimensional velocity profiles were to be measured using a hot-film probe. Unfortunately, the expense involved in the purchase of the probes from DISA was too large for our budget and the proposed experiment was cancelled. For completeness we have included the address of DISA in the bibliography. As far as we know they are the only suppliers of hot-film and hot-wire measuring equipment in this country.

3. THE SINGLE SIDED FLAT LINEAR INDUCTION PUMP

3.1 Introduction

Here we obtain expressions for the EM field induced in an electrically conducting half space by a SLIM placed on its surface. These expressions are used to obtain estimates for the electrical and mechanical characteristics of a SLIP.

As we have indicated in chapter one, the idea of imposing a travelling wave along the surface of a conductor to model an induction motor is not new. In this sense, our solutions to Maxwell's equations given below, are not original. However, to our knowledge,our subsequent analysis of the variation of the EM field and our analysis of the SLIP, is new.

We assume the half space moves with a constant velocity parallel to the direction of travel of the SLIM excitation. Consideration is given to the series-wound and parallel-wound excitations and we discuss their different properties. The Lorentz body force acting on the half space is derived and then substituted in the Navier-Stokes equations which govern fluid flow. An exact, stationary solution, for both the fixed and free surface boundary conditions, is possible provided we assume no vertical fluid motion occurs. Using an approximate analysis we discuss the effect of a surface shear stress on the induced velocity profiles.

Combining the expressions for the induced EM field and the velocity profiles induced by the Lorentz force gives a first approximation for the MHD action of a SLIP. A second approximation is made, obtaining the slip as a function of the Hartmann number, by successive iteration. Because all solutions are obtained as a function of the slip - and therefore the Hartmann number - the characteristics of a SLIP are analysed in this context.

3.2 The Induced Electromagnetic Field

Figure 3.1 illustrates the simplified model of a SLIM used in the following analysis. Cartesian coordinate axes are chosen with origin on the interface between regions I and II with the z axis pointing vertically

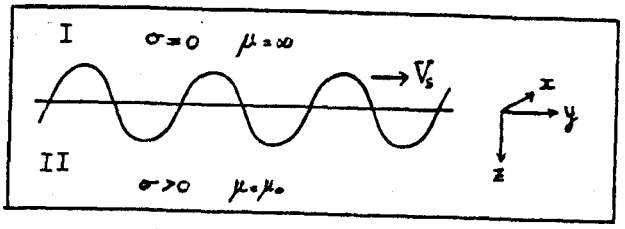

Fig 3.1 An Idealised FLIM

downward. Region I represents the stator core of the SLIM and is taken to be of zero conductivity and infinite magnetic permeability. Region II ($z > 0$) is an electrical conductor with magnetic permeability equal to that of free space, μ_0. We assume that a travelling wave excitation of the form $e^{i(\omega t - \alpha y)}$ is specified along $z=0$ and that $B_t = 0$ there. We further assume the induced EM field is also of the travelling wave form and write

$$\underline{B}(\underline{r},t) = B(z)\, e^{i(\omega t - \alpha y)} \qquad \underline{J}(\underline{r},t) = J(z)\, e^{i(\omega t - \alpha y)} \qquad \underline{E}(\underline{r},t) = E(z)\, e^{i(\omega t - \alpha y)} \tag{1}$$

where only the real parts of $\underline{B}$, $\underline{J}$ and $\underline{E}$ have physical significance. For boundary conditions we choose the case S, (1.47), and case P, (1.48), excitations on Z=0 and impose damping as $z \to \infty$. The half space $z > 0$ is assumed to move with a constant velocity

$$\underline{V} = [0, V, 0] \tag{2}$$

Substituting (2) in Maxwell's equation (1.11) and simplifying, using (1), we obtain the induction equation in region II:

$$\frac{d^2\underline{B}}{dz^2} = \left\{ \alpha^2 + i\left(\frac{\omega}{\eta} - \frac{\alpha V}{\eta}\right) \right\} \underline{B} \tag{3}$$

We now introduce a scale length h (the molten tin depth) and introduce the dimensionless variables $y^* = y/h$, $z^* = z/h$ and $\alpha^* = \alpha h$. All references to y, z and α from here onwards refer to their dimensionless forms but we shall ignore the star superscripts for convenience. Thus (3) becomes

$$\frac{d^2\underline{B}}{dz^2} = 4^2 \underline{B} \tag{4}$$

where $$\psi^2 = \alpha^2 (1 + i s R_m) \tag{5}$$

Here $S = (V_s - V)/V_s$ is the slip, $R_m = h V_s / \alpha \eta$ is the magnetic Reynolds number and $V_s = \omega h/\alpha$ is the synchronous speed of the excitation. For an open magnetic circuit the magnetic gap is $\pi h/\tau$ and Laithwaite's goodness factor (1.55) becomes identical to R_m. The solution to (4) may be written in the form $\underline{B} = \underline{C} e^{-\psi z}$ where $\underline{C}$ is a constant to be found. However, because B_1 is zero on $Z=0$, it is zero everywhere. For this problem Maxwell's equations (1.1) and (1.4) become respectively

$$\frac{dB_3}{dz} = i\alpha B_2 \tag{6}$$

$$\mu_0 h J_1 = -\left(i\alpha B_3 + \frac{dB_2}{dz}\right) \qquad J_2 = 0 \qquad J_3 = 0 \tag{7}$$

Writing $\psi = \psi_1 + i\psi_2$ it is easy to show that

$$\psi_{1,2} = \frac{\alpha}{\sqrt{2}} \left\{ (1 + s^2 R_m^2)^{1/2} \pm 1 \right\}^{1/2} \tag{8}$$

(a) Case S. Here $B_2(0) = \mu_0 K_s$ where K_s is the stator surface current density. The solution for $B_2(z)$ is easily shown to be

$$B_2(z) = \mu_0 K_s e^{-\psi z} \tag{9}$$

Substituting (9) in (6) we find

$$B_3(z) = -\left(\frac{i\alpha}{\psi}\right) \mu_0 K_s e^{-\psi z} \tag{10}$$

Substituting (9) and (10) in (7) we have

$$J_1(z) = \left(\frac{i\alpha^2 s R_m}{h\psi}\right) K_s e^{-\psi z} \tag{11}$$

Remembering only the real parts of $\underline{B}$ and $\underline{J}$ have physical significance we obtain for the induced EM field in II

$$\mathcal{R}\left\{ \underline{B}(z) e^{i(\omega t - \alpha y)} \right\} = \mu_0 K_s \cos\phi \, e^{-\psi_1 z} \underline{e}_2 + \mu_0 K_s \frac{\alpha}{|\psi|} \cos\left(\phi + \tfrac{3\pi}{2} - \theta\right) e^{-\psi_1 z} \underline{e}_3 \tag{12}$$

$$\mathcal{R}\left\{ \underline{J}(z) e^{i(\omega t - \alpha y)} \right\} = K_s \left(\frac{\alpha^2 s R_m}{h|\psi|}\right) \cos\left(\phi + \tfrac{\pi}{2} - \theta\right) e^{-\psi_1 z} \underline{e}_1 \tag{13}$$

where $$\theta = \tan^{-1}(\psi_2/\psi_1) \qquad \phi = \omega t - \alpha y + \psi_2 z \tag{14}$$

The Lorentz body force $\underline{F}$ is given by $\underline{F} = \mathcal{R}\{\underline{J}\} \wedge \mathcal{R}\{\underline{B}\}$, (1.28), and we obtain after a little manipulation (substituting for θ from (1.4))

$$\mathcal{F}_2 = \alpha Q_s e^{-2\psi_1 z}\left\{1 - \frac{\alpha^2}{|\psi|^2}\cos 2\phi - \frac{2\psi_1\psi_2}{|\psi|^2}\sin 2\phi\right\} \tag{15}$$

$$\mathcal{F}_3 = Q_s e^{-2\psi_1 z}\left\{\psi_2 - \psi_2\cos 2\phi + \psi_1 \sin 2\phi\right\} \tag{16}$$

where $Q_s = \mu_0 K_s^2 \alpha^2 s R_m / 2k|\psi|^2$ and $\mathcal{F}_1 = 0$. We note that the first terms of (15) and (16) are time independent - they correspond to the time-averaged Lorentz forces (§ 1.4.4).

Associated with the EM field is a skin depth δ where

$$\delta = \psi_1^{-1} \tag{17}$$

The force has a skin depth $\frac{1}{2}\delta$.

It is instructive to examine in finer detail the dependence of $\underline{\mathcal{B}}$ and $\underline{J}$ upon the slip and magnetic Reynolds number. We have assumed in the above analysis that K_s is constant. From (9) we see that $\mathcal{B}_2$ is also constant on $Z=0$. However examination of $\mathcal{B}_3$ and J_1 indicates that these quantities vary with s and R_m on the surface of the conductor. Denoting the magnitude of $\mathcal{B}_3$ and J_1 on $Z=0$ by $\mathcal{B}_m$ and J_o respectively, we see from (10) and (11) that

$$\mathcal{B}_m = \frac{\mu_0 K_s}{(1+s^2R_m^2)^{1/4}} \qquad J_o = \frac{\alpha K_s}{k}\cdot\frac{sR_m}{(1+s^2R_m^2)^{1/4}} \tag{18}$$

where we have written, using (8), $|\psi| = \alpha(1+s^2R_m^2)^{1/4}$. For $s \neq 0$ we find $\mathcal{B}_m = \mu_0 K_s$ and $J_o = 0$ when $R_m = 0$, as expected. When R_m is large we have $\mathcal{B}_m = O(R_m^{-1/4})$ and $J_o = O(R_m^{1/2})$. Thus for large R_m, the normal magnetic field disappears and the electric current density increases, apparently without bound. However, associated with an increase in R_m is a decrease in the skin depth (17) which forces the electric current to cluster near $Z=0$. The total current $\mathcal{J}^T$ below the surface of the conductor is found by integrating (11) from $Z=0$ to $Z=\infty$. We find

$$\mathcal{R}\{\mathcal{J}^T\} = K_s\cdot\frac{sR_m}{(1+s^2R_m^2)^{1/2}}\cos(\omega t - \alpha y + \pi/4 - 2\theta) \tag{19}$$

As $R_m \to \infty$, (14) gives $\theta \to \pi/4$ and we see from (19) that an induced surface current density appears, equal in magnitude and phase to the inducing stator

current, and demagnetisation of the induced field is complete.

The variation of $\mathcal{B}_m$ and J_0 together with the time averaged components of the body force, (15) and (16), as the slip varies, is shown in figure 3.2.

(b) Case P. Here $\mathcal{B}_3(0) = \mathcal{B}_m$, (1.48) where $\mathcal{B}_m$ is the peak normal magnetic induction. The solutions for $\underline{\mathcal{B}}(z)$ and $\underline{J}(z)$ can be found in a similar manner to those of (a). We obtain

$$\mathcal{B}(z) = \left(\frac{i\psi}{\alpha}\right) \mathcal{B}_m e^{-\psi z} \underline{e}_2 + \mathcal{B}_m e^{-\psi z} \underline{e}_3 \tag{20}$$

$$J(z) = -\left(\frac{\alpha s R_m}{\mu_0 h}\right) \mathcal{B}_m e^{-\psi z} \underline{e}_1 \tag{21}$$

Taking real parts we obtain

$$\mathcal{R}\left\{\underline{\mathcal{B}}(z) e^{i(\omega t - \alpha y)}\right\} = \frac{|\psi|}{\alpha} \mathcal{B}_m \cos(\phi + \tfrac{\pi}{2} + \vartheta) e^{-\psi_1 z} \underline{e}_2 + \mathcal{B}_m \cos\phi\, e^{-\psi_1 z} \underline{e}_3 \tag{22}$$

$$\mathcal{R}\left\{\underline{J}(z) e^{i(\omega t - \alpha y)}\right\} = \left(\frac{\alpha s R_m}{\mu_0 h}\right) \mathcal{B}_m \cos(\phi + \pi) e^{-\psi_1 z} \underline{e}_1 \tag{23}$$

Substituting for ϑ from (15) and using (1.28) we obtain the following expressions for the induced body force (with $\mathcal{F}_1 = 0$).

$$\mathcal{F}_2 = \alpha \Phi_m e^{-2\psi_1 z}\left\{1 + \cos 2\phi\right\} \tag{24}$$

$$\mathcal{F}_3 = \Phi_m e^{-2\psi_1 z}\left\{\psi_2 + \psi_2 \cos 2\phi + \psi_1 \sin 2\phi\right\} \tag{25}$$

where $\Phi_m = s R_m \mathcal{B}_m^2 / 2\mu_0 h$. The first terms of (24) and (25) correspond, as before, to the time averaged forces. The skin depth is as before, (17).

The case S solutions can be recovered by substituting for $\mathcal{B}_m$ using the first of (18). Here, however, $\mathcal{B}_m$ is held constant. We already know that the EM field is excluded from the conductor when $R_m \to \infty$ and the continuity conditions in this case would require $\mathcal{B}_m$ to be zero on $Z=0$. Examination of (20) on $Z=0$ apparently leads to a contradiction, because a discontinuity in $\mathcal{B}_3(z)$ occurs. However, this discontinuity has been imposed by us and does not appear from the solution of Maxwell's equations. Our analysis is thus correct provided $R_m \neq \infty$. We see from (20) and (21) that the magnitudes of $\mathcal{B}_2$ and J_1 on $Z=0$ are respectively

$$\mathcal{B}_0 = \mathcal{B}_m \left(1 + s^2 R_m^2\right)^{1/4} \qquad J_0 = \frac{\alpha s R_m \mathcal{B}_m}{\mu_0 h} \tag{26}$$

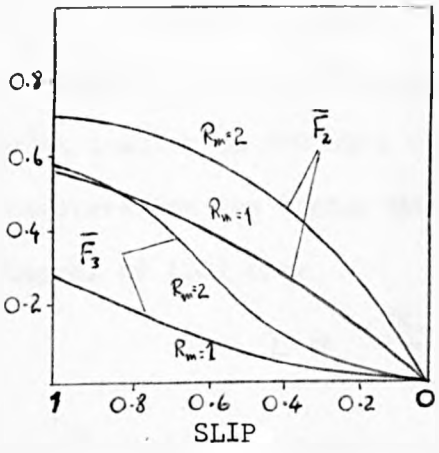

(a) FORCE : CASE S

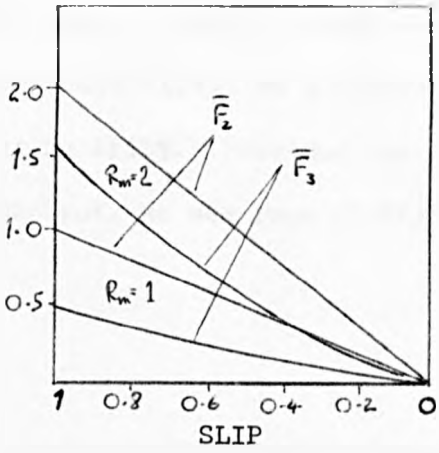

(b) FORCE : CASE P

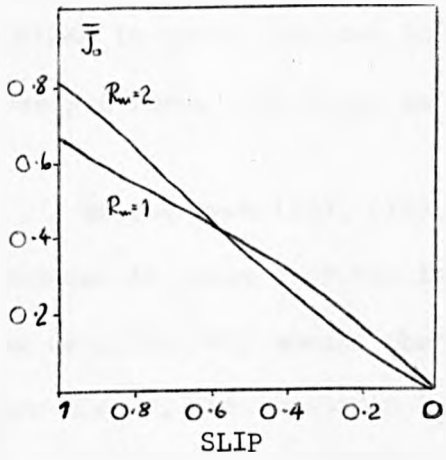

(c) CURRENT DENSITY CASE S

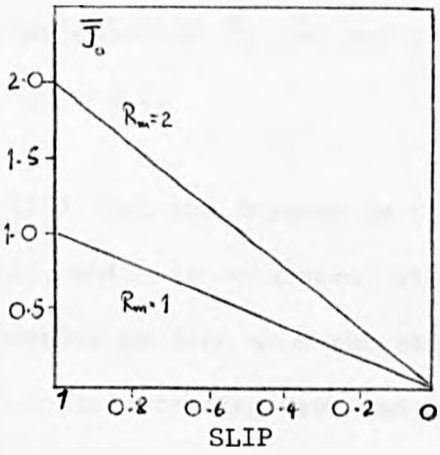

(d) CURRENT DENSITY CASE P

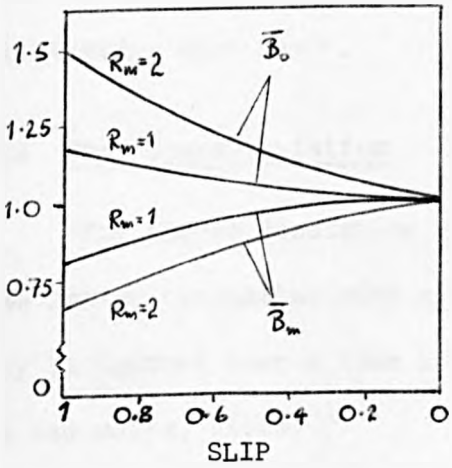

(e) TANGENTIAL FIELD ($\bar{B}_0$) CASE P
NORMAL FIELD ($\bar{B}_m$) CASE S

NOTATION	CASE S	CASE P
$\bar{F}_2$	$F_2/(\alpha\mu_0 K_s^2/2L)$	$F_2/(\alpha B_m^2/2\mu_0 L)$
$\bar{F}_3$	$F_3/(\alpha\mu_0 K_s^2/2L)$	$F_3/(\alpha B_m^2/2\mu_0 L)$
$\bar{B}_0$	---	B_0/B_m
$\bar{B}_m$	$B_m/\mu_0 K_s$	---
$\bar{J}_0$	$J_0/(K_s\alpha/L)$	$J_0/(\alpha B_m/\mu_0 L)$

Fig. 3.2 THE EM FIELD ON $\bar{z} = 0$ AS A FUNCTION OF SLIP AND MAGNETIC REYNOLDS NUMBER.

How is it possible to hold $\mathcal{B}_m$ constant when s and R_m vary? We answer this question by use of Ampéres circuital rule (1.49) on a circuit linking the excitation on Z=0 with the region at infinity. Provided the physical parameters for the stator MMF remain constant, we see from (1.46) and the integral of (20) that

$$I \propto \frac{\mathcal{B}_m}{(1+s^2 R_m^2)^{1/4}} \tag{27}$$

where I is the excitation current. To maintain the constant voltage operation with $\mathcal{B}_m$ constant, the load current through the stator windings must decrease with increasing s and R_m according to (27).

The time averaged components of the body force, (24) and (25), are similar to those obtained in (a). The variation of $\mathcal{B}_o$, J_o and the time averaged force with slip, is shown in figure 3.2.

We see from (12), (13) and (22), (23) that the induced EM field is advanced in phase over the inducing field, which is consistent with Lenz's law (§ 1.2). Why should the induced currents be zero when the slip is zero? When $S=0$, the conductor 'sees' a sinusoidal standing wave and it can easily be shown using Maxwell's equations that in this special case no electric currents are induced. This result indicates why the 'no load' condition ($S=0$) gives maximum efficiency - no mechanical work is expended and the ohmic losses are confined to the stator. Least efficiency will occur at starting when $S=1$.

3.3 Pump Characteristics

The forces consist of a time independent and time dependent component. The latter oscillates with a frequency twice that of the inducing field and may be ignored over a time interval greater than its period of oscillation. We can write, (1.29)

$$\underline{f}(y,z,t) = \underline{F}(z) + \underline{f}^t(y,z,t) \tag{28}$$

We shall work with the time averaged (§ 1.4.4) component of the force, $\underline{F}(z)$, in the following analysis of an idealised SLIP.

(a) The electromechanical power developed by the pump P_m is given by

$$P_m = \int_{VOL} E \cdot \underline{v} \, d(vol) \tag{29}$$

where $\underline{v}$ is given in (2) and (vol) is the volume swept by the SLIP in the fluid.

(b) The power loss from ohmic heating in the fluid, P_r, is given by

$$P_r = \frac{1}{2\sigma} \int_{VOL} \underline{J} \cdot \underline{J}^* \, d(vol) \tag{30}$$

where $\underline{J}$ is given in (11) and (21).

(c) The hydraulic power loss, P_h, may be estimated from the results for flow in a rectangular pipe of cross section A and length $2b$, equivalent to the volume swept by the SLIP, ($A = 2a\,h$ where $2a$ is the SLIP width). The pressure drop ΔP across the length of the SLIP is given by (BARNA,1969)

$$\Delta P = C_h \cdot \frac{2b}{D_e} \cdot \rho \frac{V^2}{2} \tag{31}$$

where C_h is the wall friction coefficient (friction factor), ρ the fluid's density and $D_e = 2A/(2a+h)$ is the equivalent diameter (the results are calculated on the basis of circular cross section). For smooth walls we may use Blasius' empirical relation, (R_e is the Reynolds number for the flow (1.24)),

$$C_h = 0.316 / R_e^{1/4} \tag{32}$$

which holds in the range $5\times10^3 < R_e < 10^5$. For larger Reynolds numbers ($5\times10^4 < R_e < 3\times10^6$) Kármáns relation is more appropriate and we have

$$1/\sqrt{C_h} = 2 \log_{10}(R_e \sqrt{C_h}) - 0.8$$

The hydraulic power loss $P_h = AV\Delta p$ and may be written in the form

$$P_h = \frac{1}{2} \rho C_h (2a+h) b \, (1-s)^3 u_s^3 \tag{33}$$

(d) The stray losses, P_s, account for primary copper loss, core loss, stray-load loss and the windage loss. ALGER (1951) gives the following formula for the primary copper loss

$$P_c = \frac{4.95 \, I^2 N^2 L_t}{10^6 \, C_1} \qquad \text{(at } 75^\circ\text{C)} \tag{34}$$

where I is the load current; N the turns in series per phase; L_t the mean

length of turn in inches; C_1 the total cross section of copper in the primary slots in square inches.

(e) The total power output is

$$P_t = P_m + P_r + P_h + P_s \tag{35}$$

(f) The electrical efficiency of the SLIP is

$$e = P_m / P_t \tag{36}$$

(g) The complex form of Poynting's Theorem may be used to calculate the power supplied to the fluid. We have

$$P_{ac} + i P_{re} = \int_S \frac{(\underline{E} \wedge \underline{B}^*)}{2\mu_0} \cdot \hat{n}\, dS \tag{37}$$

where P_{ac} is the active power ($P_{ac} = P_m + P_r$) and P_{re} is the reactive (oscillatory) power; S' is the surface of the contained fluid below the SLIP whose unit normal is $\hat{n}$. The electric field $\underline{E}$ is given by (1.8) and we have

$$\underline{E} = \frac{1}{\sigma} \underline{J} - \underline{V} \wedge \underline{B} \tag{38}$$

The true internal power of a machine is the RMS current x RMS voltage x power factor (pf), where the power factor (cos θ) is given by (M. HARRIS, 1967)

$$\cos\theta = P_{ac} / (P_{ac}^2 + P_{re}^2) \tag{39}$$

Performing the substitution in (a) and integrating, we obtain

$$P_m = \frac{C_s \cdot s(1-s) R_m}{(1+s^2R_m^2)^{\frac{1}{2}}\left[(1+s^2R_m^2)^{\frac{1}{2}}+1\right]^{1/2}} \quad (S); \quad \frac{C_p \cdot s(1-s) R_m}{\left[(1+s^2R_m^2)^{1/2}+1\right]^{1/2}} \quad (P) \tag{40}$$

where $C_s = \sqrt{2}\, V_s A \mu_0 K_s^2 L^2 / 4$ and $C_p = \sqrt{2}\, V_s A B_m^2 L^2 / 4\mu_0$. From (b) we obtain the ohmic loss as

$$P_s = \frac{C_s \cdot s^2 R_m}{(1+s^2R_m^2)^{\frac{1}{2}}\left[(1+s^2R_m^2)^{\frac{1}{2}}+1\right]^{1/2}} \quad (S); \quad \frac{C_p \cdot s^2 R_m}{\left[(1+s^2R_m^2)^{\frac{1}{2}}+1\right]^{\frac{1}{2}}} \quad (P) \tag{41}$$

For an idealised SLIP where winding and stator losses are negligible, (35), (36) and (40), (41) give for the idealised efficiency

$$e = 1 - s \tag{42}$$

Result (42) is the standard idealised efficiency for both rotary and linear induction machines. Further discussion on the efficiency of both compensated

and uncompensated pumps may be found in BLAKE (1956). Substituting (38) in (37) and performing the integration we find

$$P_{ac} = \frac{C_s \cdot sR_m}{(1+s^2R_m^2)^{\frac{1}{2}}\left[(1+s^2R_m^2)^{\frac{1}{2}}+1\right]^{\frac{1}{2}}} \quad (S) \; ; \quad \frac{C_p \cdot sR_m}{\left[(1+s^2R_m^2)^{\frac{1}{2}}+1\right]^{\frac{1}{2}}} \quad (P) \quad (43)$$

$$P_{re} = \frac{C_s \cdot \left[(1+s^2R_m^2)^{\frac{1}{2}}+1\right]^{\frac{1}{2}}}{(1+s^2R_m^2)^{\frac{1}{2}}} \quad (S) \; ; \quad C_p \cdot \left[(1+s^2R_m^2)^{\frac{1}{2}}+1\right]^{\frac{1}{2}} \quad (P) \quad (44)$$

The ratio of reactive power to active power is the same in both cases and is given by

$$\text{power ratio} = \frac{\left[(1+s^2R_m^2)^{\frac{1}{2}}+1\right]}{sR_m} \quad (45)$$

The power factor is obtained from (39) and is also the same in both cases. We have

$$\cos\theta = \frac{sR_m/\sqrt{2}}{(1+s^2R_m^2)^{\frac{1}{4}}\left[1+(1+s^2R_m^2)^{\frac{1}{2}}\right]^{\frac{1}{2}}} \quad (46)$$

The power factor for a SLIM is very low - when $s \sim \frac{1}{R_m}$, $\cos\theta \sim 0.3$. Results (43) to (46) are appropriate where the skin depth of the EM field is less than the conductor depth (ι). When the converse is true we can neglect the skin effect and obtain the results

$$P_{ac} = \frac{C_s \cdot sR_m}{(1+s^2R_m^2)^{\frac{1}{2}}}\left(\frac{\alpha L}{\sqrt{2}}\right) \quad (S) \; ; \quad C_p \cdot sR_m \left(\frac{\alpha L}{\sqrt{2}}\right) \quad (P) \quad (47)$$

$$P_{re} = \frac{C_s \cdot \left[(1+s^2R_m^2)^{\frac{1}{2}}+1\right]}{(1+s^2R_m^2)^{\frac{1}{2}}}\left(\frac{\alpha L}{\sqrt{2}}\right) \quad (S) \; ; \quad C_p \cdot \left[(1+s^2R_m^2)^{\frac{1}{2}}+1\right]\left(\frac{\alpha L}{\sqrt{2}}\right) \quad (P) \quad (48)$$

The power ratio and power factor are as before. Results (43) to (48) may be compared with those obtained by WANG and DUDZINSKY (1967) for a DLIP with a slit channel. They find

$$P_{ac} \propto \frac{sR_m}{1+s^2R_m^2} \quad (S) \; ; \quad sR_m \quad (P)$$

$$P_{re} \propto \frac{1}{1+s^2R_m^2} \quad (S) \; ; \quad 1 \quad (P)$$

$$\cos\theta = sR_m/(1+s^2R_m^2)^{\frac{1}{2}}$$

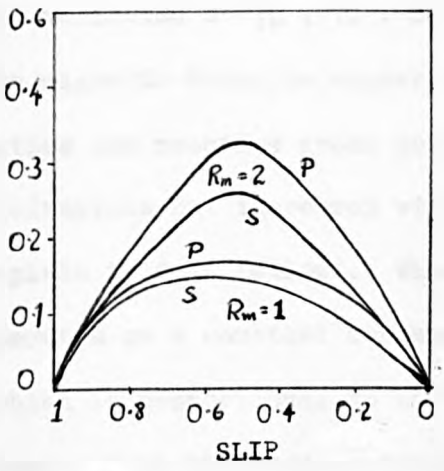

(a) $\bar{P}_m = P_m / C_s$

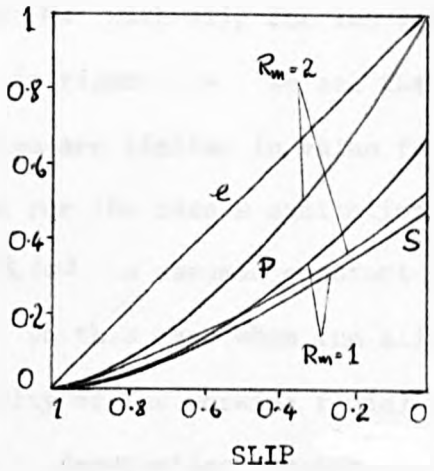

(b) $\bar{P}_s = P_s / C_s$
$e = 1 - s$

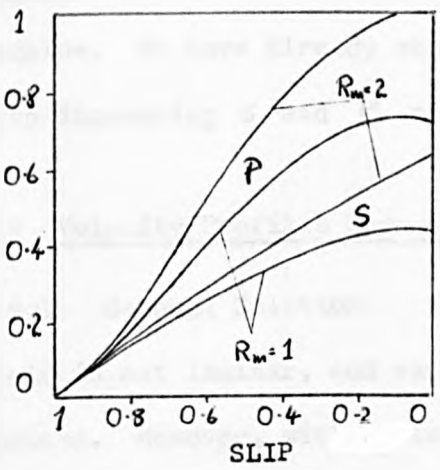

(c) $\bar{P}_{ac} = P_{ac} / C_s$

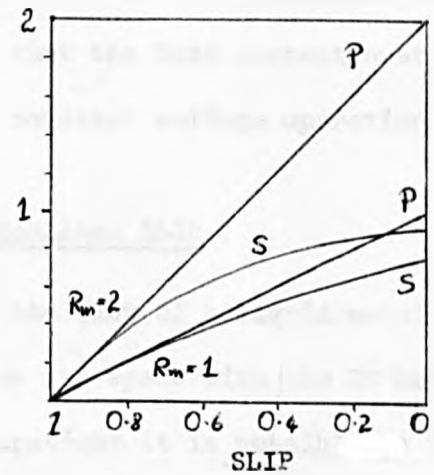

(d) $\bar{P}_{ac} = P_{ac} / (C_s \propto L/\sqrt{2})$

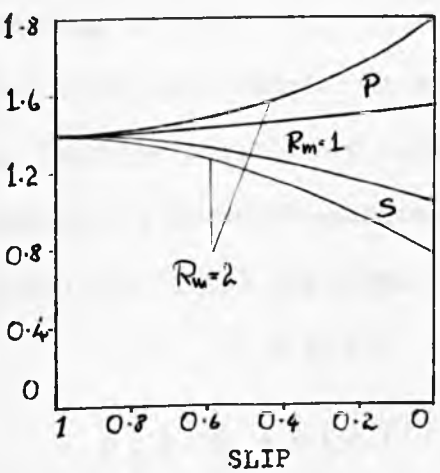

(e) $\bar{P}_{re} = P_{re} / C_s$

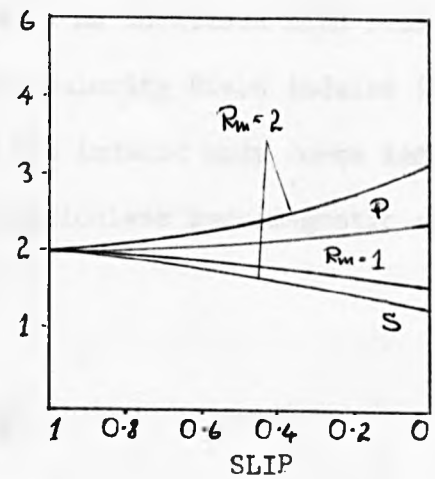

(f) $\bar{P}_{re} = P_{re} / (C_s \propto L/\sqrt{2})$

Fig. 3.3 Power Densities

The variation of P_m, P_r, e, P_{ac} and P_{re} with slip for two values of the magnetic Reynolds number is shown in figure 3.4. We see that the active and reactive gross power densities are limited in value for case S excitations but increases without bound for the case P excitation. We explain this as follows. When K_s or $B_z(o)$ is assumed constant the machine operates as a constant current device. In this case when the slip s, or R_m (which is proportional to the conductivity of the working fluid) becomes large enough the induced current tends to demagnetise the imposed field. When B_m, the normal magnetic induction, is held constant the machine operates as a constant voltage device. For a sheet rotor the active power P_{ac} becomes a linear function of slip, (47), as in a classical induction machine. We have already shown, (27), that the load current must decrease with increasing s and R_m to maintain constant voltage operation.

3.4 Velocity Profiles Induced By An Idealised SLIP

3.4.1 General Solution. In general the flow of a liquid metal in an EM field is not laminar, and varies in time and space with the EM body force induced. However, with certain configurations it is possible to linearise the Navier-Stokes hydromagnetic equation and obtain stationary solutions for the velocity field.

Here we present an exact solution to the hydrodynamic equations assuming the body force is that induced by an idealised SLIM over a conducting half space. We show that the velocity field induced is stationary and that the oscillatory components of the induced body force induce an oscillatory pressure gradient. The dimensionless hydromagnetic equations (1.22) and (1.23) are respectively:

$$\nabla . \underline{v} = 0 \tag{49}$$

$$\rho \left\{ L^2 \frac{\partial \underline{v}}{\partial t} + L(\underline{v}.\nabla)\underline{v} \right\} = -L \nabla P + L^2 \underline{f} + \nu \nabla^2 \underline{v} \tag{50}$$

Where the Lorentz body force $\underline{f}$ is given by (15), (16) and (22), (23). If we assume $\frac{\partial P}{\partial x} = 0$ and no vertical flow is induced, then (49) implies laminar

flow occurs and the velocity is purely a function of z. We have

$$\underline{v} = V(z)\,\underline{e}_2 \tag{51}$$

Linearisation of (50) is now possible. We obtain

$$\frac{d^2V}{dz^2} = h\frac{\partial P}{\partial y} - h^2 f_2 \tag{52}$$

$$\frac{\partial P}{\partial z} = h f_3 \tag{53}$$

From (52) and (53) we find, on eliminating v, that the pressure P satisfies the Poisson equation

$$\frac{\partial^2 P}{\partial y^2} + \frac{\partial^2 P}{\partial z^2} = h\left(\frac{\partial f_2}{\partial y} + \frac{\partial f_3}{\partial z}\right) \tag{54}$$

Using (15), (16) and (20), (27) the right of (54) becomes respectively

$$2Q_s e^{-2\psi_1 z} h\left\{-\psi_1\psi_2 + \frac{2\psi_1\psi_2\alpha^2}{|\psi|^2}\cos 2\phi - \left[\frac{(\psi_1^2-\psi_2^2)\alpha^2}{|\psi|^2} + |\psi|^2\right]\sin 2\phi\right\} \tag{55}$$

$$2Q_m e^{-2\psi_1 z} h\left\{-\psi_1\psi_2 - 2\psi_1\psi_2\cos 2\phi\right\} \tag{56}$$

We seek a solution to (54) for $P(y,z,t)$ which is consistent with (55) and (56). Writing

$$P(y,z,t) = 2Q_{s,m}\, e^{-2\psi_1 z} h\left\{A'_{s,m} + A''_{s,m}\cos 2\phi + A'''_{s,m}\sin 2\phi\right\}$$

then direct substitution of P in (54) gives $A'_{s,m}, A''_{s,m}, A'''_{s,m}$ by comparison of terms. After some lengthy algebra we obtain

$$P(y,z,t) = Q_s\cdot\frac{h}{2}\cdot e^{-2\psi z}\left\{-\frac{\psi_2}{\psi_1} + \frac{[\alpha^2(\psi_1^2-\psi_2^2)+|\psi|^4]}{2\psi_1\psi_2\cdot|\psi|^2}\cos 2\phi + \frac{\alpha^2}{|\psi|^2}\sin 2\phi\right\} + h\left(\frac{\partial P}{\partial y}\right)_0 y. \tag{57}$$

$$P(y,z,t) = Q_m\cdot\frac{h}{2}\cdot e^{-2\psi z}\left\{-\frac{\psi_2}{\psi_1} - \sin 2\phi\right\} + h\left(\frac{\partial P}{\partial y}\right)_0 y. \tag{58}$$

Where we have assumed the constant applied external gradient $h\left(\frac{\partial P}{\partial y}\right)_0$ is given. By differentiating P w.r.t z we can recover (52). Thus we have shown that all the y and t variation is contained in the induced pressure and the solution to (51) for $V(z)$ may be carried out since the right of (51) now contains only z variation, and constant terms. We have

$$\frac{\nu}{h^2}\frac{d^2V}{dz^2} = \left(\frac{\partial P}{\partial y}\right)_0 - \alpha Q_{s,m}\, e^{-2\psi_1 z} \tag{59}$$

The solution to (59) is

$$V(z) = -S V_s q H_m^2 e^{-2\mu_1 z} + \frac{L^2}{\nu}\left(\frac{\partial P}{\partial y}\right)_0 \frac{z^2}{2} + C_1 z + C_2 \qquad (60)$$

where we have substituted for Q_s and Q_m, writing

$$q = \alpha^2/8\mu_1^2|\mu|^2 \quad \text{CASE S;} \qquad 1/8\mu_1^2 \quad \text{CASE P} \qquad (61)$$

The Hartmann number $H_m = BL\left(\frac{\sigma}{\nu}\right)^{1/2}$ where $B = \mu_0 K_s$ or B_m, and C_1, C_2 are constants of integration, (which are found from the boundary conditions).

3.4.2. Surface Shear Stress Analysis. Because the plant SLIP is capable of pumping the liquid tin both with and without the glass sheet on its upper surface, we must consider both the fixed and free surface boundary conditions. However, a more general analysis is possible using the idealised configuration in figure 3.4

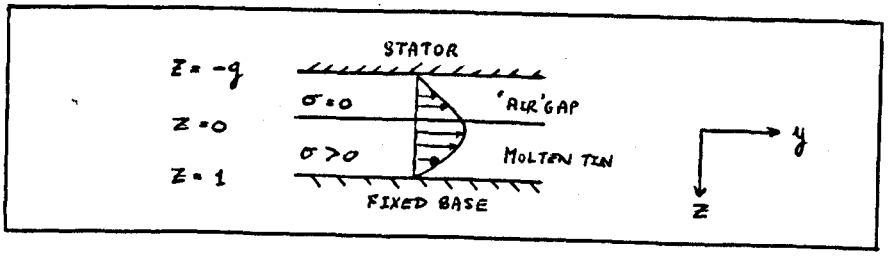

Fig. 3.4 Idealized Configuration

To obtain simple expressions we assume all flow is laminar and steady. The stator is replaced by a smooth surface height g (dimensionless) above the molten tin surface $z=0$. The region between $z=0$ and $z=-g$ is assumed to be of zero conductivity and of viscoscity ν_1. This region will model the air gap or the glass ribbon. We recover the fixed and free surface boundary conditions by taking limiting cases for the viscoscity. If $\left(\frac{\partial P}{\partial y}\right)_0$ is zero in the gap, the velocity profile induced by the moving molten tin is a simple shear flow. Denoting the solution to (60) for the gap by V_1, we have

$$V_1(z) = \frac{KL}{\nu_1}(z+g) \qquad (62)$$

where we have assumed $V_1(-g)=0$, (viscous condition at a fixed boundary, (1.40)), and the shear stress K on $z=0$ is specified ($\nu_1 \frac{dV_1}{dz} = KL$ on $z=0$, (1.41)). For the molten tin we have $V(1)=0$ and (by equilibrium of surface

shear stress) $\nu \frac{dv}{dz} = KL$ on $z=0$. Solving (60) with these boundary conditions we obtain

$$V(z) = sV_s\, q\, H_m^2 \left\{ e^{-2\psi_1} - e^{-2\psi_1 z} + 2\psi_1(1-z) \right\} - \frac{h^2}{2\nu}\left(\frac{\partial p}{\partial y}\right)_0 (1-z^2) - \frac{KL}{\nu}(1-z) \qquad (63)$$

The first term of (63) arises from the magnetic forces, the second from the pressure gradient and the third from the specified shear stress. Along the interface $z=0$ we must have continuity of the velocity (1.40) and so, on equating (62) and (63), we find

$$K = K_0 \cdot \frac{\nu}{h}\left(g\,\frac{\nu}{\nu_1} + 1 \right)^{-1} \qquad (64)$$

where $$K_0 = sV_s\, q\, H_m^2 \left\{ 2\psi_1 + e^{-2\psi_1} - 1 \right\} - \frac{h^2}{2\nu}\left(\frac{\partial p}{\partial y}\right)_0 \qquad (65)$$

When $\nu_1 \sim \infty$ we recover the fixed surface boundary conditions, and the magnitude of the surface shear stress is $\frac{K_0 \nu}{h}$ When $\nu_1 \sim 0$ we recover the free surface boundary conditions and K becomes zero.

Equations (63) to (65) completely specify the velocity profile induced. We shall consider the two limiting cases of K separately.

3.4.3 Free Surface. When $K = 0$ (63) reduces to

$$V(z) = sV_s\, q\, H_m^2 \left\{ e^{-2\psi_1} - e^{-2\psi_1 z} + 2\psi_1(1-z) \right\} - \frac{h^2}{2\nu}\left(\frac{\partial p}{\partial y}\right)_0 (1-z^2) \qquad (66)$$

Equation (66) gives the free surface velocity profile induced in the molten tin by an idealised SLIP excitation. However, the parameter ψ_1 is a function of the slip and the slip is obtained from a knowledge of V, the average velocity of the working fluid. The average velocity may be found by integrating (66) from $z=0$ to $z=1$. Using the notation of TKACHENKO (1970) we may write (66) as the sum of MHD induced and pressure induced average velocities, (V_m and V_p respectively)

$$V(z) = V_m \left\{ \frac{e^{-2\psi_1} - e^{-2\psi_1 z} + 2\psi_1(1-z)}{\left(\frac{e^{-2\psi_1}-1}{2\psi_1}\right) + e^{-2\psi_1} + \psi_1} \right\} + V_p \cdot \frac{3}{2}(1-z^2) \qquad (67)$$

where $$V = \int_0^1 V(z)\, dz = V_m + V_p \qquad (68)$$

and $$V_m + V_p = sV_s\, q\, H_m^2 \left\{ \left(\frac{e^{-2\psi_1}-1}{2\psi_1}\right) + e^{-2\psi_1} + \psi_1 \right\} - \frac{h^2}{3\nu}\left(\frac{\partial p}{\partial y}\right)_0 \qquad (69)$$

3.4.4. Fixed Surface. When $\psi_1 \sim \infty$ (62) reduces to

$$V(z) = sV_s\, q\, Hm^2 \left\{ z e^{-2\psi_1} - e^{-2\psi_1 z} + 1 - z \right\} - \frac{h^2}{2\nu}\left(\frac{\partial p}{\partial y}\right)_0 z(1-z) \qquad (70)$$

which may be written as

$$V(z) = V_m \left\{ \frac{z e^{-2\psi_1} - e^{-2\psi_1 z} + 1 - z}{\left(\frac{e^{-2\psi_1}-1}{2\psi_1}\right) + \frac{1}{2}(1+e^{-2\psi_1})} \right\} + 6\, V_p\, z(1-z) \qquad (71)$$

where V is again given by (68), and

$$V_m + V_p = sV_s\, q\, Hm^2 \left\{ \left(\frac{e^{2\psi_1}-1}{2\psi_1}\right) + \frac{1}{2}\left(e^{-2\psi_1}+1\right) \right\} - \frac{h^2}{12\nu}\left(\frac{\partial p}{\partial y}\right)_0 \qquad (72)$$

3.4.5 MHD Effects. From (68), (69) and (72) we obtain the following result (writing $sV_s = V_s - V$)

$$V = \frac{q\, Hm^2 R\, V_s}{1 + q\, Hm^2 R} + \frac{P^\circ}{1 + q\, Hm^2 R} \qquad (73)$$

where $R = \left(\frac{e^{-2\psi_1}-1}{2\psi_1}\right) + e^{-2\psi_1} + \psi_1 \qquad P^\circ = -\frac{h^2}{3\nu}\left(\frac{\partial p}{\partial y}\right)_0$ free surface (74)

$$R = \left(\frac{e^{-2\psi_1}-1}{2\psi_1}\right) + \frac{1}{2}\left(e^{-2\psi_1}+1\right) \qquad P^\circ = -\frac{h^2}{12\nu}\left(\frac{\partial p}{\partial y}\right)_0$$ fixed surface (75)

The slip S is given by

$$S = \frac{1}{1 + q\, Hm^2 R} - \frac{P^\circ / V_s}{1 + q\, Hm^2 R} \qquad (76)$$

We see that MHD back reaction effects are included in (73) and (76). For small Hm there is little interaction between the magnetic field and the molten tin - the velocity V arises predominantly from the applied pressure gradient. As $Hm \to \infty$, $V \to V_s$ and the field is 'frozen into' the fluid. The slip in this case is zero.

Equations (73) and (76) are non linear in V and S respectively, because q and R are functions of ψ, which, by (5), is a function of V. The roots of these equations may be found using standard iterative procedures (for example, the modified bisection method). The parameter q is given in (61)

The value of S obtained from (76), can now be substituted back into (67) and (70) to give second approximation solutions which include the MHD effects.

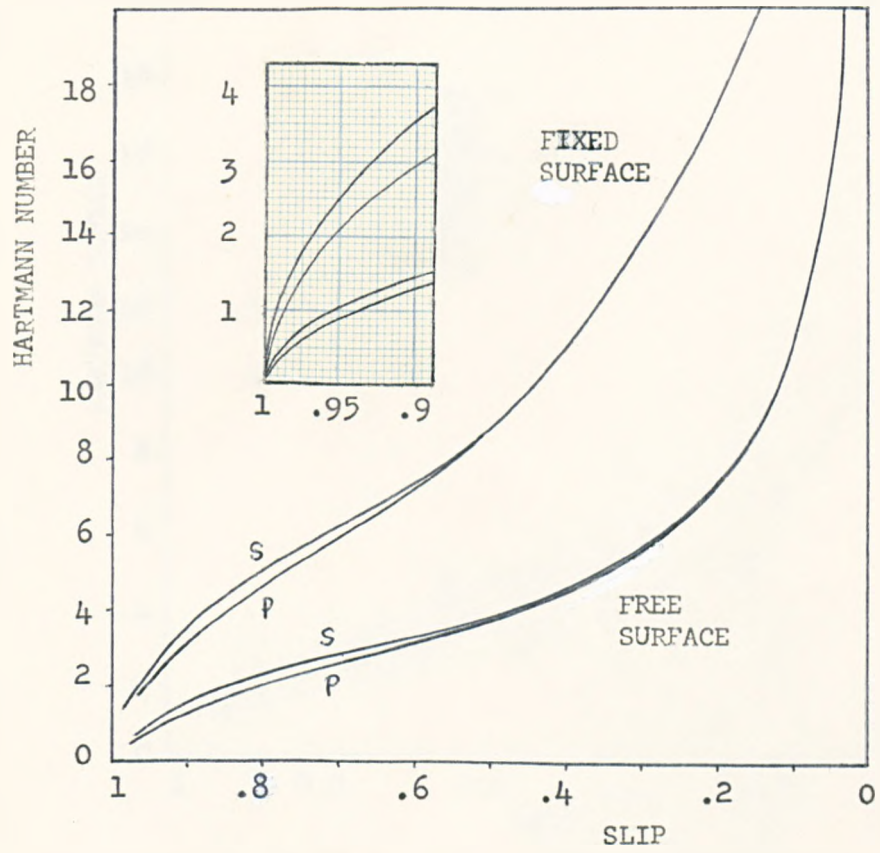

Fig.3.5 $R_m = 1$ $\tau = 15.24$ cm (6 in)

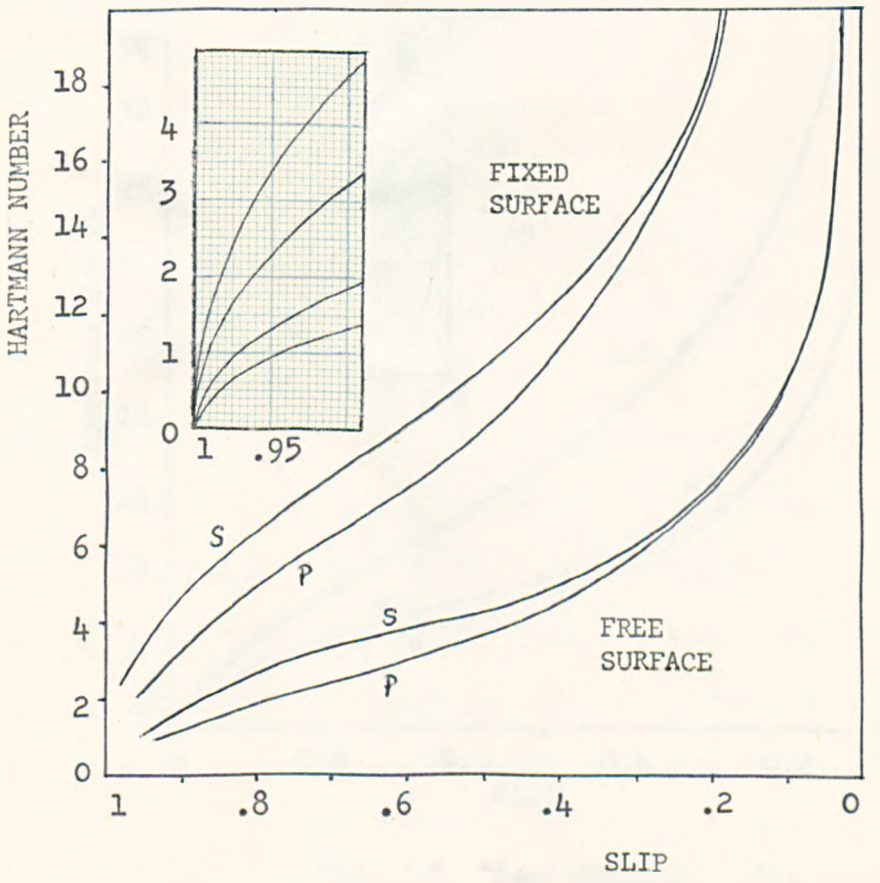

Fig. 3.6 $R_m = 2$ $\tau = 15.24$ cm (6 in)

Fig. 3.7 Free Surface (τ = 15·24 cms)

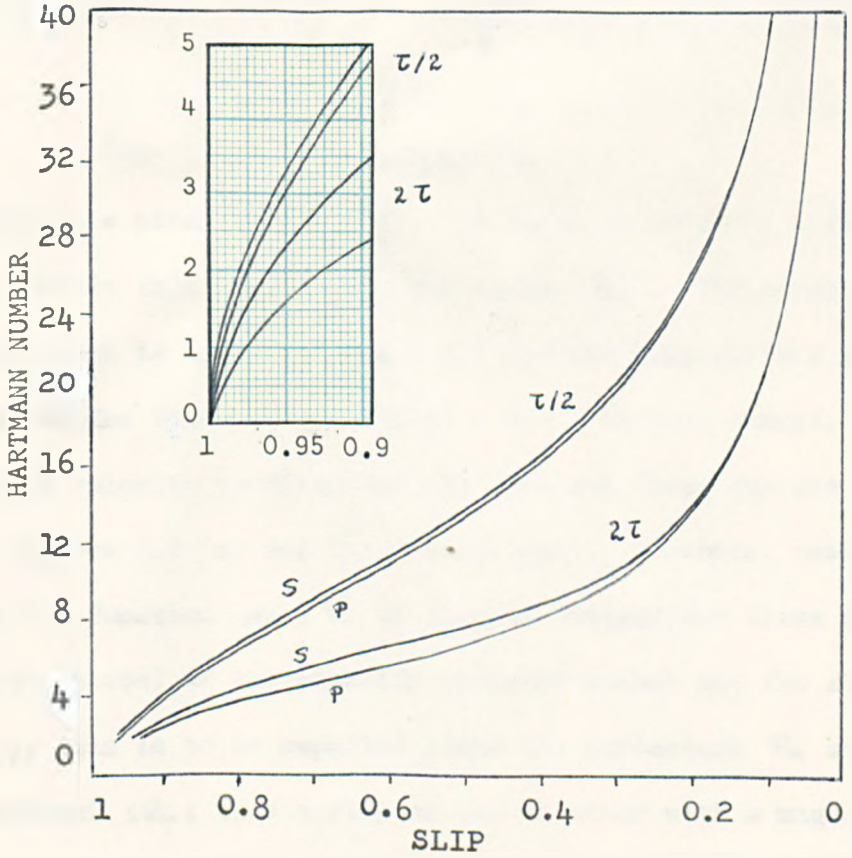

Fig. 3.8 Fixed Surface (τ = 15·24 cms)

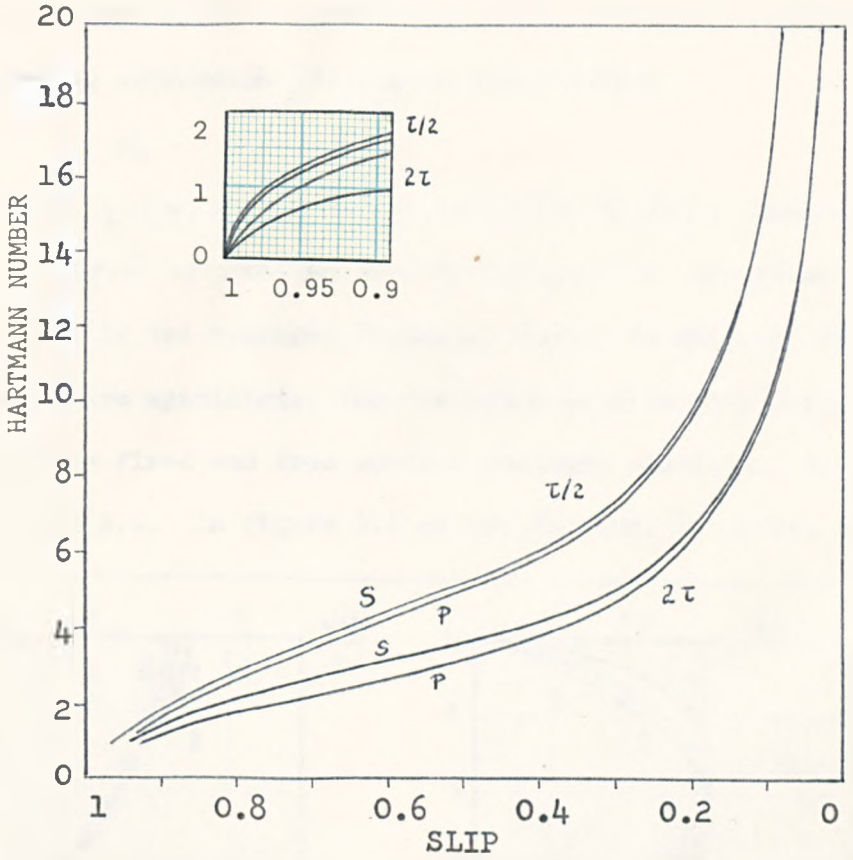
HARTMANN NUMBER
SLIP
20
18
16
14
12
10
8
6
4
2
0
1
0.8
0.6
0.4
0.2
0
τ/2
2τ
S
P
S
P
2
1
0
1
0.95
0.9
τ/2
2τ

When the external applied pressure gradient is zero we obtain, using (76), the following expression for the Hartmann number

$$H_m = \left(\frac{1 - s}{q s R} \right)^{1/2} \qquad (77)$$

where, from (61), $q = q(\psi_1)$ and from (74) and (75), $R = R(\psi_1)$. However from (8) we have $\psi_1 = \psi_1(\alpha, R_m, s)$ and so $H_m = H_m(\alpha, R_m, s)$. The value of H_m obtained from (77) is the required Hartmann number to maintain the flow when α, R_m and S are specified. The variation of slip with Hartmann number for both the fixed and free surface boundary conditions is shown in figures 3.5 and 3.6. In figure 3.5 we set R_m equal to unity, and

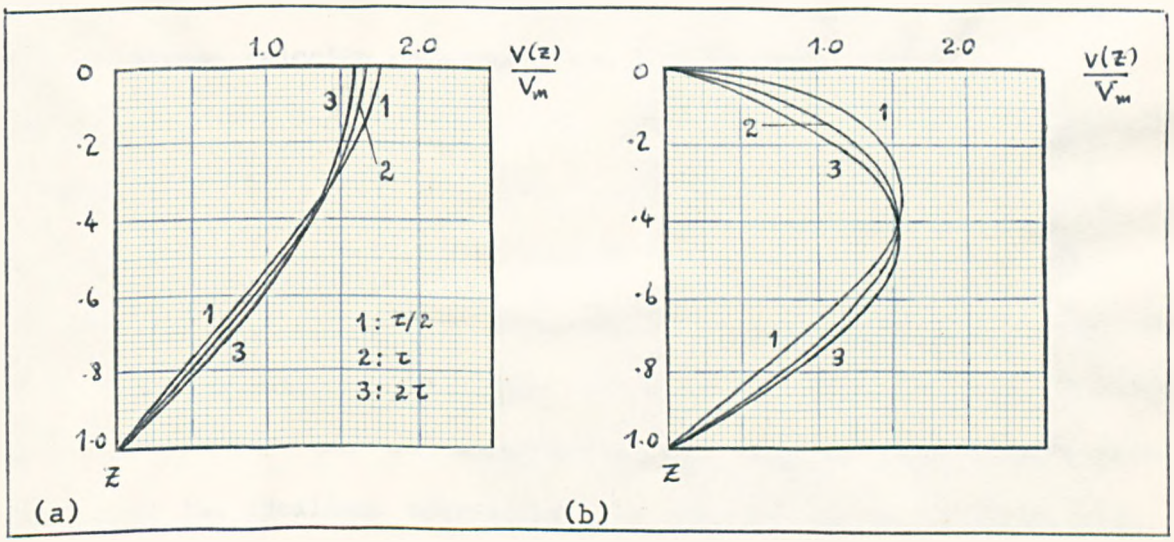

Fig. 3.9 Velocity Profiles

the dimensional pole pitch $\tau = \pi h / \alpha$ is taken as 152mm (6 inches); in figure 3.6 we retain this value of τ but double R_m. The effect of a change in pole pitch is shown in figure 3.7 for the free surface slip and in figure 3.8 for the fixed surface slip; ($R_m = 1$ in both cases).

The induced velocity profiles for the free and fixed surface flows are shown in figures 3.9 (a) and (b) respectively. Numerical results indicate that the function $V(z) / V_m$ is largely independent (less than one per cent variation) of the magnetic Reynolds number and the slip. Mathematically, this is to be expected since the parameters R_m and S occur only in the product $S R_m$; thus a slip of 0.1 together with a magnetic Reynolds number of value 2 is equivalent to a slip 0.2 with a magnetic Reynolds number of value unity. When the applied pressure gradient is

zero the average velocity V is equal to V_m and so for a given Hartmann number V may be obtained from the graphs in figures 3.5 to 3.8, using the relation $V = (1-s)V_s$.

The Hartmann number for the flow is determined primarily by the scale magnetic field ($\mu_0 K_s$ or B_m) . The stator surface current density was derived in §1.5 for an idealised SLIM, but can we apply the formula (1.46) in the design of a real linear motor? In §3.5 we show that this is so.

3.4.6 Example: The MHD Experiment. From table 2.1 we see that the average mercury velocity underneath the SLIM is about 10 cm/sec and thus with $V_s = 4.6$ m/sec we have $s \sim 1$. The magnetic Reynold's number is equal to 0.23. Substituting for s and R_m in (46) we find that the power factor is 0.11. Comparison with the measured power factor (table 2.1) indicates that our idealised theoretical analysis produces a power factor rather different than was observed. One of the reasons for this difference may lie in the fact that the experimental SLIM was less than a wavelength long and so the idealised travelling wave analysis may be inappropriate.

3.4.7 Example: The Float Bath Linear Motor. Using the data of table 1.1 we find H_m , the Hartmann number for the flow, is equal to 25 when $K_s = 7850$ A/m. From figure 3.8 we find the appropriate steady state idealised slip produced by the SLIP is about 0.3. With R_m equal to 1 we find the ideal characteristics are:

(a) from (29), the mechanical power developed $P_m = 0.7$ Watts.

(b) from (30), the ohmic loss $P_r = 1.74$ Watts, (corresponding to a temperature rise in the molten tin of 0.4 ^{o}C/sec).

(c) from (32) and (33), the hydraulic power loss $P_f = 18$ Watts when the Reynolds number $R_e \sim 10^6$.

(d) from (34), the winding loss $P_c = 19$ Watts.

(e) from (35), the total power output $P_e = 39.43$ Watts.

(f) from (36), the electrical efficiency $e = 0.02$.

(g) from (45) the power ratio = 6.8 .

(h) from (46), the power factor $\cos\theta = 0.14$.

3.5 The Force Acting On A Sheet Rotor

Recently HAWORTH (1976) has completed a simple experiment to assess the driving force produced by the linear motors used in Pilkington's float bath. He supported an aluminium sheet (1.6mm thick) on bakelite rollers which rested on a bakelite sheet placed on the stator face of an inverted SLIM. The force on the conducting sheet ($\sigma_{Al} = 28.6\,\sigma_{Fe}$), acting tangential to the stator face, was measured by vertically hanging weights (adjusted to maintain a stationary sheet), attached to the aluminium sheet by a thin cord taken over a free running pulley. The experiment was performed with 8-pole (49.75 turns) 12-pole (79.75 turns) and 16-pole (109.75 turns) three phase SLIMs. The internal parameters of each machine are the same as those given in table 1.1. The results indicated that the force developed in the aluminum sheets was given by the empirical relation:

$$F = \{0.025\,,\ 0.04\,,\ 0.054\}I^2 \text{ grams} \quad (8\text{-pole},12\text{-pole},16\text{-pole}) \quad (78)$$

where I was the electric current supplied. The width of the sheets (203mm) allowed 50mm overlap at the edges, and their length (0.76m, 1.1m, 1.372m for the 8, 12, and 16-pole machines respectively) allowed 100mm overlap at each end. Because the skin depth of the induced EM field (1cm) is much greater than the sheet thickness we assume the field has little decay with depth. From (15) the force developed, when $S = 1$ is thus given by

$$F \sim \frac{1}{2} \cdot \frac{\alpha}{L} \cdot \mu_0 K_s^2 \times (\text{vol}) \text{ Newtons}$$

where $(\text{vol})\text{m}^3$ is the volume of aluminium. Substituting for the appropriate parameters in K_s (1.46)we find

$$F \sim \{0.066\,,\ 0.113\,,\ 0.16\}\,I^2 \text{ grams} \quad (79)$$

In his DLIM study BOLTON (1969) indicates the transverse edge effect (see §1.5)may be accounted for by a factor of approximately 0.7 in the surface current density at the stator face. The longitudinal end effect can be included through LIELPETER and TUTIN's (1959) factor of 0.8-0.9. Thus the force can be reduced to about one half of its value in (79), and we obtain very good agreement with (78). Thus the formula for K_s, given by (1.46) should produce reliable quantative estimates for the induced forces in the molten tin.

3.6 A Finite SLIP

The results of §3.4 are, as we noted, only applicable in the steady state analysis of an idealised excitation of infinite expanse. Here we consider an approximation to the flow developed when this excitation is made finite in length.

Consider the open sided SLIP, ABCD, shown in figure 3.10. The working

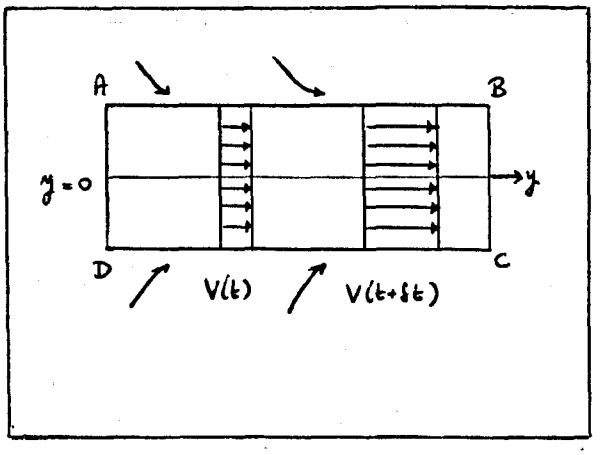

Fig. 3.10 Idealized Model

fluid is drawn into the SLIP from the end AD and accelerated until a maximum flow rate is attained at the exit end BC. If we ignore end and edge effects, we may assume the idealised pumping force (15) is maintained across the SLIP, and thus to a good approximation, we may assume the working fluid moves with no transverse or vertical variation underneath the motor. From figures 3.2 (a) and (b)we see that the

pumping force may be considered proportional to the slip S, (certainly when $S \gg 0$); averaging (1.15) across the channel depth and setting $S = 1$ in the ψ-terms, we obtain, for the approximate pumping force

$$F = sT = s\left\{ \frac{\alpha R_m}{2L} \cdot \frac{\mu_0 K_s^2}{(1+R_m^2)^{1/2}} \cdot \left(\frac{1-e^{-2\psi_1}}{2\psi_1}\right)\right\} \qquad (80)$$

where T is measured in Newtons / m^3; $s = (V_s - V)/V_s$ is the slip; and $V = dy/dt$ is the fluid velocity — the direction of y is taken parallel with the travelling wave. We now apply Newton's second law to the slug flow underneath the motor, where the inducing force is given by (80), and write

$$\rho \frac{d^2y}{dt^2} = \left(V_s - \frac{dy}{dt}\right) \cdot T/V_s \qquad (81)$$

where ρ is the density of the working fluid. Equation (81) is a reduction of the hydrodynamic equation (1.81) and is applicable when (i) the inertia terms are small, (ii) when the fluid viscoscity can be neglected, and (iii) when the external pressure gradient is zero. However, even when these conditions are not satisfied the solutions to (81) gives an estimate of the flow development in the SLIP. Given $y = 0$ and $V = V_0$ when $t = 0$, the solutions to (81) are

$$y = V_s\left(t - \frac{1}{\beta} + \frac{1}{\beta}e^{-\beta t}\right) + V_0(1-e^{-\beta t}) \sim \frac{1}{2}\beta(V_s - V_0)t^2 + V_0 t \quad (\beta t \ll 1) \qquad (82)$$

$$V = V_s(1-e^{-\beta t}) + V_0 e^{-\beta t} \sim \beta(V_s - V_0)t + V_0 \quad (\beta t \ll 1) \qquad (83)$$

where $\beta = T/\rho V_s$

3.6.1 Example: The MHD Experiment. Using the data of table 2.2 in the expression for T (80) we find $T \sim 240$ N/m^3. With $V_s = 4.6$ m/sec, $\rho = 13.6$ gms/cc we have $\beta \sim 8.8 \times 10^{-2}$ sec^{-1}. Using the approximate results (when $\beta t \ll 1$) of (82) and (83), with y (the distance between stations (c) and (d) (figure 2.1)) equal to 12 cms, and V_0 (from table 2.1) equal to 9cm/sec, we find the time taken for the mercury to traverse the distance y is 1.1 secs, and the final velocity is 13 cm/sec.

This final value for the velocity agrees reasonably well with that given in table 2.1 , for station (*d*).

3.6.2 Example: The Float Bath SLIP. Using the data of table 1.1 in the expression for T (80) we find $T \sim 204\ N/m^3$. With $V_s = 7.6$ m/sec and $\rho = 6.8$ gms/cc we find $\beta \sim 3.9 \times 10^{-3}\ sec^{-1}$.

(a) Assuming the input velocity (v_0) is zero, we find the time taken (using (82)) for the molten tin to traverse the length of the motor (0.6m) is 6.4 secs. The final velocity is obtained from (83) and we find its value is 19 cm/sec.

(b) Assuming the input velocity is 20 cm/sec (for example), the appropriate time is about 2.6 seconds and the final velocity is 27 cm/sec.

The results of (a) describe the flow at 'start up' when $v_0 = 0$. For a motor of width 10 cm and a molten tin depth of 6.4 cm we obtain a mass-flow rate of 8.3 Kg/sec. It is clear from the results of (b) that when the fluid velocity is non-zero at the SLIP entrance end (as is the case for a non-zero pressure gradient, and also axial alignment of the SLIM with the ribbon flow) the pumping ability of the SLIP decreases, and the SLIM becomes a 'stirrer'.

4. THE EFFECT OF A SUPERIMPOSED SHEAR FLOW ON AN IDEALISED SLIP.

4.1 Introduction

Consider the float glass process. The moving glass ribbon induces a shear flow in the molten tin in regions away from the SLIP. As a section of the ribbon passes below the SLIP the shear flow is modified by the EM field. This chapter attempts to assess the flow modification when the SLIP is aligned parallel to, and transverse to, the direction of motion of the ribbon.

We have previously considered (Chapter 3) the flow induced in an electrically conducting liquid by an idealised SLIP when the upper surface of the liquid is constrained to be both free and fixed. The EM body force was calculated from a knowledge of EM field induced in a conducting half space moving with a constant velocity parallel to the direction of the SLIP excitation. This choice of motion allowed us to obtain simple solutions to Maxwell's equations, and later, to include MHD effects by suitable iterations. Here however, we impose the shear velocity $\underline{V}_{sh}$ on the half space, where

$$\underline{V}_{sh} = \left[u_0 \left(1 - \frac{z}{L}\right),\ V_0 \left(1 - \frac{z}{L}\right),\ 0 \right] \qquad (1)$$

The parameters u_0 and V_0 are constants (with dimensions of velocity); L is a scale length (the tin depth) and z is the vertical ordinate. The actual velocity $\underline{V}$ of the half space is taken as

$$\underline{V}(z) = \underline{V}_{sh}(z) + \underline{V}_h \equiv [u, v, 0] \qquad (2)$$

where $\underline{V}_h$ is a velocity (yet to be specified) which allows the simplification of Maxwell's equations and the inclusion of some MHD effects, as in Chapter 3.

Below (§4.2) we obtain the EM field induced in the half space for both the parallel and transverse alignments of the SLIP. In §4.3 we give an estimate of the velocity profiles induced in a liquid inductor of finite depth by a SLIP in the transverse alignment. For the reasons discussed in §4.2.2, it has not been possible to obtain the induced velocity profiles when the shear flow is imposed parallel to the direction of the SLIP excitation.

4.2 The Induced Electromagnetic Field.

Figure 4.1 illustrates the simplified model of the SLIM used in the following analysis. Cartesian coordinate axes are chosen with origin on the interface between regions I and II with the z axis pointing vertically downwards. Region I represents the stator core of a SLIM and is taken to

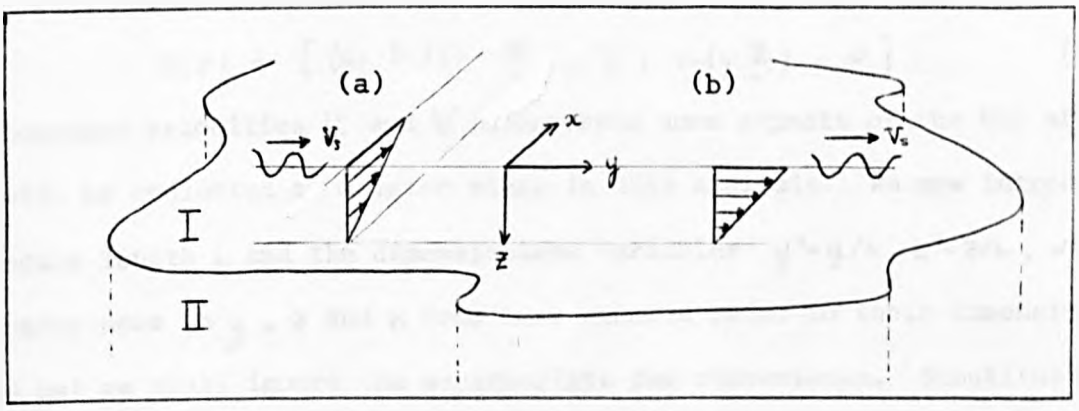

Fig. 4.1 The Models Under Consideration

be of zero conductivity and infinite magnetic permeability. Region II (the half space $z>0$) is taken to be of non-zero conductivity and of magnetic permeability equal to that of free space, μ_0. We assume that a travelling wave excitation of the form $e^{i(\omega t-\alpha y)}$ is applied along the surface $z=0$ and that $B_1=0$ there (but not necessarily elsewhere). We assume that no x variation exists and so we have $\frac{\partial}{\partial x}=0$. We further assume that the EM field may be written in the form

$$\underline{\mathcal{B}}(\underline{r},t)=\underline{B}(z)e^{i(\omega t-\alpha y)} \qquad \underline{\mathcal{J}}(\underline{r},t)=\underline{J}(z)e^{i(\omega t-\alpha y)} \tag{3}$$

where only the real parts of $\underline{\mathcal{B}}$ and $\underline{\mathcal{J}}$ have physical significance. For boundary conditions we choose the case S and case P excitations((1.47) and (1.48) respectively) and impose damping as $z\to\infty$. Using (2) and (3) in Maxwell's equation (1.11) we obtain the induction equation for region II.

$$\eta\frac{d^2\underline{B}}{dz^2}=i\omega\underline{B}-i\alpha V(z)\underline{B}-B_3\left[\frac{du}{dz},\frac{dv}{dz},0\right] \tag{4}$$

In the derivation of (4) we have used Maxwell's solenoidal relation (1.1). We see from (4) that the velocity $u(z)$ occurs only in its differentiated form. Thus the MHD approximation can only be performed if the x component of V_1 is a function of z. Since the MHD back reaction is proportional to

the field line deformation, we may assume the x component of $\underline{V}_f$ can be taken as a shear flow. This problem does not arise for $V(z)$ and so we can follow the procedure of §3.2 for the y component of $\underline{V}_f$. Finally we have

$$\underline{V}_f(z) = \left[-U\left(1-\frac{z}{L}\right),\ V,\ 0\right] \tag{5}$$

where the minus sign in the x component indicates that the magnetic field lines will oppose the shear flow. Combining (1), (2) and (5) we have

$$\underline{V}(z) = \left[(U_0-U)\left(1-\frac{z}{L}\right),\ V+V_0\left(1-\frac{z}{L}\right),\ 0\right] \tag{6}$$

The constant velocities U and V incorporate some aspects of the MHD effects and will be evaluated at a later stage in this analysis. We now introduce the scale length L and the dimensionless variables $y^*=y/L$, $z^*=z/L$, $\alpha^*=\alpha/L$. All references to y, z and α from here onwards refer to their dimensionless forms but we shall ignore the superscripts for convenience. Substituting (6) in (4) we obtain

$$\frac{d^2\underline{B}}{dz^2} = \Psi^2\underline{B} + B_3\left[R_{m1}, R_{m2}, 0\right] \tag{7}$$

where

$$\Psi^2 = \alpha^2(1+iSR_m) \tag{8}$$

the slip

$$S(z) = 1 - \frac{V}{V_s} - \frac{V_0}{V_s}(1-z) \tag{9}$$

In (8) $R_m = V_s L/\omega\eta$ is the magnetic Reynolds number based on the synchronous velocity $V_s = \omega L/\alpha$ of the travelling wave. The parameters $R_{m1} = \frac{(U_0-U)L}{\eta}$ and $R_{m2} = V_0 L/\eta$ are magnetic Reynolds numbers based on the imposed shear flow. For this problem the dimensionless form of Maxwell's equations (1.1) and (1.4) become respectively

$$\frac{dB_3}{dz} = i\alpha B_2 \tag{10}$$

$$\mu_0 L\underline{J} = \left[-\left(i\alpha B_3 + \frac{dB_2}{dz}\right),\ \frac{dB_1}{dz},\ i\alpha B_1\right] \tag{11}$$

Because $B_1(z)$ is not zero (cf. §3) we see that the current density vector is three dimensional in nature. The solutions to (7) and (11), for the magnetic field and current density respectively, will be found for two special cases of the above configuration.

4.2.1 Transverse Alignment. The shear flow configuration transverse to the direction of motion of the travelling wave is shown in figure 4.1(a) Because V_0 is now zero, we have $R_{m_2}=0$. The slip (9) reduces to the standard form

$$S = (V_s - V)/V_s \tag{12}$$

The solution to (7) is of the form $\underline{B} = \underline{C}\, e^{-\psi z} + \underline{P}_I e_1$, where $\underline{P}_I(z)$ is a particular integral, and $\underline{C}$ is a constant of integration. The boundary conditions give $C_1 = 0$ because P_I is shown to be zero on $z=0$. From equations (7), (10) and (11) we obtain (using the methods of §3.2) the EM field induced in region II:

(a) Case S. Here $B_2(0) = \mu_0 K_s$, (1.47), where K_s is the stator surface current density. We find

$$\underline{B} = \mu_0 K_s e^{-\psi z}\left[\left(\frac{i\alpha}{\psi}\right) R_{m_1}\left(\frac{z}{2\psi}\right),\ 1,\ -\frac{i\alpha}{\psi}\right] \tag{13}$$

$$\underline{J} = \frac{K_s}{h} e^{-\psi z}\left[\frac{i\alpha^2 s R_m}{\psi},\ \left(\frac{-i\alpha}{2\psi}\right) z R_{m_1} + \left(\frac{i\alpha}{\psi}\right)\frac{R_{m_1}}{2\psi},\ -\frac{\alpha^2 z}{2\psi^2}\cdot R_{m_1}\right] \tag{14}$$

From (3.8) we obtain

$$\psi_{1,2} = \frac{\alpha}{\sqrt{2}}\left\{\left(1 + s^2 R_m^2\right)^{1/2} \pm 1\right\}^{1/2} \tag{15}$$

Remembering only the real parts of $\underline{B}$ and $\underline{J}$ have physical significance, the true EM field in II becomes

$$\mathcal{R}\left\{\underline{B}(z) e^{i(\omega t - \alpha y)}\right\} = e^{-\psi_1 z}\mu_0 K_s\left[R_{m_1}\frac{\alpha z}{2|\psi|^2}\cos\left(\phi - 2\theta + \tfrac{\pi}{2}\right),\ \cos\phi,\ -\frac{\alpha}{|\psi|}\cos\left(\phi - \theta + \tfrac{\pi}{2}\right)\right] \tag{16}$$

$$\mathcal{R}\left\{\underline{J}(z) e^{i(\omega t - \alpha y)}\right\} = \frac{K_s}{h} e^{-\psi_1 z}\left[\frac{\alpha^2 s R_m}{|\psi|}\cos\left(\phi - \theta + \tfrac{\pi}{2}\right),\ -\frac{\alpha z}{2|\psi|}R_{m_1}\cos\left(\phi - \theta + \tfrac{\pi}{2}\right) + \right.$$

$$\left. \frac{R_{m_1}\alpha}{2|\psi|^2}\cos\left(\phi - 2\theta + \tfrac{\pi}{2}\right),\ -\frac{R_{m_1} z}{2|\psi|^2}\cos(\phi - 2\theta)\right] \tag{17}$$

where $\theta = \tan^{-1}\left(\frac{\psi_2}{\psi_1}\right)$ and $\phi = \omega t - \alpha y - \psi_2 z$ (18)

The Lorentz body force $\underline{F}$ is given by $\underline{F} = \mathcal{R}\{\underline{J}\} \wedge \mathcal{R}\{\underline{B}\}$, (1.28), and we obtain using (16) and (17)

$$\mu_0 F_1 = \frac{R_{m_1}\alpha^2 z}{4|\psi|^2 h}(\mu_0 K_s)^2 e^{-2\psi_1 z}(1 + \cos 2\theta) - \frac{\alpha^2 R_{m_1}}{4|\psi|^3 h}(\mu_0 K_s)^2 e^{-2\psi_1 z}\left\{\cos\theta + \cos(2\phi - \theta)\right\} \tag{19}$$

$$\mu_0 F_2 = \frac{\alpha^3 R_m . s}{2|\psi|^2 h}(\mu_0 K_s)^2 e^{-2\psi_1 z}\left\{1 - \cos(2\phi - \theta)\right\} + \frac{R_{m_1}^2 \alpha^3 z^2}{8|\psi|^2 h}(\mu_0 K_s)^2 e^{-2\psi_1 z}\sin(2\phi - 4\theta) \tag{20}$$

$$\mu_0 F_3 = -\frac{R_{m_1}^2 \alpha^2 z}{8|\psi|^4 . h}(\mu_0 K_s)^2 e^{-2\psi_1 z}\left\{1 - \cos(2\phi - 4\theta)\right\} + \frac{\alpha^2 s R_m}{2|\psi|^2 . h}(\mu_0 K_s)^2 e^{-2\psi_1 z}\left\{\sin\theta - \sin(2\phi - \theta)\right\}$$

$$+ \frac{R_{m_1}^2 \alpha^2 z^2}{8|\psi|^2 h}(\mu_0 K_s)^2 e^{-2\psi_1 z}\left\{\cos\theta - \cos(2\phi - \theta)\right\} \tag{21}$$

(b) Case $\mathcal{P}$. Here $\mathcal{B}_3(0) = \mathcal{B}_m$, (1.48), where $\mathcal{B}_m$ is the peak normal magnetic induction on $z=0$, We find

$$\underline{\mathcal{B}} = \mathcal{B}_m e^{-4z}\left[-R_{m1}\frac{z}{2\mathcal{H}}, \frac{i\mathcal{H}}{\alpha}, 1\right] \tag{22}$$

$$\underline{\mathcal{J}} = \frac{\mathcal{B}_m}{\mu_0 L} e^{-4z}\left[-\alpha S R_m, \tfrac{1}{2}R_{m1}z - \frac{1}{2\mathcal{H}}R_{m1}, -\frac{i\alpha z}{2\mathcal{H}}R_{m1}\right] \tag{23}$$

The real parts of $\underline{\mathcal{B}}$ and $\mathcal{J}$ are:

$$\mathcal{R}\{\underline{\mathcal{B}}(z)e^{i(\omega t-\alpha y)}\} = \mathcal{B}_m e^{-4_1 z}\left[-R_{m1}\frac{z}{2|4|}\cos(\phi-\theta), \frac{|4|}{\alpha}\cos(\phi+\theta-\tfrac{\pi}{2}), \cos\phi\right] \tag{24}$$

$$\mathcal{R}\{\underline{\mathcal{J}}(z)e^{i(\omega t-\alpha y)}\} = \frac{\mathcal{B}_m}{\mu_0 L} e^{-4_1 z}\left[-\alpha S R_m\cos\phi, R_{m1}\frac{z}{2}\cos\phi - \frac{R_{m1}}{2|4|}\cos(\phi-\theta),\right.$$
$$\left. -\frac{\alpha z}{2|4|}\cdot R_{m1}\cdot\cos(\phi-\theta+\tfrac{\pi}{2})\right] \tag{25}$$

where θ and ϕ are given in (18). The Lorentz body force $\underline{\mathcal{F}}$ is given by (1.28), and we obtain using (24) and (25)

$$\mu_0\mathcal{F}_1 = \frac{R_{m1}\cdot\mathcal{B}_m^2\cdot z}{4L}e^{-2\mathcal{H}z}(1+\cos 2\theta) - \frac{R_{m1}\cdot\mathcal{B}_m^2}{4|4|L}e^{-2\mathcal{H}z}\{\cos\theta+\cos(2\phi-\theta)\} \tag{26}$$

$$\mu_0\mathcal{F}_2 = \frac{\alpha S R_m\cdot\mathcal{B}_m^2}{2L}e^{-2\mathcal{H}z}(1+\cos 2\phi) - \frac{R_{m1}\mathcal{B}_m^2\alpha z^2}{8|4|^2L}e^{-2\mathcal{H}z}\sin(2\phi-2\theta) \tag{27}$$

$$\mu_0\mathcal{F}_3 = -\frac{R_{m1}^2\mathcal{B}_m^2 z}{8|4|^2L}e^{-2\mathcal{H}z}\{1+\cos(2\phi-2\theta)\} + \frac{\alpha S R_m\mathcal{B}_m^2}{2\alpha L}|4|e^{-2\mathcal{H}z}\{\sin\theta+\sin(2\phi+\theta)\}$$
$$+\frac{R_{m1}^2\mathcal{B}_m^2\cdot z^2}{8|4|L}e^{-2\mathcal{H}z}\{\cos\theta+\cos(2\phi-\theta)\} \tag{28}$$

Results (13) to (28) may be compared with the EM field solutions given in §3.2. The magnetic induction vector is now fully three dimensional although the extra component, $\mathcal{B}_1$, is of order R_{m1}, which may be neglected when $R_{m1} \ll 1$. Additional components $\mathcal{J}_2$ and $\mathcal{J}_3$ are added to the current density vector but these components are also of order R_{m1}. The Lorentz force may be written, in the usual way, as the sum of a time dependent term $\underline{\mathcal{F}}^t$ and a time independent term $\underline{F}$:

$$\underline{\mathcal{F}} = \underline{\mathcal{F}}^t + \underline{F} \tag{29}$$

We see that $\mathcal{F}_2$ is unchanged from its value in §3.2 but an extra component $\mathcal{F}_1$ exists. This force, which is proportional to R_{m1}, tries to counteract the stretching and bending of the magnetic field lines by the imposed shear flow. Later we shall evaluate R_{m1} in terms of the Hartmann number using a similar analysis to that in §3.4.

4.2.2 Parallel Alignment. The shear flow configuration parallel to the direction of motion of the travelling wave is shown in figure 4.1 (b). Because U_0 is now zero we must have $R_{m1}=0$. Because there are now no inducing terms for $B_1(z)$ in (7), the boundary conditions on $z=0$ imply that this component of magnetic induction is zero everywhere.

(i) Exact formulation. We can reduce the induction equation (7) to the form

$$\frac{d^2\underline{B}}{d\zeta^2} - \zeta\underline{B} = [\,0,\ r^{-2/3}.R_{m2}B_3,\ 0\,] \tag{30}$$

In the derivation of (30) we have made the transformation

$$\zeta = (\gamma^2 + rz)\,r^{-2/3} \tag{31}$$

where

$$r = i\alpha^2 R_{m2} \tag{32}$$

and

$$\gamma^2 = \alpha^2\left\{1 + iR_m\left(1 - \frac{V+V_0}{V_s}\right)\right\} \tag{33}$$

The solution to (30) may be written as a linear combination of the two independent Airy functions $Ai(\zeta)$, $Bi(\zeta)$, (see ABRAMOWITZ and STEGUN, 1965). The basic properties of these functions have been included in Appendix I for completeness. As $\zeta\to\infty$, $Bi(\zeta)\to\infty$ and so the solution to (30) is of the form $\subseteq Ai(\zeta)$ where $\subseteq$ is a constant to be found from the boundary conditions.

Introducing the notation

$$\zeta_0 = \gamma^2 r^{-2/3} \quad ; \quad S = 1 - \frac{V+V_0}{V_s} \tag{34}$$

the solutions for the EM field can be shown to be

Case S:

$$\underline{B} = \mu_0 K_s\left[0,\ \frac{Ai'(\zeta)}{Ai'(\zeta_0)},\ \frac{r^{2/3}Ai(\zeta)}{R_{m2}\,Ai'(\zeta_0)}\right] \tag{35}$$

$$\mu_0\underline{J} = \frac{\mu_0 K_s}{h}\left[-\alpha S\,\frac{R_m}{R_{m2}}.r^{2/3}\,\frac{Ai(\zeta)}{Ai'(\zeta_0)},\ 0,\ 0\right] \tag{36}$$

Case P:

$$\underline{B} = B_m\left[0,\ \frac{R_{m2}}{r^{2/3}}.\frac{Ai'(\zeta)}{Ai(\zeta_0)},\ \frac{Ai(\zeta)}{Ai(\zeta_0)}\right] \tag{37}$$

$$\mu_0\underline{J} = \frac{B_m}{h}\left[-S\alpha R_m.\frac{Ai(\zeta)}{Ai(\zeta_0)},\ 0,\ 0\right] \tag{38}$$

The time averaged forces (1.31) are calculated as

Case S $$\underline{F} = \frac{\mu_0 K_s^2 \mathcal{R}}{2k}\left[0,\ s\propto \frac{R_m}{R_{m2}}\,|\tau|^{2/3}\left|\frac{Ai(\xi)}{Ai'(\xi_0)}\right|^2,\ -\alpha s\frac{R_m}{R_{m2}}\tau^{2/3}\frac{Ai(\xi)Ai'(\xi^*)}{|Ai(\xi_0)|^2}\right] \quad (39)$$

Case P $$\underline{F} = \frac{B_m^2}{2\mu_0 k}\mathcal{R}\left[0,\ s\propto R_m\left|\frac{Ai(\xi)}{Ai(\xi_0)}\right|^2,\ -\alpha s R_m R_{m2}(\tau^*)^{-4/3}\frac{Ai(\xi)Ai'(\xi^*)}{|Ai(\xi_0)|^2}\right] \quad (40)$$

Results (35) to (40) exactly describe the EM field and Lorentz force induced in a conducting half space by a travelling wave excitation when the specified shear flow is imposed. A comparison may be made with the results of §3.2. We see that a shear flow imposed parallel to the direction of the travelling wave does not induce a body force transverse to this direction - as we would expect from consideration of the symmetry of the problem. The electric currents (36), (38) and the time averaged forces (39), (40) are, as before, proportional to the slip, although in this case we see from the latter of (34) that a velocity V_0, representative of the imposed flow is also included in S.

It is apparent that the hydrodynamic analysis of §3.3 may equally be applied here. The slip in Chapter 3 was given by $S=(V_s-V)/V_s$ so if we replace V there by $V+V_0$, (using the latter of (34)), we find the average velocity here for the flow across the width of the channel, V, may be written in a form similar to (3.73) as

$$V = \frac{(V_s - V_0)\,Hm^2 . A}{1+Hm^2 A} + \frac{P^0}{1+Hm^2 A} \quad (41)$$

where Hm is the Hartmann number $(\mu_0 K_s (\frac{\rho}{\nu})^{1/2}$ or $R_m (\frac{\rho}{\mu})^{1/2})$ and P^0 an applied pressure gradient. The parameter A arises from integrating the terms containing in (39) and (40), as we have done in §3.41. Unfortunately there do not appear to be simple expressions for the required indefinite integrals and we have been unable to represent the integrals in terms of known functions. However, we see from (41) that it is the maximum value of the imposed shear velocity, (V_0), which dominates the back reaction effects by decreasing the synchronous velocity of the SLIP excitation relative to the conductor. When $V_0 << V_s$, the shear flow has little effect on the fluid motion and the

results of §3.4 are applicable. In this case the motion of the glass ribbon is included by assuming the velocity in the surface $z=0$ is equal to V_0, the velocity of the ribbon.

We now consider an approximate analysis of the parallel configuration.

(ii) J.W.K.B. approximation. The third component of (30) is

$$\frac{d^2B_z}{d\zeta^2} - \zeta B_z = 0 \tag{42}$$

An approximate solution to (42) may be obtained using the JWKB 'phase memory' method, which is applicable when ζ is large. Using (31) we find

$$B_z = \frac{C\, e^{-\int_0^z (\gamma^2+\tau z)^{1/2} dz}}{(\gamma^2+\tau z)^{1/4}} + O\left(\{\gamma^2+\tau z\}^{-9/4}\right) \tag{43}$$

where C is a constant to be found from the boundary conditions. If the case P boundary condition is applied, we find from (10) and (11), using (43)

$$\underline{B} \sim B_m \gamma^{1/2} e^{2\gamma^3/3\tau} e^{-\frac{2}{3\tau}(\gamma^2+\tau z)^{3/2}} \left[0,\ \frac{i(\gamma^2+\tau z)^{1/4}}{\alpha},\ (\gamma^2+\tau z)^{-1/4} \right] \tag{44}$$

$$J_1 \sim -\frac{\alpha B_m}{\mu_0 h} \cdot \gamma^{1/2} \cdot \zeta R_m \cdot e^{2\gamma^3/3\tau} e^{-\frac{2}{3\tau}(\gamma^2+\tau z)^{3/2}} \tag{45}$$

The time averaged Lorentz body force (1.31) is

$$\underline{F} \sim \frac{1}{2} R\left\{ \left(\frac{\zeta R_m \cdot B_m}{\mu_0 h}\right) e^{-\frac{2}{3}\left|\frac{(\gamma^2+\tau z)^{3/2}}{\tau}\right|} \cdot e^{\left|\frac{2\gamma^3}{3\tau}\right|} \cdot |\gamma^{1/2}|^2 \cdot \left[0,\ \frac{\alpha}{(\gamma^2+\tau z)^{1/4}},\ \frac{i(\gamma^2+\tau z)^{1/4}}{\alpha} \right] \right\} \tag{46}$$

Equations (44) to (46) are in fact the asymptotic forms of (37), (38) and (40), when γ is assumed large. The results of §3.2 may be recovered by expanding $(\gamma^2+\tau z)^{n/4}$, $(n=1 \text{ or } 6)$, as a power series neglecting terms of order $(\tau z/\gamma^2)^2$. This indicates that the imposed shear flow may be neglected unless $\tau = o(\gamma^2)$, that is, unless $R_{m2} \sim 1$.

When $R_{m2} \gg 1$, the imposed shear flow drags the magnetic field lines through the conductor and this reduces the magnitude of the normal magnetic field. This effect is equivalent to an increase in the electrical conductivity since the field lines become clustered at the surface of the conductor. Because τ is proportional to R_{m2}, (32), we can identify a skin depth $o(R_{m2}^{-1})$ for the EM field.

In their asymptotic form, the solutions to (30) do provide an adequate

description of the EM field variation. Unfortunately the induced body force (46) remains rather complicated. The process of substituting this force into the hydrodynamic equations and integrating w.r.t. z to find the induced velocity profiles has not been found tractable. There does not appear to be a solution to the indefinite integral (from(46))

$$\int (\gamma^2+rz)^{n/4}\, e^{-|(\gamma^2+rz)^{3/2}|}\, dz \qquad n = 1 \text{ or } -1$$

which can be written in terms of known functions.

The comments of (i) regarding the induced flow are equally appropriate here, but the parameter A is now obtained from (46). If the velocity profiles in this parallel configuration are required, we feel a different approach to the problem may prove more successful.

4.3 The Induced Velocity Profiles

We shall only consider the flow induced in a liquid conductor for the transverse configuration (§4.2.1). The dimensionless equations governing fluid flow ((1.22) and (1.23)) are:

$$\nabla \cdot \underline{V} = 0 \tag{47}$$

$$\rho\left\{ \frac{\partial \underline{V}}{\partial t} + L(\underline{V}\cdot\nabla)\underline{V} \right\} = -L\nabla P + L^2 \underline{\mathcal{F}} + \nu \nabla^2 \underline{V} \tag{48}$$

We have already noted the similarity between $\mathcal{F}_2$ in §4.2.1 and $\mathcal{F}_2$ in §3.2, and it was shown in §3.3 that a stationary solution exists for the velocity component parallel to the direction of the travelling wave. We shall assume the velocity $\underline{V}$ may be written in the form

$$\underline{V} = \left[u(z) + \ell\ell(y,z,t) \;,\; v(z) + \ell(y,z,t) \;,\; 0 \right] \tag{49}$$

The inertia term $(\underline{V}\cdot\nabla)\underline{V}$ becomes (with $\frac{\partial}{\partial x} = 0$)

$$(\underline{V}\cdot\nabla)\underline{V} = v(z)\frac{\partial \ell\ell}{\partial y}\underline{e}_1 \tag{50}$$

Taking the divergence of (48) using (49) and (50), we find the pressure satisfies the Poisson equation,

$$\nabla^2 P = L\left(\frac{\partial \mathcal{F}_1}{\partial y} + \frac{\partial \mathcal{F}_2}{\partial z} \right) \tag{51}$$

The third component of (48) gives

$$\frac{\partial P}{\partial z} = h\, \mathcal{F}_3 \tag{52}$$

Combining (51) and (52), we see that $\left(\frac{\partial P}{\partial y} - h\mathcal{F}_2\right)$ is independent of y, and so, as in §3.4, a stationary solution for the second component of $\underline{v}$ is possible and we may set $V(y,z,t)$ equal to zero.

Using (29), (49) and (50), we can reduce (48) to

$$\nu\left(\frac{\partial^2}{\partial y^2} + \frac{\partial^2}{\partial z^2}\right) u - \rho\left(h^2 \frac{\partial \ell l}{\partial t} + V(z)\frac{\partial \ell l}{\partial y}\right) = -h^2\, \mathcal{F}_1^t(y,z,t) \tag{53}$$

$$\nu \frac{d^2 u}{dz^2} = h\left(\frac{\partial P}{\partial x}\right)_0 - h^2 F_1(z) \tag{54}$$

$$\nu \frac{d^2 v}{dz^2} = h\left(\frac{\partial P}{\partial y}\right)_0 - h^2 F_2(z) \tag{55}$$

Here, the terms $\left(\frac{\partial P}{\partial x}\right)_0$, $\left(\frac{\partial P}{\partial y}\right)_0$ represent the constant applied external pressure gradient. It is apparent that ℓl will have the same time variation as $\mathcal{F}_1^t$: so ℓl will oscillate with an angular frequency twice that of the inducing field and thus may be ignored when discussing the overall motion of the liquid.

Equation (55) is identical to (3.59) and so the results of §3.4.4 hold here. The pressure P can be obtained from (51) by inspection, and we can obtain solutions similar to (3.57) and (3.58). The slip (12) is thus given by (3.76). Substituting for $F_1(z)$ in (54) we obtain (writing $R_{m_1} = \frac{(u_0 - U)h}{\nu}$)

$$\frac{d^2 u}{dz^2} = \frac{h}{\nu}\left(\frac{\partial P}{\partial x}\right)_0 - (u_0 - U) H_m^2 \cdot p\left(z - \frac{\psi_1}{|\psi|^2}\right) e^{-2\psi_1 z} \tag{56}$$

where $p = \frac{\alpha^2}{4|\psi|^2}$ Case S; $\frac{1}{4}$ Case P (57)

and $H_m = Bh\left(\frac{\sigma}{\nu}\right)^{1/2}$ is the Hartmann number, with $B = \mu_0 K_1$ or B_m. The solution to (56) subject to the boundary conditions, $u(0) = u_0$, $u(1) = 0$ (see §1.4.7) is (writing $\beta = \frac{\psi_1}{|\psi|^2}$)

$$u(z) = u_0(1-z) + \frac{1}{2\nu}\left(\frac{\partial P}{\partial x}\right)_0 z(z-1) - (u_0 - U) H_m^2 \cdot \frac{2p}{(2\psi_1)^3}\left\{ z e^{-2\psi_1}\left[1 + \psi_1(1-\beta)\right] - e^{-2\psi_1 z}\left[1 + \psi_1(z-\beta)\right] + (1-z)(1-\psi_1\beta) \right\} \tag{58}$$

Following the procedure of §3.4.4 we may write (58) in the form

$$u(z) = 2U_{sh}(1-z) + 6U_1(z-1)z - \frac{U_m}{R_1}\left\{ z e^{-2\psi_1}\left[1 + \psi_1(1-\beta)\right] + \frac{\psi_1}{(2\psi_1)^2}\left(e^{-2\psi_1} - 1\right) + (1-z)(1-\psi_1\beta) \right\} \tag{59}$$

where $$R_1 = \tfrac{1}{2} e^{-2\psi_1}\left(1+\tfrac{1}{\psi_1}\right)\left[1+\psi_1(1-\beta)\right] + \frac{\psi_1}{(2\psi_1)^2}\left(e^{-2\psi_1}-1\right) + \tfrac{1}{2}(1-\psi_1\beta)\left(1-\tfrac{1}{\psi_1}\right) \qquad (60)$$

$$U = \int_0^1 u(z)\,dz = U_M + U_P + U_m \qquad (61)$$

$$U_M + U_P = \tfrac{1}{2}u_0 - \frac{1}{12\nu}\left(\frac{\partial P}{\partial x}\right)_0 \qquad (62)$$

$$U_m = (u_0 - U)\,\frac{H_m^2 \cdot 2\beta R_1}{(2\psi_1)^3} \qquad (63)$$

In the above U is the average velocity of the liquid conductor across the channel, U_M is the average velocity of the imposed shear flow, U_P the average velocity induced by the pressure gradient, and U_m is the average velocity induced by the back reaction of the EM field. Equations (59) to (63) describe the flow induced by the SLIP when the glass ribbon moves transverse to the direction of the travelling wave.

4.3.1 MHD Effects. From (61) to (63) we obtain the following expression for the average velocity U experienced by the liquid conductor

$$U = U_M \frac{1 + 2R_2 H_m^2}{1 + R_2 H_m^2} + \frac{U_P}{1 + R_2 H_m^2} \qquad (64)$$

where $$R_2 = -2\beta \cdot R_1 / (2\psi_1)^3 \qquad (65)$$

As $H_m \to 0$, (64) gives $U \to U_M + U_P$ as we would expect. When $H_m \to \infty$ the term containing the average velocity due to the pressure gradient, U_P, becomes zero because the magnetic field lines resist the motion, but the term containing U_M remains finite. This apparent contradiction is explained as follows. When H_m is finite, the shear flow we impose is 'seen' by the whole depth of liquid conductor, but as $H_m \to \infty$, the flow becomes stationary below the surface $z=0$. However, the liquid 'sees' its surface moving with an imposed velocity u_0, and since this is the only part of the liquid which is moving we can say $U = u_0$, agreeing with (64) when $H_m \gg 1$.

The average velocity due to the EM field U_m is obtained from (63) and (64) we have

$$U_m = \frac{U_M H_m^2 R_2}{1 + R_2 H_m^2} \qquad (66)$$

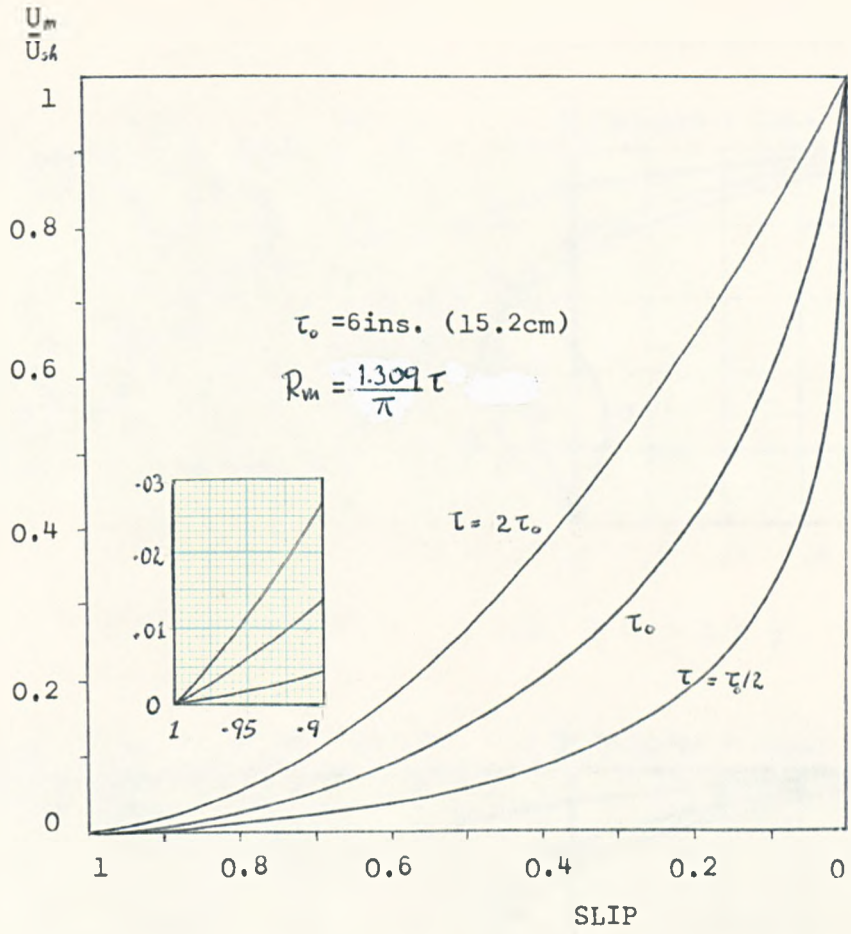

Fig. 4.2 The Transverse Motion Induced for a given Axial Slip

The variation of U_m / U_{sh} with axial slip and pole pitch (τ) is shown in figure 4.2. We consider three values of the pole pitch: $\frac{1}{2}\tau_o$, τ_o and $2\tau_o$, where τ_o (1.309) is the pole pitch of the float bath motor (15.2 cms), (see table 1.1). The magnetic Reynolds number (R_m) is set equal to unity for $\tau = \tau_o$. We note that for a given Hartmann number (H_m) the axial slip is obtained from figures 3.5 and 3.8. The results are identical for the case S and case P analyses.

The profiles induced by the action of the EM field (the third expression on the right of (59)) are shown, together with the total velocity profile, (59), when $U_p = 0$, in figure 4.3 (a) (for a slip of 0.1) and in figure 4.3 (b) (for a slip of 0.9). In both graphs we show the variation over three values of τ, (as above). It is clear that in this steady state configuration back flow occurs as the magnetic field lines

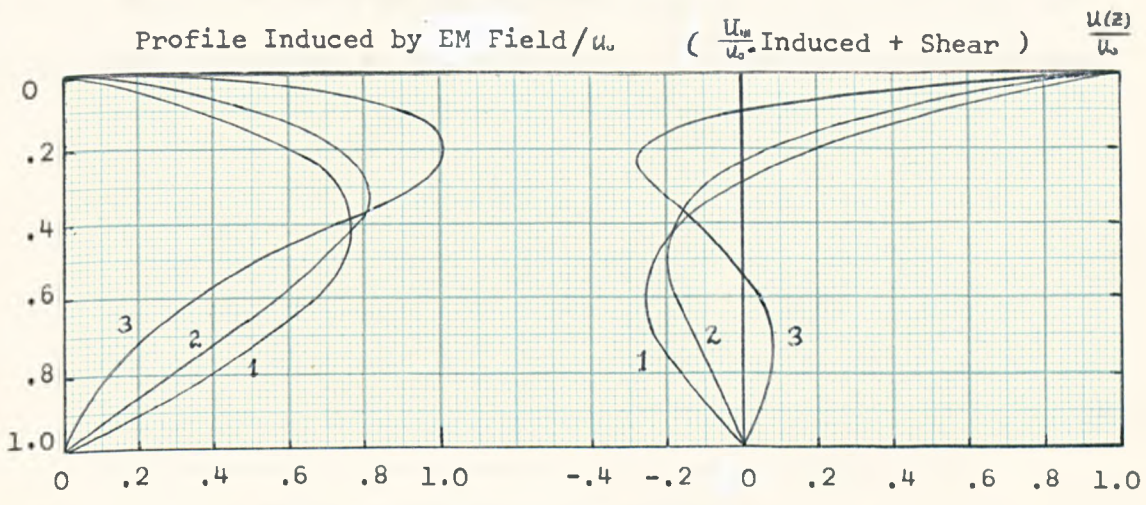

Fig. 4.3(a) Axial Slip s = 0.1 (1: $2\tau_o$ 2: τ_o 3: $\tau_o/2$)

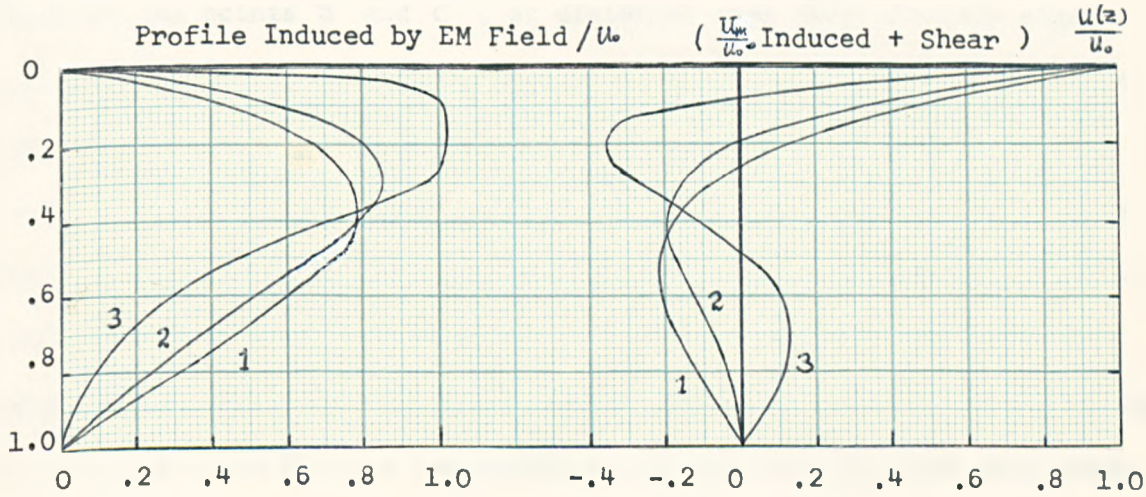

Fig. 4.3(b) Axial Slip s=0.9 $R_m = \frac{1309}{\pi} \cdot \tau$ $\tau_o = 15{\cdot}2$ cm

resist the motion of the imposed shear flow. Note that unlike the profiles of figures 3.4(a) and 3.4(b), here there is a noticable dependence upon the magnitude of the axial slip.

4.4 A Finite Width SLIP

The results of §4.3 are applicable to the steady state analysis of an idealised SLIP. However, if the SLIP is of finite width, does the working liquid have sufficient time to develop backflow?

Consider a section through an infinitely long SLIP, of finite width (figure 4.4) with an imposed shear flow as shown. The origin for the

coordinate system is taken at the entrance edge A of the SLIP and the axis is chosen transverse to the SLIP axis. A possible flow development

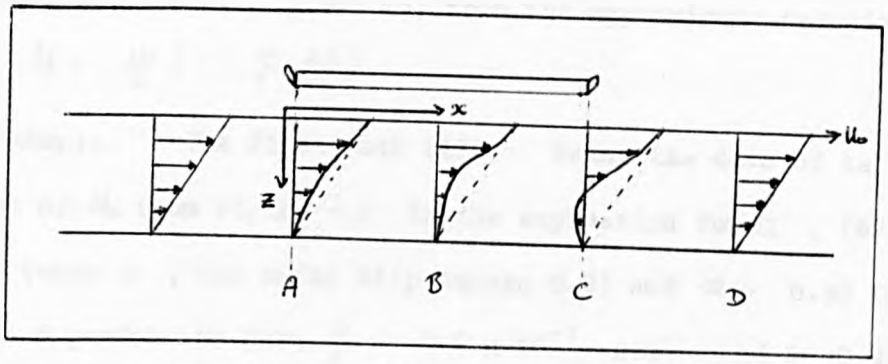

Fig. 4.4 Possible Flow Profiles

is shown at the points B and C ; at distances away from the exit edge of the SLIP (D) the profile returns to that of an imposed shear flow. (In practice an inflow of material must occur in regions below the SLIP to maintain continuity of flow). At A , because $U = U_{sh}$, there is no force induced in the conducting liquid along the x axis. However at B (and C) the deformation of the magnetic field lines induces a force in the liquid so as to resist the flow. If we consider (as in §3.5) the motion of a 'slug' of fluid beneath the SLIP we can obtain an estimate of the flow development using Newton's second law. The transverse force produced by the SLIP can be obtained from (19) and (26); taking the force on $z = o$ as representative we can write:

$$\rho \frac{dU}{dt} = (U - u_0)\, Q \qquad \text{where} \qquad Q = \frac{\psi_1}{141^2} \cdot p \cdot H\omega^2 \tag{67}$$

where ρ is the density of the working fluid; U is the average velocity of the fluid along the x axis and u_0 is the speed of the glass ribbon. The parameter p is given by (57). The solution to (67) for the velocity U given the initial conditions $U = u_0/2$ when $t = o$ is

$$U = u_0 - \frac{u_0}{2} e^{Qt/\rho} \sim \frac{u_0}{2}\left(1 - \frac{Qt}{\rho}\right) \qquad \frac{Qt}{\rho} \ll 1 \tag{68}$$

Using (68) we can describe the effects to be expected in the float bath configuration. The solution for U is of course invalid when $\frac{Qt}{\rho} > 1$ since U must always be finite , but we may consider the solution for $\frac{Qt}{\rho} \ll 1$

as a reasonable estimate of the decrease in U with time. If the width of the slip is d then the time taken for the slug to traverse the SLIP is approximately $2d/u_o$, and so, from the approximate solution in (68), we have $U \sim \frac{u_o}{2}\left(1 - \frac{Q}{\ell}\cdot\frac{2d}{u_o}\right)$

4.4.2 Example. The Float Bath SLIP. Using the data of table 1.1 and the values of H_w from figure 3.5 in the expression for Q, (67), we find $Q \sim 0.4$ (when S, the axial slip equals 0.9) and $Q \sim 0.33$ (when $S = 0.1$) With $\rho = 6.8$ gms/cc we have $\frac{Q}{\rho} \sim 0.5 \times 10^{-3}$ sec^{-1} ($S = 0.9$) and $\frac{Q}{\rho} \sim 0.02$ sec^{-1} ($S = 0.1$). Thus for the average velocity U, given by (68), to change by 10 per cent we require $t > 50$ seconds ($S = 0.9$) and $t > 0.5$ seconds ($S = 0.1$). For a SLIP of width 10 cms (4 inches) this requires a ribbon speed (u_o) less that 0.4 cm/sec ($S = 0.9$) or less than 40 cm/sec ($S = 0.1$).

The case S and case P analyses produce identical results.

We conclude that there is very little modification to the imposed shear flow in the float bath when the ribbon moves at its normal (see table 1.1) speed and the external applied pressure gradients are small.

5. THE BOUNDARY LAYER REGIONS OF A SLIP

5.1 Introduction

In this chapter we present a heuristic analysis of the physical processes involved in the boundary layer regions of a SLIP. In §5.2 we use the singular perturbation method to illustrate the importance of certain physical parameters in the decay of the EM field. In §5.3 we consider a rectangular excitation and obtain $1/e$ folding lengths for the EM field decay both parallel and normal to the secondary conductor surface. Finally, in §5.3 we use an order of magnitude argument to compare the EM fields induced in the boundary layer regions under the case S and case P analyses.

5.2 Shear Flow Parallel to the SLIP Axis

This problem has been analysed in Chapter 4; in §4.2.2 we obtained exact solutions for the induced EM field in terms of Airy's functions. These solutions were however extremely complicated and only yielded information concerning the behaviour of the EM field when asymptotic estimates were used. However it is possible to avoid a complex analysis of the induction equations if all we require is a knowledge of the asymptotic behaviour of the EM field. The method of approach used below is the Singular Perturbation technique (VAN DYKE, 1964). This technique may be used when a small parameter ϵ occurs as a coeffieient of the highest derivative in a differential equation. Over much of the range this term can be considered negligible and the differential equation may be reduced to one of lower order. The solution to this reduced equation is called the 'outer solution'. In certain regions (the boundary layers), the highest order derivative becomes large. A solution in these regions (the 'inner solution') is obtained by performing a transformation of the coordinates sufficient to remove the ϵ coefficient. The complete solution obtained is thus discontinuous, but an estimate of the continuous

solution may be obtained by matching the inner and outer solutions in an intermediate region.

We shall use the model, notation and equations of Chapter 4 in the following analysis. First we give a brief description of the problem. An idealised SLIM is placed on the surface of an electrically conducting half space ($z>0$) which is assumed to move with a constant velocity V, together with an imposed shear velocity, $V_0(1-\frac{z}{L})$, parallel with the direction of the travelling wave excitation, (figure 5.1).

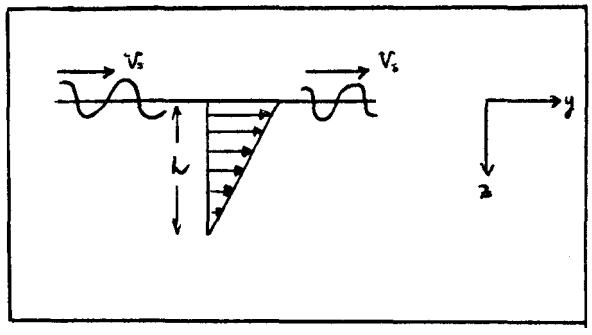

Fig 5.1 The Idealized Configuration

The velocity V arises from the 'drag' of the magnetic field lines through the conductor; we can identify a slip S_0 given by

$$S_0 = 1 - \left(\frac{V+V_0}{V_s}\right) \qquad (1)$$

where $V_s = \omega L/\alpha$, (α dimensionless), is the synchronous velocity of the excitation. The parameter S_0 is the slip at the surface of the conductor. When the shear-inducing glass ribbon moves at the speed of the travelling wave, $(V_0 \sim V_s)$, the drag on the conducting liquid is small and so $V \sim 0$. In this case $S_0 \sim 0$, and the shear flow influences the induced EM field to a great extent. When V_0 is small $(V_0 \ll V_s)$ the motion of the glass ribbon may be neglected. In this section we discuss the decay of the EM field into the conductor when the parameters α, R_m and R_{m2} are separately considered large, $(R_m = V_s L/\alpha\eta$ is the magnetic Reynolds number based on the wave velocity and $R_{m2} = V_0 L/\eta$ is the magnetic Reynolds number based on the ribbon velocity).

We shall assume $B_1 = 0$ throughout. For boundary conditions we use

the case P excitation ($B_3 = B_m$ on $z=0$) and decay of the EM field as $z \to \infty$. The reduced (dimensionless) forms of Maxwell's equations (1.11), (1.1) and (1.4) appropriate for this problem have been derived in Chapter 4. We have respectively

$$\frac{d^2\underline{B}}{dz^2} = \alpha^2(1+is R_m)\,\underline{B} + R_{m2}\,B_3\,\underline{e}_2 \tag{2}$$

$$\frac{dB_3}{dz} = i\alpha B_2 \tag{3}$$

$$\mu_{oh}\,\underline{J} = -\left(i\alpha B_3 + \frac{dB_2}{dz}\right)\underline{e}_1 \tag{4}$$

where
$$S(z) = 1 - \frac{V}{V_s} - \frac{V_o}{V_s}(1-z) \tag{5}$$

It is clear from (2) that the outer solutions, when α, R_m and R_{m2} are large are the trivial cases with $\underline{B}=\underline{0}$. Consequently we shall only consider the inner solutions.

5.2.1 α Large. Writing $\alpha = 1/\epsilon$, (2) becomes

$$\epsilon^2 \frac{d^2B_2}{dz^2} = (1+is R_m)\,B_2 + \epsilon^2 R_{m2}\,B_3 \tag{6}$$

$$\epsilon^2 \frac{d^2B_3}{dz^2} = (1+is R_m)\,B_3 \tag{7}$$

From the definition of R_m we see that $R_m = O(\epsilon^2)$. We shall assume that $R_{m2} = O(1)$. Equations (3) and (4) become respectively

$$\epsilon \frac{dB_3}{dz} = i\alpha B_2 \qquad J_1 = -\frac{1}{\mu_{oh}}\left(\frac{i}{\epsilon}B_3 + \frac{dB_2}{dz}\right) \tag{8}$$

The inner solution is found by writing $z = \epsilon^n \zeta$ where n is chosen so as to include the highest order differential in (6) and (7) when ϵ is made small. When $n=1$ and $\epsilon \to 0$, (6) and (7) reduce to

$$\frac{d^2B_2}{d\zeta^2} \sim B_2 \qquad \frac{d^2B_3}{d\zeta^2} \sim B_3 \tag{9}$$

and (8) becomes

$$\frac{dB_3}{d\zeta} \sim iB_2 \qquad \epsilon J_1 \sim -\frac{1}{\mu_{oh}}\left(iB_3 + \frac{dB_2}{d\zeta}\right) \tag{10}$$

The solutions to(9) using the first of (10) and the assumed boundary conditions are

$$B_2 \sim iB_m e^{-\zeta} \qquad B_3 \sim B_m e^{-\zeta} \tag{11}$$

Substituting (11) in the second of (10) leads to $J_1 \sim 0$. Substituting back for z in (11) we find the $1/e$ folding length for the EM field decay is ϵ $(= 1/\alpha)$. Thus an increase in α (which implies a decrease in the pole pitch) effectively reduces R_m (which is proportional to the conductivity and angular frequency of the excitation) and the skin depth of the EM field tends towards that for a non-conductor.

5.2.2 R_m Large. Writing $R_m = 1/\epsilon$, (2) becomes

$$\epsilon \frac{d^2 B_2}{dz^2} = \alpha^2 (1+is) B_2 + \epsilon R_{m2} B_3 \qquad (12)$$

$$\epsilon \frac{d^2 B_3}{dz^2} = \alpha^2 (1+is) B_3 \qquad (13)$$

We shall assume both α and R_{m2} are of order unity. When there is no pressure gradient we may assume $s>0$. If we neglect the product zV_0 (since $z \ll 1$ in the boundary layer) the variable slip s becomes equal to s_0 . Using the transformation $z = \epsilon^{1/2}\xi$, (12), (13), (3) and (4) become respectively

$$\frac{d^2 B_2}{d\xi^2} = i\alpha^2 s B_2 + \epsilon (\alpha^2 B_2 + R_{m2} B_3) \qquad (14)$$

$$\frac{d^2 B_3}{d\xi^2} = i\alpha^2 s B_3 + \epsilon \alpha^2 B_3 \qquad (15)$$

$$\frac{dB_3}{d\xi} = i\alpha \epsilon^{1/2} B_2 \qquad J_1 = -\frac{1}{\mu_0 L}\left(i\alpha B_3 + \frac{1}{\epsilon^{1/2}} \frac{dB_2}{d\xi}\right) \qquad (16)$$

A first approximation solution to (14) and (15) is obtained by letting $\epsilon \to 0$. We find the trivial case $\underline{B} \sim \underline{0}$, $J_1 \sim 0$ is recovered, agreeing with the known results for an infinitely conducting medium. A second approximation solution to (14) and (15) is found by assuming $B_3(\xi) = o(\epsilon^{1/2})$. The solutions obtained on letting $\epsilon \to 0$ in this case can be shown to be

$$B_2 \sim -B_m \sqrt{\frac{s}{i\alpha}}\, e^{-\xi\sqrt{i\alpha^2 s}} \qquad B_3 \sim \epsilon^{1/2} B_m e^{-\xi\sqrt{i\alpha^2 s}} \qquad J_1 \sim \frac{B_m}{\mu_0 L} s\, e^{-\xi\sqrt{i\alpha^2 s}} \qquad (17)$$

Equations (17) indicate a skin depth $(\alpha^2 s R_m/2)^{-1/2}$ may be associated with the decay of the EM field. Because $0 \ll s \ll 1$, we know $s^{1/2} \sim 1$ and conclude that the skin depth is largely independent of the slip. However we see from (17) that the electric current (and thus the induced body force) is proportional

to the slip. The tendency of the conductor to exclude the EM field is clearly shown by the order of $\mathcal{B}_3$ in (17). When the conductivity becomes infinite ($\epsilon \to 0$) the normal magnetic field disappears and the discontinuity in the tangential field at the surface of the conductor sets up a surface current density, (see §1.4.6).

5.2.3. $R_{m_2} = o(R_m)$. Here the imposed shear flow is as important as the inducing excitation in the evaluation of the induced EM field. Because $V_0 \sim V_3$, the surface of the conductor 'sees' a stationary excitation and so $V \sim 0$. Thus S is proportional to z. A boundary layer transformation can be made but the solution to (2) still involves the Airy function. However we can assess the effect of an imposed shear flow assuming the simplified model of figure 5.2.

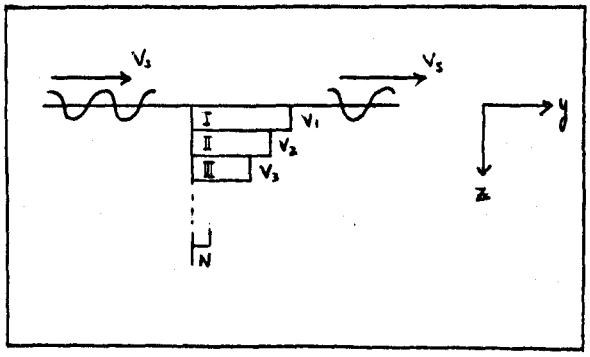

Fig. 5.2 Simplified Shear Model

We divide a depth L of the conductor into N regions and let each region move with a constant velocity parallel with the direction of the travelling wave. Denoting the velocity of region r by V_r, we assume $V_{r+1} < V_r$ and so $S_{0,r+1} > S_{0,r}$ (where from (5), $S_{0,r} = 1 - \frac{V_r + V_0}{V_3}$). If $V_1 \sim V_3$, $S_{0,1} \sim 0$ and the decay of the EM field is that of §5.2.1. In region II, $V_2 < V_3$ so $S_{0,2} > 0$ and the rate of decay is that given in §5.2.2 which is greater than the rate of decay in region I. This process may be continued until the N'th region is reached. There we assume $V_N = 0$ and $S_{0,N} = 1$. In this region we see the maximum rate of decay is achieved. By letting $N \to \infty$ and adjusting the velocities, the imposed shear flow can

be recovered. There is thus a gradual increase in the rate of decay of the EM field with depth into the conductor. We can obtain an expression for the magnitude of the EM field at any depth as follows.

Using the simplified shear model above the magnitude of the EM field at a depth z_r, lying inside region r is proportional to $\exp\left\{-\frac{L}{N}\left(\sum_r' \alpha_r\right)\right\} \cdot \exp\left\{-\alpha_r\left(\frac{rL}{N} - z_r\right)\right\}$. Here α_r is the decay parameter of region r obtained from the induction equation (2). We have $\alpha_r = \alpha\left(1 + i S_r R_m\right)^{1/2}$, with, from (5), $S_r = 1 - \frac{V_r}{V_s} - \frac{V_o}{V_s}(1 - z_r)$. Letting $N \to \infty$, we can write $\frac{L}{N} \sim \delta z_r$, and replace $\sum_r'$ by an integral. The exponential factor representing the EM field decay is then given by $\int_0^z \alpha\left(1 + i S_r R_m\right)^{1/2} dz_r$, which gives, on performing the substitution for S_r, the expression previously obtained in §4.2.2.(ii), which was obtained from the asymptotic expansion of the Airy function.

5.3 Finite Excitation.

Here we give an estimate for the boundary layer scale lengths of the EM field induced in an electrically conducting half space by a SLIM, using a rectangular travelling wave excitation of constant magnitude. Cartesian axes are chosen with origin at the centre of the rectangular excitation and z axis pointing into the conductor, (figure 5.3). The excitation is taken to be of length $2b$ metres and width $2a$ metres to allow comparison of the results obtained here with those of later chapters. (Here we consider a simplified form of this rectangular excitation).

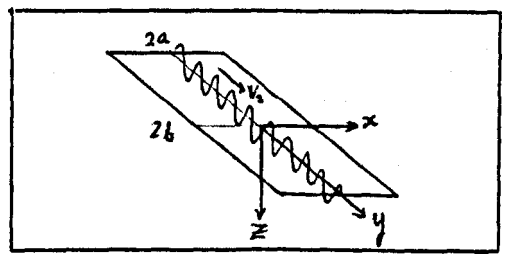

Fig. 5.3 The Rectangular Excitation

The conductor is assumed to move with a constant velocity $\underline{V}$ given by

$$\underline{V} = [U, V, 0] \qquad (18)$$

We introduce a scale length L (the molten tin depth) and the dimensionless variables $x^* = x/L$, $y^* = y/L$, $z^* = z/L$, $\alpha^* = \alpha L$, $a^* = a/L$, $b^* = b/L$. All parameters will be assumed dimensionless from now on, so we ignore the star superscripts. Substituting (18) in (1.11) we obtain the dimensionless induction equation for the conducting region $z > 0$

$$\left(\frac{\partial^2}{\partial x^2} + \frac{\partial^2}{\partial y^2} + \frac{\partial^2}{\partial z^2} \right) \underline{B} = \left(R_{m_1} \frac{\partial}{\partial x} + R_{m_2} \frac{\partial}{\partial y} + i\alpha^2 R_m \right) \underline{B} \qquad (19)$$

Here we have written $\underline{B}(\underline{r},t) = \underline{B}(\underline{r}) e^{i\omega t}$; $R_m = V_s L/\alpha\eta$, $R_{m_1} = UL/\eta$ and $R_{m_2} = VL/\eta$ are magnetic Reynolds numbers for the motion and $V_s = \omega L/\alpha$ is the synchronous wave velocity.

Suppose we can identify a large parameter (which we write as $\frac{1}{\epsilon}$ for ϵ small) in the right of (19), then we can apply the singular perturbation method of §5.2 to obtain boundary layer approximations for the induced EM field. Because the differential terms on the left of (19) are all of the same form we see that there are four main boundary layer regions:

Region I	$o\left(\frac{\partial}{\partial z}\right) \gg o\left(\frac{\partial}{\partial x}, \frac{\partial}{\partial y}\right)$	(idealised configuration)
Region II	$o\left(\frac{\partial}{\partial z}\right) \sim o\left(\frac{\partial}{\partial y}\right) \gg o\left(\frac{\partial}{\partial x}\right)$	(end regions)
Region III	$o\left(\frac{\partial}{\partial z}\right) \sim o\left(\frac{\partial}{\partial x}\right) \gg o\left(\frac{\partial}{\partial y}\right)$	(edge regions)
Region IV	$o\left(\frac{\partial}{\partial z}\right) \sim o\left(\frac{\partial}{\partial y}\right) \sim o\left(\frac{\partial}{\partial x}\right)$	(corner regions)

These regions, with the exception of IV, are shown in figures 5.4, (cross section in the (y,z) plane) and 5.5, (cross section in the (x,z) plane), together with the outer regions where $\underline{B} = \underline{0}$. Region IV corresponds to the corner areas and will not be considered in the analysis below. The

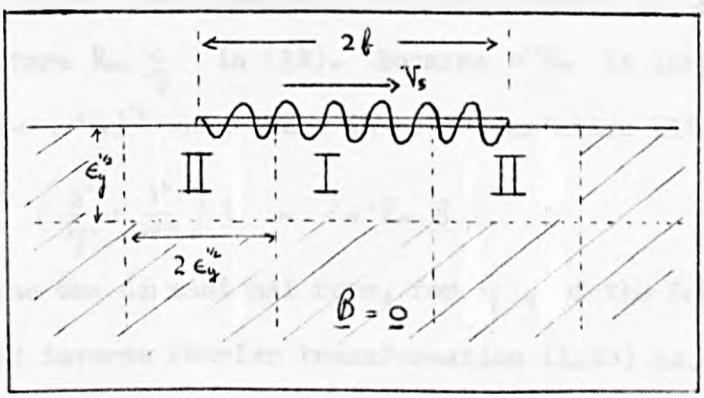

Fig. 5.4 Cross Section in the (y,z) Plane

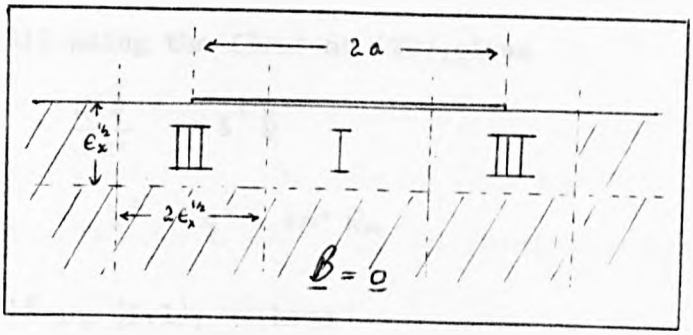

Fig. 5.5 Cross Section in the (x,z) Plane

EM field solutions in I are those previously obtained in chapters 3 and 4 for an idealised excitation of infinite extent. The width of regions II and III will be the order of twice the skin depth (which is approximately $\epsilon^{1/2}$).

5.3.1 Infinite Width Excitation. The configuration for this problem is shown in figure 5.4. We have previously noted (§1.5.3) that the discontinuity in the excitation at $y = \pm b$ introduces pulsating components in regions II. Because the EM field in II does not 'see' a pure travelling wave we would expect the variation with distance to be largely independent of the wave number α. This is certainly true beyond the excitation where the induced fields arise largely from the end teeth of the motor. Thus we can obtain first approximation solutions for the induced EM field in II using the following boundary conditions on $z=0$, using the form of (1.47) and (1.48):

$$\text{Case S}: \quad B_z(\underline{r})\Big|_{z=0} = \mu_0 K_s \, \delta(y) \qquad \text{Case P}: \quad B_z(\underline{r})\Big|_{z=0} = B_m \, \delta(y) \tag{20}$$

where $\delta(y)$ is the Dirac delta function. As usual we impose damping of the EM field at infinity. For simplicity we shall assume R_{m2} is small enough to neglect the term $R_{m2}\frac{\partial}{\partial y}$ in (19). Because $\alpha^2 R_m$ is large, this neglect is valid if $R_m \ll (\alpha^2 R_m)^{-\frac{1}{2}}$ when there is no x variation (19) reduces to

$$\left(\frac{\partial^2}{\partial y^2} + \frac{\partial^2}{\partial z^2}\right)\underline{B} = i\alpha^2 R_m \underline{B} \tag{21}$$

We now define the one dimensional form, for y, of the fourier transformation (1.32) and inverse Fourier transformation (1.33) as, respectively

$$\hat{M}(q,z) = \int_{-\infty}^{\infty} M(y,z)\, e^{+iqy}\, dy \qquad M(y,z) = \frac{1}{2\pi}\int_{-\infty}^{\infty} \hat{M}(q,z)\, e^{-iqy}\, dq \tag{22}$$

Transforming (21) using the first of (22), gives

$$\frac{d^2\hat{\underline{B}}}{dz^2} = \gamma^2 \hat{\underline{B}} \tag{23}$$

where $$\gamma^2 = q^2 + i\alpha^2 R_m \tag{24}$$

Transforming $\nabla.\underline{B}=0$, (1.1), we have

$$\frac{d\hat{B}_3}{dz} = iq\,\hat{B}_2 \tag{25}$$

The boundary conditions (20) transform to

$$\text{Case S}: \hat{B}_2(q,0) = 2\pi\mu_0 K_s \qquad \text{Case P}: \hat{B}_3(q,0) = 2\pi B_m \tag{26}$$

The solution to (23) is obtained in the form $\hat{\underline{B}} = \underline{C} e^{-\gamma z}$, where the constant $\underline{C}$ is found from the boundary conditions on $z=0$. Using (25) and (26) we find, (with $B_1=0$):

$$\text{Case S}: \quad \frac{1}{2\pi}\hat{\underline{B}} = \mu_0 K_s . e^{-\gamma z}\underline{e}_2 - \frac{iq}{\gamma}.\mu_0 K_s e^{-\gamma z}\underline{e}_3 \tag{27}$$

$$\text{Case P}: \quad \frac{1}{2\pi}\hat{B}_3 = \frac{i\gamma}{q} B_m e^{-\gamma z}\underline{e}_2 + B_m e^{-\gamma z}\underline{e}_3 \tag{28}$$

Inverting (27) and (28) by the latter of (22) and using the symmetry of the kernels we find

$$\text{Case S}: \quad B_2 = 2\mu_0 K_s \int_0^\infty e^{-\gamma z}\cos qy\, dq \qquad B_3 = -2\mu_0 K_s \int_0^\infty \frac{q}{\gamma} e^{-\gamma z}\sin qy\, dq \tag{29}$$

$$\text{Case P}: \quad B_2 = 2B_m \int_0^\infty \frac{\gamma}{q} e^{-\gamma z}\sin qy\, dq \qquad B_3 = 2B_m \int_0^\infty e^{-\gamma z}\cos qy\, dq \tag{30}$$

The integrals in (29) and (30) are given in BATEMAN (1954), (p.16 and p.75) Performing the integration, we find after simplification that:

$$\text{Case S}: \quad \underline{B} = 2\mu_0 K_s \left\{ z\,\underline{e}_2 - y\,\underline{e}_3 \right\} \frac{K_1\left(\sqrt{2iR_m(y^2+z^2)}\right)}{(y^2+z^2)^{1/2}} \tag{31}$$

$$\text{Case P}: \quad B_3 = 2B_m . z . \frac{K_1\left(\sqrt{2iR_m(y^2+z^2)}\right)}{(y^2+z^2)^{1/2}}, \quad B_2 = \int_{-\infty}^{y} \frac{dB_3}{dz}.dy \tag{32}$$

In (31) and (32), $K_1(\phi)$ is Bessel's modified function of the second kind of order unity. We have not been able to obtain the solution for B_2 in the case P analysis in closed form. It is immediately apparent that, in

some circumstances, the choice of a case S or case P analysis should be governed, not by physical constraints, but by the ease with which we can obtain closed solutions. The form of (31) and (32) does not yield a great deal of information, but using the asymptotic form of $K_1(\phi)$, viz:

$$K_1(\phi) \sim \sqrt{\frac{\pi}{2\phi}}\, e^{-\phi} \qquad \phi >> 1 \tag{33}$$

we see that the EM field decays with an exponential factor $\{ i\alpha^2 R_m (y^2+z^2)\}^{1/2}$ We see that both the skin depth and longitudinal decay scale length are of the same order, and equal to $\left(\frac{\alpha^2 R_m}{2}\right)^{1/2} = \epsilon_y^{1/2}$, (figure 5.4). Using (1.4) we can obtain expressions for the induced electric currents and from (1.3.1) expressions can be derived for the induced body force. In this simplified model however, these results are of little interest.

5.3.2 Infinite Length Excitation. The configuration for this problem is shown in figure 5.5. Regions III are the edge effect regions previously described in §1.5.3. The only y variation arises from the travelling wave source, so we assume the magnetic field varies as the source and write $\underline{B}(y) = \underline{B}(x,z)e^{-i\alpha y}$. Using similar arguments as in §5.3.1 for the neglect of R_{m_2} we neglect R_{m_1} in (19) and the induction equation reduces to

$$\left(\frac{\partial^2}{\partial x^2} + \frac{\partial^2}{\partial z^2}\right)\underline{B} = \alpha^2(1+isR_m)\,\underline{B} \tag{34}$$

where $S = 1 - V/V_s$ is the slip. The one dimensional form, for x, of the Fourier transformation (1.32) and inverse Fourier transformation (1.33) are defined as, respectively

$$\hat{M}(p,z) = \int_{-\infty}^{\infty} M(x,z)e^{ipx}\,dx \qquad M(x,z) = \frac{1}{2\pi}\int_{-\infty}^{\infty} \hat{M}(p,z)\,e^{-ipx}\,dp \tag{35}$$

Transforming (24) using the first of (35), gives

$$\frac{d^2\hat{\underline{B}}}{dz^2} = \gamma^2\hat{\underline{B}} \tag{36}$$

where

$$\gamma^2 = p^2 + \alpha^2(1+isR_m) \tag{37}$$

Transforming $\nabla.\underline{B} = 0$, (1.1), we have, (compare (25)),

$$\frac{d\hat{B}_3}{dz} = i\alpha\hat{B}_2 \tag{38}$$

We use the boundary conditions (20) and (26) replacing y by x and q by ρ. The solutions to (36) are thus identical to those of (23), given by (27) and (28), but q is replaced by α, and γ is given by (37). Making these substitutions and inverting (27) and (28) using the second of (35) gives, using the symmetry of the kernels

$$\text{Case } S: \quad \mathcal{B}_2 = 2\mu_0 K_s \int_0^\infty e^{-\gamma z} \cos \rho x \, d\rho \; ; \; \mathcal{B}_3 = -2i\mu_0 K_s \int_0^\infty \frac{\alpha e^{-\gamma z}}{\gamma} \cos \rho x \, d\rho \qquad (39)$$

$$\text{Case } P: \quad \mathcal{B}_2 = \frac{2B_m i}{\alpha} \int_0^\infty \gamma e^{-\gamma z} \cos \rho x \, d\rho \; ; \; \mathcal{B}_3 = 2B_m \int_0^\infty e^{-\gamma z} \cos \rho x \, d\rho \qquad (40)$$

As we would expect, the solutions are all even in x. These integrals may be evaluated using the results given in BATEMAN (p.17), and they can be written in terms of Bessel's modified functions $K_0(\phi)$, $K_1(\phi)$ and $K_2(\phi)$. The asymptotic expansions of these functions are all of the form (33), so we conclude the EM field decays with an exponential factor $\mathcal{R}\left\{\alpha^2(1+is R_m)(y^2+z^2)\right\}^{1/2}$. We see that both the skin depth and transverse decay scale length are of the same order and equal to $\frac{\sqrt{2}}{\alpha}\left\{(1+s^2R_m^2)^{1/2}+1\right\}^{-1/2} = \epsilon_x^{1/2}$, (figure 5.5). From (3.17) and (3.8) we see that the skin depth for regions I and III is the same. However we would expect the curvature of the field lines at the edges of the excitation to decrease the skin depth there, and so $\epsilon_x^{1/2}$ must be regarded as an upper bound for the folding lengths. Unfortunately we do not have any information concerning the decay of the EM field away from the edge of the excitation towards region I. This decay is largely dependent on the width of the excitation, and our Dirac function boundary condition can only give an upper bound for the folding length.

5.4 Choice of Boundary Condition

Here we give an order of magnitude argument which illustrates the differences between the case S and case P analyses. We assume an excitation of the type used in the previous section (§5.3) is specified on the surface of a conducting half space. We shall also refer to figures 5.4 and 5.5. In §5.2 we used a singular perturbation technique

to obtain the width of the boundary layers and showed in §5.2.2 that the boundary layer transformation when the conductivity is large contains the small parameter

Using standard notation, writing $\underline{\mathcal{B}}(x,t) = \underline{B}(x)e^{i(\omega t - ay)}$, $\underline{J}(x,t) = \underline{J}(x)e^{i(\omega t - ay)}$ the equation $\nabla . \underline{\mathcal{B}} = 0$, (1.1), and the equation for the electric current density, (1.4), become respectively (assuming $\mathcal{B}_1 = 0$)

$$\frac{\partial B_2}{\partial y} + \frac{\partial B_3}{\partial z} = i\alpha B_2 \tag{41}$$

$$\mu_0 k \underline{J} = \left[\frac{\partial B_3}{\partial y} - \frac{\partial B_2}{\partial z} - i\alpha B_3 , -\frac{\partial B_2}{\partial x} , \frac{\partial B_3}{\partial x} \right] \tag{42}$$

We now obtain estimates for the behaviour of both $\underline{B}$ and $\underline{J}$ in the four regions of §5.3.

(i) Region I. Here the conductor 'sees' a travelling wave of infinite expanse and the only variation in y is that of the travelling wave itself. Thus (41) implies $o(B_3) = \delta\, o(B_2)$, and to maintain the same strength of field in the case S and case P analyses we require $B_m \sim \delta \mu_0 K_s$. Because there is no x variation, the electric currents are all transverse to the direction of the travelling wave. Their magnitude is decided by the tangential magnetic field and we have $o(\mu_0 k J_1) \sim \frac{1}{\delta} o(B_2)$.

(ii) Region II. Here the y variation appears not only from the travelling wave but also from the discontinuity of the excitation. For large conductivity, with α of order unity, (41) implies $o(B_3) \sim o(B_2)$, since the y and z boundary layers have similar width. To maintain a similar strength field in the S and P analysies we require $B_m \sim \mu_0 K_s$. There is no x variation here so the electric currents are as in (i). However we see from (42) that $o(\mu_0 k J_1) \sim \frac{2}{\delta} o(B_2)$ and so an increase in magnitude of the electric current density occurs in both analyses towards the end regions of the excitation.

(iii) Region III. Here the only variation appears in the travelling wave and now the x variation is non-zero. Equation (41) indicates that

$o(B_3) \sim \delta\, o(B_2)$ as in region I. However, (42) indicates the electric current density is now three dimensional. It is apparent that

$o(\mu_0 J_1) \sim \frac{1}{\delta}\, o(B_1)$, $o(\mu_0 J_2) \sim \frac{1}{\delta}\, o(B_2)$ and $o(\mu_0 J_3) \sim o(B_2)$.

Thus the induced vertical currents may be considered small, and circulation of the currents occurs mainly in the (x,y) plane.

(iv) Region IV. The behaviour of the EM field in this transition region must be found by a suitable matching of the fields in regions I, II and III.

In the case $\mathcal{S}$ analysis we hold B_2 constant along the length of the excitation, whilst B_3 is held constant in case $\mathcal{P}$. Using the arguments of (i) to (iv) we can obtain the approximate variation of the EM field as shown in figures 5.6 and 5.7 .

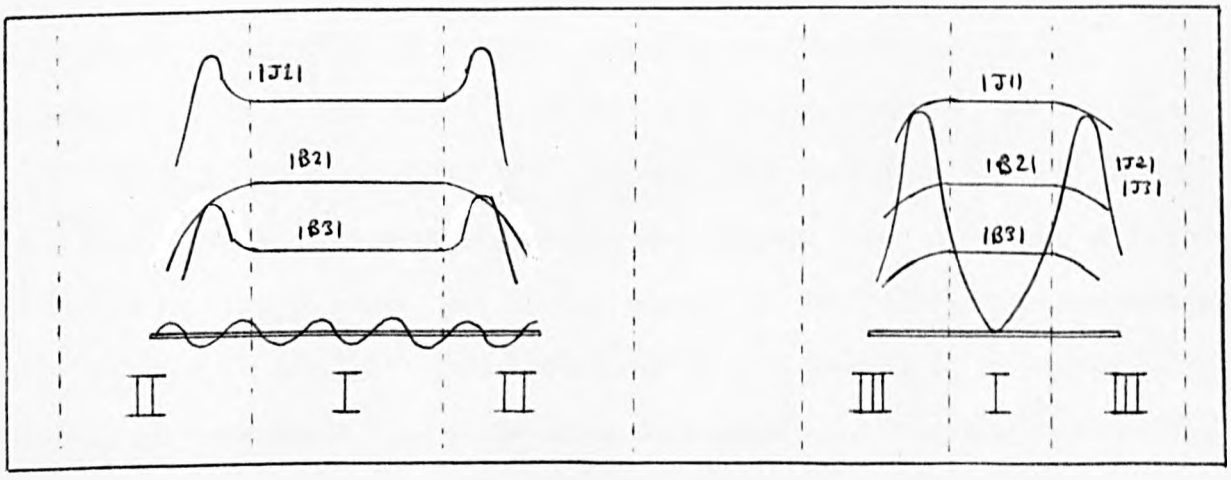

Fig. 5.6 Approximate Boundary Layer Variation. Case $\mathcal{S}$.

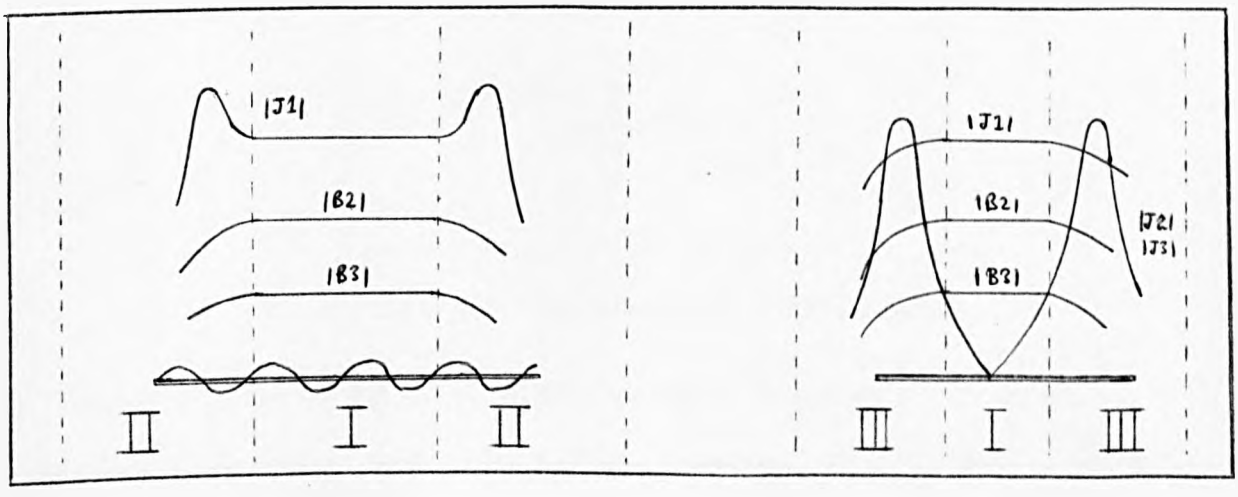

Fig. 5.7 Approximate Boundary Layer Variation. Case $\mathcal{P}$.

It appears that major differences between the two types of analysis occur only in the entrance and exit regions of the excitation. The case S analysis is characterised by a rapid increase in the magnitude of the electric current and normal magnetic fields there, whilst the case P analysis produces a rapid decay of the magnitude of the tangential magnetic field and a slow rise in the magnitude of the electric current. These results may be applied to the induced body force given by (1.31). It is easily shown that in region II both the normal and tangential forces for the case S analysis are of order $\frac{1}{s}$ times those of the case P analysis. Thus it appears that any fluid motion induced by a series wound SLIP is largely impulsive and occurs mainly in the entrance and exit regions of the SLIP. In a parallel wound SLIP we expect the motion to be gradually induced over the full length of the pump.

6. THE EFFECT OF CURVATURE ON THE INDUCED ELECTROMAGNETIC FIELD

6.1 Introduction

Here we are concerned with the structure of a SLIM and the effect this may have on the skin depth of the induced EM field. We have already obtained (chapters 3 and 4) a skin depth for the EM field induced by an idealised travelling wave excitation. We have also discussed (in §5.3) the effects of a finite travelling wave excitation and we have obtained some estimates for the boundary layer decay lengths. It is clear however that the EM field produced by a SLIM will decay smoothly with distance from the motor. The width and length of the SLIM also has some influence on the decay parameters. Because the magnetic field lines remain closed, it is clear they return from beyond the SLIM domain and so will lie parallel to the stator face in regions close to the perimeter of the SLIM. The skin depth of the induced EM field will thus vary from place to place. The models we consider here attempt to incorporate these curvature effects into the skin depth parameter; to do this we use the following configuration.

Cartesian coordinate axes are chosen on the surface of an electrically conducting half space $(z>o)$ as shown in figure 6.1. A magnetic induction excitation with sinosoidal variation in magnitude is applied along the surface of the conductor. (The form of this variation will be given later).

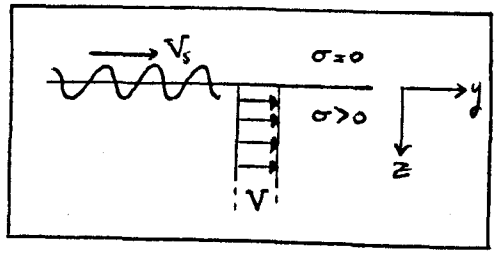

Fig. 6.1 The Idealized Configuration

We assume the conductor moves with a constant velocity, V , parallel with the direction of the y axis. The notation $\underline{\mathcal{B}}(t,t) = \underline{B}(t)e^{i\omega t}$ and

$\mathcal{J}(r,t) = \underline{J}(r)\, e^{i\omega t}$ is used, where only the real parts of $\underline{\mathcal{B}}$ and $\mathcal{J}$ have physical significance. Introducing the dimensionless variables

$$x^* = x/L,\ y^* = y/L,\ z^* = z/L,\quad R_0 = \omega L^2/\eta,\quad R_{m_2} = VL/\eta$$

where L is a scale length (taken to be the molten tin depth), Maxwell's equations (1.1), (1.4) and (1.11) become (dropping the star superscripts for convenience):

$$\frac{\partial B_1}{\partial x} + \frac{\partial B_2}{\partial y} + \frac{\partial B_3}{\partial z} = 0 \tag{1}$$

$$\mu_0 L \underline{J} = \left[\frac{\partial B_3}{\partial y} - \frac{\partial B_2}{\partial z},\ \frac{\partial B_1}{\partial z} - \frac{\partial B_3}{\partial x},\ \frac{\partial B_2}{\partial x} - \frac{\partial B_1}{\partial y} \right] \tag{2}$$

$$\left(\frac{\partial^2}{\partial x^2} + \frac{\partial^2}{\partial y^2} + \frac{\partial^2}{\partial z^2} \right) \underline{B} = i \left(R_0 - R_{m_2} \right) \underline{B} \tag{3}$$

We shall also write $\mathcal{R} = R_0 - R_{m_2}$. The solutions of (2) and (3) form a complete description of the induced three dimensional EM field. Previously we have assumed $B_1(r) = 0$ but this condition will not be applied here. However it has been shown (eg. SCHWARTZ et al, 1964) that the induced vertical currents are dissipated rapidly by the displacement current, and so without loss of generality we shall assume $J_3(r) = 0$. Thus we have

$$\frac{\partial B_2}{\partial x} = \frac{\partial B_1}{\partial y} \tag{4}$$

In §6.2 we use an approximation to the EM field produced by a single tooth of a SLIM to give an estimate of the skin depth for the induced EM field. This process is also used in §6.3 but there we apply a suitably adjusted travelling magnetic field which includes the dimensions of the SLIM.

6.2 Single Tooth Approximation

Provided the coil-wound teeth of a SLIM do not lie too close to one another (the degree of closeness will be decided by the $1/e$ folding length for horizontal decay, which is of the order of the skin depth) we may assume there is no induction interaction between separate teeth. Thus the excitation produced by a SLIM may be considered as a linear combination of suitably phased magnetic sources. We now show that it is entirely

possible to produce a travelling magnetic field from such a combination.

Consider the array of sources shown in figure 6.2. Their

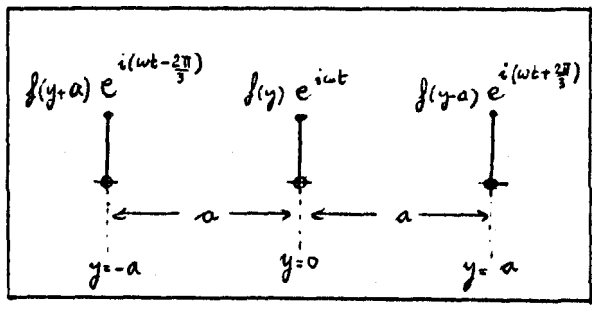

Fig. 6.2 An Array Of Phased Sources

one dimensional EM behaviour is governed by the function $f(y)$. We require of course, $f(y)\to 0$ as $|y|\to\infty$. We suppose the distance between adjacent sources, a, is small (which is certainly true in regions away from the SLIP when the appropriate scale length is the length of the motor). The three phase current supplied is assumed balanced (see §1.5.2) so the phase difference between adjacent teeth is $2\pi/3$ radians. Using the complex form for the time dependence, $e^{i\omega t}$, we find the total magnetic field $F(y)$ produced by the three sources of figure 6.1 is (writing $\frac{\partial f}{\partial y}=f'$, etc).

$$F(y) = \left\{ f(y+a)\,e^{-i\frac{2\pi}{3}} + f(y) + f(y-a)\,e^{i\frac{2\pi}{3}} \right\} e^{i\omega t}$$

$$\sim \left\{ a^2 f''(y)\cos\tfrac{2\pi}{3} - 2ia\,f'(y)\sin\tfrac{2\pi}{3} \right\} e^{i\omega t}$$

$$= aA\,e^{i(\omega t - g(y))} \qquad (5)$$

where $$A^2 = (\sqrt{3}f')^2 + (\tfrac{a}{2}f'')^2 \quad \text{and} \quad g(y) = \tan^{-1}\left(\frac{2\sqrt{3}f'(y)}{a f''(y)}\right) \qquad (6)$$

Thus $F(y)$ given by (5) is certainly of the travelling wave form. However it is unlikely that the form of $f(y)$ will produce a linear $g(y)$, and so the travelling wave will not be a pure sinusoidal one.

Consider now a single coil-wound tooth of width $2d$ (dimensionless) and length $2l$ (dimensionless). A complete description of its EM field can be made using Fourier series. To a first approximation we may assume the normal magnetic induction at the surface of the conductor (figure 6.1)

is given as

$$\mathcal{B}_3 = \mathcal{B}_m \cos \alpha x \cdot \cos \beta y \tag{7}$$

where $\mathcal{B}_m$ is the magnitude of $\mathcal{B}_3$ at the centre of the tooth; $\alpha = \frac{\pi}{2d}$ and $\beta = \frac{\pi}{2\ell}$. The variation of $\mathcal{B}_3$ over the tooth is shown in figure 6.3. Because we are only interested in the effect of curvature on the EM field it does not matter that the source field (7) is cyclic in the x and y directions. Solving (3) for $\mathcal{B}_3$ by the separation of variables technique, subject to (8) on $z=0$ and decay as $z \to \infty$, we find

$$\mathcal{B}_3 = \mathcal{B}_m \cos \alpha x \cdot \cos \beta y \cdot e^{-\gamma z} \tag{8}$$

where
$$\gamma^2 = \alpha^2 + \beta^2 + i R \tag{9}$$

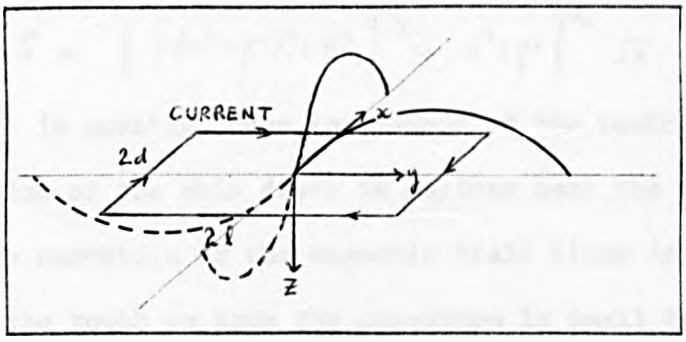

Fig. 6.3 Normal Magnetic Field

Substituting (8) in (1), using (4) we find

$$\mathcal{B}_1 = \frac{\alpha \mathcal{B}_m}{(\alpha^2+\beta^2)\gamma} \sin \alpha x \cdot \cos \beta y \cdot e^{-\gamma z} \tag{10}$$

$$\mathcal{B}_2 = \frac{\beta \mathcal{B}_m}{(\alpha^2+\beta^2)\gamma} \cos \alpha x \cdot \sin \beta y \cdot e^{-\gamma z} \tag{11}$$

From (2) using (8) to (11) we find

$$\mu_0 J_1 = \frac{i \beta R \mathcal{B}_m}{\gamma(\alpha^2+\beta^2)} \cos \alpha x \cdot \sin \beta y \cdot e^{-\gamma z} \tag{12}$$

$$\mu_0 J_2 = \frac{-i \alpha R \mathcal{B}_m}{\gamma(\alpha^2+\beta^2)} \sin \alpha x \cdot \cos \beta y \cdot e^{-\gamma z} \tag{13}$$

Equations (12) and (13) may be compared with (11) and (10). We see that

the spatial variation of B_2 is identical to that of J_1 and that of B_1 is identical to J_2 . This mathematical result is of course only applicable to the idealised model of figure 6.3. However later work (Chapter 10) using more realistic models also indicates a certain correspondence between the above pairs. Integrating $\nabla \times \underline{B} = \mu_0 \underline{J}$, (1.4), over a surface S leads to the result $\int_S \underline{J}.d\underline{S} = \oint_C \underline{B}.d\underline{l}$ where C is the perimeter of S . Thus the magnitude of the induced electric current at a point depends on the curvature of the magnetic field lines there, so the mathematical result connecting the magnetic induction and induced electric current is consistent with the physical analysis.

The skin depth δ for the induced EM field is obtained from the real part of $e^{-\gamma z}$; we find

$$\delta = \left\{ \left[(\alpha^2+\beta^2)^2 + R^2 \right]^{1/2} + \alpha^2+\beta^2 \right\}^{-1/2} \cdot \sqrt{2} \qquad (14)$$

In our model δ is constant over the domain of the tooth. In practice, δ will be the value of the skin depth in regions near the perimeter of the tooth where the curvature of the magnetic field lines is at a maximum the centre of the tooth we know the curvature is small so the penetration is greater and the skin depth increases. The value of δ there is found by setting $\alpha=\beta=0$ in (14). The skin depth is increased by increasing the width or length of the SLIM (since $\alpha = \frac{\pi}{2d}$, $\beta = \frac{\pi}{2l}$), as we would expect, because then the overall curvature of the magnetic field lines decreases.

From (1.31) we obtain for the time averaged force

$$\underline{F} = \frac{B_m^2 R}{2\mu_0 k} \left(\alpha^2 \sin^2\alpha x . \cos^2\beta y + \beta^2 \cos^2\alpha x . \sin^2\beta y \right) e^{-2z\delta} \Re\left\{\frac{i}{\gamma}\right\} \underline{e}_3 \qquad (15)$$

This force exhibits a 'doughnut' shape with a central depression, raised edges (coinciding with the tooth perimeter) and outer decay. It bears a strong resemblence to the vertical force obtained in Chapter 10 for a three dimensional tooth. Unfortunately our model does not allow the existence of horizontal force components (apart from purely oscillatory

terms) and so cannot be applied directly in an analysis of the SLIM. However, we feel the simple results of this section do provide a reasonable description of the EM field and vertical force induced by a single tooth.

6.3 Travelling Magnetic Field Analysis

In Chapters 3 and 4 we analysed the EM field induced in a conducting half space by a travelling magnetic field of infinite expanse. In Chapter 5 we briefly discussed the effect of a finite travelling wave and its effect on the conductor when using case S and case P analyses. Later (Chapters 7 and 9) we give an exact analysis of the rectangular excitation but we have been unable to obtain all of the results in closed form. Here we introduce finite effects by supposing the excitation has a sinosoidal variation in magnitude superimposed on the standard travelling magnetic field.

In the analysis below we make use of the complex plane and introduce the two independent imaginary numbers *i and j, where

$$i^2 = -1 \qquad j^2 = -1 \quad \text{but} \quad i \neq j \quad \text{so} \quad ij \neq -1 \tag{16}$$

The use of (16) below greatly simplifies the solution of Maxwell's induction equation. Choosing cartesian axes with origin at the centre of the SLIM we impose the general travelling wave excitation on the surface $z = 0$, (see figure 6.4).

$$B_3(x,y,0) = B_m \cos(\lambda x + \mu y)\, e^{-i(\alpha_1 x + \alpha_2 y)} \tag{17}$$

$$= \underset{j}{\mathcal{R}} \left\{ B_m e^{j(\lambda x + \mu y)} e^{-i(\alpha_1 x + \alpha_2 y)} \right\} \tag{18}$$

Here $\lambda = \frac{\pi}{2d}$, $\mu = \frac{\pi}{2l}$ where $2d$ is the width of the SLIM and $2l$ is its length; $\alpha_1 = \omega L / V_1$ and $\alpha_2 = \omega L / V_2$ are wave numbers parallel to the x and y axes respectively based on the wave velocity $\underline{V} = [V_1, V_2, 0]$. The notation $\underset{j}{\mathcal{R}}$, $\underset{i}{\mathcal{R}}$ is used to denote the 'real part of' with respect to j and i respectively. The parameter α_1 is included mainly for reasons of symmetry; its value is non zero only when the teeth are skewed on the stator face.

* Also used by PARK (1974). See §11.8.2

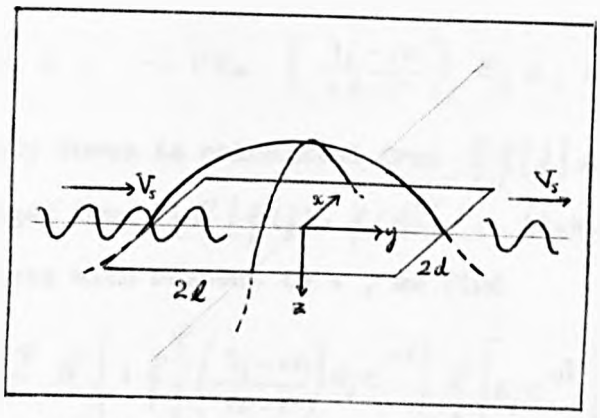

Fig. 6.4 The SLIM Excitation

We have chosen a non-symmetric excitation (17) for convenience. A more accurate representation of the normal magnetic induction would be $B_3(x,y,0) = B_m \cos\lambda x \cdot \cos\mu y \cdot e^{-i(\alpha_1 x + \alpha_2 y)}$ which has lines of symmetry parallel to the coordinate axes. The problem in this case can be simplified by the introduction of the imaginary parameter κ, where $\kappa^2 = -1$ and κ is not the same as i or j in (16). We would then be able to write $B_3(x,y,0) = \sum_\kappa \sum_j \{ B_m e^{j\lambda x} e^{\kappa\mu y} e^{-i(\alpha_1 x + \alpha_2 y)} \}$ However, because we are only interested in the effect of curvature on the skin depth, we can ignore the skew fields and their periodicity along the coordinate axes.

The solution to (3) for B_3, subject to (18) may be accomplished using the separation of variables technique. We find

$$B_3(\underline{r}) = B_m E_j E_i e^{-\gamma z} \tag{19}$$

where $$E_j = e^{j(\lambda x + \mu y)} \qquad E_i = e^{-i(\alpha_1 x + \alpha_2 y)} \tag{20}$$

and $$\gamma^2 = iR - (\lambda_j - i\alpha_1)^2 - (\mu_j - i\alpha_2)^2 \tag{21}$$

Substituting (19) in (1) using (4) and (3) we find

$$B_1(\underline{r}) = B_m \cdot \gamma \cdot \left(\frac{\lambda_j - i\alpha_1}{iR - \gamma^2}\right) E_j E_i e^{-\gamma z} \tag{22}$$

$$B_2(\underline{r}) = B_m \gamma \left(\frac{\mu_j - i\alpha_2}{iR - \gamma^2}\right) E_j E_i e^{-\gamma z} \tag{23}$$

Substituting (19), (22) and (23) in (2) we find

$$\mu_0 J_1 = iR \cdot B_m \left(\frac{\mu_j - i\alpha_2}{iR - \gamma^2}\right) E_j E_i e^{-\gamma z} \tag{24}$$

$$\mu_0 L J_z = -i R B_m \left(\frac{\lambda_j - i\alpha_1}{iR - \gamma^2} \right) E_j \Xi_i e^{-\gamma z} \tag{25}$$

The Lorentz body force is calculated from $\underset{i}{\mathcal{R}}\underset{j}{\mathcal{R}}\{\underline{J}\} \wedge \underset{i}{\mathcal{R}}\underset{j}{\mathcal{R}}\{\underline{B}\}$. Using the time averaged form $\frac{1}{2}\underset{i}{\mathcal{R}}\left[\underset{j}{\mathcal{R}}(\underline{J}) \wedge \underset{j}{\mathcal{R}}(\underline{B}^*)\right]$, (1.41), where $*$ is the complex conjugate with respect to i , we find

$$F_1 = -\frac{B_m^2 R}{2\mu_0 L} \underset{i}{\mathcal{R}} \left\{ i \underset{j}{\mathcal{R}} \left[\left(\frac{\lambda_j - i\alpha_1}{iR - \gamma^2} \right) E_j e^{-\gamma z} \right] \cdot \underset{j}{\mathcal{R}} \left[E_j e^{-\gamma^* z} \right] \right\} \tag{26}$$

$$F_2 = \frac{B_m^2 R}{2\mu_0 L} \underset{i}{\mathcal{R}} \left\{ i \underset{j}{\mathcal{R}} \left[\left(\frac{\mu_j - i\alpha_1}{iR - \gamma^2} \right) E_j e^{-\gamma z} \right] \underset{i}{\mathcal{R}} \left[E_j e^{-\gamma^* z} \right] \right\} \tag{27}$$

$$F_3 = -\frac{B_m^2 R}{2\mu_0 L} \underset{i}{\mathcal{R}} \left\{ i \underset{j}{\mathcal{R}} \left[\left(\frac{\mu_j - i\alpha_2}{iR - \gamma^2} \right) E_j e^{-\gamma z} \right] \cdot \underset{j}{\mathcal{R}} \left[\gamma^* \left(\frac{\mu_j + i\alpha_2}{iR + \gamma^* \gamma^*} \right) E_j e^{-\gamma^* z} \right] + i \underset{j}{\mathcal{R}} \left[\left(\frac{\lambda_j - i\alpha_1}{iR - \gamma^2} \right) E_j e^{-\gamma z} \right] \cdot \underset{i}{\mathcal{R}} \left[\gamma^* \left(\frac{\lambda_j + i\alpha_1}{iR + \gamma^* \gamma^*} \right) E_j e^{-\gamma^* z} \right] \right\} \tag{28}$$

Because γ is a function of both i and j we could write $\gamma = \gamma_1(j) + i\,\gamma_2(j)$ or $\gamma = \psi_1(i) + j\,\psi_2(i)$. Using the latter representation, we have from (21)

$$\gamma^2 = (iR + \lambda^2 + \mu^2 + \alpha_1^2 + \alpha_2^2) + j\,(2i[\lambda\alpha_1 + \mu\alpha_2]) \tag{29}$$

$$\equiv (iR + \beta) + 2j \cdot i \cdot \xi \tag{30}$$

$$\therefore \quad \psi_1 = \left[(\beta^2 - R^2 - 4\xi^2 + 2iR\beta)^{1/2} + iR + \beta \right]^{1/2} / \sqrt{2} \tag{31}$$

Writing $\psi_1 = \phi_1 + i\,\phi_2$ we find, after a great deal of algebra

$$\phi_1 = \frac{1}{2} \left\{ \left(A^2 + 4R^2\beta^2 + R^2 + \beta^2 + \beta\sqrt{2} \left[(A^2 + 4R^2\beta^2)^{1/2} + A \right]^{1/2} + R\sqrt{2} \left[(A^2 + 4R^2\beta^2)^{1/2} - A \right]^{1/2} \right)^{1/2} + \frac{1}{\sqrt{2}} \left[(A^2 + 4R^2\beta^2)^{1/2} + A \right]^{1/2} + \beta \right\} \tag{32}$$

where $A = \beta^2 - R^2 - 4\xi^2$. Usually $\alpha_1 = 0$ and $\alpha_2 = O(1)$, so if the length of the SLIM is large ($2\ell > 2\pi$) we may neglect the ξ - term of (30), and set $\mu = 0$. In this case γ is independent of j and we find

$$\phi_1 \sim \left[\left(R^2 + \{\alpha_2^2 + \lambda^2\}^2 \right)^{1/2} + \alpha_2^2 + \lambda^2 \right]^{1/2} / \sqrt{2} \tag{33}$$

The skin depth δ for the EM field is equal to ϕ_1^{-1} . A comparison of (33)

may be made with (14), (in §6.2). As the width of the SLIM increases δ increases because $\lambda \left(= \frac{\pi}{2d}\right)$ decreases. When both λ and μ equal zero (corresponding to a travelling wave excitation of infinite expanse) and the teeth are not skewed ($\alpha_1 = 0$) we recover the results for $\underline{\mathcal{E}}$, $\underline{\mathcal{I}}$ and $\underline{f}$ of Chapter 3.

6.4 Summary

In this chapter we have obtained expressions for the skin depth of the induced EM field which include curvature effects. These results provide a better approximation to the $1/e$ folding lengths for the boundary layer decay obtained in §5.3. Using the notation of figures 5.3 and 5.4 the new values of $\epsilon_y'^{\epsilon}$ and $\epsilon_x'^{\epsilon}$ are obtained from (14) and (33) respectively. The skin depth in region IV (the corner region defined in §5.3) is obtained from (32).

7. ELECTROMAGNETIC INDUCTION IN A UNIFORM HALF SPACE BY A RECTANGULAR TRAVELLING MAGNETIC FIELD

7.1 Introduction

Here we obtain expressions for the EM field induced in a conducting half space by a rectangular travelling magnetic field applied on the surface of the half space. The half space is assumed to move with a constant velocity $\bar{V}$ parallel with the direction of the travelling wave. Cartesian coordinate axes are chosen with origin at one corner of the excitation (which is of length 2b metres and width 2a metres) with the z axis pointing into the conductor (figure 7.1). The region above the conductor is

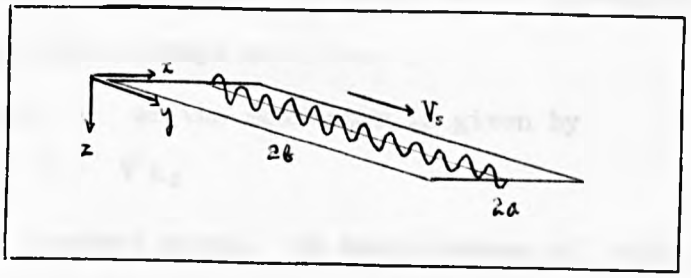

Fig. 7.1 The Rectangular Excitation

assumed to be non-conducting and of infinite permeability. The permeability of the conductor is assumed to be that of free space.

A closed solution in three dimensions for the induced EM field does not seem to be possible for this problem, so we consider two special cases; the first is when the excitation is of infinite width (figure 7.2) and the second is when the excitation is of infinite length (figure 7.3)

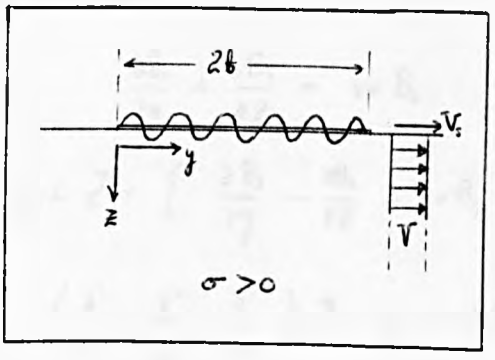

Fig. 7.2 Infinite Width Excitation

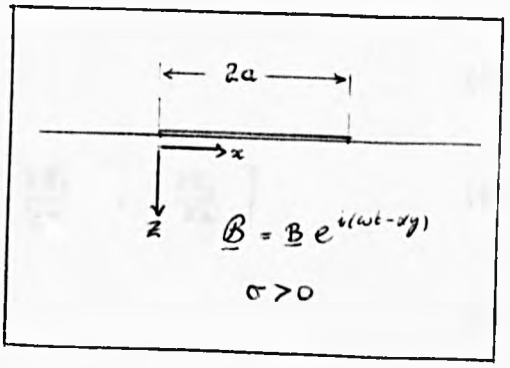

Fig 7.3 Infinite Length Excitation

We assume the excitation is of constant magnitude over its width and length. The unit block functions S_x and S_y are defined in terms of the Heaviside unit step function $H(s)$ as follows

$$S_x \equiv S_x(2a, x) = H(x) - H(x-2a) \tag{1}$$

$$S_y \equiv S_y(2b, y) = H(y) - H(y-2b) \tag{2}$$

The boundary conditions on the surface $z=0$ for the magnetic field are obtained by combining the case S and case P idealised conditions ((1.47) and (1.48) respectively) with (1) and (2). We have, on $z=0$,

$$\mathcal{B}_2 = \mu_0 K_s S_s e^{i(\omega t - \alpha y)} \ (S) \qquad \mathcal{B}_3 = \mathcal{B}_m S_s e^{i(\omega t - \alpha y)} \ (P) \tag{3}$$

where s is taken as x for the infinite length excitation and y for the infinite width excitation. We shall assume throughout that $\mathcal{B}_1 = 0$ and that the EM field decays as $z \to \infty$.

The velocity $\underline{V}$ of the conductor is given by

$$\underline{V} = V \underline{e}_2 \tag{4}$$

where V is a constant speed. We shall assume all solutions to Maxwells equations are of the travelling wave form specified in (3), and we write $\underline{\mathcal{B}}(\underline{r},t) = \underline{B}(\underline{r}) e^{i(\omega t - \alpha y)}$, $\underline{\mathcal{J}}(\underline{r},t) = \underline{J}(\underline{r}) e^{i(\omega t - \alpha y)}$. Introducing a scale length L (which we take to be the molten tin depth) we define the following dimensionless variables: $x^* = x/L$, $y^* = y/L$, $z^* = z/L$ $\alpha^* = \alpha L$, $a^* = a/L$ and $b^* = b/L$. In the analysis below all variables are assumed dimensionless so we discard the star superscripts. Maxwell's dimensionless equations are obtained from (1.1), (1.4) and (1.11); we find

$$\frac{\partial B_2}{\partial y} + \frac{\partial B_3}{\partial z} = i\alpha B_2 \tag{5}$$

$$\mu_0 L \underline{J} = \left[\frac{\partial B_3}{\partial y} - \frac{\partial B_2}{\partial z} - i\alpha B_3 , -\frac{\partial B_3}{\partial x} , \frac{\partial B_2}{\partial x} \right] \tag{6}$$

$$\left(\frac{\partial^2}{\partial x^2} + \frac{\partial^2}{\partial y^2} + \frac{\partial^2}{\partial z^2} \right) \underline{B} = \Psi^2 \underline{B} \tag{7}$$

where

$$\Psi^2 = \alpha^2 (1 + is R_m) \tag{8}$$

and $S = (V_s - V)/V_s$ is the slip; $V_s = \omega\tau/\alpha$ is the synchronous wave speed and $R_m = V_s\tau/\alpha\eta$ is the magnetic Reynolds number based on the wave speed.

We now define the appropriate form of the Fourier transformation (1.32) and inverse Fourier transformation (1.33), for use in this chapter. The one dimensional exponential Fourier transformation of the function $M(\xi,z)$ with respect to ξ, and the corresponding inverse transformation are defined as follows

$$\hat{M}(\eta,z) = \int_{-\infty}^{\infty} M(\xi,z)\, e^{+i\xi\eta}\, d\xi \qquad M(\xi,z) = \frac{1}{2\pi}\int_{-\infty}^{\infty} \hat{M}(\eta,z)\, e^{-i\xi\eta}\, d\eta \tag{10}$$

where ξ is taken as x and η is taken as p for the infinite length excitation, and ξ is taken as y with η as q for the infinite width excitation. The one dimensional convolution result for the functions $M(\xi,z)$, $N(\xi,z)$ is obtained from (1.35). We have

$$\mathcal{F}_1^{-}\left\{\hat{M}(\eta,z)\,\hat{N}(\eta,z)\right\} = \int_{-\infty}^{\infty} M(\xi',z)\, N(\xi-\xi',z)\, d\xi' \tag{11}$$

7.2 Infinite Width Excitation

Here $\frac{\partial}{\partial x} = 0$ and Maxwell's equations (5) to (7) transform to (using the first of (10)):

$$\frac{d\hat{B}_3}{dz} = i(\alpha+q)\,\hat{B}_2 \tag{12}$$

$$\mu_0\tau\,\hat{\underline{J}} = \left[-\frac{d\hat{B}_2}{dz} - i(\alpha+q)\,\hat{B}_3\ ,\ 0\ ,\ 0\right] \tag{13}$$

$$\frac{d^2\underline{\hat{B}}}{dz^2} = \gamma^2\,\underline{\hat{B}} \tag{14}$$

where $$\gamma^2 = \psi^2 + q^2 \tag{15}$$

Transforming the boundary conditions (3) we obtain

$$\hat{B}_2(q,0) = \mu_0 K_s\,\hat{S}_y \quad (S) \qquad \hat{B}_3(q,0) = B_m\,\hat{S}_y \quad (P) \tag{16}$$

where $$\hat{S}_y = \frac{e^{2ihq} - 1}{iq} \tag{17}$$

The solution to (14) may be written in the form $\underline{C}\,e^{-\gamma z}$ where $\underline{C}$ is

a vector, independent of z, to be found from the boundary conditions (16). Using (12) to (14) we can easily show the solutions in transform space are

$$\text{Case } S: \quad \hat{\underline{B}} = \mu_0 K_s \hat{S}_y \left[0, \; 1, \; -\frac{i(\alpha+q)}{\gamma} \right] e^{-\gamma z} \tag{18}$$

$$\hat{\underline{J}} = \frac{\mu_0 K_s}{\mu_0 h} \hat{S}_y \left[\frac{i\alpha^2 s R_m - 2\alpha q}{\gamma}, \; 0, \; 0 \right] e^{-\gamma z} \tag{19}$$

$$\text{Case } P: \quad \hat{\underline{B}} = B_m \hat{S}_y \left[0, \; \frac{i\gamma}{\alpha+q}, \; 1 \right] e^{-\gamma z} \tag{20}$$

$$\hat{\underline{J}} = \frac{B_m}{\mu_0 h} \hat{S}_y \left[\frac{i\alpha^2 s R_m - 2\alpha q}{\alpha+q}, \; 0, \; 0 \right] e^{-\gamma z} \tag{21}$$

Applying the inverse Fourier transformation (the second of (10)) to (18) to (21) we obtain the following integral solutions in real space:

$$\text{Case } S: \quad \underline{B} = \frac{\mu_0 K_s}{2\pi} \int_{-\infty}^{\infty} \hat{S}_y \left[0, \; 1, \; -\frac{i(\alpha+q)}{\gamma} \right] e^{-\gamma z} e^{-iqy} dq \tag{22}$$

$$\underline{J} = \frac{\mu_0 K_s}{2\pi \mu_0 h} \int_{-\infty}^{\infty} \hat{S}_y \left[\frac{i\alpha^2 s R_m - 2\alpha q}{\gamma}, 0, 0 \right] e^{-\gamma z} e^{-iqy} dq \tag{23}$$

$$\text{Case } P: \quad \underline{B} = \frac{B_m}{2\pi} \int_{-\infty}^{\infty} \hat{S}_y \left[0, \; \frac{i\gamma}{\alpha+q}, \; 1 \right] e^{-\gamma z} e^{-iqy} dq \tag{24}$$

$$\underline{J} = \frac{B_m}{2\pi \mu_0 h} \int_{-\infty}^{\infty} \hat{S}_y \left[\frac{i\alpha^2 s R_m - 2\alpha q}{\alpha+q}, \; 0, \; 0 \right] e^{-\gamma z} e^{-iqy} dq \tag{25}$$

We notice that the case P integral solutions for B_z and J_1 are Cauchy Principal Value integrals with a singularity at $q = -\alpha$. This singularity can be removed using, for example, the method of Appendix II. For B_z we obtain the result

$$B_z = \frac{B_m}{2\pi} e^{i\alpha y} \int_{-\infty}^{y} e^{-i\alpha \xi} d\xi \int_{-\infty}^{\infty} \hat{S}_y \gamma e^{-\gamma z} e^{-iq\xi} dq \tag{26}$$

A similar expression can be obtained for J_1. We now use the convolution result (11) for the inversion of (22) to (25). For integrals with kernals of the form $\hat{S}_y \theta(q)$ the following result holds:

$$\frac{1}{2\pi} \int_{-\infty}^{\infty} \hat{S}_y \hat{\theta}(q) e^{-i\alpha y} dq = \int_{y-2h}^{y} \theta(\xi) d\xi \tag{27}$$

where $\theta(\xi) = \mathcal{F}_1^{-}\{\hat{\theta}(q)\}$ and the functions $\hat{\theta}(q)$ can be obtained from (22) to (25) by observation. Using the form of (26) for B_z and J_1 in the

case P solutions we can identify a basic kernal from which the remaining kernals may be found, viz: $\hat{\theta}(q) = e^{-\gamma z}/\gamma$. Applying the inverse transformation (the second of (10)) we have

$$\theta(\zeta) = \frac{1}{2\pi}\int_{-\infty}^{\infty} \frac{e^{-\gamma z}}{\gamma} e^{-iqy}\,dq = \frac{1}{\pi}\int_{0}^{\infty} \frac{e^{-\gamma z}}{\gamma} \cos qy \cdot dq$$

$$= \frac{1}{\pi} K_0(\Psi) \qquad \text{(BATEMAN p.17)} \qquad (28)$$

where $$\Psi = \psi (y^2 + z^2)^{1/2} \qquad (29)$$

and K_0 is Bessel's modified function of the second kind of order zero. The remaining functions $\theta(\zeta)$ can be found by differentiating (28) partially with respect to y or with respect to z using the recurrence relations of Appendix I. Finally, using (26), (27) and (28) we can reduce (22) to (25) to the form:

Case S : $$B_2 = \frac{\mu_0 K_s}{\pi} \cdot \psi^2 z \cdot I_y\left\{\frac{K_1(\Psi)}{\Psi}\right\} \qquad (30)$$

$$B_3 = -\frac{i\mu_0 K_s}{\pi}\left(\alpha I_y\left\{K_0(\Psi)\right\} - i\, K_0(\Psi)\Big|_{y-2b}^{y}\right) \qquad (31)$$

$$J_1 = \frac{\mu_0 K_s}{\mu_0 h \pi}\left(i\alpha^2 s R_m\, I_y\left\{K_0(\Psi)\right\} - 2i\alpha\, K_0(\Psi)\Big|_{y-2b}^{y}\right) \qquad (32)$$

Case P : $$B_2 = -\frac{B_m}{\pi} e^{i\alpha y} \frac{\partial}{\partial z}\left(\psi^2 z \int_{-\infty}^{y} I_y\left\{\frac{K_1(\Psi)}{\Psi}\right\} e^{-i\alpha y}\,dy\right) \qquad (33)$$

$$B_3 = \frac{B_m}{\pi} \cdot \psi^2 z \cdot I_y\left\{\frac{K_1(\Psi)}{\Psi}\right\} \qquad (34)$$

$$J_1 = \psi^2 z \cdot \frac{B_m}{\pi\mu_0 h} e^{i\alpha y}\left(i\alpha^2 s R_m \int_{-\infty}^{y} I_y\left\{\frac{K_1(\Psi)}{\Psi}\right\} e^{-i\alpha y}\,dy - 2\alpha \int_{-\infty}^{y} \frac{K_1(\Psi)}{\Psi}\Big|_{y-2b}^{y} e^{-i\alpha y}\,dy\right) \qquad (35)$$

where $$I_y\left\{\theta(y)\right\} = \int_{y-2b}^{y} \theta(y)\,dy \qquad (36)$$

and $$\theta(y)\Big|_{y-2b}^{y} = \theta(y) - \theta(y-2b) \qquad (37)$$

Here the function K_1 is Bessel's modified function of order unity. We can recover the infinite expanse of excitation solutions (chapter 3) by

setting $y = b$, letting $b \to \infty$ and then using the following relations:

$$\int_0^\infty \frac{K_\nu\left(\psi\sqrt{z^2+\xi^2}\right)}{\sqrt{z^2+\xi^2}^{\nu}}\,\xi^{2\mu+1}\,d\xi = \frac{2^\mu \Gamma(\mu+1)\, K_{\nu-\mu-1}(\psi z)}{\psi^{\mu+1} z^{\nu-\mu-1}} \quad \text{(GRADSHTEYN, p.705)} \quad (38)$$

with $$K_{\pm\frac{1}{2}}(\psi z) = \sqrt{\frac{\pi}{2\psi z}}\, e^{-\psi z} \quad \text{(GRADSHTEYN, p.967)} \quad (39)$$

where $\Gamma(\mu+1)$ is the Gamma function (GRADSHTEYN, p.933).

Unfortunately we have been unable to obtain closed solutions to the integral in (36) with kernals of the type given in (28). It is possible to approximate (36) assuming $2b \gg 1$, and then evaluating the integral when $y = 2b + \epsilon$ for ϵ small. However this process merely indicates that EM field decays beyond the edge $y = 2b$. Alternatively we can calculate the curvature of the EM field by differentiating the results (30) to (35) with respect to y , but this leads to complicated algebra and the behaviour of the EM field is difficult to ascertain. Some information can be obtained regarding the skin depth of the EM field if we assume ψ is large and use the asymptotic result

$$K_n(\Psi) \sim \sqrt{\frac{\pi}{2\Psi}}\, e^{-\Psi} \qquad n = 0,1 \quad \psi \gg 1 \qquad (40)$$

Relation (40) indicates that the $1/e$ folding lengths in the y and z directions are of the same order and equal to $1/\alpha\{\psi\}$, agreeing with chapters 5 and 6.

Numerical tables do exist for the Bessel functions of complex argument (eg: LOWAN, 1947) but evaluation of the modified functions from these tables is extremely arduous and cumbersome. Thus a direct quadrature evaluation of $I_y\{\theta(y)\}$ is difficult. Perhaps the best approach (and it is the approach adopted here) is to use the integral formulation for $K_n(\Psi)$ given in (for example) ABRAMOWITZ and STEGUN (1965):

$$K_n(\Psi) = \int_0^\infty e^{-\Psi\cosh t}\cosh nt\, dt \qquad (|\arg\Psi| < \pi/2) \qquad (41)$$

The form of (41) allows the use of Gaussian quadrature in the evaluation of $I_y\{\theta(y)\}$ and if we reverse the order of integration we can produce numerical solutions of high accuracy. Unfortunately this approach is not

very useful for (31) and (35) because we require a numerical evaluation of three successive integrals. Computational results for the dimensionless EM field components $B2\left(=B_2/\{\frac{\mu_0 K_0}{\pi}\}\right)$, (30), $B3\left(=B_3/\{\frac{\mu_0 K_0}{\pi}\}\right)$, (31), and $J1\left(=J_1/\{\frac{K_0}{\Delta\pi}\}\right)$, (32), are shown in figures 7.4 (a), 7.4 (b) and 7.5 respectively. The physical parameters used in the computation are those listed in table 1.1 for the Pilkington Float Linear Motor. Using these dimensionless components we can calculate the dimensionless time-averaged body force induced (1. 31) The two body force components, F2 and F3, are shown in figures 7.6 (a) and (b). The computation was performed using Gaussian quadrature over $[0, \infty)$ and Patterson's updated Gaussian method over $[y-2\delta, y]$. Both algorithms are available as subroutines in the Nottingham Algorithm Group's (NAG) computer library.

We can describe the physical nature of the results as follows. The symmetry of B2 (figure 7.4 (a)) has been imposed on the system by the boundary conditions on $z=0$. As we would expect this component of magnetic induction is well-behaved. The asymmetry of B3 (figure 7.4 (b)) and J1 (figure 7.5) is due to the motion of the magnetic field through the conductor. At the entrance end of the excitation the magnetic field lines are dragged through the conductor and a slight flattening occurs there which reduces the normal magnetic field, and (by Stoke's theorem) reduces the magnitude of the induced electric currents. However, because the magnetic field lines are closed loops, the curvature of the magnetic field must increase rapidly at the entrance edge $(y=0)$ to allow the flux linkage, and so both B3 and J1 increase in magnitude there. At the exit end of the excitation $(y=9.0)$ the magnetic field lines push through the conductor forcing the magnetic flux to return from beyond the excitation in the form of a shallow loop lying mostly parallel with the surface of the conductor. This explains the decrease in B3 and the increase in J1 (due to the increased curvature of the magnetic field lines) at $y=9.0$ The large electric currents induced in a secondary, at the entrance and exit ends of a finite excitation, are often referred to as 'shunt end

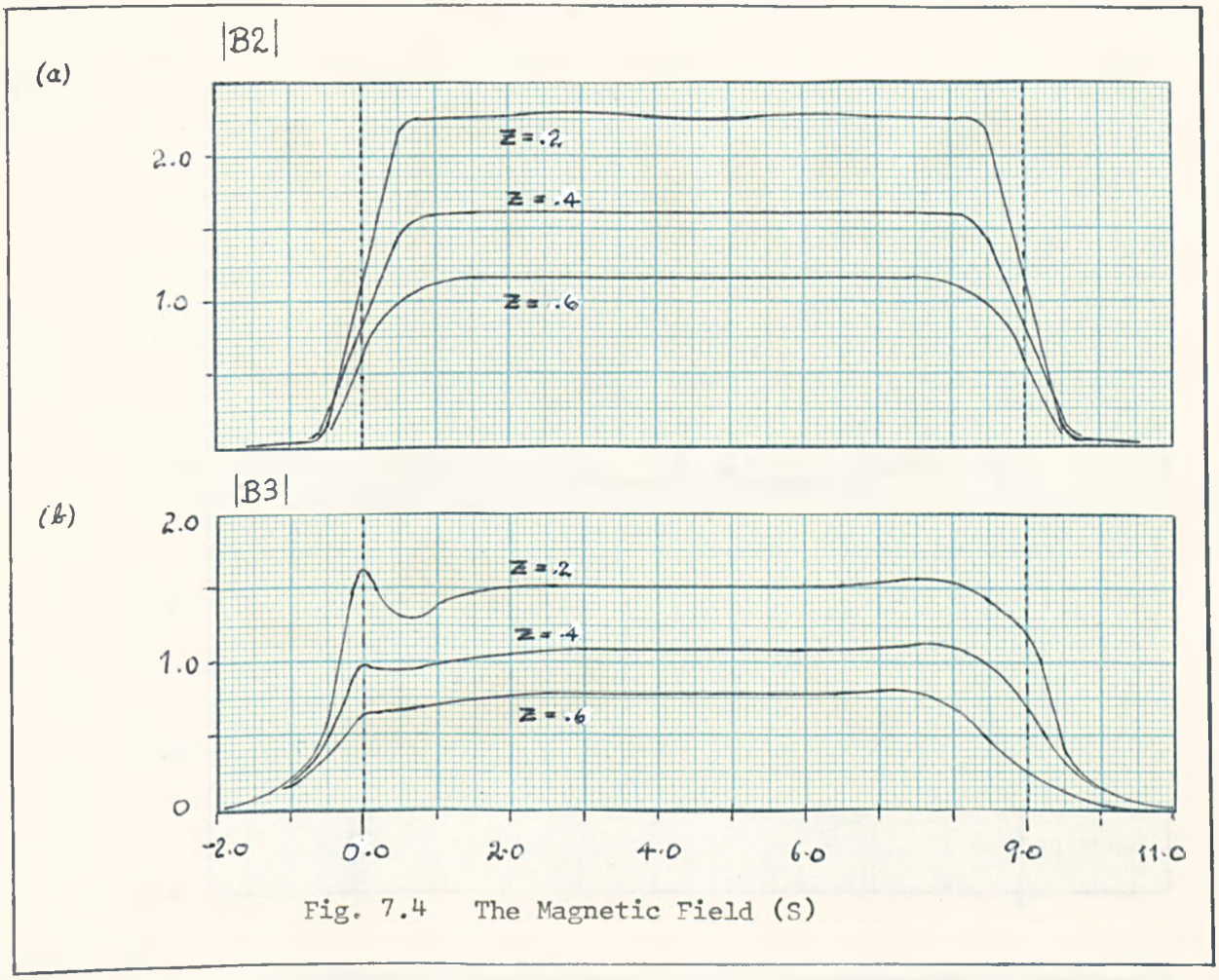

Fig. 7.4 The Magnetic Field (S)

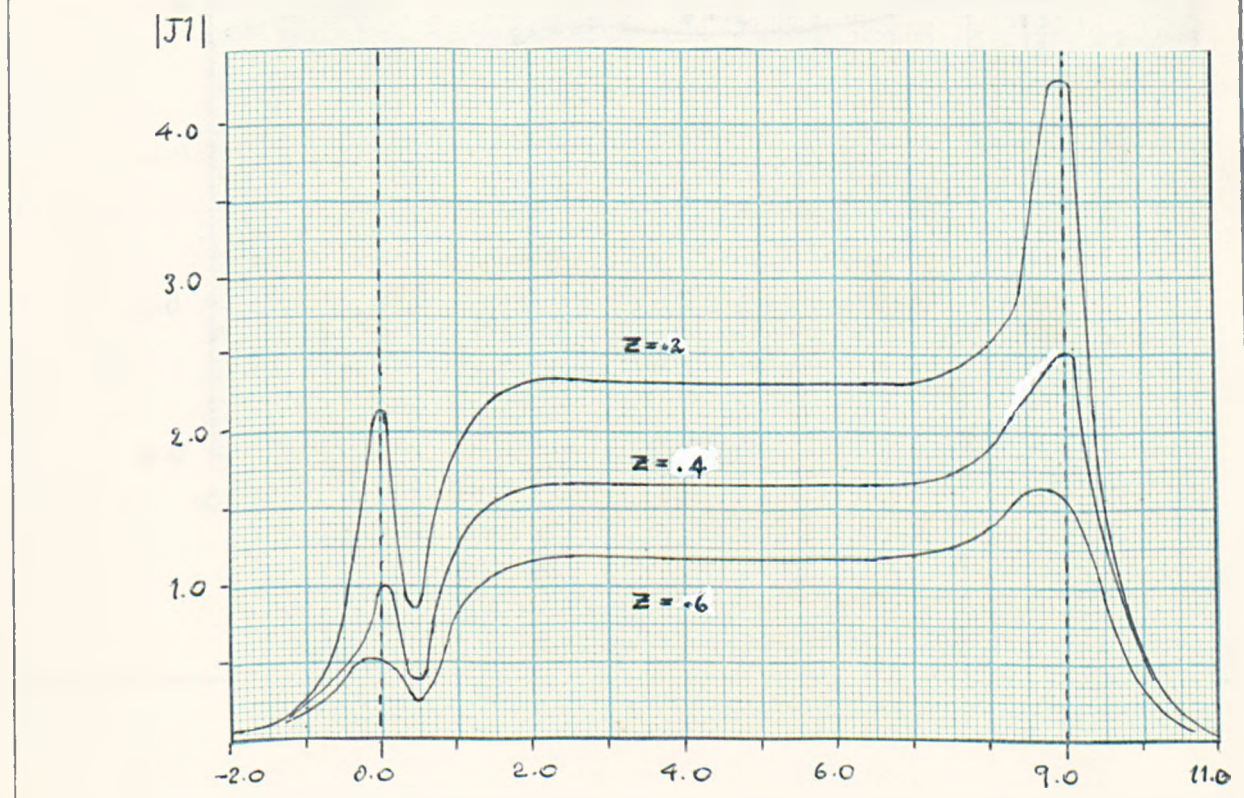

Fig. 7.5 The Electric Current Density (S)

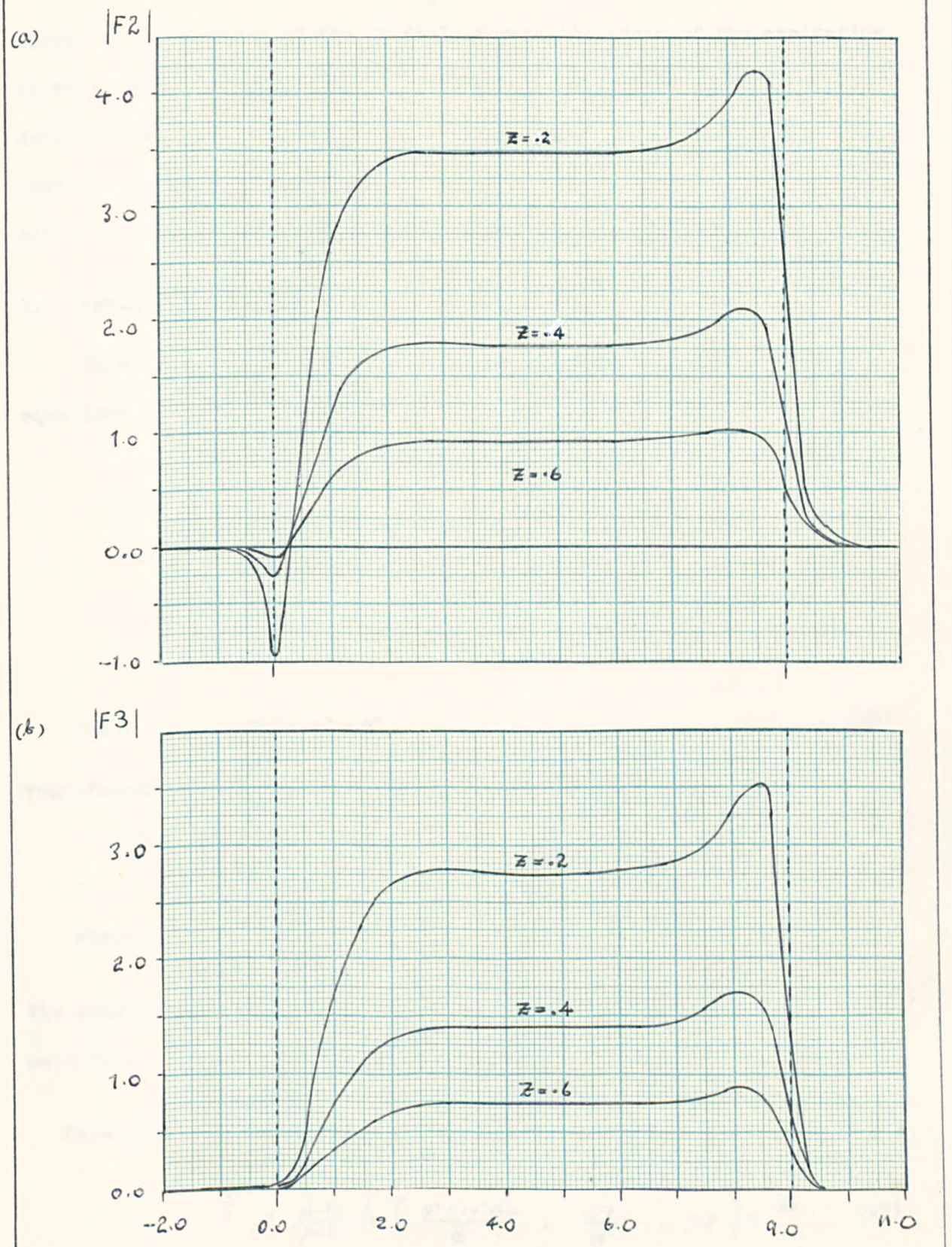

Fig. 7.6 The Induced EM Body Forces

currents'. The decay of the EM field beyond the edges of the excitation is very rapid and does in fact correspond to the estimated lengths of decay obtained in chapters 5 and 6. From figures 7.6 (a) and (b) we see that the body force components are approximately of the same order and may be considered constant along the length of the excitation.

7.3 Infinite Length Excitation

Here $\frac{\partial}{\partial x} \neq 0$ but $\frac{\partial}{\partial y} = 0$ (with the notation of §7.1). Maxwell's equations (5) to (7) transform to (using the first of (10)):

$$\frac{d\hat{B}_3}{dz} = i\alpha \hat{B}_2 \tag{42}$$

$$\mu_0 h \hat{\underline{J}} = \left[-\frac{\partial \hat{B}_2}{\partial z} - i\alpha \hat{B}_3 \;,\; ip\hat{B}_3 \;,\; -ip\hat{B}_2 \right] \tag{43}$$

$$\frac{d^2\hat{\underline{B}}}{dz^2} = \phi^2 \hat{\underline{B}} \tag{44}$$

where $$\phi^2 = \gamma^2 + p^2 \tag{45}$$

Transforming the boundary conditions we obtain

$$\hat{B}_2(p,0) = \mu_0 K_s \hat{S}_x \quad (S) \qquad \hat{B}_3(p,0) = B_m \hat{S}_x \quad (P) \tag{46}$$

where $$\hat{S}_x = (e^{2ipa} - 1)/ip \tag{47}$$

The solutions to (44) are found using the same method as that in §7.2, we obtain

Case S: $$\hat{\underline{B}} = \mu_0 K_s \hat{S}_x \left[0 \;,\; 1 \;,\; -\frac{i\alpha}{\phi} \right] e^{-\phi z} \tag{48}$$

$$\hat{\underline{J}} = \frac{\mu_0 K_s}{\mu_0 h} \hat{S}_x \left[\frac{p^2 + i\alpha^2 s R_m}{\phi} \;,\; \frac{\alpha\gamma}{\phi} \;,\; ip \right] e^{-\phi z} \tag{49}$$

Case P: $$\hat{\underline{B}} = B_m \hat{S}_x \left[0 \;,\; \frac{i\phi}{\alpha} \;,\; 1 \right] e^{-\phi z} \tag{50}$$

$$\hat{\underline{J}} = \frac{B_m}{\mu_0 h} \hat{S}_x \left[i\left(\frac{p^2 + i\alpha^2 s R_m}{\alpha}\right) \;,\; ip \;,\; \frac{\phi p}{\alpha} \right] e^{-\phi z} \tag{51}$$

Applying the inverse Fourier transformation (the latter of (10)) to (48)

to (51), we obtain

$$\text{Case } S: \quad \underline{B} = \frac{\mu_0 K_s}{2\pi} \int_{-\infty}^{\infty} \hat{S}_x \left[0,\ 1,\ -\frac{i\alpha}{\phi} \right] e^{-\phi z} e^{-i\rho x} d\rho \tag{52}$$

$$\underline{J} = \frac{K_s}{2\pi h} \int_{-\infty}^{\infty} \hat{S}_x \left[\frac{\rho^2 + i\alpha^2 s R_m}{\phi},\ \frac{\alpha \rho}{\phi},\ i\rho \right] e^{-\phi z} e^{-i\rho x} d\rho \tag{53}$$

$$\text{Case } P: \quad \underline{B} = \frac{B_m}{2\pi} \int_{-\infty}^{\infty} \hat{S}_x \left[0,\ \frac{i\phi}{\alpha},\ 1 \right] e^{-\phi z} e^{-i\rho x} d\rho \tag{54}$$

$$\underline{J} = \frac{B_m}{2\pi \mu_0 h} \int_{-\infty}^{\infty} \hat{S}_x \left[i\left(\frac{\rho^2 + i\alpha^2 s R_m}{\alpha}\right),\ i\rho,\ \frac{\phi \rho}{\alpha} \right] e^{-\phi z} e^{-i\rho x} d\rho \tag{55}$$

The integrals in (52) to (55) are identical in form to those in (22) to (25). Applying the convolution result (11) and using a similar analysis as that in §7.2 , we can write (52) to (55) in the following form. .

$$\text{Case } S: \quad \underline{B} = \frac{\mu_0 K_s}{\pi} \left[0,\ \psi^2 z\, I_x\left\{ \frac{K_1(\mp)}{\mp} \right\},\ -i\alpha\, I_x\{K_0(\mp)\} \right] \tag{56}$$

$$\underline{J} = \frac{K_s}{\pi h} \left[i\alpha^2 s R_m\, I_x\{K_0(\mp)\} + \psi^2 z \frac{K_1(\mp)}{\mp}\Big|_{x-2a}^{x},\ i\alpha K_0(\mp)\Big|_{x-2a}^{x},\ -\psi^2 z \frac{K_1(\mp)}{\mp}\Big|_{x-2a}^{x} \right] \tag{57}$$

$$\text{Case } P: \quad \underline{B} = \frac{B_m}{\pi} \left[0,\ -i\frac{\partial}{\partial z}\left(\frac{\psi^2 z}{\alpha} I_x\left\{ \frac{K_1(\mp)}{\mp} \right\} \right),\ \psi^2 z\, I_x\left[\frac{K_1(\mp)}{\mp} \right] \right] \tag{58}$$

$$\underline{J} = \frac{B_m}{\pi \mu_0 h} \left[\psi^2 z \left(-\alpha s R_m\, I_x\left\{ \frac{K_1(\mp)}{\mp} \right\} - \frac{i}{\alpha} \frac{\partial}{\partial x} \left\{ \frac{K_1(\mp)}{\mp}\Big|_{x-2a}^{x} \right\},\ -\psi^2 z \frac{K_1(\mp)}{\mp}\Big|_{x-2a}^{x},\ -i\frac{\partial}{\partial z}\left\{ \frac{\psi^2 z}{\alpha} \cdot \frac{K_1(\mp)}{\mp}\Big|_{x-2a}^{x} \right\} \right] \tag{59}$$

In (56) to (59) we use the notation of (36) and (37) with y replaced by x and $2b$ replaced by $2a$.

The infinite expanse solutions of chapter 3 can be recovered by setting x equal to a and letting $a \to \infty$, using the results of (38) and (39). Using the asymptotic approximation for $K_1(\mp)$, (40), we see that the $1/e$ folding lengths for the decay of the EM field is equal to $1/\mathcal{R}(\psi)$ for both the x and z coordinate axes, agreeing with the results of chapter 5.

A numerical approach similar to that of §7.2 is used here for the evaluation of the EM field solutions (56) to (59), and the results are shown in figures 7.7 to 7.9 (for the case S solutions) and in figures 7.10

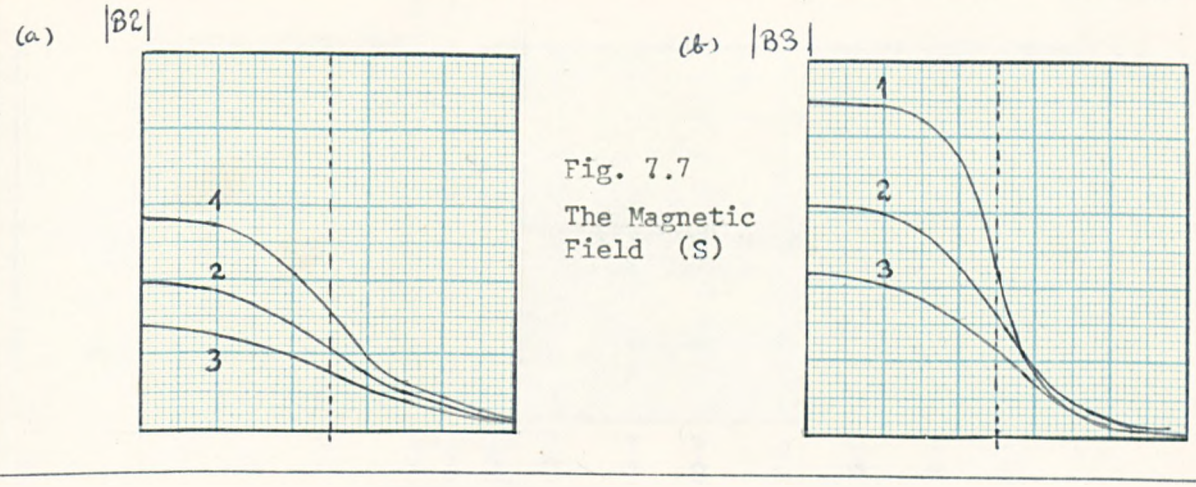

Fig. 7.7
The Magnetic Field (S)

1: z=·2 2: z=·4 3: z=·6

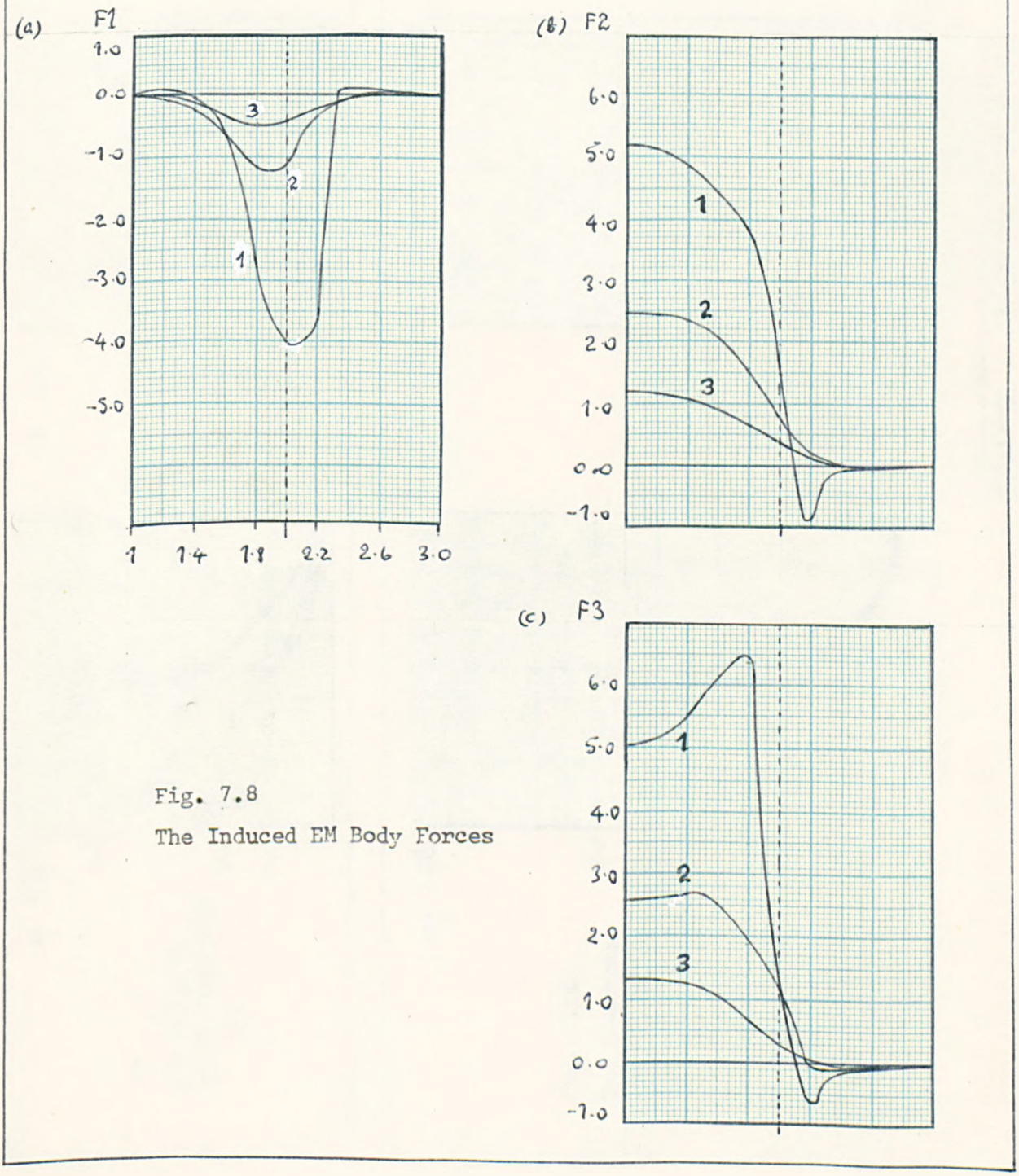

Fig. 7.8
The Induced EM Body Forces

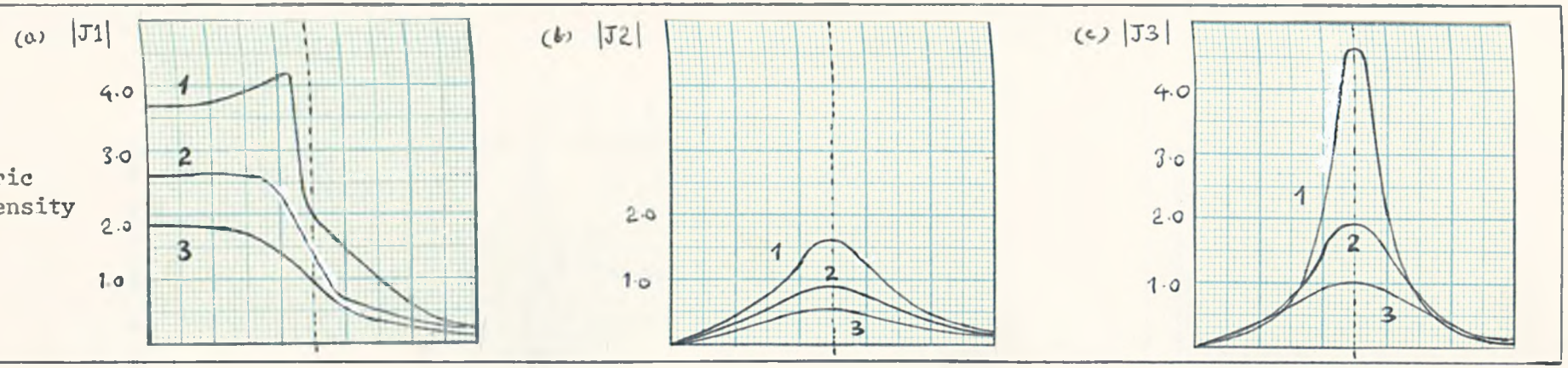

Fig. 7.9
The Electric Current Density (S)

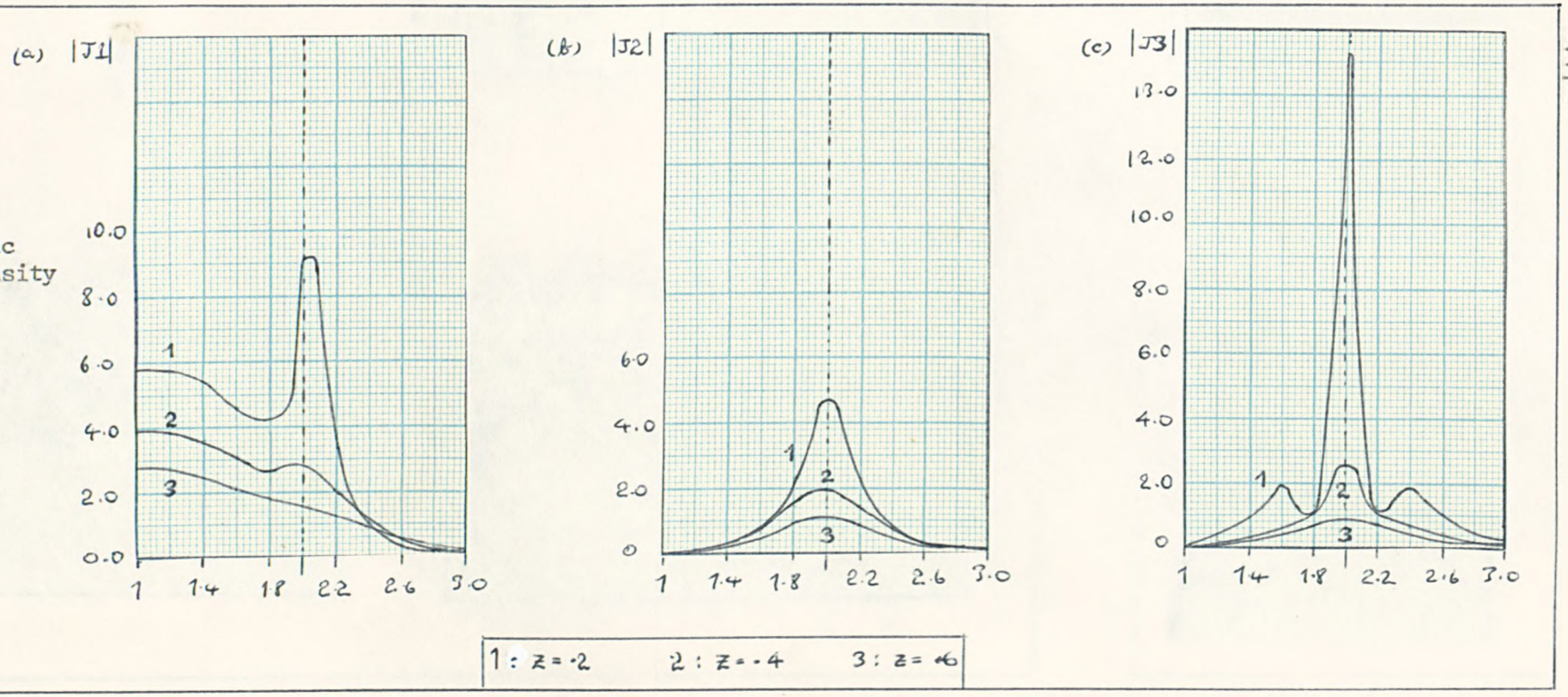

Fig. 7.10
The Electric Current Density (S)

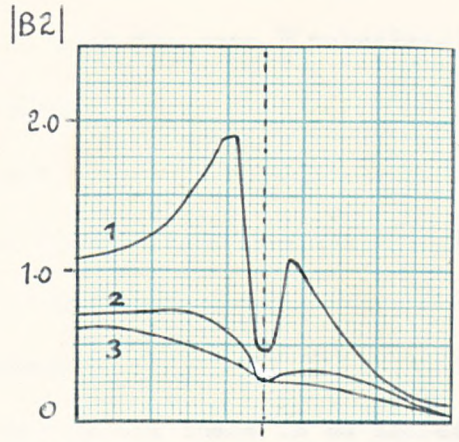

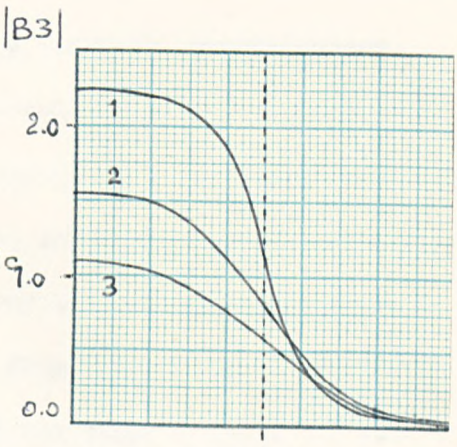

Fig. 7.11
The Magnetic Field (P)

1 : Z = -2 2 : Z = -4 3 : Z = -6

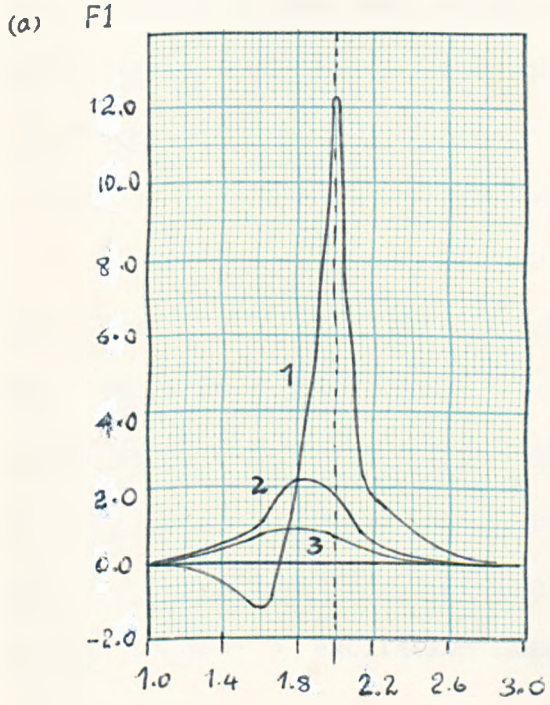

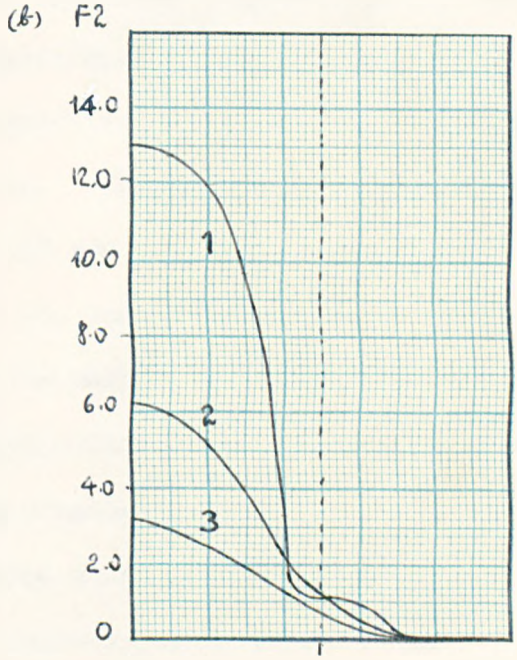

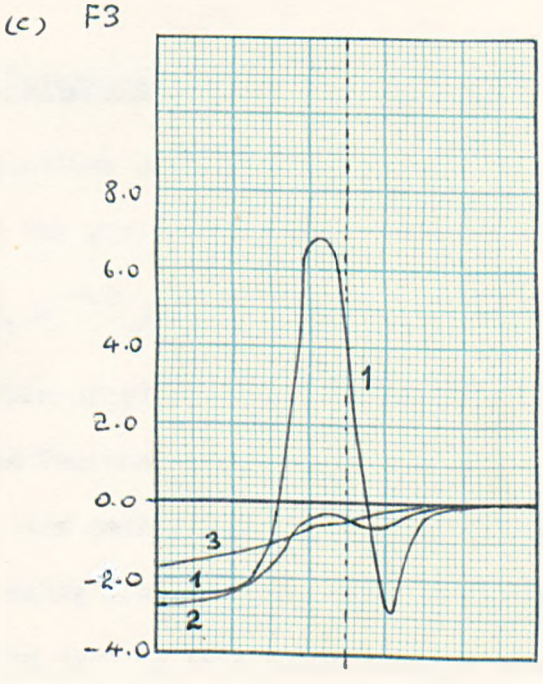

Fig. 7.12
The Induced EM Body Forces (P)

to 7.12 (for the case P solutions). The graphs show the dimensionless variation of the induced EM field (magnetic induction / ($\frac{\mu_0 K_0}{\pi}$ or $\frac{B_m}{\pi}$) and electric current density / ($\frac{K_0}{\pi L}$ or $\frac{B_m}{\pi \mu_0 L}$)). Because of the axial symmetry of the solutions we have only shown the induced EM field from $x > 1.0$. The form of the induced EM field for this configuration is similar to that described by the heuristic analysis of §5.4. From figures 7.9 (a) and 7.10 (a) we see there is an increase in J_1 at the edge $(x=2.0)$ of the excitation; this is merely a physical requirement of the conservation equation $\nabla . \underline{J} = 0$. The minimum at $x=2.0$ in figure 7.11 (a) arises because there is a reversal in the decay of the normal induction (figure 7.11 (b)) with depth there. The diagrams are mostly self-explanatory, but there is a striking contrast in the EM field solutions of the two methods of analysis - expecially in the induced EM body force. The pumping force (F2), (figure 7.8 (b), for case S , and figure 7.12 (b) for case P) has similar variation for the two analyses, however the remaining components of the body force are quite different and the two methods of analysis produce almost opposite effects. Apart from local circulation, the overall flow in the (x,z) plane can be estimated from consideration of F2 and F3; it appears that the case S excitation induces anti-clockwise circulation whilst the case P excitation induces clockwise circulation of the working fluid.

7.4 Fourier Inversion Using Contour Integration.

It is clear that the integral solutions of §7.2 ((22) to (25)) and §7.3 ((52) to (55)) may be written in the general form

$$I = \int_{-\infty}^{\infty} M(q,x)\, e^{-\gamma z}\, \hat{f}_y\, e^{-iqy}\, dq \qquad (60)$$

where we have chosen to use the notation of §7.2. From (15) we see that the function $\gamma = \gamma(q)$ is a double-valued function in the complex q-plane. Writing $\gamma = \sqrt{(q-a_1)(q-a_2)}$, the points a_1, a_2 are called branch points and $\gamma(q)$ is discontinuous on any contour encircling a_1 or a_2 . However, $\gamma(q)$ can be made continuous in the complex plane by cutting this plane along a line

joining a_1 and a_2 (the branch cut) and forming a Riemann surface, (see KNOPP, 1947). Thus (60) may now be evaluated along a contour in the complex q-plane using Cauchy's residue theorem. However, in the construction of a suitable contour care must be taken if we wish to apply Jordan's Lemma (see, for example, GOODSTEIN, 1965). Basically, this lemma allows the neglect of a line integral taken along a contour at infinity provided the kernal of the integral decays there. Consider the function $\hat{S}e^{-iqy}$ where from (17) $\hat{S}_y = (e^{2ibq}-1)/iq$. The behaviour of each of the two parts of this function in the upper and lower half planes of complex q-space must be separately examined to ensure applicability of Jordan's lemma. Three regions are constructed as follows (we use the notation C^+ to denote the upper half of the q-plane and C^- to denote the lower half).

$$\left.\begin{array}{lll} \text{Region I} & (y<0) & \Re\{iq(2b-y)\}<0 \text{ in } C^+ \;;\; \Re\{-iqy\}<0 \text{ in } C^+ \\ \text{Region II} & (0<y<2b) & \Re\{iq(2b-y)\}<0 \text{ in } C^+ \;;\; \Re\{-iqy\}<0 \text{ in } C^- \\ \text{Region III} & (y>2b) & \Re\{iq(2b-y)\}<0 \text{ in } C^- \;;\; \Re\{-iqy\}<0 \text{ in } C^- \end{array}\right\} \quad (61)$$

Similar regions (corresponding to $x<0$, $0<x<2a$, $x>2a$) can be constructed for the infinite length excitation analysis. Finally we consider the function $e^{-\gamma z}$. This decays exponentially with z along any contour provided $\Re(\gamma)>0$ on that contour. Incorporating this constraint with those of (61), we can construct a suitable contour in the complex q-plane (which loops the branch cut) allowing evaluation of the integral relation I in (60). Unfortunately the results we have obtained using this method are extremely cumbersome and difficult to interpret and so are not included here. We have also been unable to obtain a closed result for the EM field solutions - the line integrals taken around the branch cut do not appear to be reducible. However, with the notation $\mathcal{E}(z,t) = \mathcal{E}(z)e^{i(\omega t-\alpha y)}$ and $\mathcal{J}(z,t) = \mathcal{J}(z)e^{i(\omega t-\alpha y)}$ some information has been obtained from the contour solutions. We find that in region II (underneath the SLIM excitation), the EM field solutions consist of the

infinite expanse solutions of chapter 3 plus end/edge effect terms. The solutions in regions I and II (outside the excitation) consist solely of end/edge effect terms. In the infinite length excitation case (§7.3) the edge effects do not alter the travelling wave structure of $\mathcal{E}$ and $\mathcal{J}$ but merely their spatial variation. However when the excitation is made finite in length (§7.2) the effects are different. In region II the end effects consist of oscillatory terms which are superimposed on the travelling wave structure of $\mathcal{E}$ and $\mathcal{J}$; these terms are caused by the discontinuity in the excitation at $y=0$ and $y=2\ell$. These oscillatory terms dominate the solutions in regions I and III (at infinity the travelling wave excitation appears as a magnetic pole); in addition, terms which include the travelling wave effects are present, but these appear to decay with distance away from the ends of the excitation. These results agree with the ideas of §1.5 and the earlier results of this chapter.

Some of the ideas used here are incorporated in the contour analysis of chapter 9. However because the integral solutions contain only even powers of γ the kernals remain single valued.

8. THE FLUID MOTION INDUCED BY A RECTANGULAR BODY FORCE

8.1 Introduction

It is clear from the complexity of the EM field induced in the working liquid of a finite SLIP (see chapter 7) that any analytic solution to the hydromagnetic equation (1.23) for the induced velocity profiles will be extremely cumbersome. However, to a first approximation, we may assume the EM body force induced in the working liquid by a rectangular SLIP is rectangular in nature and of exponential decay with depth. For simplicity we assume the working liquid occupies the half space $z>0$, (figure 8.1). Choosing the origin at the centre of the rectangular force, which is taken to be of length $2b$ metres and width $2a$ metres, the body

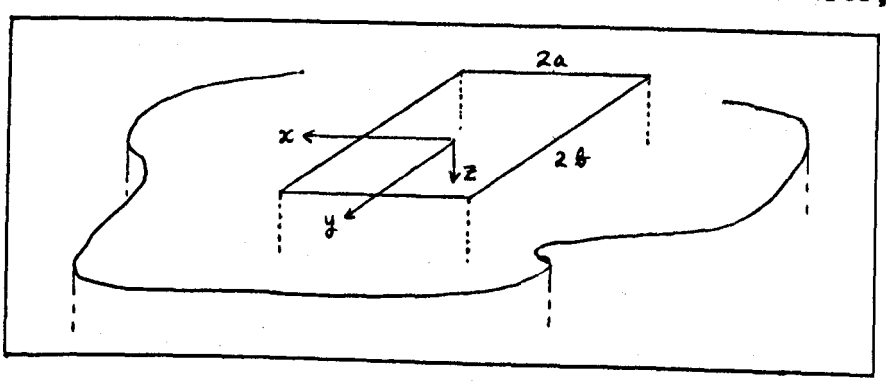

Fig. 8.1 The Rectangular Force

force we apply is

$$\underline{F} = \mathcal{B}_0^2 \sigma [f_1, f_2, f_3] e^{-\beta z} S_x(a,x) S_y(b,y) \qquad (1)$$

where $S_x(a,x) = H(x+a) - H(x-a)$ $\qquad S_y(b,y) = H(y+b) - H(y-b)$ $\qquad (2)$

and $H(x)$ is the Heaviside unit step function. In (1) $\mathcal{B}_0$ is constant with dimensions of magnetic field; σ is a constant with dimensions of electrical conductivity; f_1, f_2, f_3 are constants and β is a positive real parameter. The parameters $\mathcal{B}_0$ and σ are included in (1) to enable the Hartmann number to be introduced into the hydrodynamic analysis below. To preserve symmetry the parameter f_1 is assumed non-zero for the moment, although it will be set to zero when we consider the velocity profiles

induced in the liquid.

Assuming the magnitude of the induced velocity profiles is sufficiently small to enable the neglect of the hydrodynamic inertia terms (the 'slow flow' approximation) we obtain exact solutions in the three dimensional Fourier transformation space for the induced velocity profiles under both the fixed and free surface boundary conditions. Unfortunately, a closed result for the inversion of these solutions does not seem to be possible. However, by reducing the problem to two dimensions and concentrating on the boundary layer regions of the induced flow, we find an analytic approximation can be made. From the simplified results we make certain deductions concerning the relative importance to the flow of the body force components induced by a SLIP.

8.2 Exact Solutions in Transform Space

The hydrodynamic equation for steady state slow flow (neglecting the inertia terms in (1.23)) is

$$\nu \nabla^2 \underline{v} = \nabla P - \underline{F} \tag{3}$$

where ν is the fluid viscosity ; $\underline{v}(\underline{r})$ its velocity; $P(\underline{r})$ the internal pressure of the fluid and $\underline{F}(\underline{r})$ the body force (given by (1)). Introducing a scale length h we define the following dimensionless variables:

$x^* = x/h$, $y^* = y/h$, $z^* = z/h$, $a^* = a/h$, $b^* = b/h$, $\beta^* = \beta h$, $P^* = Ph/\nu$

and $H_M = B_0 h \left(\frac{\sigma}{\nu}\right)^{1/2}$ (the Hartmann number). We write $f_i^* = f_i / H_M^2$ $(i = 1,3)$. Because all parameters will be assumed dimensionless from now on we shall ignore the star superscripts. Equation (3) becomes

$$\nabla^2 \underline{v} = \nabla P - [f_1, f_2, f_3]\, S_x S_y e^{-\beta z} \tag{4}$$

We also require the continuity equation (1.22)

$$\nabla \cdot \underline{v} = 0 \tag{5}$$

we now define respectively the two-dimensional forms of the Fourier transformation (1.32) and inverse Fourier transformation (1.33) of the function $M(x,y,z)$:

$$\mathcal{F}_2^+\{M(x,y,z)\} = \hat{M}(p,q,z) = \int_{-\infty}^{\infty}\int_{-\infty}^{\infty} M(x,y,z)\, e^{i(px+qy)}\, dx\, dy \tag{6}$$

$$\mathcal{F}_2^-\{\hat{M}(p,q,z)\} = M(x,y,z) = \frac{1}{(2\pi)^2}\int_{-\infty}^{\infty}\int_{-\infty}^{\infty} \hat{M}(p,q,z)\, e^{-i(px+qy)}\, dp\, dq \tag{7}$$

Using the notation $\mathcal{F}_1^+\{S_x(a,x)\} = \hat{S}_x$ and $\mathcal{F}_2^+\{S_y(b,y)\} = \hat{S}_y$, the transformed form of (4) in component form is:

$$\left(\frac{d^2}{dz^2} - \kappa^2\right)\hat{u} = -ip\hat{P} - \hat{S} f_1 e^{-\beta z} \tag{8}$$

$$\left(\frac{d^2}{dz^2} - \kappa^2\right)\hat{v} = -iq\hat{P} - \hat{S} f_2 e^{-\beta z} \tag{9}$$

$$\left(\frac{d^2}{dz^2} - \kappa^2\right)\hat{w} = \frac{d\hat{P}}{dz} - \hat{S} f_3 e^{-\beta z} \tag{10}$$

where $$\kappa^2 = p^2 + q^2 \tag{11}$$

and the notation $\underline{v} = [u, v, w]$, $\hat{S} = \hat{S}_x \hat{S}_y$ is employed. The transformation of the continuity equation (5) yields

$$\frac{d\hat{w}}{dz} = ip\hat{u} + iq\hat{v} \tag{12}$$

Applying the operator $\left(\frac{d^2}{dz^2} - \kappa^2\right)$ to (12) using (8) to (10) we obtain the biharmonic equation

$$\left(\frac{d^2}{dz^2} - \kappa^2\right)^2 \hat{w} = \left\{\kappa^2 f_3 + \beta(ipf_1 + iqf_2)\right\}\hat{S}\, e^{-\beta z} \tag{13}$$

If the velocity $\hat{w}$ becomes zero as $z \to \infty$, the solution to (13) may be written as

$$\hat{w} = (A + Bz)e^{-\kappa z} + Re^{-\beta z}\hat{S} \tag{14}$$

where $$R = \left\{\kappa^2 f_3 + \beta(ipf_1 + iqf_2)\right\} \Big/ (\beta^2 - \kappa^2)^2 \tag{15}$$

In (14) the parameters A and B arise as 'constants' (ie: independent of z) of integration; we have $A = A(p,q)$ and $B = B(p,q)$. Using (8) to (10), and (12), we obtain the harmonic equation for $\hat{P}(z)$:

$$\left(\frac{d^2}{dz^2} - \kappa^2\right)\hat{P} = -\left\{\beta f_3 + ipf_1 + iqf_2\right\}\hat{S}\, e^{-\beta z} \tag{16}$$

If $\hat{P} \to 0$ as $z \to \infty$ the solution to (16) can be written as

$$\hat{P} = Ce^{-\kappa z} - Qe^{-\beta z}\hat{S} \tag{17}$$

where $$Q = \left\{ \beta f_3 + ip f_1 + iq f_2 \right\} \Big/ (\beta^2 - \kappa^2) \tag{18}$$

and $C = C(p,q)$. Substituting (17) in (10) using (14) we find $C = 2B$. Substituting (17) in (8) and (9) and solving for $\hat{u}$ and $\hat{v}$ we obtain

$$\hat{u} = -ip\left\{ D e^{-\kappa z} - \frac{Cz}{2\kappa} e^{-\kappa z} \right\} + \left\{ \frac{ipQ - f_1}{\beta^2 - \kappa^2} \right\} \hat{S} e^{-\beta z} \tag{19}$$

$$\hat{v} = -iq\left\{ E e^{-\kappa z} - \frac{Cz}{2\kappa} e^{-\kappa z} \right\} + \left\{ \frac{iqQ - f_2}{\beta^2 - \kappa^2} \right\} \hat{S} e^{-\beta z} \tag{20}$$

where $D = D(p,q)$ and $E = E(p,q)$. We require four equations to evaluate the functions A, B, D, and E; these equations are supplied by the boundary conditions on the surface $z = 0$.

8.2.1 Fixed Surface Solutions. On the surface $z = 0$, from (1.40) we have $\underline{v} = \underline{0}$, therefore $\hat{\underline{v}} = \underline{0}$ on $z = 0$, and by (12) $\frac{d\hat{w}}{dz} = 0$ on $z = 0$. Applying these conditions to (14), (19) and (20) we find

$$A = -R\hat{S} \; ; \; B = R(\beta - \kappa)\hat{S} \; ; \; ip D = \left(\frac{ipQ - f_1}{\beta^2 - \kappa^2} \right) \hat{S} \; ; \; iq E = \left(\frac{iqQ - f_2}{\beta^2 - \kappa^2} \right) \hat{S}$$

and the solutions for the velocity and pressure become

$$\hat{u} = \left\{ \frac{ipz}{\kappa} \cdot e^{-\kappa z} \cdot R(\beta + \kappa) - \left(\frac{ipQ - f_1}{\beta^2 - \kappa^2} \right) \left(e^{-\kappa z} - e^{-\beta z} \right) \right\} \hat{S} \tag{21}$$

$$\hat{v} = \left\{ \frac{iqz}{\kappa} \cdot e^{-\kappa z} R(\beta + \kappa) - \left(\frac{iqQ - f_2}{\beta^2 - \kappa^2} \right) \left(e^{-\kappa z} - e^{-\beta z} \right) \right\} \hat{S} \tag{22}$$

$$\hat{w} = \left\{ Rz e^{-\kappa z} (\beta - \kappa) - R\left(e^{-\kappa z} - e^{-\beta z} \right) \right\} \hat{S} \tag{23}$$

$$P = \left\{ 2R(\beta - \kappa) e^{-\kappa z} - Q e^{-\beta z} \right\} \hat{S} \tag{24}$$

8.2.2 Free Surface Solutions. On $z = 0$ by (1.41) we have $\frac{du}{dz} = 0$ $\frac{dv}{dz} = 0$ and $w = 0$ so $\frac{d\hat{u}}{dz} = 0$, $\frac{d\hat{v}}{dz} = 0$ and $\hat{w} = 0$ on $z = 0$. Also by (12) $\frac{d^2\hat{w}}{dz^2} = 0$ on $z = 0$. Applying these conditions to (14), (19) and (20) we find

$$A = -R \; ; \; B = \frac{(\beta^2 - \kappa^2)}{2\kappa} R \; ; \quad \begin{Bmatrix} ipD \\ iqE \end{Bmatrix} = \frac{\beta/\kappa}{\beta^2 - \kappa^2} \begin{Bmatrix} ipQ - f_1 \\ iqQ - f_2 \end{Bmatrix} - \frac{(\beta^2 - \kappa^2)R}{2\kappa^3} \begin{Bmatrix} ip \\ iq \end{Bmatrix}$$

and the solutions for the velocity and pressure become:

$$\hat{u} = \left\{ \left(\frac{ipQ - f_1}{\beta^2 - \kappa^2} \right) \left(e^{-\beta z} - \frac{\beta}{\kappa} e^{-\kappa z} \right) + \frac{ip}{2\kappa^3} (\beta^2 - \kappa^2) R(1 + \kappa z) e^{-\kappa z} \right\} \hat{S} \tag{25}$$

$$\hat{v} = \left\{ \left(\frac{iqQ - f_2}{\beta^2 - \kappa^2} \right) \left(e^{-\beta z} - \frac{\beta}{\kappa} e^{-\kappa z} \right) + \frac{iq}{2\kappa^2} (\beta^2 - \kappa^2) R (1 + \kappa z) e^{-\kappa z} \right\} \hat{S} \tag{26}$$

$$\hat{w} = \left\{ (\beta^2 - \kappa^2) \frac{zR}{2\kappa} + R (e^{-\beta z} - e^{-\kappa z}) \right\} \hat{S} \tag{27}$$

$$\hat{p} = \left\{ (\beta^2 - \kappa^2) \frac{R}{\kappa} e^{-\kappa z} - Q e^{-\beta z} \right\} \hat{S} \tag{28}$$

8.3 Reduction of the Problem to Two Dimensions

Consider the function $\hat{S}\hat{M}(p,q,z)$. Its inverse Fourier transformation (7) may be evaluated using the two-dimensional form of the convolution theorem (1.34), viz:

$$\mathcal{F}_2^{-} \left\{ \hat{M}(p,q,z) \hat{N}(p,q,z) \right\} = \int_{-\infty}^{\infty} \int_{-\infty}^{\infty} M(\xi,\eta,z) N(x-\xi, y-\eta, z) \, d\xi \, d\eta \tag{29}$$

Using the properties of $\mathcal{F}\{\hat{S}\}$, (2), it is easy to show that

$$\mathcal{F}_2^{-} \left\{ \hat{S} \hat{M}(p,q,z) \right\} = \int_{x-a}^{x+a} \int_{y-b}^{y+b} M(\xi,\eta,z) \, d\xi \, d\eta \tag{30}$$

When $\hat{M}(p,q,z) \equiv \hat{M}(\kappa,z)$ where κ is given by (11) we can derive the result (see Appendix

$$M(\xi,\eta,z) = \frac{1}{(2\pi)^2} \int_{-\infty}^{\infty} \int_{-\infty}^{\infty} \hat{M}(\kappa,z) e^{-i(p\xi+q\eta)} \, dp \, dq = \frac{1}{2\pi} \cdot \int_0^{\infty} \hat{M}(\kappa,z) \cdot \kappa J_0(\kappa\rho) \, d\kappa \tag{31}$$

where $J_0(\kappa\rho)$ is Bessel's function of order zero and $\rho^2 = \xi^2 + \eta^2$. If the transformed solutions are of the form $ip\hat{M}(\kappa,z)$ or $iq\hat{M}(\kappa,z)$ we find their inverse can be written as in the right of (31) but with $J_0(\kappa\rho)$ replaced by $J_1(\kappa\rho)$ (see Appendix I), Bessel's function of order unity. However, from the second of (31) we see that the operator relations $ip = -\frac{\partial}{\partial \xi}$, $iq = -\frac{\partial}{\partial \eta}$ can be used. Substituting these relations in Q, (18), and R, (15), we find

$$Q \equiv \left(\beta f_3 - f_1 \frac{\partial}{\partial \xi} - f_2 \frac{\partial}{\partial \eta} \right) \cdot \frac{1}{(\beta^2 - \kappa^2)} \tag{32}$$

$$R \equiv \left(\kappa^2 f_3 - \beta f_1 \frac{\partial}{\partial \xi} - \beta f_2 \frac{\partial}{\partial \eta} \right) \cdot \frac{1}{(\beta^2 - \kappa^2)^2} \tag{33}$$

The transformed solutions in §8.2.1 and §8.2.2 can now be written in integral form using the operator form of Q and R ((32) and (33)) and the convolution results (30). Unfortunately, we have been unable to

obtain a closed analytic solution for the real-space results. A numerical approach is possible, (although not performed here), because the form of (31) allows the use of Gaussian quadrature over $[0, \infty)$ and the kernal of (30) is well behaved for reasonable values of x and y ($|x|<2a$ and $|y|<2b$, say). However if we reduce the problem to two dimensions an analytic approximation is possible.

A plan view of the body force is given in figure 8.2. Region A corresponds to the case of zero y-dependence, whilst region B corresponds

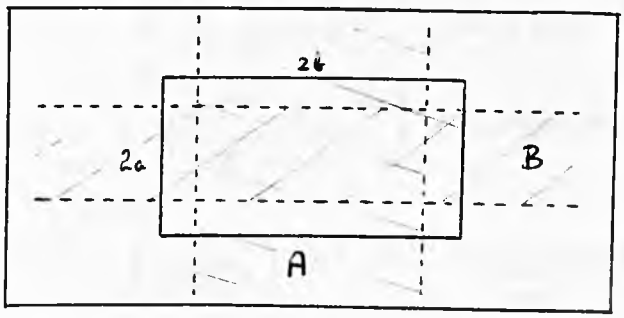

Fig. 8.2 The Two-Dimensional Regions Under Consideration

to zero x - dependence. We further simplify the problem by setting $f_1 = 0$.

8.3.1 Region A $\left(\frac{\partial}{\partial y}=0\right)$. With $f_1 = 0$, (32) and (33) reduce to

$$Q = \beta f_2 / (\beta^2 - \kappa^2) \quad ; \quad R = \kappa^2 f_2 / (\beta^2 - \kappa^2)^2 \tag{34}$$

This region corresponds to a body force of infinite length; letting $b \to \infty$ in the second of (2) we find $S_y(b,y) = 1$ and so $\hat{S}_y(b,q) = 2\pi\,\delta(q)$ (the Dirac delta function). Thus for this region, the inverse transformation (30) reduces to

$$\mathcal{F}_2^{-1}\left\{\hat{S}\,\hat{M}(p,q,z)\right\} = 2\pi \int_{x-a}^{x+a} M(\xi,0,z)\,d\xi \tag{35}$$

where $M(\xi,0,z)$ is given by (31) with $\rho = |\xi|$.

Substituting for Q and R in (21) to (24) and (25) to (28) using (34) and (35), the inverted solutions for the velocity and pressure distributions become (with $f_1 = 0$ and $\eta = 0$):

(i) Fixed boundary

$$u = f_3 \int_{x-a}^{x+a} \int_{0}^{\infty} \left\{ -\frac{\partial}{\partial \xi} \cdot \frac{z e^{-\kappa z}}{\kappa} \cdot \frac{\kappa^2(\beta+\kappa)}{(\beta^2-\kappa^2)^2} + \frac{\partial}{\partial \xi} \cdot \frac{\beta\,(e^{-\kappa z} - e^{-\beta z})}{(\beta^2-\kappa^2)^2} \right\} \kappa J_0(\kappa\rho)\,d\kappa\,d\xi \tag{36}$$

$$V = f_2 \int_{x-a}^{x+a} \int_0^\infty \left(\frac{e^{-\kappa z} - e^{-\beta z}}{\beta^2 - \kappa^2} \right) \kappa J_0(\kappa\rho)\, d\kappa\, d\xi \tag{37}$$

$$W = f_3 \int_{x-a}^{x+a} \int_0^\infty \left\{ \frac{\kappa^2 z(\beta-\kappa) e^{-\kappa z}}{(\beta^2-\kappa^2)^2} - \kappa^2 \frac{(e^{-\kappa z} - e^{-\beta z})}{(\beta^2-\kappa^2)^2} \right\} \kappa J_0(\kappa\rho) \tag{38}$$

$$P = f_3 \int_{x-a}^{x+a} \int_0^\infty \left\{ \frac{2\kappa^2(\beta-\kappa) e^{-\kappa z}}{(\beta^2-\kappa^2)^2} - \frac{\beta e^{-\beta z}}{\beta^2-\kappa^2} \right\} \kappa J_0(\kappa\rho) \tag{39}$$

(ii) Free boundary

$$u = f_3 \int_{x-a}^{x+a} \int_0^\infty \left\{ \beta \frac{\partial}{\partial \xi} \cdot \frac{\left(\frac{\beta}{\kappa} e^{-\kappa z} - e^{-\beta z}\right)}{(\beta^2-\kappa^2)^2} - \frac{\partial}{\partial \xi} \cdot \frac{\kappa^2}{(\beta^2-\kappa^2)^2} \cdot \frac{(\beta^2-\kappa^2)}{2\kappa^3} (1+\kappa z) e^{-\kappa z} \right\} \kappa J_0(\kappa\rho)\, d\kappa\, d\xi \tag{40}$$

$$V = f_2 \int_{x-a}^{x+a} \int_0^\infty \left(\frac{e^{-\kappa z} - \frac{\beta}{\kappa} e^{-\beta z}}{\beta^2-\kappa^2} \right) \kappa J_0(\kappa\rho)\, d\kappa\, d\xi \tag{41}$$

$$W = f_3 \int_{x-a}^{x+a} \int_0^\infty \frac{\kappa^2}{(\beta^2-\kappa^2)^2} \left\{ e^{-\beta z} - e^{-\kappa z} + \frac{(\beta^2-\kappa^2)}{2\kappa} z e^{-\kappa z} \right\} \kappa J_0(\kappa\rho)\, d\kappa\, d\xi \tag{42}$$

$$P = f_3 \int_{x-a}^{x+a} \int_0^\infty \left\{ \frac{\kappa(\beta^2-\kappa^2) e^{-\kappa z}}{(\beta^2-\kappa^2)^2} - \frac{\beta e^{-\kappa z}}{(\beta^2-\kappa^2)} \right\} \kappa J_0(\kappa\rho)\, d\kappa\, d\xi \tag{43}$$

8.3.2 Region $\mathcal{B}\left(\frac{\partial}{\partial x} = 0\right)$. With $f_1 = 0$, (32) and (33) reduce to

$$Q \equiv \left(\beta f_3 - f_2 \frac{\partial}{\partial \eta}\right) \cdot \frac{1}{\beta^2-\kappa^2} \quad ; \quad R \equiv \left(\kappa^2 f_3 - \beta f_2 \frac{\partial}{\partial \eta}\right) \cdot \frac{1}{(\beta^2-\kappa^2)^2} \tag{44}$$

Using a similar reasoning as in §8.2.1 for $S_x(a,y)$, the inverse transformation (30) reduces to

$$\mathcal{F}_2^- \left\{ \hat{S}\, \hat{M}(p,q,z) \right\} = 2\pi \int_{y-t}^{y+t} M(0,\eta,z)\, d\eta \tag{45}$$

where $M(0,\eta,z)$ is given by (31) with $\rho = |\eta|$.

Substituting for Q and R in (21) to (24) and (25) to (28), using (44) and (45), the inverted solutions for the velocity and pressure distributions become (with $f_1 = 0$ and $\rho = 0$):

(i) Fixed boundary

$$u = 0 \tag{46}$$

$$V = \int_{y-t}^{y+t} \int_0^\infty \left\{ -\frac{\partial}{\partial \eta} \cdot \frac{z}{\kappa} e^{-\kappa z} \frac{(\beta-\kappa)}{(\beta+\kappa)} \left(f_3 \kappa^2 - \beta f_2 \frac{\partial}{\partial \eta}\right) + \left[\frac{\partial}{\partial \eta} \frac{\left(\beta f_3 - f_2 \frac{\partial}{\partial \eta}\right)}{\beta^2-\kappa^2} + f_2 \right] \left(\frac{e^{-\kappa z} - e^{-\beta z}}{\beta^2-\kappa^2} \right) \right\}$$

$$\times \kappa J_0(\kappa\rho)\, d\kappa\, d\xi \tag{47}$$

$$W = \int_{y-b}^{y+b}\int_{0}^{\infty} \frac{f_3 k^2 - \beta f_2 \frac{\partial}{\partial \eta}}{(\beta^2-k^2)^2}\left\{ z(\beta-k)e^{-kz} - e^{-kz} + e^{-\beta z}\right\} k J_0(k\rho)\, dk\, d\eta \qquad (48)$$

$$P = \int_{y-b}^{y+b}\int_{0}^{\infty} \left\{ 2\left(f_3 k^2 - \beta f_2 \frac{\partial}{\partial \eta}\right)\frac{(\beta-k)e^{-kz}}{(\beta^2-k^2)} - \frac{(f_3\beta - f_2\,\partial/\partial\eta)\,e^{-\beta z}}{(\beta^2-k^2)}\right\} k J_0(k\rho)\, dk\, d\eta \qquad (49)$$

(ii) Free boundary

$$u = 0 \qquad (50)$$

$$V = \int_{y-b}^{y+b}\int_{0}^{\infty} \left\{ \left[\frac{-\frac{\partial}{\partial\eta}(\beta f_3 - f_2\frac{\partial}{\partial\eta})}{(\beta^2-k^2)^2} - \frac{f_2}{(\beta^2-k^2)}\right]\left(e^{-\beta z} - \frac{\beta}{k}e^{-kz}\right) - \frac{\partial}{\partial\eta}\frac{(k^2 f_3 - \beta f_2\frac{\partial}{\partial\eta})(1+kz)e^{-kz}}{2k^3(\beta^2-k^2)}\right\}$$

$$\times\, k J_0(k\rho)\, dk\, d\eta \qquad (51)$$

$$W = \int_{y-b}^{y+b}\int_{0}^{\infty} \left\{ \frac{(\beta^2-k^2)z}{2k} + e^{-\beta z} - e^{-kz}\right\} \frac{k^2 f_3 - \beta f_2 \frac{\partial}{\partial\eta}}{(\beta^2-k^2)^2}\cdot k J_0(k\rho)\, dk\, d\eta \qquad (52)$$

$$P = \int_{y-b}^{y+b}\int_{0}^{\infty} \left\{ \frac{e^{-kz}}{k}\left(\frac{k^2 f_3 - \beta f_2\frac{\partial}{\partial\eta}}{\beta^2-k^2}\right) - \left(\frac{\beta f_3 - f_2\frac{\partial}{\partial\eta}}{\beta^2-k^2}\right)e^{-\beta z}\right\} k J_0(k\rho)\, dk\, d\eta \qquad (53)$$

8.4 Integral Evaluation

Examination of the results in §8.3.1 and §8.3.2 indicates that we require an evaluation of certain integrals whose general form is represented by

$$I^n_{m,r}(\beta,\rho,z) = \int_0^\infty \frac{k^n J_r(k\rho)\, e^{-kz}}{(\beta^2-k^2)^m}\, dk \qquad \Re\{\beta\} > 0 \qquad (54)$$

where m, n and r are positive integers. The integral $I^n_{m,r}$ is Cauchy Principal Value* with a singularity at $k=\beta$ when β is real. Because the kernel of $I^n_{m,r}$ is continuous either side of this singularity we can differentiate through the integral sign (see Appendix II) and write

$$I^n_{m,r} = \frac{(-1)^{n+m-1}}{(2\beta)^{m-1}}\cdot\frac{\partial^{(m)}}{\partial z^{(m)}}\cdot\frac{\partial^{(m-1)}}{\partial\beta^{(m-1)}}\cdot\left\{ I^0_{1,r}(\beta,\rho,z)\right\} \qquad m \geq 1 \qquad (55)$$

where

$$I^0_{1,r} = \int_0^\infty \frac{J_r(k\rho)\, e^{-kz}}{\beta^2-k^2}\, dk \qquad (56)$$

$$= \frac{1}{2\beta}\left\{ F^0_{1,r} + G^0_{1,r}\right\} \qquad (57)$$

and

$$F^0_{1,r}(\beta,\rho,z) = \int_0^\infty \frac{J_r(k\rho)\, e^{-kz}}{\beta-k}\, dk \qquad (58)$$

* for m odd

$$G^{\circ}_{i,r}(\beta,\rho,z) = \int_0^{\infty} \frac{J_r(k\rho)e^{-kz}}{\beta+k}\,dk \tag{59}$$

Substituting (57) into (55) we have

$$I^{n}_{m,r} = (-1)^{m-1}\frac{\partial^{(m-1)}}{\partial\beta^{(m-1)}}\left\{\frac{1}{2\beta}\left(F^{n}_{i,r}+G^{n}_{i,r}\right)\right\} = (-1)^{m-1}\frac{\partial^{(m-1)}}{\partial\beta^{(m-1)}}\left\{\frac{1}{2}\left(F^{n-1}_{i,r}-G^{n-1}_{i,r}\right)\right\} \tag{60}$$

where the form of $F^{n}_{i,r}$ and $G^{n}_{i,r}$ is specified by (54).

The integrals (54), (58) and (59) are of the Laplacian type, but we have been unable to find evaluations of either their general or particular forms in the published literature. However, using the method of Appendix II we can reduce the integrals to expressions which are the sum of closed and integral results. First, we define the Laplace transformation of $J_r(k\rho)$ as

$$\mathcal{L}\{J_r(k\rho)\} = \bar{J}_r(z) = \int_0^{\infty} J_r(k\rho)e^{-kz}\,dk \tag{61}$$

$$= \rho^{r}(\rho^2+z^2)^{-1/2}\left\{z+(\rho^2+z^2)^{1/2}\right\}^{-r} \quad \text{BATEMAN (p.182)} \tag{62}$$

We now reduce (58) and (59) using (61); the dashes denote differentiation with respect to z :

(a) Consider $F^{\circ}_{i,r}(\beta,\rho,z)$. We have

$$F^{\circ}_{i,r}(\beta,\rho,z)\cdot e^{\beta z} = \int_0^{\infty} \frac{J_r(k\rho)e^{z(\beta-k)}}{\beta-k}\,dk$$

so
$$\left(F^{\circ}_{i,r}\,e^{\beta z}\right)' = e^{\beta z}\bar{J}_r(z) \tag{63}$$

thus
$$F^{\circ}_{i,r} = e^{-\beta z}\left\{\int_0^{z}\bar{J}_r(\phi)e^{\beta\phi}\,d\phi + F^{\circ}_{i,r}(\beta,\rho,0)\right\} \tag{64}$$

(b) Consider $G^{\circ}_{i,r}(\beta,\rho,z)$. We have

$$G^{\circ}_{i,r}(\beta,\rho,z)\,e^{-\beta z} = \int_0^{\infty} \frac{J_r(k\rho)\,e^{-z(\beta+k)}}{\beta+k}\,dk$$

so
$$\left(G^{\circ}_{i,r}\,e^{-\beta z}\right)' = -e^{-z\beta}\bar{J}_r(z) \tag{65}$$

thus
$$G^{\circ}_{i,r} = e^{\beta z}\left\{-\int_0^{z}\bar{J}_r(\phi)e^{-\beta\phi}\,d\phi + G^{\circ}_{i,r}(\beta,\rho,0)\right\} \tag{66}$$

Performing the differentiation on the left of (63) or (65) produces recurrence relations for $F^{n}_{i,r}$ and $G^{n}_{i,r}$ which can be used as an addition

to their counterparts of (55). From OBERHETTINGER (p.34) we obtain the result

$$G^{\circ}_{1,r}(\beta,\rho,0) \equiv \int_0^{\infty} \frac{J_r(k\rho)}{\beta+k}\,dk = \pi \lim_{\nu \to r} \left\{ \frac{\overline{J}_{\nu}(\beta\rho) - J_{\nu}(\beta\rho)}{\sin \nu\pi} \right\} \tag{67}$$

where $\overline{J}_{\nu}(\beta\rho)$ is Anger's function of order ν . The following relation is given in LUKE (p.83):

$$\pi \left\{ \frac{\overline{J}_{\nu}(\beta\rho) - J_{\nu}(\beta\rho)}{\sin \nu\pi} \right\} = \int_0^{\infty} e^{-\beta\rho \sinh t - \nu t}\,dt \qquad \Re(\beta\rho) > 0 \tag{68}$$

and WATSON (p.313) gives, when $\nu = r$

$$\int_0^{\infty} e^{-\beta\rho \sinh t - rt}\,dt = \frac{(-1)^{r+1}}{2} \left\{ S_r(\beta\rho) + \pi E_r(\beta\rho) + \pi Y_r(\beta\rho) \right\} \tag{69}$$

where $S_r(\beta\rho)$ is the Schlafli polynomial of order r ; $E_r(\beta\rho)$ is Weber's function of order r and $Y_r(\beta\rho)$ is Bessel's modified function of the first kind of order r . The function $E_r(\beta\rho)$ can be written in terms of the Struve function of order r , $H_r(\beta\rho)$, (Appendix I) . The properties of these special functions may be found in the texts of GRADSHTEYN, WATSON, ABRAMOWITZ and STEGUN, or LUKE, but, for completeness, their basic properties and recurrence relations are included in Appendix I. Combining (66) and (67) yields the result for $G^{\circ}_{1,r}(\beta,\rho,0)$. The evaluation of $F^{\circ}_{1,r}(\beta,\rho,0)$ can be performed using OBERHETTINGER's result (p.37) for $I^{\circ}_{1,r}(\beta,\rho,0)$ in (57). We have

$$I^{\circ}_{1,r}(\beta,\rho,0) \equiv \int_0^{\infty} \frac{J_r(k\rho)}{\beta^2 - k^2}\,dk = -\frac{1}{\beta} \cdot \frac{\pi}{2} E_r(\beta\rho) \tag{70}$$

thus $$F^{\circ}_{1,r}(\beta,\rho,0) \equiv \int_0^{\infty} \frac{J_r(k\rho)}{\beta - k}\,dk = \frac{(-1)^r}{2} \left\{ S_r(\beta\rho) + \pi E_r(\beta\rho) + \pi Y_r(\beta\rho) \right\} - \pi E_r(\beta\rho) \tag{71}$$

OBERHETTINGER (p.37) lists a particular case of (71), when $r = 0$, and agreement is found. We shall require the following particular results

$$F^{\circ}_{1,0}(\beta,\rho,0) \equiv \int_0^{\infty} \frac{J_0(k\rho)}{\beta - k}\,dk = (H_0 + Y_0)\frac{\pi}{2} \qquad \left(H_0 \equiv H_0(\beta\rho) \,;\, Y_0 \equiv Y_0(\beta\rho) \right) \tag{72a}$$

$$G^{\circ}_{1,0}(\beta,\rho,0) \equiv \int_0^{\infty} \frac{J_0(k\rho)}{\beta + k}\,dk = (H_0 - Y_0)\frac{\pi}{2} \tag{72b}$$

$$F^{\circ}_{1,2}(\beta,\rho,0) \equiv \int_0^{\infty} \frac{J_2(k\rho)}{\beta - k}\,dk = \left\{ \frac{2}{\beta^2\rho^2} + \frac{2}{\beta\rho}(H_1 + Y_1) - (H_0 + Y_0) \right\} \frac{\pi}{2} \tag{72c}$$

$$G^{\circ}_{1,2}(\beta,\rho,0) \equiv \int_0^{\infty} \frac{J_2(k\rho)}{\beta+k}\,dk = \left\{ -\frac{2}{\beta^2\rho^2} + \frac{2}{\beta\rho}(H_1 - Y_1) - (H_0 - Y_0) \right\} \frac{\pi}{2} \qquad (72d)$$

We supplement (60) with the following results for $I^{n}_{m,r}(\beta,\rho,0)$ obtained from OBERHETTINGER (p.37)

$$O^{\circ}_{1,0}(\beta,\rho,0) \equiv \int_0^{\infty} \frac{k J_0(k\rho)}{\beta^2 - k^2}\,dk = \frac{\pi}{2} Y_0 \qquad (73a)$$

$$O^{1}_{2,0}(\beta,\rho,0) \equiv \int_0^{\infty} \frac{k J_0(k\rho)}{(\beta^2 - k^2)^2}\,dk = -\frac{\pi}{2} \cdot \frac{\rho}{2\beta} \cdot Y_1 \qquad (73b)$$

and

$$O^{3}_{2,0}(\beta,\rho,0) \equiv \int_0^{\infty} \frac{k^3 J_0(k\rho)}{(\beta^2 - k^2)^2}\,dk = \left(\frac{1}{2} \cdot \rho\beta \cdot Y_1 - Y_0 \right) \frac{\pi}{2} \qquad (73c)$$

The expressions for $I^{n}_{m,r}(\beta,\rho,z)$ are obtained using (60), (72) and (73). Writing $\sinh \beta z \equiv s$, $c \equiv \cosh \beta z$, $s_\phi \equiv \sinh \beta(\phi - z)$, $c_\phi \equiv \cosh \beta(\phi - z)$ $\phi s_\phi \equiv \beta(\phi - z) s_\phi$, $\phi c_\phi \equiv \beta(\phi - z) c_\phi$, $t = \beta\rho$, $\bar{J}_r \equiv \bar{J}_r(\phi)$ $\frac{2}{\pi}\int_0^{z} \{\ldots\}\,d\phi \equiv P\{\ldots\}$ and $\frac{d}{dt} \equiv '$ we find

$$I^{\circ}_{1,0} = \frac{\pi}{2\beta}\left(P\{\bar{J}_0 \cdot s_\phi\} - s Y_0 + \bar{c} H_0 \right)$$

$$I^{1}_{1,0} = \frac{\pi}{2}\left(P\{\bar{J}_0 \cdot c_\phi\} + c Y_0 - s H_0 \right)$$

$$I^{2}_{1,0} = \frac{\pi\beta}{2}\left(P\{\bar{J}_0 \cdot s_\phi\} + P\{\bar{J}_0\} - s Y_0 + c H_0 \right)$$

$$I^{2}_{1,0} = \beta^2\frac{\pi}{2}\left(P\{\bar{J}_0 c_\phi\} - \bar{J}_0(z) + c Y_0 - s H_0 \right)$$

$$I^{\circ}_{2,0} = \frac{\pi}{4\beta^3}\left(P\{\bar{J}_0 \cdot s_\phi\} - P\{\bar{J}_0 \cdot \phi c_\phi\} - s Y_0 + c H_0 - \beta z\{ s H_0 - c Y_0 \} - t\{ s Y_1 + c(\tfrac{2}{\pi} - H_1) \} \right)$$

$$I^{1}_{2,0} = -\frac{\pi}{4}\left(P\{\bar{J}_0 \cdot \phi s_\phi\} + \beta z\{ s Y_0 - c H_0 \} - t\{ c Y_1 + s(\tfrac{2}{\pi} - H_1) \} \right)$$

$$I^{2}_{2,0} = -\frac{\pi}{4\beta}\left(P\{\bar{J}_0 \cdot \phi c_\phi\} + c H_0 - s Y_0 + \beta z\{ s H_0 - c Y_0 \} + P\{\bar{J}_0 \cdot s_\phi\} - t\{ s Y_1 + c(\tfrac{2}{\pi} - H_1) \} \right)$$

$$I^{3}_{2,0} = -\frac{\pi}{4}\left(P\{\bar{J}_0 \cdot \phi s_\phi\} + 2P\{\bar{J}_0 \cdot c_\phi\} + 2\{ c Y_0 - s H_0 \} + \beta z\{ s Y_0 - c H_0 \} + t\{ c Y_1 + s(\tfrac{2}{\pi} - H_1) \} \right)$$

$$I^{4}_{2,0} = -\frac{\beta\pi}{4}\left(3P\{\bar{J}_0 \cdot s_\phi\} + P\{\bar{J}_0 \cdot \phi c_\phi\} - \frac{2}{\beta}\bar{J}_0(z) + 3\{ c H_0 - s Y_0 \} + \beta z\{ s H_0 - c Y_0 \} - t\{ s Y_1 + c(\tfrac{2}{\pi} - H_1) \} \right)$$

$$I^{0}_{2,2} = \frac{\Pi}{4\beta^2}\left(P\{\bar{J}_2 . S_\phi\} - P\{\bar{J}_2 . \varphi C_\phi\} + \frac{2}{t^2}\{\beta z . c - 3s\} + \frac{2H_1}{t}\{2c - \beta z . s\}\right.$$

$$+ \frac{2Y_1}{t}\{\beta z . c - 2s\} + H_0\{\beta z . c - c\} + Y_0\{s - \beta z . c\} + 2s Y_1' + tcH_0'$$

$$\left. - t s Y_0' - 2c H_1' \right)$$

$$I^{1}_{2,2} = -\frac{\Pi}{4\beta^2}\left(P\{\bar{J}_2 . \varphi S_\phi\} + \frac{2}{t^2}\{\beta z . s - 2c\} + \frac{2H_1}{t}\{s - \beta z . c\} + \frac{2Y_1}{t}\{\beta z . s - c\}\right.$$

$$\left. + H_0 . \beta z . c - Y_0 . \beta z . s + 2c Y_1' + ts H_0' - t . c . Y_0' - 2s H_1' \right)$$

$$I^{2}_{2,2} = \frac{\Pi}{4\beta}\left(-P\{\bar{J}_2 . S_\phi\} - P\{\bar{J}_2 . \varphi C_\phi\} + \frac{2}{t^2}\{\beta z . c - s\} - \beta z . s . \frac{2H_1}{t} + \beta z . c . \frac{2Y_1}{t}\right.$$

$$\left. + H_0\{c + \beta z . s\} - Y_0\{\beta z . c + s\} + 2s Y_1' + t . c . H_0' - ts Y_0' - 2c H_1' \right)$$

The above expressions for $I^{n}_{m,r}(\beta, \rho, z)$ are exact. It is clear that to evaluate the real-space solutions of §8.3.1 and §8.3.2 we require an evaluation of finite integrals (of the type (35) and (45)) whose kernals are a combination of the functions $I^{n}_{m,r}$ above. Unfortunately this we have been unable to achieve. However, the functions Y_0, H_0, Y_1 and H_1 together with $\int_0^{\phi} H_0(\psi)d\psi$ etc. are tabulated in ABRAMOWITZ and STEGUN and so a numerical approach is possible. But because the complexity of the results for $I^{n}_{m,n}(\beta, \rho, z)$ renders an evaluation using the special-function tables extremely cumbersome we choose to simplify the expressions for $I^{n}_{m,r}$. Our interest is mainly concerned with the behaviour of the solutions in the regions close to the surface of the liquid where z is small. To simplify the analysis we define a new variable $\epsilon = \beta z$ and expand the expressions $I^{n}_{m,r}$ in powers of ϵ retaining the first and second order terms, for ϵ small. Writing $\theta = z\phi$ and $I^{n}_{m,r}(\beta, \rho, z) \equiv I^{n,\epsilon}_{m,r}(\beta, \rho, \epsilon)$ we obtain

$$I^{0,\epsilon}_{1,0} = \frac{\Pi}{2\beta}(H_0 - \epsilon Y_0) + o(\epsilon^2)$$

$$I^{1,\epsilon}_{1,0} = \frac{\Pi}{2}(Y_0 - \epsilon H_0) + \epsilon \int_0^1 \frac{d\theta}{(\epsilon^2\rho^2 + t^2)^{1/2}} + o(\epsilon^2)$$

$$I^{2,\epsilon}_{1,0} = \beta\left\{ \frac{\Pi}{2}(H_0 - \epsilon Y_0) + \epsilon \int_0^1 \frac{d\theta}{(\epsilon^2\rho^2 + t^2)^{1/2}} \right\} + o(\epsilon^2)$$

$$I^{3,\epsilon}_{1,0} = \beta^2\left\{(\gamma_0-\epsilon H_0)\frac{\pi}{2} + \epsilon\int_0^1 \frac{d\theta}{(\epsilon^2\theta^2+t^2)^{1/2}} - \frac{1}{(\epsilon^2+t^2)^{1/2}}\right\} + o(\epsilon^2)$$

$$I^{0,\epsilon}_{2,0} = \frac{\pi}{4\beta^2}\left\{H_0 - t\left(\frac{2}{\pi} - H_1 + \epsilon\gamma_1\right)\right\} + o(\epsilon^2)$$

$$I^{1,\epsilon}_{2,0} = \frac{\pi}{4\beta^2}\left\{\epsilon H_0 + t\left(\frac{2\epsilon}{\pi} - \epsilon H_1 + \gamma_1\right)\right\} + o(\epsilon^2)$$

$$I^{2,\epsilon}_{2,0} = \frac{\pi}{4\beta}\left\{2\epsilon\gamma_0 - H_0 - t\left(\frac{2}{\pi} - H_1 + \epsilon\gamma_1\right)\right\} + o(\epsilon^2)$$

$$I^{3,\epsilon}_{2,0} = -\epsilon\int_0^1 \frac{d\theta}{(\epsilon^2\theta^2+t^2)^{1/2}} - \frac{\pi}{4}\left\{2\gamma_0 - 3\epsilon H_0 - t\left(\frac{2}{\pi} - H_1\right)\epsilon - t\gamma_1\right\} + o(\epsilon^2)$$

$$I^{4,\epsilon}_{2,0} = \frac{-\epsilon\beta}{(\epsilon^2+t^2)^{1/2}} - \frac{\pi\beta}{4}\left\{3H_0 - 4\epsilon\gamma_0 - t\left(\epsilon\gamma_0 + \frac{2}{\pi} - H_1\right)\right\} + o(\epsilon^2)$$

$$I^{0,\epsilon}_{2,2} = \frac{\pi}{4\beta^2}\left\{\frac{4H_1}{t} - H_0 + tH_0' - 2H_1'\right\} + o(\epsilon)$$

$$I^{1,\epsilon}_{2,2} = \frac{-\pi}{4\beta^2}\left\{-\frac{4}{t^2} - \frac{2\gamma_1}{t} + 2\gamma_1' - t\gamma_0'\right\} + o(\epsilon)$$

$$I^{2,\epsilon}_{2,2} = \frac{\pi}{4\beta}\left\{H_0 + tH_0' - 2H_1'\right\} + o(\epsilon)$$

For the expressions $I^{n}_{m,2}$ we have expanded up to $o(\epsilon)$ because we require these expressions only in the free surface results of §8.3.2 where the surface profiles correspond to $\epsilon = 0$. Before presenting the final solutions we give the following integral results

$$\int_0^{t_1}\int_0^1 \frac{d\theta\,dt}{(\epsilon^2\theta^2+t^2)^{1/2}} = \left[t\sinh^{-1}\left(\frac{\epsilon}{t}\right) + \epsilon\ln\left(t+\sqrt{t^2+\epsilon^2}\right)\right]_0^{t_1}$$

$$\therefore \int_{t_0}^{t_1}\int_0^1 \frac{d\theta\,dt}{(\epsilon^2\theta^2+t^2)^{1/2}} = \epsilon\left\{\begin{array}{ll}\ln(t_1/t_0) & t_1, t_0 \gg \epsilon > 0 \\ \ln|(4t_1t_0)| & t_1, |t_0| \gg \epsilon,\ t_1 > 0,\ t_0 < 0\end{array}\right\} + o(\epsilon^2)$$

$$\equiv \epsilon L_N\Big|_{t_0}^{t_1} \quad \text{(notation)} \qquad (74)$$

8.5 Approximate Solutions

The solutions given below describe the velocity and pressure distributions close to the surface $z=0$ (for fixed surface solutions) and on the surface $z=0$ (for free surface solutions). They are valid

for $|\xi| > \epsilon$ (region A) and $|\eta| > \epsilon$ (region B). In view of the physical data of table 1.1 (the float bath configuration) we have chosen $a = 1$ $b = 4$ and $\beta = 3$.

8.5.1 Region A

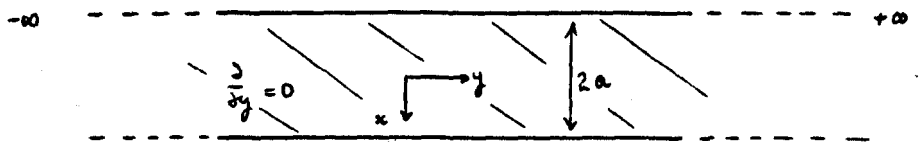

(i) Fixed surface. The integral solutions (36) to (39) can be written in terms of $I^{n}_{m,r}(\beta,\rho,z)$. We find

$$u = f_3 \left[-z\beta I^{2}_{2,0} + z I^{2}_{2,0} + \beta \left(I^{1}_{2,0} - O^{1}_{2,0} e^{-\beta z} \right) \right]^{\xi = x+a}_{\xi = x-a} \tag{75}$$

$$v = f_2 \int_{x-a}^{x+a} \left\{ I^{1}_{1,0} - O^{1}_{1,0} e^{-\beta z} \right\} d\xi \tag{76}$$

$$w = f_3 \int_{x-a}^{x+a} \left\{ z\beta I^{3}_{2,0} - z I^{4}_{2,0} - I^{3}_{2,0} + e^{-\beta z} O^{3}_{2,0} \right\} d\xi \tag{77}$$

$$p = f_3 \int_{x-a}^{x+a} \left\{ 2\beta I^{3}_{2,0} - z I^{4}_{2,0} - \beta e^{-\beta z} O^{1}_{1,0} \right\} d\xi \tag{78}$$

Expressions (75) to (78) are exact, but because of the difficulty in their evaluation we choose to approximate using the results for $I^{n,\epsilon}_{m,r}$ and relation (72). We obtain the following simplified forms

$$u = \frac{\epsilon f_3 \pi}{2\beta} \left[H_0 - Y_0 + t \left(\frac{2}{\pi} - H_1 + Y_1 \right) \right]^{\xi = x+a}_{\xi = x-a} + O(\epsilon^2) \tag{79}$$

$$v = \frac{\epsilon \pi}{2\beta} f_2 \left\{ \frac{2\epsilon}{\pi} L_N \Big|^{\xi = x+a}_{\xi = x-a} - \int_{x-a}^{x+a} (H_0 - Y_0)\, d\xi \right\} + O(\epsilon^2) \tag{80}$$

$$w = \epsilon \cdot \frac{f_3}{\beta} \cdot \epsilon L_N \Big|^{\xi = x+a}_{\xi = x-a} + O(\epsilon^2) \tag{81}$$

$$p = \frac{\pi}{2\beta} f_3 \left\{ 2 \int_{x-a}^{x+a} (H_0 - Y_0)\, d\xi + \left[t (H_0 - Y_0)\, \mathrm{sign}(\xi) \right]^{\xi = x+a}_{\xi = x-a} \right\} + O(\epsilon^2) \tag{82}$$

where $t = \beta|\xi|$, $H_0 \equiv H_0(t)$, $Y_0 \equiv Y_0(t)$ and $\mathrm{sign}(\xi) = \begin{cases} 1 & \xi > 0 \\ -1 & \xi < 0 \end{cases}$.

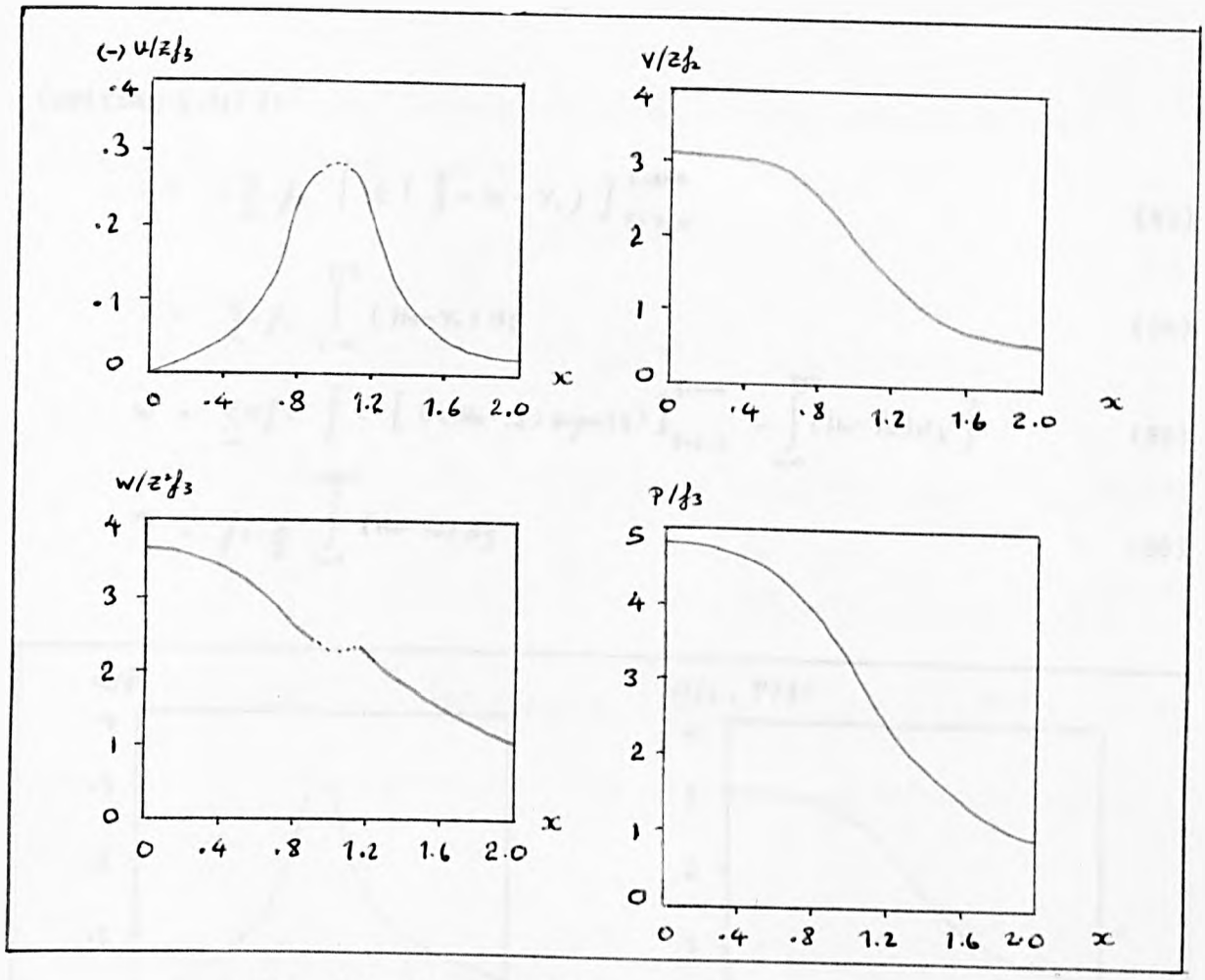

Fig. 8.4 Fixed Surface. Region A

The velocity and pressure distributions obtained from (71) to (82) are shown in figure 8.4. From (a) we see that the largest input velocity occurs at the edge of the excitation, and, as we would expect is only dependent on the imposed vertical force. This force forces the fluid downwards in the central region of the SLIP and this fluid motion draws in fluid from the edges. It appears that circulation transverse to the SLIP axis sits over the full width of the excitation. As we would expect from the symmetry of the problem, the axial velocity depends only upon the magnitude of f_z .

(ii) Free surface. Following (i) we can write the integral solutions (40) to (43) in terms of $I^{n}_{m,r}(\beta,\rho,z)$. However because we are mainly concerned with the surface profiles we evaluate the solutions for u, v and P directly on $z=0$. Of course $w=0$ on $z=0$, so we use the expressions for $I^{n,e}_{m,r}$ in its calculation. We find after some manipulation

(writing $t=|\xi|$):

$$u = -\frac{\pi}{4} f_3 \left[t \left(\frac{2}{\pi} - |H_0 + Y_1| \right) \right]_{\xi = x-a}^{\xi = x+a} \tag{83}$$

$$v = \frac{\pi}{2} f_2 \int_{x-a}^{x+a} (H_0 - Y_0)\, d\xi \tag{84}$$

$$w = \frac{\pi e f_3}{4} \left\{ - \left[t (H_0 - Y_0) \operatorname{sign}(\xi) \right]_{\xi = x-a}^{\xi = x+a} - \int_{x-a}^{x+a} (H_0 - Y_0)\, d\xi \right\} \tag{85}$$

$$P = f_3 \frac{\pi}{2} \int_{x-a}^{x+a} (H_0 - Y_0)\, d\xi \tag{86}$$

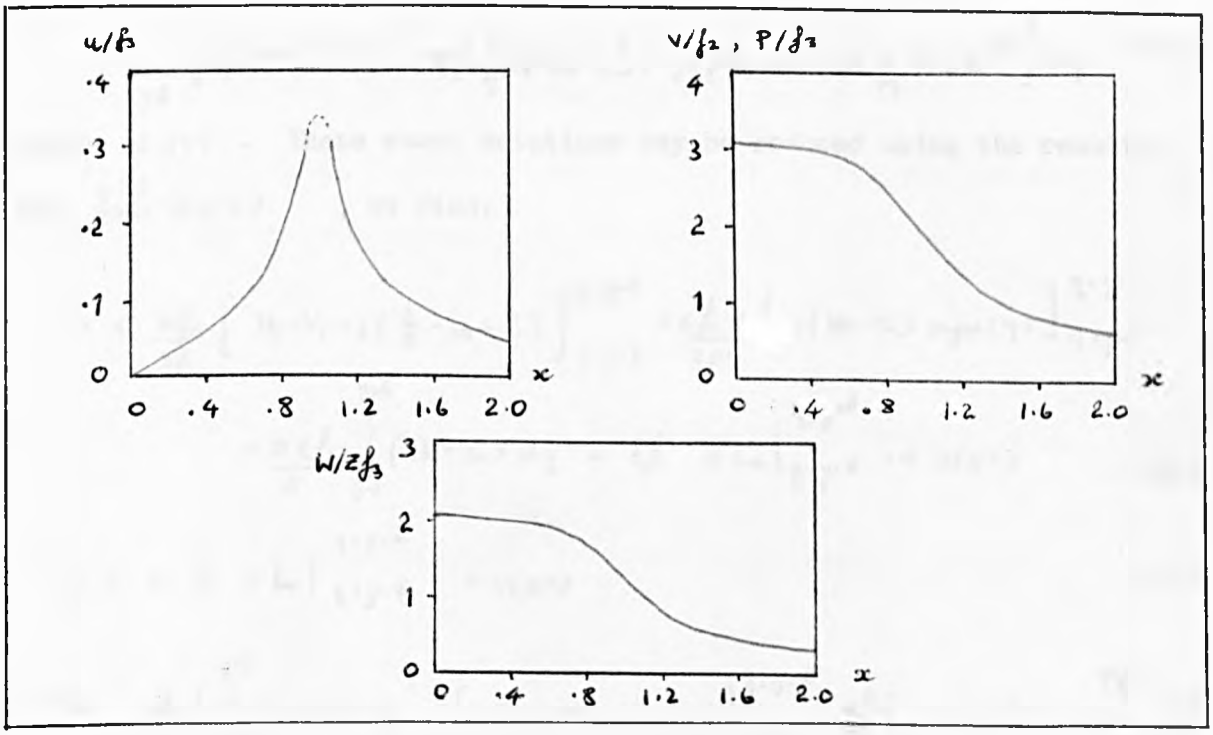

Fig. 8.5 Free Surface. Region B

The profiles obtained from (83) to (86) are shown in figure 8.5. Similar observations to those made in (i) can be made.

8.5.2 Region B .

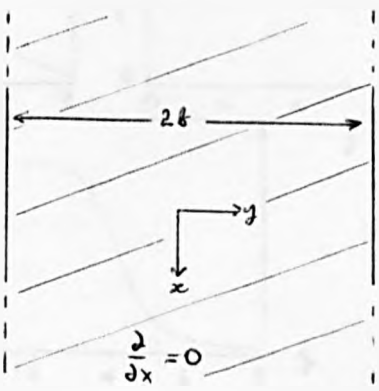

(i) Fixed surface. Writing the integral solutions (46) to (49) in terms of $I^{n}_{m,r}(\beta,\rho,z)$ we find

$$u = 0 \tag{87}$$

$$v = \int_{y-b}^{y+b} \left\{ -\frac{\partial}{\partial\eta} f_3 \left(z\beta I^{2}_{2,0} - z I^{3}_{1,0} \right) + \beta f_2 \frac{\partial^2}{\partial\eta^2} \left(z\beta I^{0}_{2,0} - z I^{1}_{2,0} \right) + \right.$$

$$\left. f_3 \beta \frac{\partial}{\partial\eta} \left(I^{1}_{2,0} - e^{-\beta z} O^{1}_{2,0} \right) - f_2 \frac{\partial^2}{\partial\eta^2} \left(I^{1}_{2,0} - e^{-\beta z} O^{1}_{2,0} \right) + f_3 \left(I^{1}_{1,0} - e^{-\beta z} O^{1}_{1,0} \right) \right\} d\eta \tag{88}$$

$$w = \int_{y-b}^{y+b} \left\{ f_3 \left(z\beta I^{3}_{2,0} - z I^{4}_{1,0} - I^{3}_{1,0} + e^{-\beta z} O^{3}_{2,0} \right) - \beta f_2 \frac{\partial}{\partial\eta} \left(z\beta I^{1}_{2,0} - z I^{2}_{1,0} - I^{1}_{1,0} - e^{-\beta z} O^{1}_{2,0} \right) \right\} d\eta \tag{89}$$

$$p = \int_{y-b}^{y+b} \left\{ 2 f_3 \left(\beta I^{3}_{2,0} - I^{4}_{1,0} \right) - 2\beta f_2 \frac{\partial}{\partial\eta} \left(\beta I^{1}_{2,0} - I^{2}_{1,0} \right) - f_3 \beta O^{1}_{1,0} e^{-\beta z} + f_2 \frac{\partial}{\partial\eta} O^{1}_{1,0} e^{-\beta z} \right\} d\eta \tag{90}$$

where $t = |\eta|$. These exact solutions may be reduced using the results for $I^{n,\epsilon}_{m,r}(\beta,\rho,\epsilon)$, we find:

$$v = \epsilon \cdot \frac{\pi f_2}{2\beta} \left[H_0 - Y_0 + t\left(\frac{2}{\pi} - H_1 + Y_1 \right) \right]_{\eta=y-b}^{\eta=y+b} + \frac{\epsilon f_2 \pi}{2\beta^2} \left[t (H_0 - Y_0) \operatorname{sign}(\eta) \right]_{\eta=y-b}^{\eta=y+b}$$

$$- \frac{\pi \epsilon f_2}{2} \int_{y-b}^{y+b} (H_0 - Y_0)\, d\eta + \epsilon f_2 \cdot \epsilon L_N \Big|_{\eta=y-b}^{\eta=y+b} + o(\epsilon^2) \tag{91}$$

$$w = \epsilon \cdot f_3 \cdot \epsilon L_N \Big|_{\eta=y-b}^{\eta=y+b} + o(\epsilon^2) \tag{92}$$

$$p = \frac{\pi f_2}{2} \left\{ 2 \int_{y-b}^{y+b} (H_0 - Y_0)\, d\eta - \left[t (H_0 - Y_0) \operatorname{sign}(\eta) \right]_{\eta=y-b}^{\eta=y+b} - \frac{\pi f_2}{2} \left[H_0 - Y_0 + t\left(\frac{2}{\pi} - H_1 + Y_1 \right) \right]_{\eta=y-b}^{\eta=y+b} \right\} \tag{93}$$

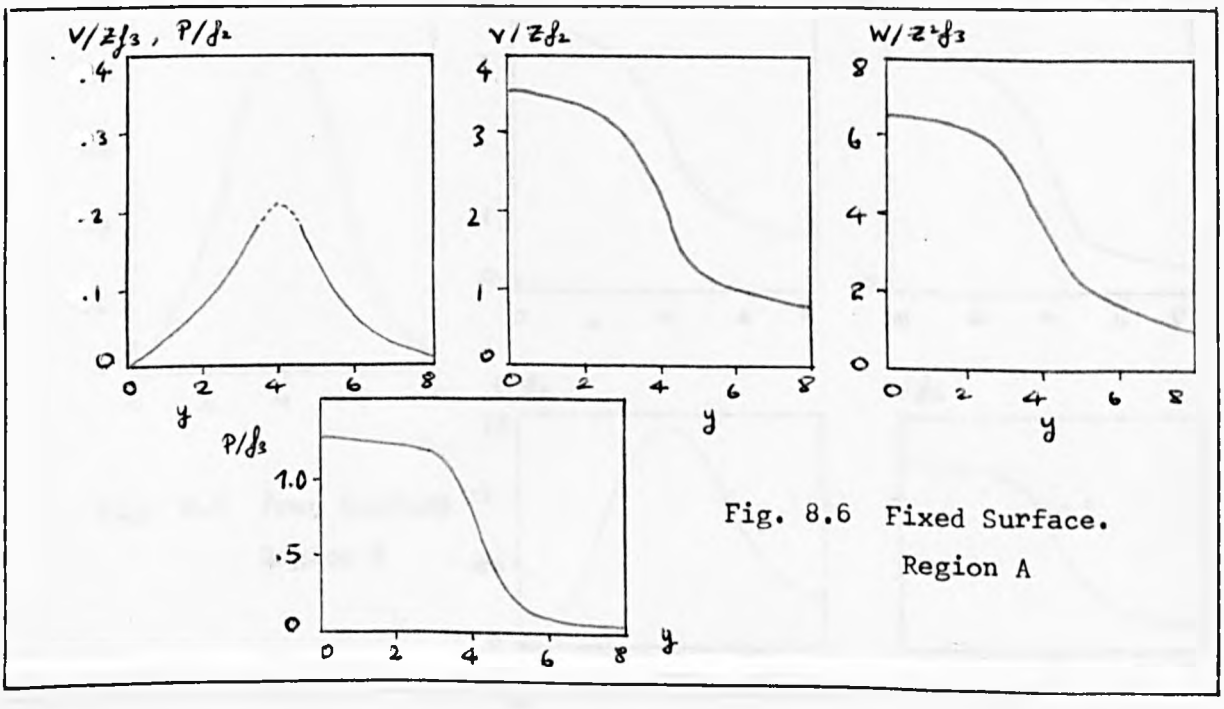

Fig. 8.6 Fixed Surface.
Region A

The profiles for $\underline{v}$ and P are shown in figure 8.6. The symmetry of the problem ensures $u=0$. Both the axial velocity v and the pressure P arise from the applied forces f_2 and f_3 . The vertical force has maximum effect on v at the entrance and exit end of the excitation, (a), as we would expect since this velocity arises because fluid is drawn in to the centre of the excitation by the downward motion of the fluid there. However, a comparison of the magnitudes in (a) and (b) indicates that the vertical force has little effect on the flow unless $f_3 >> f_2$. We see from (b) that the flow extends fully across the width of the excitation. A small amount of eirculation will occur since $w \neq 0$ but the effects will not be noticeable unless f_2 is small.

(ii) Free surface. On $z=0$ (apart from w), the free surface integral solutions (50) to (53) reduce to (with $t=|\eta|$):

$$u=0 \tag{94}$$

$$v = -\frac{\pi}{2} f_3 \left[t\left(\frac{2}{\pi} - H + Y_1\right) \right]_{\eta=y-b}^{\eta=y+b} + f_2 \cdot \frac{\pi}{2} \int_{y-b}^{y+b} (H_0 - Y_0)\, d\eta + f_2 \left[-\mathrm{sign}(\eta) \cdot t \cdot (H_0 - Y_0) \right]_{\eta=y-b}^{\eta=y+b} \tag{95}$$

$$w = \frac{\epsilon\pi}{4} f_3 \left\{ \left[-t(H_0 - Y_0)\, \mathrm{sign}(\eta) \right]_{\eta=y-b}^{\eta=y+b} - \int_{y-b}^{y+b} (H_0 - Y_0)\, d\eta \right\} + \frac{\epsilon\pi}{4} f_2 \left[t\left(\frac{2}{\pi} - H + Y_1\right) \right]_{\eta=y-b}^{\eta=y+b} \tag{96}$$

$$P = f_3 \cdot \frac{\pi}{2} \int_{y-b}^{y+b} (H_0 - Y_0)\, d\eta - f_2 \cdot \frac{\pi}{2} \left[H_0 - Y_0 \right]_{\eta=y-b}^{\eta=y+b} \tag{97}$$

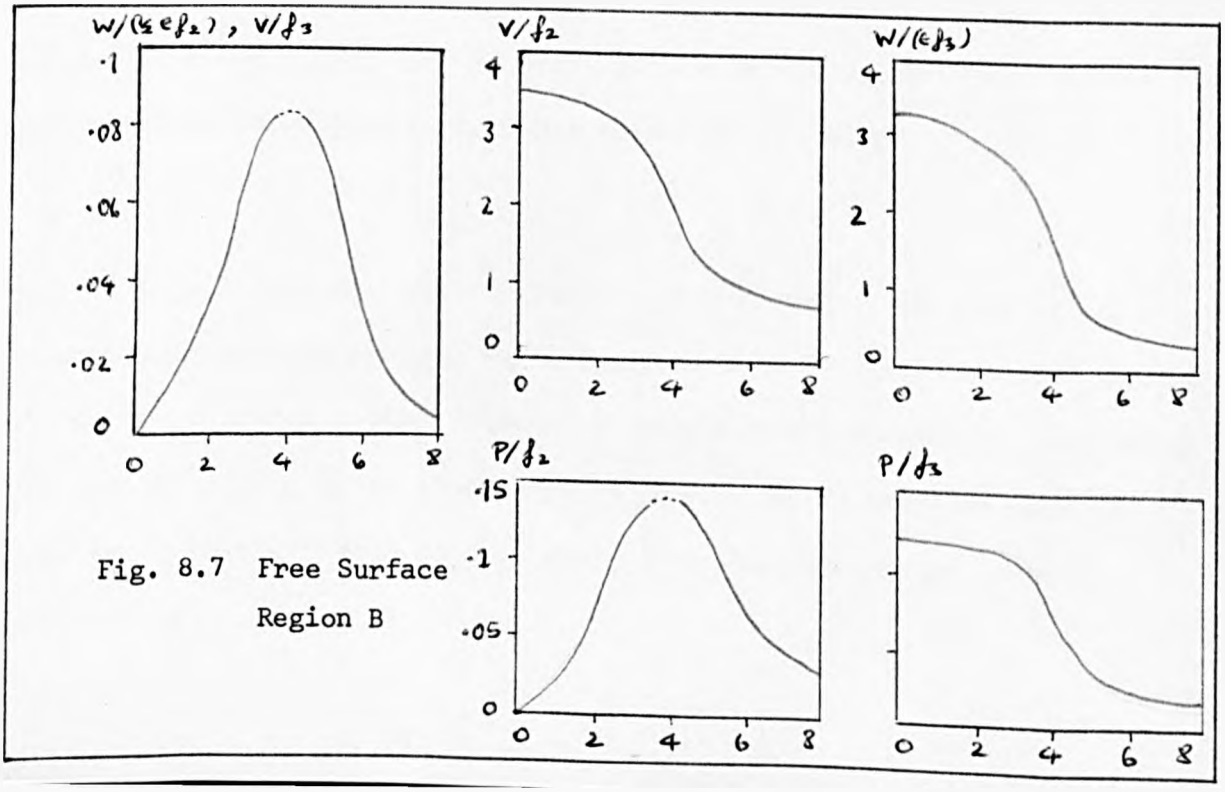

Fig. 8.7 Free Surface Region B

The profiles obtained from (95) to (97) are shown in figure 8.7. Similar observations can be made as in (i) for these solutions.

9. A REALISTIC MODEL FOR THE SLIM

9.1 Introduction

Until now we have assumed in our analysis of the SLIP that the excitation is applied on the surface of an electrically conducting half space. Here the excitation is assumed to be rectangular in shape (of length ℓ metres and width a metres) and is applied at a height h metres above the surface of an electrical conductor (of thickness L metres), (figure 9.1). Cartesian coordinate axes are chosen as shown, with the origin O taken at one corner of the projection of the excitation onto the surface of the conductor.

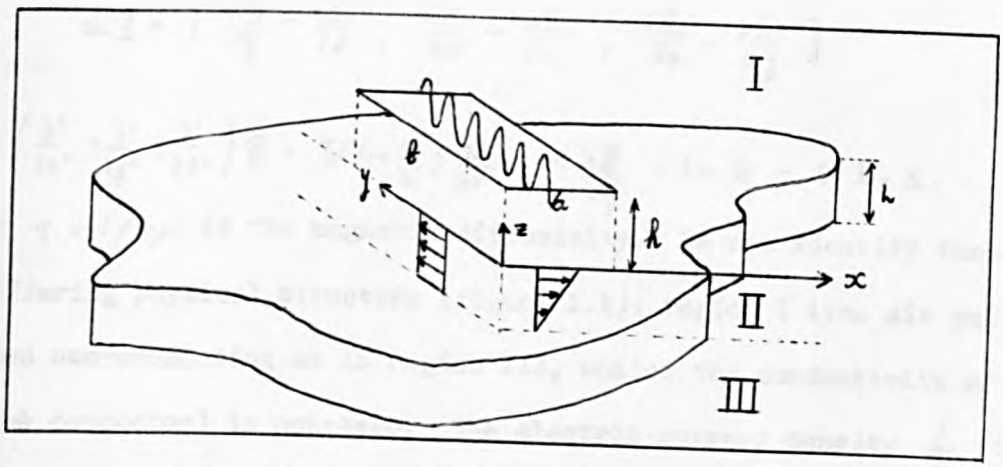

Fig. 9.1 The Realistic Model

Here, the z axis is chosen to point away from the conductor. The conductor is assumed to move with a velocity $\underline{V}$, where

$$\underline{V} = [\, U(1+z/L)\,,\ V\,,\ 0\,] \qquad (1)$$

and U, V are constants with dimensions of velocity. The form of (1) allows the inclusion of some MHD effects as well as the shear flow induced by the float bath's moving ribbon. A more detailed discussion concerning the use of (1) was given in chapters 3 and 4. As in previous work we consider both the series-wound (case S) and parallel-wound (case P) excitations.

In §9.2 we derive the three dimensional Fourier transformed EM field solutions to this problem. For the limiting cases (when a or b becomes infinite) we recover the infinite expanse excitation solutions (§9.3), the finite length excitation solutions (§9.4) and the finite width solutions (§9.5). Finally, in §9.6, we discuss the application of the results of this chapter to the velocity profile analysis of an open-sided SLIP.

9.2 Analysis Of Maxwell's Equations

Writing $\underline{B}(\underline{r},t) = \underline{B}(\underline{r})e^{i\omega t}$, $\underline{J}(\underline{r},t) = \underline{J}(\underline{r})e^{i\omega t}$, Maxwell's equations (1.1), (1.4) and (1.11) become respectively, using (1):

$$\frac{\partial B_1}{\partial x} + \frac{\partial B_2}{\partial y} + \frac{\partial B_3}{\partial z} = 0 \tag{2}$$

$$\mu_0 \underline{J} = \left[\frac{\partial B_3}{\partial y} - \frac{\partial B_2}{\partial z}, \frac{\partial B_1}{\partial z} - \frac{\partial B_3}{\partial x}, \frac{\partial B_2}{\partial x} - \frac{\partial B_1}{\partial y} \right] \tag{3}$$

$$\eta \left(\frac{\partial^2}{\partial x^2} + \frac{\partial^2}{\partial y^2} + \frac{\partial^2}{\partial z^2} \right) \underline{B} = U(1+\underline{z}) \frac{\partial \underline{B}}{\partial x} + V \frac{\partial \underline{B}}{\partial y} + i\omega \underline{B} - U B_3 \underline{e}_1 \tag{4}$$

where $\eta = 1/\sigma\mu$ is the magnetic diffusivity. We can identify three regions of differing physical structure (figure 1.1); region I (the air gap) is assumed non-conducting as is region III, whilst the conductivity of region II (the conductor) is non-zero. The electric current density $\underline{J}$ is related to the total electric field $\underline{E}'$ by $\underline{J} = \sigma \underline{E}'$ (1.7). The magnetic permeability is taken to be that of free space (μ_0) throughout.

Taking the scale length as h, we define the following dimensionless variables: $x^* = x/h$, $y^* = y/h$, $z^* = z/h$, $a^* = a/h$, $b^* = b/h$, $k^* = kh$, $R_0 = \omega h^2/\eta$, $R_{m1} = Uh/\eta$, $R_{m2} = Vh/\eta$ and $\alpha^* = \alpha h$. Here R_{m1} and R_{m2} are the magnetic Reynolds numbers for the motion of the conductor and α is the wavenumber of the travelling wave excitation. All parameters will be assumed dimensionless from now on so we shall ignore the star superscripts. The dimensionless forms of (3) and (4) become ((2) remains the same)

Region II:
$$\mu_0 h \underline{J} = \left[\frac{\partial B_3}{\partial y} - \frac{\partial B_2}{\partial z}, \frac{\partial B_1}{\partial z} - \frac{\partial B_3}{\partial x}, \frac{\partial B_2}{\partial x} - \frac{\partial B_1}{\partial y} \right] \tag{5}$$

$$\left(\frac{\partial^2}{\partial x^2} + \frac{\partial^2}{\partial y^2} + \frac{\partial^2}{\partial z^2} \right) \underline{B} = R_{m1}(1+z) \frac{\partial \underline{B}}{\partial x} + R_{m2} \frac{\partial \underline{B}}{\partial y} + iR \underline{B} - R_{m1} B_3 \underline{e}_1 \tag{6}$$

Regions I and III: $$\underline{0} = \left[\frac{\partial B_3}{\partial y} - \frac{\partial B_2}{\partial z} , \frac{\partial B_1}{\partial z} - \frac{\partial B_3}{\partial x} , \frac{\partial B_2}{\partial x} - \frac{\partial B_1}{\partial y} \right] \quad (7)$$

$$\left(\frac{\partial^2}{\partial x^2} + \frac{\partial^2}{\partial y^2} + \frac{\partial^2}{\partial z^2} \right) \underline{B} = i R_e \underline{B} \quad (8)$$

The two dimensional form of the Fourier transformation (1.32), of the function $M(x,y,z)$, is defined as

$$\mathcal{F}_2^+ \{ M(x,y,z) \} = \hat{M}(p,q,z) = \int_{-\infty}^{\infty} \int_{-\infty}^{\infty} M(x,y,z)\, e^{i(px+qy)}\, dx\, dy \quad (9)$$

and the corresponding inverse transformation (1.33) is defined as

$$\mathcal{F}_2^- \{ \hat{M}(p,q,z) \} = M(x,y,z) = \frac{1}{(2\pi)^2} \int_{-\infty}^{\infty} \int_{-\infty}^{\infty} \hat{M}(p,q,z)\, e^{-i(px+qy)}\, dp\, dq \quad (10)$$

Applying the transformation (9) to (10) we find

$$\frac{d\hat{B}_3}{dz} = ip\hat{B}_1 + iq\hat{B}_2 \quad (11)$$

Transforming (5) to (8) we obtain

Region II: $$\mu_0 h \underline{\hat{J}} = \left[-iq\hat{B}_3 - \frac{d\hat{B}_2}{dz} , \frac{d\hat{B}_1}{dz} - ip\hat{B}_3 , -ip\hat{B}_2 + iq\hat{B}_1 \right] \quad (12)$$

$$\frac{d^2\underline{B}}{dz^2} = \gamma^2 \underline{B} - R_{m1} [\hat{B}_3, 0, 0] \quad (13)$$

where $$\gamma^2 = k^2 + i \{ R_e - p R_{m1}(1+z) - q R_{m2} \} \quad (14)$$

and $$k^2 = p^2 + q^2 \quad (15)$$

Regions I and III:

$$\frac{d\hat{B}_2}{dz} = -iq\hat{B}_3 \quad ; \quad \frac{d\hat{B}_1}{dz} = -ip\hat{B}_3 \quad ; \quad iq\hat{B}_1 = ip\hat{B}_2 \quad (16)$$

$$\frac{d^2\underline{B}}{dz^2} = k^2 \underline{B} \quad (17)$$

We now solve the above expressions to obtain the EM field induced in the conductor. For the finite width case, (when $\frac{\partial}{\partial x} \neq 0$), we shall take the velocity to be constant along the direction of the x axis thereby avoiding the complexity of Airy functions, (see chapter 3) which arise as solutions to (14). Unfortunately, ignoring the shear profile removes the term $R_{m1}\hat{B}_3$ from (13) because this term arose from the derivative of the shear velocity. However, this does not affect the overall description of the induced EM field when R_{m1} is small, but it does remove the vertical

component of the electric current density which arises solely from the term $R_{m1}\hat{B}_3$.

The boundary condition on $z=h$ is

$$(S)\quad B_z(x,y,h)=\mu_0 K_s e^{-i\alpha y} S_x S_y \;;\; (P)\quad B_3(x,y,h)=B_m e^{-i\alpha y} S_x S_y \qquad (18)$$

where $$S_x \equiv S_x(x,a)=H(x)-H(x-a)\,,\quad S_y \equiv S_y(y,b)=H(y)-H(y-b) \qquad (19)$$

where $H(x)$ is the Heaviside unit step function; thus S_x and S_y are unit block functions of length a and b respectively. Transforming (18) using (9) we have, on $z=h$

$$(S)\quad \hat{B}_z(p,q,h)=\mu_0 K_s \hat{S} \;;\; (P)\quad \hat{B}_3(p,q,h)=B_m \hat{S} \qquad (20)$$

where $$\hat{S} \equiv \hat{S}_x(p,a)\,\hat{S}_y(q-\alpha,b) \qquad (21)$$

with $$\hat{S}_x(p,a)=\frac{e^{ipa}-1}{ip} \qquad \hat{S}_y(q-\alpha,b)=\frac{e^{ib(q-\alpha)}-1}{i(q-\alpha)} \qquad (22)$$

The solutions to (13) and (17) subject to (11) are easily found using standard techniques. Introducing the vector functions $\underline{M}(p,q)$, $\underline{N}(p,q)$ $P(p,q)$, $Q(p,q)$ and $\underline{R}(p,q)$ as 'constants' of integration and applying the condition that the EM field decays as $z\to-\infty$, we find

Region I: $$\underline{\mathcal{B}}=\underline{M}e^{\kappa z}+\underline{N}e^{-\kappa z} \qquad (23)$$

Region II: $$\underline{\mathcal{B}}=\underline{P}e^{\gamma z}+\underline{Q}e^{-\gamma z}+PI(z)\,\underline{e}_z \qquad (24)$$

Region III: $$\underline{\mathcal{B}}=\underline{R}e^{\kappa z} \qquad (25)$$

where $PI(z)$ is the particular integral of (13), which is non-zero when $R_{m1}\neq 0$.

9.2.1 The Evaluation of the Constants of Integration. It has been stated (1.39) that the magnetic induction $\underline{\mathcal{B}}$ is continuous across a boundary. Because all media interfaces are in the (x,y) plane both $\hat{\underline{\mathcal{B}}}$ and (by (11)) $\frac{d\hat{B}_3}{dz}$ are continuous across a boundary. Assuming the

case S boundary conditions on $z=h$ (the first of (20)) is applied, we have

(i) on $z=h$

Using (23) and (20) $$M_2 e^{\kappa h} + N_2 e^{-\kappa h} = \mu_0 K_s \hat{S} \tag{26}$$

Using the first of (16) $\kappa M_2 = -iq M_3$ and $\kappa N_2 = -iq N_3$

Thus (26) becomes $$M_3 e^{\kappa h} - N_3 e^{-\kappa h} = \frac{i\kappa}{q} \cdot \mu_0 K_s \hat{S}. \tag{27}$$

(ii) on $z=0$

Using (23) and (24) $$M_2 + N_2 = P_2 + Q_2 \tag{28}$$

$$M_3 + N_3 = P_3 + Q_3 \tag{29}$$

$$\kappa (M_3 - N_3) = \gamma (P_3 - Q_3) \tag{30}$$

(iii) on $z=-1$

Using (24) and (25) $$P_2 e^{-\gamma} + Q_2 e^{\gamma} = R_2 e^{-\kappa} \tag{31}$$

$$P_3 e^{-\gamma} + Q_3 e^{\gamma} = R_3 e^{-\kappa} \tag{32}$$

$$\gamma (P_3 e^{-\gamma} - Q_3 e^{\gamma}) = \kappa R_3 e^{-\kappa} \tag{33}$$

Using the first of (16) $$\kappa R_2 = -iq R_3 \tag{34}$$

Equations (26) to (34) give nine independent equations in the nine unknowns which can now be found by, for example, direct substitution. Expressions for these constants are listed in Appendix III . To find the constants for $\mathcal{B}_1$ we use the third of (16) and continuity of $\hat{\mathcal{B}}_1$ across the boundaries to obtain

in region I: $$M_1 = \frac{p}{q} M_2 \qquad N_1 = \frac{p}{q} N_2 \tag{35}$$

in region II $$R_1 = \frac{p}{q} R_2 \tag{36}$$

on $z=0$ $$P_1+Q_1 = M_1+N_1 - PI(0) \tag{37}$$

on $z=-1$ $$P_1e^{-\gamma}+Q_1e^{\gamma} = R_1e^{-\kappa} - PI(-1) \tag{38}$$

when $R_{m1}=0$, (and so $PI(z)=0$), we find $P_1=\frac{p}{q}P_2$ and $Q_1=\frac{p}{q}Q_2$ The third component of (12) indicates that in this case no vertical currents are induced in the conductor. This is a steady-state result and is consistent with the knowledge that induced vertical currents are subject to free decay with time (see chapter 5).

9.2.2 The Solutions in Transform Space. Substituting for the constants of integration in (23) to (25) we can obtain the magnetic induction vector and using (12) we can obtain the induced electric current. The results are:

Case S :

Region I: (the lower sign is to be taken for $\hat{B}_z$)

$$\hat{\underline{B}} = \frac{\mu_0 K_s.\hat{S}}{4q\Delta_s\gamma}\,[p,q,ik]\left(\left\{\left(\frac{\gamma+\kappa}{\gamma-\kappa}\right)^2e^{2\gamma}-1\right\}e^{\kappa z} \pm \left\{e^{2\gamma}-1\right\}\left\{\frac{\gamma+\kappa}{\gamma-\kappa}\right\}e^{-\kappa z}\right)(\gamma-\kappa)^2e^{-\gamma} \tag{39}$$

Region II: $$\hat{\underline{B}} = \frac{\mu_0 K_s.\hat{S}}{q\Delta_s}\,[p\Pi,q\Pi,ik^2\Phi] + \frac{\mu_0 K_s.\hat{S}.R_{m1}}{2\gamma^2 q\Delta_s}\,[ik^2\zeta,0,0]\,\Pi \tag{40}$$

$$\mu_0\hat{J} = \frac{\mu_0 K_s.\hat{S}}{q\Delta_s}.\,[-q,p,0](\gamma^2-k^2)\Phi + \frac{\mu_0 K_s.\hat{S}.R_{m1}}{2\gamma^2 q\Delta_s}.[0,ik^2G,-qk^2\zeta\Pi] \tag{41}$$

where $$\zeta(k,z) = \sinh\gamma z/\sinh\gamma - z \tag{42}$$

$$G(k,z) = \Pi\left\{\frac{\gamma\cosh\gamma z}{\sinh\gamma}-1\right\} + \zeta\gamma^2\Phi \tag{43}$$

and $$\Phi(k,z) = \cosh\gamma(1+z) + \frac{\kappa}{\gamma}\sinh\gamma(1+z) \tag{44}$$

$$\Pi(k,z) = \gamma\sinh\gamma(1+z) + \kappa\cosh\gamma(1+z) \tag{45}$$

$$\Delta_s(k,h) = \gamma\sinh\gamma\cosh kh + \kappa\cosh\gamma e^{kh} + \frac{\kappa^2}{\gamma}\sinh\gamma.\sinh kh \tag{46}$$

Region III: $$\hat{\underline{B}} = \mu_0 K_s.\hat{S}.[p,q,ik].\frac{\kappa e^{\kappa(1+z)}}{q\Delta_s} \tag{47}$$

Case P :

There is a relationship between the boundary conditions in (20) which can be obtained from (39). Using the value of $\hat{\mathcal{B}}_z$ on $z=h$ we see that the case P solutions are obtained by replacing $\mu_0 K_s$ in (39) to (47) by $(-i\eta \mathcal{B}_m \Delta_s / \kappa^2 \Delta_m)$ where

$$\Delta_m(\kappa,h) = \frac{\gamma}{\kappa}\sinh\gamma\sinh\kappa h + \cosh\gamma e^{\kappa h} + \frac{\kappa}{\gamma}\sinh\gamma\cdot\cosh\kappa h \qquad (48)$$

We note that the terms containing R_{m1} in (40) and (49) are only to be included when $\frac{\partial}{\partial x}=0$ $(p=0)$. The solutions in region II have been written in a form which allows the use of contour integration for the Fourier transformation inversion. An alternative formulation is given in Appendix which is more helpful when describing the physical behaviour of the EM field.

9.3 Infinite Expanse Excitation

Here, the functions $S_x(x,a)$ and $S_y(y,b)$ in (19) are evaluated when both a and b become infinitely large. In this case we have $S_x=1$, $S_y=1$ so $\hat{S}_x = 2\pi\delta(p)$, $\hat{S}_y = 2\pi\delta(q)$ thus using (21) $\hat{S} = (2\pi)^2\delta(p)\delta(q-\alpha)$ where $\delta(p)$ is the Dirac delta function. Applying the inverse transformation (10) to (40) and (41) using this value of $\hat{S}$ we obtain the following solutions in real space:

Region II ; Case S :

$$\underline{\mathcal{B}} = \frac{\mu_0 K_s}{\Delta_s}[0,\Pi,i\alpha\Phi] - \frac{\mu_0 K_s R_{m1}}{2\gamma^2\Delta_s}[i\alpha\zeta\Pi,0,0] \qquad (49)$$

$$\mu_0 \underline{J} = \frac{\mu_0 K_s}{\Delta_s}(\gamma^2-\alpha^2)[-\Phi,0,0] - \frac{\mu_0 K_s R_{m1}}{2\gamma^2\Delta_s}[0,i\alpha G,-\alpha^2\zeta\Pi] \qquad (50)$$

where $\Phi=\Phi(\alpha,z)$, $\Pi=\Pi(\alpha,z)$, $\Delta_s=\Delta_s(\alpha,h)$, $G=G(\alpha,z)$, $\zeta=\zeta(\alpha,z)$

and from (14) $$\gamma^2 = \alpha^2 + i(R_0 - \alpha R_{m2}) = \alpha^2(1+isR_m) \qquad (51)$$

where $s=(V_s-V)/V_s$ is the slip; $R_m = Vh/\alpha\eta$ is the magnetic Reynold's number based on the wavespeed $V_s = \omega h/\alpha$.

Case $\mathcal{P}$: The solutions here are identical to those in (49) and (50) apart form the parameter μ_s which should be replaced by the term $(-i\beta_m \Delta_s / \alpha \Delta_m)$ where $\Delta_m = \Delta_m(\alpha, z)$, (48).

If we set $h=0$ and neglect upgoing waves we can reduce (49) and (50) to the solutions previously obtained in chapters 3 and 4 (this process is made easier using the form of the solutions in Appendix III . From (46) and (48) we see that the magnitude of the EM field decreases with an increase in h . When $\alpha h > 1$ we identify the decay factor $e^{-\alpha h}$ but for smaller values of αh the decay factor is not quite so apparent however $(\coth \alpha h)^{-1}$ is a good approximation.

9.4 Finite Length, Infinite Width Excitation

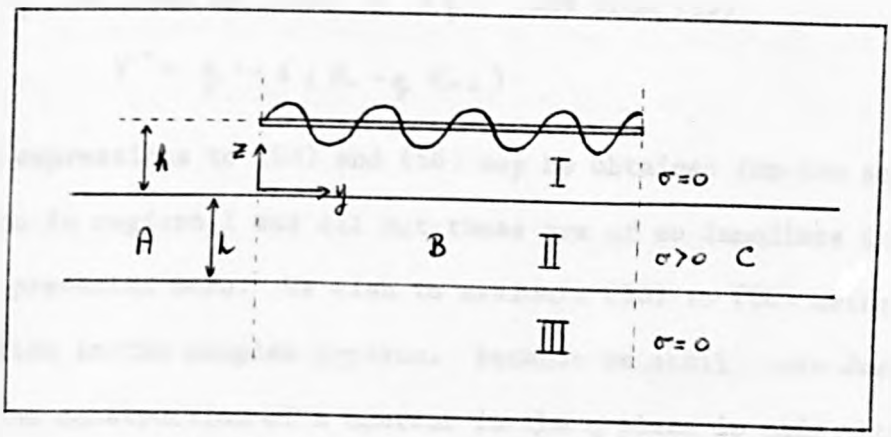

Fig. 9.2 Two Dimensional Model

A section through the configuration of figure 9.1 is shown in figure 9.2. We consider an excitation finite in length but infinite in width (so $\frac{\partial}{\partial x} = 0$) . The function $S_x(x,a)$ (the first of (19)) equals unity when a becomes infinite so $\hat{S}_x = 2\pi \delta(p)$. Thus from (21) we have $\hat{S} = 2\pi \delta(p) \hat{S}_y(q-\alpha, b)$ where (from the second of (22))

$$\hat{S}_y(q-\alpha, b) = \frac{e^{ib(q-\alpha)} - 1}{i(q-\alpha)} \tag{52}$$

Applying the inverse transformation (10) to (40) and (41) with the value of $\hat{S}$ above we obtain the following integral expressions for the EM field

induced in the electrical conductor:

Case S :

$$\underline{B} = \frac{\mu_0 K_s}{2\pi}\int_{-\infty}^{\infty}\left\{\frac{[0,\Pi,iq\Phi]}{\Delta_s} - \frac{R_{m1}[iq\zeta\Pi,0,0]}{2\gamma^2\Delta_s}\right\}\hat{S}_y e^{-iqy}\,dq \qquad (53)$$

$$\mu_0 k\underline{J} = \frac{\mu_0 K_s}{2\pi}\int_{-\infty}^{\infty}\left\{\frac{[-1,0,0](\gamma^2-q^2)\Phi}{\Delta_s} - \frac{R_{m1}[0,iqG,-q^2\zeta\Pi]}{2\gamma^2\Delta_s}\right\}\hat{S}_y e^{-iqy}\,dq \qquad (54)$$

Case P :

$$\underline{B} = \frac{B_m}{2\pi}\int_{-\infty}^{\infty}\left\{\frac{[0,-i\Pi,q\Phi]}{q\Delta_m} - \frac{R_{m1}[\zeta\Pi,0,0]}{2\gamma^2\Delta_m}\right\}\hat{S}_y e^{-iqy}\,dq \qquad (55)$$

$$\mu_0 k\underline{J} = \frac{B_m}{2\pi}\int_{-\infty}^{\infty}\left\{\frac{[i,0,0](\gamma^2-q^2)\Phi}{q\Delta_m} - \frac{R_{m1}[0,G,iq\zeta\Pi]}{2\gamma^2\Delta_m}\right\}\hat{S}_y e^{-iqy}\,dq \qquad (56)$$

where $\hat{S}_y$ is given by (50); $k^2 = q^2$ and from (15)

$$\gamma^2 = q^2 + i(R_0 - q R_{m2}) \qquad (57)$$

Similar expressions to (53) and (56) may be obtained for the magnetic induction in regions I and III but these are of no immediate interest and are not presented here. We wish to evaluate (53) to (56) using contour integration in the complex q-plane. Because we shall use Jordan's Lemma, the construction of a contour in the q-plane is made according to the behaviour of the function $\hat{S}e^{-iqy}$ (see §7.4). Denoting the upper half q-plane by C^+ and the lower half by C^- we identify three regions according to the decay of the two terms of $\hat{S}e^{-iqy}$, which by (52) are: $\dfrac{e^{-ib\alpha}e^{iq(b-y)}}{i(q-\alpha)}$ and $\dfrac{e^{-iqy}}{i(q-\alpha)}$. The regions are:

Region A $(y<0)$: e^{-iqy} decays in C^+ ; $e^{iq(b-y)}$ decays in C^+

Region B $(0<y<b)$: e^{-iqy} decays in C^- ; $e^{iq(b-y)}$ decays in C^+

Region C $(y>b)$: e^{-iqy} decays in C^- ; $e^{iq(b-y)}$ decays in C^-

At first sight it may be thought that we have to consider the branch point $\gamma = 0$. However, expanding the hyperbolic functions of δ (present

in Π, Φ, Δ_s and Δ_m) in a power series indicates that γ only occurs as an even power and so branch points do not arise. The function $\kappa = \sqrt{q^2}$ (which contains two imaginary branch points at $\sigma_+ i$, $\sigma_- i$) is single valued in the complex q-plane. From (52) we see there is a simple pole at $q = \alpha$ for all the solutions and there is also a simple pole at $q = 0$ in the case $\mathcal{P}$ solutions (55) and (56). Both poles lie on the real axis. Two simple poles χ^+, χ^- are obtained from the R_{m1} terms when $\gamma^2 = 0$. Using (57) we see that

$$\chi^{\pm} = \mp A \sin\frac{\theta}{2} + i\left(R_{m2} \pm A\cos\frac{\theta}{2}\right) \quad \text{where} \quad A^2 = R_{m2}^4 + 16R_0^2 \quad \text{and} \quad \theta = \tan^{-1}\left(\frac{4R_0}{R_{m2}^2}\right) \qquad (58)$$

Following NASAR and DEL CID 1973(a) we use the iterative method of Muller (see CONTE and DE BOOR, 1965) to find the complex zeros of Δ_s and Δ_m In general there will be an infinite number of them, but we only use a small number of zeros in the integral evaluations below. Denoting a zero of Δ (either Δ_s or Δ_m) by $q = \psi_j$; we can factorise Δ as $\Delta(q) = (q - \psi_j)\, D(q)$ where $D(q)$ is a polynomial in q. The residue of Δ at the simple pole ψ_j is equal to $D(\psi_j)$. However differentiating Δ with respect to q we have $\Delta'(q) = D(q) + (q - \psi_j) D'(q)$ and so $D(\psi_j) = \Delta'(\psi_j)$

The contours around which we choose to evaluate (53) to (56) are shown in figure 9.3. Included in this diagram are the infinite radius semi-circles Γ^+, Γ^- around which the line integral contribution vanishes by Jordan's Lemma. The roots of Δ are denoted by $\psi_j^{\pm}$ (in C^+ and C^- respectively).

Indentations around the poles at $q = \alpha$ and $q = 0$ are also shown.

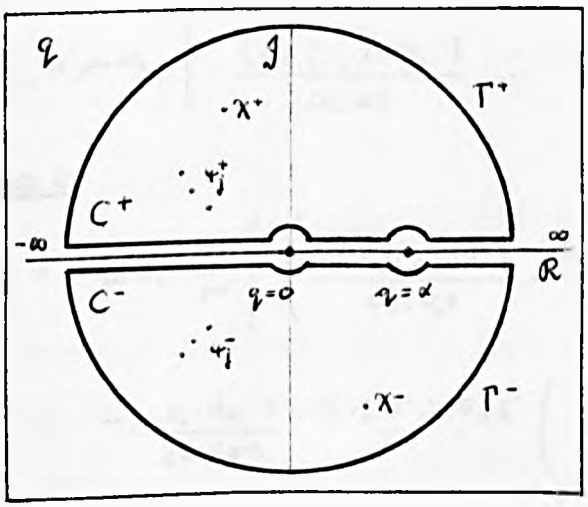

Fig. 9.3 Contours in the Complex q-plane

Using Cauchy's Residue theorem and standard contour integration methods (some of which were described in §7.4) we can invert (53) to (57) and obtain exact expressions for the EM field in real space. The following notation is used to simplify the algebra: $\Pi(\psi_j^\pm) = \Pi_j^\pm$, $\Phi(\psi_j^\pm) = \Phi_j^\pm$, $\gamma(\psi_j^\pm) = \gamma_j^\pm$, $\Pi(\chi^\pm) = E^\pm$, $\Phi(\chi^\pm) = D^\pm$, $\zeta(\psi_j^\pm) = \zeta_j^\pm$, $\zeta(\chi^\pm) = \zeta^\pm$, $G(\psi_j^\pm) = G_j^\pm$, $G(\chi^\pm) = G^\pm$. Subscripts α and o are used when we consider the contribution from the poles $q = \alpha$ and $q = o$ respectively. We note the contribution from the loops at $q = \alpha$ and $q = o$ is half that obtained from the residues at those points. We also use the notation $\lim_{q \to \chi^\pm} \left\{ \frac{q - \chi^\pm}{\gamma^\pm} \right\} = \frac{\pm 1}{\chi^+ - \chi^-} \equiv r^\pm$.

The case S solutions for the magnetic induction vector are:

Region A

$$\underline{B} = \mu_o K_s \sum_{j=0}^{\infty} \left\{ \left(\frac{[0, \Pi_j^+, i\psi_j^+ \Phi_j^+]}{\Delta_s'(\psi_j^+)} - \frac{R_{m1} \Pi_j^+ [i\zeta_j^+ \psi_j^+, 0, 0]}{2(\gamma_j^+)^2 \Delta_s'(\psi_j^+)} \right) \left(\frac{e^{ik(\psi_j^+ - \alpha)}}{\psi_j^+ - \alpha} \right) e^{-i\psi_j^+ y} \right\}$$

$$- \frac{\mu_o K_s . R_{m1} r^+ E^+ [i\zeta^+ \chi^+, 0, 0]}{2\Delta_s(\chi^+)} \cdot \left(\frac{e^{ik(\chi^+ - \alpha)}}{\chi^+ - \alpha} \right) e^{-i\chi^+ y} \qquad (59)$$

Region B

$$\underline{B} = \mu_o K_s \sum_{j=0}^{\infty} \left\{ \left(\frac{[0, \Pi_j^-, i\psi_j^- \Phi_j^-]}{\Delta_s'(\psi_j^-)} - \frac{R_{m1} \Pi_j^- [i\zeta_j^- \psi_j^-, 0, 0]}{2(\gamma_j^-)^2 \Delta_s'(\psi_j^-)} \right) \cdot \frac{e^{-i\psi_j^- y}}{(\psi_j^- - \alpha)} \right.$$

$$\left. - \left(\frac{[0, \Pi_j^+, i\psi_j^+ \Phi_j^+]}{\Delta_s'(\psi_j^+)} - \frac{R_{m1} \Pi_j^+ [i\zeta_j^+ \psi_j^+, 0, 0]}{2(\gamma_j^+)^2 \Delta_s'(\psi_j^+)} \right) \cdot \frac{e^{ik(\psi_j^+ - \alpha)} e^{-i\psi_j^+ y}}{(\psi_j^+ - \alpha)} \right\}$$

$$- R_{m1} . \mu_o K_s . \left\{ \frac{r^- [i\chi^- \zeta^-, 0, 0] E^- e^{-i\chi^- y}}{2\Delta_s(\chi^-) . (\chi^- - \alpha)} + \frac{r^+ [i\chi^+ \zeta^+, 0, 0] E^+ e^{i\chi^+ y} e^{ik(\chi^+ - \alpha)}}{2\Delta_s(\chi^+) . (\chi^+ - \alpha)} \right\}$$

$$+ \mu_o K_s . \left\{ \frac{[0, \Pi_\alpha, i\alpha \Phi_\alpha]}{\Delta_s(\alpha)} - \frac{R_{m1} [i\alpha \zeta_\alpha, 0, 0] \Pi_\alpha}{2(\gamma_\alpha)^2 \Delta_s(\alpha)} \right\} e^{-i\alpha y} \qquad (60)$$

Region C

$$\underline{B} = \mu_o K_s . \sum_{j=0}^{\infty} \left\{ \left(\frac{[0, \Pi_j^-, i\psi_j^- \Phi_j^-]}{\Delta_s'(\psi_j^-)} - \frac{R_{m1} . \Pi_j^- [i\zeta_j^- \psi_j^-, 0, 0]}{2(\gamma_j^-)^2 . \Delta_s'(\psi_j^-)} \right) \left(\frac{1 - e^{ik(\psi_j^- - \alpha)}}{\psi_j^- - \alpha} \right) e^{-i\psi_j^- y} \right\}$$

$$- \frac{\mu_o K_s . R_{m1} r^- . [i\zeta^- \chi^-, 0, 0] E^-}{2\Delta_s(\chi^-)} \left(\frac{1 - e^{ik(\chi^- - \alpha)}}{\chi^- - \alpha} \right) e^{-i\chi^- y} \qquad (61)$$

In the evaluation of (59) to (61) we find the contribution from the branch point at $q=0$ is zero. Notice that the last term of (60) is equal to (49), thus the magnetic induction in the central region of the excitation is made up of the idealised result (49) plus end effects (the remaining terms of (60). The magnetic induction in regions A and C arise solely from these end effect phenomena.

The case S solution for the electric current density is:

Region A

$$\mu_0 h \underline{J} = -\mu_0 K_s \sum_{j=0}^{\infty}{}' \left\{ \left(\frac{[-i(R_0-\psi_j^+ R_{m2}),0,0]\,\Phi_j^+}{\Delta_s'(\psi_j^+)} - \frac{R_{m1}\,[0, i\psi_j^+ G_j^+, -(\psi_j^+)^2 \zeta_j^+ \pi_j^+]}{2(\gamma_j^+)^2\,\Delta_s'(\psi_j^+)} \right) \times \left(\frac{1-e^{ih(\psi_j^+-\alpha)}}{\psi_j^+-\alpha} \right) e^{-i\psi_j^+ y} \right\} + \frac{\mu_0 K_s r^+ R_{m1}}{2\Delta_s(\chi^+)}\,[0, i\chi^+ G^+, -(\chi^+)^2 E^+ \zeta^+] \left(\frac{1-e^{ih(\chi^+-\alpha)}}{\chi^+-\alpha} \right) e^{-i\chi^+ y} \quad (62)$$

Region B

$$\mu_0 h \underline{J} = \mu_0 K_s \sum_{j=0}^{\infty}{}' \left\{ \left(\frac{[-i(R_0-\psi_j^- R_{m2}),0,0]\,\Phi_j^-}{\Delta_s'(\psi_j^-)} - \frac{R_{m1}\,[0, i\psi_j^- G_j^-, -(\psi_j^-)^2 \zeta_j^- \pi_j^-]}{2(\gamma_j^-)^2\,\Delta_s(\psi_j^-)} \right) \frac{e^{-i\psi_j^- y}}{\psi_j^- - \alpha} - \left(\frac{[-i(R_0-\psi_j^+ R_{m2}),0,0]\,\Phi_j^+}{\Delta_s'(\psi_j^+)} - \frac{R_{m1}\,[0, i\psi_j^+ G_j^+, -(\psi_j^+)^2 \zeta_j^+ \pi_j^+]}{2(\gamma_j^+)^2\,\Delta_s'(\psi_j^+)} \right) \frac{e^{ih(\psi_j^+-\alpha)} e^{-i\psi_j^+ y}}{\psi_j^+ - \alpha} \right\}$$

$$- R_{m1}\mu_0 K_s \left\{ \frac{r^-\,[0, i\chi^- G^-, -(\chi^-)^2 \zeta^- E^-]\, e^{-i\chi^- y}}{2\Delta_s(\chi^-)\,(\chi^- - \alpha)} + \frac{r^+\,[0, i\chi^+ G^+, -(\chi^+)^2 \zeta^+ E^+]\, e^{ih(\chi^+-\alpha)} e^{-i\chi^+ y}}{2\Delta_s(\chi^+)\,\chi^+ - \alpha} \right\}$$

$$\mu_0 K_s \left\{ \frac{[-i(R_0-\alpha R_{m2}),0,0]\,\Phi_\alpha}{\Delta_s(\alpha)} - \frac{R_{m1}\,[0, i\alpha G_\alpha, -\alpha^2 \zeta_\alpha \pi_\alpha]}{2\gamma_\alpha^2\,\Delta_s(\alpha)} \right\} e^{-i\alpha y} \quad (63)$$

Region C

$$\mu_0 h \underline{J} = \mu_0 K_s \sum_{j=0}^{\infty}{}' \left\{ \left(\frac{[-i(R_0-\psi_j^- R_{m2}),0,0]\,\Phi_j^-}{\Delta_s'(\psi_j^-)} - \frac{R_{m1}\,[0, i\psi_j^- G_j^-, -(\psi_j^-)^2 \zeta_j^- \pi_j^-]}{2(\gamma_j^-)^2\,\Delta_s'(\psi_j^-)} \right) \times \left(\frac{1-e^{ih(\gamma_j^- - \alpha)}}{\psi_j^- - \alpha} \right) e^{-i\psi_j^- y} \right\} - \frac{R_{m1}\mu_0 K_s r^-\,[0, i\chi^- G^-, -(\chi^-)^2 E^- \zeta^-]}{2\Delta_s(\chi^-)} \left(\frac{1-e^{ih(\chi^- - \alpha)}}{\chi^- - \alpha} \right) e^{-i\chi^- y} \quad (64)$$

The comments made previously concerning the magnetic induction apply equally to the electric current density.

The case P solutions for the magnetic induction and electric current density (setting R_{m1} equal to zero for brevity) are:

Region A

$$\underline{B} = B_m \sum_{j=0}^{\infty}{}' \left\{ \frac{[0, -i\Pi_j^+, \psi_j^+ \Phi_j^+]}{\psi_j^+ \Delta_m'(\psi_j^+)} \left(\frac{e^{ib(\psi_j^+ - \alpha)} - 1}{\psi_j^+ - \alpha} \right) e^{-i\psi_j^+ y} \right\} + \frac{B_m [0, -i\Pi_0, 0]}{\Delta_m(0)} \frac{(e^{-ib\alpha} - 1)}{(-\alpha)} \quad (65)$$

$$\mu_0 h \underline{J} = B_m \sum_{j=0}^{\infty}{}' \left\{ \frac{[i\Phi_j^+, 0, 0]}{\psi_j^+ \Delta_m'(\psi_j^+)} \left(\frac{e^{ib(\psi_j^+ - \alpha)} - 1}{\psi_j^+ - \alpha} \right) e^{-i\psi_j^+ y} \right\} + \frac{B_m [\Phi_0 i, 0, 0]}{\Delta_m(0)} \frac{(e^{-ib\alpha} - 1)}{(-\alpha)} \quad (66)$$

Region B

$$\underline{B} = B_m \sum_{j=0}^{\infty}{}' \left\{ \frac{[0, -i\Pi_j^+, \psi_j^+ \Phi_j^+]}{\psi_j^+ \Delta_m'(\psi_j^+)} \cdot \frac{e^{ib(\psi_j^+ - \alpha)}}{(\psi_j^+ - \alpha)} e^{-i\psi_j^+ y} + \frac{[0, -i\Pi_j^-, \psi_j^- \Phi_j^-]}{\psi_j^- \Delta_m'(\psi_j^-)} \frac{e^{-i\psi_j^- y}}{(\psi_j^- - \alpha)} \right\}$$

$$+ B_m \frac{[0, -i\Pi_0, 0]}{\Delta_m(0)} \frac{(e^{-ib\alpha} + 1)}{(-\alpha)} + B_m \frac{[0, -i\Pi_\alpha, \alpha \Phi_\alpha]}{\alpha \Delta_m(\alpha)} e^{-i\alpha y} \quad (67)$$

$$\mu_0 h \underline{J} = B_m \sum_{j=0}^{\infty}{}' \left\{ \frac{[i\Phi_j^+, 0, 0]}{\psi_j^+ \Delta_m'(\psi_j^+)} \frac{e^{ib(\psi_j^+ - \alpha)} e^{-i\psi_j^+ y}}{(\psi_j^+ - \alpha)} + \frac{[i\phi_j^-, 0, 0] e^{-i\psi_j^- y}}{\psi_j^- \Delta_m'(\psi_j^-) \cdot (\psi_j^- - \alpha)} \right\}$$

$$B_m \frac{[i\Phi_0, 0, 0]}{\Delta_m(0)} \frac{(e^{-ib\alpha} + 1)}{(-\alpha)} + \frac{B_m [i\Phi_\alpha, 0, 0] e^{-i\alpha y}}{\alpha \Delta_m(\alpha)} \quad (68)$$

Region C

$$\underline{B} = -B_m \sum_{j=0}^{\infty}{}' \left\{ \frac{[0, -i\Pi_j^-, \psi_j^- \Phi_j^-]}{\psi_j^- \Delta_m'(\psi_j^-)} \left(\frac{e^{ib(\psi_j^- - \alpha)}}{\psi_j^- - \alpha} - 1 \right) e^{-i\psi_j^- y} - \frac{B_m [0, -i\Pi_0, 0]}{\Delta_m(0)} \frac{(e^{-ib\alpha} - 1)}{(-\alpha)} \right\} \quad (69)$$

$$\mu_0 h \underline{J} = B_m \sum_{j=0}^{\infty}{}' \left\{ \frac{[i\Phi_j^-, 0, 0]}{\psi_j^- \Delta_m'(\psi_j^-)} \left(\frac{e^{ib(\psi_j^- - \alpha)}}{\psi_j^- - \alpha} - 1 \right) e^{-i\psi_j^- y} - \frac{B_m [i\Phi_0, 0, 0]}{\Delta_m(0)} \frac{(e^{-ib\alpha} - 1)}{(-\alpha)} \right\} \quad (70)$$

Again, the comments made for the magnetic induction in (59) to (61) apply equally to (65) to (70). However we see that B_2 and J_1 in this case contain an evaluation at the pole $q=0$. This contribution (which is removed as $|y| \to \infty$) is a major cause of the end effects in regions A and C. If $(e^{-ib\alpha} - 1)$ equals zero the end effect terms largely disappear; thus for maximum efficiency we require $b = \frac{2n\pi}{\alpha}$ $(= n\lambda$ or $2n\tau$ where λ is the wavelength of the excitation and τ the pole pitch). This

observation has also been made by LAITHWAITE (1965) using a one dimensional analysis. His result was obtained by specifying that $\int_0^{\ell} J_1 dy = 0$ (ie: the net surface produced by the stator is zero). The above constraint can be avoided by changing to a Gramme-ring winding (for a description see LAITHWAITE, 1975) which allows the use of fractional pole pitch machines.

9.4.1 Example. We evaluate the expressions above using the physical and electrical data of table 1.1 (the float bath configuration).

The first nine roots of $\Delta_s(q)$, (48), are tabulated in figures 9.4 (for C^+) and 9.5 (for C^-) for three values of h (corresponding to 0.5 inches, 1.5 inches and 3 inches). Similarly the first nine roots of $\Delta_m(q)$ are tabulated in figures 9.6 (for C^+) and figure 9.7 (for C^-) The positions of these roots in the complex q-plane are also shown; extra roots have been plotted for completeness. From (58) we find

$$\chi^+ = -1.1511 + i\,1.1611 \qquad \chi^- = 1.1511 - i\,1.1411$$

The EM field solutions (59) to (70) were evaluated using these values of $\psi_j^{\pm}$ and $\chi^{\pm}$. The results are shown in figure 9.8 (case S ; variation with z , h =0.5 inches), figure 9.9 (case P ; variation with z, h =0.5 inches), figure 9.10 (case S ; variation with h , $z=0$) and figure 9.11 (case P ; variation with h , $z=0$). Note that in these results we have set $R_{m1} = 0$ and $R_{m2} = 0.02$. The diagrams show the dimensionless EM fields: $\underline{B} = \underline{B}/(\mu k_s \text{ or } B_m)$, $\underline{J} = \underline{J}/(L/k_s \text{ or } \mu_0 L/B_m)$ The dimensionless time-averaged forces are recalculated using (1.31).

It is clear from figures 9.4 to 9.7 that the larger h is, the more roots are required. In fact, for h =0.2 we found six roots were sufficient to produce results within a tolerance of 5 per cent. However, for h =1.2 we required around twelve roots to produce the same accuracy. We did in fact compute the first fifteen roots of Δ_s and Δ_m in C^+ and C^- - these roots follow the same line and seperation indicated by the diagrams of figures 9.4 to 9.7.

○ H= .2	Δ_s
-.107087E+01	.180398E+01
-.164833E+01	.435162E+01
-.198247E+01	.700232E+01
-.221810E+01	.964948E+01
-.239937E+01	.122885E+02
-.290128E+01	.227965E+02
-.279512E+01	.201719E+02
-.299756E+01	.254211E+02
-.308501E+01	.280450E+02

△ H= .6	
-.537595E+00	.137241E+01
-.119466E+01	.331381E+01
-.149067E+01	.724013E+01
-.132490E+01	.531822E+01
-.172795E+01	.112080E+02
-.164429E+01	.923798E+01
-.183681E+01	.131639E+02
-.192068E+01	.151485E+02
-.198565E+01	.171073E+02

▫ H= 1.2	
-.234310E+00	.942988E+00
-.751731E+00	.258796E+01
-.950733E+00	.534506E+01
-.108416E+01	.669791E+01
-.877821E+00	.379368E+01
-.123317E+01	.110226E+02
-.122385E+01	.958164E+01
-.133898E+01	.138731E+02
-.132753E+01	.124559E+02
-.110768E+01	.817788E+01

Fig. 9.4 Complex Roots of Δ_s in C^+

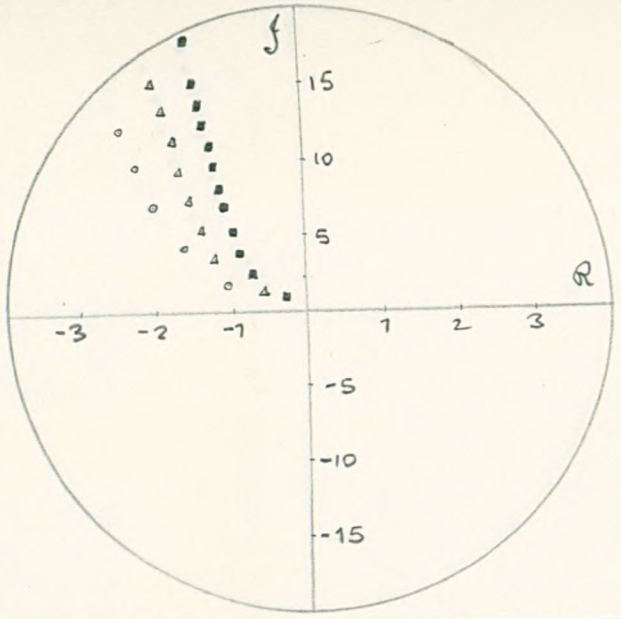

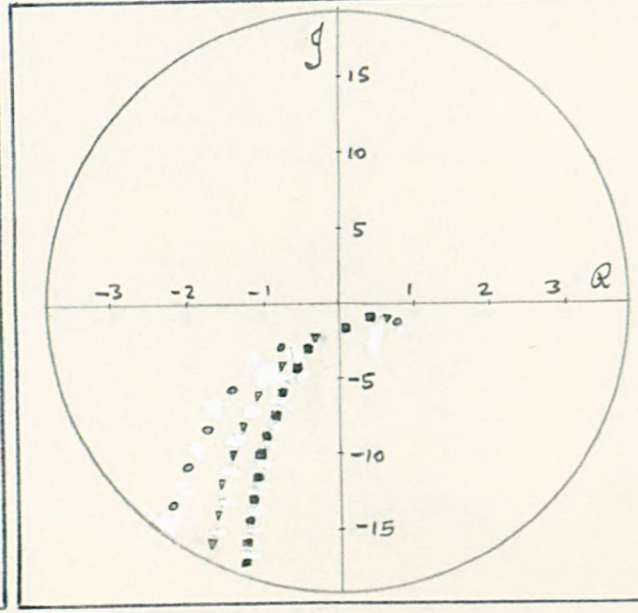

Fig. 9.5 Complex Roots of Δ_s in C^-

○ H= .2	Δ_s
.755555E+00	-.107981E+01
-.826421E+00	-.291010E+01
-.145049E+01	-.563316E+01
-.179384E+01	-.830559E+01
-.203742E+01	-.109552E+02
-.222783E+01	-.135960E+02
-.238196E+01	-.162334E+02
-.250848E+01	-.188678E+02
-.261432E+01	-.214986E+02

△ H= .6	
.614272E+00	-.919074E+00
-.351355E+00	-.224182E+01
-.822062E+00	-.421260E+01
-.116105E+01	-.623442E+01
-.132287E+01	-.823620E+01
-.147819E+01	-.101934E+02
-.168558E+01	-.141560E+02
-.160487E+01	-.121882E+02
-.191020E+01	-.200615E+02

▫ H= 1.2	
.417090E+00	-.815561E+00
.853845E-01	-.161188E+01
-.473655E+00	-.307797E+01
-.614132E+00	-.453667E+01
-.828254E+00	-.599938E+01
-.894137E+00	-.740965E+01
-.101465E+01	-.888249E+01
-.120121E+01	-.131476E+02
-.114007E+01	-.117493E+02
-.107220E+01	-.102785E+02

○ H= .2	Δ_M
-.151528E+01	.308885E+01
-.185099E+01	.570479E+01
-.210032E+01	.833753E+01
-.230232E+01	.109687E+02
-.247257E+01	.135995E+02
-.261773E+01	.162302E+02
-.304009E+01	.267333E+02
-.294952E+01	.241109E+02
-.285146E+01	.214867E+02

△ H= .6	
-.994753E+00	.246404E+01
-.145084E+01	.627540E+01
-.120857E+01	.426822E+01
-.168592E+01	.102044E+02
-.155464E+01	.825918E+01
-.179587E+01	.121952E+02
-.196032E+01	.161202E+02
-.186782E+01	.141577E+02
-.208781E+01	.200567E+02

▨ H= 1.2	
-.475262E+00	.183431E+01
-.907564E+00	.316955E+01
-.105577E+01	.603718E+01
-.107302E+01	.741879E+01
-.118040E+01	.890090E+01
-.122292E+01	.102817E+02
-.861188E+00	.456800E+01
-.143053E+01	.160170E+02
-.136663E+01	.146101E+02
-.128083E+01	.117577E+02

Fig. 9.6 Complex Roots of Δ_m in C^+.

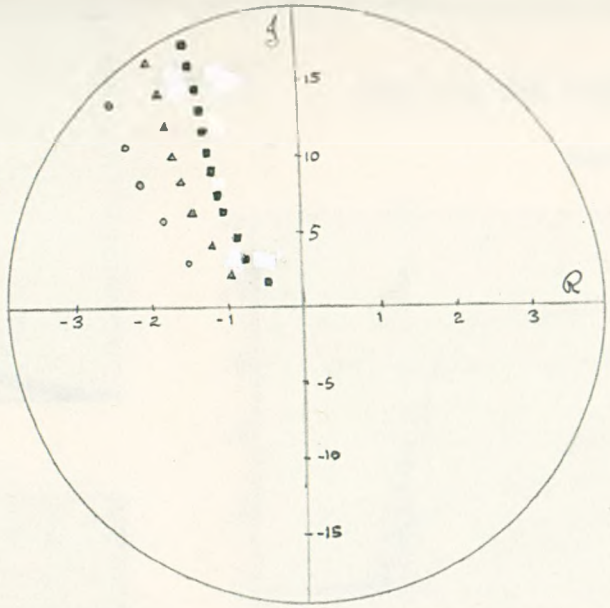

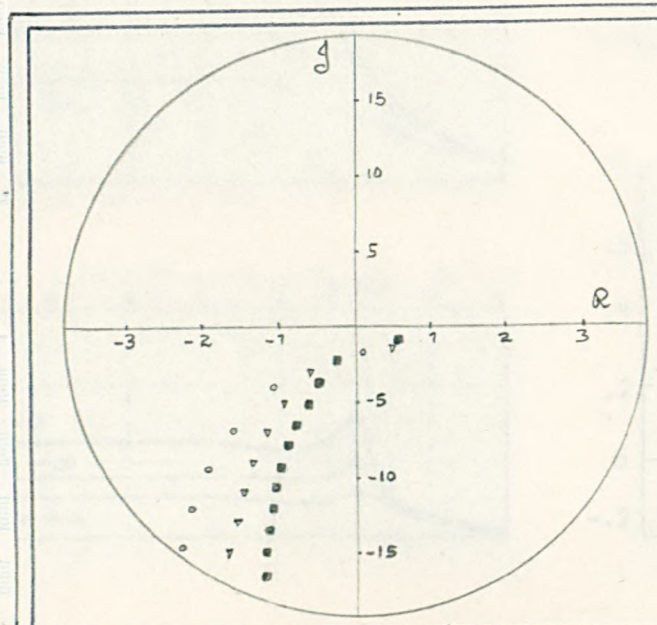

Fig. 9.7 Complex Roots of Δ_m in C^-.

○ H= .2	Δ_M
.804292E-01	-.170172E+01
-.113947E+01	-.425284E+01
-.163594E+01	-.695600E+01
-.193660E+01	-.962759E+01
-.214778E+01	-.122805E+02
-.230989E+01	-.149210E+02
-.244351E+01	-.175534E+02
-.255909E+01	-.201819E+02
-.266087E+01	-.228094E+02

△ H= .6	
.422116E+00	-.142955E+01
-.676339E+00	-.320606E+01
-.100591E+01	-.525892E+01
-.123446E+01	-.721570E+01
-.142447E+01	-.921996E+01
-.153095E+01	-.111993E+02
-.165031E+01	-.131600E+02
-.174151E+01	-.151480E+02
-.180846E+01	-.171096E+02

▨ H= 1.2	
.518503E+00	-.117628E+01
-.289006E+00	-.238494E+01
-.547903E+00	-.377799E+01
-.722862E+00	-.529456E+01
-.875987E+00	-.668464E+01
-.106158E+01	-.957267E+01
-.941945E+00	-.816005E+01
-.109119E+01	-.110167E+02
-.120664E+01	-.138722E+02
-.118655E+01	-.124506E+02

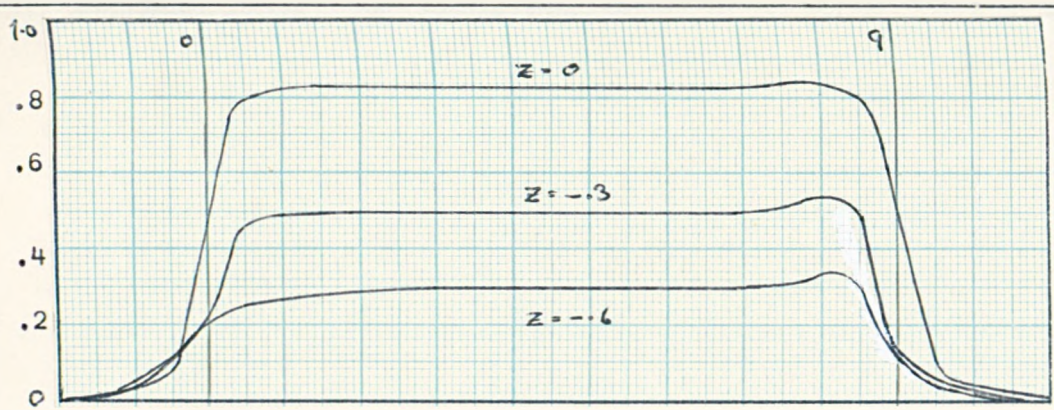
1.0
.8
.6
.4
.2
0
0
9
z = 0
z = -.3
z = -.6

(a) B2

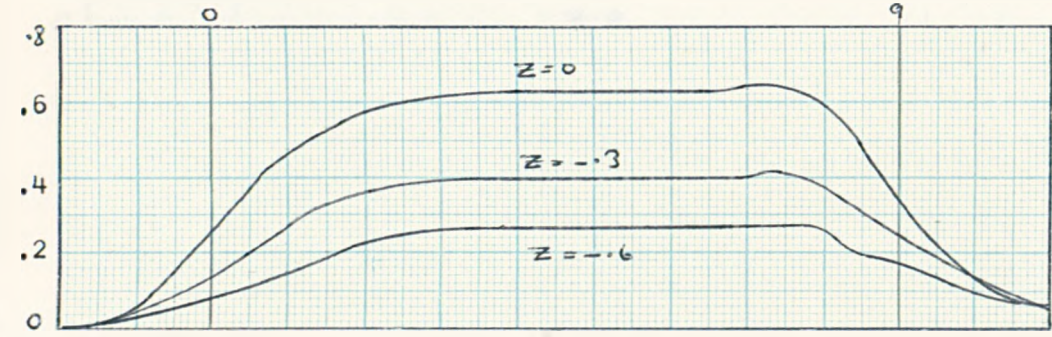
.8
.6
.4
.2
0
0
9
z = 0
z = -.3
z = -.6

(b) B3

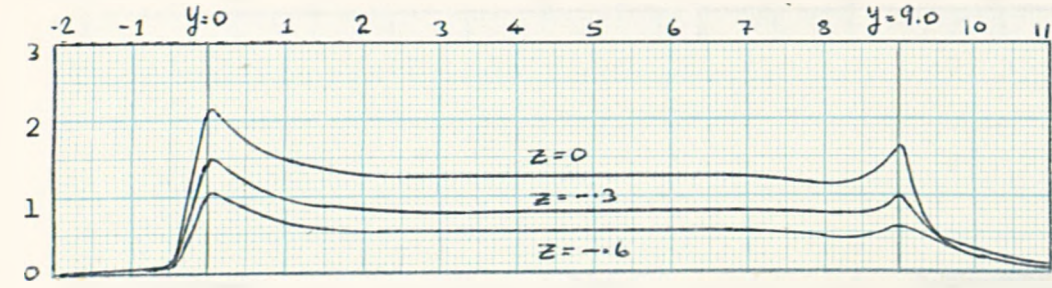
-2
-1
y=0
1
2
3
4
5
6
7
8
y=9.0
10
11
3
2
1
0
z=0
z=-.3
z=-.6

(c) J1

Fig. 9.8 The Induced EM Field. Case S

Variation with z (H= .2)

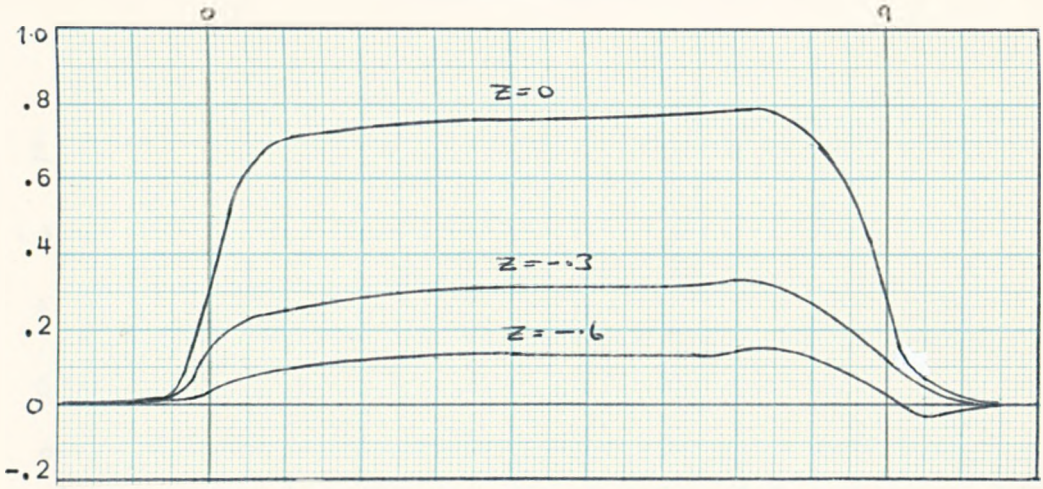

(d) F2

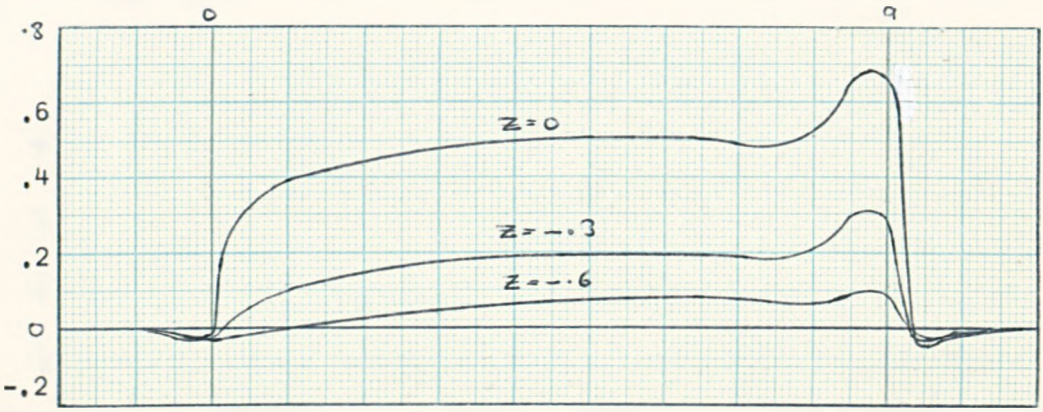

(e) (-)F3

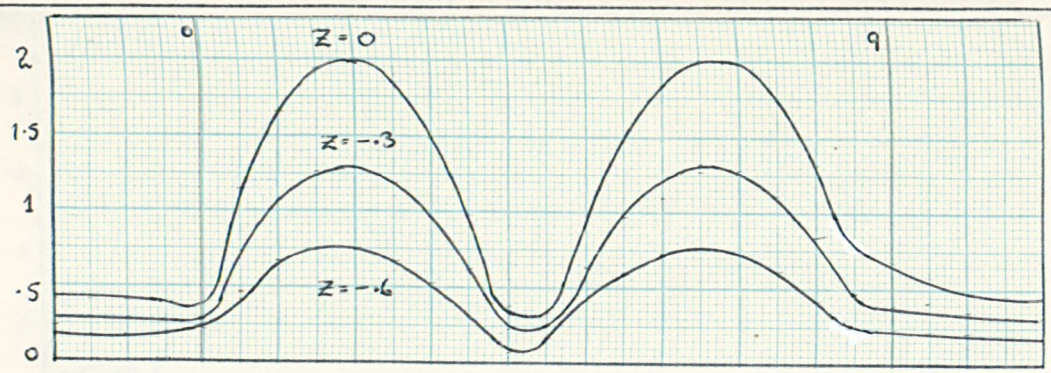
0
9
2
1·5
1
·5
0
Z = 0
Z = -·3
Z = -·6

(a) B2

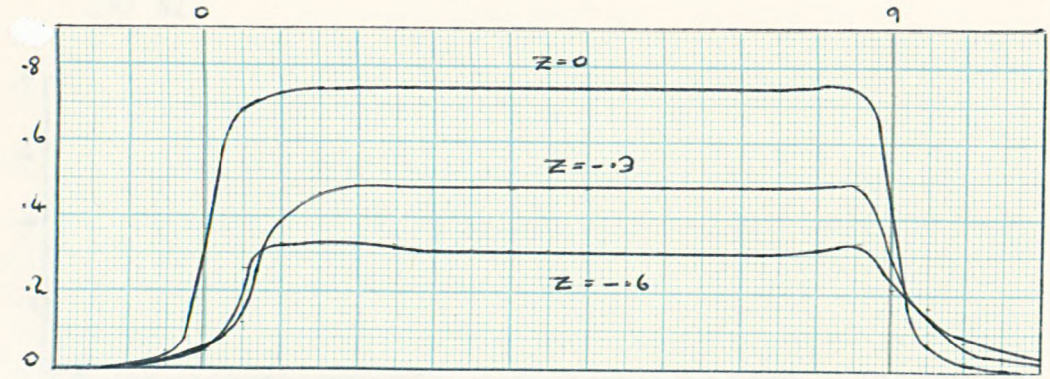
0
9
·8
·6
·4
·2
0
Z = 0
Z = -·3
Z = -·6

(b) B3

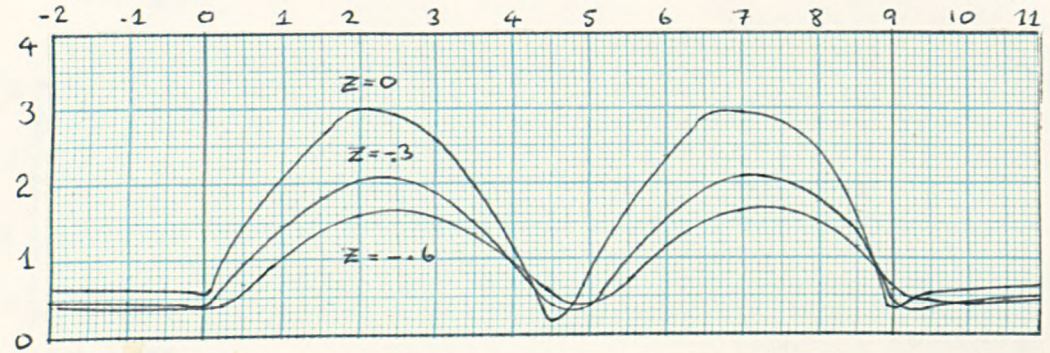
-2
-1
0
1
2
3
4
5
6
7
8
9
10
11
y
4
3
2
1
0
Z = 0
Z = -·3
Z = -·6

(c) J1

Fig. 9.9 The Induced EM Field. Case P

Variation with z (H= .2)

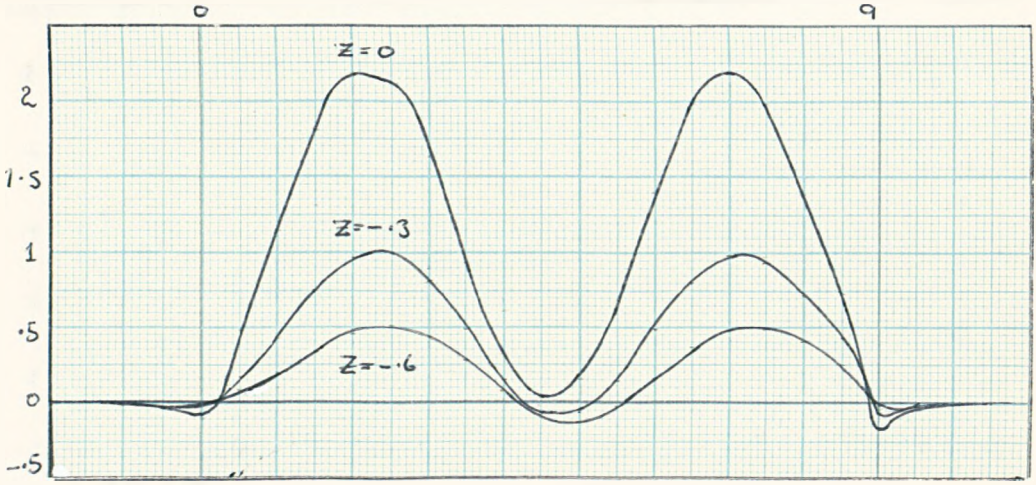

(a) F2

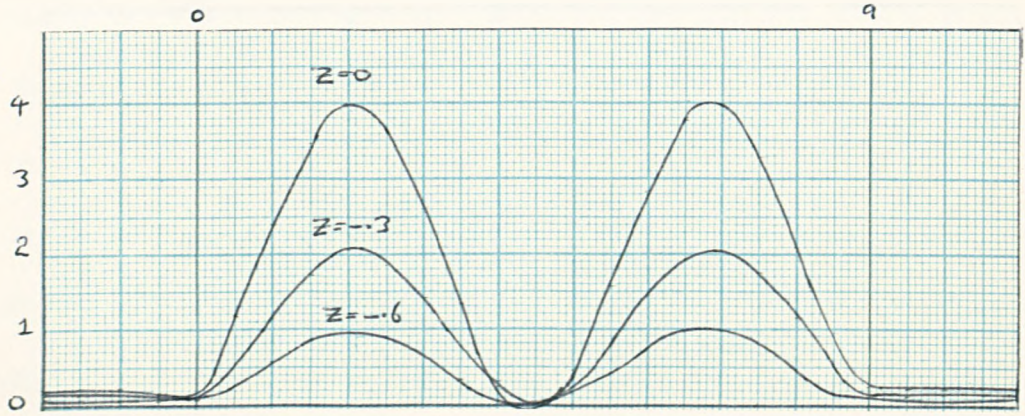

(e) (-) F3

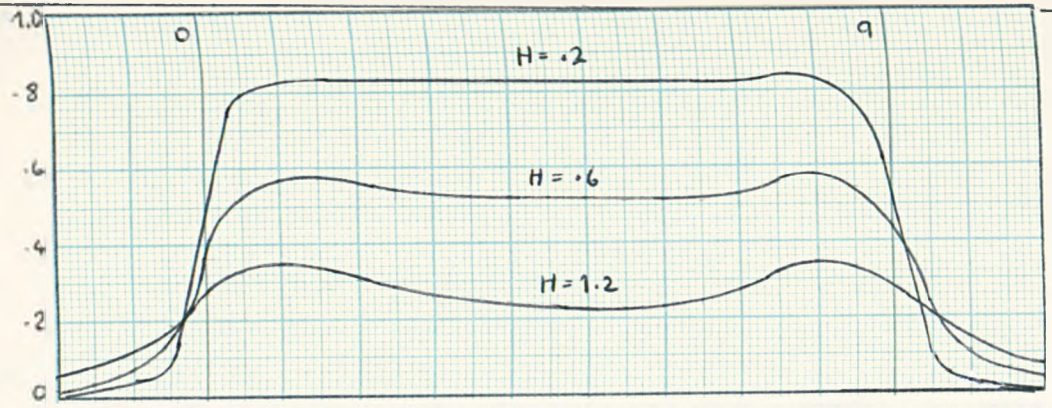
1.0
.8
.6
.4
.2
0
0
9
H = .2
H = .6
H = 1.2

(a) B2

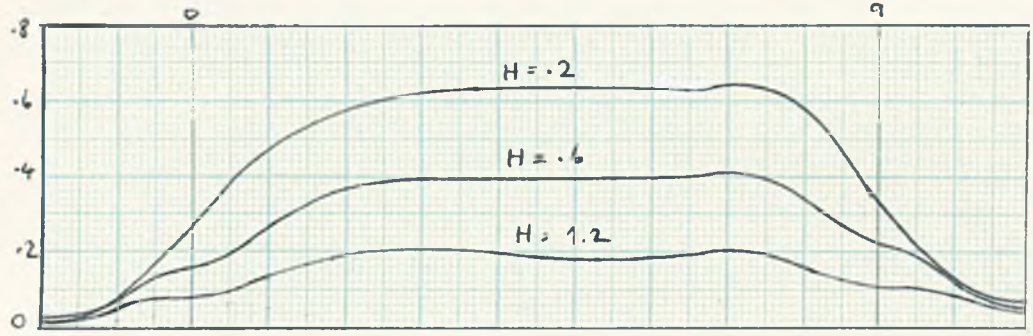
.8
.6
.4
.2
0
0
9
H = .2
H = .6
H = 1.2

(b) B3

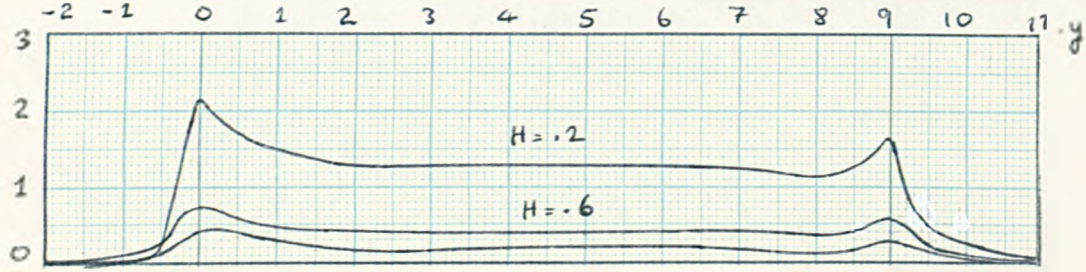
-2 -1 0 1 2 3 4 5 6 7 8 9 10 11
3
2
1
0
H = .2
H = .6

(c) J1

Fig. 9.10 The Induced EM Field. Case S

Variation with H (z=0)

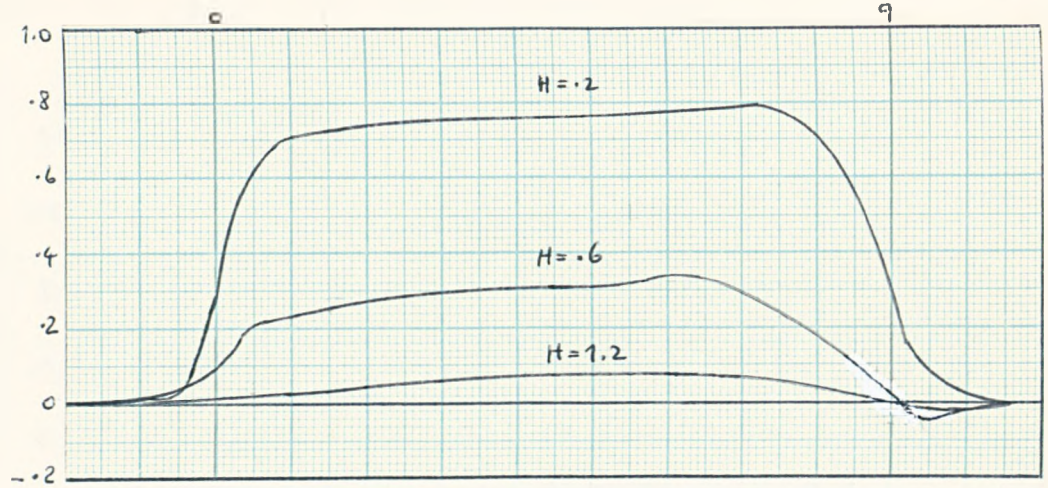

(d) F2

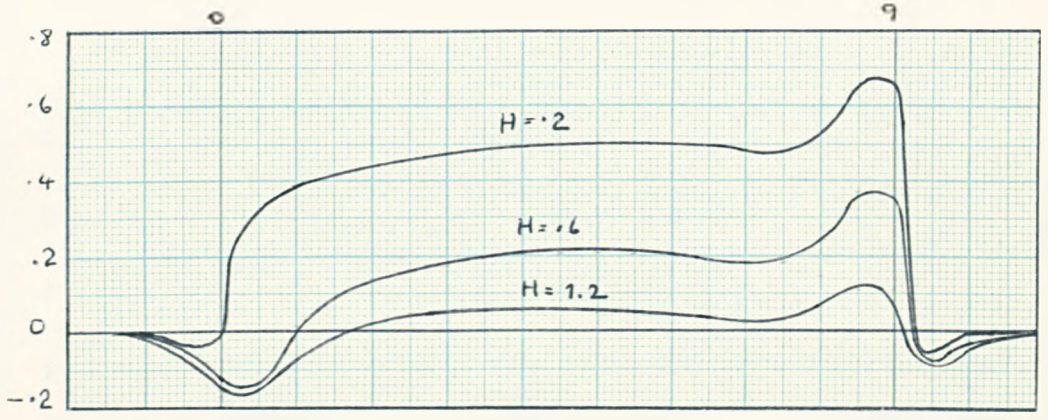

(e) (-) F3

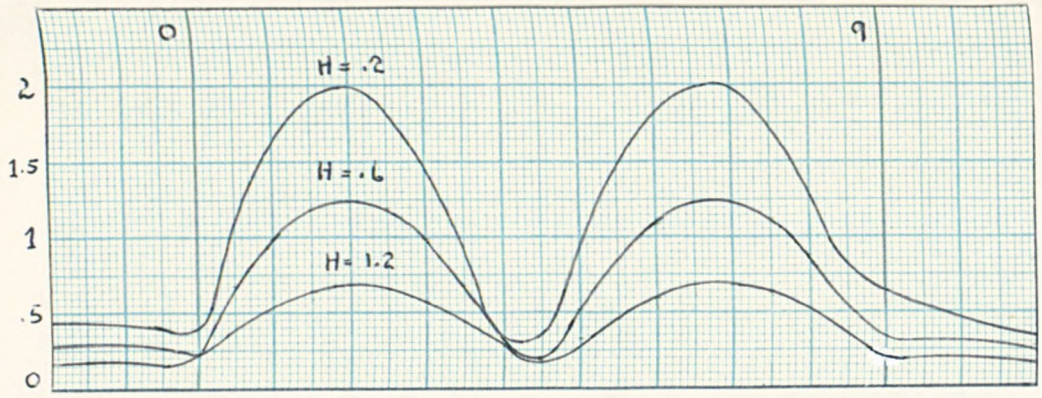
0
9
H = .2
H = .6
H = 1.2
2
1.5
1
.5
0

(a) B2

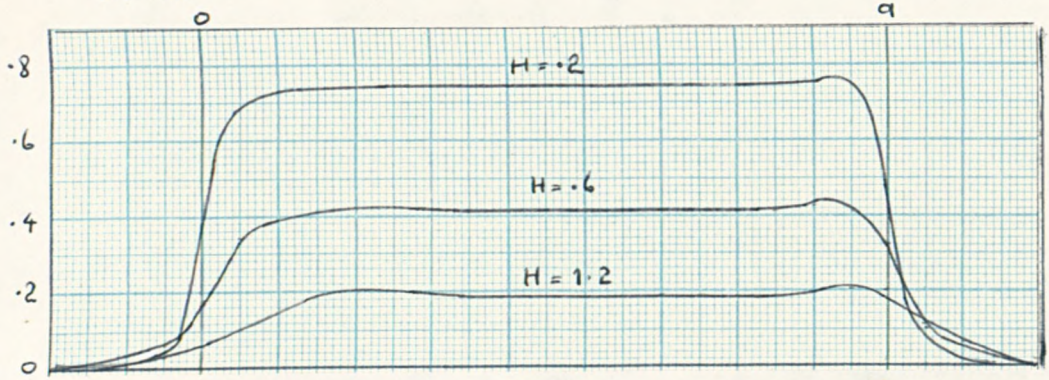
0
9
H = .2
H = .6
H = 1.2
.8
.6
.4
.2
0

(b) B3

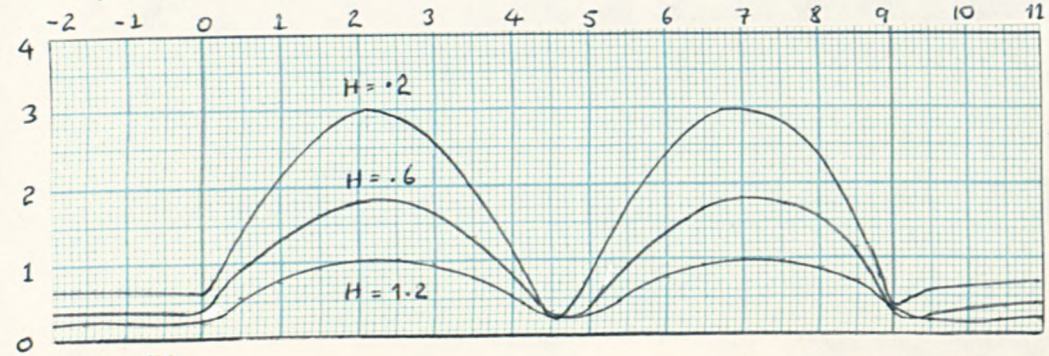
-2 -1 0 1 2 3 4 5 6 7 8 9 10 11 y
H = .2
H = .6
H = 1.2
4
3
2
1
0

(c) J1

Fig. 9.11 The Induced EM Field. Case P

Variation with H (z=0)

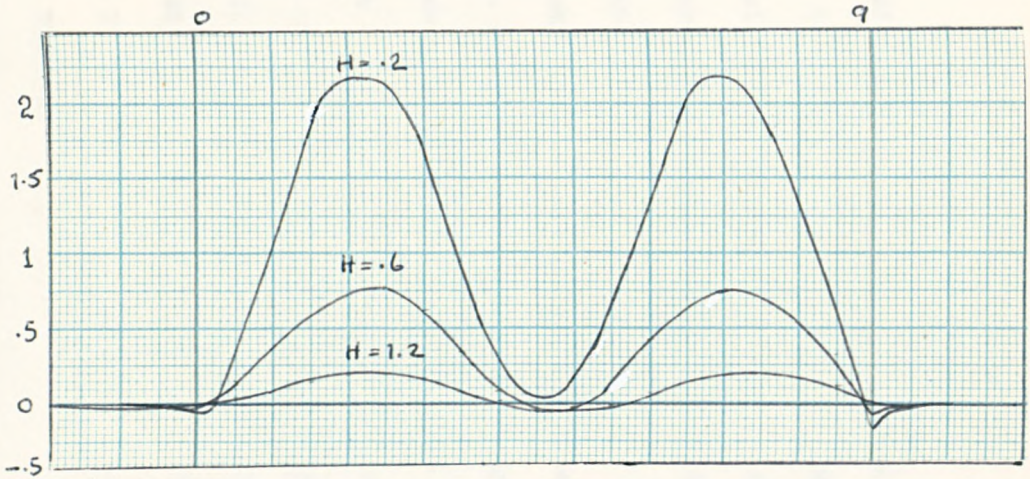

(d) F2

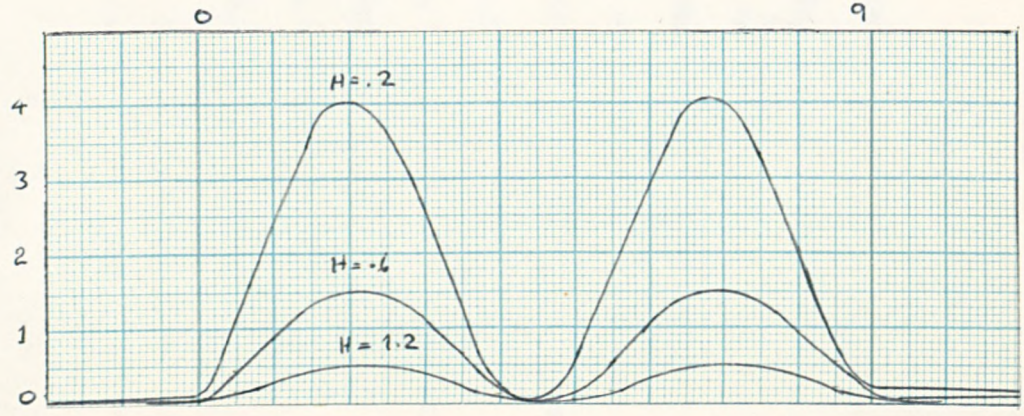

(e) (→ F3

Discussion of the results: The z and h variation of the EM fields in figures 9.8 to 9.11 is largely self explanatory. A good agreement in terms of spatial variation and magnitude is found between the case S results of figure 9.8 and figures 7.4 to 7.6 of chapter 7. (Note that a factor of π occurs when relating these two sets of results, because of the assumed dimensionless forms). The applied uniform stator surface current density induces a uniform and well-behaved EM field in the conducting secondary. However if each coil in the same phase is connected in parallel (case P) so as to produce a uniform normal magnetic induction, the stator surface current density is forced to assume a form similar to that of a single coil placed along the length of the stator.

This explains the features of J_1 and J_2 in the case P results of figures 9.9 to 9.11. Note that the magnitude of the potential levitating force is twice that of the pumping force. It is apparent that parallel connection will induce a large amount of circulation in liquid conductor secondaries; thus a parallel connected SLIP has greater potential for stirring (but not pumping) than its series wound counterpart.

Calculations were also performed to assess the contribution from the imposed shear flow to the induced electric currents and magnetic induction. The case S results are shown in figure 9.12 for several values of z . Great difficulty with convergence was encountered close to the end regions $y=0$ and $y=q$, (the graphs show the result of including fifteen roots of $\Delta_s(q)$). Physically, because the fields are obtained from the curvature produced when the EM field (induced by the stator excitation) is bent to one side of the stator axis, we would expect a gradual decrease in magnitude of all the extra components towards the ends of the excitation where the magnetic field lines are both less dense and less 'taut'. The dashed lines in figure 9.12 are extrapolations of the results based on the above reasoning. The calculated results do, however, give a true indication of the field variation in the central regions of the excitation.

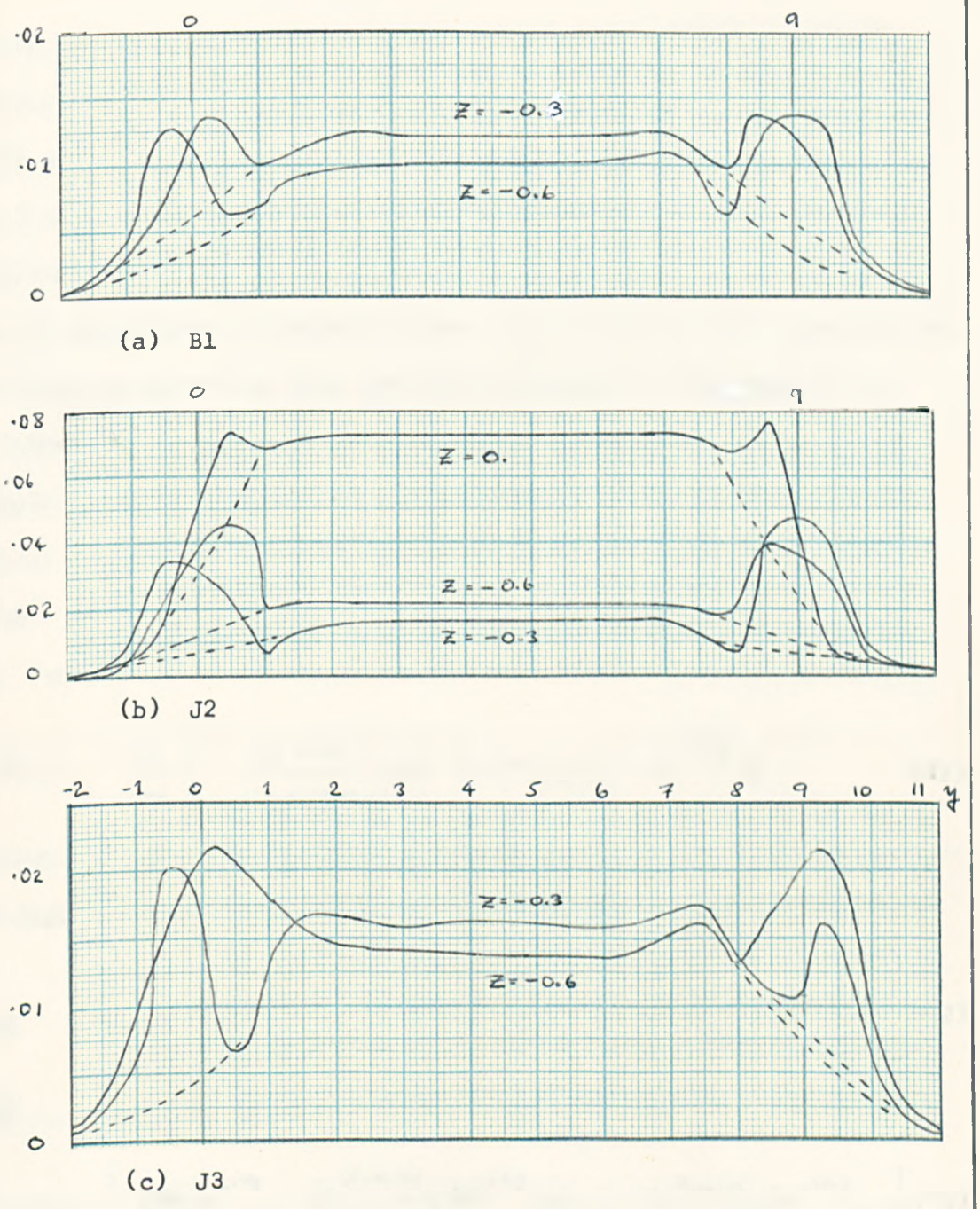

Fig. 9.12 The EM Field Induced by the Applied Shear Flow (H= .2)

Because $J1 = o(1)$, it is clear that we require $R_{m1} > 10$ for the effect of an imposed shear flow to become noticeable.

9.4.2 Sudan's Compensating Method. The compensating method proposed by SUDAN (1963) is to modify the transformation of the stator surface current density (for the case S solutions) to remove the two zero-order modes of the Fourier series solutions for the EM field, (59) to (64). The

zero order modes arise from the solution of $\Delta_s(q)=0$ and are given in figures 9.4 and 9.5. The contribution from these modes is removed if the transform of the stator surface current density, $K_s\hat{S}$ (where $\hat{S}$ is given by (52)) is made to include the term $(q-\psi_0^+)(q-\psi_0^-)$ in the numerator. The resulting expression needs a pole of order q^3 in the denominator to satisfy the conditions of Jordan's Lemma. The actual current distribution is then given by inverting this modified expression. The evaluation of the subsequent integral is easily performed since the contour contains only simple poles on the real axis if the denominator is taken as $(q-\alpha)(q-\alpha_1)(q-\alpha_2)$, where α_1 and α_2 are (real) wave numbers to be specified. We thus require the complex stator surface current density $K_s(y)$ to be

$$K_s(y) = \frac{K_s}{2\pi i}\int_{-\infty}^{\infty} \frac{(e^{ib(q-\alpha)}-1)}{(q-\alpha)(q-\alpha_1)(q-\alpha_2)}\cdot(q-\psi_0^+)(q-\psi_0^-)\cdot e^{-iqy}\,dq \qquad (71)$$

This integral is evaluated similarly to (53) and (54). The resulting current distribution is given by; (writing $Q(q)=(q-\psi_0^+)(q-\psi_0^-)$):

Region A
$$K_s(y) = \tfrac{1}{2}K_s\left\{\frac{(e^{ib(\alpha_1-\alpha)}-1)e^{-i\alpha_1 y}}{(\alpha_1-\alpha)(\alpha_1-\alpha_2)}Q(\alpha_1) + \frac{(e^{ib(\alpha_2-\alpha)}-1)e^{-i\alpha_2 y}}{(\alpha_2-\alpha)(\alpha_2-\alpha_1)}Q(\alpha_2)\right\} \qquad (72)$$

Region B
$$K_s(y) = \tfrac{1}{2}K_s\left\{\frac{2Q(\alpha)e^{-i\alpha y}}{(\alpha-\alpha_1)(\alpha-\alpha_2)} + \frac{(e^{ib(\alpha_1-\alpha)}+1)e^{-i\alpha_1 y}}{(\alpha_1-\alpha)(\alpha_1-\alpha_2)}Q(\alpha_1) + \frac{(e^{ib(\alpha_2-\alpha)}+1)e^{-i\alpha_2 y}}{(\alpha_2-\alpha)(\alpha_2-\alpha_1)}Q(\alpha_2)\right\} \qquad (73)$$

Region C
$$K_s(y) = (-)\times(72)$$

Equations (72) and (73) represent the superposition of three separate travelling wave windings with wave numbers α , α_1 and α_2 . The magnitude of each winding is obtained from consideration of individual terms. From practical considerations we require $K(y)$ to be zero in regions A and C (when $y<0$ and $y>b$). Thus we require

$$\left.\begin{aligned} e^{ib(\alpha_1-\alpha)}-1=0 \quad &\Rightarrow \alpha_1 = \alpha + \frac{2m\pi}{b} \qquad m \text{ integer } (\neq 0)\\ e^{ib(\alpha_2-\alpha)}-1=0 \quad &\Rightarrow \alpha_2 = \alpha + \frac{2n\pi}{b} \qquad n \text{ integer } (n\neq m \text{ or } 0)\end{aligned}\right\} \qquad (74)$$

The modified form of $K_s(y)$ can now be substituted in (59) to (64) which can be evaluated as before. In theory, any of the Fourier series modes can be removed by the above method, but in practice the physical dimensions of the machine are the deciding influence. Without further analysis little can be inferred about the optimum choice of m and n. However, in their investigation of a slit channel DLIP MHD generator, PIERSON (1970) and SUDAN (1963) use $m=-1$, $n=1$. For the float bath linear motor $b \sim 8\tau$ and so (with $\alpha = \pi/\tau$) $\alpha_1 \sim 0.75$ and $\alpha_2 \sim 1.25$ for these values of m and n. Further investigation on the effect of the values of m and n on the pumping ability of the SLIP is required. However, from the results of chapter 3 it is clear that an increase in flow rate occurs for an increase in R_m $(= V_s L/\alpha\eta)$, the magnetic Reynolds number based on the synchronous velocity of the excitation. Thus we require wave numbers smaller than α for an increase in the pumping ability of a compensated SLIP, and wave numbers greater than α for an increase in the stirring ability of a compensated SLIP.

We note that Sudan's method of end compensation can only be used with versatility when there is more than one slot per pole.

9.5 Infinite Length, Finite Width Excitation.

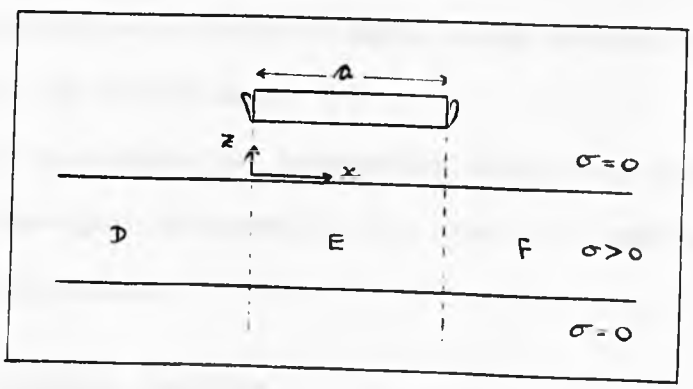

Fig. 9.13 Section in the (x,z)-plane

A section through the configuration of figure 9.1 is shown in figure 9.13. We consider an excitation finite in width but infinite in length (so $\frac{\partial}{\partial y} = -i\alpha$ since all y variation is contained in the travelling wave).

The function $S_y(y,b)$ (the second of (19)), equals e^{-iqy} when $b \to \infty$, so $\hat{S}_y = 2\pi\,\delta(q-\alpha)$. Thus from (21) we have $\hat{S} = 2\pi\,\delta(q-\alpha)\,\hat{S}_x(p,a)$ where (from the first of (22))

$$\hat{S}_x(p,a) = (e^{ipa}-1)/ip \tag{75}$$

Applying the inverse transformation (10) to (40) and (41) with the above value of $\hat{S}$ we obtain the following integral expressions for the EM field induced in the electrical conductor (case S solutions only):

$$\underline{B} = \mu_0 K_s\, e^{-i\alpha y} \int_{-\infty}^{\infty} \frac{[p\pi, \alpha\pi, i\kappa^2\Phi]}{\alpha\Delta_s} \cdot \hat{S}_x\, e^{-ipx}\, dp \tag{76}$$

$$\underline{J} = \mu K_s\, e^{-i\alpha y} \int_{-\infty}^{\infty} \frac{[-\alpha, p, 0]}{\kappa\Delta_s} \cdot (\gamma^2-\kappa^2)\,\Phi\,\hat{S}_x\, e^{-ipx}\, dp \tag{77}$$

where $\kappa^2 = \alpha^2 + p^2$ and $\gamma^2 = \kappa^2 + i(R_0 - \kappa R_{m2})$ (78)

We can evaluate (76) and (77) using contour integration in the complex p-plane as in §9.4. We identify three regions of interest; region D ($x<0$) region E ($0<x<a$) and region F ($x>a$) . As before the choice of contour for each region is made to ensure the applicability of Jordan's Lemma. However we see that there are branch points at $\kappa=0$, ie: $p=\pm i\alpha$, and a branch line must be constructed, (see §7.4), joining $p=i\alpha$ with $p=-i\alpha$. Thus we not only require a summation over the residues of but also the evaluation of a finite integral which arises from a line integration around the branch loop.

We choose not to perform the integration above since extensive results for this have been obtained in §7.3 when $h=0$ and the conductor is treated as a half space.

9.6 The Induced Velocity Profiles.

The problem of viscous flow into a finite applied EM field is extremely complex. Some progress has been made with Hartmann-type flow (see §1.8) but apart from the work of KOZYRENKO (1971 a, 1971 b) we are not aware of any work with finite travelling wave fields.

Below we give a brief order-of-magnitude argument for the expected flow development.

9.6.1 Finite Length, Infinite Width Excitation.

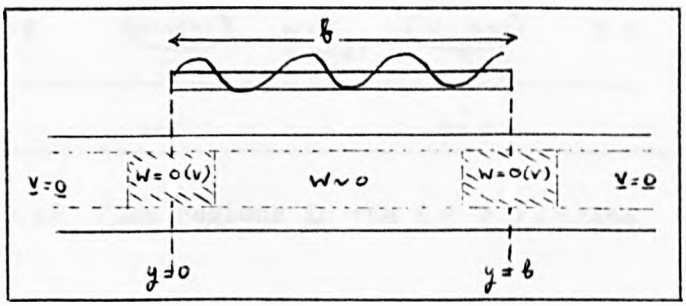

Fig. 9.14 Flow regions in the (y,z)-plane

Consider the flow of a viscous conducting liquid into the SLIP shown in figure 9.14. We can separate the flow into thin boundary layers close to the surfaces $z=o$ and $z=-1$, and a free stream in the centre of the channel. In the boundary layers we can assume the velocity is one dimensional (parallel with the y axis) and of small magnitude. Over most of the free stream flow, the velocity may also be considered one dimensional and parallel with the y axis. However, close to the entrance and exit regions, $y=o$ and $y=b$ respectively, there is a rapid change in the velocity with y. From the continuity equation $\nabla.\underline{v}=0$ we see that $\frac{\partial v}{\partial y}+\frac{\partial w}{\partial z}=0$ and so since $o(\frac{\partial}{\partial y})\sim o(\frac{\partial}{\partial z})$, (see §5.3) we find $w=o(v)$ there. Thus circulation in the (y,z) plane occurs mainly in the entrance and exit regions of the SLIP. The extent of this circulation can be estimated from the graphs in figure 9.8, the results of chapter 5 or from the Fourier series solutions of §9.4. Using the latter our estimate of the $1/e$ folding length for the induced body forces (and thus the circulating flow) is $1/\mathcal{R}\{24.3\}$ for the entrance end and $1/\mathcal{R}\{24.7\}$ for the exit end (see figure 9.14).

9.6.2. Finite Width, Infinite Length Excitation.

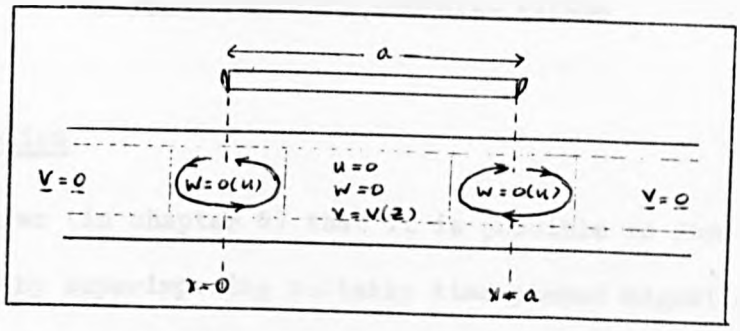

Fig. 9.15 Flow regions in the (x, z)- plane

Following §9.6.1 we can identify a free stream and a boundary layer for the flow (figure 9.15). In the central region of the SLIP the fluid is induced to move along the y axis (into the paper) with a velocity dependent only on z . From $\nabla \underline{v} = 0$ we have $\frac{\partial u}{\partial x} + \frac{\partial w}{\partial z} = 0$ and so $w = o(u)$ in the regions where $\frac{\partial}{\partial x} = o(\frac{\partial}{\partial z})$, (at $x=0$ and $x=a$). The width of these circulatory regions is of the same order as the width of the regions in §9.6.1. We conclude that the conducting liquid is drawn in from the regions outside the excitation (where $\underline{v} = \underline{0}$) towards the central axis where $V(z)$ dominates. The flow pattern would resemble a helical spiral (figure 9.16).

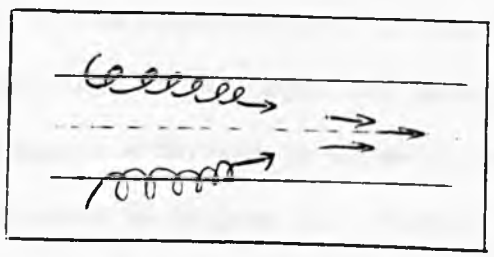

Fig. 9.16 Spiral flow pattern.

10. ELECTROMAGNETIC INDUCTION IN A UNIFORM PLANE SHEET BY AN OSCILLATING MAGNETIC DIPOLE

10.1 Introduction

We have shown (in chapter 6) that it is possible to form a travelling magnetic field by superimposing suitably time-phased magnetic sources. Thus providing we can neglect mutual induction effects between adjacent teeth it is possible to deduce the total EM field of a LIM from a knowledge of the EM field produced by a solitary tooth. The field of a single tooth (which resembles that of a bar magnet) may be approximated by (for example) the superposition of magnetic dipole sources over a tooth volume.

The EM field produced by a magnetic dipole source placed in free space is well known, but when electric conductors are introduced into the configuration the source field is modified by the secondary fields generated in the conductors, and simple analytical expressions for the total EM field are difficult to obtain. For the SLIM/SLIP configuration, the secondary can be represented by a conducting slab of infinite extent, and the primary can be modelled by placing the magnetic dipole above the slab with its axis normal to the slab surface. If the slab is of finite depth continuity conditions at its upper and lower surfaces must be considered before complete solutions to Maxwell's equations can be obtained. This problem is considered in chapter 11. Here we consider the physically simpler and more tractable problem of a slab with conductivity σ and thickness d, where d is allowed to become infinitely small but $\lim_{d \to 0} (\sigma d) = \kappa$, where κ is the integrated conductivity (which is non-zero). This 'thin sheet' configuration is applicable to problems where the skin depth of the induced EM field is greater than the slab thickness.

The most important work on thin sheets was that of PRICE (1949) who obtained the boundary condition at the surface of the sheet in terms

of the non-uniform distribution of conductivity and the scalar magnetic potentials of the inducing and induced fields. Other methods and further references are given in the review of ASHOUR (1973). The problem considered here and the solutions we obtain are not new - RIKITAKE (1966) derives integral expressions for the magnetic potential using Price's method - but our solutions are obtained using a different method of analysis. Using this method, which was first suggested by RODEN (1964) and later modified by HUTSON et al (1972), we derive a linear integral equation connecting the electric current density at the surface of the conductor with the inducing magnetic potential. Integral solutions to this equation for the current density are obtained using Fourier transformation techniques.

10.2 The Integral Equation

The method of derivation is that given in Hutson et al. We consider a particular result of their more general analysis. An integral solution is obtained for the EM field produced by an oscillating vertical magnetic dipole placed above a thin sheet of constant integrated conductivity occupying the plane $z=0$ of cartesian coordinate space, (figure 10.1) The z axis is chosen so as to point into the conductor.

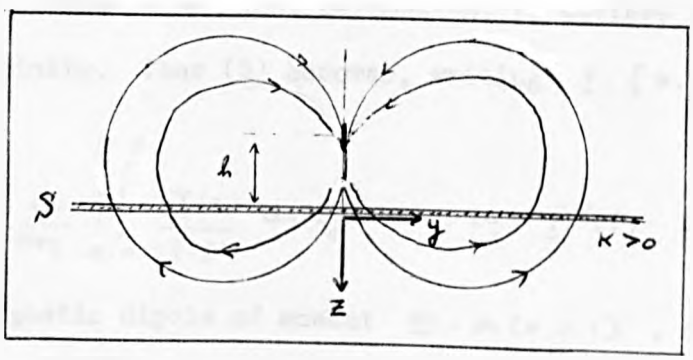

Fig. 10.1 Thin Sheet Model

Suppose $\underline{A}^i(r,t)$ is the vector potential of the induced magnetic induction vector $\underline{B}^i(r,t)$ defined such that

$$\underline{B}^i = \nabla \wedge \underline{A}^i \quad \text{and} \quad \nabla . \underline{A}^i = 0 \qquad (1)$$

Denoting the scalar electric potential by $\psi(\underline{r},t)$ the electric field $\underline{\mathcal{E}}(\underline{r},t)$ is given by

$$\underline{\mathcal{E}} = -\frac{\partial \underline{\mathcal{A}}^i}{\partial t} - \frac{\partial \underline{\mathcal{A}}^\infty}{\partial t} - \kappa \nabla \psi \tag{2}$$

where $\underline{\mathcal{A}}^\infty(\underline{r},t) = \underline{A}^\infty(\underline{r},t)$ is the magnetic vector potential of the dipole field in absence of the conductor S. We assume all the EM field solutions have the same time variation as the source and write: $\underline{\mathcal{B}}(\underline{r},t) = \underline{B}(\underline{r})e^{i\omega t}$, $\underline{\mathcal{E}}(\underline{r},t) = \underline{E}(\underline{r})e^{i\omega t}$, $\underline{\mathcal{J}}(\underline{r},t) = \underline{J}(\underline{r})e^{i\omega t}$, $\underline{\mathcal{A}}(\underline{r},t) = \underline{A}(\underline{r})e^{i\omega t}$ and $\psi(\underline{r},t) = \psi(\underline{r})e^{i\omega t}$. We similarly define the fields with superscript i and ∞.

Using Ohm's law (1.7) the current density $\underline{J}(\underline{r})$ in S becomes

$$\underline{J} = \kappa \underline{E} = -i\omega\kappa(\underline{A}^i + \underline{A}^\infty) - \kappa \nabla \psi \tag{3}$$

We also have (FERRARO, 1954)

$$\underline{A}^i(\underline{r}) = \frac{\mu_0}{4\pi} \iint_S \frac{\underline{J}(\underline{r}')}{|\underline{r}-\underline{r}'|} ds' \tag{4}$$

where the integration is with respect to the primed variable. Combining (3) and (4) we have the result (writing $\eta = \frac{1}{\kappa\mu_0}$)

$$\underline{J}(\underline{r}) + \frac{i\omega}{4\pi\eta} \iint_S \frac{\underline{J}(\underline{r}')}{|\underline{r}-\underline{r}'|} ds' + \kappa \nabla \psi(\underline{r}) = -i\omega\kappa \underline{A}^\infty(\underline{r}) \quad \text{in } S \tag{5}$$

For an infinitesimal horizontal current loop (vertical magnetic dipole) we have $J_3 = E_3 = A_3^\infty = 0$ and (5) gives $\frac{\partial \psi}{\partial z} = 0$. From (3) since $\nabla \cdot \underline{J} = 0$ we have $\nabla^2 \psi = 0$, and so ψ must be constant to satisfy the decay conditions at infinity. Thus (5) becomes, writing $\underline{r} = [x,y,z]$, $\underline{r}' = [x',y',z']$:

$$\underline{J}(\underline{r}) + \frac{i\omega}{4\pi\eta} \int_{-\infty}^{\infty}\int_{-\infty}^{\infty} \frac{\underline{J}(\underline{r})}{|\underline{r}-\underline{r}'|} dx'dy' = -i\omega\kappa \underline{A}^\infty(\underline{r}) \tag{6}$$

For a vertical magnetic dipole of moment $\underline{m} = m[0,0,1]$, situated at the position $[0,0,-h]$ in free space, the result of Ferraro (p gives

$$\underline{A}^\infty(\underline{r}) = m[y,-x,0] \Big/ \left\{x^2+y^2+(z+h)^2\right\}^{3/2} \tag{7}$$

This choice of $\underline{m}$ corresponds to a magnetic dipole orientated towards the

conductor when $t = 0$.

Equation (6) is an integral equation of the Fredholm type with a symmetric kernel. We now derive integral solutions to (6) for $\underline{J}(t)$ using the Fourier transformation technique.

10.3 Solutions in Transform Space

From (1.32) and (1.33) we define the two dimensional Fourier transformation and inverse transformation of the function $M(x,y,z)$ as, respectively,

$$\mathcal{F}_2^+\left\{M(x,y,z)\right\} = \hat{M}(p,q,z) = \int_{-\infty}^{\infty}\int_{-\infty}^{\infty} M(x,y,z)\, e^{i(px+qy)}\, dx\, dy \tag{8}$$

$$\mathcal{F}_2^-\left\{\hat{M}(p,q,z)\right\} = M(x,y,z) = \frac{1}{(2\pi)^2}\int_{-\infty}^{\infty}\int_{-\infty}^{\infty} \hat{M}(p,q,z)\, e^{-i(px+qy)}\, dp\, dq \tag{9}$$

The two dimensional form of the convolution result (1.35) is

$$\mathcal{F}_2^-\left\{\hat{M}(p,q,z)\,\hat{N}(p,q,z)\right\} = \int_{-\infty}^{\infty}\int_{-\infty}^{\infty} M(x',y',z)\, N(x-x', y-y', z)\, dx'\, dy' \tag{10}$$

Transforming (6) using (8) and relation (10), we find

$$\hat{\underline{J}} + \frac{i\omega}{4\pi\eta}\cdot\hat{\underline{J}}\cdot\mathcal{F}_2^+\left\{\frac{1}{|r|}\right\} = -i\omega\chi\,\hat{\underline{A}}^{\infty} \tag{11}$$

The solution for $\hat{\underline{J}}$ in (11) may be written in two ways:

$$\hat{\underline{J}} = \left[\frac{-i\omega\chi\,\hat{\underline{A}}^{\infty}}{1 + \frac{i\omega}{4\pi\eta}\mathcal{F}_2^+\left\{\frac{1}{|r|}\right\}}\right] \tag{12}$$

$$\text{or} \qquad \hat{\underline{J}} = -i\omega\chi\,\underline{A}^{\infty} + \left[\frac{(i\omega\chi)(i\omega/4\pi\eta)\,\hat{\underline{A}}^{\infty}\,\mathcal{F}_2^+\left\{\frac{1}{|r|}\right\}}{1 + \frac{i\omega}{4\pi\eta}\mathcal{F}_2^+\left\{\frac{1}{|r|}\right\}}\right] \tag{13}$$

The form of (13) makes clear the relationship: total current = source currents + induced currents; however, for ease of analysis we use the result of (12).

Transforming (7) using (8) we have

$$\hat{\underline{A}}^{\infty}(p,q,z) = m\int_{-\infty}^{\infty}\int_{-\infty}^{\infty} \frac{[y,-x,0]\, e^{i(px+qy)}}{\left\{x^2+y^2+(z+h)^2\right\}^{3/2}}\, dx\, dy \tag{14}$$

The evaluation of the integral on the right of (14) is accomplished using symmetry arguments for the reduction of the exponential factor in the kernel to trigonometric functions, and the following integral results given in the text of BATEMAN (1954):

$$\int_0^\infty \frac{\cos px\, dx}{\{x^2+y^2+z^2\}^{3/2}} = \frac{p}{(y^2+z^2)^{1/2}} \cdot K_1\left(p\sqrt{y^2+z^2}\right) \qquad \text{(p.11)}$$

$$\int_0^\infty \frac{y\, K_1(p\sqrt{y^2+z^2})}{(y^2+z^2)^{1/2}} \sin qy\, dy = \frac{\pi q\, e^{-zK}}{2pK} \qquad \text{(p.112)}$$

where $$K^2 = p^2+q^2 \qquad (15)$$

and $K_1(\zeta)$ is Bessel's modified function of the second kind of order unity.

We find $$\hat{\underline{A}}^\infty = \frac{2i\omega\pi}{K}\,[q, -p, 0]\, e^{-K(z-h)} \qquad (16)$$

We also require the transformation of $\frac{1}{|\xi|}$. Using (8) we have

$$\mathcal{F}_2^+\left\{\frac{1}{|\xi|}\right\} = \int_{-\infty}^{\infty}\int_{-\infty}^{\infty} \frac{e^{i(px+qy)}}{(x^2+y^2+z^2)^{1/2}}\, dx\, dy \qquad (17)$$

Using symmetry arguments for the kernel of (19) and the following integral results from Bateman

$$\int_0^\infty \frac{\cos px\, dx}{(x^2+y^2+z^2)^{1/2}} = K_0\left(p\sqrt{y^2+z^2}\right) \qquad \text{(p.11)}$$

$$\int_0^\infty K_0(p\sqrt{y^2+z^2}) \cos qy\, dy = \frac{\pi}{2}\cdot\frac{e^{-Kz}}{K} \qquad \text{(p.49)}$$

where K is given in (15) and $K_0(\zeta)$ is Bessel's modified function of the second kind of zero order; (17) becomes:

$$\mathcal{F}_2^+\left\{\frac{1}{|\xi|}\right\} = \frac{2\pi}{K} e^{-Kz} \qquad (18)$$

Substituting (18) and (16) in (12) we obtain the following result for the transformation of the electric current density:

$$\hat{\underline{J}} = 2\pi\kappa\omega m\, [q, -p, 0]\, e^{-hK}/(K+i\beta) \qquad (19)$$

where we have written $\beta = \omega/2\eta$. Transforming (4) using (8) we find

$$\hat{\underline{A}}^i = \frac{\mu_0}{4\pi}\cdot\hat{\underline{J}}\cdot\mathcal{F}_2^+\left\{\frac{1}{|\xi|}\right\} \qquad (20)$$

Substituting (18) and (19) in (20) we find

$$\hat{\underline{A}}^i = \mu_0 \pi . \chi \omega m . \frac{[q, -p, 0]}{\kappa(\kappa + i\beta)} . e^{-\kappa(h+z)} \tag{21}$$

The induced magnetic induction $\underline{B}^i = \nabla \wedge \underline{A}^i$. It is easy to show using (21), that

$$\underline{B}^i = (\pi \mu_0 \chi \omega m) . \frac{[-p, -q, i\kappa]}{(\kappa + i\beta)} . e^{-\kappa(h+z)} \tag{22}$$

10.4 Solutions in Real Space

The magnetic induction vector $\underline{B}$ for the total field is given by

$$\underline{B} = \underline{B}^i + \underline{B}^\infty \tag{23}$$

where $\underline{B}^\infty = \nabla \wedge \underline{A}^\infty$ becomes, using (7),

$$\underline{B}^\infty = m \left[-3x(z+h), -3y(z+h), (x^2+y^2) - 2(z+h)^2\right] \left\{x^2+y^2+(z+h)^2\right\}^{-3/2} \tag{24}$$

Inverting (19) and (22) using (9) we find

$$\underline{J} = \frac{m \chi \omega}{2\pi} \int_{-\infty}^{\infty}\int_{-\infty}^{\infty} \frac{[q, -p, 0]}{(\kappa + i\beta)} . e^{-\kappa h} . e^{-i(px+qy)} \, dp \, dq \tag{25}$$

$$\underline{B}^i = \frac{\mu_0 \chi \omega m}{4\pi} \int_{-\infty}^{\infty}\int_{-\infty}^{\infty} \frac{[-p, -q, i\kappa]}{(\kappa + i\beta)} . e^{-\kappa(h+z)} . e^{-i(px+qy)} \, dp \, dq \tag{26}$$

Unfortunately is does not appear possible to write the integral expressions in (25) and (26) in terms of known functions. However, some information can be gained using the analyses below.

10.4.1 Series Expansion Method. If β is assumed large (implying a large integrated conductivity since $\beta = \omega \mu_0 \chi / 2$), the following result can be used:

$$(\kappa + i\beta)^{-1} = (i\beta)^{-1} \sum_{n=0}^{\infty}{}' \kappa^n (-i\beta)^{-n} \tag{27}$$

Substituting (27) in (25) and (26) using the following integral results (Bateman)

$$\int_0^\infty e^{-\kappa z} \cos px \, . \, dp = zq \, . \, K_1 \left(q\sqrt{x^2+z^2}\right) / (x^2+z^2)$$

$$\int_0^\infty q \, K_1\left(q\sqrt{x^2+z^2}\right) \cos qy \, dq = \frac{\pi}{2} \, . \, \frac{(x^2+z^2)^{1/2}}{(x^2+y^2+z^2)^{1/2}}$$

the solutions for $\underline{J}$ and $\underline{B}^i$ may be written:

$$\mu_0 \underline{J} = 6m\,[y,-x,0] \sum_{n=0}^{\infty}{}' (i\beta)^{-n} \frac{\partial^{(n)}}{\partial h^{(n)}} \left\{ \frac{h}{(x^2+y^2+h^2)^{5/2}} \right\} \tag{28}$$

$$\underline{B}^i = m \sum_{n=0}^{\infty}{}' (i\beta)^{-n} \frac{\partial^{(n)}}{\partial h^{(n)}} \left\{ \frac{3\,[x,y,0]\,(h+z)}{(x^2+y^2+(z+h)^2)^{5/2}} - [0,0,\tfrac{\partial}{\partial x}]\,\frac{h+z}{(x^2+y^2+(h+z)^2)^{3/2}} \right\} \tag{29}$$

The total magnetic induction is then given by (23). Results (28) and (29) are exact but, unfortunately, convergence is extremely slow. For a first order approximation $(n=0)$ we see that the total normal magnetic field $(\underline{B}^i+\underline{B}^\infty).\underline{e}_3$ equals zero on $z=0$, as we would expect since this is the infinite conductivity case $(\beta>>1)$. In this case the discontinuity in the tangential magnetic induction at S' accounts for the surface current density and the boundary condition (1.38) is satisfied. The behaviour of the electric current density is dominated by that of its zero mode. From (28) we see that along $x=0$ and $y=0$ the electric current is at its maximum magnitude when $y=\pm h/2$ and $x=\pm h/2$ respectively. These points correspond to regions where the magnetic field spontaneously forms inside the conducting sheet at a time $t=0^+$ (see chapter 12) and their position agrees with the physical reasoning of that chapter.

For a finite β further terms must be included in the evaluation of $\underline{J}$ and $\underline{B}$ and the series must be summed numerically. This is not performed here.

10.4.2 Simplified Solutions. Consider the function $M(x,y,z)$; if $\hat{M}(p,q,z) \equiv \hat{M}(K,z)$ where K is given by (15) we can derive the result (see Appendix II):

$$M(x,y,z) = \frac{1}{(2\pi)^2}\int_{-\infty}^{\infty}\int_{-\infty}^{\infty} \hat{M}(K,z)\,e^{-i(px+qy)}\,dp\,dq = \frac{1}{2\pi}\int_0^{\infty} \hat{M}(K,z).K\,J_0(K\rho)\,dK \tag{30}$$

where $J_0(K\rho)$ is Bessel's function of order zero, and $\rho^2 = x^2+y^2$. If the transformed solutions are of the form $ip\,\hat{M}(K,z)$ or $iq\,\hat{M}(K,z)$ we find their inverse can be written as in the right of (30) but with $J_0(K\rho)$ replaced by $J_1(K\rho)$, Bessel's function of order unity (see Appendix II).

However, using the operator notation $\frac{\partial}{\partial x} = -ip$, $\frac{\partial}{\partial y} = -iq$ and the form of (30), the results (25) and (26) can be reduced to:

$$\mu_0 \underline{I} = 2m\beta i \left[\frac{\partial}{\partial y}, -\frac{\partial}{\partial x}, 0 \right] \int_0^\infty \frac{k . J_0(k\rho) e^{-kh}}{(k+i\beta)} dk \qquad (31)$$

$$\underline{B}' = m\beta i \left[\frac{\partial^2}{\partial x \partial z}, \frac{\partial^2}{\partial y \partial z}, -\left(\frac{\partial^2}{\partial x^2} + \frac{\partial^2}{\partial y^2}\right) \right] \int_0^\infty \frac{J_0(k\rho) e^{-k(h+z)}}{(k+i\beta)} dk \qquad (32)$$

The use of operators in (31) and (32) ensures the convergence of the integrals. It is clear that we require an evaluation of the integral I , where

$$I(h) = \int_0^\infty \frac{J_0(k\rho) e^{-kh}}{k+i\beta} . dk \qquad (33)$$

Integrals of this type have been encountered in chapter 8. It does not seem possible to write I in terms of known functions - except for particular values of β and h . We can expand $J_0(k\rho)$ as a power series and integrate term by term but this leads to a summation of sine and cosine-integral functions. A numerical approach is possible using Gaussian quadrature over $[0,\infty)$. Alternatively I can be reduced using the method of Appendix II.

Because we require simple results (a full numerical evaluation of the EM field of a SLIM is performed in chapter 11) we merely consider the behaviour of I when β is large and h is small, corresponding to a dipole source placed close to a sheet of large conductivity. We have the result

$$I(0) = \int_0^\infty \frac{J_0(k\rho)}{(k+i\beta)} dk = H_0(i\beta\rho) - Y_0(i\beta\rho) \qquad \text{(OBERHETTINGER p.6)}$$

$$= K_0(\beta\rho) - i\left\{ I_0(\beta\rho) - L_0(\beta\rho) \right\} \qquad (34)$$

where $H_0(\xi)$ is Struve's function of order zero; $Y_0(\xi)$, $K_0(\xi)$ and $I_0(\xi)$ are Bessel functions of order zero and $L_0(\xi)$ is Struve's modified function of order zero. Basic definitions and recurrence relations for these functions are given in Appendix I ; further relations are given in the texts of ABRAMOWITZ and STEGUN (1965) and GRADSHTEYN (1965). From Appendix we have the asymptotic results ($\beta\rho >> 1$)

$$K_0(\beta\rho) \sim \sqrt{\frac{\pi}{2}} \cdot \frac{e^{-\beta\rho}}{(\beta\rho)^{1/2}} \qquad I_0(\beta\rho) - K_0(\beta\rho) \sim \left\{ \frac{1}{\beta\rho} - \frac{1}{(\beta\rho)^3} \right\} \cdot \frac{\pi}{2} \qquad (35)$$

We can now obtain expressions for the asymptotic behaviour (β large, $h < \frac{1}{\beta\ell}$) of $\underline{J}$ and $\underline{B}^i$ on S' by substituting (34) in (31) and (32), using (35) and carrying out the differentiation. We find

$$\mu_0 \underline{J} \sim 2m\beta^2 [y, -x, 0] \left\{ \sqrt{\frac{\pi\beta}{2}} \frac{e^{-\beta\ell}}{\rho^{1/2}} - i \frac{3\pi}{2\beta^5\rho^5} \right\} \tag{36}$$

$$\underline{B}^i \sim m\beta^2 [x, y, 0] \left\{ \sqrt{\frac{\pi\beta}{2}} \cdot \frac{e^{-\beta\ell}}{\rho^{1/2}} - i \frac{3\pi}{2\beta^5\rho^5} \right\}$$
$$- m\beta [0, 0, 1] \left\{ \frac{\pi}{2\beta\rho^3} + i\sqrt{\frac{\pi\beta}{2}} \cdot \frac{e^{-\beta\ell}}{\rho^{1/2}} \right\} \tag{37}$$

Results (36) and (37) describe the decay of $\underline{J}$ and $\underline{B}^i$ at distances away from the dipole source. The total magnetic induction is given by (23).

Because the physical variation of the electric current density and magnetic induction is described by the form of $\mathcal{R}\{\underline{J} e^{i\omega t}\}$ and $\mathcal{R}\{\underline{B} e^{i\omega t}\}$ respectively, we see that $\mathcal{R}\{\underline{J}\}$ and $\mathcal{R}\{\underline{B}\}$ describe the field at $t = 0$ whilst $\mathcal{I}\{\underline{J}\}$ and $\mathcal{I}\{\underline{B}\}$ describe the field at $t = \frac{\pi}{2\omega}$. From (36) and (37) we see that the induced currents and tangential magnetic induction decay exponentially in S' at $t = 0$ when the source field is at its maximum. When $t = -\frac{\pi}{2\omega}$ the source field is momentarily zero and these fields decay inversely proportional to (distance)^4. Similar arguments may be applied to the normal magnetic induction. As in §10.4.1 , the total normal magnetic induction on S' is zero at $t = 0$. This agrees with physical reasoning since we have only considered the first term in the β -expansion and this corresponds to the infinitely conducting case.

A full consideration of the behaviour of the magnetic field produced by an oscillating magnetic dipole placed above a plane conductor is given in chapter 12.

11. A COMPLETE LINEAR MOTOR ANALYSIS

11.1 Introduction

Using a more detailed model than in previous chapters we obtain integral expressions for the EM field induced in a plane secondary conductor by a LIM. This model takes into account both the presence of the LIM core and the three dimensional structure of the stator face. The integral expressions are evaluated numerically using the physical data for the float bath SLIM (table 1.1) and the structure of the induced EM field is shown in three dimensional graphic form.

11.2 Single Tooth Analysis

Our starting point, as in chapter 10, is an analysis of the EM field produced by a solitary tooth. In that chapter it was suggested that a tooth's EM field could be found by the superposition of magnetic dipole sources over the volume of a tooth. This procedure is adopted here but instead of a magnetic dipole we shall use the electric current filament suggested by CLEMMOW and DOUGHERTY (1969) as the basic constituent in our field analysis. The magnetic dipole configuration can be recovered by 'bending' the current filament into a closed infinitesimal current loop (this we achieve using line integration techniques). Our assumption that the EM field of a LIM can be deduced from a linear addition of individual sources is equivalent to the physical assumption that we can neglect mutual induction between adjacent teeth. Thus our results will be valid providing the tooth pitch c_τ (the distance between adjacent teeth) is large enough - we may arbitrarily define the minimum tooth pitch in terms of the folding length for the idealised EM field of a solitary tooth obtained in §6.2 which is given by (6.14). Thus as far as a solitary tooth is concerned the stator core is of infinite length along the motor axis (except for the end teeth which 'see' a semi-infinite stator core). The core is of course finite in width. Mathematically it is far easier to

consider a stator core of infinite expanse in the plane of the stator face since this avoids complicated corner and edge boundary conditions. Because soft iron tends to enhance a magnetic field (it increases the number of magnetic field lines per unit area) it is clear that an overhang

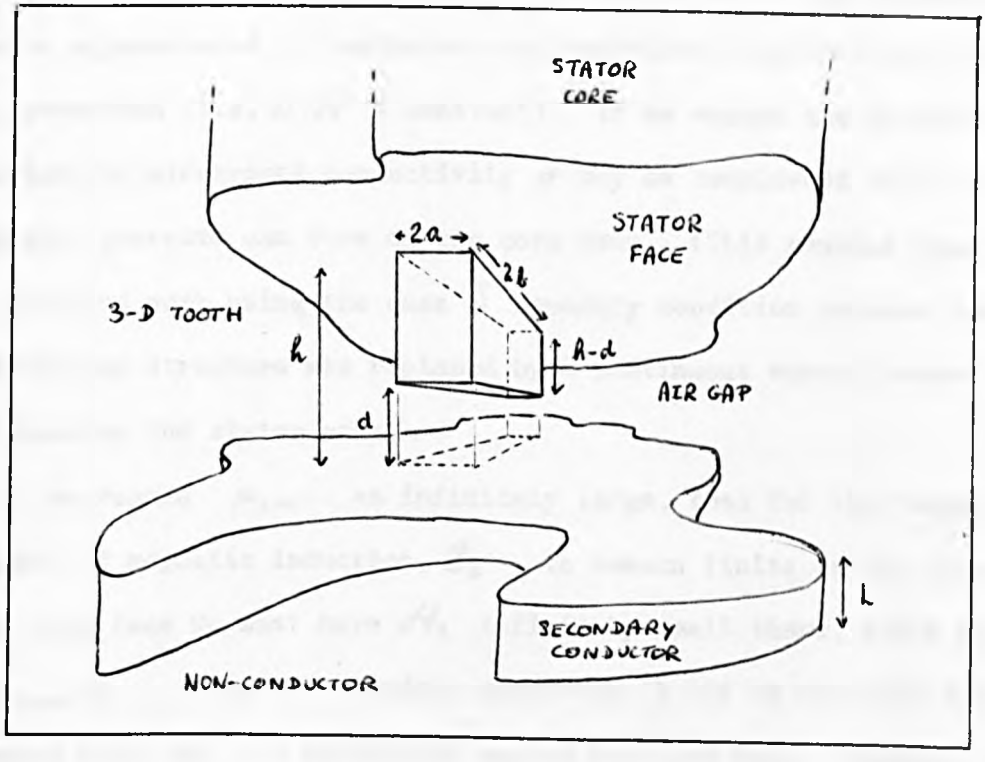

Fig. 11.1 The Single Tooth Configuration

of stator core will slightly exaggerate the true extent of a tooth's EM field. However this does not affect the applicability of the results obtained here to the design and performance of linear motors with finite cores.

The single tooth model is shown in figure 11.1. A tooth of length $2b$ m, width $2a$ m, and height $(h-d)$m , is placed on the lower side of a stator core as shown. Cartesian axes are chosen with origin on the surface of a plane electrical conductor (thickness L metres) and the z axis is chosen to point away from the surface. The base of the tooth is assumed to be at a height d metres above the conductor and the stator core occupies the region $z > h$.

We introduce the soft iron stator core into the mathematical analysis through a boundary condition (to be specified) at $z = h$. The magnetic

permeability of soft iron is very large (typically $\mu_{iron} \sim 10^4$) and it is normally field dependent. The iron is also subject to hysteresis effects - changes in magnetic flux density lag behind changes in the applied field. Here we assume (as in all of this thesis) that hysteresis effects may be ignored (but see JAMIESON (1968)* for an analysis where the hysteresis curve is approximated by Heaviside step functions) and that the iron is fully saturated (i.e. $\mathcal{B}/\mathcal{H}$ = constant). If we assume the stator is laminated its electrical conductivity σ may be considered zero and so no surface currents can form on the core face. (This remains consistent with previous work using the case S boundary condition because there the tooth gap structure was replaced by a continuous current sheet which was placed on the stator core).

If we regard μ_{iron} as infinitely large, then for the tangential component of magnetic induction, $\mathcal{B}_t$, to remain finite on the iron side of the core face we must have $\mathcal{H}_t$ infinitely small there, since by (1.5) $\mathcal{B}_t = \mu_{iron} \mathcal{H}_t$. From the boundary condition (1.38) we see that for a laminated core $\mathcal{H}_t$ is continuous across the core face. However, in the air gap, $\mathcal{B}_t = \mu_0 \mathcal{H}_t$ and so we conclude the boundary condition on the magnetic induction at the core face is $\mathcal{B}_t = 0$. The normal component of magnetic induction is continuous across the stator face by (1.39).

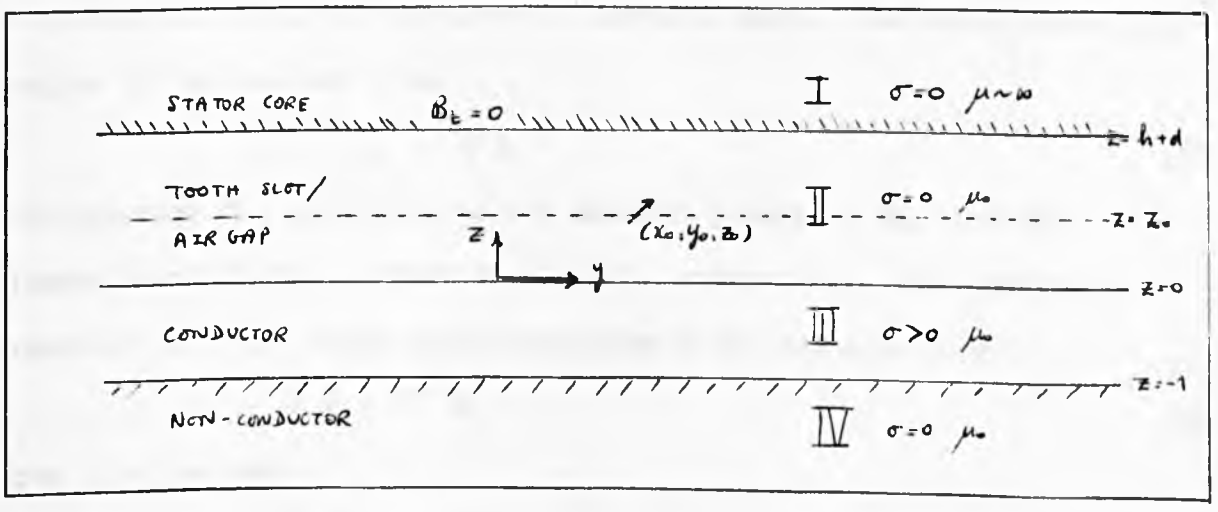

Fig. 11.2 The Mathematical Model

* JAMIESON R A (1968) *Eddy-current effects in solid, unslotted iron rotors*, Proc. IEE, 115, 6, 813-820.

The mathematical model we use is shown in figure 11.2. Region I $(z>h)$ is the stator core, region II $(h>z>0)$ is the tooth/slot/air gap region, region III $(0>z>-L)$ is the electrical conductor and region IV $(z<-L)$ is a non-conductor. The magnetic permeability of I is taken to be infinite but in all other regions it is taken to be that of free space, μ_0 .

11.3 The Field Equations

11.3.1 The Working Equations Of Region II . Clemmow and Dougherty define an electric current filament $\underline{j}(\underline{r})$ at the point $\underline{r}=\underline{r}_0$ to be

$$\underline{j}(\underline{r}) = \underline{c}\,\delta(x-x_0)\,\delta(y-y_0)\,\delta(z-z_0) = \underline{c}\,\delta(\underline{r}-\underline{r}_0) \qquad (1)$$

where $\underline{c}$ is a constant vector* defining the orientation of the filament and $\delta(s)$ is the Dirac delta function. We place the time varying filament $\underline{j}\,e^{i\omega t}$ at the point $\underline{r}=\underline{r}_0$ in region II . In what follows we assume all solutions to Maxwell's equations have the same time variation as the source and write (with the usual notation) $\underline{\mathcal{B}}(\underline{r},t) = \underline{B}(\underline{r})\,e^{i\omega t}$, $\underline{\mathcal{E}}(\underline{r},t) = \underline{E}(\underline{r})\,e^{i\omega t}$, $\underline{\mathcal{J}}(\underline{r},t) = \underline{J}(\underline{r})\,e^{i\omega t}$. It is clear from (1) that $\underline{j}(\underline{r})$ does not satisfy the charge continuity equation $\nabla.\underline{j}=0$, (1.6), at $\underline{r}=\underline{r}_0$. This discrepancy can be rectified by introducing a potential $\Phi(\underline{r}) = L\phi(\underline{r})$ (where L is a scale length) which sets up a space charge at $\underline{r}=\underline{r}_0$ allowing continuity of the electric currents there. The total current in region II is defined to be

$$\underline{J}^T = \underline{j} - \nabla\Phi \qquad (2)$$

The function Φ is related to the electric potential Φ_e but the dimension of Φ/Φ_e is that of electric conductivity. The continuity equation $\nabla.\underline{J}^T=0$ is satisfied providing Φ is chosen so that

$$\nabla.\underline{j} = \nabla^2\Phi \qquad (3)$$

From (1.4) we have

$$\nabla\wedge\underline{B} = \mu_0\underline{J}^T \qquad (4)$$

Taking the curl of (4) using the relation curl curl = grad div - ∇^2, we

* , with dimensions of current density

find, using (2) and the relation curl grad = 0,

$$\nabla^2 \underline{B} = -\mu_0 \nabla \wedge \underline{j} \tag{5}$$

We now define the dimensionless variables $x^* = x/h$, $y^* = y/h$, $z^* = z/h$, $a^* = a/h$, $b^* = b/h$, $d^* = d/h$, $h^* = h/h$, $c^* = c/h$, $x_0^* = x_0/h$, $y_0^* = y_0/h$ and $z_0^* = z_0/h$ where h is a scale length (taken to be the thickness of the conducting region). We shall also write $\underline{B}^* = \underline{B}/\mu_0 h$. Only starred variables will be used from now on so we ignore the star superscripts.

Substituting for $\underline{j}$ in (3) using (1) we find the 'current' potential $\phi(\underline{r})$ satisfies the following dimensionless equation

$$\left(\frac{\partial^2}{\partial x^2}+\frac{\partial^2}{\partial y^2}+\frac{\partial^2}{\partial z^2}\right)\phi = \left(c_1\frac{\partial}{\partial x}+c_2\frac{\partial}{\partial y}+c_3\frac{\partial}{\partial z}\right)\delta(x-x_0)\,\delta(y-y_0)\,\delta(z-z_0) \tag{6}$$

Similarly from (5) we obtain the following dimensionless equation for $\underline{B}$

$$\left(\frac{\partial^2}{\partial x^2}+\frac{\partial^2}{\partial y^2}+\frac{\partial^2}{\partial z^2}\right)\underline{B} = -\left[c_3\frac{\partial}{\partial y}-c_2\frac{\partial}{\partial z},\ c_1\frac{\partial}{\partial z}-c_3\frac{\partial}{\partial x},\ c_2\frac{\partial}{\partial x}-c_1\frac{\partial}{\partial y}\right]\delta(\underline{r}-\underline{r}_0) \tag{7}$$

In dimensionless component form (4) becomes, using (2) and (1)

$$\left[\frac{\partial B_3}{\partial y}-\frac{\partial B_2}{\partial z},\ \frac{\partial B_1}{\partial z}-\frac{\partial B_3}{\partial x},\ \frac{\partial B_2}{\partial x}-\frac{\partial B_1}{\partial y}\right] = \left[c_1,c_2,c_3\right]\delta(\underline{r}-\underline{r}_0) - \left[\frac{\partial\phi}{\partial x},\frac{\partial\phi}{\partial y},\frac{\partial\phi}{\partial z}\right] \tag{8}$$

11.3.2 The Equations of Region III . In the conductor the electric current density $\underline{J}$ is that induced by the source in region II ; it is related to the induced magnetic induction $\underline{B}$ by (1.4). We have

$$\underline{J} = \left[\frac{\partial B_3}{\partial y}-\frac{\partial B_2}{\partial z},\ \frac{\partial B_1}{\partial z}-\frac{\partial B_3}{\partial x},\ \frac{\partial B_2}{\partial x}-\frac{\partial B_1}{\partial y}\right] \tag{9}$$

where $\underline{B}$ is obtained by solving (1.11). We shall assume the conductor moves with a constant velocity V parallel with the y axis. Writing $\underline{v} = V\underline{e}_2$ the dimensionless form of (1.11) becomes

$$\left(\frac{\partial^2}{\partial x^2}+\frac{\partial^2}{\partial y^2}+\frac{\partial^2}{\partial z^2}\right)\underline{B} = iR_0\,\underline{B} + R_{m2}\frac{\partial \underline{B}}{\partial y} \tag{10}$$

where $R_0 = \frac{\omega h^2}{\eta}$, and $R_{m2} = \frac{Vh}{\eta}$ is the magnetic Reynolds number for the motion of the conductor.

11.3.3 The Equations of Region IV . Here the conductivity is zero, so (1.4) reduces to the following equations

$$\frac{\partial B_3}{\partial y} = \frac{\partial B_2}{\partial z} \quad ; \quad \frac{\partial B_1}{\partial z} = \frac{\partial B_3}{\partial x} \quad ; \quad \frac{\partial B_2}{\partial x} = \frac{\partial B_1}{\partial y} \tag{11}$$

(1.11) becomes $$\left(\frac{\partial^2}{\partial x^2}+\frac{\partial^2}{\partial y^2}+\frac{\partial^2}{\partial z^2}\right)\underline{B} = \underline{0} \tag{12}$$

In all three regions we have from (1.1)

$$\frac{\partial B_1}{\partial x}+\frac{\partial B_2}{\partial y}+\frac{\partial B_3}{\partial z} = 0 \tag{13}$$

The three dimensional partial differential equations (6), (7), (10) and (13) are solved for ϕ and $\underline{B}$ using the Fourier transformation technique of previous chapters. The nature of the discontinuities in these equations and the boundary conditions for the EM field are made clearer by considering the transformed differential equations in the three regions.

11.4 The Transformed Field Equations

The two dimensional form of the Fourier transformation (1.32) for the function $M(x,y,z)$ is defined to be

$$\hat{M}(p,q,z) = \mathcal{F}_2^+\left\{M(x,y,z)\right\} = \int_{-\infty}^{\infty}\int_{-\infty}^{\infty} M(x,y,z)\, e^{i(px+qy)}\,dx\,dy \tag{14}$$

The corresponding inverse transformation (1.33) is defined as

$$M(x,y,z) = \mathcal{F}_2^-\left\{\hat{M}(p,q,z)\right\} = \frac{1}{(2\pi)^2}\int_{-\infty}^{\infty}\int_{-\infty}^{\infty} \hat{M}(p,q,z)\, e^{-i(px+qy)}\,dp\,dq \tag{15}$$

11.4.1 Region II . Applying the transformation (14) to (6) we obtain for the function $\hat{\phi}(p,q,z)$:

$$\left(\frac{d^2}{dz^2}-\kappa^2\right)\hat{\phi} = \left(-ipc_1 - iqc_2 + c_3\frac{d}{dz}\right)e^{i(px_0+qy_0)}\,\delta(z-z_0) \tag{16}$$

The Fourier Transformation of (7) becomes

$$\left(\frac{d^2}{dz^2}-\kappa^2\right)\hat{B}_1 = e^{i(px_0+qy_0)}\left(iqc_3+c_2\frac{d}{dz}\right)\delta(z-z_0) \tag{17}$$

$$\left(\frac{d^2}{dz^2}-\kappa^2\right)\hat{B}_2 = -e^{i(px_0+qy_0)}\left(ipc_3+c_1\frac{d}{dz}\right)\delta(z-z_0) \tag{18}$$

$$\left(\frac{d^2}{dz^2}-\kappa^2\right)\hat{B}_3 = ie^{i(px_0+qy_0)}\left(pc_2-qc_1\right)\delta(z-z_0) \tag{19}$$

The Fourier transformation of (8) becomes

$$-iq\,\hat{B}_3 - \frac{d\hat{B}_2}{dz} = ip\,\hat{\phi} + c_1 e^{i(px_0+qy_0)}\,\delta(z-z_0) \tag{20}$$

$$ip\,\hat{B}_3 + \frac{d\hat{B}_1}{dz} = iq\,\hat{\phi} + c_2 e^{i(px_0+qy_0)}\,\delta(z-z_0) \tag{21}$$

$$-ip\hat{B}_2 + iq\hat{B}_1 = c_3 e^{i(px_0+qy_0)}\delta(z-z_0) - \frac{d\hat{\phi}}{dz} \tag{22}$$

where in (16) to (22)

$$K^2 = p^2 + q^2 \tag{23}$$

11.4.2 Region III . The transformed forms of (9) and (10) are respectively

$$\hat{\underline{J}} = \left[-iq\hat{B}_1 - \frac{d\hat{B}_2}{dz},\ \frac{d\hat{B}_1}{dz} + ip\hat{B}_2,\ -ip\hat{B}_2 + iq\hat{B}_1\right] \tag{24}$$

$$\frac{d^2\hat{\underline{B}}}{dz^2} = \gamma^2\underline{B} \tag{25}$$

where $$\gamma^2 = K^2 + i(R_0 - qR_{m_2}) \tag{26}$$

11.4.3 Region IV . The transformed forms of(11) and (12) are respectively

$$-iq\hat{B}_2 = \frac{d\hat{B}_1}{dz} \quad ; \quad \frac{d\hat{B}_1}{dz} = -ip\hat{B}_2 \quad ; \quad p\hat{B}_2 = q\hat{B}_1 \tag{27}$$

$$\frac{d^2\hat{\underline{B}}}{dz^2} = K^2\hat{\underline{B}} \tag{28}$$

In all three regions we have, transforming (13)

$$\frac{d\hat{B}_3}{dz} = ip\hat{B}_1 + iq\hat{B}_2 \tag{29}$$

11.5 Boundary Conditions

11.5.1 Physical Conditions. From (1.38) and (1.39) we see that $\underline{B}$ is continuous across a boundary; because all boundaries in this problem are in the (x,y) plane we conclude that both $\hat{\underline{B}}$ and $\frac{d\hat{B}_3}{dz}$ (by (29)) are continuous across the interfaces at $z=0$ and $z=-1$. For reasons mentioned in §11.2, we take both B_1 and B_2 equal to zero at the stator face, so $\hat{B}_1 = 0$ and $\hat{B}_2 = 0$ on $z = h$.

Physically, because region II is non-conducting it is clear that the normal component of $\underline{J}^T$ should vanish on the stator face (which is consistent with the specification that B_1 and B_2 are zero there) and also vanish on the surface on the conductor. Thus we require $\frac{\partial\phi}{\partial z} = 0$ (and so $\frac{d\hat{\phi}}{dz} = 0$) on $z=0$ and $z=-1$. Finally we assume the EM field

decays as $z \to -\infty$ in region IV .

11.5.2 Discontinuity Conditions on $z = z_0$. Consider the equation $\frac{d^2\psi}{dz^2} - k^2\psi = \alpha\,\delta(z-z_0)$, where $\psi = \psi(z)$. Integrating across the discontinuity at $z = z_0$ we find $\left[\frac{d\psi}{dz}\right]_{z_0^-}^{z_0^+} - k^2\int_{z_0^-}^{z_0^+}\psi\,dz = \alpha$. This result indicates that $\frac{d\psi}{dz}$ is discontinuous across $z = z_0$ by the amount α .

An examination of the equation $\frac{d^2\psi}{dz^2} - k^2\psi = \alpha\frac{d}{dz}\cdot\delta(z-z_0)$ is made clearer using the substitution $\psi = \frac{d\theta}{dz}$. After substitution we find $\frac{d}{dz}\left\{\frac{d^2\theta}{dz^2} - k^2\theta\right\} = \frac{d}{dz}\left\{\alpha\,\delta(z-z_0)\right\}$, which implies $\frac{d^2\theta}{dz^2} - k^2\theta = \alpha\,\delta(z-z_0) + \beta$ where β is a constant. This equation is similar to that considered earlier. Integrating across the discontinuity at $z = z_0$ leads to the result : $\frac{d\theta}{dz}$ (which equals $\psi(z)$) is discontinuous by an amount α there. Applying the above analysis in (16) to (19) it is clear that the results of table 11.1 hold (writing $E = e^{i(px_0+qy_0)}$)for the discontinuities across $z = z_0$.

Field	$\hat{\phi}$	$\frac{d\hat{\phi}}{dz}$	$\hat{B}_1$	$\hat{B}_2$	$\frac{d\hat{B}_1}{dz}$	$\frac{d\hat{B}_2}{dz}$	$\frac{d\hat{B}_3}{dz}$
Discontinuous by:	Ec_3	$-E(ipc_1+iqc_2)$	Ec_2	$-Ec_1$	$E.iqc_3$	$-E.ipc_3$	$iE(pc_2-qc_1)$

Table 11.1 The Field Discontinuities at $z = z_0$

We note that the results of table 11.1 satisfy the discontinuity conditions required by (20) to (22).

11.6 Solutions in Transform Space

11.6.1 $\hat{\phi}(p,q,z)$. Subject to the condition $\frac{d\hat{\phi}}{dz} = 0$ on $z = h$ and $z = 0$, we see the solution for $\hat{\phi}$ in region II $(h > z > 0)$ is of the form:

$$\hat{\phi} = \begin{cases} D_1 \cosh k(h-z) & z > z_0 \\ D_2 \cosh kz & z < z_0 \end{cases} \qquad (30)$$

Applying the discontinuity conditions of table 11.1 for $\hat{\phi}$ and $\frac{d\hat{\phi}}{dz}$ we obtain two equations connecting the two constants $D_1 = D_1(p,q)$ and $D_2 = D_2(p,q)$:

$$\left.\begin{aligned} D_1 \cosh \kappa(h-z_0) - D_2 \cosh \kappa z_0 &= EC_3 \\ D_1 \sinh \kappa(h-z_0) + D_2 \sinh \kappa z_0 &= iE(pC_1+qC_2)/\kappa \end{aligned}\right\} \quad (31)$$

The solutions obtained to (31) for D_1 and D_2 (which are given in Appendix IV) can be substituted in (30) to give the following solution for $\hat{\phi}(p,q,z)$:

$$\hat{\phi} = E \cdot \begin{cases} \dfrac{C_3 \sinh \kappa z_0 \cosh \kappa(h-z)}{\sinh \kappa h} + \dfrac{i(pC_1+qC_2)\cosh \kappa z_0 \cosh \kappa(h-z)}{\kappa \sinh \kappa h} & (z > z_0) \\ \dfrac{-C_3 \sinh \kappa(h-z_0)\cosh \kappa z}{\sinh \kappa h} + \dfrac{i(pC_1+qC_2)\cosh \kappa z \cosh \kappa(h-z_0)}{\kappa \sinh \kappa h} & (z < z_0) \end{cases} \quad (32)$$

11.6.2 $\hat{\underline{B}}(p,q,z)$

(i) Region II . Subject to the condition $\hat{B}_1 = 0$, $\hat{B}_2 = 0$ on $z = h$, we see from (17) and (18) that the solutions for $\hat{B}_1$ and $\hat{B}_2$ in $0 < z < h$ are

$$\hat{B}_{1,2} = \begin{cases} L_{1,2} \sinh \kappa(h-z) & z > z_0 \\ M_{1,2} e^{\kappa z} + N_{1,2} e^{-\kappa z} & z < z_0 \end{cases} \quad (33)$$

where L_1, L_2 etc. are constants (functions of p and q only). Applying the discontinuity conditions of table 11.1 for $\hat{B}_1$, $\hat{B}_2$, $\frac{d\hat{B}_1}{dz}$ and $\frac{d\hat{B}_2}{dz}$ we find

$$\begin{Bmatrix} L_1 \\ L_2 \end{Bmatrix} \sinh \kappa(h-z_0) - \begin{Bmatrix} M_1 \\ M_2 \end{Bmatrix} e^{\kappa z_0} - \begin{Bmatrix} N_1 \\ N_2 \end{Bmatrix} e^{-\kappa z_0} = \begin{Bmatrix} EC_2 \\ -EC_1 \end{Bmatrix} \quad (34)$$

$$-\begin{Bmatrix} L_1 \\ L_2 \end{Bmatrix} \cosh \kappa(h-z_0) - \begin{Bmatrix} M_1 \\ M_2 \end{Bmatrix} e^{\kappa z_0} + \begin{Bmatrix} N_1 \\ N_2 \end{Bmatrix} e^{-\kappa z_0} = \frac{iE}{\kappa} \begin{Bmatrix} qC_3 \\ -pC_3 \end{Bmatrix} \quad (35)$$

(ii) Region III . The solution to (25) may be written in the form

$$\hat{\underline{B}} = \underline{P} e^{\gamma z} + \underline{Q} e^{-\gamma z} \quad (36)$$

where $\underline{P}$ and $\underline{Q}$ are constant vectors.

(iii) Region IV. The solution to (28) may be written in the form

$$\hat{\underline{B}} = \underline{R}\, e^{\kappa z} \tag{37}$$

where $\underline{R}$ is a constant vector.

It is clear that applying the boundary conditions discussed in §11.5 produces a system of algebraic linear equations connecting the constants in (34) to (37). This system can be solved either by matrix methods (using Cramer's rule) or by direct substitution. To avoid unnecessary complication we shall use only the boundary conditions relevant to our direct substitution approach outlined below.

(a) Our starting point is the solution for L_2 and N_2 in terms of M_2 by combining the lower of (34) and (35). Thus we have $L_2 = L_2(M_2)$ and $N_2 = N_2(M_2)$

(b) On $z=0$ $\hat{B}_2$ is continuous. Using (36) and the lower of (33) we find $P_2+Q_2 = M_2+N_2$. Combining this result with (a) gives $P_2 = P_2(Q_2, M_2)$

(c) On $z=-1$ $\hat{B}_2$ is continuous. Using (36) and (37) we find $P_2 e^{-\gamma} + Q_2 e^{\gamma} = R_2 e^{-\kappa}$. Using (b) we see that $Q_2 = Q_2(R_2, M_2)$

(d) The normal component of magnetic induction, $\hat{B}_3$, in region II is now found in terms of L_2 (in $z>z_0$) and M_2, N_2 (in $z<z_0$) using (20) and the results for $\hat{\phi}$ and $\hat{B}_2$ in (30) and (33) respectively. Thus we have (using (a))

$$\hat{B}_3 = \begin{cases} \hat{B}_3(L_2) & z>z_0 \text{ , where } L_2 = L_2(M_2) \\ \hat{B}_3(M_2, N_2) & z<z_0 \text{ , where } N_2 = N_2(M_2) \end{cases}$$

(e) On $z=0$, $\hat{B}_3$ and $\frac{d\hat{B}_3}{dz}$ are continuous. Using (36) and (d) we can find both P_3 and Q_3 in terms of M_2 . Thus we have $P_3 = P_3(M_2)$, $Q_3 = Q_3(M_2)$

(f) In region IV, we have, from the third of (27) using (37), $R_1 = qR_2/p$. The second of (27) gives the result $\hat{B}_2 = \frac{i\kappa R_2}{q} e^{\kappa z}$

(g) On $z=-1$, both $\hat{B}_3$ and $\frac{d\hat{B}_3}{dz}$ are continuous. Using (36) and (f) we can eliminate R_2 to give $P_3 = P_3(Q_3)$ and then substituting for P_3 gives

$R_2 = R_2(Q_3)$.

(h) Combining the results of (e) and (g) gives the expression $P_3(M_2) = P_3(Q_3(M_2))$ which enables an algebraic expression to be found for M_2.

(i) Having found M_2 we can obtain algebraic expressions for P_3 and Q_3 (using (e)), R_2 (using (g)), Q_2 and P_2 (using (b)), L_2 and N_2 (using (a)). Thus $\hat{B}_3$ is now completely specified in region II by (d).

(j) The expression for $\hat{B}_1$ in the three regions can be found by repeating the above analysis. However, the procedure can be shortened by using the symmetry of (34) and (35). In many of the equations for we can immediately obtain their correct form by replacing $(-EC_4)$ by (EC_3) and $(-pC_3)$ by (qC_3) in the appropriate expression for $\hat{B}_2$.

Direct substitution of the constants into (33), (36), (37), (d) and (f) leads to a complete description of the magnetic induction in the three regions. Expressions for the constants above are given in Appendix IV. We see from these expressions that:

(i) The vertical component of the electric current filament C_3 only appears in the expressions for L_1, L_2, M_1, M_2, N_1 and N_2. We conclude that vertical source currents in region II do not affect the magnetic field (nor the electric currents)induced in region III. This is perhaps to be expected since we specified that the normal component of electric current should be zero on the conductor surface. The conductor, of course, screens the source from region IV so the magnetic field is also independent of C_3 there.

(ii) The following relations hold; $pP_2 = qP_1$ and $pQ_2 = qQ_1$. From the third component of (24) it is clear that these relations specify the condition that $\hat{J}_3$ (and so J_3) is zero inside region III. We conclude that the induced currents are all in the plane of the conductor. Physically, unless free charges are available in the plane conductor, the electric current cannot form closed loops out of the (x,y) plane.

Because we have neglected displacement currents (see chapter 1) the time of relaxation for the conductor becomes infinitely large and free charges are instantly dissipated. However, by (1.9), if $\nabla.(\underline{v}\wedge\underline{B})\neq 0$ the motion of the conductor itself induces free charges (for example when $V=V(z)$) and J_3 is not necessarily zero everywhere. Mathematically, we see by taking the curl of (10) using (9), that J_3 also satisfies (10); however the only solution to (25) (the transform of (10) subject to $\hat{J}_3 = 0$ on $z=0$ and $z=-1$ when $\underline{v}=V\underline{e}_2$ is the trivial one.

For brevity we shall give the solution for $\hat{\underline{B}}$ inside region III (the conductor) only(see Appendix IV for the remaining solutions). We find

$$\left\{\begin{matrix}\hat{B}_1\\ \hat{B}_2\end{matrix}\right\} = E.\left\{\begin{matrix}p\\ q\end{matrix}\right\} \frac{\gamma(qC_1-pC_2)}{k^2\Delta}\left\{\left(\frac{\gamma+k}{\gamma-k}\right)e^{2\gamma}e^{\gamma z}-e^{-\gamma z}\right\}.\cosh k(h-z_0) \qquad (38)$$

$$\hat{B}_3 = \frac{iE(qC_1-pC_2)\cosh k(h-z_0)}{\Delta}\left\{\left(\frac{\gamma+k}{\gamma-k}\right)e^{2\gamma}e^{\gamma z}+e^{-\gamma z}\right\} \qquad (39)$$

where $$\Delta = \left\{\left(\frac{\gamma+k}{\gamma-k}\right)e^{2\gamma}-1\right\}\gamma\cosh kh + \left\{\left(\frac{\gamma+k}{\gamma-k}\right)e^{2\gamma}+1\right\}k\sinh kh \qquad (40)$$

The electric current density is given by (24) but for brevity it is not included here.

11.7 Tooth Construction

From the analysis of §11.6.2 it is clear that for region III (the conductor), unlike region II (the air gap/stator face), only components of the source currents parallel with the conductor surface have any influence on the induced EM field. Thus as far as stator losses are concerned, vertical source currents merely produce ohmic losses and so the stator windings should be layered parallel with the stator face. Henceforth we shall assume $C_3=0$.

11.7.1 Coil Configurations. Writing $E=e^{i(px_0+qy_0)}$ in (38) and (39) we see that the terms $C_1e^{i(px_0+qy_0)}$ and $C_2e^{i(px_0+qy_0)}$ appear in the transformed field expressions. These terms arise from the current element positioned

at the point (x_0, y_0) in the plane $z = z_0$ in real space (figure 11.3). Writing $x_0 = u + x_\epsilon$ and $y_0 = v + y_\epsilon$ the position of the current element

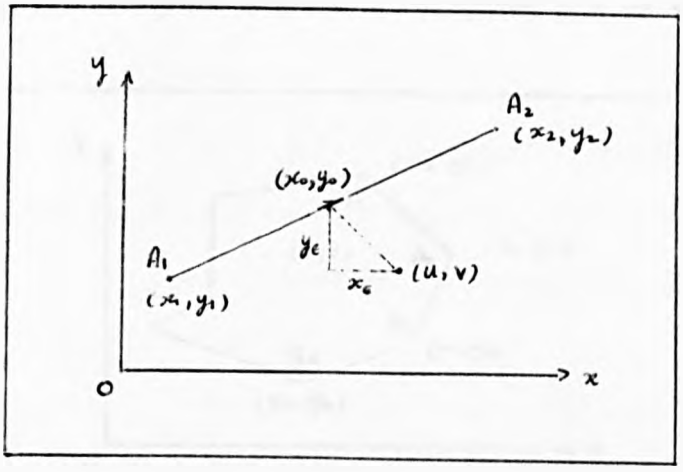

Fig. 11.3 The Plane $z = z_0$

in relation to the fixed reference point (u,v) can be obtained by choosing appropriate values for x_ϵ and y_ϵ. If the orientation of the element is along the line $y = \alpha x + \beta$, we may write $\underline{\ell} = [1, \alpha, 0]\, I\, \delta x_\epsilon$ where δx_ϵ is a small positive increment in the direction of the x-axis and I the magnitude of the applied current. Thus we have, for a current element

$$E(qc_1 - pc_2) = I\, e^{i(up+vq)}\, e^{i(p+\alpha q)x_\epsilon}\, (q - p\alpha)\, \delta x_\epsilon \qquad (41)$$

Note that the choice of $\underline{\ell}$ here implies the alternating current is flowing in the direction of $\overrightarrow{AB}$ at $t = 0$.

Combining an infinite number of current elements along the line $y = \alpha x + \beta$ between the points (x_1, y_1) and (x_2, y_2), (see figure 11.3), is equivalent to integrating (41) with respect to x_ϵ between x_1 and x_2. This infinite summation produces a finite line current for which

$$E(qc_1 - pc_2) = I\, e^{i(up+vq)}\, (q - p\alpha) \int_{x_1}^{x_2} e^{i(p+\alpha q)x_\epsilon}\, dx_\epsilon \qquad (42)$$

We note that this result can be extended to include the effects of a current sheet. For example, writing $x_1 = x_1' + \epsilon$, $x_2 = x_2' + \epsilon$ and integrating (42) with respect to ϵ from 0 to ℓ includes the effect of a trapezoidal current sheet (of length ℓ and slant height $y_2 - y_1$) whose vertices lie at the points (x_1', y_1), $(x_1' + \ell, y_1)$, $(x_2' + \ell, y_2)$, (x_2', y_2).

It is clear from figure 11.4 that any closed current loop can be obtained by combining the appropriate number of finite line currents. If the polygonal loop has N sides and the N vertices lie at the points

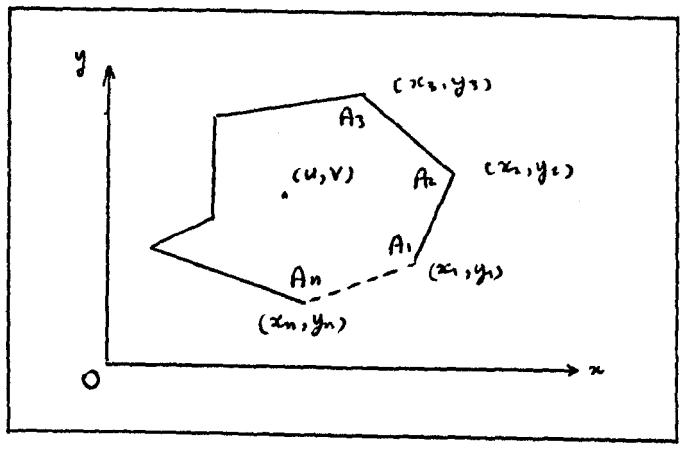

Fig. 11.4 An Arbitrary Polygonal Current Loop

(x_1,y_1), (x_2,y_2), ..., (x_N,y_N) , then the appropriate form of $E(qc_1-pc_2)$ for the loop when the current is anti-clockwise in direction at $t=0$ is from (42)

$$E(qc_1-pc_2) = I e^{i(pu+qv)} \sum_{n=1}^{N} \frac{q-\alpha_n p}{i(q+\alpha_n p)} \left\{ e^{i(p+\alpha_n q)x_{n+1}} - e^{i(p+\alpha_n q)x_n} \right\} \quad (43)$$

where $(x_{N+1}, y_{N+1}) = (x_1, y_1)$ and $\alpha_n = \frac{y_{n+1}-y_n}{x_{n+1}-x_n}$ is the slope of the n'th side of the polygon. For a rectangular coil of length $2b$ and width $2a$ we find (writing $\kappa^2 = p^2+q^2$) using (43)

$$E(qc_1-pc_2) = \frac{4i\kappa^2 I \sin(pa)\sin(qb)\, e^{i(up+vq)}}{pq} \quad (44)$$

If we require a loop with curvature (eg. circle or ellipse) we may use the parametric form of the curve's cartesian equation. As an example we shall consider the elliptical current loop whose semi-major axis is of length n and semi-minor axis is of length m . Using the parametric form $(m\cos\theta, n\sin\theta)$ we can write $(x_0,y_0) = (u,v)+(m\cos\theta, n\sin\theta)$. An element of the elipse is orientated in the direction $\underline{s} = I.[-n\sin\theta, m\cos\theta, 0]\delta\theta$ (for anti-clockwise current at $t=0$) where $\delta\theta$ is a small angle. Summing current elements around the ellipse is equivalent to integrating

with respect to θ from 0 to 2π, so for an ellipse we have

$$E(c_1 q - p c_2) = -I.e^{i(up+vq)} \int_0^{2\pi} (nq\sin\theta + mp\cos\theta)\, e^{i(\rho m\cos\theta + nq\sin\theta)}\, d\theta$$

$$= 2\pi I.\ \psi J_1(\psi).\ e^{i(up+vq)} \qquad (45)$$

where $\psi^2 = m^2p^2 + n^2q^2$ and $J_1(\psi)$ is Bessel's function of order unity. In the derivation of (45) we have used the results of Appendix Setting $m = n = r$ (so $\psi = r\kappa$) produces the appropriate expression for a circular current loop of radius r.

We can obtain expressions for an infinitesimal rectangular current loop and infinitesimal circular current loop using the limiting forms of (44) and (45) respectively. Letting a, b and r become small it is clear that both expressions (using $J_1(\psi) \sim \frac{1}{2}.\psi$ when ψ is small) reduce to the vertical magnetic dipole form

$$E(c_1 q - c_2 p) = iM.\kappa^2.e^{i(pu+qv)} \qquad (46)$$

where $\lim_{\substack{a\to 0\\ b\to 0}} \{4abI\} = M$ (using (44)) and $\lim_{r\to 0} \{\pi r^2 I\} = M$ (using (45)). Here M (which is of dimension current x area) is the strength of the dipole.

11.7.2. Tooth Configuration. In §11.2 it was suggested that the magnetic field produced by a solitary tooth could be found by the superposition of an infinite number of dipole sources over the tooth's volume. If we write $(u,v) = (u',v') + (u_\epsilon, v_\epsilon)$ in (46), where (u',v') is a reference point and integrate (46) with respect to u_ϵ and v_ϵ over the surface S, which is taken as a section through a tooth of length $2b$ and width $2a$, we produce expression (44). This shows that the effect of a superposition of dipole sources over a surface S is equivalent to the effect of a line current placed on its boundary. A superposition of dipole sources over a tooth volume is therefore equivalent to placing finite current sheets on the containing sides. For a tooth placed at a height d above the conductor and of length $(h-d)$ this is achieved by integrating (38) and (39) with respect to z_0 from $z_0 = d$ to $z_0 = h$ using expression (44).

Hitherto we have assumed that the tooth is placed normal to the face of the stator. However, our analysis, apart from assuming all coil windings are parallel with the stator face, places no restriction on the structure of a vertical section through the tooth. For example, consider the teeth of figure 11.5. The first tooth is a circular cone of generator angle α

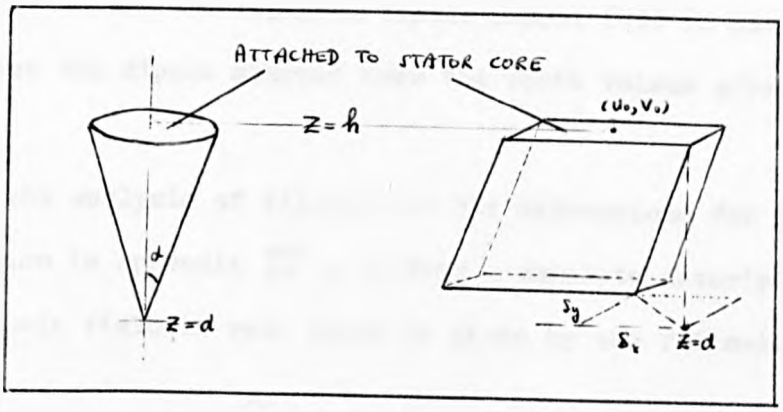

Fig. 11.5 Tooth Configurations

and the second a rectangular skewed tooth normal to the stator face. For the cone we have $r(z_0) = \tan\alpha \cdot (z_0 - d)$ where r is the cone radius at $z = z_0$. With this value of r in (45), the magnetic field induced by the cone in the conductor is obtained by integrating (38) and (39) with respect to z_0 from $z_0 = d$ to $z_0 = h$. For the slanted tooth we write $(u, v) = (u_0, v_0) + (\delta_x, \delta_y)\cdot\frac{h - z_0}{h - d}$ where δ_x and δ_y indicate the extent of the skew along the x and y axes at $z = d$, and $[u_0, v_0, h]$ is the position of the centre of the tooth at the core face. Here, however, we restrict our analysis to the single tooth of rectangular cross section placed normal to the stator core.

We note that expressions for the magnetic field induced in a secondary conductor by a polygonal DC current coil can be obtained by substituting (43) in (38) and (39) with ω (the angular frequency of the time variation) equal to zero. Thus the field expressions obtained by LEE and MENENDEZ (1974) and MENENDEZ and LEE (1975) for a non-conducting region IV of magnetic permeability μ can be obtained from our general analysis.

11.8 Solutions in Real Space

The real space solutions for the magnetic field of the tooth are obtained by substituting (44) in (38) and (39), integrating with respect to z_o from $z_o = d$ to $z_o = h$, and then inverting the expressions using the inverse transform (15). However, the form of the solutions is less cumbersome if we use the magnetic dipole result (46) in place of (44) and superpose the dipole sources over the tooth volume after Fourier inversion.

Using the analysis of §11.6.2 and the expressions for the constants of integration in Appendix IV, we find a complete description of the magnetic dipole field in real space is given by the following expressions: (with $R_{m_2} = 0$)

$$B_1(\text{II}, z > z_o) = M\frac{(u-x)}{\rho}\int_0^\infty \frac{\sinh\kappa(h-z)}{\sinh\kappa h}\cdot\kappa^2\left\{-\cosh\kappa z_o + \gamma\left[\left(\frac{\gamma+\kappa}{\gamma-\kappa}\right)e^{2\gamma}-1\right]\frac{\cosh\kappa(h-z_o)}{\Delta}\right\}J_1(\kappa\rho)\,d\kappa \tag{47}$$

$$B_1(\text{II}, z < z_o) = M\frac{(u-x)}{\rho}\int_0^\infty \frac{\cosh\kappa(h-z_o)}{\sinh\kappa h}\cdot\kappa^2\left\{\sinh\kappa z + \gamma\left[\left(\frac{\gamma+\kappa}{\gamma-\kappa}\right)e^{2\gamma}-1\right]\frac{\sinh\kappa(h-z)}{\Delta}\right\}J_1(\kappa\rho)\,d\kappa \tag{48}$$

$$B_1(\text{III}) = M\frac{(u-x)}{\rho}\int_0^\infty \frac{\gamma\cosh\kappa(h-z_o)}{\Delta}\cdot\kappa^2\left\{\left(\frac{\gamma+\kappa}{\gamma-\kappa}\right)e^{2\gamma}e^{\gamma z}-e^{-\gamma z}\right\}J_1(\kappa\rho)\,d\kappa \tag{49}$$

$$B_1(\text{IV}) = M\cdot\frac{2(u-x)}{\rho}\int_0^\infty \frac{\cosh\kappa(h-z_o)}{(\gamma-\kappa)\Delta}\cdot\kappa^3\gamma\, e^{\kappa(z+1)}e^{\gamma}J_1(\kappa\rho)\,d\kappa \tag{50}$$

where
$$\rho^2 = (u-x)^2 + (v-y)^2 \tag{51}$$

The appropriate expressions for B_2 are obtained by replacing the factor $(u-x)/\rho$ by $(v-y)/\rho$ in (47) to (50).

$$B_3(\text{II}, z > z_o) = M\int_0^\infty \frac{\cosh\kappa(h-z)}{\sinh\kappa h}\cdot\kappa^2\left\{-\cosh\kappa z_o + \gamma\left[\left(\frac{\gamma+\kappa}{\gamma-\kappa}\right)e^{2\gamma}-1\right]\frac{\cosh\kappa(h-z_o)}{\Delta}\right\}J_0(\kappa\rho)\,d\kappa \tag{52}$$

$$B_3(\text{II}, z < z_o) = M\int_0^\infty \frac{\cosh\kappa(h-z_o)}{\sinh\kappa h}\kappa^2\left\{-\cosh\kappa z + \gamma\left[\left(\frac{\gamma+\kappa}{\gamma-\kappa}\right)e^{2\gamma}-1\right]\frac{\cosh\kappa(h-z)}{\Delta}\right\}J_0(\kappa\rho)\,d\kappa \tag{53}$$

$$B_3(\text{III}) = -M\int_0^\infty \frac{\cosh\kappa(h-z_0)}{\Delta}\cdot\kappa^3\cdot\left\{\left(\frac{\gamma+\kappa}{\gamma-\kappa}\right)e^{2\gamma}e^{\gamma z}+e^{-\gamma z}\right\}J_0(\kappa\rho)\,d\kappa \qquad (54)$$

$$B_3(\text{IV}) = -2M\int_0^\infty \frac{\cosh\kappa(h-z_0)}{(\gamma-\kappa)\Delta}\cdot\gamma\kappa^3 e^{\kappa(1+z)}e^{\gamma}\,J_0(\kappa\rho)\,d\kappa \qquad (55)$$

In the derivation of (47) to (55) we have used the inverse Fourier transformation result:

$$\int_{-\infty}^{\infty}\int_{-\infty}^{\infty} F(\kappa)\,e^{-i(px+qy)}\,dp\,dq = 2\pi\int_0^\infty \kappa F(\kappa)\,J_0(\kappa\sqrt{x^2+y^2})$$

which is discussed in Appendix II .

Integrating (49) and (54) with respect to u from $-a$ to a, v from $-b$ to b and z_0 from d to h, gives the following simplified expressions for the magnetic field induced in the conductor by a tooth of rectangular cross section with axis passing through the origin.

$$B_1 = M\int_0^\infty \frac{\gamma\sinh\kappa(h-d)}{\Delta}\cdot\kappa^2\cdot\left\{\left(\frac{\gamma+\kappa}{\gamma-\kappa}\right)e^{2\gamma}e^{\gamma z}-e^{-\gamma z}\right\}\int_{v=-b}^{v=b}\left\{J_0(\kappa\rho_x^+)-J_0(\kappa\rho_x^-)\right\}dv\,d\kappa \qquad (56)$$

$$B_2 = M\int_0^\infty \frac{\gamma\sinh\kappa(h-d)}{\Delta}\cdot\kappa^2\left\{\left(\frac{\gamma+\kappa}{\gamma-\kappa}\right)e^{2\gamma}e^{\gamma z}-e^{-\gamma z}\right\}\int_{u=-a}^{u=a}\left\{J_0(\kappa\rho_y^+)-J_0(\kappa\rho_y^-)\right\}du\,d\kappa \qquad (57)$$

$$B_3 = -M\int_0^\infty \frac{\sinh\kappa(h-d)}{\Delta}\cdot\kappa^3\left\{\left(\frac{\gamma+\kappa}{\gamma-\kappa}\right)e^{2\gamma}e^{\gamma z}+e^{-\gamma z}\right\}\int_{u=-a}^{u=a}\int_{v=-b}^{v=b} J_0(\kappa\rho)\,du\,dv\,d\kappa \qquad (58)$$

where $$\rho_x^\pm = \left[(a\mp x)^2+(v-y)^2\right]^{1/2}\ ;\quad \rho_y^\pm = \left[(u-x)^2+(b\mp y)^2\right]^{1/2} \qquad (59)$$

and ρ is given by (51). The electric current density is found by inverting (24) using (38) and (39) or by substituting (50) to (58) in (9). We find, for the special case $R_{m_2}=0$:

$$J_1 = -iM\int_0^\infty R_0\cdot\frac{\sinh\kappa(h-d)}{\Delta}\cdot\kappa^2\left\{\left(\frac{\gamma+\kappa}{\gamma-\kappa}\right)e^{2\gamma}e^{\gamma z}+e^{-\gamma z}\right\}\int_{u=-a}^{u=a}\left\{J_0(\kappa\rho_y^+)-J_0(\kappa\rho_y^-)\right\}du\,d\kappa \qquad (60)$$

$$J_2 = iM\int_0^\infty R_0\cdot\frac{\sinh\kappa(h-d)}{\Delta}\cdot\kappa^2\left\{\left(\frac{\gamma+\kappa}{\gamma-\kappa}\right)e^{2\gamma}e^{\gamma z}+e^{-\gamma z}\right\}\int_{v=-b}^{v=b}\left\{J_0(\kappa\rho_x^+)-J_0(\kappa\rho_x^-)\right\}dv\,d\kappa \qquad (61)$$

with, of course, $J_3=0$. The integrals in (56) to (61) were evaluated numerically using Gaussian quadrature over $[0,\infty)$ and Patterson's updated Gaussian method over $[-b,b]$ and $[-a,a]$. Both algorithms are available

as subroutines in the Nottingham Algorithm Group's (NAG) computer library. The NAG library also contains a function subroutine for the evaluation of the Bessel function $J_0(\kappa\rho)$ to five decimal places. The degree of accuracy obtained in any quadrature routine depends on the number of sampling points used, so we must speak in terms of 'relative accuracy'. For values of $|x|$ and $|y|$ less than $2a$ and $2b$ respectively we estimate the error in our results to be at the most 2 per cent. At greater distances from the tooth the error rises to 5 per cent except for $\mathcal{B}_3$ where it may be as large as 10 per cent (due to the triple integration required by (58)).

The values of the parameters used in (56) to (61) are taken from the float bath data listed in table 1.1. Their dimensionless values are given in table 11.2. When these parameters include a pole pitch of 76mm (from table 1.1) the set of parameters is referred to as 'Data 1'. For a pole pitch of half this value (38mm) the set of parameters is referred to as 'Data 2'.

Tooth Width ($2a$)	1.6	Tooth Length ($2b$)	0.2	
Height of stator face above conductor surface (d)	0.2 (12mm)			
Height of stator core above conductor surface (h)	1.05			
Height of tooth ($h-d$)	0.85			
Pole Pitch (τ)	1.2	Slot Width (w_s)	0.6	Data 1
Tooth Pitch (c)	0.8			
Pole Pitch (τ)	0.6	Slot Width (w_s)	0.2	Data 2
Tooth Pitch (c)	0.4			

Table 11.2 Dimensionless Parameters

Results for the modulus of magnetic induction are shown in figures 11.6 (variation with depth) and 11.11 to 11.13 (on $z = 0$). The electric current density is shown in figures 11.7 (variation with depth) 11.15 and

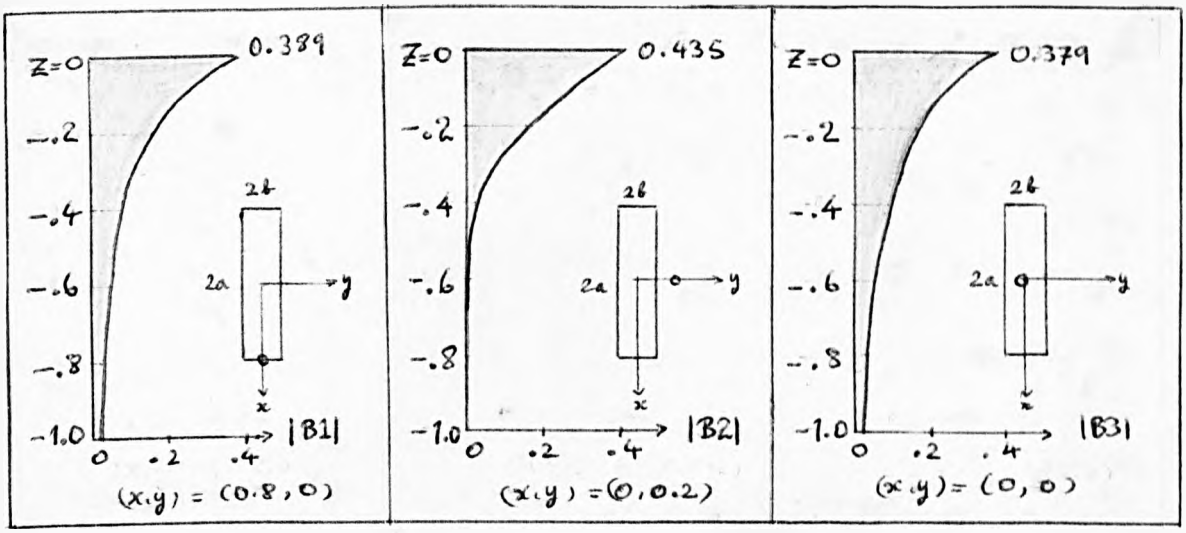

Fig. 11.6 Variation of Magnetic Field With Depth

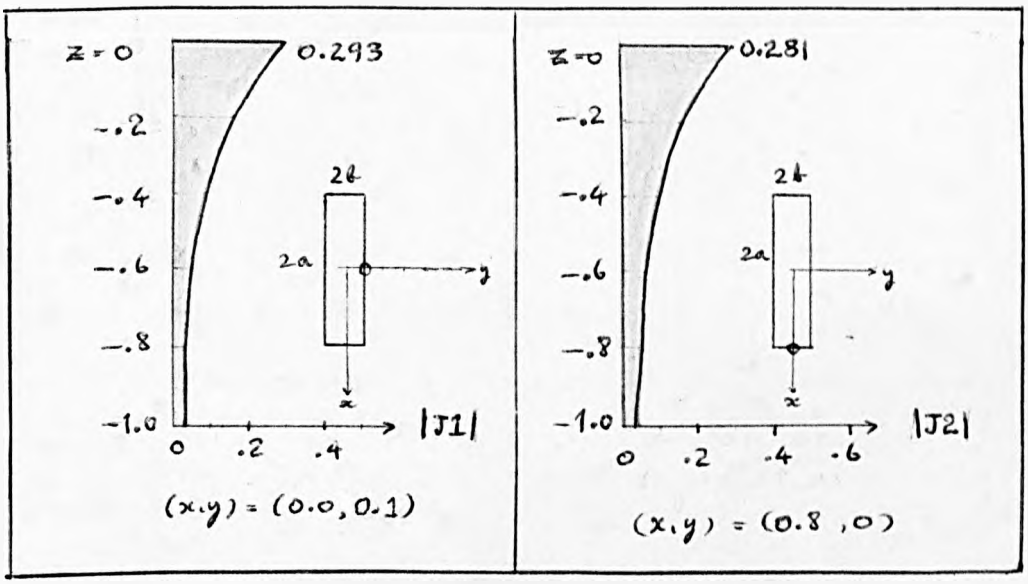

Fig. 11.7 Variation of Electric Current Density with Depth

11.16 (on $z=0$). We have used the notation $[B1, B2, B3] = \underline{B}/M$, $[J1, J2, J3] = \underline{J}/M$ where M is the strength of the tooth ($M = 4ab\mathcal{I}$) . The time averaged body force $[JB1, JB2, JB3] = \frac{1}{2}\mathcal{R}\{\underline{J} \wedge \underline{B}^*\} / M^2$, (1.31), is shown in figures 11.8 to 11.10 (variation with depth) and 11.17 to 11.19 (on $z=0$). We have also evaluated the inverse of (32) for the current potential; its modulus on $z=0$ is shown in figure 11.14, where $PT = \phi/M$.

In all of the above results we have neglected back reaction effects ($R_{mz} = 0$).

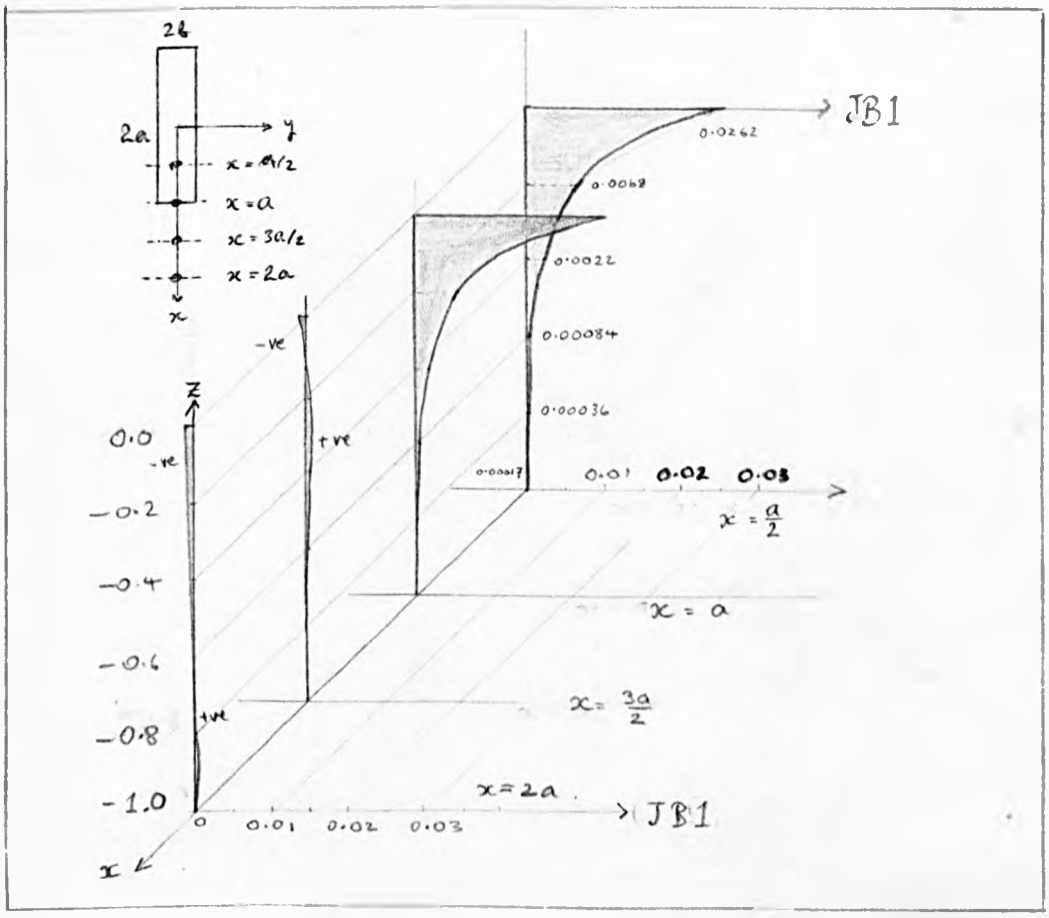

Fig. 11.8 Body Force Variation (X-cpt.) With Depth (y=0)

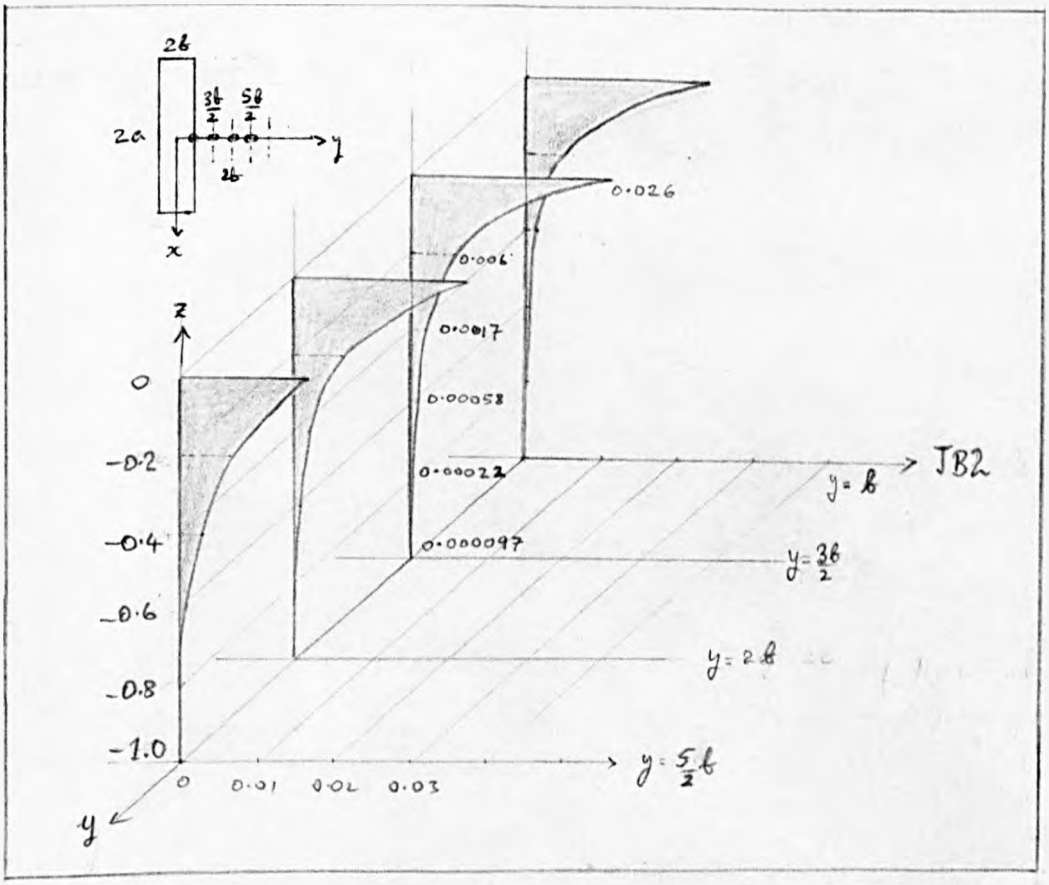

Fig. 11.9 Body Force Variation (Y-cpt.) With Depth (x=0)

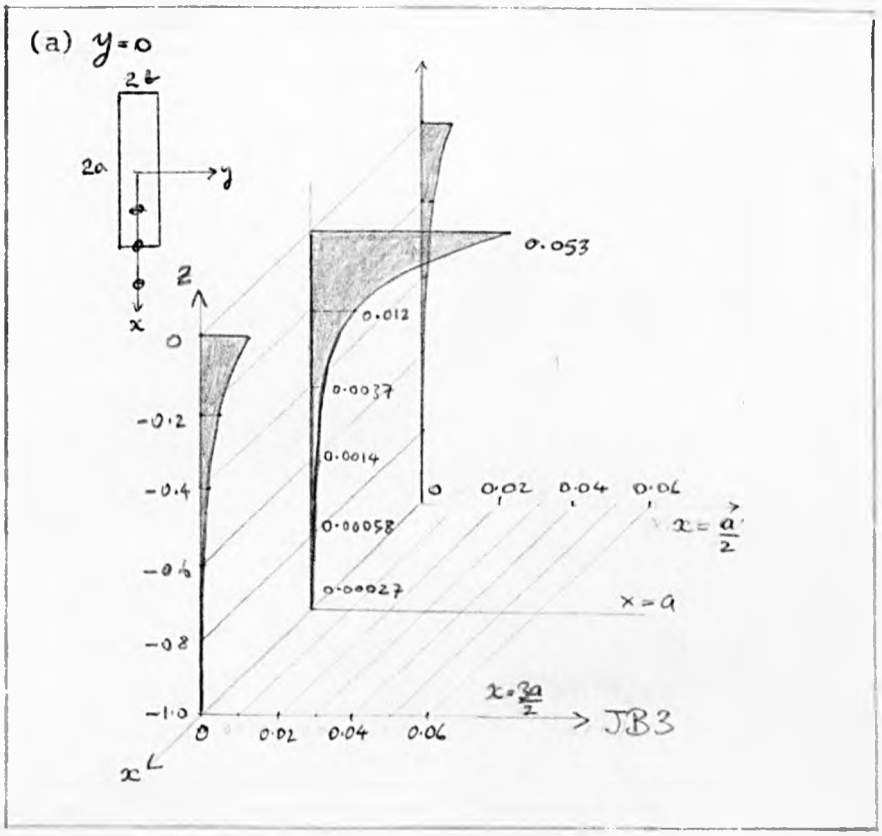

Fig. 11.10 Body Force Variation (Z-cpt.) With Depth

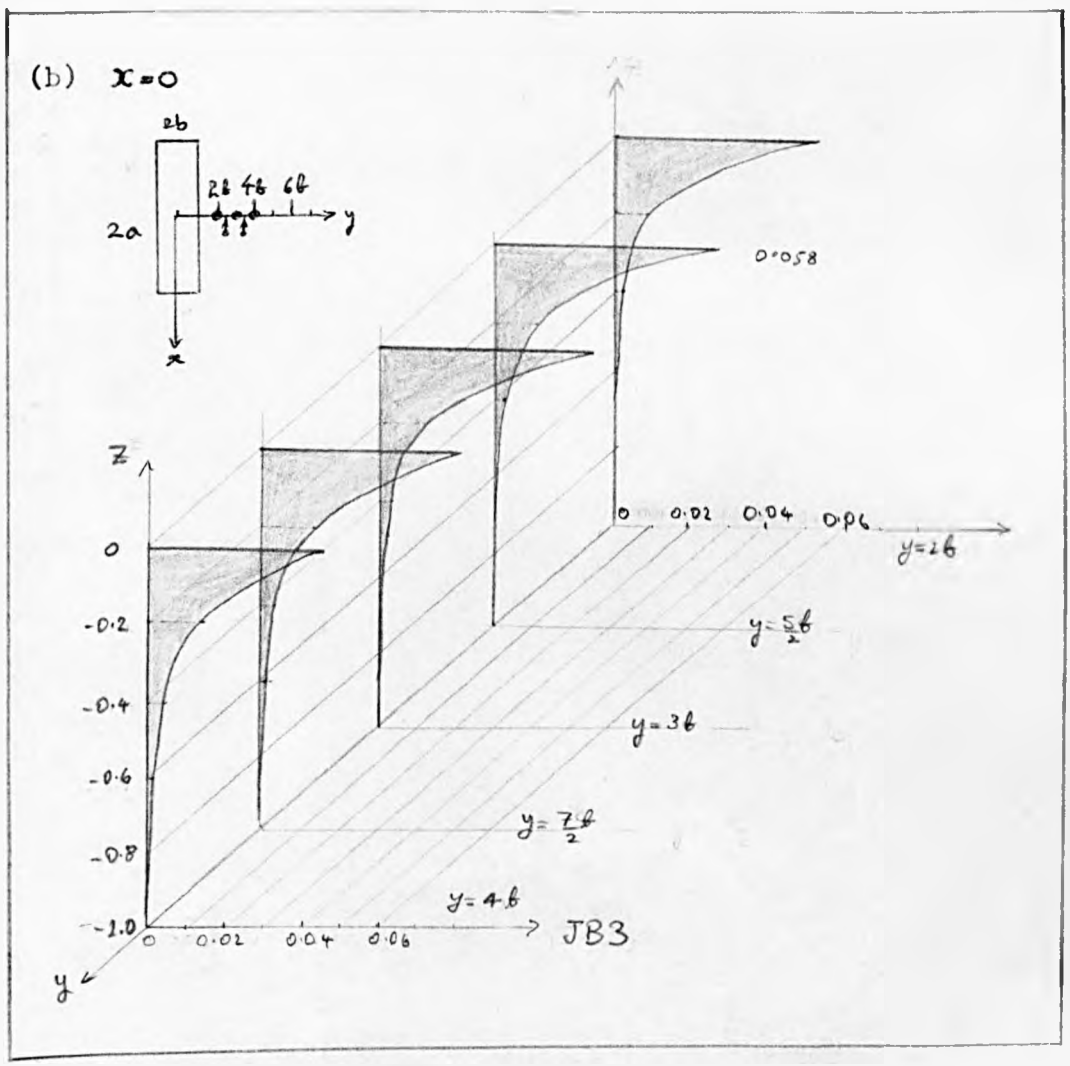

Fig. 11.11

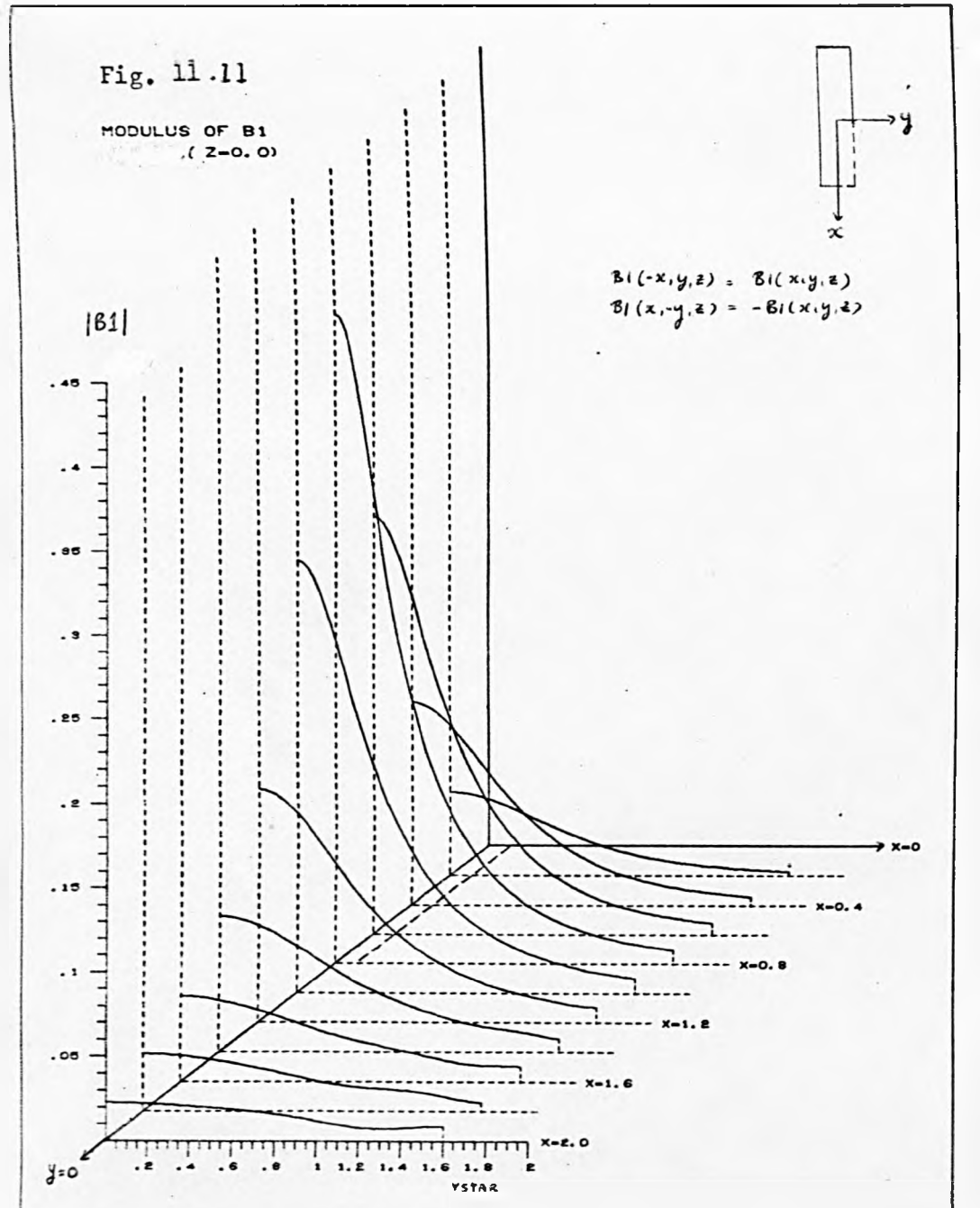
MODULUS OF B1
(Z=0.0)
|B1|
Bi(-x,y,z) = Bi(x,y,z)
Bi(x,-y,z) = -Bi(x,y,z)
y
x
.45
.4
.35
.3
.25
.2
.15
.1
.05
X=0
X=0.4
X=0.8
X=1.2
X=1.6
X=2.0
y=0
.2 .4 .6 .8 1 1.2 1.4 1.6 1.8 2
YSTAR

Fig. 11.12

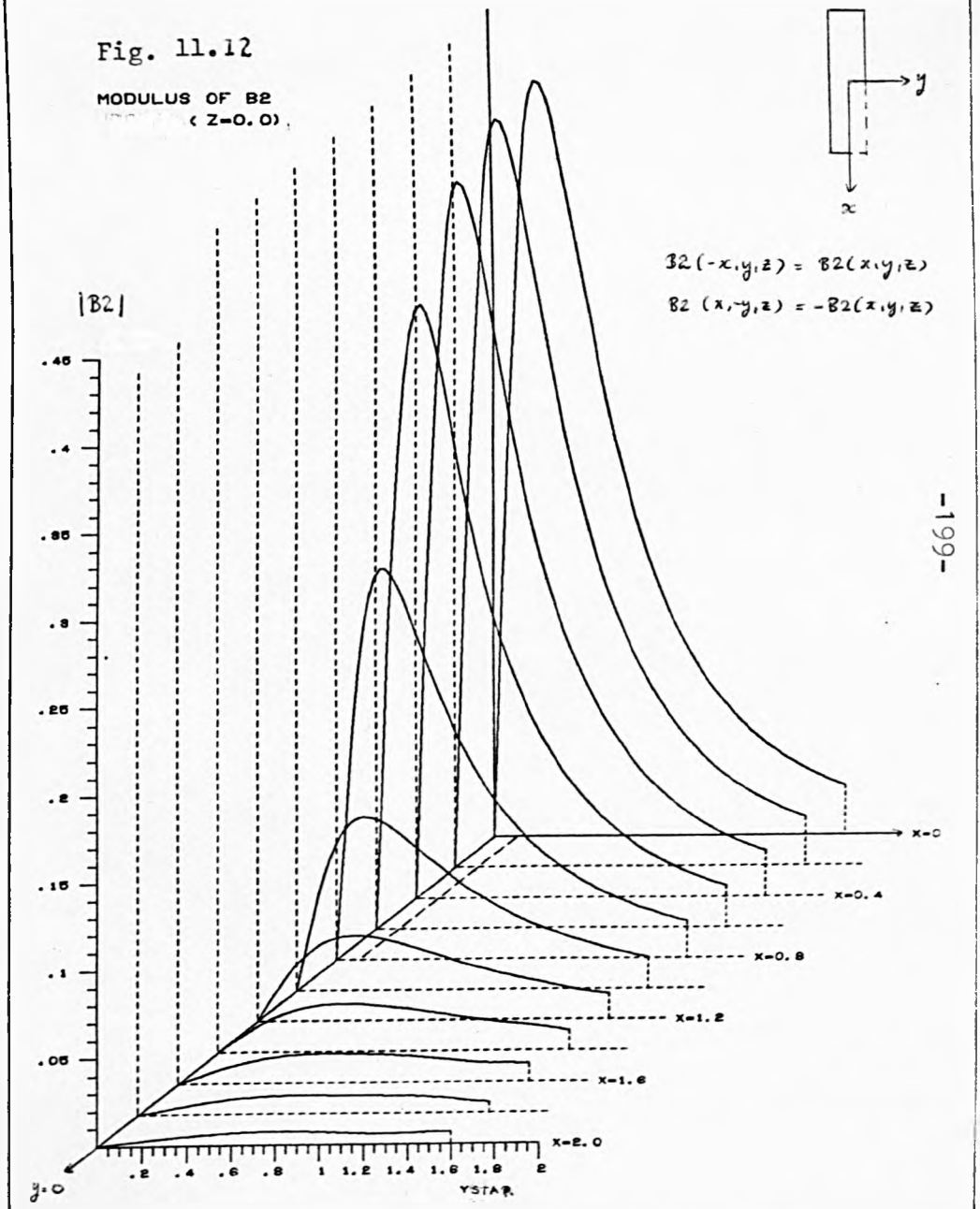
MODULUS OF B2
(Z=0.0)
|B2|
B2(-x,y,z) = B2(x,y,z)
B2 (x,-y,z) = -B2(x,y,z)
y
x
.45
.4
.35
.3
.25
.2
.15
.1
.05
x=0
x=0.4
x=0.8
x=1.2
x=1.6
x=2.0
.2 .4 .6 .8 1 1.2 1.4 1.6 1.8 2
y=0
YSTAR

Fig. 11.13

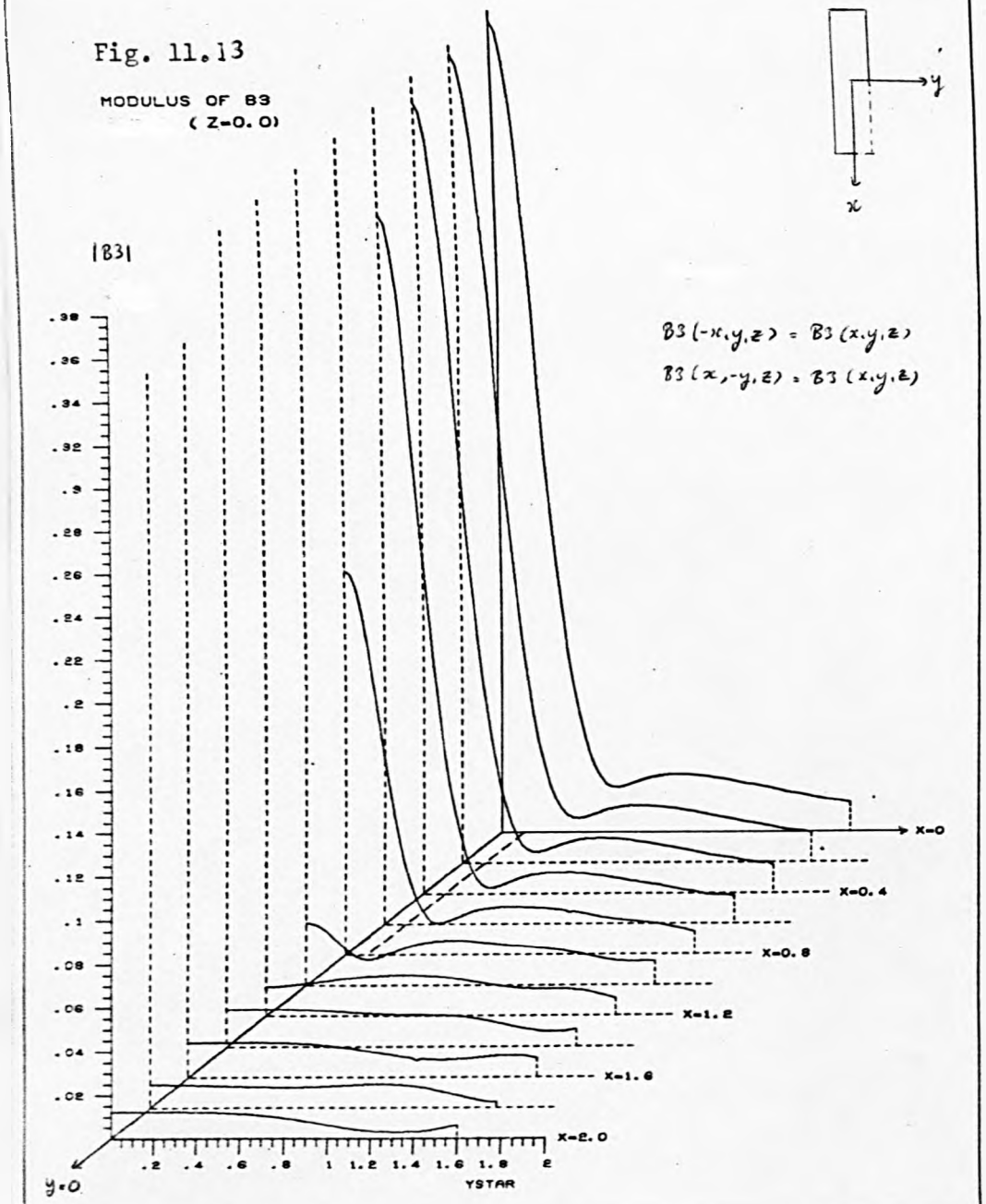

Fig. 11.14

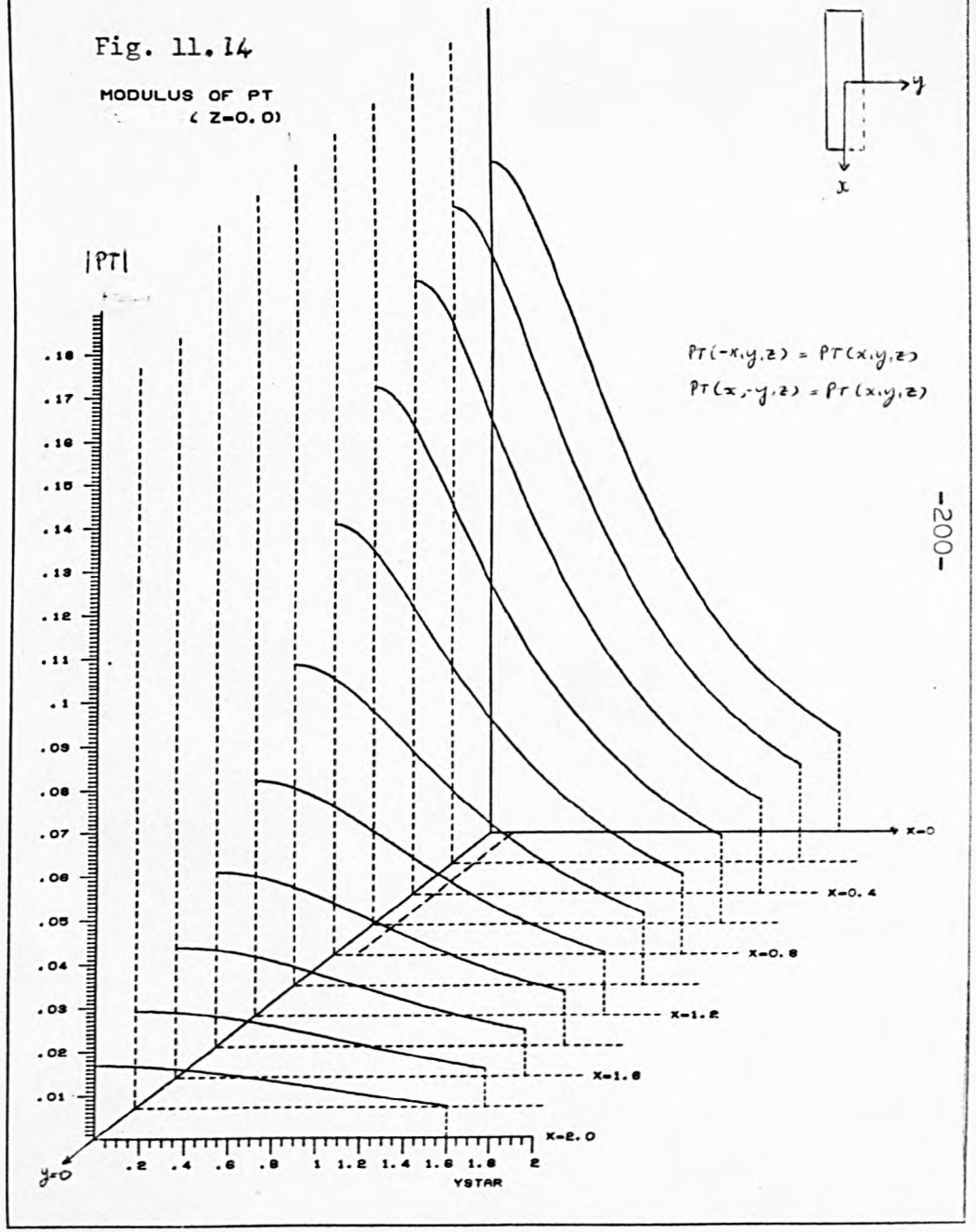

Fig. 11.15

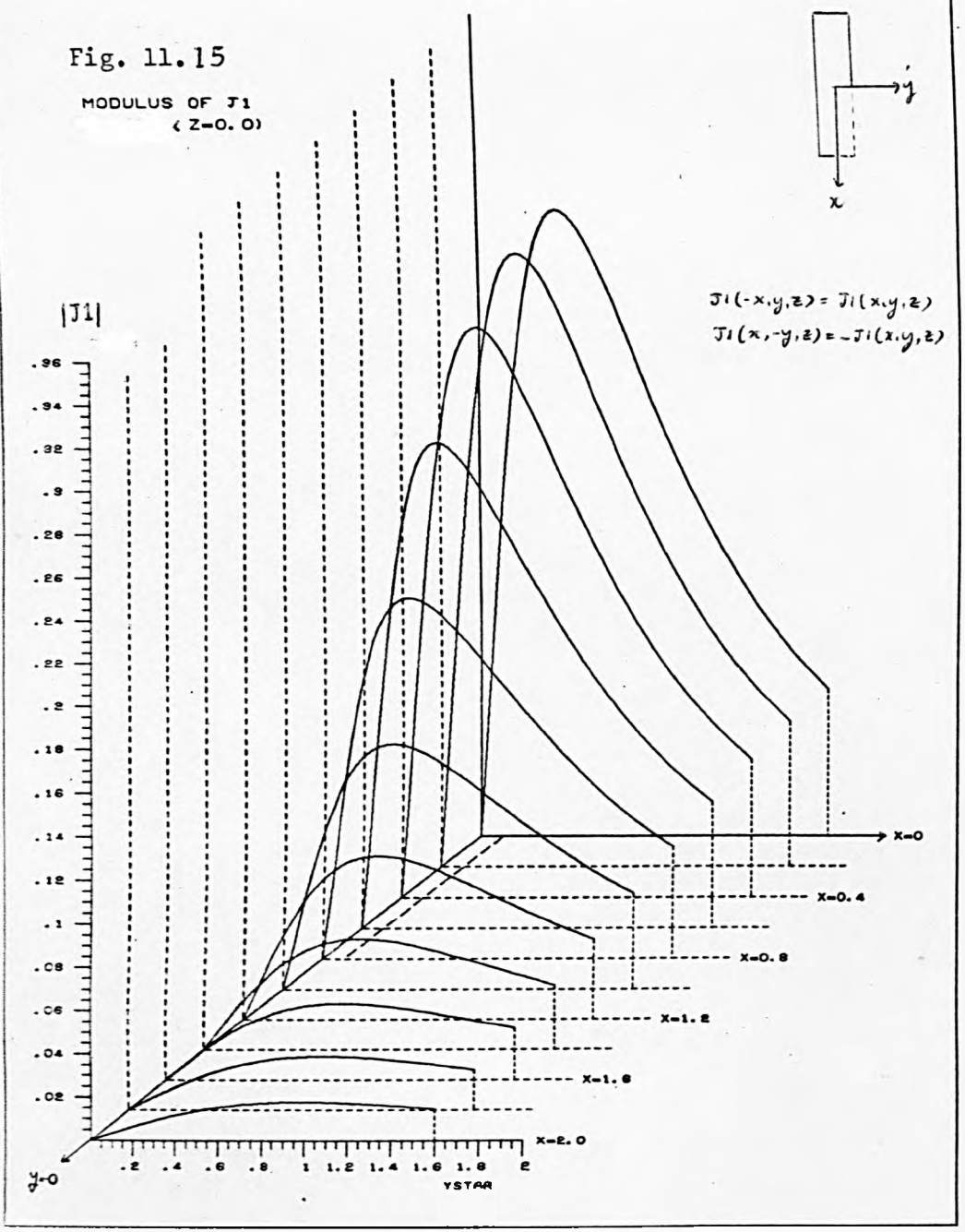

Fig. 11.16

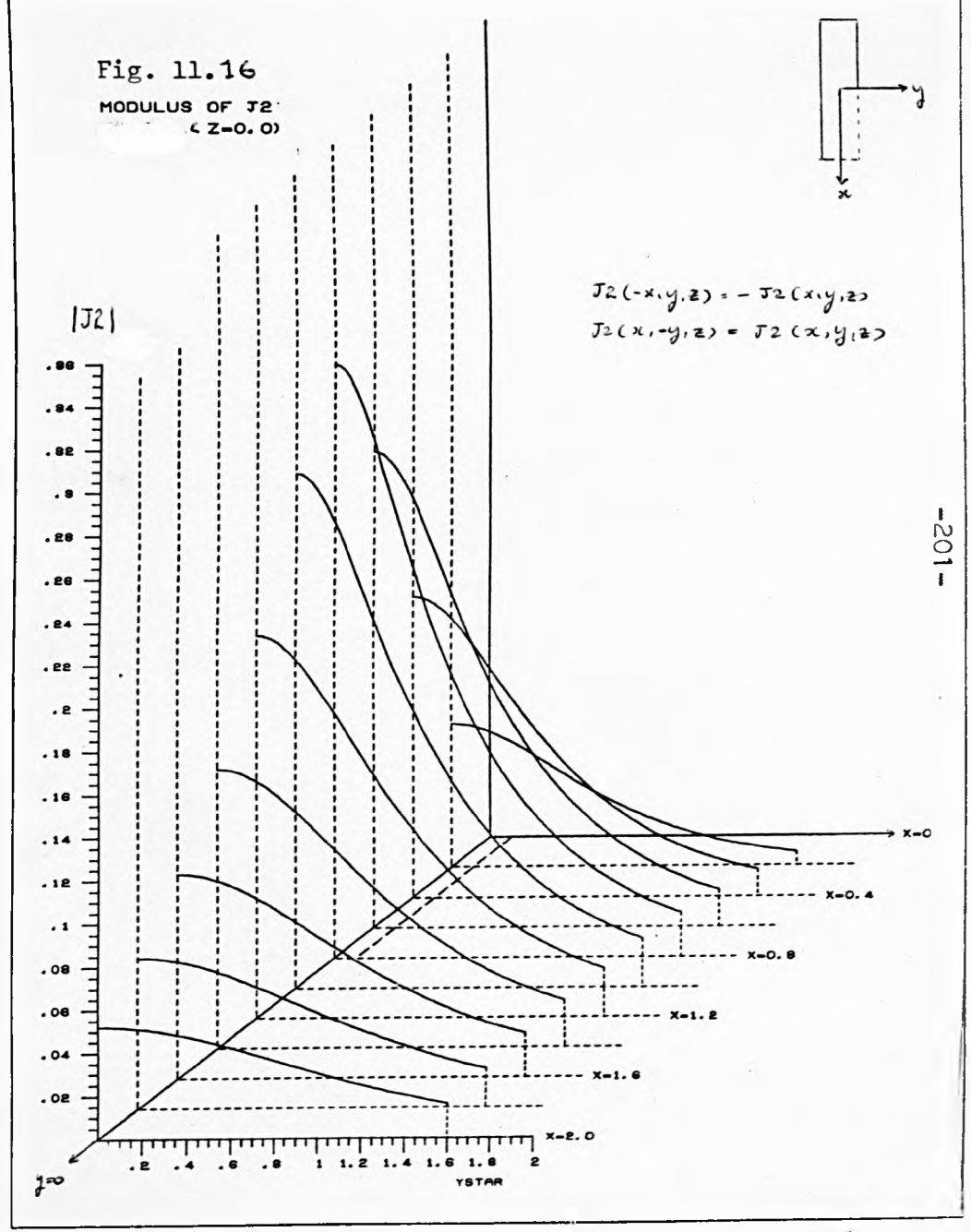

Fig. 11.17

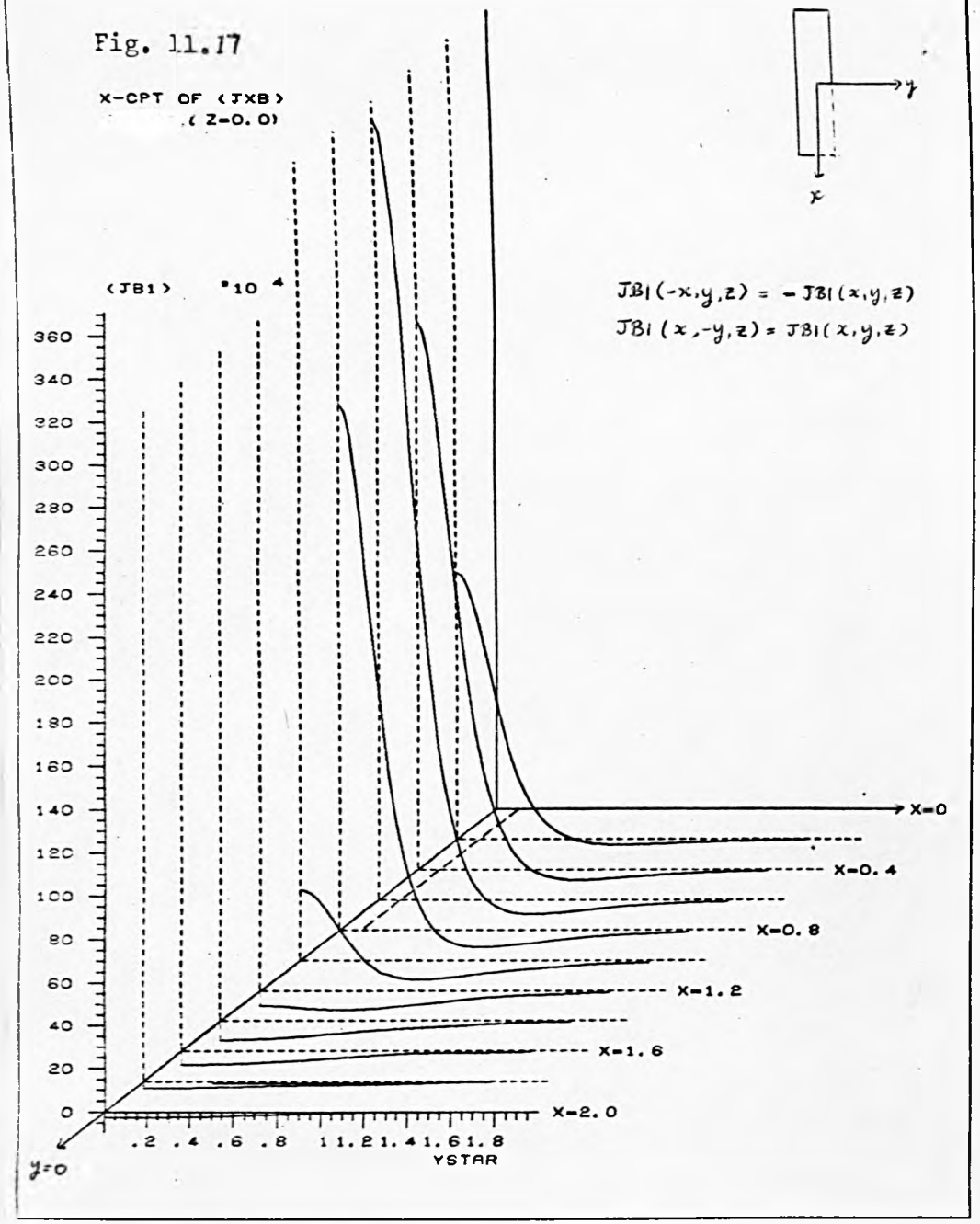

Fig. 11.18

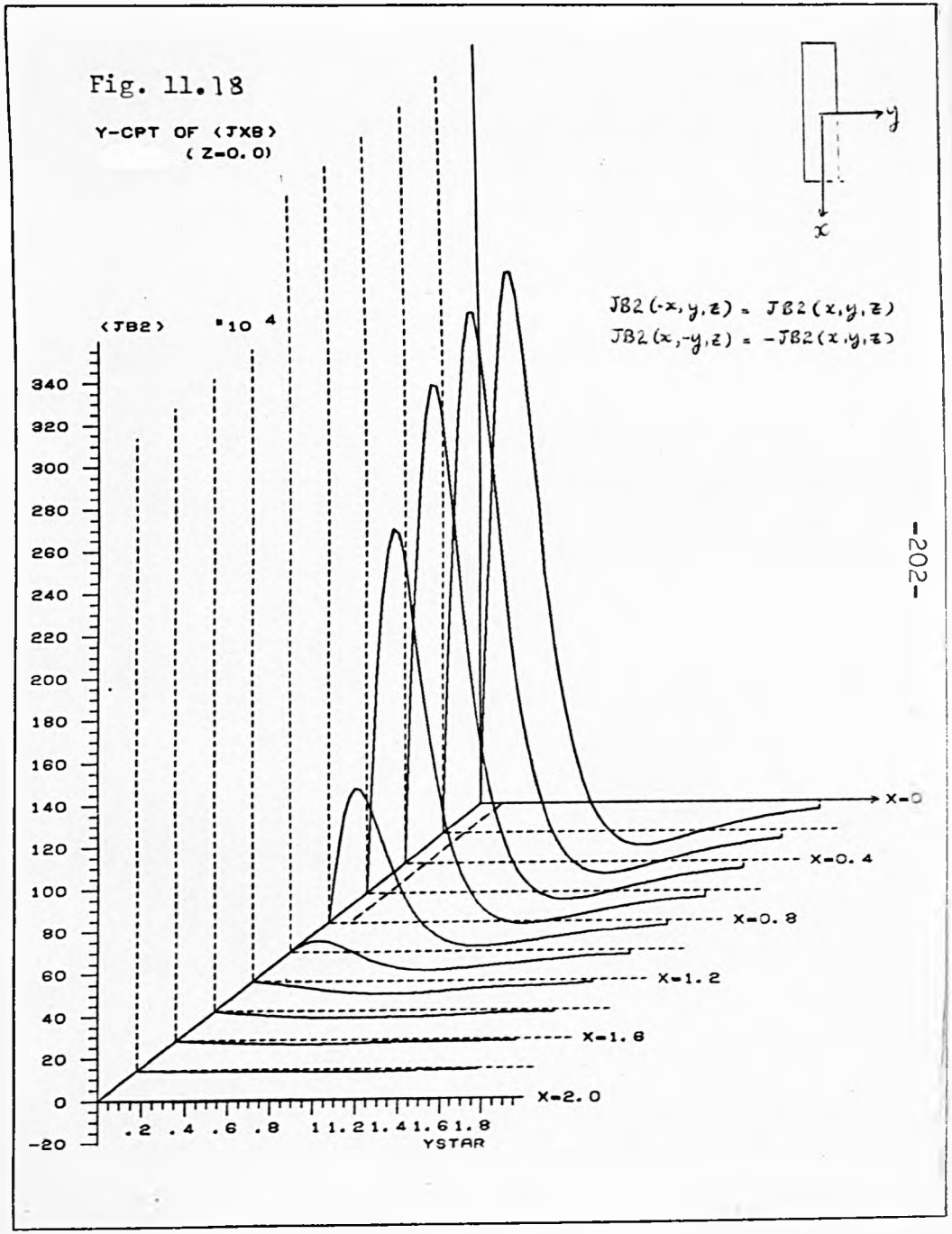

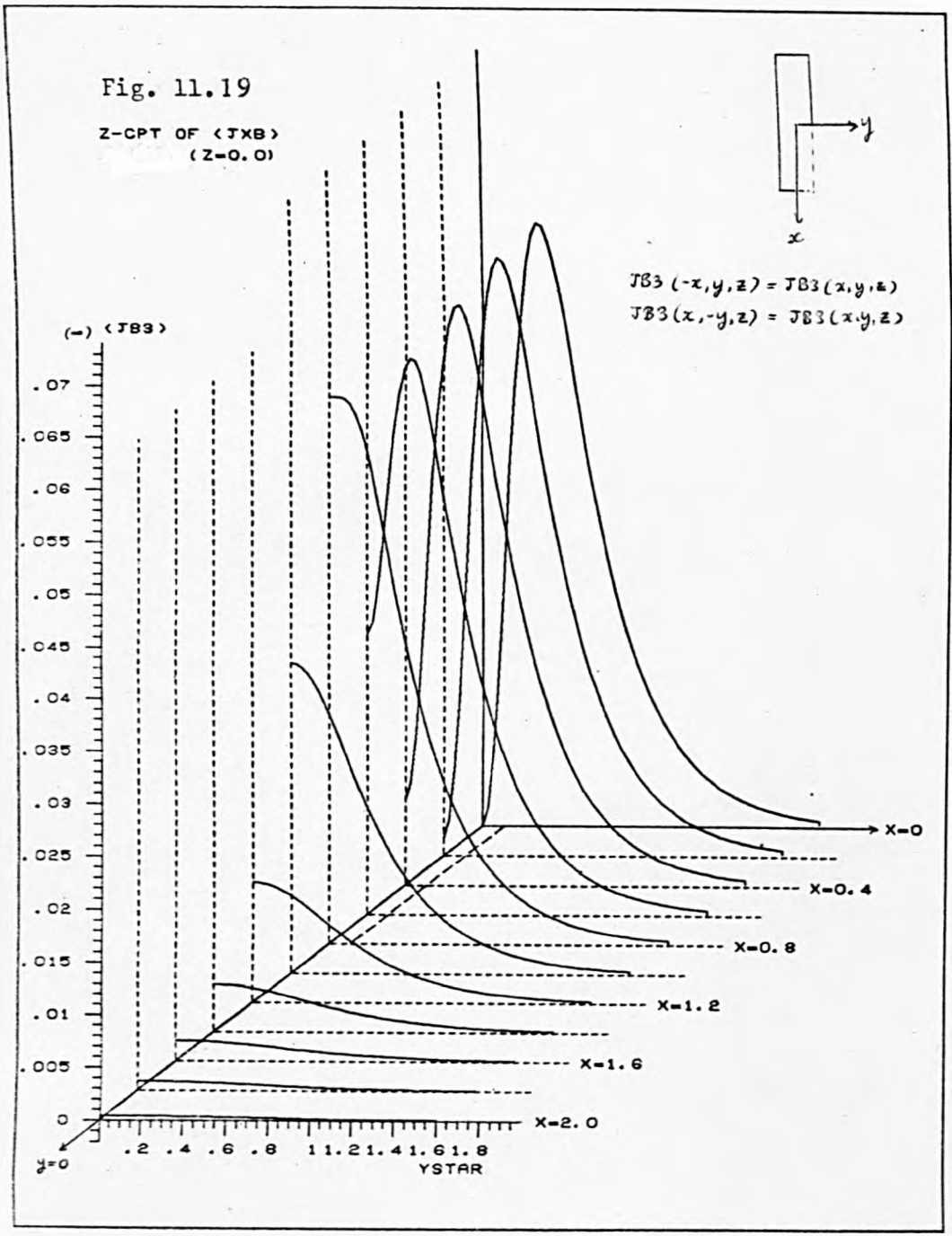
Fig. 11.19
Z-CPT OF ⟨JXB⟩
(Z=0.0)
y
x
JB3(-x,y,z) = JB3(x,y,z)
JB3(x,-y,z) = JB3(x,y,z)
(-) ⟨JB3⟩
.07
.065
.06
.055
.05
.045
.04
.035
.03
.025
.02
.015
.01
.005
0
X=0
X=0.4
X=0.8
X=1.2
X=1.6
X=2.0
y=0
.2 .4 .6 .8 1 1.2 1.4 1.6 1.8
YSTAR

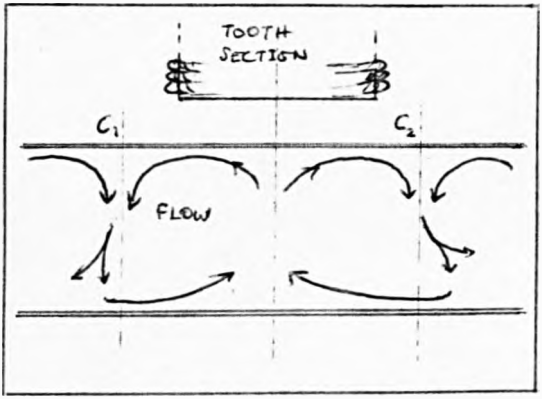

Fig. 11.20 Possible flow pattern for sections in the (x,z) or (y,z) planes

11.8.1 Observations On The Results. We briefly note the more important espects of the results. Figures 11.6 to 11.10 clearly show an exponential decay with depth although the actual rate of decay depends on the position in the plane of the tooth (see chapter 6). We see that the variation of $|J_1|$ and $|\mathcal{B}_2|$ is similar, as is the variation of $|J_2|$ and $|\mathcal{B}_1|$ This result has been noted in the idealised analysis of §6.2 where it has been physically explained using Stoke's theorem. It is clear from figures 11.17 to 11.19 that the induced body force components all have their maxima around the perimiter of the projection of the tooth in the conductor. At the centre of this projection the body force is of course zero since induced currents are zero there. Although it appears that the normal body force is always of a 'levitator' nature it is clear that the force in the plane of the tooth reverses direction beyond the tooth perimeter. From an analysis of the body force variation we conclude that the overall flow induced in molten tin by a solitary tooth is similar to that shown in figure 11.20. (The cross section in the diagram may be taken as the (x,z)- or (y,z)-plane). The points C_1 and C_2 are points beyond the perimeter of the tooth corresponding to points where the direction of the tangential body force changes.

Writing $\underline{\mathcal{B}} = \mathcal{B}_R + i\mathcal{B}_I$, we have the result $\mathcal{R}\{\underline{\mathcal{B}}e^{i\omega t}\} = |\underline{\mathcal{B}}|\, e^{i(\omega t+\phi)}$ where $\phi = \tan^{-1}(\mathcal{B}_I/\mathcal{B}_R)$. Thus $|\underline{\mathcal{B}}|$ gives the behaviour of the magnetic induction averaged over a period of osciilation $(\frac{2\pi}{\omega})$ whilst its behaviour at any time t is given by $\mathcal{B}_R\cos\omega t - \mathcal{B}_I \sin\omega t$. Similarly for ϕ and $\mathcal{I}$. The significance of the real and imaginary parts of the EM field is fully considered in chapter 12 so we shall not present a discussion here. However, graphs of these fields are included in Appendix IV , and their structure is analysed there using the magnetic field line theory described in chapter 12.

11.8.2 Application Of The Theory To Geophysics. One of the methods of analysing the structure of the Earth depends on making electrical or

or electromagnetic measurements, at the surface, of the effect of artificial or natural (tellaric) currents in the Earth. Artificial currents can be produced by conductive, inductive or transient (pulse) methods but we shall only consider the second of these here. Telluric currents (which are believed to arise from ionospheric currents) can be represented theoretically by line currents or current sheets placed above the Earth's surface (see CAGNAIRD, 1953) whilst the source for the inductive method (usually current coils or cables) can be modelled by a magnetic dipole or line current array (see WAIT, 1951). A connected problem is the use of ground-based magnetic dipoles to probe the magnetosphere (for example FRASER-SMITH and BUBENIK, 1974). Because the Earth is usually assumed to be a horiaontally stratified half space, it is clear that the method of solution of the induction problem developed in this chapter for the analysis of a SLIM may equally be applied in the above areas of geophysics. By removing the stator core boundary condition at $z = h$, the expressions (47) to (55), which describe the field of a vertical magnetic dipole placed at a height z_0 above the conductor surface, can be reduced to the well-known expressions for a magnetic dipole placed above a two-layer Earth (see for example*, WEAVER and THOMPSON,(1970) -asymptotic expansion for large z_0). Neglecting up going waves reduces (47) to (55) to the well known results for a magnetic dipole outside a semi-infinite conductor (see for example*, GORDON, (1951a) - evaluation for $z_0 = 0$). References for other source configurations can be found in the review of WEAVER (1973). Apart from various asymptotic reductions and some special cases it does not seem possible to write the integral expressions in (47) to (50) in terms of known functions. However approximate expressions for the EM field produced by a horizontal line current and horizontal magnetic dipole placed above a conducting half space, have been derived by PARK (1974) and WEAVER (1971) respectively. Both authors use an image method whereby an image source is placed at a complex depth below the conductor surface.

* and Appendix IV

Although we do not claim that the theory described in this chapter for the analysis of EM induction is stratified media is as significant as that developed by PRICE (1950), GORDON (1951b) or WEAVER (1970), (see WEAVER (1973) for a résumé of the authors' methods), it is clear that we can duplicate many of the published results with relative ease and the initial use of a current element source allows more complex primary source configurations to be constructed.

11.9 The EM Field of a SLIM

As we have described in §11.2 the EM field of a SLIM is found by combining the EM field of individual, suitably phased and positioned, coil-wound teeth. The diagrams in figures 11.11 to 11.19 show the extent to which we have evaluated a tooth's field - we have obtained data for the region $0 < x < 5a/2$, $0 < y < 2\tau$, where τ is the pole pitch of the float bath motor. Using symmetry arguments we can obtain a complete set of data for the rectangle $|x| < 5a/2$, $|y| < 2\tau$, (the symmetry properties for the field components are shown in their respective diagrams).

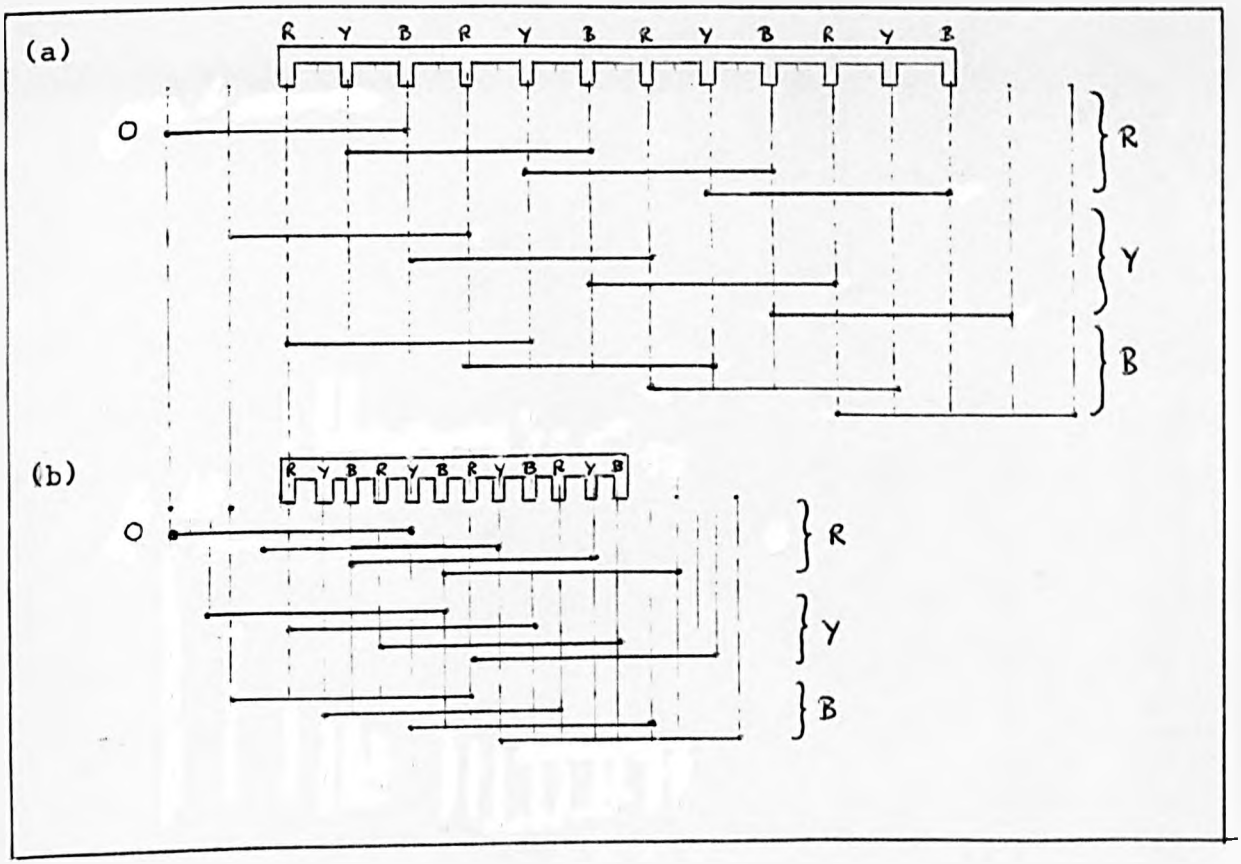

Fig. 11.21 The extent of a tooth's influence

Axial sections through two FLIMs are shown in figures 11.21 (a) (the float bath motor (Data 1) - see figure 1) and 11.21 (b), (Data 2), together with the extent of each tooth's influence. Suppose that $f(y)e^{i\omega t}$ represents the behaviour of an EM field component for a single tooth (when x and z are fixed), where $f(y)$ is a complex function, then the field of the motor is given by $f^M(y)e^{i\omega t}$, where

$$f^M(y) = e^{i\theta}\sum_{n=1}^{q}\sum_{m=1}^{3}\alpha_{mn}\, f(y+g(c))\left\{H(y+g(c))-H(y-g(c))\right\}e^{2i(m-1)\pi/3} \qquad (62)$$

In (62), the point $y=0$ is chosen as the point O in figures 11.21(a) and (b); θ is a parameter which specifies the phase of the colour groups at $t=0$; c is the tooth pitch; $g(c)=c(1-m-3n)$, (Data 1), or $g(c)=-c(1+m+3n)$, (Data 2); $H(\xi)$ is the Heaviside unit step function and the summation is over the three phases with four teeth per phase. The parameter α_{mn} equals 0.5 if $m+n$ = 2 or 7, otherwise it equals unity - this is to include the effect of half-wound end teeth. It is clear from the nature of (62) that $f^M(y)$ will only be a smooth function if the rate of decay of $f(y)$ is sufficiently large to ensure that no jumps occur at the point where adjacent tooth-fields overlap.

Because only real expressions have physical meaning, the actual field $F=\mathcal{R}\{f^M e^{i\omega t}\}$ becomes, on writing $f^M=F_R+iF_I$, $F=|f^M|\cos\{\omega t+\tan^{-1}(\frac{F_I}{F_R})\}$. For a full description of the behaviour of F for a SLIM we require an evaluation of (62) over the range of values of x and z . However, we are mainly concerned with the induced EM field - the character of which is indicated by the fields behaviour on $z=0$ (the conductor surface). In figures 11.22 to 11.37 we show* the variation with x and y of the magnitude of the functions $|f^M|$ and $\cos h(y)$, where $h(y)=\tan^{-1}\{\frac{F_I}{F_R}\}$, along the plane $z=0$, when the pole pitch is that in Data 1 (the data for the float bath FLIM - see figure 11.21 (a)). The discrete function f^M is found by substituting the data obtained from (56) to (61), (which specifies the

* The graphs were plotted using H Williamson's FORTRAN subroutine HIDE (Algorithm 420, Hidden-Line Plotting Program, Communications of the ACM, 15, 2, 1972).

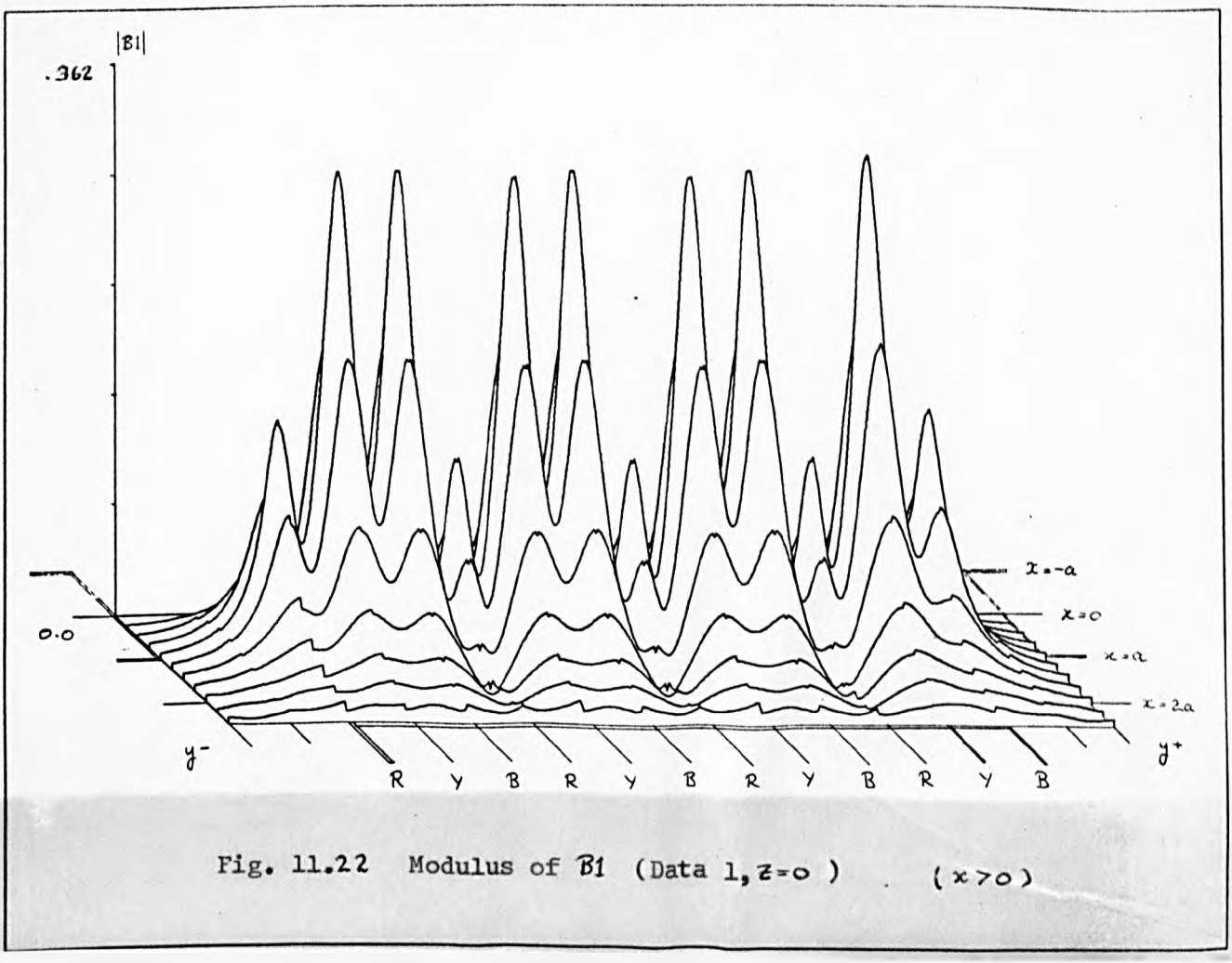

Fig. 11.22 Modulus of $\mathcal{B}1$ (Data 1, $z=0$) $(x>0)$

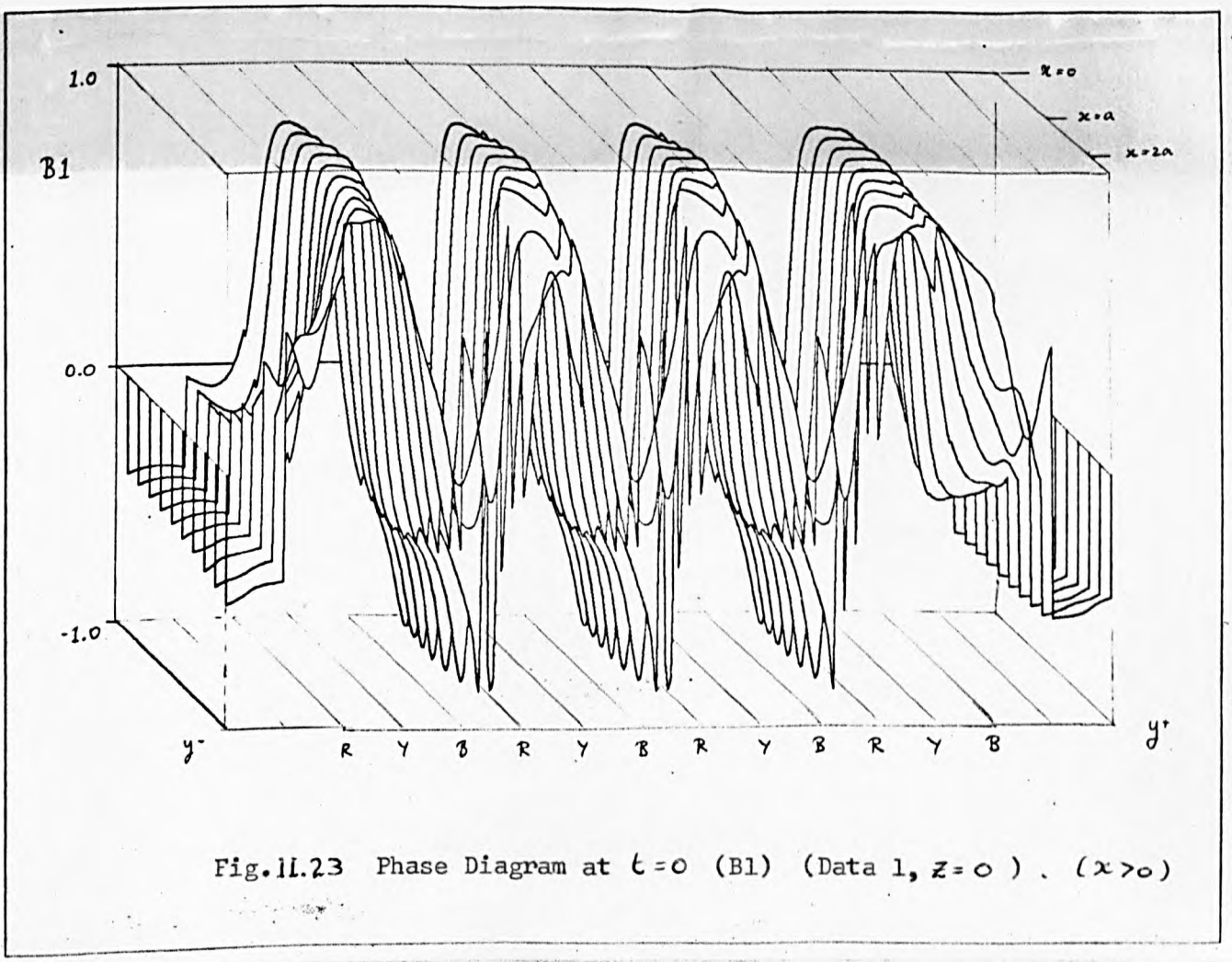

Fig. 11.23 Phase Diagram at $t=0$ (B1) (Data 1, $z=0$) . $(x>0)$

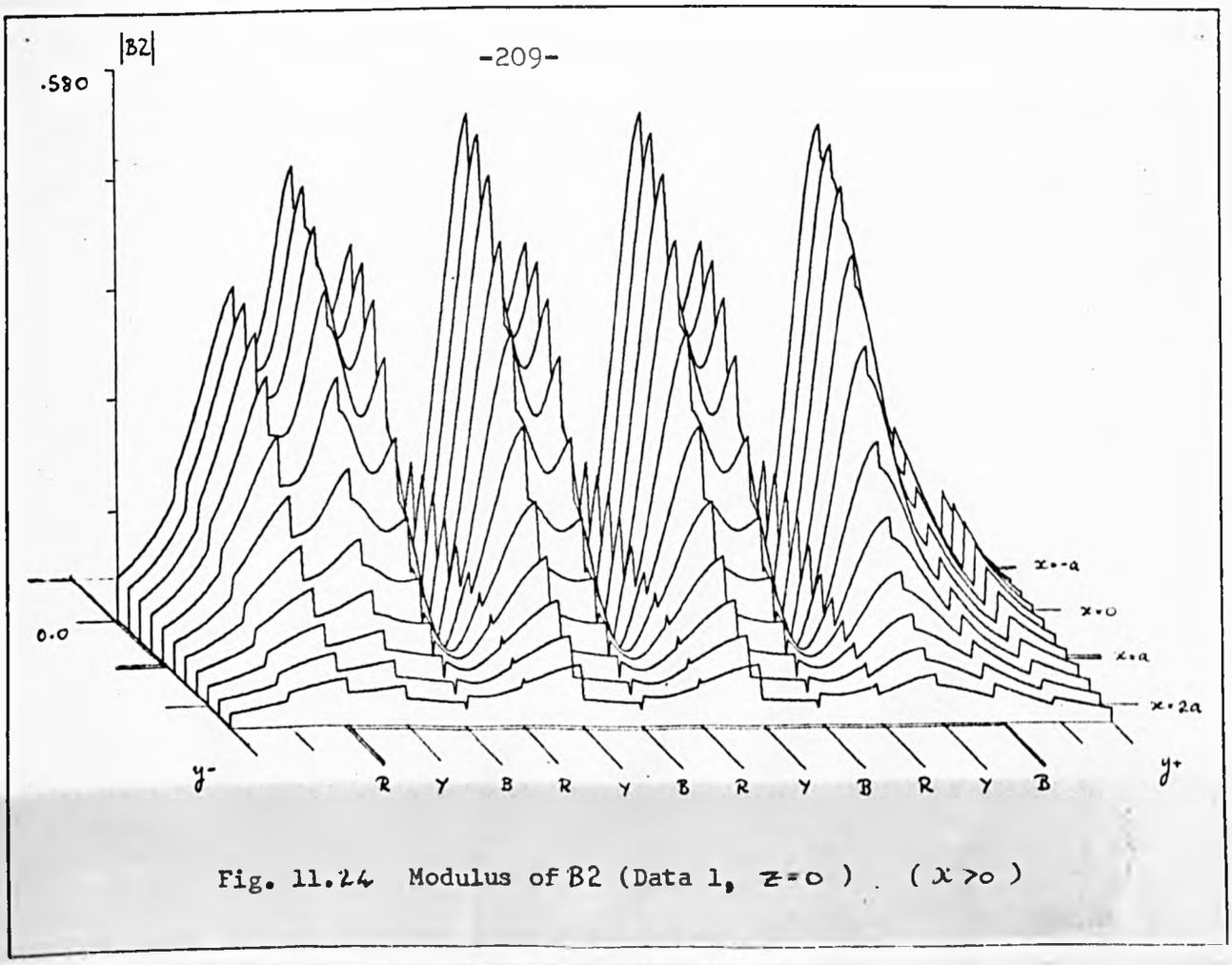

Fig. 11.24 Modulus of B2 (Data 1, $z=0$) ($x>0$)

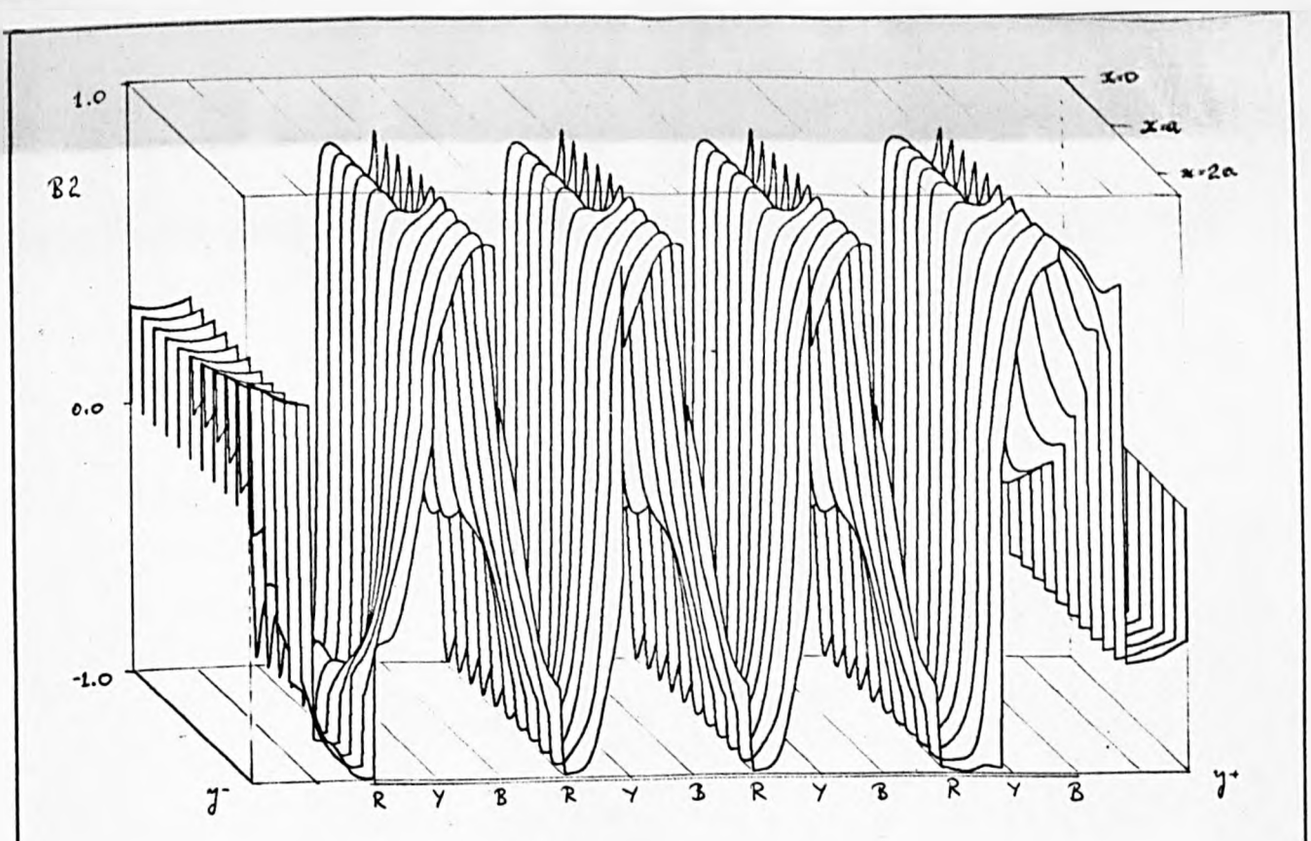

Fig. 11.25 Phase Diagram at $t=0$ (B2) (Data 1, $z=0$) ($x>0$)

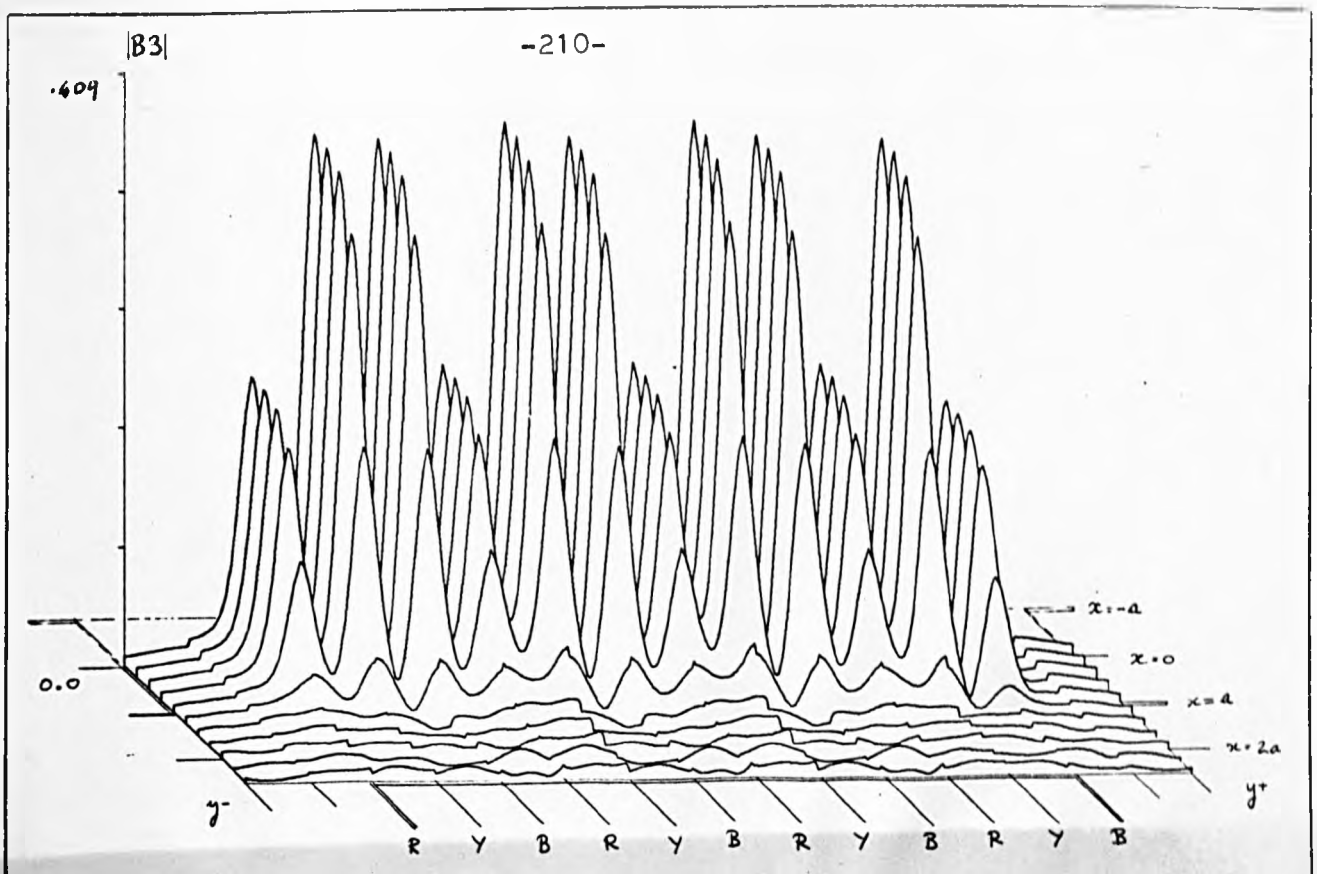

Fig. 11.26 Modulus of B3 (Data 1, z=0) (x>0)

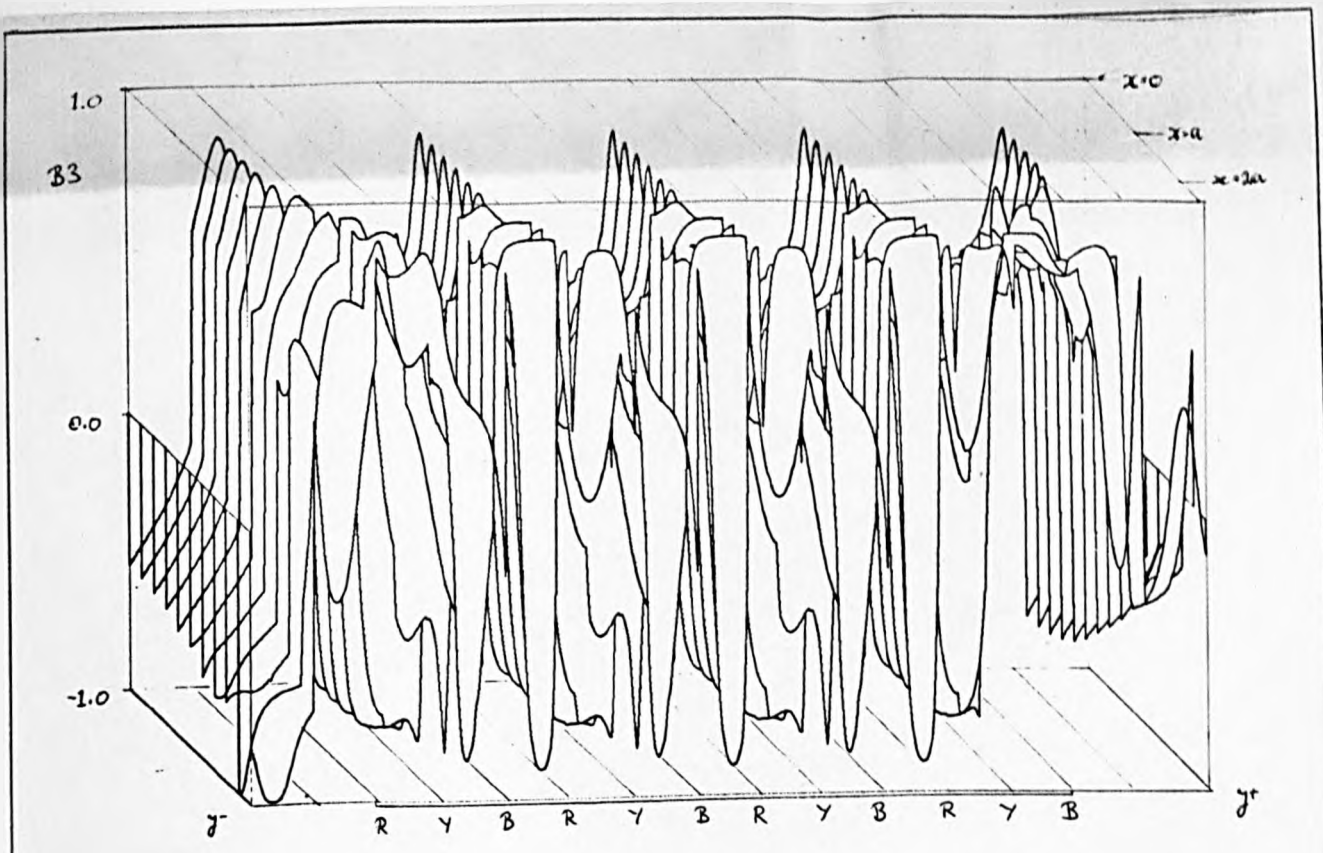

Fig. 11.27 Phase Diagram at t=0 (B3) (Data 1, z=0) (x>0)

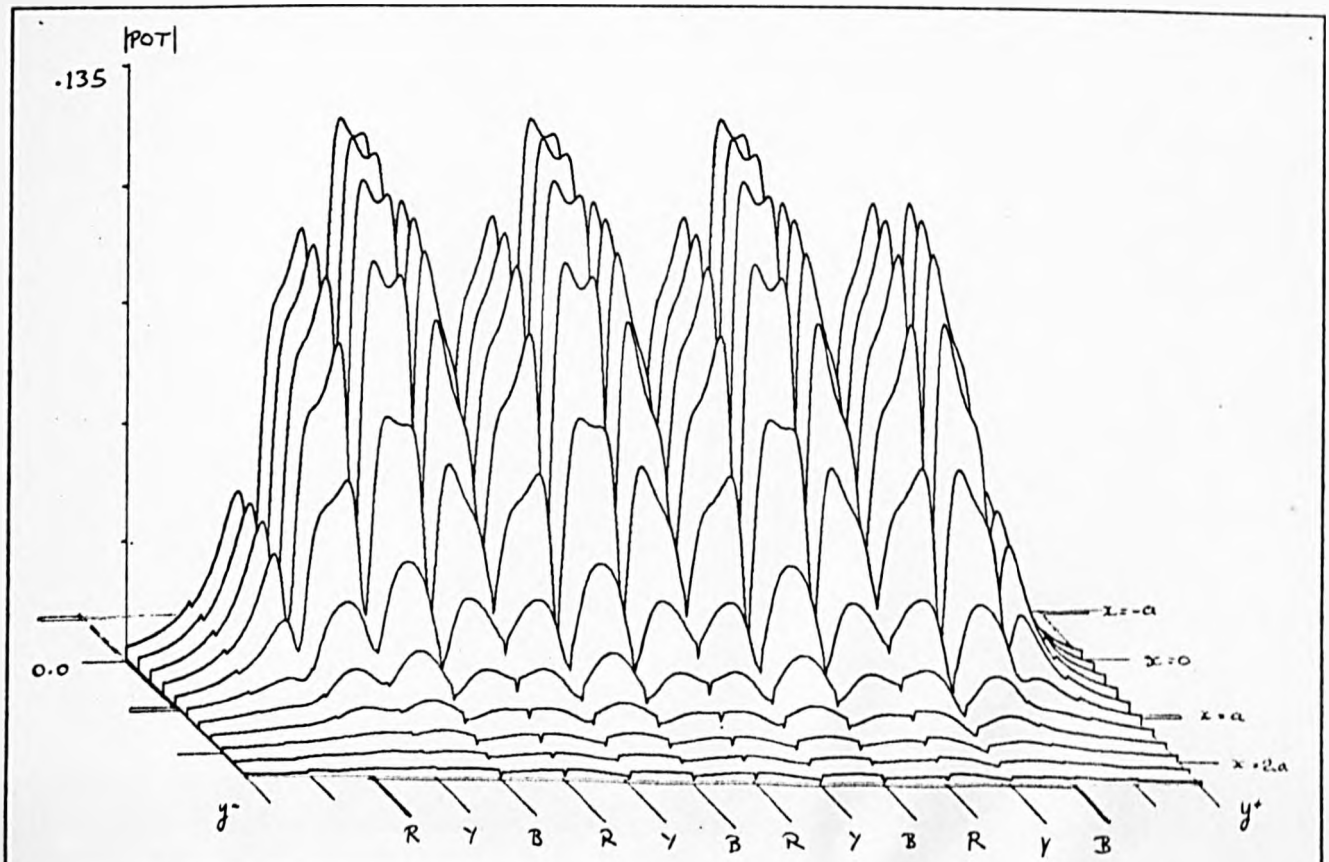

Fig. 11.28 Modulus of POT (Data 1, Z=0). (x>0)

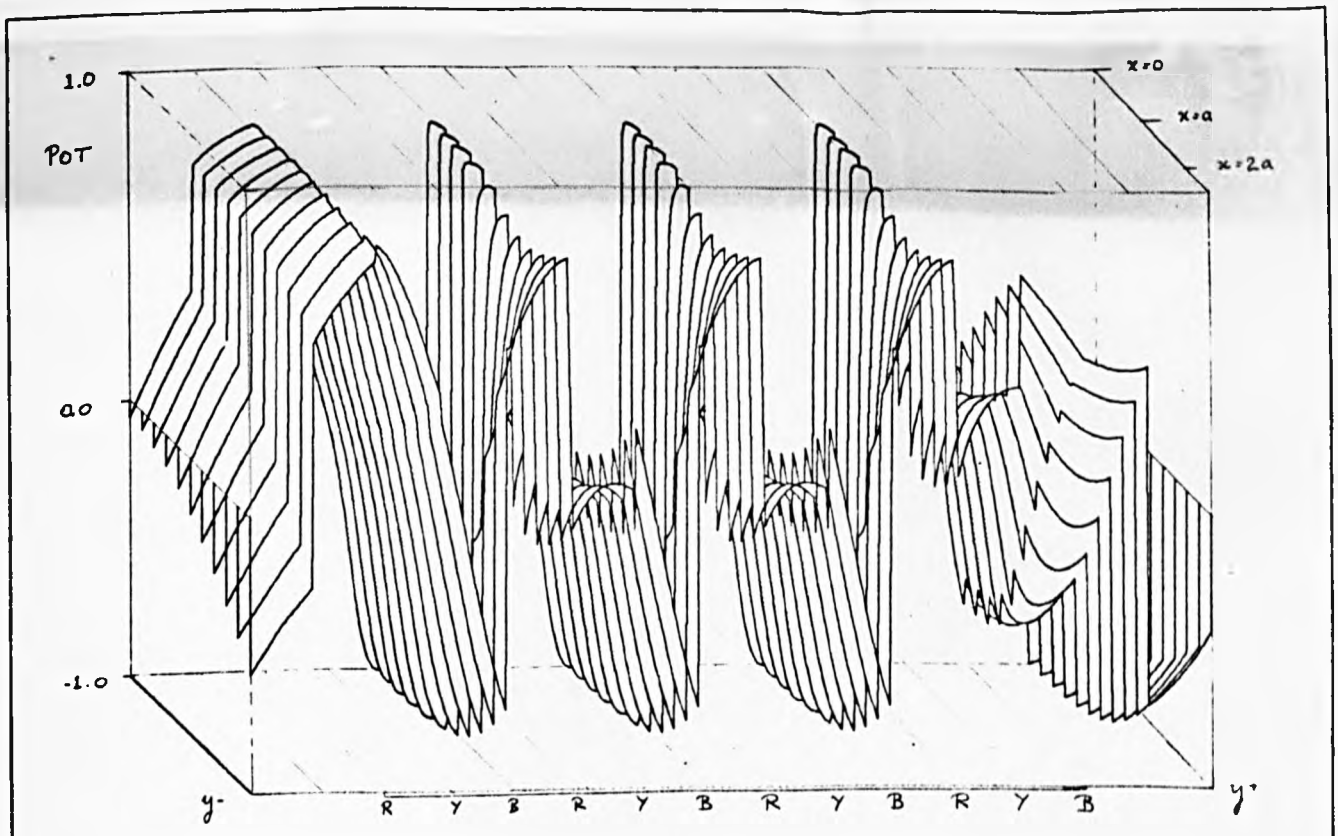

Fig. 11.29 Phase Diagram at t=0 (POT) (Data 1, Z=0) (x>0)

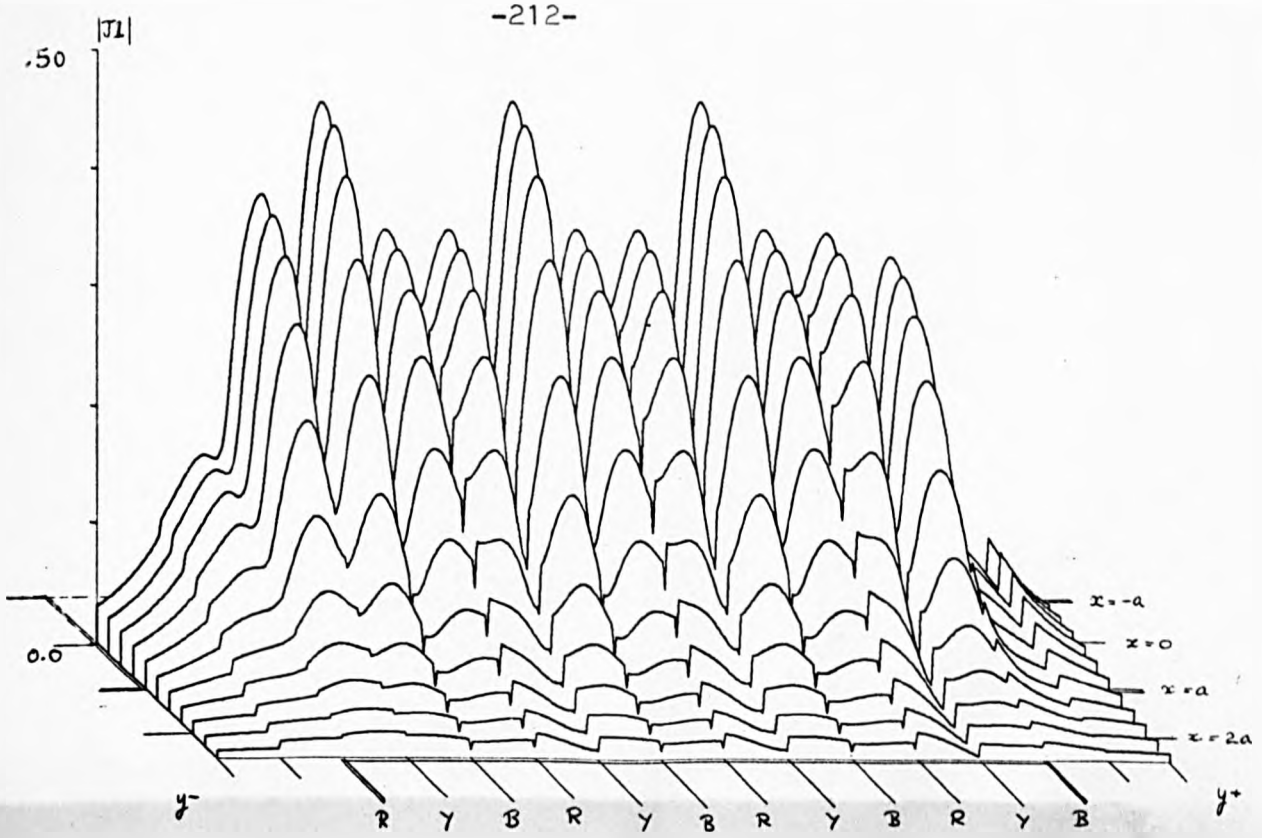

Fig. 11.30 Modulus of J1 (Data 1, z=o) . (x>o)

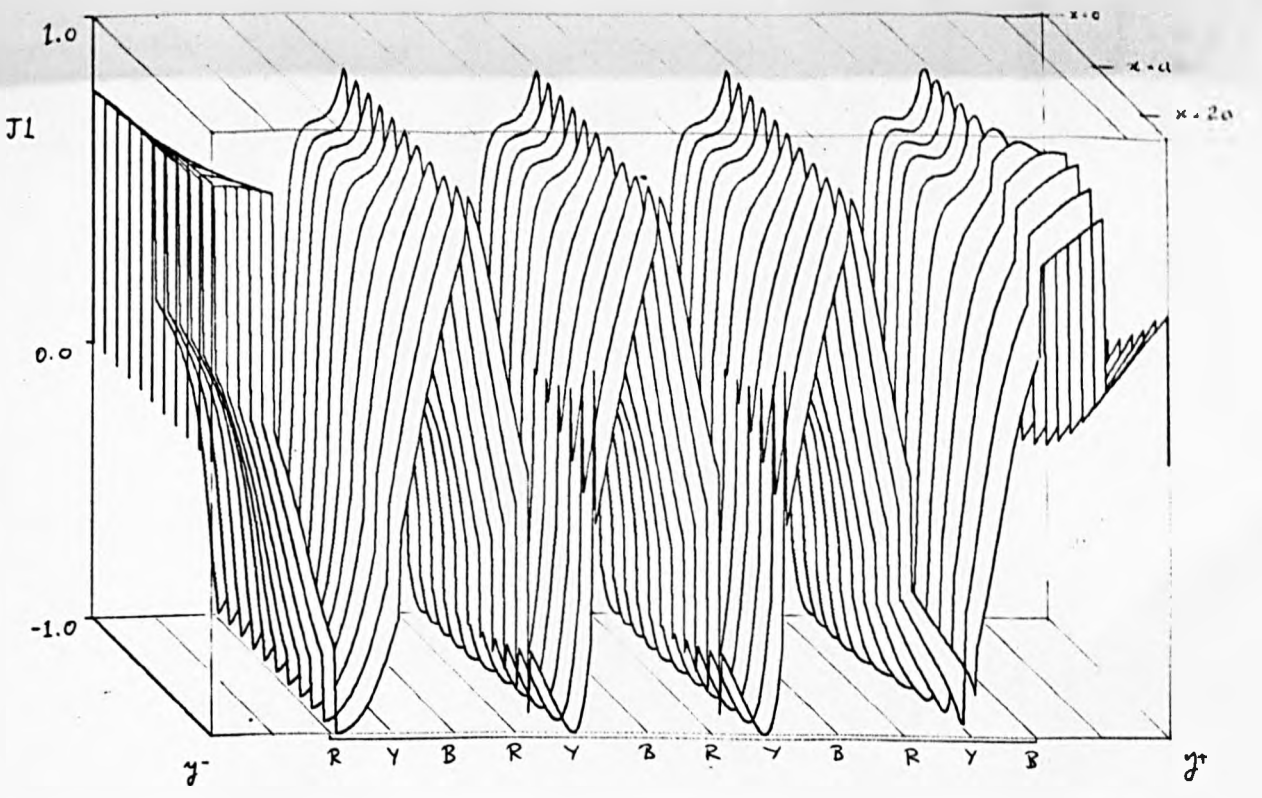

Fig.11.31 Phase Diagram at t=o (J1) (Data 1, z=o) (x>o)

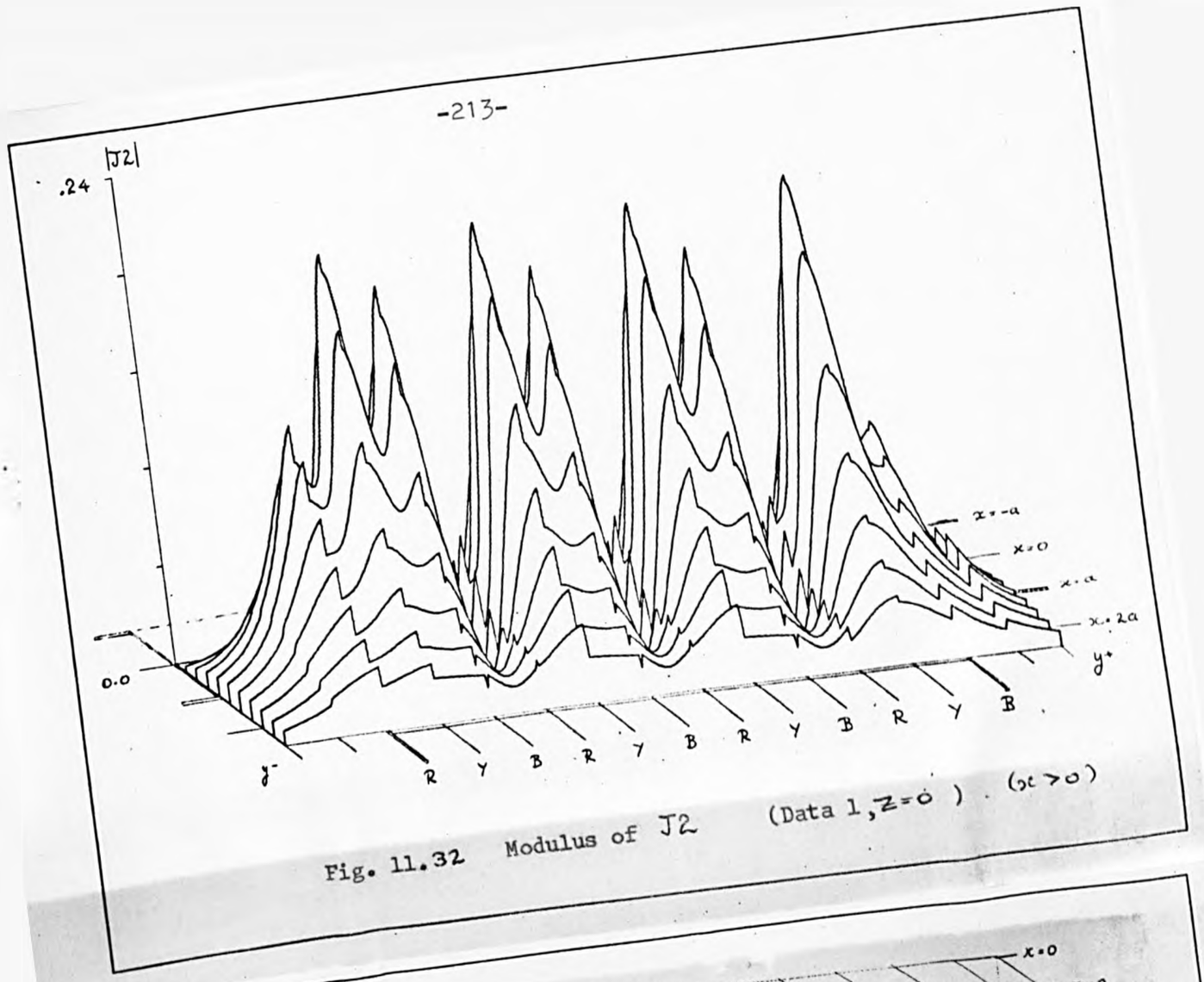

Fig. 11.32 Modulus of J2 (Data 1, Z=0) (x>0)

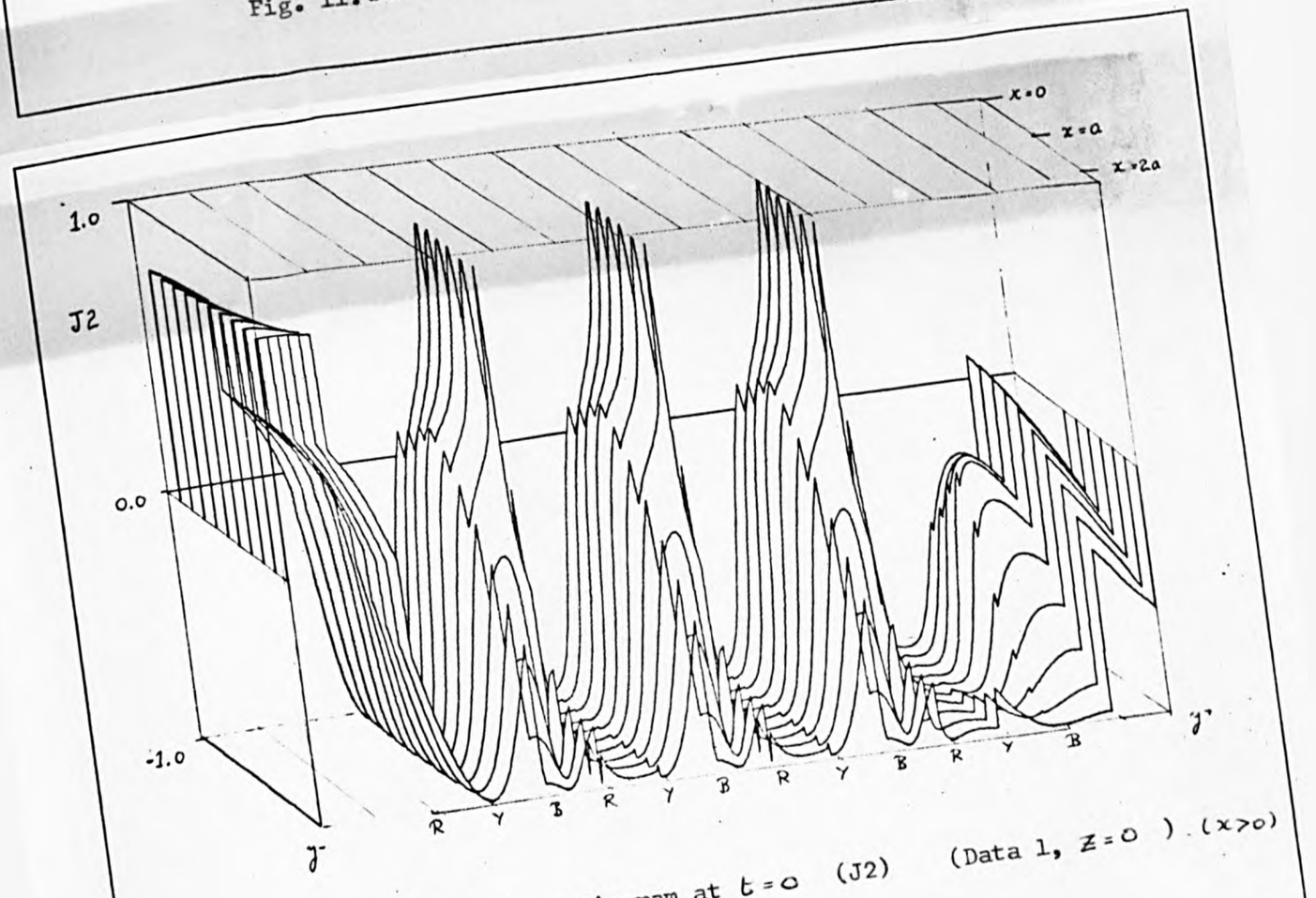

Fig. 11.33 Phase Diagram at t=0 (J2) (Data 1, Z=0) (x>0)

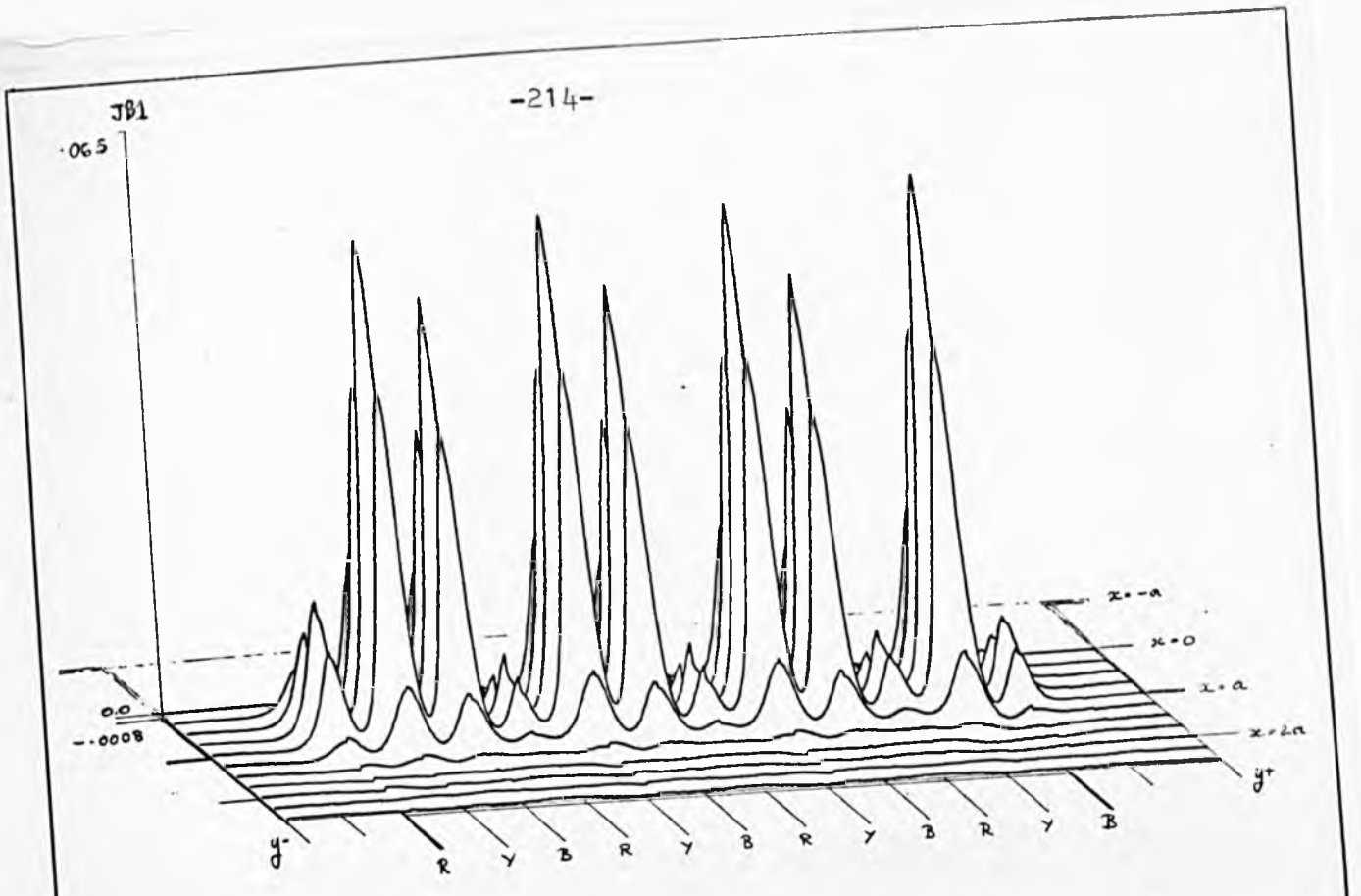

Fig. 11.34 X-cpt. of Body Force (Data 1 , Z = 0) . (x > 0)

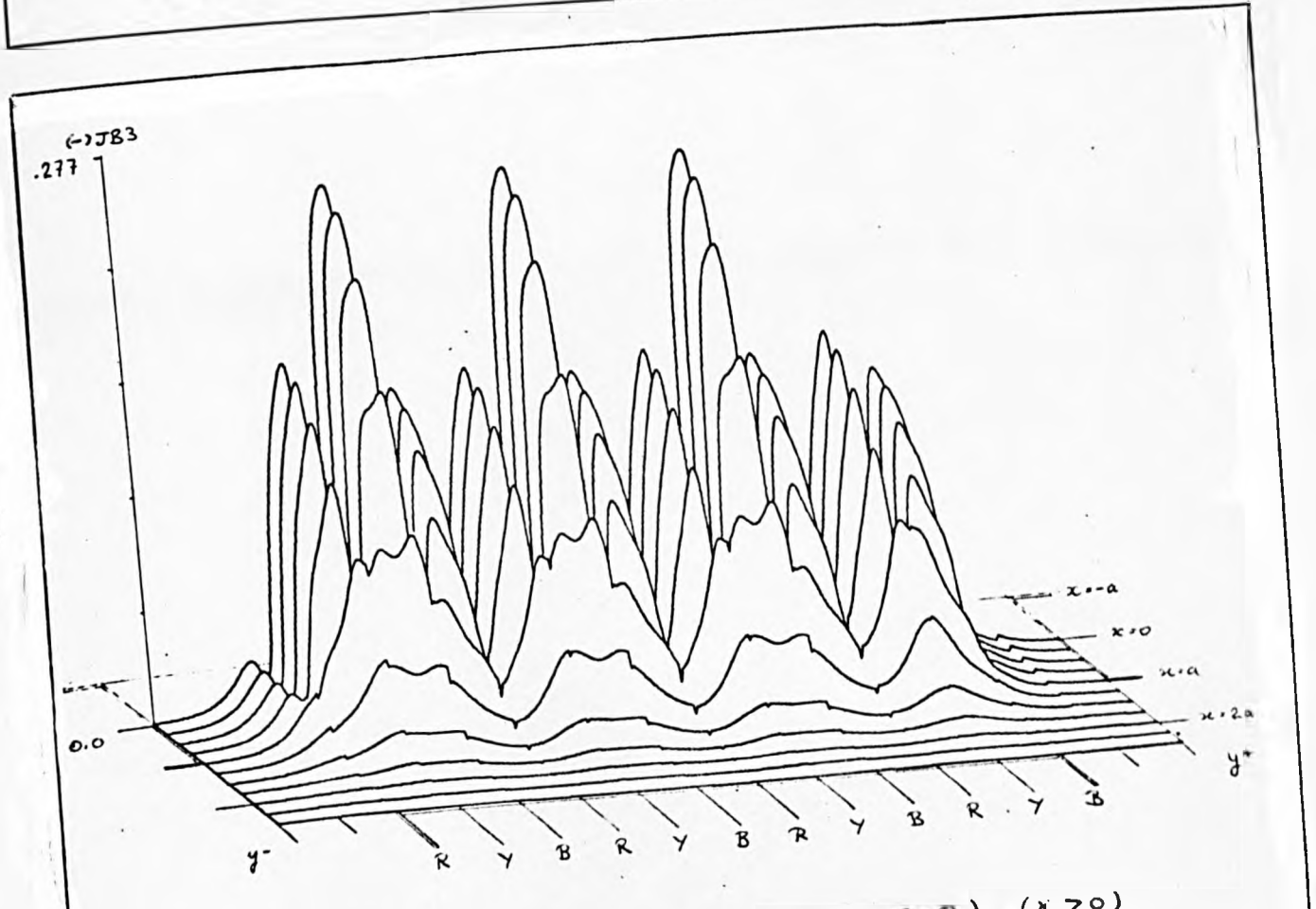

Fig. 11.35 Z-cpt. of Body Force (Data 1 , Z = 0) (x > 0)

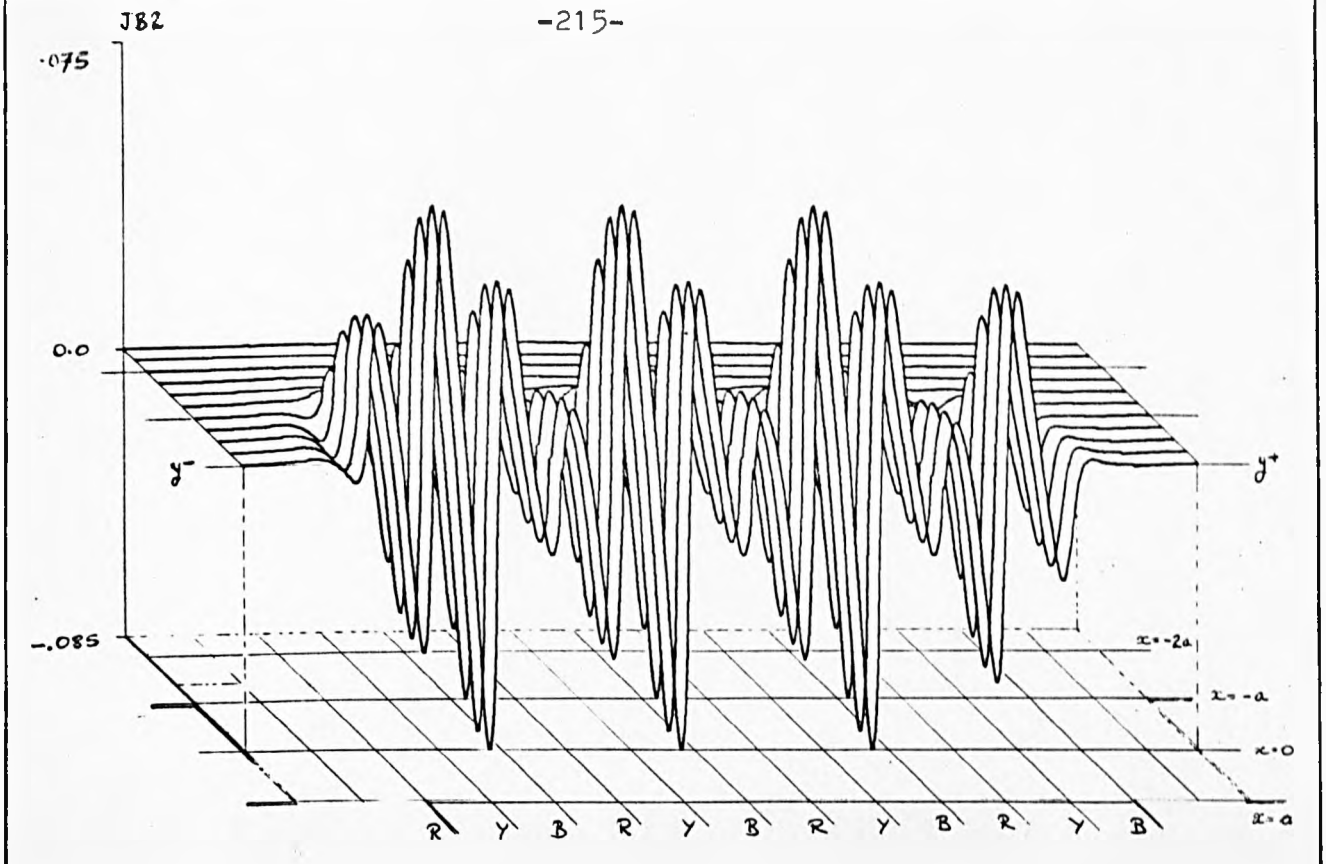

Fig. 11.36 Y-cpt. of Body Force (Data 1, z=0). ($x<0$)

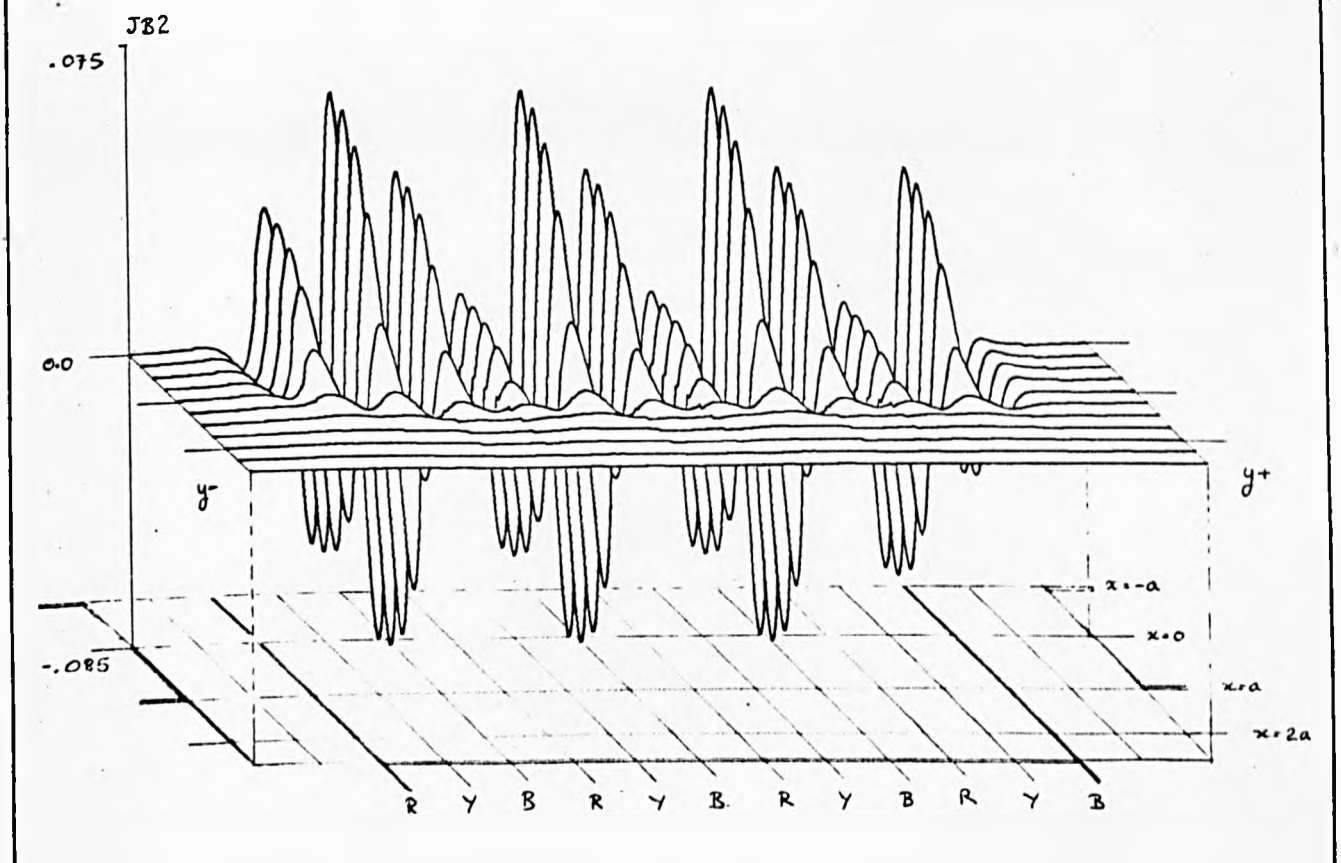

Fig. 11.37 Y-cpt. of Body Force (Data 1, z=0). ($x>0$)

function $f(y)$), into (62). In the derivation of the results we have set θ equal to zero which means that the magnitude of the colour group Y is at a maximum when $t=0$ (ie: the phase of Y is zero at $t=0$). Corresponding graphs for the induced EM field and body forces in the Data 2 configuration (reduced pole pitch - see figure 11.21 (b)) are shown in figures 11.39 to 11.47.

11.9.1 Some Observations on the Results. Clearly, a FLIM consists of a combination of groups of teeth - each group containing three teeth (R-Y-B) - so we would expect the source field (and induced field) to be cyclic along the FLIM axis (with adjustments for the half-wound end teeth). This behaviour is clearly seen in the results of figures 11.22 to 11.37 and figures 11.39 to 11.47.

(i) Data 1. Because we would expect $\cos h(y)$ to be a well-behaved function a comparison between the phase and modulus diagrams indicates the validity of the modulus results. The phase diagrams for B1 (figure 11.23) and J1 (figure 11.31) indicate that figures 11.22 ($|B1|$) and 11.30)($|J1|$) are accurate representations of the appropriate induced fields. Figure 11.27 indicates that the form of $|B3|$ (figure 11.26) is accurate for the region $x<2a$. However, in the phase diagrams of B2 (figure 11.25), PoT (figure 11.29) and J2 (figure 11.33) the effect of combining finite sets of data is clearly seen by the discontinuities in the plot. For the potential, PoT , the phase diagram indicates that the regions between the red(R) and yellow (Y) phases are irregular, but it is difficult to interpret the error (if any) in $|PoT|$ (figure 11.28) because the plot is smooth there. The phase diagram for J2 indicates that the peaks in $|J2|$ (figure 11.32) at the second, third and fourth red (R) tooth should be removed, however the overall form of the plot appears to be correct. A comparison between the phase diagram and modulus diagram for B2 (figures 11.24, 11.25) leads us to believe that a more accurate result for $|B2|$ is that indicated by the dashed line in figure 11.38.

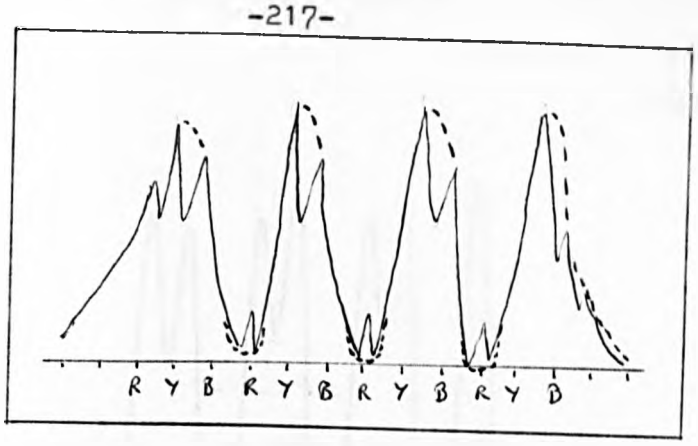

Fig. 11.38 Corrected form of $|B_z|$.

Incorporating the above discussion in the body force diagrams, we conclude that the form of J_{B1} ($= \frac{1}{2}\mathcal{R}\{J_2 B_3^*\}$, figure 11.34) is correct, apart from the peaks along the second, third and fourth R-teeth, that the form of J_{B3} ($= -\frac{1}{2}\mathcal{R}\{J_1 B_2^*\}$, figure 11.35) appears reasonably correct, but it is difficult to compensate for the suggested change in B_2, and that the plot of J_{B2} ($= \frac{1}{2}\mathcal{R}\{J_1 B_3^*\}$, figure 11.36 ($x<0$) and figure 11.37 ($x>0$) gives an accurate representation of the structure of the induced pumping force. We see that this force is sometimes positive, sometimes negative, and conclude that the direction of the axial motion of the working fluid in a SLIP varies according to position and that the overall pumping action of the SLIP is an averaged (nett) effect. We see that the vertical force is always of a levitator nature and that its maximum magnitude is four times greater than that of the horizontal force. Although we cannot deduce the form of the flow of the working fluid parallel with the SLIP axis, the flow transverse to the pump will be concentrated at the four regions indicated by the peaks in figure 11.34 and is likely to be of the form shown in figure 11.20. It is clear from figures 11.34 to 11.37 that the body force's influence is almost confined to the area mapped by the projection of the SLIP in the conductor.

Finally we note that the phase diagrams indicate the EM field is of the travelling wave form since $\cos h(y) \sim \cos \alpha y$, where $\alpha = 2\pi/\lambda$ is the wave number and $\lambda = 2\tau$ is the wavelength of the excitation.

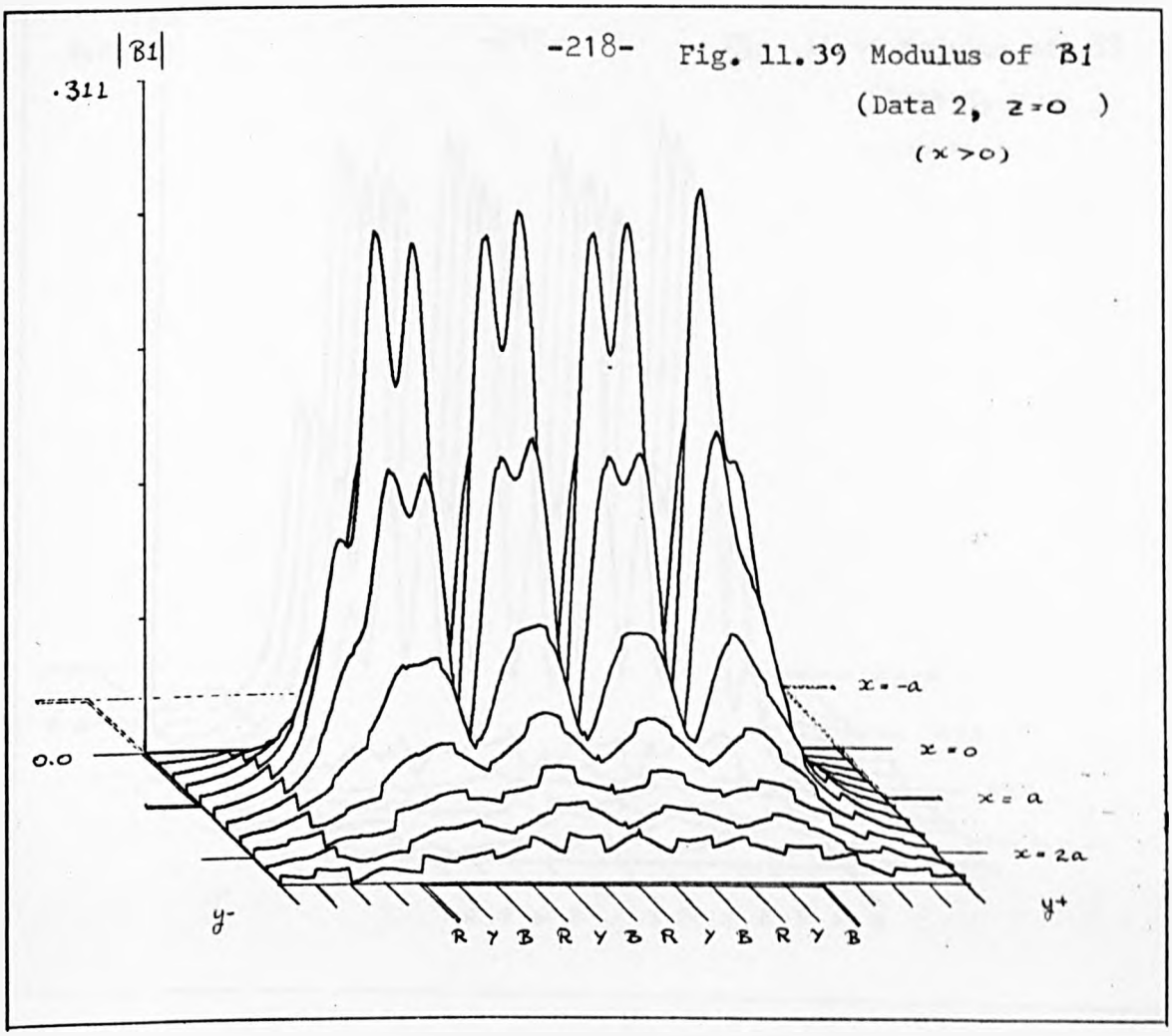

Fig. 11.39 Modulus of B1
(Data 2, z=0)
(x>0)

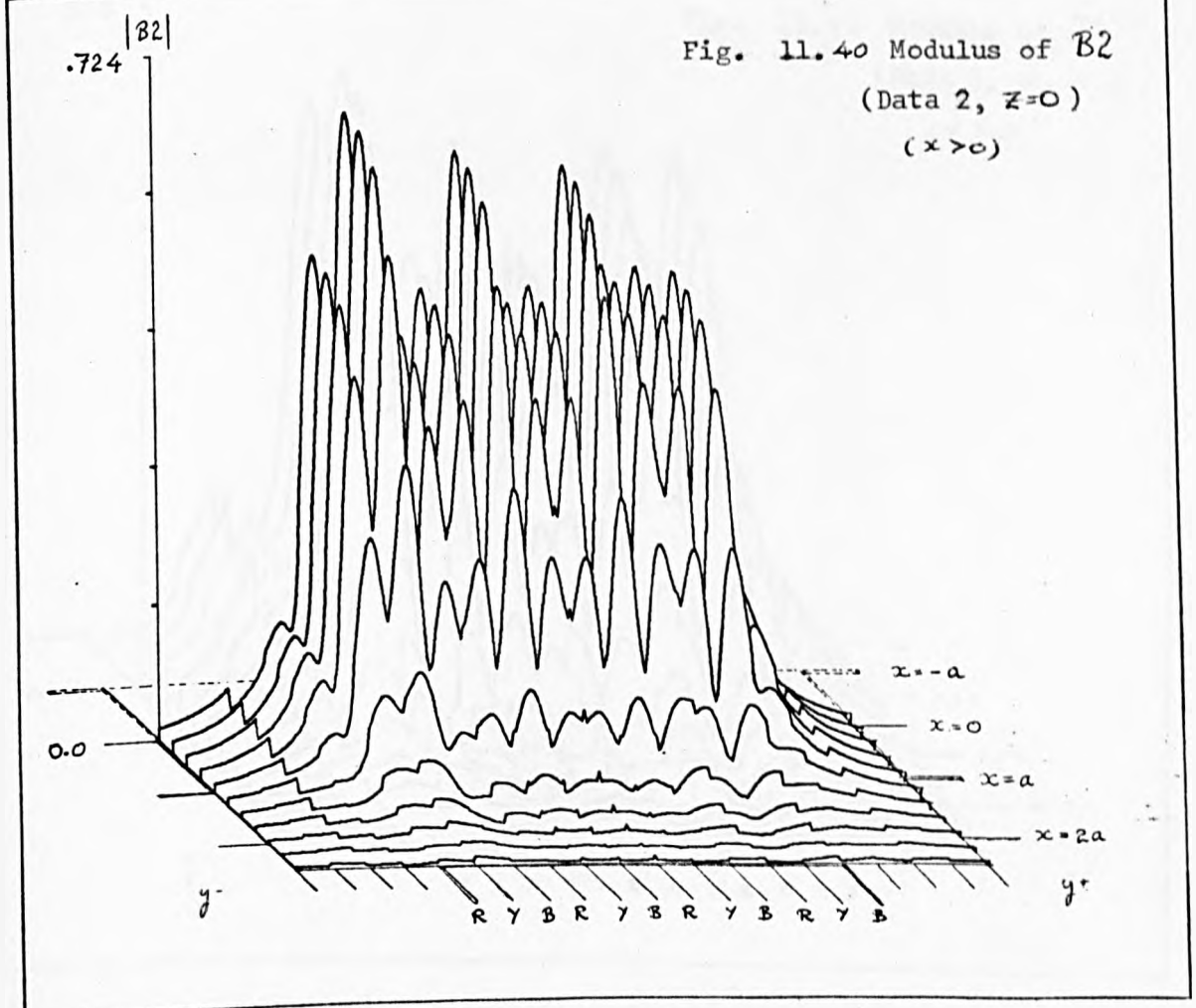

Fig. 11.40 Modulus of B2
(Data 2, z=0)
(x>0)

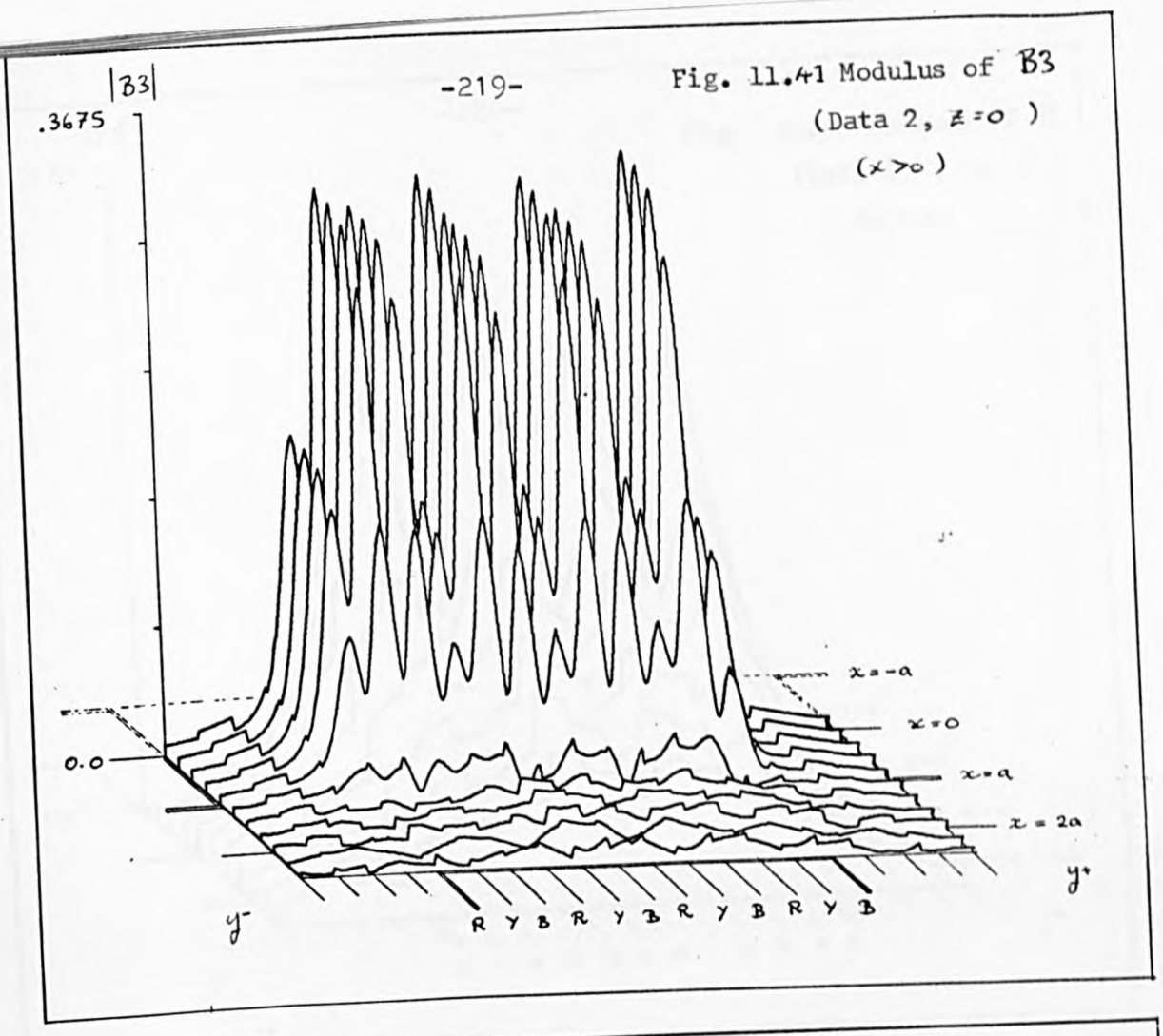

Fig. 11.41 Modulus of B3
(Data 2, z=0)
(x>0)

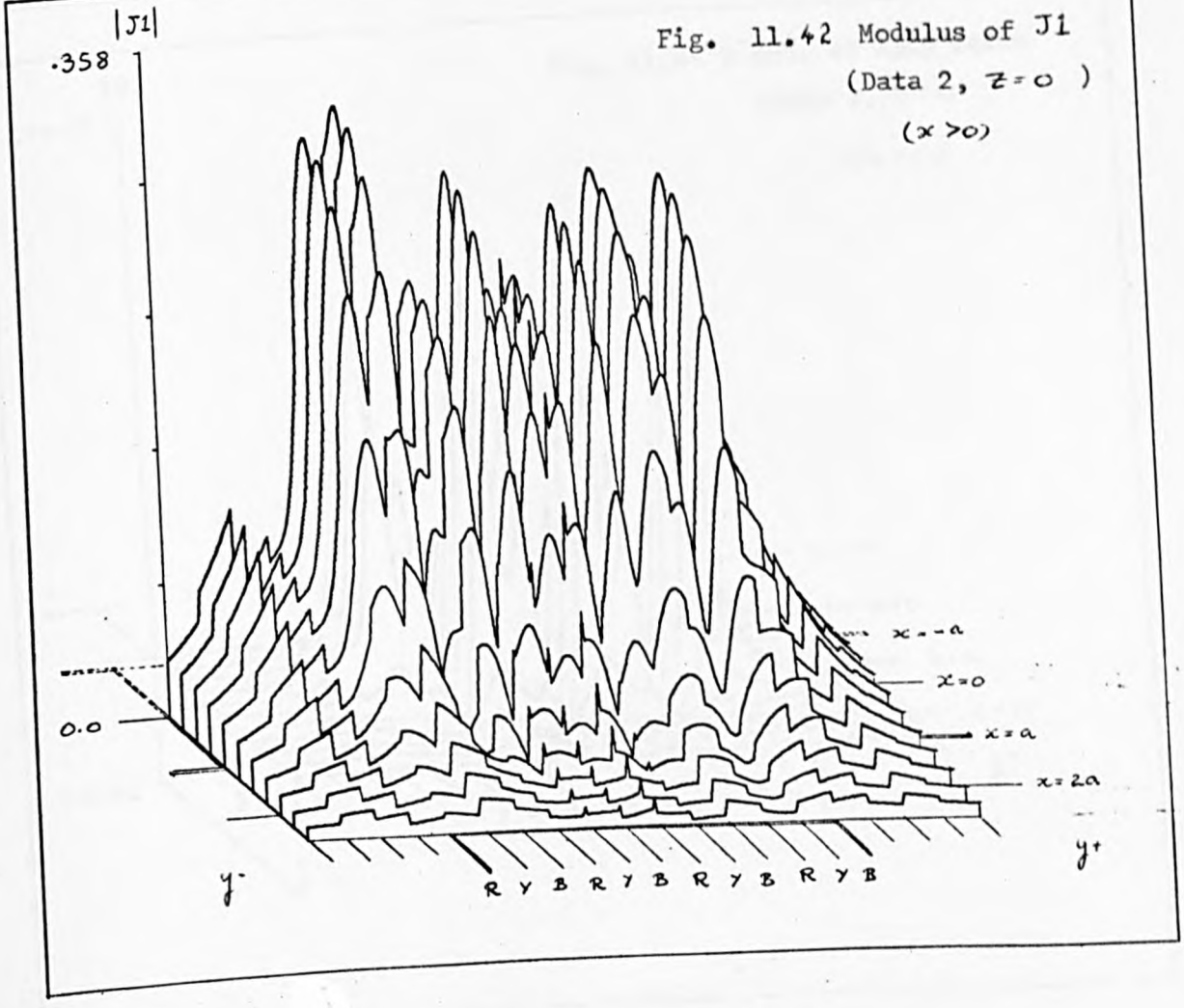

Fig. 11.42 Modulus of J1
(Data 2, z=0)
(x>0)

Fig. 11.43 Modulus of J2
(Data 2, z=0)
(x > 0)

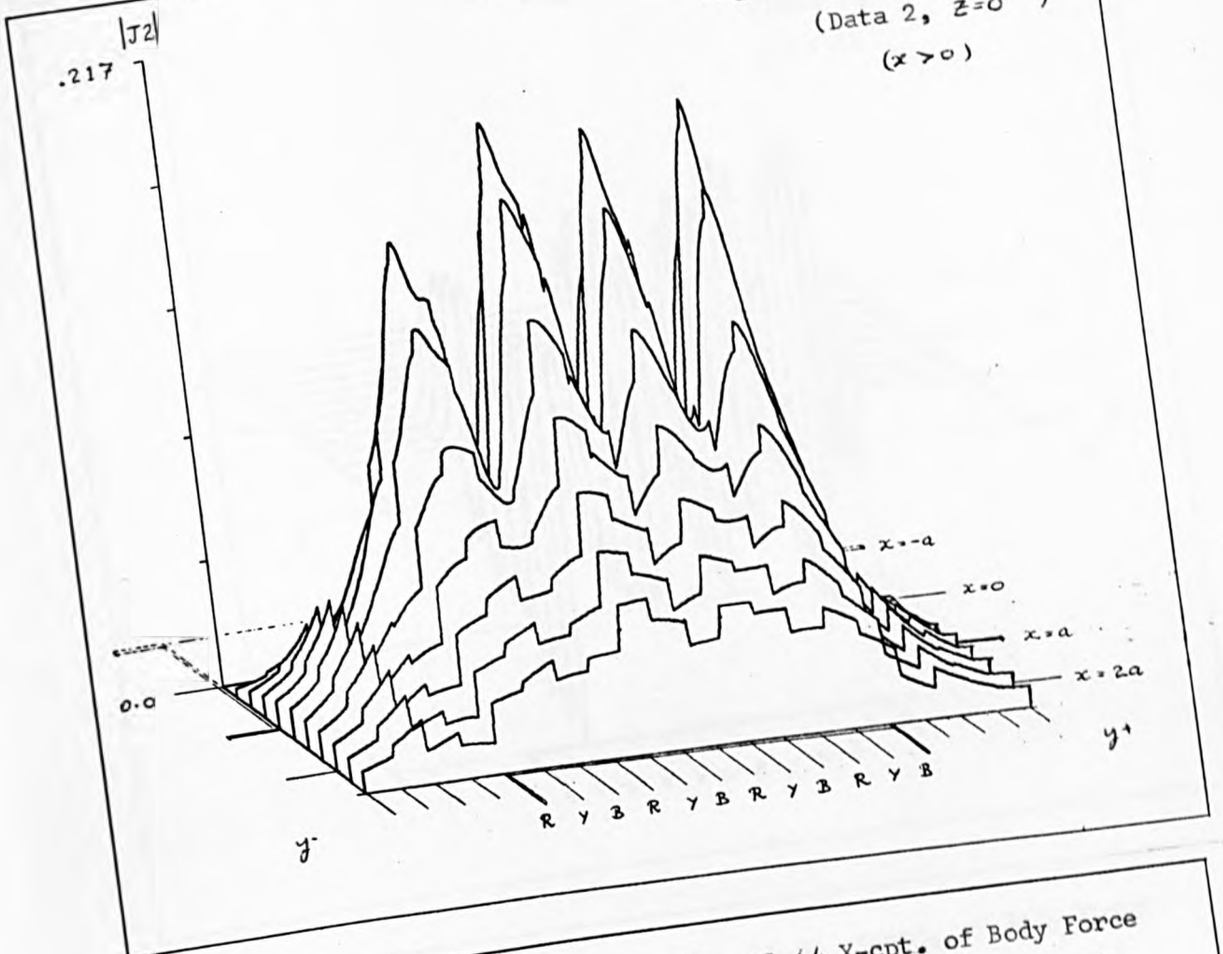

Fig. 11.44 X-cpt. of Body Force
(Data 2, z=0)
(x > 0)

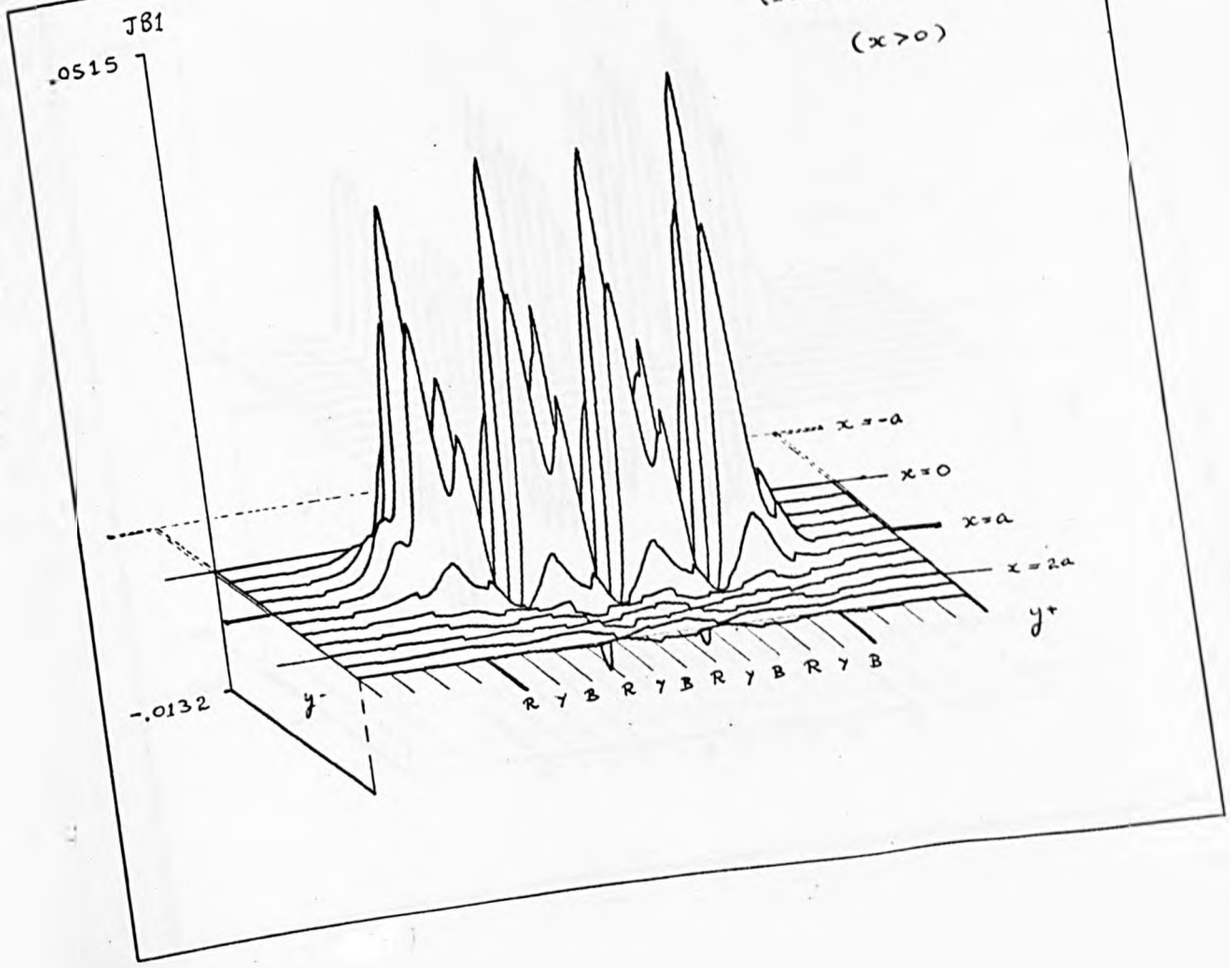

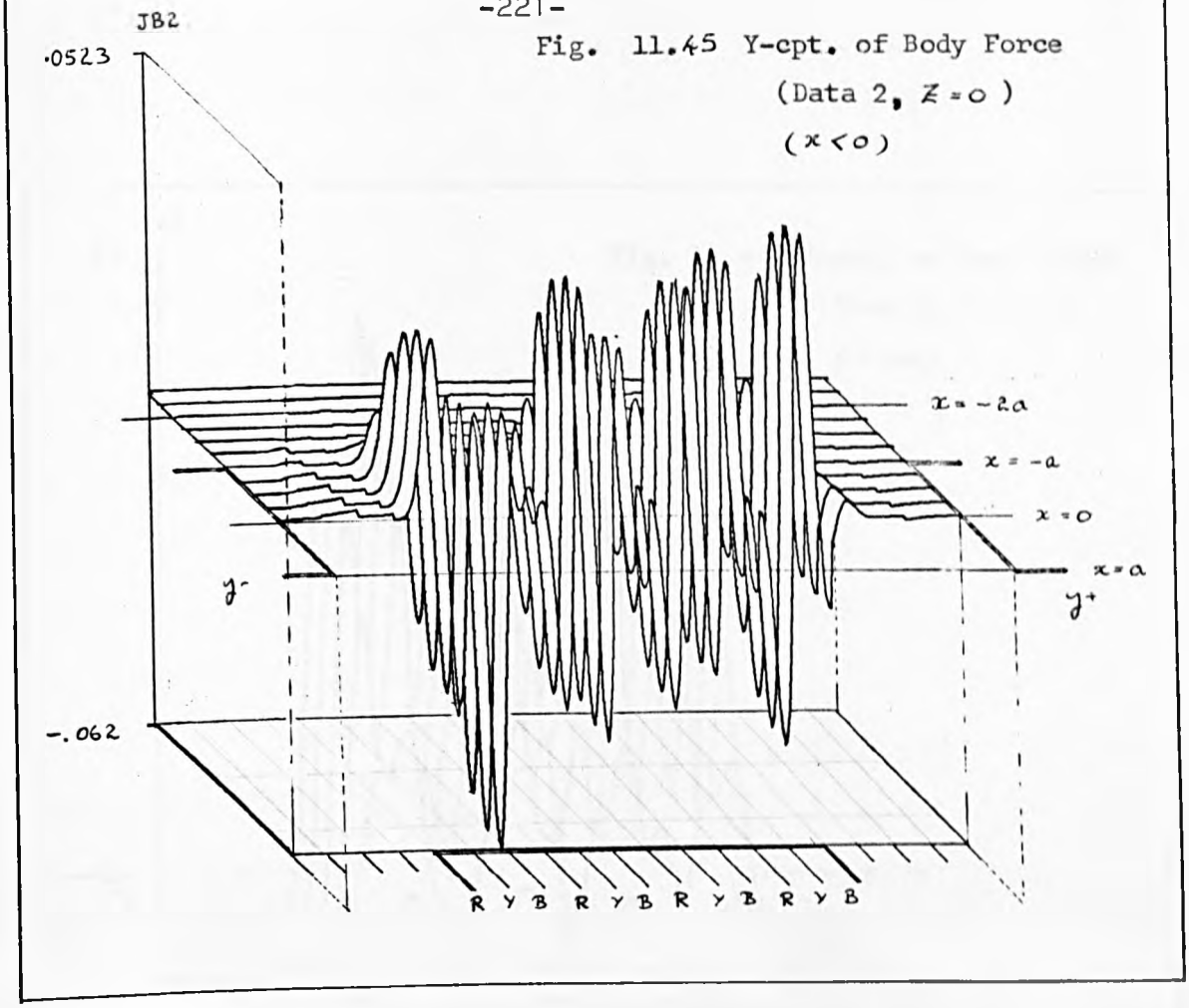

Fig. 11.45 Y-cpt. of Body Force
(Data 2, $z = 0$)
($x < 0$)

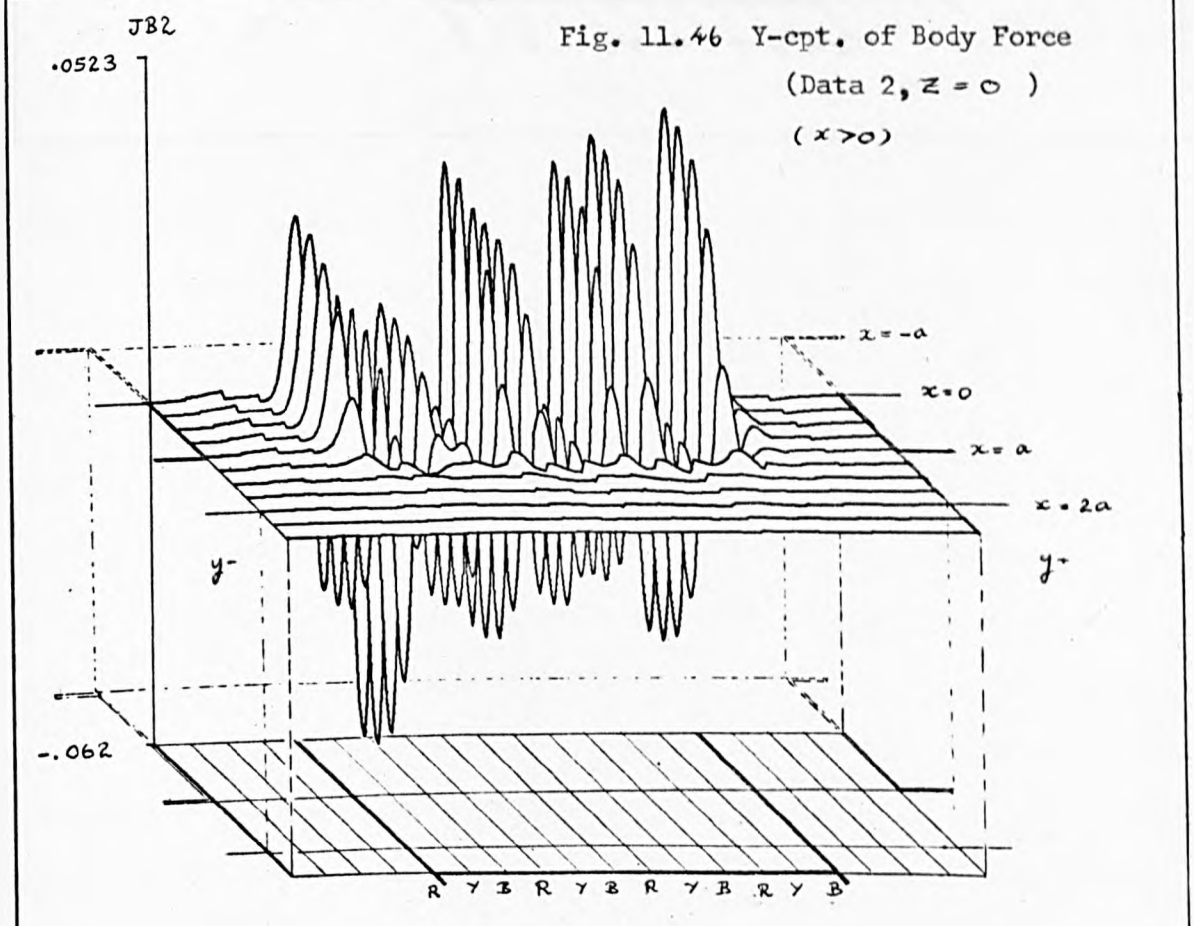

Fig. 11.46 Y-cpt. of Body Force
(Data 2, $z = 0$)
($x > 0$)

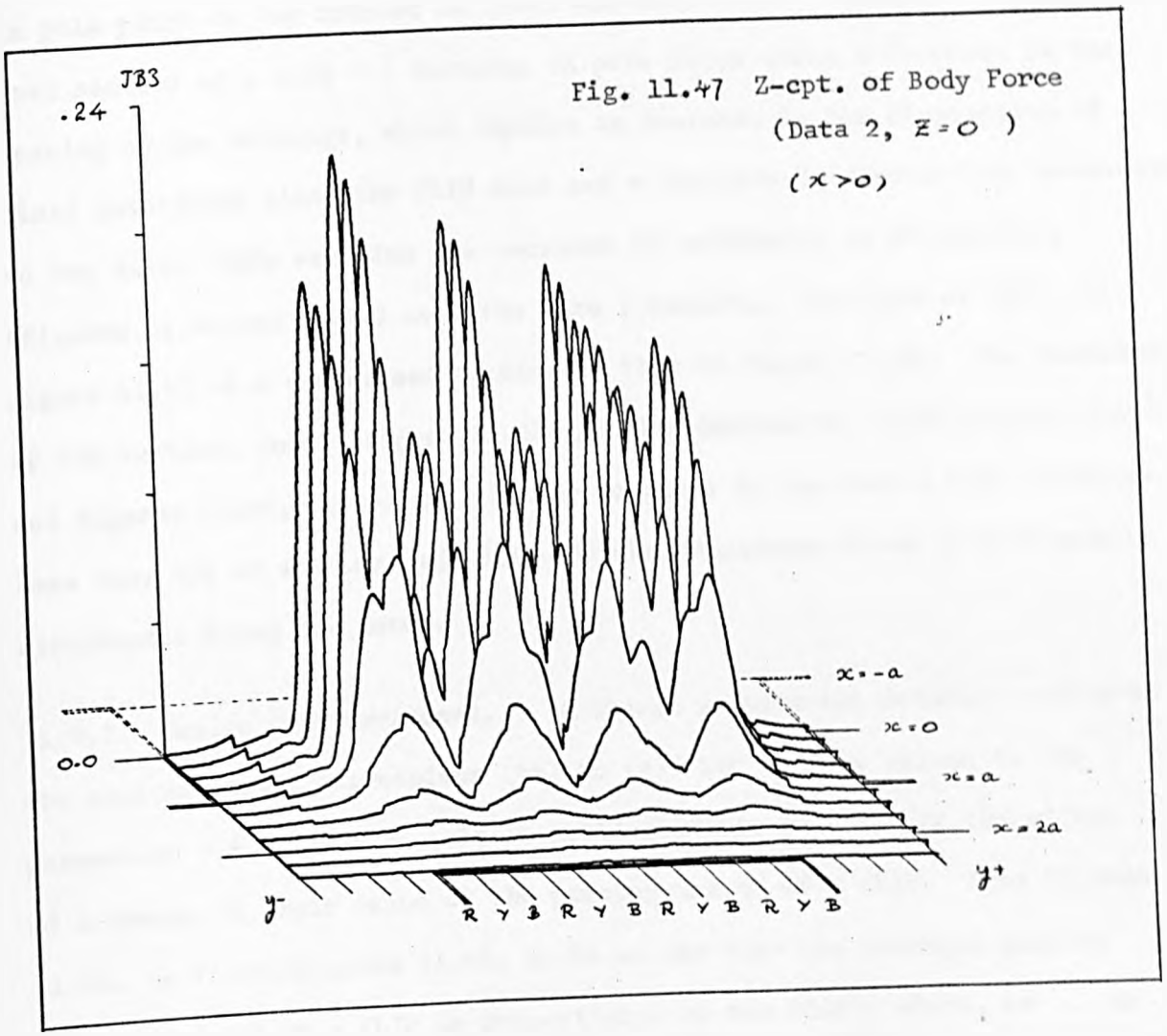

Fig. 11.47 Z-cpt. of Body Force
(Data 2, $\bar{z}=0$)
($x>0$)

(ii) Data 2. Here we are mainly concerned with the effect of a change in pole pitch on the induced EM field and body force. Consider a longitudinal section of a FLIM - a decrease in pole pitch means a decrease in the spacing of the windings, which implies an increase in the fluctuation of field quantities along the FLIM axis and a decrease in fluctuation transverse to the axis. This explains the increase in uniformity of $|B_1|$ and $|J_2|$, (figures 11.40 and 11.42) over the Data 1 results. The form of $|B_3|$ in figure 11.41 is a compressed version of that in figure 11.26. The structures of the vertical force (figure 11.47) and the horizontal force (figure 11.44 and figures 11.45, 11.46) are similar to those in the Data 1 case although here they are of smaller magnitude and the transverse force is more evenly distributed along the motor.

11.9.2 Design Considerations. Although we have not actually evaluated the solitary tooth expressions (56) to (61) for various values of the parameters a, b, d and h, it is still possible to estimate the effect of a change in their value on the pumping action of a SLIP. From figures 11.36, 11.37 and figures 11.45, 11.46 we see that the averaged pumping force produced by a SLIP is proportional to the SLIP's width, $2a$. We have previously observed (figure 11.18 and §11.8.1) that the force produced by a solitary tooth pushes fluid symmetrically away from the tooth axis - this is clearly the reason why the pumping force of a SLIP has an oscillatory nature. Thus we would expect the pumping efficiency of a SLIP to increase if we can construct a stator face in such a way that the working fluid 'sees', not an array of phased teeth, but a continuous excitation. For example this is achieved by increasing the parameter (the height of the teeth above the fluid) but this decreases the magnitude of the induced EM field. Perhaps the most effective method for the SLIP's discussed in this chapter (where the coil width ~ tooth length and coil height ~ tooth height) is to increase the ratio tooth length $(2b)$: tooth height (h). This is in agreement with rotary machine theory (eg. SAY 1963) Other factors influencing the design of a SLIP are discussed in chapter 13.

12. MAGNETIC INDUCTION IN AN ELECTRICAL CONDUCTOR DUE TO OSCILLATING SOURCE FIELDS EXPLAINED AND ANALYSED IN TERMS OF MAGNETIC MERGING

12.1 Neutral Points

In chapter 11 we obtained integral expressions for the EM field of a tooth of a FLIM. From these expressions we have calculated and illustrated the variation of the magnetic field and electric current density on the surface of a conductor. The EM field at any time is given by the expression $\mathcal{R}\cos\omega t - \mathcal{I}\sin\omega t$, where $\mathcal{R}$ and $\mathcal{I}$ are the real and imaginary components of the field. However it is quite difficult to evaluate this expression by merely observing the appropriate diagrams and performing the manipulation. Fortunately there is another approach - magnetic field line topology. This extremely valuable tool was first discussed by DUNGEY (1968a) in the context of electrodynamic phenomena and later by DUNGEY (1968b) and SWEET (1968) to explain the electrical discharge theory of solar flares. It should be noted that magnetic field lines are a mathematical device and do not exist physically. The following analysis is due to DUNGEY (1968a).

From Maxwell's solenoidal equation $\nabla.\underline{B}=0$ we see that the magnetic flux $\int_S \underline{B}.d\underline{S}$ through any cross section is constant. This equation also allows the representation of the magnetic field by a vector potential $\underline{A}$ such that $\underline{B}=\nabla\wedge\underline{A}$. Integrating the latter expression over a surface S bounded by a contour C gives the result $\oint_C \underline{A}.d\underline{r}$ is constant along a tube of flux. For two dimensional phenomena we may write $\underline{A} = A(x,y)\,\underline{e}_3$ and so A is constant on a tube of flux. We shall assume a line of force is equivalent to a very thin tube of flux, and so A is constant along a line of force. The electric current density $J = \frac{1}{\mu}\nabla\wedge\underline{A}$, and so $\mu_0 J = -\nabla^2 A\,\underline{e}_3$. Now suppose the system is in equilibrium, then the nett force acting on a line of force is zero. The Lorentz body force

is given by the expression $\mathcal{J} \wedge \underline{\mathcal{B}}$. We have assumed that μ , the magnetic permeability is constant everywhere. The total force on the line of force is $\int_C \mathcal{J} \wedge \underline{\mathcal{B}} \cdot d\underline{r} = \int_S \nabla \wedge (\mathcal{J} \wedge \underline{\mathcal{B}}) \cdot d\underline{S}$. The latter vector result can now be evaluated. With $\nabla \cdot \underline{\mathcal{B}} = 0$, $\nabla \cdot \mathcal{J} = 0$ and, because of the symmetry, $(\mathcal{J} \cdot \nabla)\underline{\mathcal{B}} = \underline{0}$, we have the result $\int_S (\underline{\mathcal{B}} \cdot \nabla)\mathcal{J} \cdot d\underline{S} = 0$ and so $\mathcal{J}$ is also constant on a line of force. At a neutral point $\underline{\mathcal{B}} = \underline{0}$ and so the latter integral is automatically satisfied and $\mathcal{J}$ can take any value. However, since $\mathcal{A}$ is also constant on a line of force we have the result $\nabla \mathcal{A} = F(\mathcal{A})$ where F is an arbitrary function of $\mathcal{A}$. This is a standard equation and an obvious solution is $\mathcal{A} = \frac{1}{2}\alpha x^2 + \beta xy + \frac{1}{2}\gamma y^2$ and we have $|\underline{\mathcal{B}}|^2 = (\alpha x + \beta y)^2 + (\beta x + \gamma y)^2$. From this result two types of neutral point can be distinguished: the lines of force in the neighbourhood of a neutral point may be elliptic or hyperbolic, and the neutral point will be called an O-type in the former case, and an X-type in the latter. At an O-type neutral point lines of force can grow out or shrink into the point. At an X-type neutral point flux is created or destroyed according to the breaking or connecting of magnetic lines of force at that point. It can be seen that in free space, when $\mathcal{J}$ equals zero, only X-type neutral points can occur. Further details may be found in Dungey (1968a), chapters three and six.

We are now in a position to analyse the EM field, at any time, without the previously described complications. The field line topology is unique at any instant of time and can be described by a suitable superposition of O-type and X-type neutral points. In §12.2 we analyse the field line topology for a dipole source, which is the building block for our FLIM analysis. This work is extended to a dipole array in §12.3. In §12.4 we describe the forces to be expected from a dipole source over one period of oscillation. Finally in §12.5 we give an explanation of one of the observations in the experiment of Chapter 2.

12.2 Oscillating Dipole Suspended Above an Electrical Conductor

Here we consider the magnetic field line topology of an oscillating magnetic dipole (period $\pi/2\omega$ seconds) placed at a point P , height h above an electrical conductor. The region $o < z < -d$ is taken to be of finite, non-zero conductivity whilst the regions $z > o$, $z < -d$ are assumed to have zero conductivity.

Starting from figure 12.1(a) the changes in the magnetic field over the interval $t = o$ to $t = 2\pi/\omega$ are explained as follows. Throughout we shall refer to one section of the axially symmetric system. The cycle begins when the dipole has maximum strength at $t = o$. The magnetic field is compressed close to the surface of the conductor, S . At infinity (denoted by dashed lines) the magnetic field is at its maximum and orientated in the direction of the dipole. As time increases the field at infinity decays with that of the dipole source and an X-type neutral point forms spontaneously on the surface of the conductor at X_1 to allow the near topology to restructure itself into an O-type neutral point O_1, just below the surface ((b) and (c)). The neutral points lie at a distance o(h) from the axis, because at high conductivities the only scale length available to the dipole is h, its height above the conductor. The induced electric currents in the conductor are now centred on O_1. As the dipole source field decays the induced currents push the neutral point X_1 upwards towards P. At $t = \pi/2\omega$ (quarter cycle, diagram (e)).the X point reaches P and disappears with the dipole field. The field at infinity is now solely due to the induced currents which are at their maximum. The second quarter of the cycle now begins with a reversal of the dipole source. To facilitate the directional change in the magnetic field the near topology restructures itself forming a partition boundary C_x with a source at X_2 and sink at X_3, (f). The neutral points X_2, X_3 are formed spontaneously with the dipole reversal, occupying positions on the axis above and below P. The increase in magnetic pressure within this

Fig. 12.1

Magnetic Field Line
Topology of a Dipole

Note: Dashed lines indicate
'at infinity'.

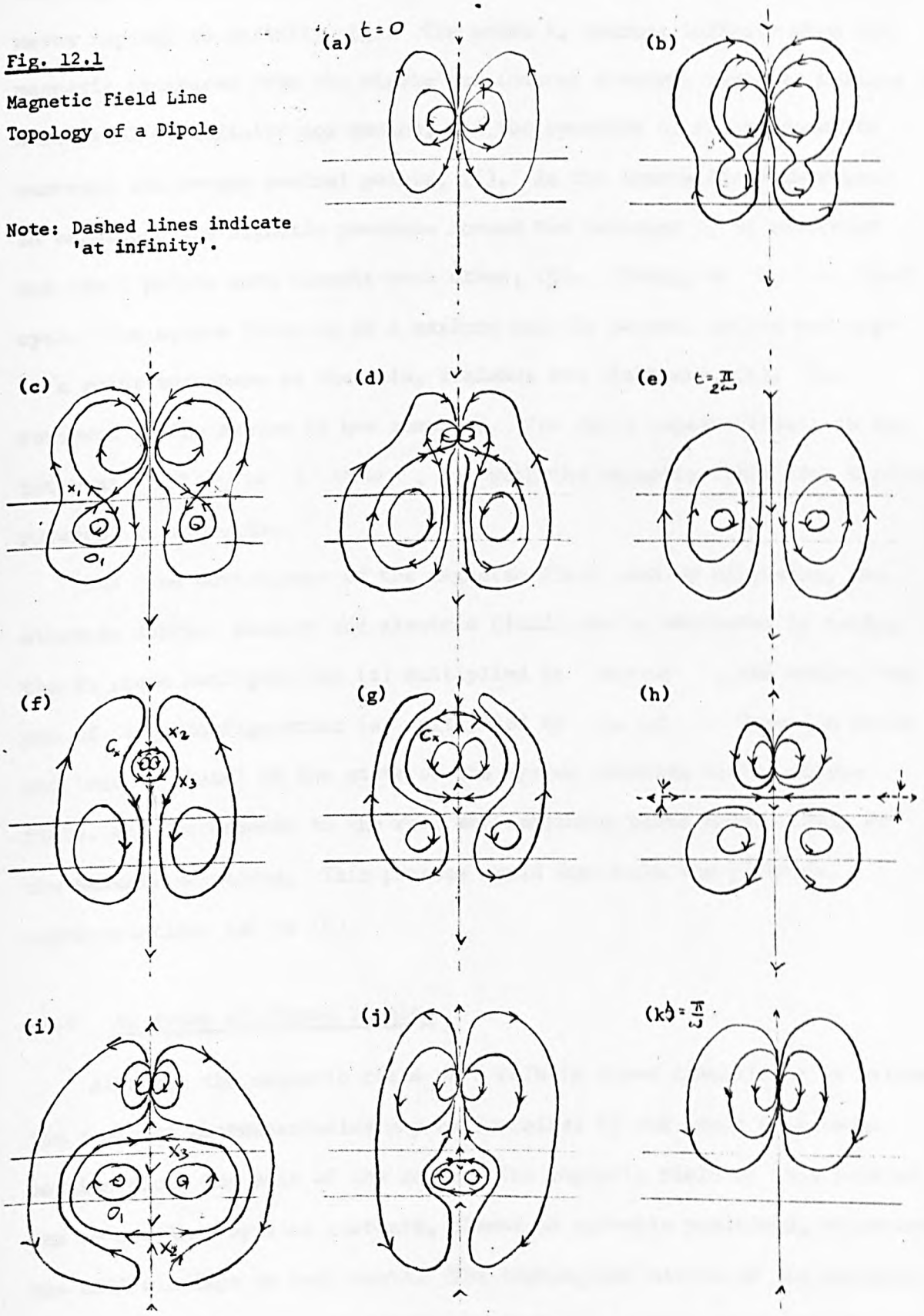

boundary forces the points X_2, X_3 to move along the axis away from P. The compression of the field lines at S retards the movement of X_3 but X_2 moves rapidly to infinity, (g). The point X_2 reaches infinity when the magnetic pressures from the dipole and induced electric currents balance (h) A reversal at infinity now occurs, and the boundary C_x flips around to surround the O-type neutral points, (i). As the source field increases in magnitude the magnetic pressure forces the boundary C_x to constrict and the O points move towards each other, (j). Finally at $t = \pi/\omega$ (half cycle) the source field is at a maximum and the neutral points converge to a point somewhere on the axis, coalesce and disappear, (k). The reversal of the system is now complete. The cycle repeats itself in the interval $t = \pi/\omega$ to $t = 2\pi/\omega$, but with the magnetic field line topology reversed in direction.

The time development of the magnetic field (and by extension, the electric current density and electric field) can be estimated by taking the in phase configuration (a) multiplied by $\cos \omega t$, and adding the out of phase configuration (e) multiplied by $-\sin \omega t$. Here 'in phase' and 'out of phase' is the state of the system relative to the source field, and corresponds to the real and imaginary parts respectively of the Maxwell solutions. This process would duplicate the pictorial representations (a) to (k).

12.3 An Array of Phased Dipoles

Although the magnetic field of a FLIM is three dimensional in nature, its dominant characteristics may be described by the study of a cross section along the axis of the motor. The magnetic field of this section can be modelled by line currents, placed in suitable positions, representing the coil windings on each tooth. The topological nature of the magnetic field of a line current is similar to that of a dipole so we can use the analysis of §12.1.

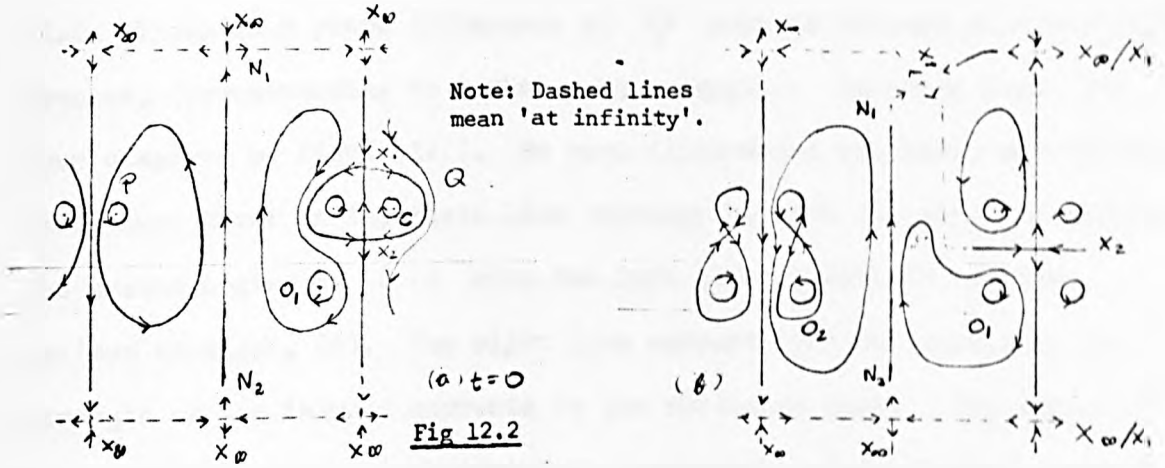

Fig 12.2 Adjacent Dipole Sources

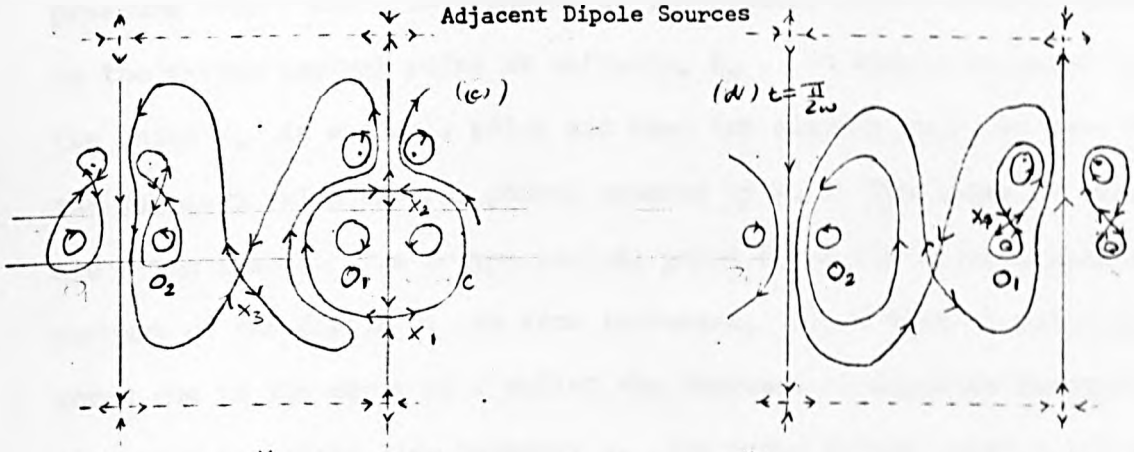

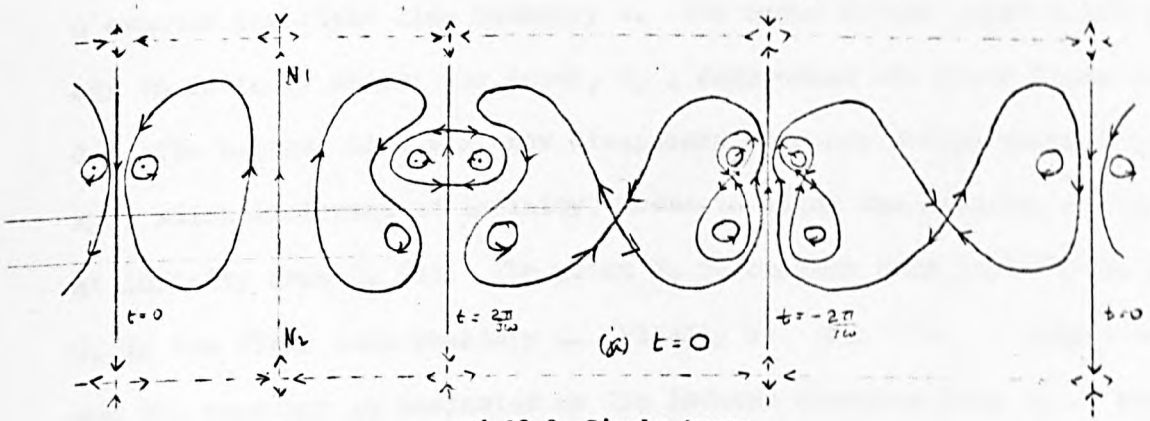

Fig12.3 Dipole Array

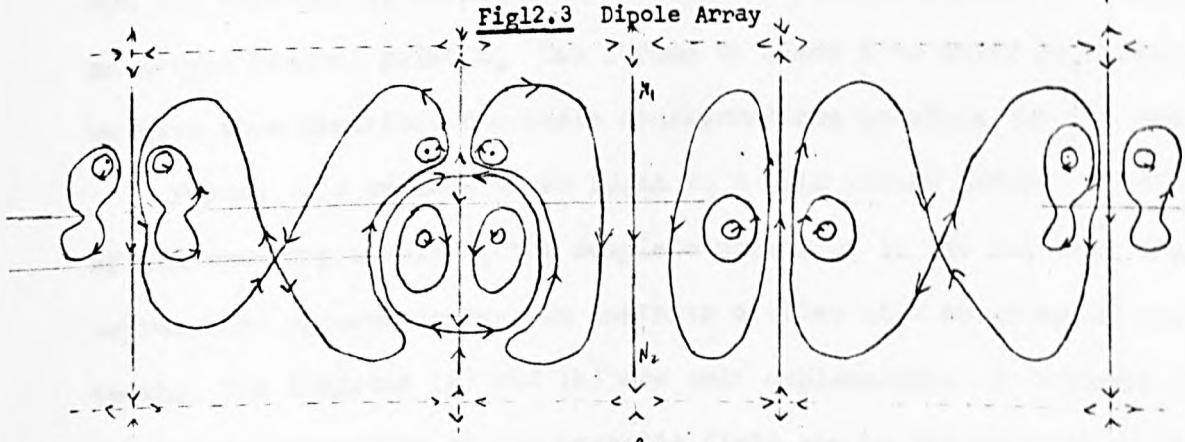

Consider the array of line currents illustrated in figures 12.2 and 12.3. There is a phase difference of $\frac{2\pi}{3}$ seconds between adjacent dipole sources, (corresponding to a three phase supply). Consider first the four diagrams of figure 12.2. We have illustrated the basic configurations which must occur in the field line topology between two adjacent sources. The system begins at $t = o$ with the left line current (P) at its maximum strenghh, (a). The right line current (Q) is increasing its strength as the induced currents in the conductor decay. The magnetic pressure from P and Q is balanced by the neutral line $N_1 N_2$ which extends to the X-type neutral point at infinity, X_∞. It should be noted that the point X_∞ is a single point and that for clarity only, we have drawn the topology with several points denoted by X_∞. The lines at infinity are drawn dashed. The O-type neutral point O_1 is the induced electric current of the dipole Q. As time increases, (b), a neutral point O_2 forms due to the decay of P whilst the increase of magnetic pressure from Q expands the field line boundary C. The upper X-type point X_1 now moves off to infinity whilst the lower, X_2, compresses the field lines due to O. The neutral line $N_1 N_2$ now disappears as a new X-type neutral point, X_3, which is formed at infinity, moves to allow the reversal of the field at infinity from Q, (c). The point X_1 re-emerges from infinity to constrict O_1 in the field line boundary C. Finally at $t = \pi/2\omega$ P blinks out and the topology is dominated by the induced currents from O_2. Meanwhile an X-type neutral point X_4 has formed to allow Q to decay in strength, (d). We have thus described the basic configurations possible for the system.

Figure 12.3 extends these ideas to a full linear motor. However because of the symmetry involved, the complete variation in the topology can be represented by considering two instants of time with an array of only four teeth. The diagrams (a) and (b) are self explanatory. It appears that the travelling nature of the magnetic field can be interpreted as the motion of the neutral line $N_1 N_2$ along the axis of the motor, (this motion will however, be extremely unsteady).

12.4 The Lorentz Force Produced By An Oscillating Magnetic Dipole.

It may be expected that the Lorentz body force induced in an electrical conductor by an oscillating magnetic dipole could be oscillatory and average to zero over a period of oscillation. However we can see from the force analysis of figure 12.1, which is shown in figure 12.4, that this is not so in general. We have drawn the induced body force as shown by the vertical and horizontal arrows, the length of which indicates the magnitude of the force at the two points P and Q on the surface of the conductor. The diagrams (a) to (f) are self explanatory, except for the lines M and N which are taken to be the regions of zero horizontal force. In diagrams (e) and (h) we illustrate the variation of the horizontal force over the period of oscillation at P and Q. It can be seen that for most positions in the conductor there will exist a non-zero time averaged force which has the potential to move an electrically conducting fluid towards the regions containing the O-type neutral points.

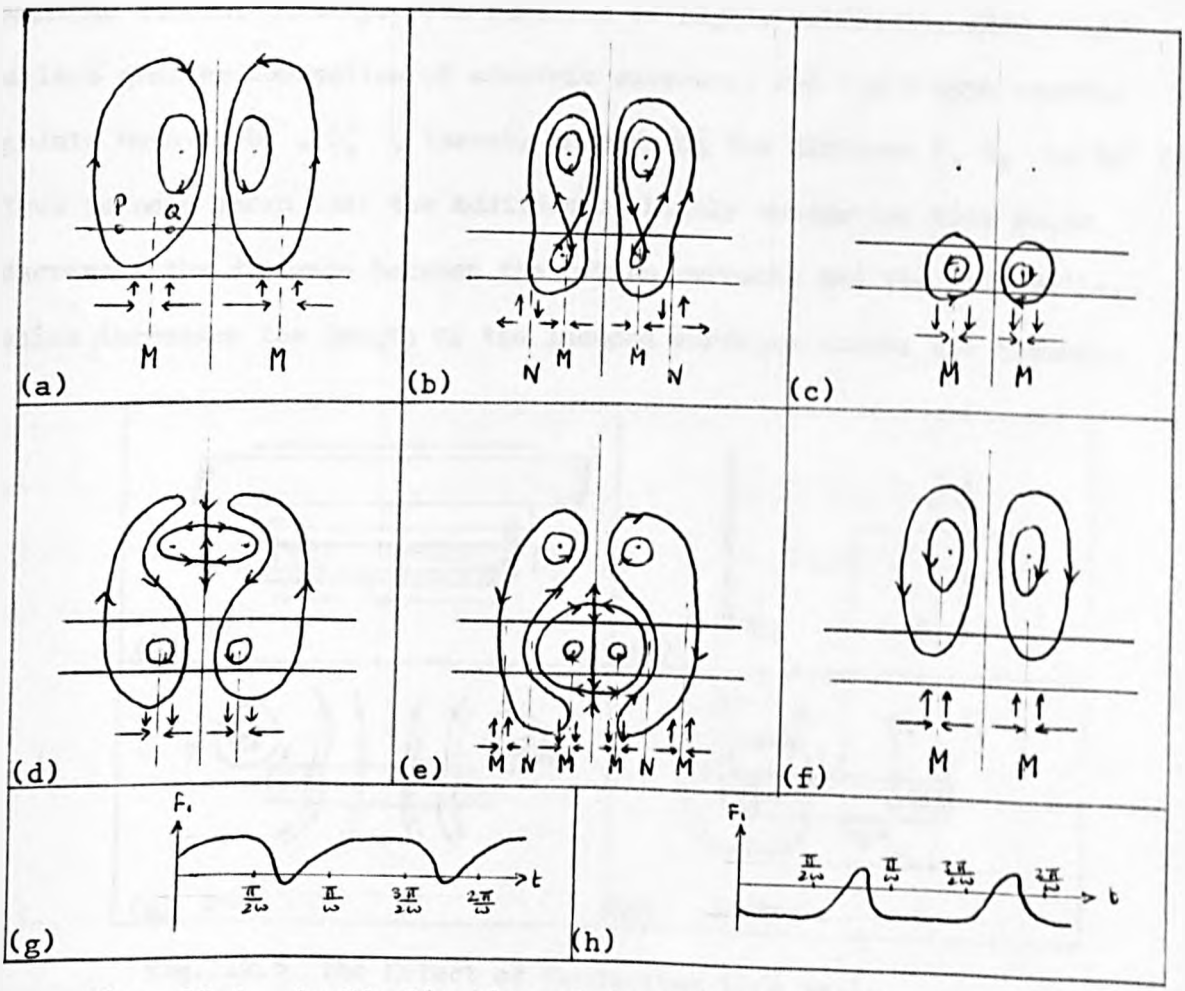

Fig. 12.4 An Idealization of the Induced Body Force

12.5 The Experiment of Chapter 2

In this section we present an explanation of the increase in flow rate for the mercury experiment (Chapter 2) when highly conducting side walls were added. A cross section of the motor/channel configuration is illustrated in figure 12.5(a) The induced currents form closed loops and these are shown in plan in (b). The regions R_1, R_2 indicate the return areas for the induced electric current.

It is possible to model the magnetic field of the cross section shown in (a) by placing line currents at P and Q on the sides of the stator, (c). At $t = 0$, the induced electric currents are at their minimum (as are the induced forces) but they gradually increase to a maximum at $t = \pi/2\omega$ (quarter cycle) when the line currents 'blink out', (d) The disappearance of the source causes two O-type neutral points to form (denoted by O_1, O_2). The distance between O_1 and O_2 (equal to 2d, say) gives the distance between return areas R_1 and R_2, because the O-points are the areas of maximum current density. The addition of highly conducting side walls allows greater conduction of electric currents, and the O-type neutral points move to O_1', O_2', thereby increasing the distance R_1 R_2 to 2d' (say) Thus we have shown that the addition of highly conducting side walls decreases the distance between the return currents and the side walls, which increases the length of the induced currents across the channel.

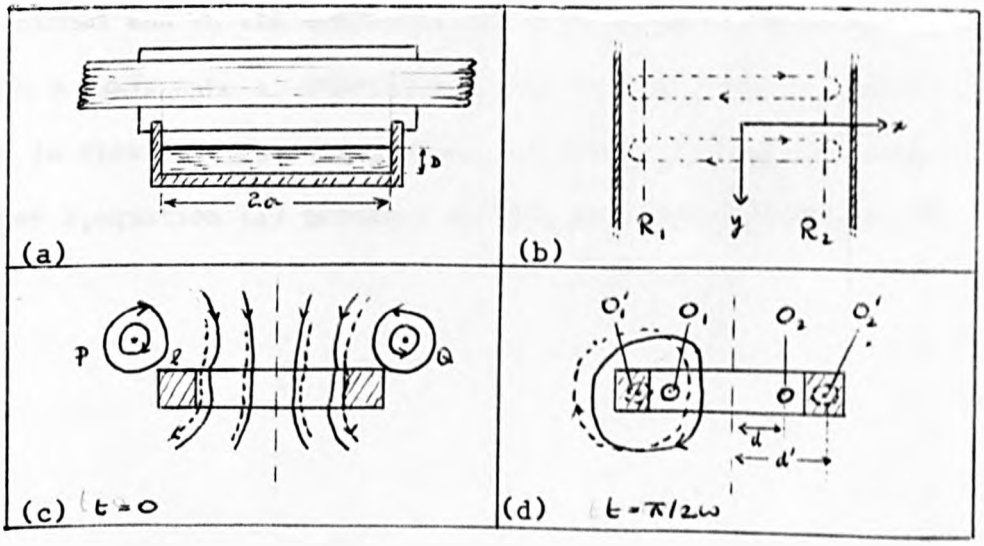

Fig. 12.5 The Effect of Conducting Side Walls.

However, in the regions between R_1 and R_2, the pumping force is that along the axis and is given by the product $J_1 B_3$ (usual notation). The total force across the channel is given by $\int_{-a}^{a} J_1 B_3 \, dx$. Because B_3 constant along this length (at a given depth), an increase in the total force is proportional to an increase in the length of J_1. If we assume two dimensional steady flow occurs beneath the motor, we may assume the average velocity is proportional to the force applied. Finally we have the result (V is the average velocity):

$$V' : V \sim d' : d \tag{1}$$

Here V' is the average velocity with highly conducting side walls. In a recent paper by HEWSON-BROWNE and KENDALL (1973) it is shown that O-type neutral points can form at a distance d_e from the edge of a conductor, where:

$$d_e \sim (4\pi\omega\mu_0\kappa)^{-1} \tag{2}$$

Here $\kappa = \sigma D$ is the integrated conductivity (D is the conductor thickness and σ its conductivity). If we assume that the addition of a <u>thin</u> highly conducting sheet ($l \ll a$) effectively increases the length of the conductor, then the decrease in distance Δd_e with the addition of the sheet may be taken as

$$\Delta d_e \sim d_e \cdot \frac{\sigma_2 l}{\sigma_1 a} \tag{3}$$

Here l is the width of the sheet, σ_2 its conductivity, a is half the width of the channel and σ_1 the conductivity of mercury. We have $d = a - d_e$ and $d' = a + \Delta d_e - d_e$. Substituting for d and d' in (1) gives the increase in flow rate for the system. With the parameter values given in chapter 2, equation (1) predicts an increase in flow rate of 20%.

13. CONCLUSION

13.1 Summary

Some of the more important results we have obtained for the single sided linear induction pump (SLIP) are:

(i) Design relations for an idealised SLIP (chapter 3)

(ii) Induced velocity profiles for an idealised SLIP (chapters 3 and 4) which take into account some MHD effects

(iii) Estimates for the rate of decay of the induced EM field with depth and beyond the edges of the motor (chapters 5 and 6)

(iv) Two-dimensional results for the induced EM field (chapters 7 and 9)

(v) Three dimensional results for the induced EM field (chapter 11)

We have also included a survey of the relevant published literature (§1.7, §1.8); an estimate of the flow profiles induced in a liquid by a rectangular body force (chapter 8); an account of an experiment performed at Pilkington's and a discussion of magnetic field line theory (chapter 12) which is applied to a linear motor's tooth (chapters 10 and 11).

Although the work is not included in this thesis, we have obtained three dimensional expressions in transform space for the velocity and pressure distribution induced in a conducting liquid of finite depth, by the force expressions derived in chapter 11 for a SLIM, in the slow flow configuration. Briefly, we can obtain the transformation of the magnetic induction $\underline{B}$ induced by a SLIM in the conductor (region III, figure 11.2) by combining suitably placed and phased magnetic induction expressions for a solitary tooth (obtained from (11.38)and(11.39)). The transformation of the induced electric current $\underline{J}$ can thus be found using (11.24).

Clearly we can write $\hat{\underline{J}}(p,q,z) = \underline{C}(\alpha e^{\gamma z} + e^{-\gamma z})$ and $\hat{\underline{B}}(p,q,z) = \underline{D}(\alpha e^{\gamma z} - e^{-\gamma z})$ where $\alpha, \beta, \gamma, \underline{C}$ and $\underline{D}$ are functions of p and q. Navier-Stokes equation for slow flow (obtained from (1.18) is $\nabla^2 \underline{v} = \nabla P - \underline{F}$, where $\underline{F} = \frac{1}{2}\mathcal{R}\{\underline{J} \wedge \underline{B}^*\} = \frac{1}{4}(\underline{J} \wedge \underline{B}^* + \underline{J}^* \wedge \underline{B})$ is the time averaged Lorentz body force. We now transform this equation using the two dimensional form of (1.32), where (for example) $\mathcal{F}_2^+\{\underline{J} \wedge \underline{B}^*\} = \int_{-\infty}^{\infty}\int_{-\infty}^{\infty} \hat{\underline{J}}(p',q',z) \wedge \hat{\underline{B}}^*(p-p', q-q', z)\, dp'dq'$ (using the convolution result (1.34)). Because $\hat{\underline{J}}$ and $\hat{\underline{B}}$ are separable in z we can now solve the ordinary differential equations in the transformed hydromagnetic equations for $\hat{\underline{v}}$ (subject to the boundary conditions specified in § 1.4.7) and $\hat{P}$, obtaining the solutions in convolution form. A Fourier inversion can then be made using (1.33). It can be seen that we require an evaluation of four successive integrals. Attempts were made to evaluate the solutions using standard numerical quadrature routines, but the amount of computation required exceeded the available computer time. Following METZ and GANDHI (1974) we attempted to use SINGLETON's (1969) fast fourier transformation (FFT) algorithm (see GENTLEMAN and SANDE, (1966)) in order to increase the speed of computation. Some results were obtained but we have disregarded them since their accuracy is questionable. Recently however SINGHAL et al (1975) have succeeded in using a Padé rational approximation for the evaluation of a two dimensional complex Laplace transform inversion. Their method may well prove useful for the inverse Fourier transformation part of our integral expressions but this remains a problem for further research.

13.2 Factors Influencing The Design of a FLIP

Although many of the results and equations obtained in this thesis are derived from idealised models they can still be used to predict the performance of a realistic SLIP, (see for example § 3.5). In the work below we shall assume the stator is series wound (case S).

Using the idealised form (3.40) for the mechanical power developed by a SLIP, P_m, we see that for a fixed slip s and pole pitch τ, we can write $P_m = K_s^2 f(R_m)$ where K_s is the stator surface current density and f a function of the Magnetic Reynolds number, R_m, based on the synchronous velocity of the excitation. Clearly $P_m \propto K_s^2$ and by figure 3.2(a) we see that an increase in the value of R_m increases the magnitude of P_m.

Consider first the parameter K_s. By (1.46) we have (for a fixed pole pitch) $K_s \propto \frac{NI\,K_w}{P}$ where N is the number of turns per phase, I the winding current, P the number of magnetic poles and $K_w = \sin\left(\frac{c_p}{\tau}\cdot\frac{\pi}{2}\right)$ is the pitch factor (c_p is the coil pitch). The simplest method of increasing K_s is therefore achieved by increasing N or I. The value of the parameters K_w and P can be adjusted by, amongst other methods, layering the stator windings or increasing the number of slots per pole (this does, of course, alter the pole pitch). These are standard procedures in rotary machine theory and are discussed in the texts of SAY (1963) and ALGER (1951). Also since Carter's fringing coefficient (1.42) gives an indication of fringing losses it is clear that losses are reduced by decreasing the width of a stator slot.

The magnetic Reynolds number $R_m = V_s/\alpha\eta$, where $V_s = \omega/\alpha$ is the synchronous wave velocity (ω is the excitation frequency), $\alpha = \pi/\tau$ is the wave number and $\eta = 1/\mu_0\sigma$ where σ is the electrical conductivity of the working fluid and μ_0 the magnetic permeability of free space. For a fixed pole pitch the only excitation parameter involved is ω. However, care must be taken to ensure that ω is not increased unduly because the skin depth for the EM field (3.17) is proportional to $\omega^{-\frac{1}{2}}$ and the fluid flow for large ω is confined to regions close to the glass ribbon's surface (see figure 3.9), which increases the surface shear stress on the glass.

Above we assumed that the pole pitch was fixed. At first sight, since $V_s = \omega\tau/\pi$, it might appear that large pole pitches are desirable. However in chapter 11 we showed that large pole pitches produce oscillatory flow beneath the SLIP and the pumping of the working fluid is then a net effect. With this in mind and the fact that (from (1.46)) $K_s \propto 1/\tau$ it is clearly desirable to have a SLIP with small pole pitches, even though this decreases the synchronous velocity of the excitation. This result can also be deduced from the idealised graphs in figures 3.5 to 3.8.

Perhaps the simplest method of increasing the pumping rate is to place two identical SLIM's adjacent to each other with their excitations fully synchronised (see figure 13.1). This should (at least) double the flow rate since a larger bulk of fluid sees an

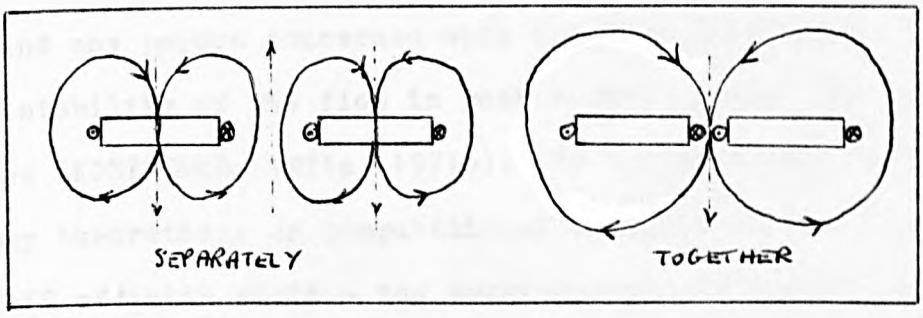

Fig. 13.1 The Effect of Placing Two SLIPs Side by Side

infinite expanse of excitation. We can increase the effective length of a SLIP by placing two identical synchronised SLIMs end to end. Since this doubles the total turns per phase and the number of pole pitches, the stator surface current density K_s remains unchanged. However, combining (3.82) and (3.83), which are idealised expressions describing the flow development in a SLIP we see that flow rate induced increases as the square root of the effective SLIP length. The above procedure may therefore prove useful.

We note that the efficiency of a SLIP can be improved using the compensating methods described in §1.5.3. Unfortunately the

compensating pole method produces a stator overhang which may be undesirable and the superimposed winding method may not be cost effective since it requires a great deal of electrical hardware.

Finally, we observe that the analysis above is unlikely to be directly applicable to parallel-wound (case $\mathcal{P}$) motors. However, following the observation made in chapter 7 that the body force induced by such motors is not conducive to pumping we choose not to discuss their design here.

13.3 Suggestions For Further Work

Apart from the few papers mentioned in the survey of §1.7 there seems to be very little published work on the flow profiles induced by an axially finite flat linear induction pump (FLIP), (whether single sided (SLIP) or double sided (DLIP), and we have not found any papers concerned with the flow development with time or the stability of the flow in such a pump, except for specific inlet profiles (KOZYRENKO, 1971a 1971b). To our knowledge there have not been any theoretical or computational analyses of the flow induced by a FLIP offinite width - the working fluid is always assumed to be fully contained in a channel which lies within the extent of the travelling wave excitation.

For an improvement in the flatness of float glass we clearly require a more detailed description of the flow induced in the baths molten tin by an open sided SLIP. In this context and with the above comments in mind we suggest the following topics as worthwhile areas of research:

(a) An analytical study of the flow development and stability of the flow in an axially finite SLIP assuming no transverse flow variation. In this context the work of KOZYRENKO (1971a, 1971b) and MERKULOV et al. (1973) is worth further consideration. It is possible that the constant applied magnetic field work of SPARROW et al. (1964) on inlet profiles, and CHEN & EATON

(1972) on stability can be extended to cater for travelling magnetic fields.

(b) A study of the flow development and stability of the movement of a body of liquid (which, in the float bath, has a shear profile) into a finite travelling magnetic field aligned transverse to the flow.

Here the approaches used by the authors in § 1.8 for an analysis of stability and flow development in the constant applied magnetic field configuration may prove useful.

(c) A full three dimensional numerical study of the coupled hydrodynamic and electromagnetic equations with boundary conditions appropriate to the float bath SLIP configuration.

A numerical approach will allow the inclusion of inertia terms for the fluid flow, and avoid the MHD approximation (the assumption that the fluid velocity $\underline{v}$ can be treated as a constant in Maxwell's equations) used in all of the analytical studies of a SLIP published to date.

Since a two-dimensional study will of necessity preceed a three dimensional one, the results of NASAR and DEL CID's (1973a, 1973b) numerical study of a SLIM may be used for comparison. If a finite difference technique is used, the results of MONSON (1972) and BREWITT-TAYLOR & WEAVER (1976) may prove useful in obtaining appropriate boundary conditions for the corners of the stator core (assuming a realistic model for the motor is used), if the magnetic permeability and electric conductivity is assumed to be different than that of free space.

APPENDIX I - Special Functions

Here we list only the particular results required in our work. Further properties of the functions below are given in the texts of ABRAMOWITZ & STEGUN (AS), GRADSHTEYN & RYZHIK (GR), LUKE (L) and WATSON (W). We use the convention that Greek letters ν, μ, etc. are written for parameters which may take arbitrary values but Latin letters, m, n, etc., for the corresponding parameters if they are restricted to integral values. The parameter z is assumed complex.

A. BESSEL Functions (AS, GR, L and W)

We use Bessel's functions of the first kind, $J_\nu(z)$; of the second kind $Y_\nu(z)$; of the modified first kind, $I_\nu(z)$, and of the modified second kind, $K_\nu(z)$.

(i) Limiting forms for Small Argument. When ν is fixed and $z \to 0$

$$J_\nu(z) \sim (\tfrac{1}{2}z)^\nu / \Gamma(\nu+1) \qquad (\nu \neq -1, -2, -3, \ldots)$$

$$Y_\nu(z) \sim -(1/\pi)\Gamma(\nu)(\tfrac{1}{2}z)^{-\nu} \quad \Re\{z\} > 0 \; ; \quad Y_0(z) \sim \tfrac{2}{\pi}\log z$$

$$I_\nu(z) \sim (\tfrac{1}{2}z)^\nu / \Gamma(\nu+1) \qquad (\nu \neq -1, -2, -3, \ldots)$$

$$K_\nu(z) \sim \tfrac{1}{2}\Gamma(\nu)(\tfrac{1}{2}z)^{-\nu} \quad \Re\{z\} > 0 \; ; \quad K_0(z) \sim -\log z$$

(ii) Asymptotic Expansions for Large Arguments. When ν is fixed and $|z| \to \infty$.

$$J_\nu(z) = \sqrt{\frac{2}{\pi z}} \left\{ \cos\left(z - \tfrac{1}{2}\nu\pi - \tfrac{1}{4}\pi\right) + e^{|\Im\{z\}|} O(|z|^{-1}) \right\} \quad (|\arg z| < \pi)$$

$$Y_\nu(z) = \sqrt{\frac{2}{\pi z}} \left\{ \sin\left(z - \tfrac{1}{2}\nu\pi - \tfrac{1}{4}\pi\right) + e^{|\Im\{z\}|} O(|z|^{-1}) \right\} \quad (|\arg z| < \pi)$$

$$I_\nu(z) = \frac{e^z}{\sqrt{2\pi z}} \left\{ 1 - \frac{4\nu^2 - 1}{8z} + O\left(\frac{1}{z^2}\right) \right\} \qquad (|\arg z| < \tfrac{\pi}{2})$$

$$K_\nu(z) = \sqrt{\frac{\pi}{2z}}\, e^{-z} \left\{ 1 + \frac{4\nu^2 - 1}{8z} + O\left(\frac{1}{z^2}\right) \right\} \qquad (|\arg z| < \tfrac{3\pi}{2})$$

(iii) Recurrence Relations. $\mathcal{B}(z)$ is any Bessel function.

$$z\,\mathcal{B}_{\nu-1}(z) + z\,\mathcal{B}_{\nu+1}(z) = 2\nu\,\mathcal{B}_{\nu}(z)$$

$$\mathcal{B}_{\nu-1}(z) - \mathcal{B}_{\nu+1}(z) = 2\frac{d}{dz}\cdot\mathcal{B}_{\nu}(z)$$

(iv) Special Results. $\mathcal{B}(z)$ is any Bessel function.

$$\mathcal{B}_{-n}(z) = (-1)^n \mathcal{B}_n(z)$$

$$\frac{d}{dz}\cdot J_0(z) = -J_1(z)$$

(v) Integral Expressions.

$$\int_0^{2\pi} e^{iz\sin\theta}\cos n\theta\, d\theta = \{1 + (-1)^n\}\pi J_n(z)$$

$$\int_0^{2\pi} e^{iz\sin\theta}\sin n\theta\, d\theta = \{1 - (-1)^n\}\pi i J_n(z)$$

$$\int_0^{\infty} e^{-z\cosh t}\cosh nt\, dt = K_n(z)$$

B. AIRY Functions (AS, L)

A pair of linearly independent solutions to the differential equation $\frac{d^2}{dz^2}\cdot w(z) - z\,w(z) = 0$ are the Airy functions $Ai(z)$ and $Bi(z)$.

(i) Limiting Forms for Small Argument.

$$Ai(z) = \frac{3^{-2/3}}{\Gamma(\frac{2}{3})}\left(1 + \frac{z^3}{3!}\right) - \frac{3^{-1/3}}{\Gamma(\frac{1}{3})}\left(z + \frac{2z^4}{4!}\right) + O(z^6)$$

$$Bi(z) = \sqrt{3}\left\{\frac{3^{-2/3}}{\Gamma(\frac{2}{3})}\left(1 + \frac{z^3}{3!}\right) - \frac{3^{-1/3}}{\Gamma(\frac{1}{3})}\left(z + \frac{2z^4}{4!}\right)\right\} + O(z^6)$$

(ii) Asymptotic Expansion for Large Arguments.

$$Ai(z) \sim \tfrac{1}{2}\pi^{-1/2} z^{-1/4} e^{-\frac{2}{3}z^{3/2}} \qquad (|\arg z| < \pi)$$

$$Bi(z) \sim \pi^{-1/2} z^{-1/4} e^{2/3 z^{3/2}} \qquad (|\arg z| < \pi/3)$$

C. STRUVE, ANGER and WEBER Functions (AS)

Here we consider the Struve function $H_\nu(z)$; modified Struve function, $L_\nu(z)$; Anger function, $\mathbf{J}_\nu(z)$ and Weber function $E_\nu(z)$.

(i) Recurrence Relations: ($' \equiv \frac{d}{dz}$)

$$H_{\nu-1} + H_{\nu+1} = \frac{2\nu}{z} \cdot H_\nu + \frac{(\frac{1}{2}z)^\nu}{\sqrt{\pi}\,\Gamma(\nu+\frac{3}{2})}$$

$$H_{\nu-1} - H_{\nu+1} = 2H_\nu' - \frac{(\frac{1}{2}z)^\nu}{\sqrt{\pi}\,\Gamma(\nu+\frac{3}{2})}$$

$$L_{\nu-1} - L_{\nu+1} = \frac{2\nu}{z} \cdot L_\nu + \frac{(z/2)^\nu}{\sqrt{\pi}\,\Gamma(\nu+\frac{3}{2})}$$

$$L_{\nu-1} + L_{\nu+1} = 2L_\nu' - \frac{(z/2)^\nu}{\sqrt{\pi}\,\Gamma(\nu+\frac{3}{2})}$$

(ii) Special Results.

$$H_0' = \frac{2}{\pi} - H_1$$

$z \to \infty$, $\quad H_0(z) - Y_0(z) \sim \frac{2}{\pi}\left\{\frac{1}{z} - \frac{1}{z^3} + \frac{1^2 3^2}{z^5}\right\} + O(\frac{1}{z^7}) \quad (|\arg z| < \pi)$

$z \to \infty$, $\quad H_1(z) - Y_1(z) \sim \frac{2}{\pi}\left\{1 + \frac{1}{z^2} - \frac{1^2 3}{z^4}\right\} + O(\frac{1}{z^6}) \quad (|\arg z| < \pi)$

$$\mathbf{J}_n(z) = J_n(z)$$

$$E_0(z) = -H_0(z)$$

$$E_1(z) = \frac{2}{\pi} - H_1(z)$$

D. SCHLAFLI Polynomial $S_n(t)$. (WA)

$$S_1(t) = \frac{2}{t} \quad S_2(t) = \frac{4}{t^2} \quad S_3(t) = \frac{2}{t} + \frac{16}{t^3} \quad S_4(t) = \frac{8}{t^2} + \frac{96}{t^4}$$

E. GAMMA Function $\Gamma(z)$. (AS)

$$\Gamma(n+1) = n! \qquad \Gamma(\tfrac{1}{2}) = \sqrt{\pi}$$

$$\Gamma(z)\,\Gamma(1-z) = -z\,\Gamma(-z)\,\Gamma(z) = \pi \operatorname{cosec} \pi z.$$

APPENDIX II - Integral Reductions

A. Fourier Integrals

Consider the integral

$$I = \int_{-\infty}^{\infty}\int_{-\infty}^{\infty} (\alpha p + \beta q)\, F(\sqrt{p^2+q^2})\, e^{-i(px+qy)}\, dp\, dq$$

where α, β are constants and F is an arbitrary function. Writing $x = \rho\cos\theta$, $y = \rho\sin\theta$, $p = \kappa\cos\vartheta$, $q = \kappa\sin\vartheta$ we can reduce I to the form

$$I = \int_0^{2\pi}\int_0^{\infty} (\alpha\cos\phi + \beta\sin\phi)\, \kappa^2 F(\kappa)\, e^{-i\kappa\rho\cos(\phi-\theta)}\, d\kappa\, d\phi$$

This expression can be further reduced by writing $\phi - \theta = \frac{\pi}{2} - \psi$ and using the integral results of $A(v)$ in Appendix I. We find

$$I = 2\pi i\,(\alpha\cos\theta + \beta\sin\theta)\int_0^{\infty} F(\kappa)\cdot\kappa^2 J_1(\kappa\rho)\, d\kappa$$

B. Laplacian Integral

Consider the integral

$$I(\alpha,\beta) = \int_0^{\infty} \frac{G(\kappa)\, e^{-\kappa\alpha}}{\kappa-\beta}\, d\kappa \qquad \Re[\alpha] > 0 \tag{II.1}$$

we have $$e^{\beta\alpha} I(\alpha,\beta) = \int_0^{\infty} \frac{G(\kappa)\, e^{-\alpha(\kappa-\beta)}}{\kappa-\beta}\cdot d\kappa$$

$$\therefore \frac{\partial}{\partial\alpha}\left\{ e^{\beta\alpha} I(\alpha,\beta)\right\} = -e^{\alpha\beta}\int_0^{\infty} G(\kappa) e^{-\alpha\kappa}\, d\kappa = -e^{\alpha\beta}\,\bar{G}(\alpha)$$

integrating, we have $$I(\alpha,\beta) = e^{-\beta\alpha}\left\{-\int_0^{\alpha} e^{\alpha\beta}\,\bar{G}(\alpha)\, d\alpha + I(0,\beta)\right\} \tag{II.2}$$

where $$I(0,\beta) = \int_0^{\infty} \frac{G(\kappa)}{\kappa-\beta}\cdot d\kappa$$

Similarly the integral

$$J(\alpha,\beta) = \int_0^{\infty} \frac{G(\kappa)}{\kappa+\beta}\cdot e^{-\kappa\alpha}\, d\kappa \qquad \Re[\alpha] > 0 \tag{II.3}$$

can be reduced to $$J(\alpha,\beta) = e^{\beta\alpha}\left\{\int_0^{\alpha} e^{-\alpha\beta}\,\bar{G}(\alpha)\, d\alpha + J(0,\beta)\right\} \tag{II.4}$$

where $$J(0,\beta) = \int_0^{\infty} \frac{G(\kappa)}{\kappa+\beta}\cdot d\kappa$$

Only for some particular values of the parameters α, β and the function $G(\kappa)$ are the integrals in (II.1) and (II.3) tabulated in the standard texts (BATEMAN, GRADSHTEYN and RYZHIK etc.). In this thesis we are mainly concerned with the value of $I(\alpha,\beta)$ and $J(\alpha,\beta)$ for α small. Usually (II.1) and (II.3) only give a first approximation (for $\alpha=0$) since expanding the exponential function, $e^{-\alpha\kappa}$, in a power series often destroys the convergence of the integrals. However, providing we can obtain a value for the Laplace transformation of $G(\kappa)$, $(\bar{G}(\alpha))$, the reduced results (II.2) and (II.4) give further approximations, since the magnitude of the integral expressions in these results are of order α . When β is real (and positive) the procedure above is a useful technique for removing the singularity at $\kappa=\beta$ in the Cauchy Principal Value (CPV) integral (II.1).

In the derivation of (II.2) and (II.4) we have assumed that we can differentiate with respect to α through the integral signs of (II.1) and (II.3). It can be shown that the conditions on the integral $I = \int_0^\infty \frac{P(\kappa,\alpha)}{\kappa-\beta} d\kappa$ for the differentiation to be valid are (i) its kernal should be continuous on $[0,\infty)$, and (ii) all the partial derivatives of its kernal should be continuous in $[0,\infty)$. The result holds even if I is CPV, as we shall show. If β is real we have

$$I = \lim_{\epsilon\to 0} \left\{ \int_0^{\beta-\epsilon} \frac{P(\kappa,\alpha)}{\kappa-\beta} d\kappa + \int_{\beta+\epsilon}^{\infty} \frac{P(\kappa,\alpha)}{\kappa-\beta} d\kappa \right\}$$

Clearly the kernal $\frac{P(\kappa,\alpha)}{\kappa-\beta}$ over the intervals $[0,\beta-\epsilon]$ and $[\beta+\epsilon,\infty)$ is continuous if $P(\kappa)$ is continuous, so providing the partial derivatives of $\frac{P(\kappa,\alpha)}{\kappa-\beta}$ exist, we can differentiate with respect to α and obtain

$$\frac{\partial I}{\partial \alpha} = \lim_{\epsilon\to 0} \left\{ \int_0^{\beta-\epsilon} \frac{\partial}{\partial\alpha} \cdot \frac{P(\kappa,\alpha)}{\kappa-\beta} d\kappa + \int_{\beta+\epsilon}^{\infty} \frac{\partial}{\partial\alpha} \frac{P(\kappa,\alpha)}{\kappa-\beta} d\kappa \right\}$$

which is the required result.

APPENDIX III - Additions to Chapter 9

Case S Constants of Integration

$$M_1 = \frac{\mu_0 K_s}{2(\gamma-k)\Delta_s} \cdot \frac{\gamma}{q}\left\{(\gamma+k)^2 e^{2\gamma} - (\gamma-k)^2\right\}$$

$$M_2 = \frac{\mu_0 K_s}{2(\gamma-k)\Delta_s}\left\{(\gamma+k)^2 e^{2\gamma} - (\gamma-k)^2\right\}$$

$$M_3 = \frac{ik\mu_0 K_s}{2q(\gamma-k)\Delta_s}\left\{(\gamma+k)^2 e^{2\gamma} - (\gamma-k)^2\right\}$$

$$N_1 = \frac{+\mu_0 K_s (\gamma+k)}{2\Delta_s}\cdot\frac{\gamma}{q}\left\{e^{2\gamma}-1\right\}$$

$$N_2 = \frac{\mu_0 K_s (\gamma+k)}{2\Delta_s}\left\{e^{2\gamma}-1\right\}$$

$$N_3 = -\mu_0 K_s \cdot \frac{ik(\gamma+k)}{2q\Delta_s}\left\{e^{2\gamma}-1\right\}$$

$$P_1 = \mu_0 K_s \cdot \frac{\gamma\gamma}{\Delta_s q}\left(\frac{\gamma+k}{\gamma-k}\right)e^{2\gamma}$$

$$P_2 = \mu_0 K_s \cdot \frac{\gamma}{\Delta_s}\left(\frac{\gamma+k}{\gamma-k}\right)e^{2\gamma}$$

$$P_3 = \mu_0 K_s \cdot \frac{ik^2}{q\Delta_s}\left(\frac{\gamma+k}{\gamma-k}\right)e^{2\gamma}$$

$$Q_1 = -\mu_0 K_s \cdot \frac{\gamma\gamma}{\Delta_s q} \qquad R_1 = \mu_0 K_s \cdot \frac{2\gamma k e^{(k+\gamma)}}{(\gamma-k)\Delta_s}\cdot\frac{\gamma}{q}$$

$$Q_2 = -\mu_0 K_s \cdot \frac{\gamma}{\Delta_s} \qquad R_2 = \mu_0 K_s \cdot \frac{2\gamma k e^{(k+\gamma)}}{(\gamma-k)\Delta_s}$$

$$Q_3 = \mu_0 K_s \cdot \frac{ik^2}{q\Delta_s} \qquad R_3 = \mu_0 K_s \cdot \frac{2ik^2\gamma e^{(k+\gamma)}}{q(\gamma-k)\Delta_s}$$

The case P solutions are recovered by replacing $\mu_0 K_s$ by $-(iq/k)(\beta_m \Delta_s/\Delta_m)$ in the above constants.

APPENDIX IV - Additions to Chapter 11

A. Expressions for the constants of integration.

$$D_1 = E C_3 \cdot \frac{\sinh \kappa z_0}{\sinh \kappa h} + \frac{iE}{\kappa} (pC_1 + qC_2) \frac{\cosh \kappa z_0}{\sinh \kappa h}$$

$$D_2 = -E C_3 \frac{\sinh \kappa (h - z_0)}{\sinh \kappa h} + \frac{iE}{\kappa} (pC_1 + qC_2) \frac{\cosh \kappa (h - z_0)}{\sinh \kappa h}$$

$$L_1 = \left\{ E C_2 \cosh \kappa z_0 - \frac{iEqC_3 \sinh \kappa z_0}{\kappa} - E\gamma \cosh \kappa (h - z_0)\, p(qC_1 - pC_2) \times \left[1 - \left(\frac{\gamma + \kappa}{\gamma - \kappa} \right) e^{2\gamma} \right] / \kappa^2 \Delta \right\} / \sinh \kappa h$$

$$M_1 = \left\{ - \frac{E C_2 \cosh \kappa (h - z_0)}{2} + E\gamma \cosh \kappa (h - z_0)\, p(qC_1 - pC_2) \cdot \frac{\left[1 - \left(\frac{\gamma + \kappa}{\gamma - \kappa} \right) e^{2\gamma} \right] e^{-\kappa h}}{2\kappa^2 \Delta} - \frac{iEqC_3 \sinh \kappa (h - z_0)}{2\kappa} \right\} / \sinh \kappa h$$

$$N_1 = \left\{ \frac{E C_2 \cosh \kappa (h - z_0)}{2} + \frac{iEqC_3 \sinh \kappa (h - z_0)}{2\kappa} + E\gamma \cosh \kappa (h - z_0)\, p(qC_1 - pC_2) \times \left[1 - \left(\frac{\gamma + \kappa}{\gamma - \kappa} \right) e^{2\gamma} \right] / 2\kappa^2 \Delta \right\} / \sinh \kappa h$$

$$L_2 = \left\{ - E C_1 \cosh \kappa z_0 + \frac{iEpC_3 \sinh \kappa z_0}{\kappa} - E\gamma \cosh \kappa (h - z_0)\, q(qC_1 - pC_2) \times \left[1 - \left(\frac{\gamma + \kappa}{\gamma - \kappa} \right) e^{2\gamma} \right] / \kappa^2 \Delta \right\} / \sinh \kappa h$$

$$M_2 = \left\{ \frac{E C_1 \cosh \kappa (h - z_0)}{2} + E\gamma \cosh \kappa (h - z_0)\, q(qC_1 - pC_2) \cdot \frac{\left[1 - \left(\frac{\gamma + \kappa}{\gamma - \kappa} \right) e^{2\gamma} \right] e^{-\kappa h}}{2\kappa^2 \Delta} + \frac{iEpC_3 \sinh \kappa (h - z_0)}{2\kappa} \right\} / \sinh \kappa h$$

$$N_2 = \left\{ - \frac{E C_1 \cosh \kappa (h - z_0)}{2} - \frac{iEpC_3 \sinh \kappa (h - z_0)}{2\kappa} - E\gamma \cosh \kappa (h - z_0)\, q(qC_1 - pC_2) \times \left[1 - \left(\frac{\gamma + \kappa}{\gamma - \kappa} \right) e^{2\gamma} \right] / 2\kappa^2 \Delta \right\} / \sinh \kappa h .$$

$$P_1 = \frac{E(\gamma+k)\, p\gamma\, (qC_1 - pC_2)\, e^{2\gamma} \cosh k(h-z_0)}{k^2(\gamma-k)\Delta}$$

$$P_2 = \frac{E(\gamma+k)\, q\, \gamma\, (qC_1 - pC_2)\, e^{2\gamma} \cosh k(h-z_0)}{k^2(\gamma-k)\Delta}$$

$$Q_1 = -\frac{Ep\gamma(qC_1 - pC_2)\, \cosh k(h-z_0)}{k^2\Delta}$$

$$Q_2 = -\frac{Eq\gamma(qC_1 - pC_2)\, \cosh k(h-z_0)}{k^2\Delta}$$

$$P_3 = \frac{iE(\gamma+k)\, e^{2\gamma}(qC_1 - pC_2)\, \cosh k(h-z_0)}{(\gamma-k)\Delta}$$

$$Q_3 = \frac{iE\,(qC_1 - pC_2)\, \cosh k(h-z_0)}{\Delta}$$

B. Transformed magnetic induction (horizontal source $C_2 = 0$)

$$\hat{B}_1(\text{II}, z<z_0) = -\frac{E\cosh k(h-z_0)}{\sinh kh}\left\{C_2 \sinh kz + p\gamma(pC_2 - qC_1)\frac{\left[\left(\frac{\gamma+k}{\gamma-k}\right)e^{2\gamma}-1\right]}{k^2\Delta}\sinh k(h-z)\right\}$$

$$\hat{B}_2(\text{II}, z<z_0) = \frac{E\cosh k(h-z_0)}{\sinh kh}\left\{C_1 \sinh kz - q\gamma(pC_2 - qC_1)\frac{\left[\left(\frac{\gamma+k}{\gamma-k}\right)e^{2\gamma}-1\right]}{k^2\Delta}\sinh k(h-z)\right\}$$

$$\hat{B}_3(\text{II}, z<z_0) = \frac{iE\cosh k(h-z_0)}{\sinh kh}\cdot(pC_2 - qC_1)\left\{-\frac{\cosh kz}{k} + \gamma\frac{\left[\left(\frac{\gamma+k}{\gamma-k}\right)e^{2\gamma}-1\right]}{k\Delta}\cosh k(h-z)\right\}$$

$$\hat{B}_1(\text{II}, z>z_0) = \frac{E\sinh k(h-z)}{\sinh kh}\left\{C_2 \cosh kz_0 - p\gamma(pC_2 - qC_1)\frac{\left[\left(\frac{\gamma+k}{\gamma-k}\right)e^{2\gamma}-1\right]}{k^2\Delta}\cosh k(h-z_0)\right\}$$

$$\hat{B}_2(\text{II}, z>z_0) = -\frac{E\sinh k(h-z)}{\sinh kh}\left\{C_1 \cosh kz_0 + q\gamma(pC_2 - qC_1)\frac{\left[\left(\frac{\gamma+k}{\gamma-k}\right)e^{2\gamma}-1\right]}{k^2\Delta}\cosh k(h-z_0)\right\}$$

$$\hat{B}_3(\text{II}, z>z_0) = \frac{iE\cosh k(h-z)}{\sinh kh}\cdot(pC_2 - qC_1)\left\{-\frac{\cosh kz_0}{k} + \gamma\frac{\left[\left(\frac{\gamma+k}{\gamma-k}\right)e^{2\gamma}-1\right]}{k\Delta}\cosh k(h-z_0)\right\}$$

$$\hat{B}_1(\text{III}) = \frac{p\gamma(qC_1-pC_2)\cdot\cosh\kappa(h-z_0)\cdot E\cdot\left[\left(\frac{\gamma+\kappa}{\gamma-\kappa}\right)e^{2h}e^{\gamma z}-e^{-\gamma z}\right]}{\kappa^2\Delta}$$

$$\hat{B}_2(\text{III}) = \frac{q\gamma(qC_1-pC_2)\cdot\cosh\kappa(h-z_0)\cdot E\cdot\left[\left(\frac{\gamma+\kappa}{\gamma-\kappa}\right)e^{2\gamma}e^{\gamma z}-e^{-\gamma z}\right]}{\kappa^2\Delta}$$

$$\hat{B}_3(\text{III}) = \frac{iE(qC_1-pC_2)\cdot\cosh\kappa(h-z_0)\left[\left(\frac{\gamma+\kappa}{\gamma-\kappa}\right)e^{2\gamma}e^{\gamma z}+e^{-\gamma z}\right]}{\Delta}$$

$$\hat{B}_1(\text{IV}) = 2E\cdot\frac{p\gamma(qC_1-pC_2)\cosh\kappa(h-z_0)\cdot e^{\kappa z}e^{(\gamma+\kappa)}}{\kappa(\gamma-\kappa)\Delta}$$

$$\hat{B}_2(\text{IV}) = 2E\cdot\frac{q\gamma(qC_1-pC_2)\cosh\kappa(h-z_0)\,e^{\kappa z}e^{(\gamma+\kappa)}}{\kappa(\gamma-\kappa)\Delta}$$

$$\hat{B}_3(\text{IV}) = 2iE\cdot\frac{\gamma(qC_1-pC_2)\cosh\kappa(h-z_0)\,e^{\kappa z}e^{(\gamma+\kappa)}}{(\gamma-\kappa)\Delta}$$

C. Vertical magnetic dipole solutions (cylindrical coordinates (r,θ,z))

(i) 2-layer Earth.

$$B_r(\text{II}, z>z_0) = M\int_0^\infty e^{-\kappa z}\cdot\kappa^2\left\{-\cosh\kappa z_0+\gamma\frac{\left[\left(\frac{\gamma+\kappa}{\gamma-\kappa}\right)e^{2\gamma}-1\right]e^{-\kappa z_0}}{\Delta_1}\right\}J_1(\kappa\rho)\,d\kappa$$

$$B_3(\text{II}, z>z_0) = M\int_0^\infty e^{-\kappa z}\kappa^2\left\{-\cosh\kappa z_0+\gamma\frac{\left[\left(\frac{\gamma+\kappa}{\gamma-\kappa}\right)e^{2\gamma}-1\right]e^{-\kappa z_0}}{\Delta_1}\right\}J_0(\kappa\rho)\,d\kappa$$

$$B_r(\text{II}, z<z_0) = M\int_0^\infty e^{-\kappa z_0}\kappa^2\left\{\sinh\kappa z+\gamma\frac{\left[\left(\frac{\gamma+\kappa}{\gamma-\kappa}\right)e^{2\gamma}-1\right]e^{-\kappa z}}{\Delta_1}\right\}J_1(\kappa\rho)\,d\kappa$$

$$B_3(\text{II}, z<z_0) = M\int_0^\infty e^{-\kappa z_0}\kappa^2\left\{-\cosh\kappa z+\gamma\frac{\left[\left(\frac{\gamma+\kappa}{\gamma-\kappa}\right)e^{2\gamma}-1\right]e^{-\kappa z}}{\Delta_1}\right\}J_0(\kappa\rho)\,d\kappa$$

$$B_r(\text{III}) = M\int_0^\infty e^{-\kappa z_0}\cdot\frac{\kappa^2\gamma}{\Delta_1}\cdot\left\{\left(\frac{\gamma+\kappa}{\gamma-\kappa}\right)e^{2\gamma}e^{\gamma z}-e^{\gamma z}\right\}J_1(\kappa\rho)\,d\kappa$$

$$B_3(\text{III}) = -M\int_0^\infty e^{-\kappa z_0}\cdot\frac{\kappa^3}{\Delta_1}\cdot\left\{\left(\frac{\gamma+\kappa}{\gamma-\kappa}\right)e^{2\gamma}e^{\gamma z}+e^{-\gamma z}\right\}J_0(\kappa\rho)\,d\kappa$$

$$B_r(\text{IV}) = 2M\int_0^\infty \frac{e^{-kz_0}k^3\gamma e^{k(z+1)}}{(\gamma-k)\Delta_1}\cdot e^{\gamma}J_1(k\rho)\,dk$$

$$B_3(\text{IV}) = 2M\int_0^\infty \frac{e^{-kz_0}k^3\gamma e^{k(1+z)}}{(\gamma-k)\Delta_1}\cdot e^{\gamma}J_0(k\rho)\,dk$$

where $$\Delta_1 = \left[\left(\frac{\gamma+k}{\gamma-k}\right)e^{2\delta}-1\right]\gamma + \left[\left(\frac{\gamma+k}{\gamma-k}\right)e^{2\gamma}+1\right]k$$

(ii) Half space.

$$B_r(\text{II}, z>z_0) = M\int_0^\infty e^{-kz}\cdot k^2\left\{-\sinh kz_0 + \frac{\gamma e^{-kz_0}}{\gamma+k}\right\}J_1(k\rho)\,dk$$

$$B_3(\text{II}, z>z_0) = M\int_0^\infty e^{-kz}\,k^2\left\{-\cosh kz_0 + \frac{\gamma e^{-kz_0}}{\gamma+k}\right\}J_0(k\rho)\,dk$$

$$B_r(\text{III}, z<z_0) = M\int_0^\infty e^{-kz_0}\cdot k^2\left\{\sinh kz + \frac{\gamma e^{-kz}}{\gamma+k}\right\}J_1(k\rho)\,dk$$

$$B_3(\text{II}, z<z_0) = M\int_0^\infty e^{-kz_0}\cdot k^2\left\{-\cosh kz + \frac{\gamma e^{-kz}}{\gamma+k}\cdot\right\}J_0(k\rho)\,dk$$

$$B_r(\text{III}) = M\int_0^\infty \gamma e^{-kz_0}\cdot\frac{k^2e^{\gamma z}}{\gamma+k}\cdot J_1(k\rho)\,dk$$

$$B_3(\text{III}) = -M\int_0^\infty e^{-kz_0}\cdot\frac{k^3e^{\gamma z}}{\gamma+k}\,J_0(k\rho)\,dk$$

D. The EM field induced by a solitary tooth

The results presented here are an addition to those of §11.16. Here we use the magnetic field line analysis of chapter 12 to discuss the structure on the conductor surface, $z=0$, of the real and imaginary parts of the (complex induced EM field shown in figures IV.1 to IV.6.

Writing $\underline{B}(I,t) = (B_R + iB_I)e^{i\omega t}$, we see that B_R corresponds to the magnetic induction induced by the tooth (since at $t=0$ the secondary

Fig. Ⅳ.1 (a)

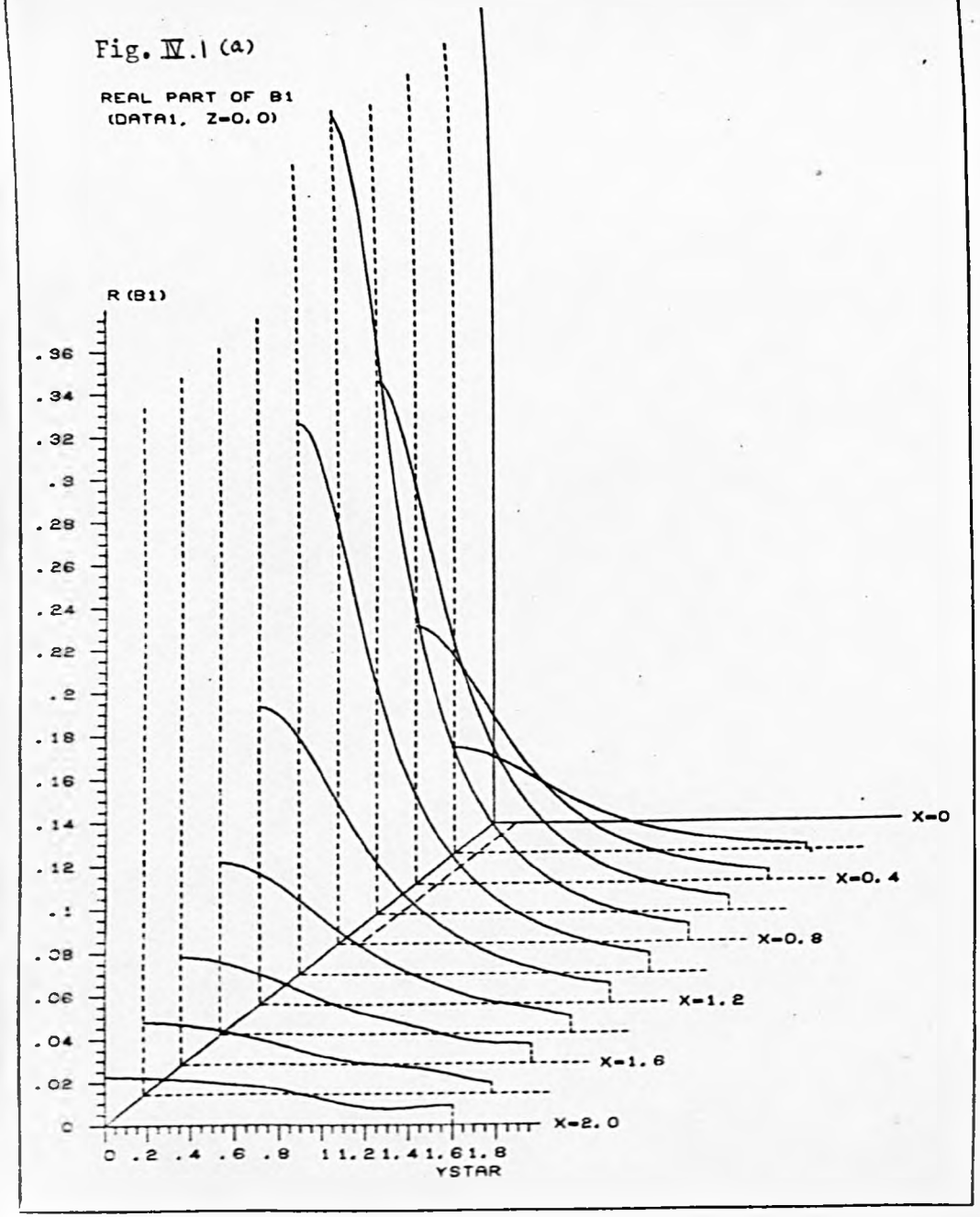

Fig. Ⅳ.1 (b)

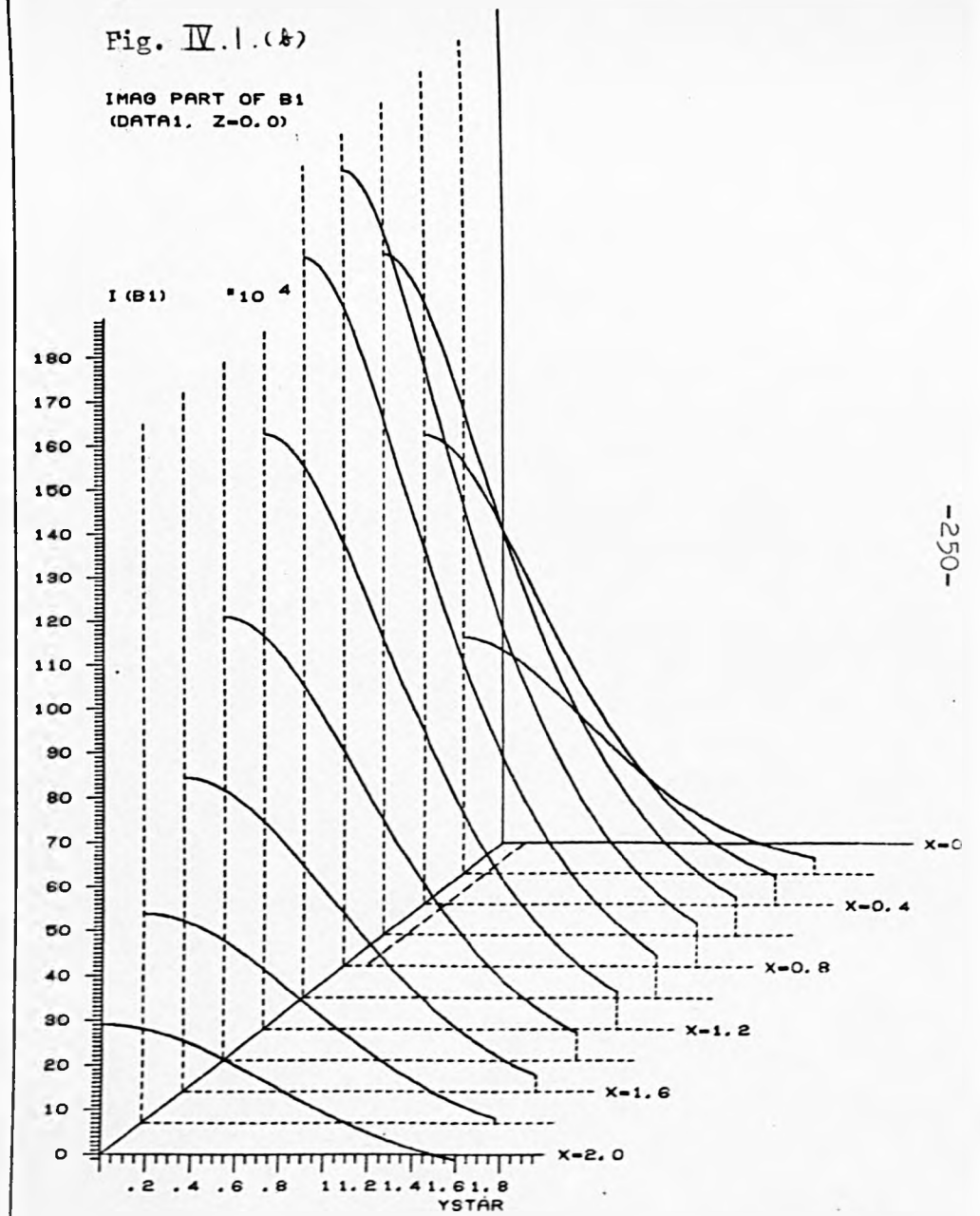

Fig. Ⅳ.26)

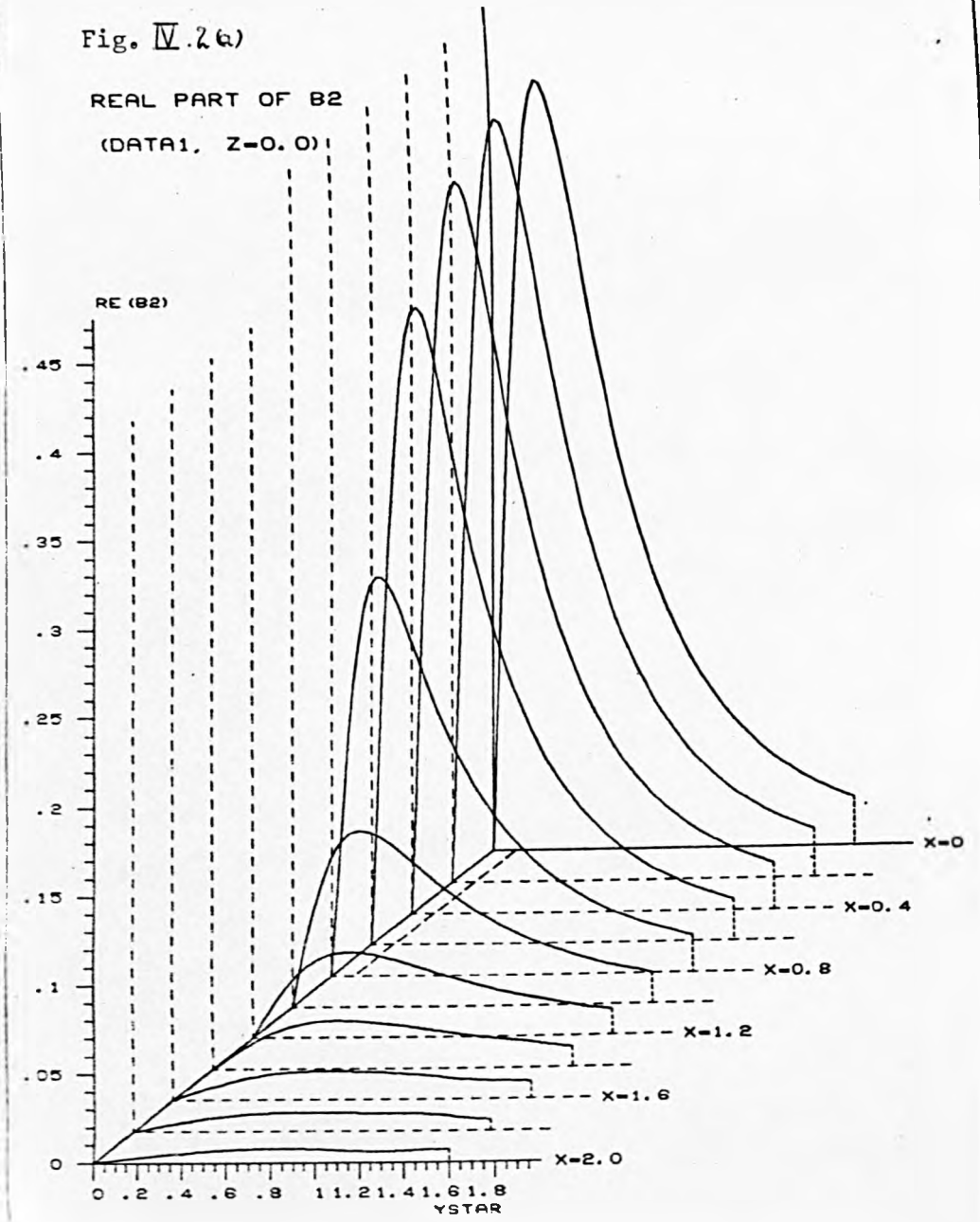
REAL PART OF B2
(DATA1, Z=0.0)
RE (B2)
.45
.4
.35
.3
.25
.2
.15
.1
.05
0
X=0
X=0.4
X=0.8
X=1.2
X=1.6
X=2.0
0 .2 .4 .6 .8 1 1.2 1.4 1.6 1.8
YSTAR

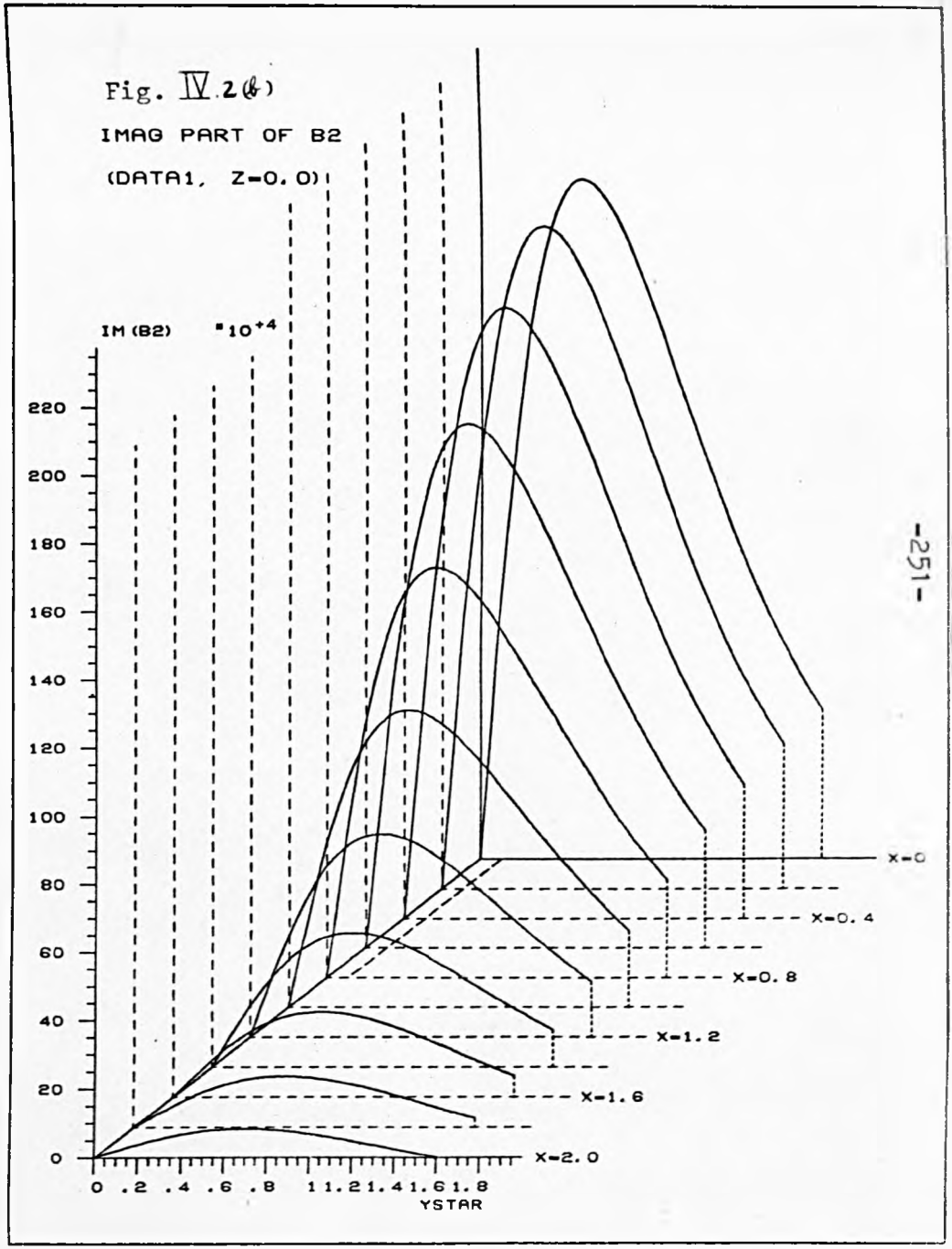
Fig. Ⅳ.2(6)
IMAG PART OF B2
(DATA1, Z=0.0)
IM(B2) *10**+4
220
200
180
160
140
120
100
80
60
40
20
0
0 .2 .4 .6 .8 1 1.2 1.4 1.6 1.8
YSTAR
X=0
X=0.4
X=0.8
X=1.2
X=1.6
X=2.0

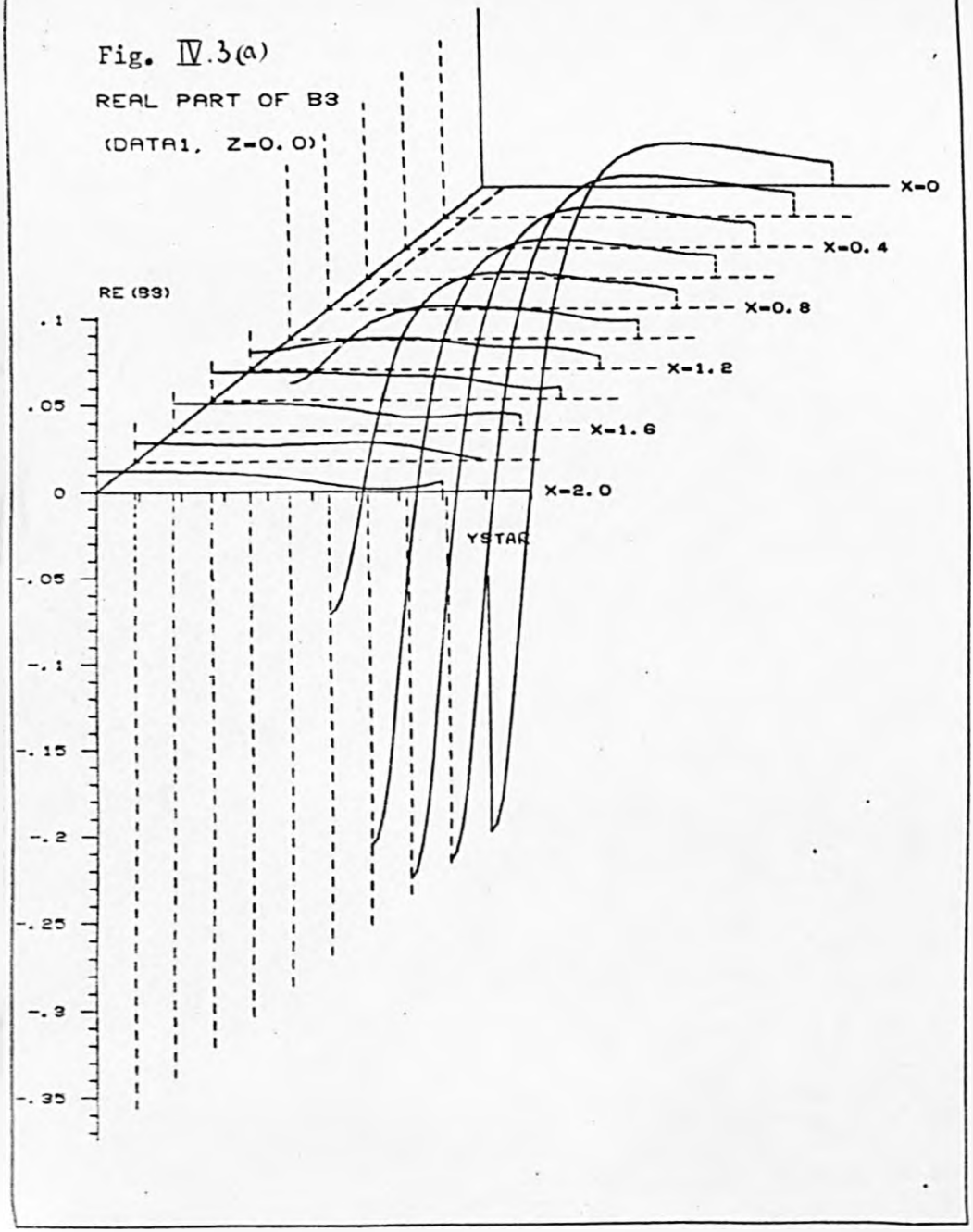
Fig. Ⅳ.3(a)
REAL PART OF B3
(DATA1, Z=0.0)
RE (B3)
.1
.05
0
-.05
-.1
-.15
-.2
-.25
-.3
-.35
X=0
X=0.4
X=0.8
X=1.2
X=1.6
X=2.0
YSTAR

Fig. Ⅳ.3(b)

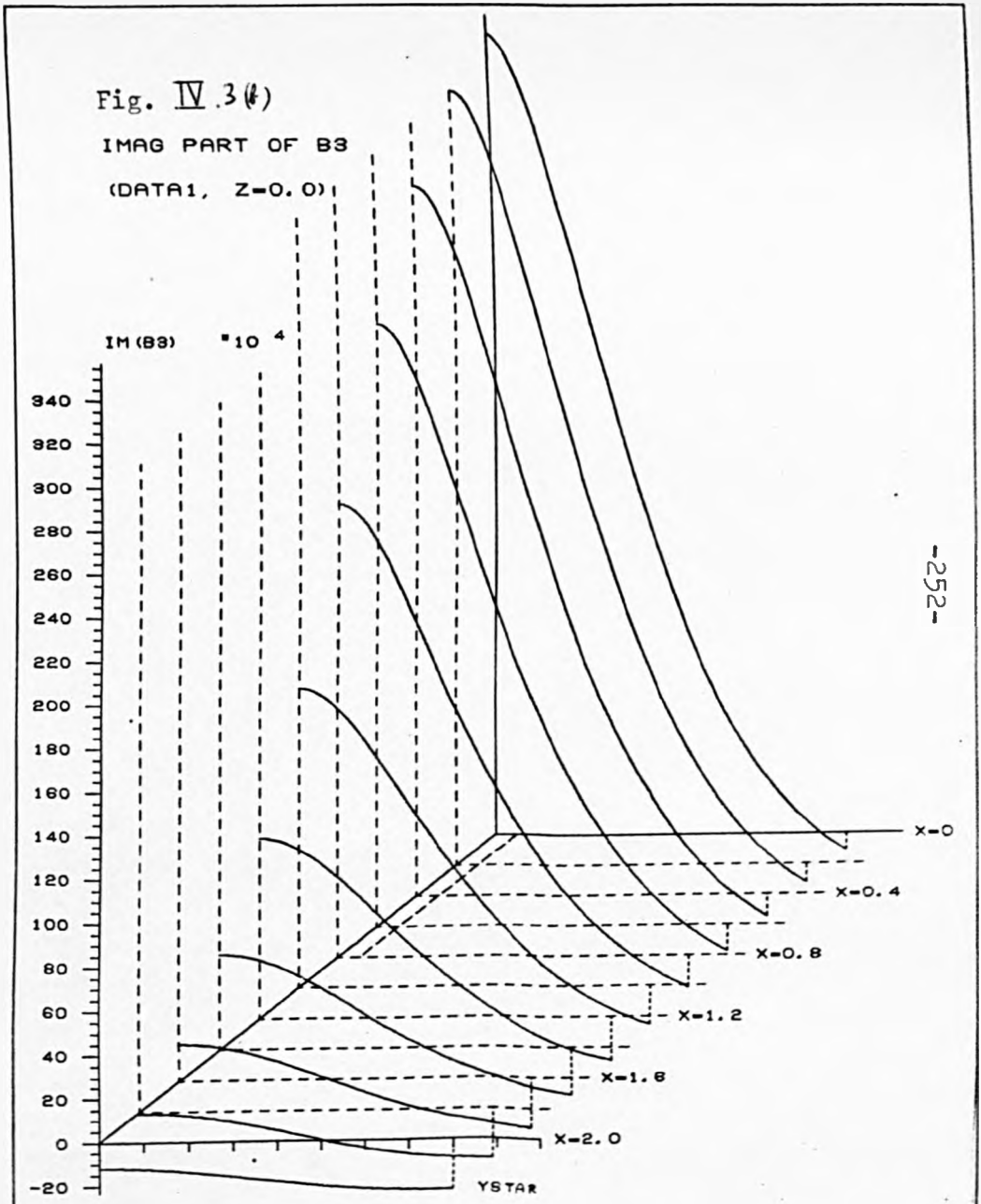
IMAG PART OF B3
(DATA1, Z=0.0)
IM(B3) *10 4
340
320
300
280
260
240
220
200
180
160
140
120
100
80
60
40
20
0
-20
X=0
X=0.4
X=0.8
X=1.2
X=1.6
X=2.0
YSTAR

Fig. IV 4(a)

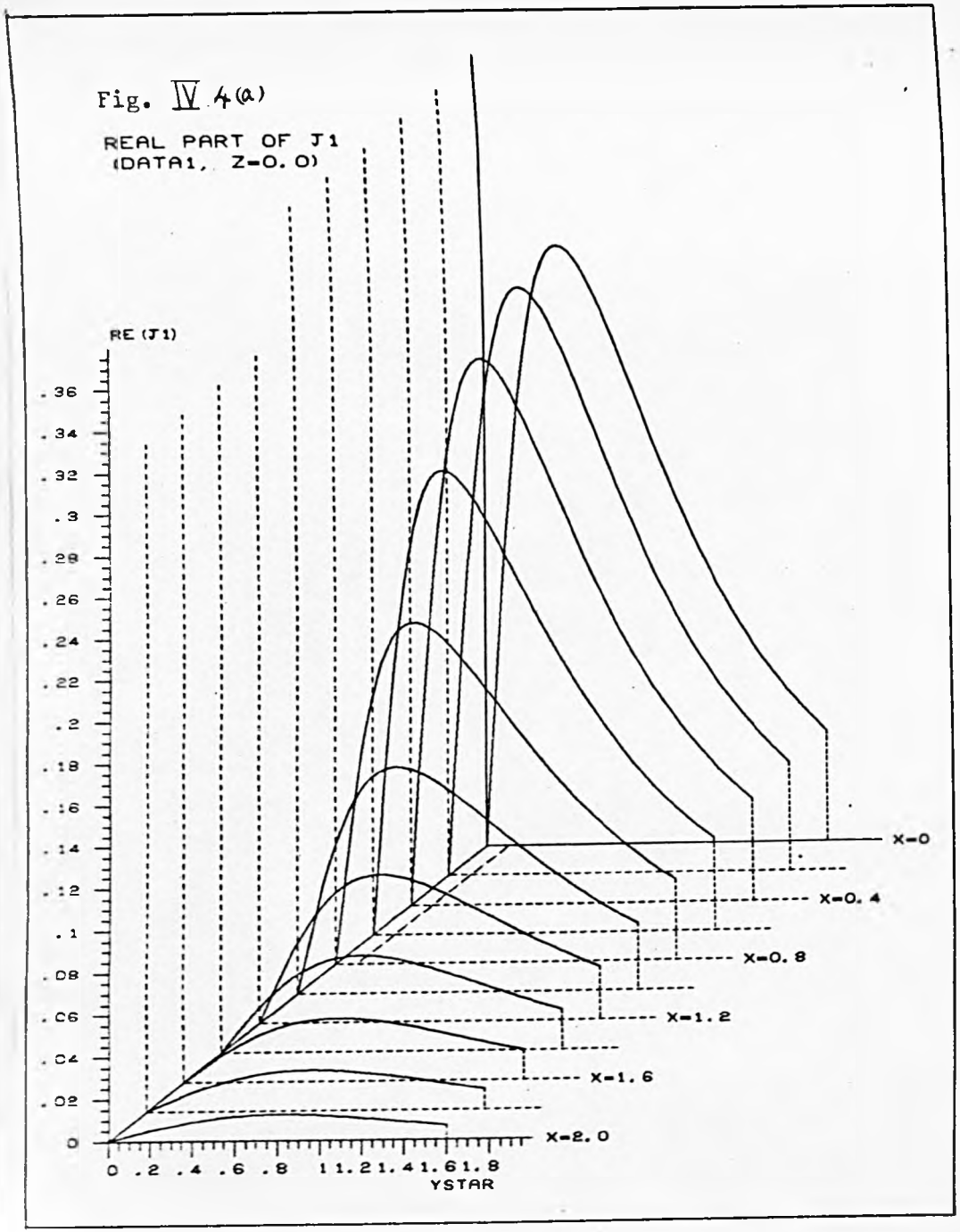

Fig. IV 4(b)

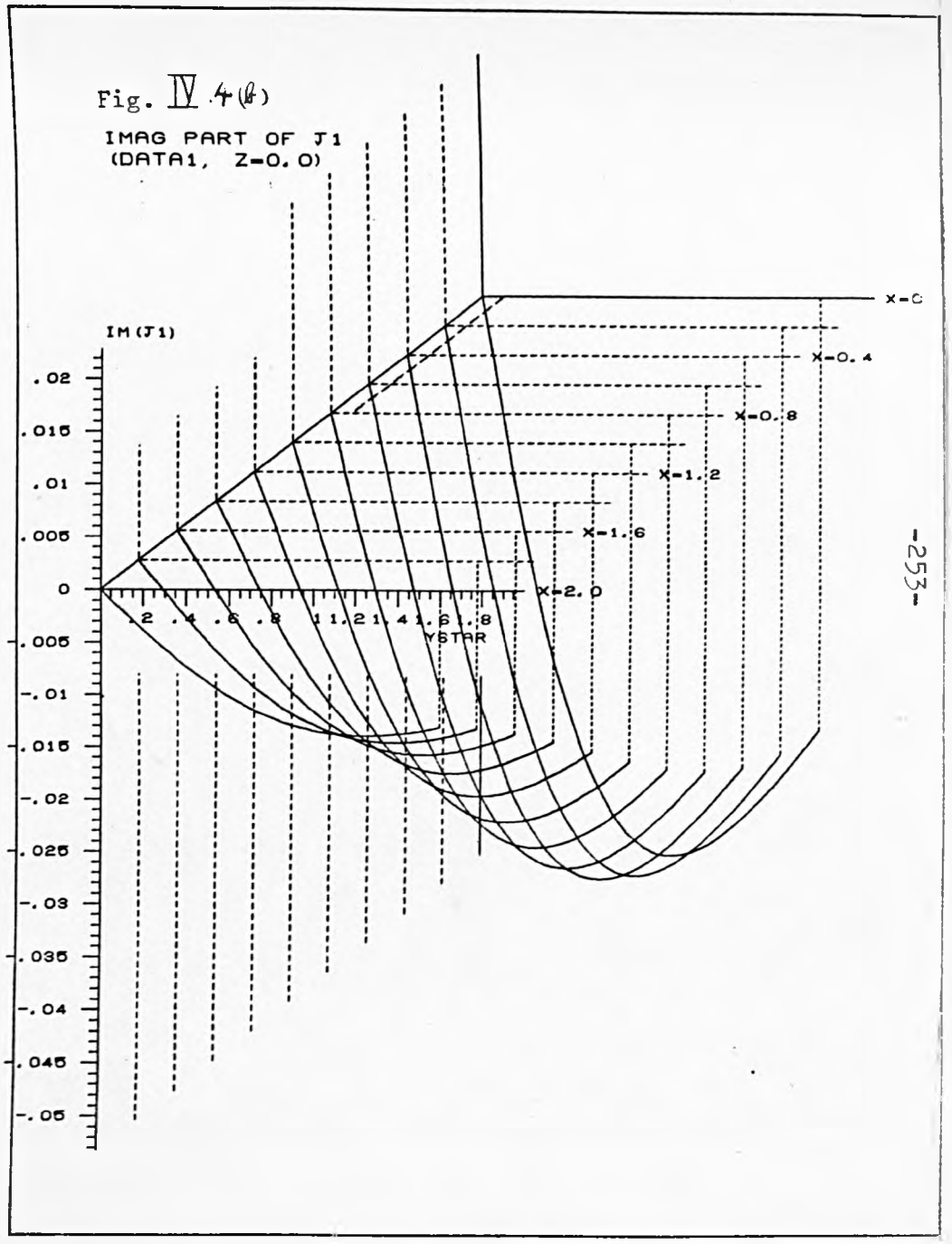

Fig. Ⅳ.5(a)

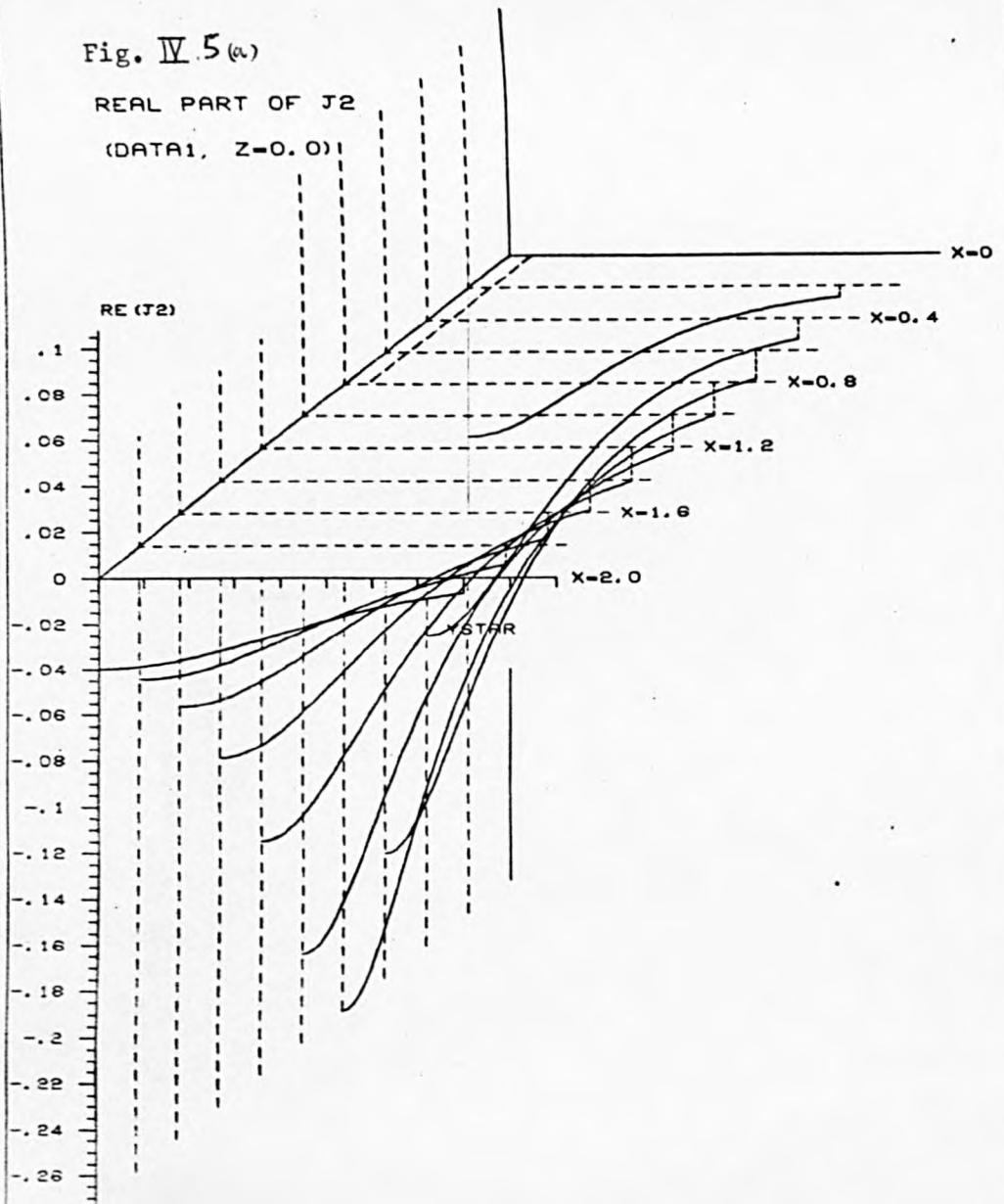
REAL PART OF J2
(DATA1, Z=0.0)
RE(J2)
.1
.08
.06
.04
.02
0
-.02
-.04
-.06
-.08
-.1
-.12
-.14
-.16
-.18
-.2
-.22
-.24
-.26
X=0
X=0.4
X=0.8
X=1.2
X=1.6
X=2.0
XSTAR

Fig. IV·5(6)

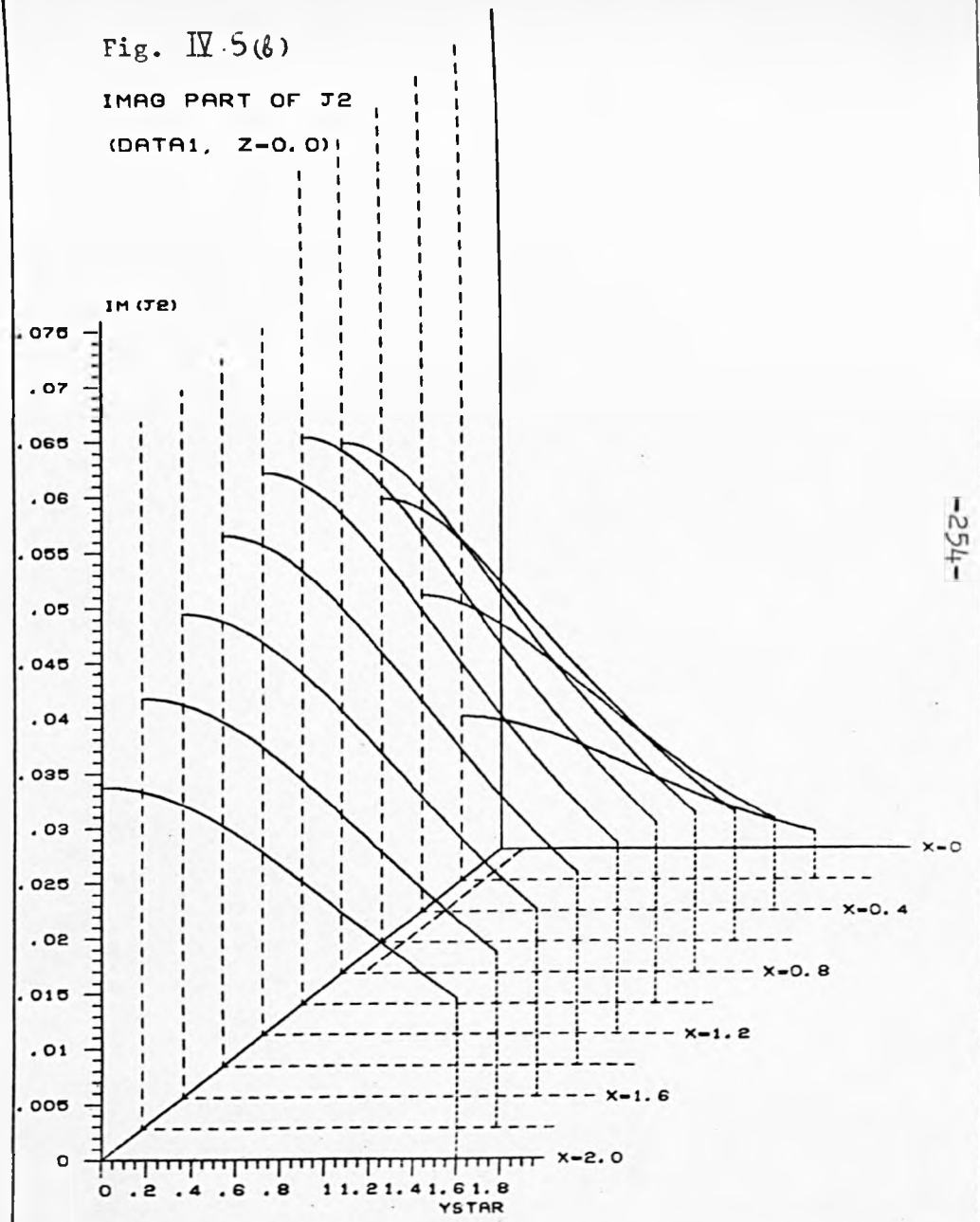
IMAG PART OF J2
(DATA1, Z=0.0)
IM (J2)
.075
.07
.065
.06
.055
.05
.045
.04
.035
.03
.025
.02
.015
.01
.005
0
0 .2 .4 .6 .8 1 1.2 1.4 1.6 1.8
YSTAR
X=0
X=0.4
X=0.8
X=1.2
X=1.6
X=2.0

Fig. Ⅳ.6.(b)

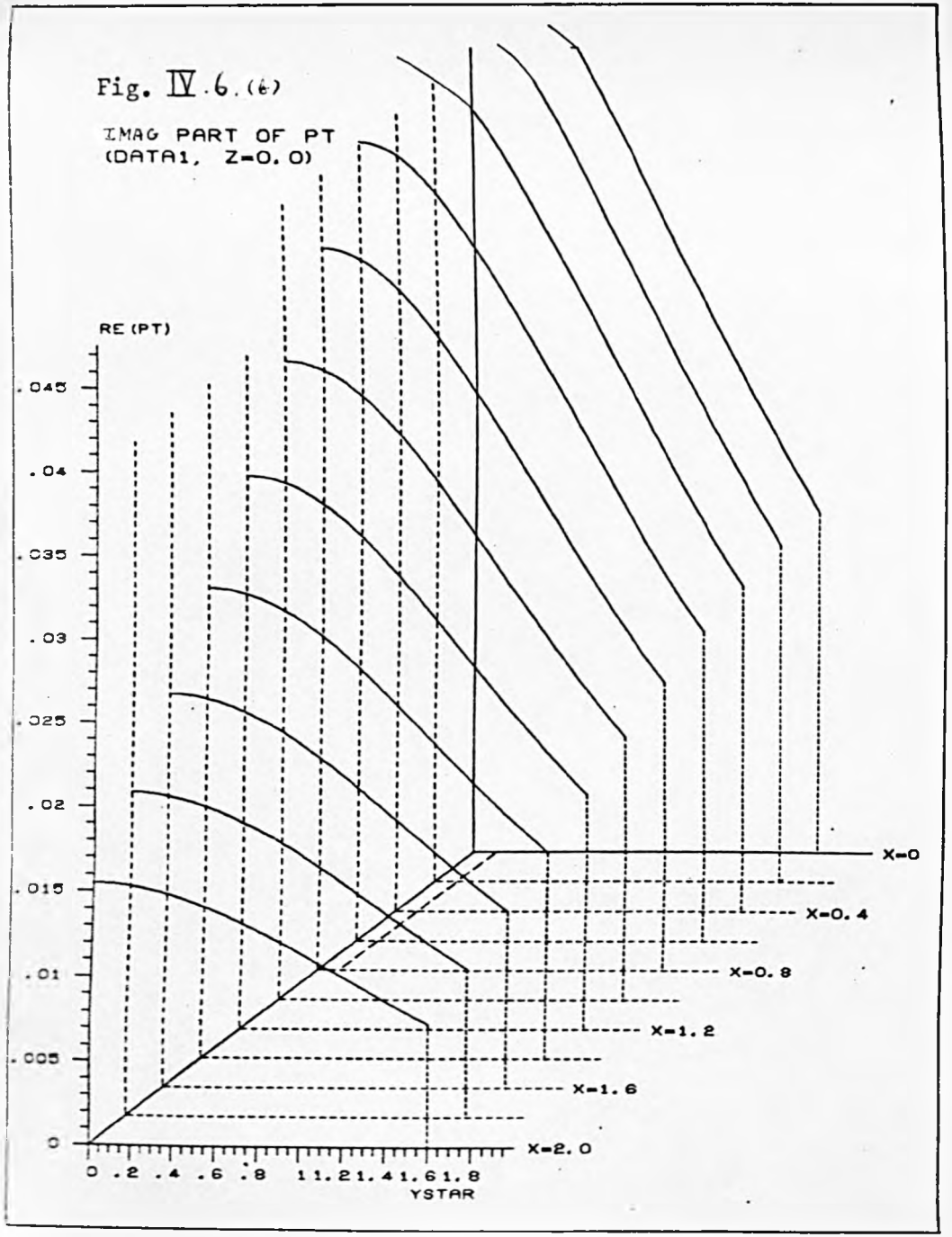

Fig. Ⅳ.6(a).

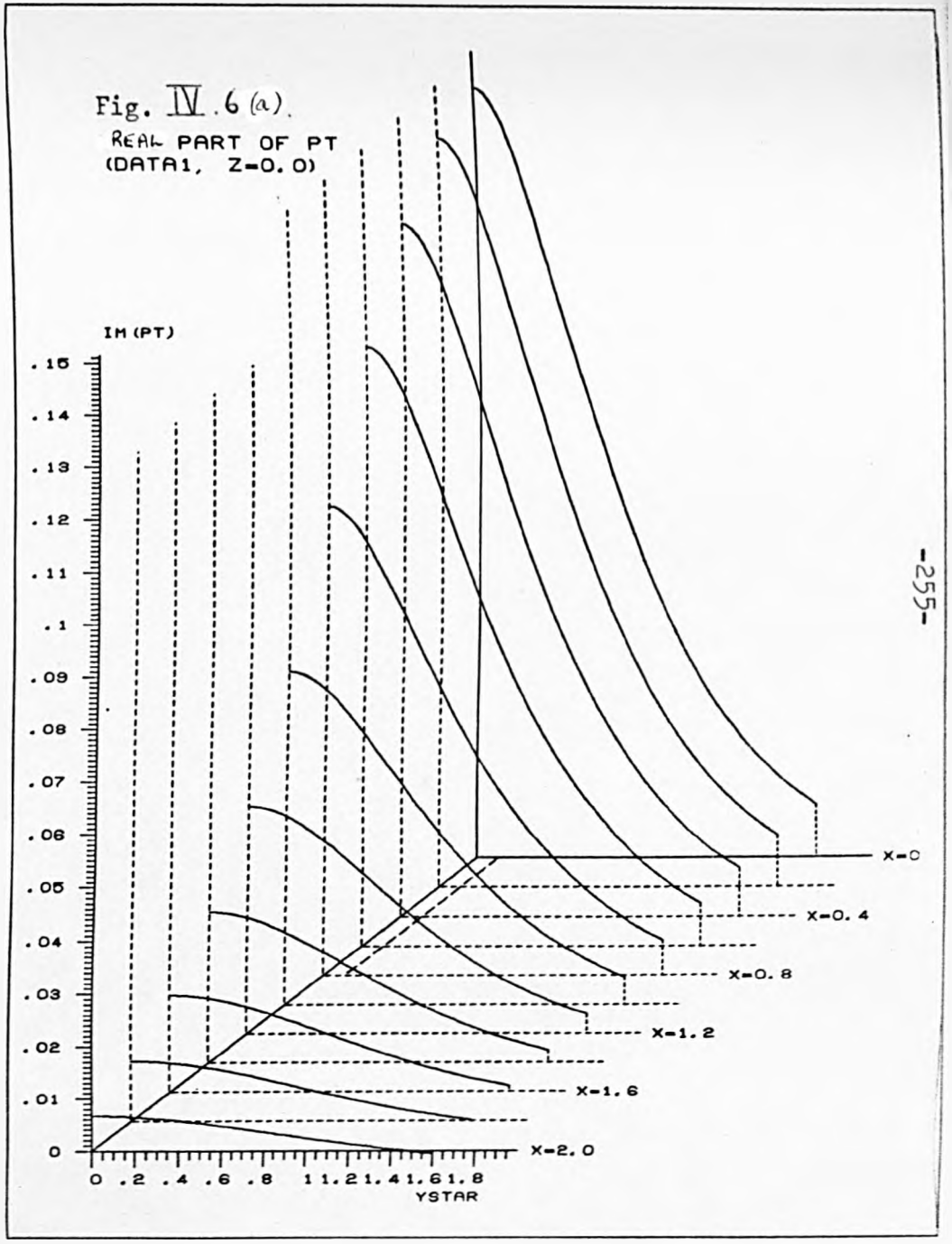

fields are momentarily zero) and $-\underline{B}_I$ corresponds to the magnetic induction produced by the induced currents (since at $t = \pi/2\omega$ the source field is momentarily zero). The magnetic induction at any time t is given by $\mathcal{R}\{\underline{B}(r,t)\} = \underline{B}_R \cos\omega t - \underline{B}_I \sin\omega t$. Similarly we may describe $\mathcal{J}(r,t) = (J_R + iJ_I)e^{i\omega t}$ and $\phi(r,t) = (\phi_R + i\phi_I)e^{i\omega t}$.

We note the following: (i) the diffusive action of the conductor is indicated by the less rapid decay with distance of the secondary field ((b) in figures IV.1 to IV.6) compared with the source field ((a) in figures IV.1 to IV.6), (ii)the magnitudes of the secondary fields are, in general, one tenth those of the source fields, (iii) the orientation of the magnetic field lines for a section along the y -axis when the tooth resembles a dipole source agrees with our magnetic field line analysis of a vertical magnetic dipole (figure 12.1) and (iv) the changes in direction of the real and imaginary parts of $\mathfrak{B}3$ (figures IV.3(a) and IV.3(b)) indicate the positions of the '0'-type neutral points between the times $t = 0$ and $t = \pi/2\omega$ (for a section along the x axis, the coil-wound tooth resembles two widely-spaced line currents, so the secondary currents are image sources).

REFERENCES

ABRAMOWITZ M. & STEGUN I.A. (1965) *Handbook of Mathematical Functions*, Dover.

ALFVÉN H. (1942) Arkiv.f.Mat. 29B, 2.

ALGER P.L. (1951) *The Nature of Polyphase Induction Machines*, Wiley/Chapman & Hall.

ARMSTRONG D.S. (1964) *Electromagnetic pumps for liquid metals*, Foundry Trade Journal, March 1964.

ASHOUR A.A. (1973) *Theoretical models for electromagnetic induction in the oceans*, Phys. Earth & Plan. Int. 7, 303-312.

BARLOW H.E.M. (1965) *Travelling-field theory of induction-type instruments and motors*, Proc. IEE, 112, 6, 1208-1214.

BARNA P.S. (1969) *Fluid Mechanics for Engineers*, Butterworths.

BATEMAN H. (1954) *Tables of Integral Transforms I*, McGraw-Hill.

BLAKE L.R. (1956) *Conduction and induction pumps for liquid metals*, Proc. IEE, 4, A, 49-63.

BLOCK F.R. (1973) *Electromagnetic runners and pumps*, E.C.S.C., Technical Research Report EUR 5082 d,e,f.

BOLDEA I. & NASAR S.A. (1975) *Quasi-1-dimensional theory of linear induction motors with half-filled primary endslots*, Proc. IEE, 122, 1, 61-66.

BOLTON H. (1969) *Transverse edge effect in sheet-rotor induction motors*, Proc. IEE, 116, 5, 725-731.

BREWITT-TAYLOR C.R. & WEAVER J.T. (1976) *On the finite difference solution of two-dimensional induction problems*, Geophys. J. R. astr. Soc, 47, 375-396.

CAGNIARD L. (1953) *Basic theory of the magneto-telluric method of geophysical prospecting*, Geophysics, 18, 605-635.

CARTER F.W. (1926) *The magnetic field of the dynamo-electric machine*, J. IEE, 64, 1115.

CERINI D.J. & ELLIOT D.G. (1968) *Performance characteristics of a single wavelength liquid-metal MHD induction generator with end-loss compensation*, AIAA Journal, 6, 3, 503-510.

CHAMPENEY D.C. (1973) *Fourier Transforms and Their Physical Applications*, London Academic Press.

CHEN T.S. & CHEN G.L. (1972) *Magnetohydrodynamic channel flow with an arbitrary inlet velocity profile*, Phys. Fluids, 15, 8, 1531-1534.

CHEN T.S. & EATON T.E. (1972) *Magnetohydrodynamic stability of the developing laminar flow in a parallel-plate channel*, Phys. Fluids, 15, 4, 592-596.

CLEMMOW P.C.& DOUGHERTY J.P.(1969) *Electrodynamics of Particles and Plasmas*, Addison-Wesley.

COCHET et al. (1972) *Possible applications of electro magnetic fields in the transport, treatment and control of liquid pig iron and steel*, Rev. Mét., 69, 1, 55-69, Translation B.I.S.I. 10341.

CONTE S.D. & DE BOOR C. (1965) *Elementary Numerical Analysis - An Algorithmic Approach*, McGraw-Hill.

COWLING T.G. (1957) *Magnetohydrodynamics*, Interscience.

CULLIN A.L. & BARTON T.H. (1958) *A simplified electromagnetic theory of the induction motor, using the concept of wave impedance*, Proc . IEE, 105C, 8, 331-336.

DISA (Dansk Industri Syndikat A/S) Technohouse, Redcliffe Way, Bristol BS1 6NU.

DUDZINSKY S.J. & WANG T.C. (1968) *MHD Induction Generator*, Proc. IEEE, 56, 9, 1420-1431.

DUNGEY J.W. (1958a) *Cosmic Electrodynamics*, C.U.P.

DUNGEY J.W. (1958b) *Electromagnetic Phenomena in Cosmical Physics*, C.U.P 135-140.

EADY J.G. (1972) *Electromagnetic transport and metering of molten metals*, Mining Technology, 54, 615, 28-31.

ELIASON C.R. & KALLING U. (1968) *The role of induction stirring in stainless steel production*, J. Metals, 20, 5, 56-61.

ELLIOT D.G.,CERINI D.J., HAYS L.G. & WEINBERG E. (1966) *Theoretical and experimental investigation of liquid metal MHD power generation*, Electricity From MHD, 2, Proceedings, Salzburg 1966, 995-1018.

ELLIOT D.G. (1969) *Effect of slots on MHD induction generator efficiency*, Energy Conversion, 10, 73-74.

ENGELN F. & PESCHKA W. (1966) *End effects on the linear induction MHD generator calculated by two-sided Laplace Transform*, Electricity From MHD, 2, Proceedings, Salzburg 1966, 937-951.

ERASLAN A.H. (1967) *Oscillatory characteristics of unsteady MHD channel flows under heaviside-type applied magnetic fields*, J. Appl. Mech., Trans. A.S.M.E., December, 854-859.

FERRARO V.C.A. (1954) *Electromagnetic Theory*, Athalone Press.

FRASER-SMITH A.C. & BUBENIK D.M. (1974) *The effect of the conducting earth on the micropulsation-generating capability of a ground-based current loop*, J. Geophys. Res., 79, 7, 1038-1045.

FUKUSHIMA K., NASAR S.A., & SAUNDERS R.M. (1963) *Electromechanical energy conversion in salient-pole structures*, IEEE Trans on Power Apparatus and Systems, October, 760-766.

GENTLEMAN W.M. & SANDE G. (1966) *Fast Fourier Transforms - for fun and profit*, Proc. A.F.I.D.S., 29, 563-578.

GOLDHAMMER A.B., MARKEY P.J. & MATHUR S.K. (1968) *Linear motors and their applications*, Electrical Times, 13 June 1968.

GOODSTEIN R.L. (1965) *Complex Functions*, McGraw-Hill.

GRADSHTEYN I.S. & RYZHIK I.M. (1965) *Tables of Integrals, Series and Products*, Academic Press.

GORDON A.N. (1951a) *The field induced by an oscillating magnetic dipole outside a semi-infinite conductor*, Q. J. Mech. Appl. Math., 4, 106-115.

GORDON A.N. (1951b) *Electromagnetic induction in a uniform semi-infinite conductor*, Q. J. Mech. Appl. Math., 4, 116-128.

HARRIS L.P. (1960) *Hydromagnetic Channel Flows*, M.I.T. Press and Wiley.

HARRIS M.R. (1967) *Analysis of power factor in linear induction generators*, Proc. IEE, 114, 8, 1179.

HAWORTH D.J. (1976) Internal Report FW/76/24/CH Pilkingtons Ltd.

HEWSON-BROWNE R.C. & Kendall P.C. (1973) *Induction in the oceans explained and analysed in terms of magnetic merging*, Geophys. J. R. astr. Soc., 34, 381-391.

HOEY D.W., HUNTER T.C. & ROBERTSON K.S. (1974) *The use of the Eldomet for anode casting*, Aust. I.M.M., North-East Queensland Branch, Regional Meeting, August 1974.

HUNT J.C.R. & SHERCLIFF J.A. (1971) *Magnetohydrodynamics at high Hartmann number*, Ann. Rev. Fluid Mech., 3, Annual Review Inc.

HUTSON V.C.L., KENDALL P.C. & MALIN S.R.C. (1972) *Computation of the solution of geomagnetic induction problems: a general method, with applications*, Geophys. J. R. astr. Soc., 28, 489-498.

HWANG C.L. & FAN L.T. (1963) *A finite difference analysis of laminar magneto-hydrodynamic flow in the entrance region of a flat rectangular duct*, Appl. Sci. Res, 10, B, 329-343.

HWANG C.L., LI K.C.,& FAN L.T. (1966) *Magnetohydrodynamic channel entrance flow with parabolic velocity at the entry*, Phys. Fluids, 9, 6, 1134-1140.

JACKSON W.D. & PIERSON E.S. (1966) *Material limitations in the MHD induction generator*, Electricity from MHD, 2, Proceedings, Salzburg 1966, 983-993.

JAMIESON R.A. (1968) *Eddy-current effects in solid, unslotted iron rotors*, Proc. IEE, 115, 6, 813-820.

JESTER J.L. & FANUCCI J.B. (1969) *Characteristics of a finite-length MHD travelling wave cylindrical accelerator or generator*, A.I.A.A. Journal, 7, 5, 864-870.

KARO D. (1963) *Electromagnetic pumps*, The Consulting Engineer, 2, 165-169.

KESAVAMURTHY N. & BEDFORD R.E. (1958) *The circuit theory and calculations of polyphase induction machines*, Proc. IEE, 115, 5, 499-508.

KIM K.I. (1970) *Incompressible fluid flow in a finite width channel with a travelling magnetic field,* Mag. Gid.* 6, 1, 140-143.

KING L.V. (1914) *On the convection of heat from small cylinders in a stream of fluid,* Phil. Trans. R. Soc., 214, 14, 373-432.

KIRILLOV I.R. & LAVRENT'EV I.V. (1972) *Integral characteristics of an induction type magnetohydrodynamic machine with a flat channel,* Mag. Gid., 4, 78-86.

KLIMAN G.B. & ELLIOT D.G. (1974) *Linear induction motor experiments in comparison with mesh/matrix analysis,* IEEE Trans., PAS-93, 1624-1633.

KNOPP K. (1947) *Theory of Functions,* II, Dover.

KOVASZNAY L.S.G. (1965) *The hot-wire anemometer,* A.C.T.A. Techn. Hung., 50 131-151.

KOZYRENKO V.E. (1971a) *On a certain effective method of investigating electromagnetic processes in magnetohydrodynamic channels I,* Mag. Gid., 2, 39-44.

KOZYRENKO V.E. (1971b) *On a certain effective method for investigating electromagnetic processes in MHD channels II,* Mag.Gid. 2, 43-48.

LAITHWAITE E.R. (1957) *Linear induction motors,* Proc. IEE, 114, 12, 461-470.

LAITHWAITE E.R., TIPPING D. & HESMONDHALGH D.E. (1960) *The application of linear induction motors to conveyors,* Proc. IEE, 117, 6, 284-294.

LAITHWAITE E.R. (1965a) *The goodness of a machine,* Proc. IEE, 112, 3, 538-541.

LAITHWAITE E.R. (1965b) *Differences between series and parallel connection in machines with asymmetric magnetic circuits,* Proc. IEE, 112, 11, 2074-2082.

LAITHWAITE E.R. (1966) *Induction Machines For Special Purposes,* Newnes.

LAITHWAITE E.R. (1975) *Linear electrical machines - a personal view,* Proc. IEEE, 63, 2, 250-290.

LEE S.W. & MENENDEZ R.C. (1974) *Force on current coils moving over a conducting sheet with application to magnetic levitation,* Proc. IEEE, 62, 5, 567-577.

LIELAUSIS O. (1975) *Liquid metal magnetohydrodynamics,* Atomic Energy Res. 13, 527-581.

LIELPETER YA. YA. & TUTIN I.A. (1959) *Method of Design of Induction Pumps for liquid metal,* Atomic Energy Commission Report, TR3602, 91-102.

LIYELPETER YA. YA. (1966) *Motion of conducting bodies in a magnetic field,* Zinatne Press (N.A.S.A. Technical Translation TTF 460, 1968).

* Mag. Gid. = Magnitnaya Gidrodinamika (English translation appears as the publication Magnetohydrodynamics.)

LING S.C. & HUBBARD P.G. (1956) *The hot-film anemometer: a new device for fluid mechanics research*, J. Aero. Sci., September 1956.

LING S.C. (1960) *Heat transfer characteristics of hot-film sensing element used in flow measurement*, Basic Eng. A.S.M.E., D82, 629-634.

LIPKIS R.E. & WANG T.C. (1971) *Single-sided linear induction motor (SLIM): a study of thrust and lateral forces*, Am. Dept. Transport Report, FRA-RT-72-25, June.

LOCK R.C. (1955) *The stability of the flow of an electrically conducting fluid between parallel planes under a transverse magnetic field*, Proc. R. Soc., 105-126.

LOWAN A.(Ed.) (1947) *Table of The Bessel Functions* $J_0(z)$ *and* $J_1(z)$ *for Complex Arguments; (1950) Table of the Bessel Functions* $Y_0(z)$ *and* $Y_1(z)$ *for Complex Arguments*, Columbia Univ. Press.

LUKE Y. (1962) *Integrals Of Bessel Functions*, McGraw-Hill.

MALCOLM D.G. (1968) *Thermo-Anemometry in Magnetohydrodynamics*, PhD. Thesis, University of Warwick, Coventry, England.

MALCOLM D.G. (1970) *Magnetohydrodynamic effects on hot-film measurements in mercury*, DISA Information, 9, 27-29.

MENENDEZ R.C. & LEE S.W. (1975) *Side force in coil sheet magnetic levitation systems*, Proc, IEEE, 63, 5, 768-776.

MERKULOV V.I. , TKACHENKO V.F. & YATSENKO V.I. (1973) *Periodic flows of conducting liquid in a travelling magnetic field*, Mag. Gid. 1, 43-48.

METZ L.S. & GANDHI O.P. (1974) *Numerical calculations of the potential due to an arbitrary charge density using the fast fourier transform*, Proc. IEEE, (Lett.), 1031-1032.

MOSON J.E. (1972) *Finite difference equations at magnetic boundaries*, Proc. IEEE (Lett.), 236.

MOSZYNSKI J.R. (1966) *End losses in MHD channels of variable cross-section and their reduction*, Electricity From MHD, Proceedings, Salzburg 1966, 1031-1038.

MULLER J.D. (1966) *A review of present electromagnetic pumps*, South African Mech. Eng., 16, 5, 105-110.

NASAR S.A. (1964) *Power: Electromagnetic theory of electrical machines*, Proc. IEE, 111, 6, 1123-1131.

NASAR S.A. (1969) *Electromagnetic fields and forces in a linear induction motor, taking into account edge effects*, Proc. IEE, 116, 4, 605-609.

NASAR S.A. & DEL CID L. (1973a) *Certain approaches to the analysis of single sided linear induction motors*, Proc. IEE, 120, 4, 477-483.

NASAR S.A. & DEL CID L. (1973b) *Propulsion and levitation forces in a single sided linear induction motor for high speed ground transportation*, Proc. IEEE, 61, 5, 638-644.

NIX G.F. & LAITHWAITE E.R. (1966) *Linear induction motors for low speed and standstill application*, Proc. IEE, 113, 6, 1044-1056.

OBERHETTINGER F. (1970) *Tables of Bessel Transforms*, Springer-Verlag.

OBERRETL K. (1973) *Dreidimensionale berechnung des linear motors mit berücksichtigung der endefekte und der wicklungsverteilung*, Archiv Fur Elertrotechnik, 55, 181-190.

OKHREMENKO N.M. (1960)*Electro-magnetic phenomena in flat induction pumps for molten metals*, Elektrichestvo, 3, 48-55.

OKHREMENKO N.M. (1965a) *An investigation of the spatial distribution of the magnetic fields and electromagnetic effects in induction pumps*, Mag. Gid., 1, 1, 97-109.

OKHREMENKO N.M. (1965b) *Transverse fringe effect in flat linear induction pumps*, Mag. Gid. 1, 3, 87-95.

OOI B.T. & WHITE D.C. (1970) *Traction and normal forces in the linear induction motor*. IEE Trans. on Power Apparatus & Systems, PAS-89, 4, 638-645.

PANHOLZER R. (1963) *Electromagnetic pumps*, Elect. Eng., 82, 2, 128-135.

PARK D. (1974) *Magnetic field at the earth's surface produced by a horizontal line current*, J. Geophys. Res., 79, 31, 4802-4804.

PETROVICH R.A. & ULMANIS L. YA. (1969) *Laminar flow of an electrically conductive fluid between parallel planes in a travelling magnetic field*, Mag. Gid., 5, 3, 57-62.

PIERSON E.S. (1970) *MHD induction machine with internal compensation for end loss*, Energy Conversion, 11, 47-53.

PIGGOT L.S. (1962) *A theory of the operation of cylindrical induction motors with squirrel-cage rotors*, Proc. IEE, 109, C, 270-282.

PILKINGTON L.A.B. (1969) *The float glass process*, Proc. Roy. Soc. Lond. A., 314, 1-25.

PILKINGTON L.A.B. (1977) *Floating to success on glass*, T.H.E.S. 21.1.77.

PRICE A.T. (1949) *The induction of electric currents in non-uniform thin sheets and shells*, Quart. J. Mech. And Math., II, 3, 283-310.

PRICE A.T. (1950) *Electromagnetic induction in a semi-infinite conductor with a plane boundary*, Q.J. Mech. Appl. Math., 3, 385-410.

REZIN M.G. (1965) *Advances in electromagnetic stirring of liquid metals*, Mag. Gid., 1, 2, 130-138.

RIGA (1972) Seventh Conference on Magnetohydrodynamics, (Latvian Inst. Phys.)

RIKITAKE T. (1966) *Electromagnetism and the Earth's Interior*, Elsevier Press.

ROBERTS P.H. (1967) *An Introduction To Magnetohydrodynamics*, Longmans.

ROBINSON T., BRAUN J.,& LINDER S. (1972) *Applications of magnetohydrodynamics in the metal industry*, Aktiebolaget Atomenergi AE 457.

RODEN R.B. (1964) *The effect of an ocean on magnetic diurnal variations*, Geophys. J. R. astr. Soc., 8, 375-388.

RYABININ A.G. & KHOZHAINOV A.I. (1969) *Non-steady-state magnetohydrodynamic flow in channels*, Mag. Gid. 5, 3, 3-7.

SABJEN M. (1965) *Hot wire anemometer in liquid mercury*, Rev. Sci. Inst. 36, 7, 945-949.

SALZBURG (1966) Symposium on Electricity From MHD.

SAY M.G. (1963) *The Performance and Design of A-C Machines*, Pitman.

SCHEIBER D. (1973) *Principles of operation of linear induction devices*, Proc. IEEE, 61, 5, 647-656.

SCHWARTZ M., GREEN S. & RUTLEDGE W.A. (1964) *Vector Analysis*, Harper & Row.

SHERCLIFF J.A. (1956) *Edge effects in electromagnetic flow meters*, J. Nuclear Energy, 3, 305-311.

SHERCLIFF J.A. (1965) *A Textbook of Magnetohydrodynamics*, Pergamon Press.

SHERCLIFF J.A. (1962) *The Theory of Electromagnetic Flow Measurement*, C.U.P.

SINGHAL K., VLACH J. & VLACH M. (1975) *Numerical inversion of multidimensional Laplace Transform*, Proc. IEEE (Lett.), 1627-1628.

SINGLETON R.C. (1969) *An algorithm for computing the mixed radix fast Fourier Transform*, IEEE Trans. Audio Electracoustics, AU17, 2, 93-100.

SLOAN D.M. (1971) *An unsteady MHD duct flow*, Appl. Sci. Res., 25, 126-136.

SLOAN D.M. (1973) *Two time scale solution for an unsteady MHD duct flow*, Appl. Sci. Res., 28, 361-380.

SMITHELLS C.J. (1955) *Metals Reference Book, Vol. II*, Butterworths.

SNEYD A. (1972) *Fluid flow generated by switching a magnetic field on or off*, J. Fluid. Mech., 209-217.

SNYDER W.T. (1965) *Magnetohydrodynamic flow in the entrance region of a parallel-plate channel*, A.I.A.A. Journal, 3, 10, 1833-1838.

SPARROW E.M., LIN S.H. & LUNDERGREN T.S. (1964) *Flow development in the hydrodynamic entrance region of tubes and ducts*, Phys. Fluids, 7, 3, 338-347.

von STARK A. (1971) *Electromagnetic pumps and conveyors for molten metals*, Foundry Trade Journal, April 1971.

STOLL R.L. & HAMMOND P. (1965) *Calculation of the magnetic field of rotating machines, Part 4,- Approximate determination of the field and the losses associated with eddy currents in conducting surfaces*, Proc. IEE, 112, 11, 2083-2094.

STUART J.T. (1954) *On the stability of viscous flow between parallel planes in the presence of co-planar magnetic field*, Proc. Roy. Soc. 221, A, 189-200.

STUDSVIK A.B. Atomenergi, Fack, S-61101 Nyköping 1, Sweden.

SUDAN R.N. (1963) *Interaction of a conducting fluid stream with a travelling wave of magnetic field of finite extension*, J. Appl. Phys. 34, 3, 641-650.

SUNDBERG Y. (1969) *Magnetic travelling fields for metallurgical processes*, IEEE Spectrum, 6, 5, 79-88.

SUTTON G.W. & CARLSON A.W. (1961) *End effects in inviscid flow in a magnetohydrodynamic channel*, J. Fluid Mech., 11, 1, 121-132.

SUTTON G.W. & SHERMAN A. (1965) *Engineering Magnetohydrodynamics*, McGraw-Hill.

TITCHMARSH E.C. (1937) *Introduction To The Theory of Fourier Integrals*, O.U.P.

TKACHENKO V.F. (1970) *Stationary flow of a conducting fluid in a travelling field*, Mag. Gid., 4, 65-70.

TKACHENKO V.F. (1972) *Influence of the paramaters of a travelling magnetic field on the flow of a viscous conducting fluid*, Mag. Gid., 3, 57-60.

TKACHENKO V.F. (1973) *Investigation of MHD phenomena in the flow of a viscous conducting fluid in a travelling magnetic field*, Mag. Gid., 2, 19-24.

TODD L. (1966) *Hartmann flow between parallel planes*, Phys. Fluids, 9, 8, 1602-1603.

TROPP É.A. (1968) *Laminar flow of a viscous conducting fluid between parallel walls in a travelling magnetic field*, Mag. Gid. 4, 4, 75-82.

TROPP É.A. (1969) *Flow of a conducting fluid in a travelling magnetic field with matched and opposed inductors*, Mag. Gid., 5, 3, 47-51.

TROPP É.A. (1972) *Longitudinal edge effect during flow of a conducting fluid in a travelling magnetic field*, Mag. Gid.,3, 111-118.

VALDAMIS YA. YA. (1966) *Longitüdinal edge effect in linear induction MHD machines*, (in LIYELPETER, 1966).

VAN DYKE M. (1964) *Perturbation Methods in Fluid Mechanics*, Academic Press.

VASIL'EV S.V., OKHREMENKO N.M. & SMIRNOVA L.G. (1965) *Experimental study of the magnetic fields in induction pumps*, Mag. Gid. 1, 2, 111-122.

VESKE T.A. (1965) *Solution of the electromagnetic field equations for a plane linear induction machine with secondary boundary effects*, Mag. Gid., 1, 1, 87-96.

VEZE A.K. & KRUMIN YU.K. (1965) *Electromagnetic force acting on an infinitely wide conducting sheet in the travelling magnetic field of plane inductors*, Mag. Gid., 1, 4, 99-107.

VEZE A.K. & MIKEL'SON A.E. (1970) *Electromagnetic effects in a conducting layer located in the field of the inductors with opposed travelling magnetic fields*, Mag. Gid., 4, 115-118.

VILNITIS A. YA. (1966) *Transverse edge effect in plane induction magneto-hydrodynamic machines*, (in LIYELPETER, 1966).

VOLDEK A.I. (1970) *Induction MHD Machines With Liquid Metal As Working Medium*, Energia, Leningrad Division.

WAIT J.R. (1951) *The magnetic dipole over the horizontally stratified earth*, Can. J. Phys., 29, 577-592.

WANG T.C. (1971) *Linear induction motor for high-speed ground transportation*, IEEE Trans. on Ind. & Gen. App.

WANG C.Y. (1974) *Stability of a current-carrying fluid with a free surface in a transverse magnetic field*, Phys. Fluids, 17, 5, 1177-1182.

WANG T.C. & DUDZINSKY S.J.(1967a) *Theoretical and experimental study of a liquid metal MHD induction generator*, A.I.A.A. Journal, 5, 1, 107-112.

WANG T.C. & DUDZINSKY S.J. (1967b) *Comparison of MHD induction generator analyses*, A.I.A.A. Journal, 5, 11, 2059-2060.

WASSERMAN R. & GRANT H. (1973) *Heated sensors for flow measurement*, Instruments and control systems, 40, 5, 59-61.

WATSON G.N. (1966) *A Treatise On The Theory of Bessel Functions*, C.U.P.

WATT D.A. (1955) *A study in the design of travelling field electromagnetic pumps for liquid metals*, A.E.R.E. ED/R 1696.

WATT D.A. (1957) *Design of travelling field induction pumps for liquid metals*, A.E.R.E. R/M 14K.

WEAVER J.T. (1970a) *The general theory of electromagnetic induction in a conducting half-space*, Geophys. J. R. astr. Soc., 22, 83-100.

WEAVER J.T. & THOMSON D.J. (1970b) *The field induced in a two-layer conductor by a magnetic dipole*, Can. J. Phys., 48, 71-79.

WEAVER J.T. (1971) *Image theory for an arbitrary quaisi-static field in the presence of a conducting half-space*, Radio-Science, 6, 6, 647-653.

WEAVER J.T. (1973) *Induction in a layered plane earth by uniform and non-uniform source fields*, Phys. Earth & Plan. Int., 7, 266-281.

WEST J.C. & HESMONDALGH D.E. (1961) *The analysis of thick-cylinder induction machines*, Proc. IEE, 477U, 172-181.

WILLIAMS F.C., LAITHWAITE E.R. & PIGGOTT L.S. (1956) *Brushless variable-speed induction motors*, Proc. IEE, 113, 6, 102-118.

WOMACK G.J. (1969) *MHD Power Generation: Engineering Aspects*, Chapman & Hall.

WOOLER P.T. (1961) *Instability of flow between parallel planes with a coplanar magnetic field*, Phys. Fluids, 4, 1, 24-27.

YAMAMURA S. (1972) *Theory of Linear Induction Motors*, Univ. Tokio Press.

YUFEREV V.S. (1967) *The laminar boundary layer of a conducting fluid when there is a stepwise change of the magnetic field*, Mag. Gid., 3, 2, 61-64.